A Celebration of a Great Partnership:
CODAR and RU COOL
1998-2025
Volume 2

The SeaSonde Papers

A Celebration of a Great Partnership: CODAR & RUCOOL 1998-2025

For four decades, the Rutgers University Center for Ocean Observing Leadership (RUCOOL) and CODAR Ocean Sensors have partnered in pioneering efforts of ocean observation, applying CODAR's SeaSonde high-frequency (HF) radar technology to address critical scientific and societal challenges. This book is a curated compilation of the scientific publications authored by our team, all of which share a common foundation: the use of SeaSonde systems to observe the coastal ocean.

Our partnership with CODAR Ocean Sensors began in 1998, driven by the need for continuous, synoptic surface current data along the New Jersey coast. At the time, there were few observational tools that could deliver this kind of coverage in real time. The SeaSonde filled that gap—and quickly became central to our research and education missions. Over the years, we have deployed these systems across from the heavily populated Mid-Atlantic coast to the tropical Caribbean and Gulf of Mexico, to the remote polar Arctic and Antarctic regions.

This body of work would not have been possible without our long-standing collaboration with Dr. Don Barrick, founder of CODAR Ocean Sensors and a pioneer in HF radar technology. Don's willingness to share his ideas and engage with ours, support field deployments, and co-develop new techniques—ranging from bistatic radar configurations to vessel detection algorithms—transformed our science and advanced the state of the art.

Each paper in this compilation represents not only a contribution to oceanography and coastal science, but also a chapter in the evolving story of radar-based ocean observing. From operational ocean forecasting and model validation to environmental response, fisheries management, and maritime security, SeaSonde technology has enabled us to turn observations into action and data into impact.

A cornerstone of this partnership has been our shared commitment to education and workforce development. At Rutgers, SeaSonde technology has not only fueled research but also served as a powerful teaching tool. Through hands-on training in the classroom, field deployments, and thesis work, our students have gained critical experience in ocean observing technologies. Together with CODAR, we have expanded the HF Radar community by hosting workshops, developing open-source tools, and fostering regional and global networks. What began as two radar stations in southern New Jersey has matured into a globally connected observing system—one in which the next generation of scientists and engineers will play a central role.

This book is intended as both a scientific record and a resource for the growing community of HF Radar users. It reflects the dedication of our students, staff, and collaborators, the vision of our funding partners, and the enduring innovation at CODAR. We hope it serves to inform, inspire, and guide those who continue to explore our dynamic coastal ocean.

– The Rutgers University HF Radar Team

A Multi-system HF Radar Array for the New Jersey Shelf Observing System (NJSOS)

Josh T. Kohut, Graduate student; *Institute of Marine and Coastal Sciences, Rutgers University, USA*. (http://marine.rutgers.edu/cool)
Scott M. Glenn, Professor; *Institute of Marine and Coastal Sciences, Rutgers University, USA*. (http://marine.rutgers.edu/cool)
Don E. Barrick, President; *Codar Ocean Sensors, Ltd., USA*. (http://www.codaros.com/)

1. Introduction

High Frequency (HF) radar technology for the remote sensing of surface current fields has experienced rapid growth and acceptance within the scientific community in the last few years (Glenn et al., 2000b). Direct measurements of receive antenna beam patterns and comparisons with current meters have demonstrated that the compact CODAR antenna designs do provide accurate direction estimates for radial current vectors, even in cluttered environments (Kohut et al., 2001; Paduan et al., 2001, Kohut and Glenn, 2002). New long-range CODAR systems demonstrated at Oregon State and Rutgers typically achieve daytime ranges of over 200 km. However, at the lower frequencies (4.4-5.1 MHz) used by the long-range systems, spatial coverage is found to be highly sensitive to radio interference and noise, especially at night. A third system utilizing bistatic technology separates the transmitter and receiver providing a larger footprint for total vector calculation that extends right to the coast. These three systems deployed in the New York Bight will establish the world's first nested multi-static HF radar array for surface current measurement. The multi-static array, combined with new ocean color remote sensing systems, vicarious calibration

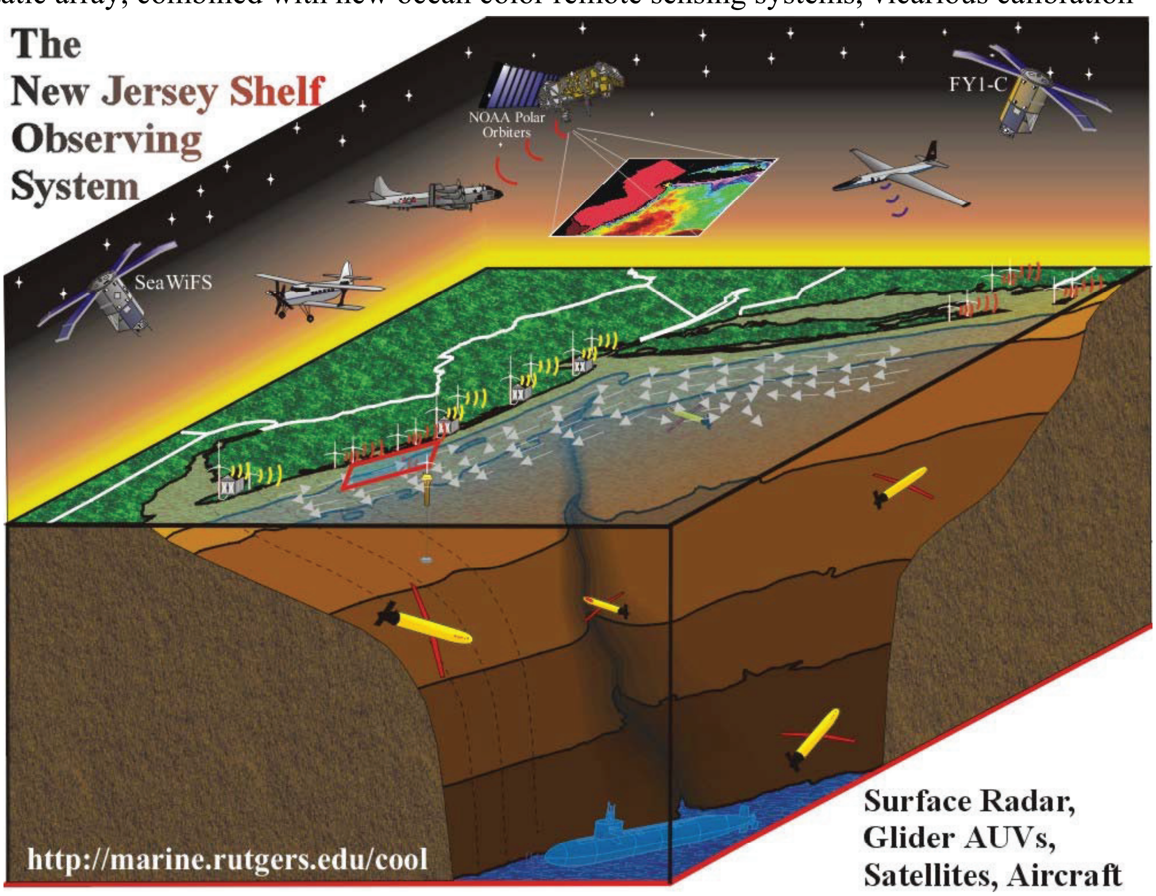

Figure 1. New Jersey Shelf Observing System (NJSOS)

capabilities, and a fleet of four long-duration autonomous underwater gliders, will establish the New Jersey Shelf Observing System (NJSOS) as a premier site for the development of new autonomous observation technologies (Figure 1). NJSOS serves as an efficient model for the developing NorthEast Observing System (NEOS) efforts to establish a complete CODAR network running from the Gulf of Maine to Cape Hatteras. This unprecedented high-quality dataset will be available for scientific studies, real time operational users, and will challenge modelers with spatially extensive assimilation/validation datasets for years to come. This paper will describe the HF radar component of this observatory focusing on the standard, long-range and bistatic CODAR SeaSonde systems.

2. Standard SeaSonde

Since 1998, Rutgers has operated a pair of standard SeaSonde (40 km) CODAR sites off the southern coast of New Jersey as part of the Longterm Ecosystem Observatory (LEO) (Figure 2). LEO is a coastal observatory centered around two underwater nodes connected to shore through a fiber optic cable (Grassle et al., 1998; Glenn et al., 2000a; Schofield et al., 2001). The CODAR system compliments many other remote and *in situ* measurements within a 30 x 30 km grid. Maps of the raw, tidal, detided, and filtered current fields, and their divergence and vorticity, are routinely generated and displayed on the Web (http://marine.rutgers.edu/cool/codar.html) in real-time. Recent validation results using the LEO ADCPs indicate that distortions in the receive antenna's beam pattern are not due to hardware configurations, but are primarily due to the local environment, which, depending on the circumstances, may not be adjustable (Kohut and Glenn, 2002). The ADCP comparisons indicate that using the measured receive antenna beam patterns optimizes system performance by improving the placement of the CODAR-derived radial current velocities in the proper directional bins. Figure 3 illustrates this point by comparing the RMS difference between the ADCP measured velocities and those derived

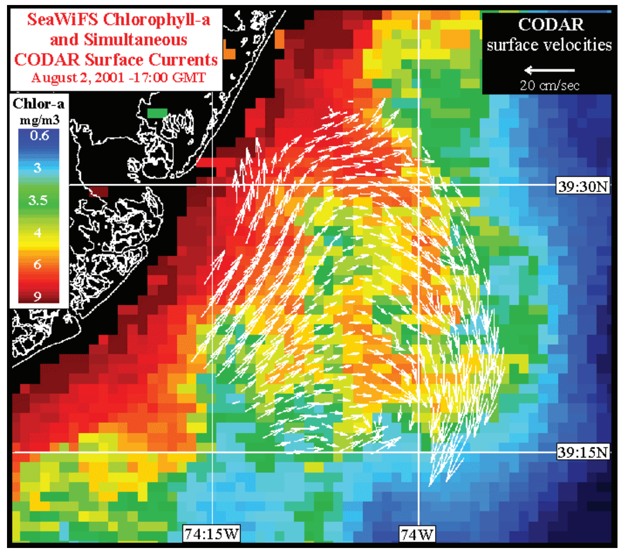

Figure 2. Standard CODAR surface currents overlaid on a SeaWiFS satellite image of Chlorophyll-a concentrations.

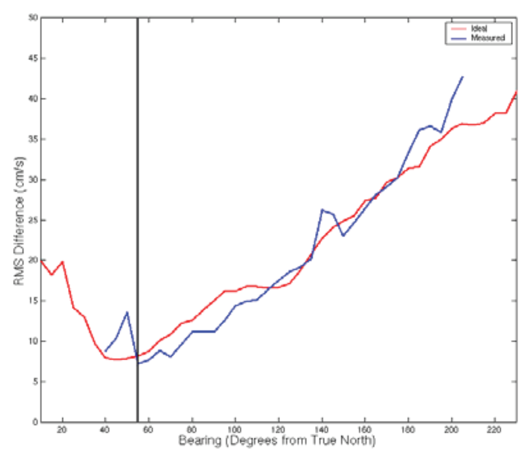

Figure 3. RMS difference between the radial component of the velocity measured by an ADCP and derived from CODAR using idealized (red) and measured (blue) receive antenna beam patterns for the Brigantine Beach CODAR system. The actual direction to the ADCP is indicated by the vertical black line

from CODAR using both idealized (cosine/sine dependent) and measured beam patterns. The idealized beam pattern produces a broad minimum with the smallest RMS offset 10 degrees from the actual direction to the ADCP (solid black line). The measured beam pattern produces a narrow minimum in the RMS located exactly in the direction of the ADCP, even in the cluttered environment of a developed New Jersey beach. The optimized CODAR current and divergence fields overlaid on satellite imagery (Figure 2) were used each summer during the annual Coastal Predictive Skill Experiments at LEO to improve biological adaptive sampling of phytoplankton distributions (Kohut et al., 1999; Schofield et al., 2001).

3. Long-range SeaSonde

In 2000, the first of five long-range SeaSonde (200 km) CODAR sites for the New Jersey Shelf Observing System (NJSOS) was deployed. Typical daytime radial coverage for the first east coast long-range CODAR site located in Loveladies, New Jersey extends as far as 200 km offshore (Figure 4). The initial deployment of the Loveladies long-range CODAR revealed an expected but surprisingly severe reduction in the nighttime coverage due to radio interference. Unlike the higher frequency (approximately 12, 24, or 48 MHz) HF radar systems that can operate at virtually any frequency without noticeable increases in the night-time radio noise, long-range CODARs should ideally operate at the quietest frequency available in the region.

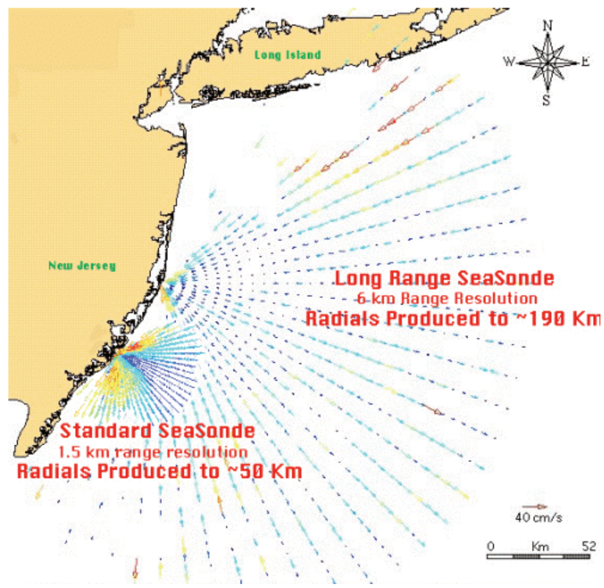

Figure 4. Comparison of radial current vectors from a long-range CODAR site located in Loveladies, NJ and a standard site in Brigantine, NJ. Radial bins are 6 km wide for the long-range system and 1.5 km wide for the standard system.

In 2001, two additional long-range sites in Wildwood and Sandy Hook New Jersey were deployed to form a long-range CODAR network. The initial approach was to establish these two sites at the extreme northern and southern extent of the New Jersey coast first, then fill in the remaining sites where additional coverage was needed. Coverage out to the shelf break is common, and extends well south of Delaware Bay (Figure 5). Vector coverage nearshore is lacking due to the standard Geometric Dilution Of Precision (GDOP) constraints on any shore-based monostatic HF Radar system deployed along a straight coast.

To improve nearshore coverage in the vicinity of LEO during the July 2001 Coastal Predictive Skill Experiment, a temporary long-range site was deployed at the Tuckerton field station. Despite the presence of barrier islands to seaward, the salt marsh on which the transmit antenna was deployed proved to be a very efficient ground plane, increasing the signal strength well beyond what was lost propagating over the barrier islands. Figure 6 illustrates the resulting 6 km resolution long-range vectors plotted on the same map as the 1.5

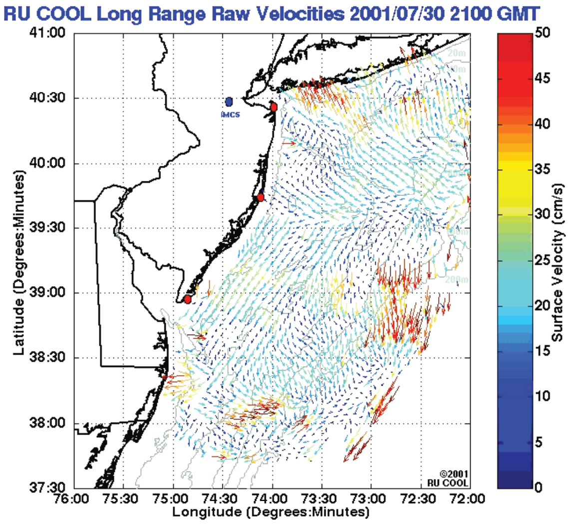

Figure 5. Total vector coverage for four long-range CODAR systems operated along the New Jersey coast.

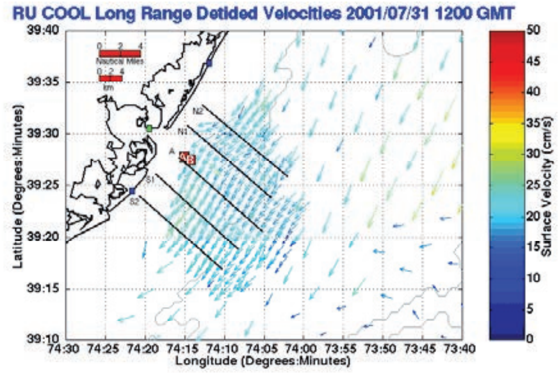

Figure 6. Enlargement showing total vector currents derived from the long range (6 km, 3 hour average) and the standard range (1.5 km, 1 hour average) CODARs in the vicinity of LEO.

km resolution vectors from the standard SeaSonde systems. The agreement is quite good in regions of overlap, and the far field vectors reveal interesting features flowing into the high-resolution field. Adding radial velocities from the single Tuckerton long-range site was critical to the accurate reproduction of total vectors nearshore. Similar maps to Figure 6 generated without the Tuckerton long-range site do not agree as well in the overlap region, an expected consequence of GDOP.

4. Bistatic SeaSonde

Existing monostatic systems use the phase of the transmitted signal to interpret the signal from the receiver, requiring the transmitter and receiver to be physically connected. Using the GPS satellite-timing signal, CODAR Ocean Sensors was able to synthesize the transmitted signal at the receiver, allowing the transmitter and receiver to be physically separated for the first time. Separating the transmitter from the receiver converts the monostatic backscatter system into a bistatic forward-scatter system (Figure 7). As the separation between transmitter and receiver grows, the constant time delay circles of the monostatic system are stretched into constant time delay ellipses with the receiver and transmitter at the foci. Just

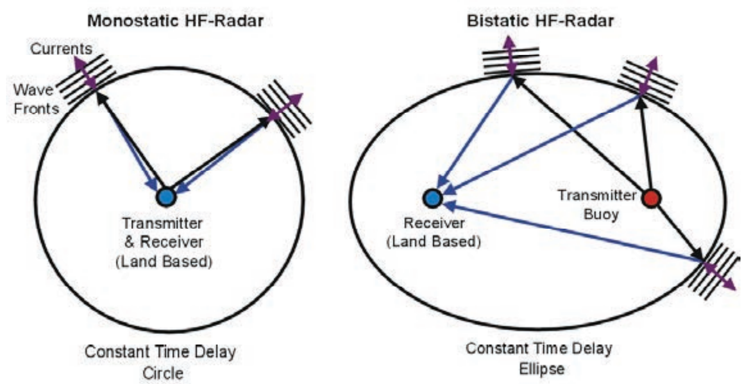

Figure 7. Illustration of the extension of monostatic backscatter to bistatic forward-scatter HF radars.

as the monostatic systems return estimates of the current component perpendicular to the constant time delay circles, bistatic systems return estimates perpendicular to the constant time delay ellipses. These current components lie along radials for the monostatic system and along hyperbolas in the bistatic system. To date there have been four bistatic SeaSonde tests including shore-to-shore, ship-to-shore, and buoy-to-shore with the standard SeaSonde and a final ship-to-shore test with the long-range SeaSonde.

4a. *Standard Bistatic SeaSonde*

The bistatic CODAR configuration was first demonstrated in Monterey Bay, California by transmitting across the bay to a receiver on the other side (Figure 8). The constant time delay ellipses are clearly visible in the spacing of the hyperbolic velocity components. The second bistatic test demonstrated ship-to-shore transmissions offshore Tuckerton, New Jersey (Figure 9). Figure 9a shows the radial current components from the shore-based transmitter and receiver operating in monostatic mode. Figure 9b illustrates the simultaneous hyperbolic current components obtained from a ship-based transmitter and a shore-based receiver operating in bistatic mode. Note that the nearshore bistatic vector components are at an angle to the coast, thereby reducing the GDOP when near-shore total vector currents are calculated. Figure 9 also illustrates that the GPS timing allows the system to operate at the same

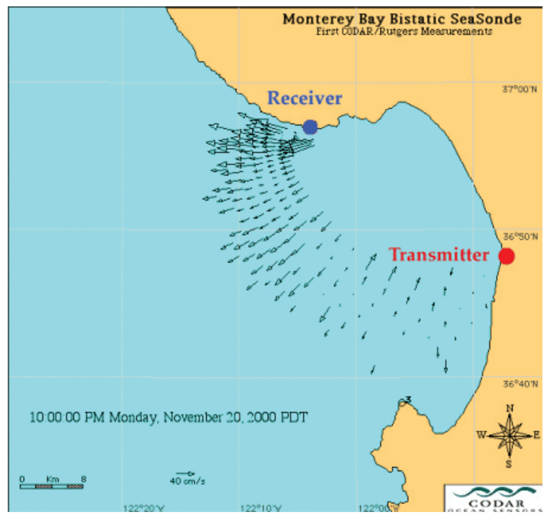

Figure 8. Demonstration of the bistatic CODAR for shore-to-shore transmissions across Monterey Bay, California.

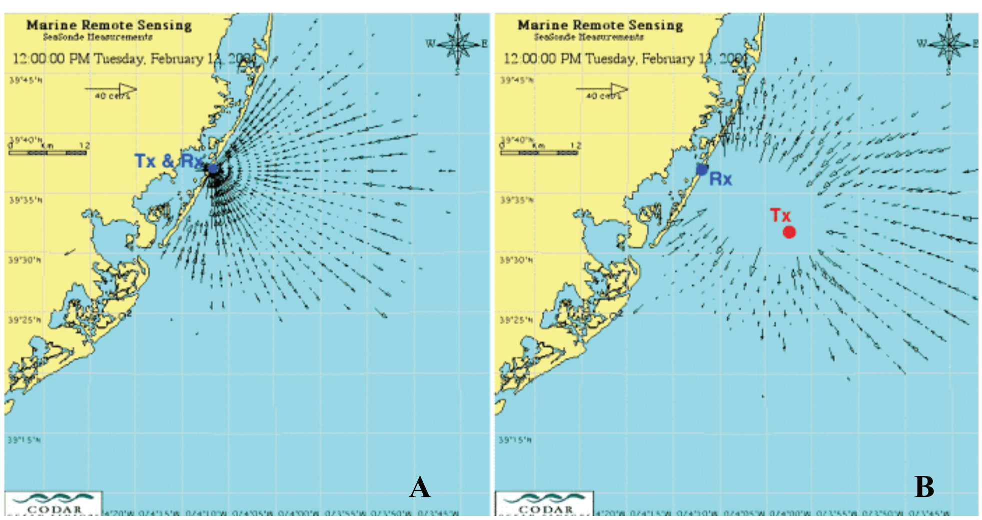

Figure 9. Demonstration of simultaneous (a) monostatic and (b) bistatic operation of a CODAR system offshore New Jersey. The transmitter (Tx) was located on shore in (a) and offshore on a boat in (b). The same shore-based receiver (Rx) was used in each case.

frequency in monostatic and bistatic mode simultaneously. Using GPS time as a reference, the timing of the frequency sweeps for each CODAR system can be adjusted so that the returns from the ship and shore transmitters can be uniquely identified. The final test with the standard bistatic system involved the deployment of a bistatic transmit buoy offshore of a standard SeaSonde shore site (Figure 10). The buoy, manufactured by the Ocean Science Group, was deployed on December 2, 2001 and is continuing to transmit a coupled signal with the shore site in Brant Beach, New Jersey. Again this system is using GPS timing to discriminate between the signal originating from the buoy and that originating from the shore site allowing bistatic and backscatter fields to be measured simultaneously.

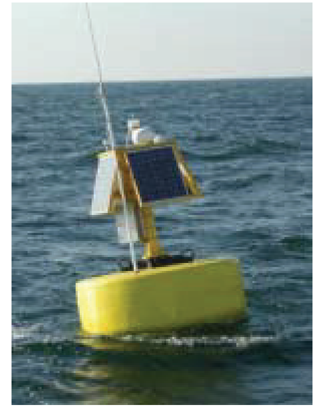

Figure 10. Standard System bistatic Buoy.

4b. Long-range Bistatic SeaSonde

The first test of the long-range bistatic system was run off the R/V Endeavor between December 1, 2001 and December 8, 2001. The ship was setup with a long-range transmitter and antenna that was coupled with the shore site in Loveladies, New Jersey. During the cruise, the transmitted signal was continuously measured in Loveladies. Once again GPS timing allowed the shore site to operate in bistatic and monostatic modes simultaneously. The cruise track included two stations located approximately 140 km offshore where the ship

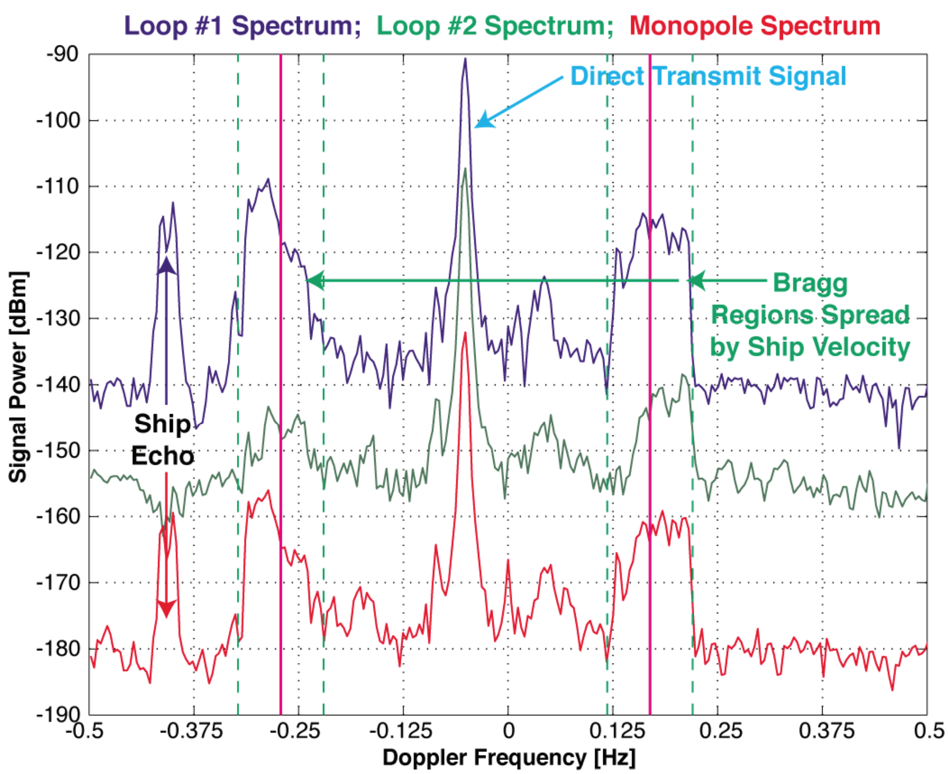

Figure 11. Bistatic cross-spectra measured at the Loveladies long-range site for loop #1 (blue), loop #2 (green), and the monopole (red). Bistatic transmit signal, ship echo, and resonant Bragg scatter peaks are shown.

remained on station for approximately 2.5 days. In addition to these stationary positions, scatter was measured while the ship was in transit. Figure 11 shows the measured cross-spectra of the ship's signal measured at the shore site. This particular cross-spectra was measured as the vessel steamed away from the Loveladies site toward the east at a speed of about seven knots. Its distance was about 40 km from the receiver at this point. The echo falls four time-delay cells later than the direct signal. A remnant of the direct signal is seen as the strongest peak in the three antenna signal spectra because it is so intense. Note that the position of the direct signal is shifted negatively, corresponding to the departing ship velocity of ~7 knots. The expected Bragg positions for resonant backscatter are shown as the vertical pink lines, symmetrically arrayed about the receding ship Doppler peak. In the fourth range cell the Bragg peaks would have been very narrow if the vessel were not moving, however the motion of the ship spreads these peaks. The theoretical limit of the spread is shown as vertical green dashed lines surrounding the Bragg positions (vertical pink lines). Observe that the measured first order region falls within these expected limits. In addition to ocean surface scatter used to measure currents, the signal may also scatter off large objects such as ships. An object must have a vertical length scale on the order of a quarter wavelength or greater to scatter the transmitted signal. For a long-range bistatic system operating at 4.8 MHz, this length scale is about 15 m. Figure 11 shows an example of a ship echo in the measured cross-spectra. Since the echo is absent in the measured Loop #2 signal, the ship is in the null of the cross-loop. The location of this ship can therefore be estimated as 40 km away at a bearing of about 161 degrees true. The measurements taken during this weeklong cruise provide the necessary data to develop algorithms to calculate surface current fields and perhaps ship tracks from measured bistatic cross-spectra.

5. Conclusions

The GPS timing that allows the transmitters and receivers to be operated at the same frequency in monostatic and bistatic mode simultaneously is a critical step for the construction of an array of CODAR systems. Using GPS time as a reference, the timing of the frequency sweeps for each CODAR system can be adjusted so that the returns from individual sites can be uniquely identified. With this information, combinations of several monostatic and/or bistatic systems all operating at the same frequency are possible. It is this discovery we choose to exploit as we redesign a nested CODAR grid for the New York Bight. By adding GPS timing to synchronize our existing long-range network, all five systems could be operated at the same optimal frequency if desired. Long-range monostatic site deployments could take advantage of the coastal geometry of the New York Bight to enable bistatic shore-to-shore transmissions as demonstrated across Monterey Bay. Bistatic operation will further decrease GDOP errors nearshore without the need to install complete monostatic systems. Offshore points within view of multiple sites will experience a significant decrease in the GDOP error of the total current vectors, since total vectors will now be estimated from N^2 rather than N components. The greater number of available components means smaller radii averaging circles in the total vector calculation can be used, enabling the network to better resolve fronts. This long-range bistatic array will provide additional current maps for total vector calculation. Successful tests of this configuration could lead to offshore long-range bistatic deployments on buoys, ships or on convenient NOAA platforms like Ambrose Light, introducing new geometries for total vector calculation. The combination of the long-range and standard bistatic CODAR systems will provide a nested grid of surface current measurements for the New York Bight with higher resolution near the shore.

6. Acknowledgements.

This work was funded by the Office of Naval Research, the National Ocean Partnership Program , and the great state of New Jersey. ADCP data provided by the Mid-Atlantic Bight National Undersea Research Center with additional support from the National Science Foundation.

7. References

Glenn, S.M., W. Boicourt, B. Parker and T.D. Dickey, 2000: Operational observation networks or ports, a large estuary and an open shelf. *Oceanography*, 13, 12-23.

Glenn, S.M., T.D. Dickey, B. Parker and W. Boicourt, 2000: Long-term real-time coastal ocean observation networks. *Oceanography*, 13, 24-34.

Grassle, J.F., S.M. Glenn and C. von Alt, 1998: Ocean observing systems for marine habitats. *OCC '98 Proceedings*, Marine Technology Society, November, 567-570.

Kohut, J.T. and S.M. Glenn. 2002: Calibration of HF radar surface current measurements using measured antenna beam patterns. *J. Atmos. Ocean. Tech*., Submitted.

Kohut, J. T., S. M. Glenn and D. E. Barrick, 1999: SeaSonde is Integral to Coastal Flow Model Development. *Hydro International,* 3, 32-35.

Kohut, J.T., S.M. Glenn and D.E. Barrick, 2001: Multiple hf-radar system development for a regional longterm ecosystem observatory in the New York bight. *American Meteorological Society: Fifth Symposium on Integrated Observing Systems*, 4-7.

Paduan, J.D., D.E. Barrick, D.M. Fernandez, Z. Hallok and C.C. Teague, 2001: Improving the accuracy of coastal hf radar current mapping. *Hydro International*, 5, 26-29.

Schofield, O., T. Bergmann, W.P. Bissett, F. Grassle, D Haidvogel, J. Kohut, M. Moline and S. Glenn, 2001: The long term ecosystem observatory: an integrated coastal observatory. *IEEE J. Ocean. Engin*., In press.

Recent Results from a Nested Multi-Static HF Radar Network for the NorthEast Observing System (NEOS).

Dr. Josh T. Kohut
Dir, HF Radar Lab., Rutgers University
kohut@imcs.rutgers.edu 1-732-932-6555 x542

Dr. Scott M. Glenn
Professor, Rutgers University
glenn@imcs.rutgers.edu 1-732-932-6555 x542

Dr. Hugh J. Roarty
Coastal Engineer, Rutgers University
hroarty@imcs.rutgers.edu 1-732-932-6555 x542

Abstract: A nested HF radar network has been deployed along the New Jersey coast as part of the New Jersey Shelf Observing System (NJSOS) and the larger regional NorthEast Observing System (NEOS). A 25 MHz standard system (range about 50 km) setup for continuous operation since 1999 includes two sites in Brant Beach and Brigantine, New Jersey. A second 5 MHz long-rang system (range about 170 km) includes four New Jersey sites set up in Wildwood, Tuckerton, Loveladies, and Sandy Hook, and one Massachusetts site in Nantucket. Both the long-range and standard-range systems provide real-time maps of surface currents, with resolutions of 1.5 km (standard) and 6 km (long-range). Recent additions to the network included GPS synchronization, which allows all long-range sites to operate on a single frequency without interfering with each other. In addition to single frequency operation, the GPS synchronization allows the existing coastal stations to be bistatically linked to each other. Without adding additional hardware, four coastal sites provide four monostatic radial current maps and 12 bistatic hyperbolic current maps simultaneously. This both increases data coverage and reduces measurement error. Two bistatic transmitting buoys (one 25 MHz and one 5 MHz) compliment the coastal sites. This operational, nested, and multistatic network provides real-time current maps for scientific and operational users.

0-933957-30-0

Intercomparison of an ADCP, ADP, standard and long-range HF RADAR: Influence of Horizontal and Vertical Shear

Hugh Roarty, Josh Kohut and Scott Glenn
Institute of Marine and Coastal Sciences
Rutgers University
71 Dudley Road
New Brunswick, NJ 08901
732-932-6555 ext. 377
hroarty@imcs.rutgers.edu

Abstract—A nested HF radar network has been deployed along the New Jersey coast as part of the New Jersey Shelf Observing System (NJSOS). A standard range (about 50 km) system setup for continuous operation since 1999 includes two sites in Brant Beach and Brigantine, New Jersey. A second longer range system (about 170 km) includes four New Jersey sites set up in Wildwood, Tuckerton, Loveladies, and Sandy Hook. The first of the long-range sites was deployed in Spring 2000. Both the long-range and standard-range systems provide real-time maps of surface currents, with resolutions of 1.5 km (standard) and 6 km (long-range). During the summer of 2001, three Workhorse ADCPs and two SonTek ADPs were deployed along a line perpendicular to the coast. All of these in situ current meters were deployed for six weeks within the footprints of the two CODAR networks. Comparisons were made between the ADCP/ADP time series and radial CODAR time series provided by the long-range and standard-range sites closest to the line of current meters. Additional comparisons were drawn between the total current fields of the standard and long-range CODAR systems with the in situ current meters. Several forcings were examined to explain the differences in the observations including vertical and horizontal shears.

I. Introduction

HF radar utilizes a high frequency radio wave to be reflected and Doppler shifted by a surface ocean wave precisely one half the wavelength of the transmitted radar wave. The radar derives a vertically averaged quantity over a depth of $\lambda/12\pi$ or possibly less, where λ is the radar wavelength [1]. Expected differences between the surface HF radar measurement and current meters depend on numerous sources of error and differences, such as geophysical variability [2]. The research conducted here on the geophysical variability may help to explain the RMS difference between HF Radar and more conventional and often-accepted techniques (i.e. current meters, drifters, ADCPs, etc.) that remains a crucial measurement issue [2].

This paper will provide the details of how the data was analyzed and compared between the ADCP and CODAR system, discuss the implication and meaning of the comparison and lastly detail future analysis and comparisons.

The first of five long-range CODAR systems was installed in the spring of 2000. The last planned system will be installed in the spring of 2003. See Figure 1 for a map indicating the location the four long-range CODAR sites (white circles along the New Jersey coastline) along with a typical total vector current map. The data from the Tuckerton CODAR site was fist utilized. This system operated at 5 MHz with a range of 180 km and a resolution of 6 km.

During the summer of 2001, three Workhorse ADCPs and two SonTek ADPs were deployed along a line perpendicular to the same coastline. Out of the five current meters, this analysis concentrated on the current record from the ADCP furthest offshore. An RD 600 kHz ADCP was deployed in 22 m of water for a period of six weeks. The water column was divided into 22 bins (Bin 1 closest to the ADCP and bin 22 closest to the surface) each with a length of 1 m. The ADCP recorded continuously for the six-week period at frequency of 0.2 Hz.

II. Data Analysis

The first comparison point is an ADCP 23.4 km offshore in 22 m of water. The shallowest bin that could be used was 4.4 m below the surface. Both the radial currents from the Tuckerton CODAR site and ADCP data were center-averaged over a 3-hour period. The ADCP measurements were then rotated into a radial and cross radial coordinate system to match the Tuckerton radial data. Figure 2 shows the

0-7803-7813-X/03/$17.00 ©2003 IEEE

comparison between the CODAR surface radial velocity and the radial current in Bin 16 of the ADCP. The RMS difference between the measurements was 6.3 cm/s over the entire record.

A closer examination of the comparison shows that the correlation between the two data sets varies with time. As discussed in the introduction there are several possible causes of this difference. Since system error should not vary over these time scales, shear in the water column was first tested.

The velocity measurements from Bins 16 through 12 were plotted along with CODAR radial measurements, as seen in Figure 3.

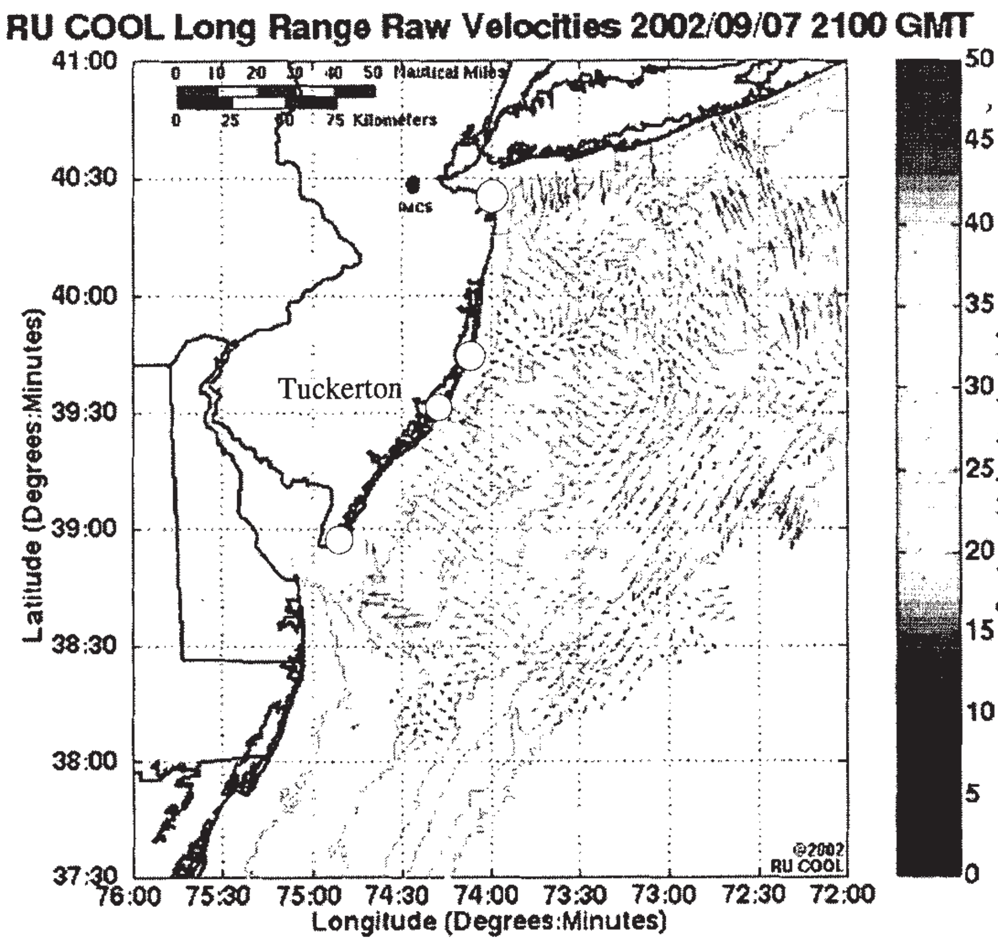

Figure 1: Location of long-range codar along New Jersey Coast

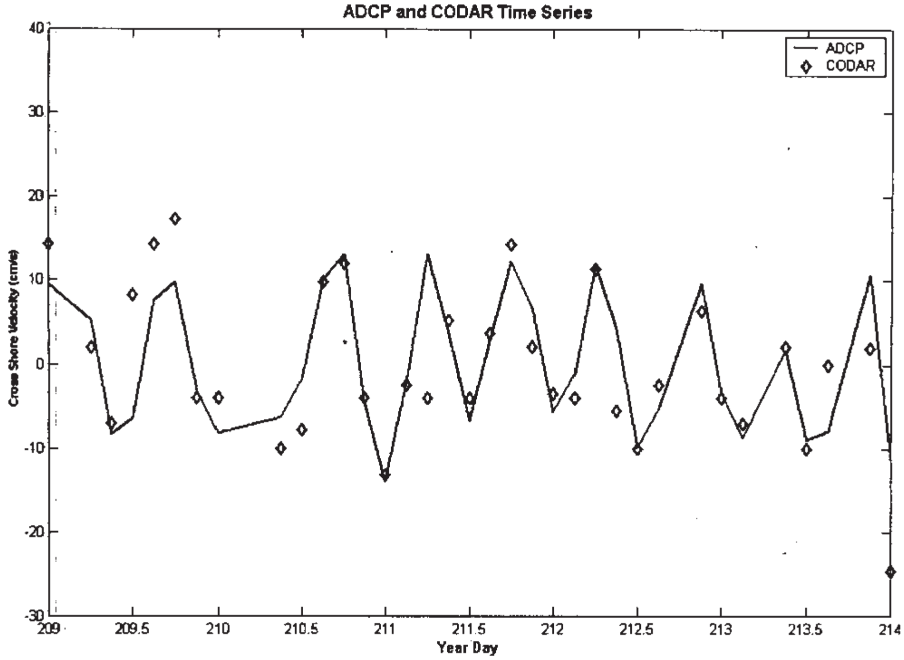

Figure 2: Comparison of long-range CODAR radial velocity with ADCP measurement

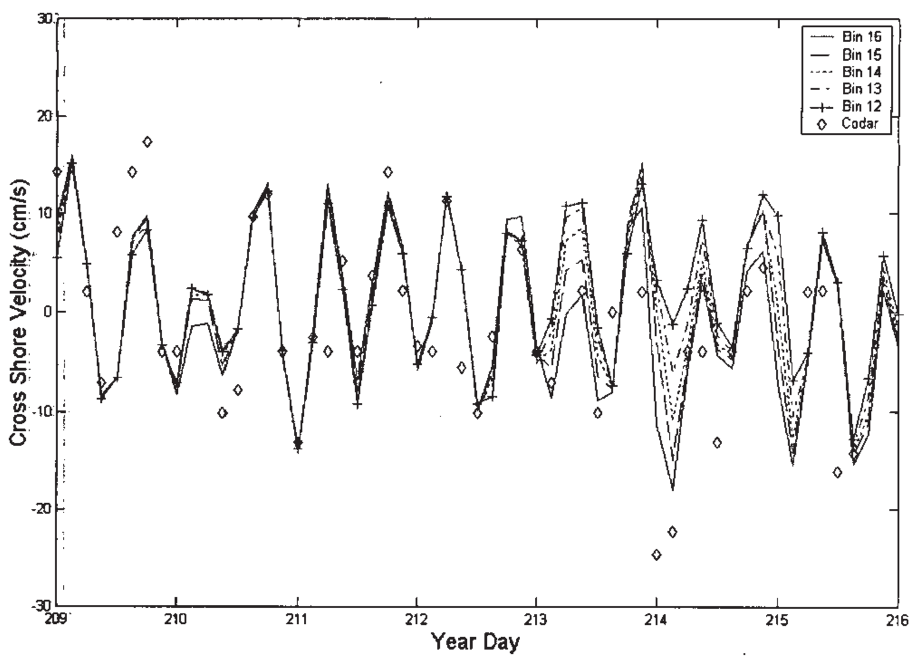

Figure 3: Long-range CODAR measurements along with ADCP measurements from 5 ADCP bins

III. Discussion

From Figure 3, velocity shear is present in the water column at the beginning of days 210 and 214. The Codar data point's magnitude follows this shear trend. An underwater jet (Magnitude of Bin 12> Magnitude of Bin 16) is present at the end of day 214 and CODAR follows that trend (CODAR point < Bin 16). Looking at the latter half of day 210, there is no shear in the water column leading to closer CODAR and ADCP measurements. Therefore, the observed RMS difference is influenced by the physical environment in which the measurements are being made.

The physical shear in the water column is shown to contribute to the difference observed in the measurements of the HF radar and ADCP. There was no clear correlation between increased shear and the local wind field, indicating that the shear may not always be wind driven.

IV. Future Analysis

There are several analysis options that can be examined to try and narrow the difference between CODAR and ADCP measurements.

- Bins closer to the surface can be used. The data analysis is simplified if the 99999 readings from the ADCP are ignored.
- Horizontal shear can be analyzed by comparing the current measurements between the 5 acoustic current meters installed.

The comparison presented here will be expanded to include data from other higher resolution (25 MHz) HF radar systems and additional in situ current meters. With this larger spatial data set, the contribution of horizontal and vertical shear to the time dependent comparisons will be explored.

V. References

[1] Stewart, R.H. and Joy, J. W. (1974). "HF radio measurements of surface currents." Deep-Sea Research, Vol. 21, 1039-1049

[2] Graber, H.C., Haus, B.K., Chapman, R.D., and Shay, L.K. (1997). "HF radar comparisons with moored estimates of current speed and direction: Expected differences and implications." *Journal of Geophysical Research*, Vol. 102, No. C8, 18,749-18766

Observed Response of the Hudson River Plume to Wind Forcing Using a Nested HF Radar Array

Josh T. Kohut, Rutgers   Hugh J. Roarty, Rutgers   Scott M. Glenn, Rutgers
Oscar Schofield, Rutgers   Robert J. Chant, Rutgers   Elizabeth Creed, Rutgers

Rutgers University, Institute of Marine and Coastal Sciences
Coastal Ocean Observation Lab
71 Dudley Rd.
New Brunswick, New Jersey 08901 USA
kohut@marine.rutgers.edu

Abstract - **One objective of the Lagrangian Transport and Transformation Experiment (LaTTE) is to determine the relative advantages of studying the Hudson River plume within the spatial and temporal context provided by an operational research observatory. Towards this end, a shelf-wide observational backbone was locally enhanced with high-resolution relocatable systems in the New York Bight apex. The permanent backbone includes local acquisition of international satellite ocean color imagery, a network of long-range High Frequency radars, and a cross-shelf Endurance line occupied by an autonomous underwater glider. The high resolution systems, including higher resolution HF Radar, glider and mooring networks, were moved to the New York Bight Apex to support the specific interdisciplinary process study. During the LaTTE field effort, datasets from the nested observation network, including a triple nested HF Radar array, were assembled in real-time at a shore-based acquisition center, and high-resolution atmospheric forecasts were performed. Surface current observations will be reviewed, with specific emphasis placed on the observed response of the Hudson River plume to local winds. The observatory results provide a spatial and temporal context for viewing the LaTTE dye release, chemical and biological results.**

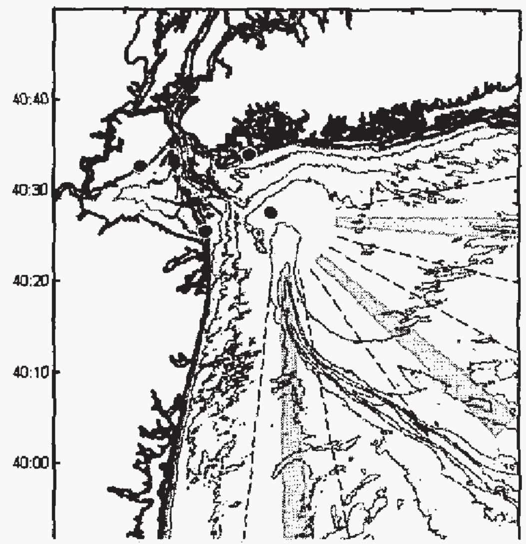

Fig. 1. Map of the Hudson River Estuary. CODAR Sites are shown as blue dots, wind measurement from a NOAA NDBC station at Ambrose Light is shown as a red dot.

I. INTRODUCTION

The Lagrangian Transport and Transformation Experiment (LaTTE) is a coordinated program of field and numerical experiments to examine processes that control the fate and transport of nutrients and chemical contaminants in the Hudson River plume, a plume that emanates from one of the United States' most urban estuaries -- the New York/New Jersey Harbor complex (Fig. 1). Urban estuarine plumes represent a major pathway for the transport of nutrients and chemical contaminants to the coastal ocean. However, the fate and transport of this material is controlled not only by the plumes dynamics but also by biological and chemical processes that are coupled to the dynamics of the plume. By conducting a series of dye experiments featuring continuous underway chemical and biological sampling with a state-of-the-art towed vehicle within the well sampled framework of an operational ocean observatory, we are able to distinguish between physical processes that transport/mix material in a buoyant plume from biological and chemical transformation processes. This allows us to quantify biological and chemical interactions in a Lagrangian perspective, and provide a means to assess their importance in determining the fate and transport of nutrients and chemical contaminants in a buoyant plume.

An ocean observatory facilitated interpretation of the dye study by placing the Lagrangian surveys in context with shelf-wide observations from satellite imagery, surface currents from a nested High Frequency (HF) radar array and far-field subsurface hydrography. The observatory was augmented with a cross shelf array of moored instruments that provided detailed estimates of subtidal circulation, stratification and Reynold stresses. Finally, data-assimilative numerical simulations provided high resolution and realistic hindcasts of the coastal ocean during the field experiments. This paper will focus on preliminary results from an intensive field effort in April of 2005. Specifically, we will discus the utility of the HF Radar nested network as an adaptive sampling tool.

0-7803-8989-1/05/$20.00 ©2005 IEEE

II. HF RADAR NESTED ARRAY

Rutgers University operates an array of 10 CODAR-type HF radar systems [1], [2]. Six of these are lower resolution long-range sites. With an operating frequency around 5 MHz, these sites measure surface currents within the upper 1.6 meters of the water column [3]. Typical spatial resolutions are on the order of 6 km with maximum ranges exceeding 200 km. Four sites along the coast of New Jersey from Wildwood to Sandy Hook provide hourly surface current maps over the entire New Jersey Shelf (Fig. 2.). These four sites form one cluster of systems within the Northeast Observing System (NEOS). A second cluster of systems include one site owned and operated by Rutgers in Nantucket MA, another owned by the UMaine and operated by Rutgers and the URI in Block Island and a

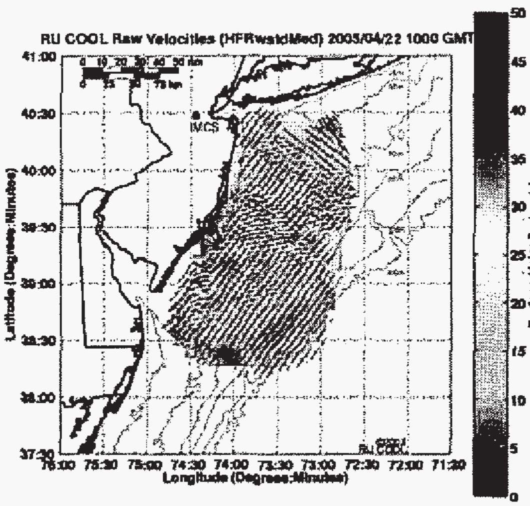

Fig. 2. Sample Hourly surface current vector map over the Mid-Atlantic Bight. Site locations are shown as green circles on the coast.

third owned and operated by UMass on Cape Cod. These three sites provide similar hourly maps from east of Cape Cod to south of Block Island. Both the New Jersey and New England clusters are using GPS synchronization so that each site is operating at the same frequency and bistatically linked to the other sites within the cluster.

Two standard range systems, currently deployed on opposite sides of the entrance to New York Harbor, are nested within the New Jersey long-range cluster. With an operating frequency of 25 MHz, these systems measure the current within the upper 30 cm of the water column. Typical spatial resolutions are on the order of 1 km with maximum ranges out to 40 km. A third sight owned and operated by Stevens Institute of Technology was deployed on Staten Island, NY. Through this collaboration, a three site total vector product covering the mouth of the estuary was produced every 30 minutes (Fig. 3.)

The first medium range system for the New York Bight has just been funded by CNTPO. This site will be deployed in Sandy Hook NJ to compliment the existing long and standard range systems already operating at Sandy Hook. The addition of this 13 MHz site makes Sandy Hook the only triple nested multi-static HF radar

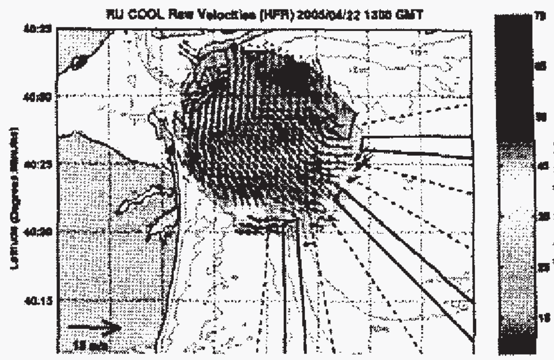

Fig. 3. Sample 30-minute surface current map at the mouth of the Hudson River estuary, nested within the long-range coverage shown in fig. 2. Site locations are shown as green circles along the coast.

test bed for ship tracking in the world. While the primary use will be for ship-tracking applications, the site will be dual-use and also produce hourly medium resolution radial currents. With an operating frequency of 13 MHz, the measured surface current is the average over the upper 60 cm of the water column. Typical spatial resolutions are on the order of 3 km with maximum ranges out to 65 km.

III. THE PULSING PLUME

Prior to the first injection, HF radar data was used to determine the spatial and temporal variability of the surface current associated with the freshwater outflow. These data showed that instead of a steady outflow from the harbor mouth, there was a series of strong pulses. These pulses were linked to the tide and local wind

Fig. 4. A freshwater pulse moving on the shelf beyond the mouth of the estuary. The surface currents are shown as red vectors overlaid on a MODIS RGB Satellite image.

forcing. An example of the surface currents associated with on these pulses is shown in Fig. 4 Preceding each pulse was a region of very high convergence. Satellite RGB imagery clearly shows the increased sediment load within this pulse as it makes its way into the coastal ocean.

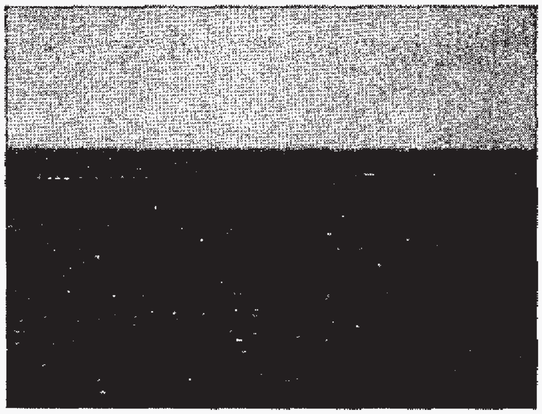

Fig. 5. Photograph taken aboard the R/V Cape Hatteras showing the surface signature of the freshwater bore.

These data were sent to the researchers aboard the R/V Cape Hatteras and R/V Oceanus so that they could view the conditions in real-time for more strategic sampling. Based on the map shown in Fig. 4., the dye was injected right into the head of the freshwater plume. The region of convergence was so strong, that researchers aboard the boat could see the bore approach the ship (Fig. 5.). The ship shuttered as the bore propagated by. The ensuing injection was tracked for the next two days.

IV. THE TRANSPORT HIGHWAY

In addition to aiding in the adaptive sampling strategy on board the vessel, the HF radar data provided a shelf wide context for the shipboard data. Long-term averages of surface currents in the MAB indicate two transport pathways to the outer shelf. One originates near the mouth of New York Harbor and moves out along the Hudson Canyon. The second, originating upshelf, enters the field from the north and moves slowly toward the south. The flow along the Hudson Canyon is an alternative pathway that is a more direct transport to the shelf/slope region of the MAB. This cross-shelf pathway is also evident in the annual and seasonal means. While the general mechanism exists over these scales, the location, width, and strength do vary.

During the last dye injection, both the satellite and long range data showed that the transport highway was present and a possible pathway for freshwater out beyond the shelf (Fig. 6). The currents associated with this highway move south along the Hudson Canyon out to the shelf edge. The sea surface temperature clearly shows the warm water along the coast associated with the Hudson River plume. One can also see the warmer water heading across the shelf.

V. SUMMARY

The HF Radar array was a critical component of the LaTTE experiment The real-time high resolution maps near the mouth of the estuary and the lower resolution maps across the entire shelf were used by the researchers on board so that the dye could be injected in the head of a freshwater bore. Without these data and the real-time link to the ships, this would not have been possible. The Observatory data has also shown a possible cross-shelf pathway for the freshwater and all that it carries. The spatial surface data sustained through the observatory provides an unprecedented look at the coastal ocean. For the first time we are able to observe a transport pathway from the bight apex near the mouth of New York Harbor out to the deep ocean beyond the shelf break. This mechanism has significant implications on the transport of materials across the shelf over many different time scales.

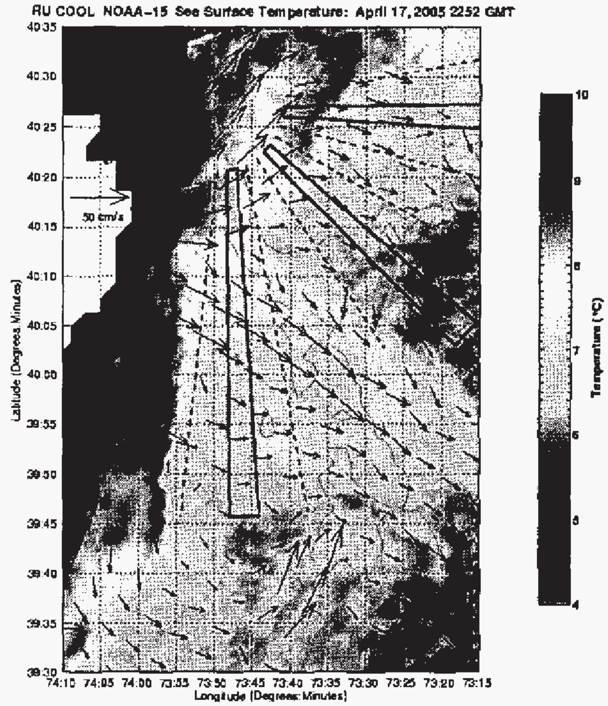

Fig. 6. Long range surface currents overlaid on satellite Sea Surface Temperatures (SST).

ACKNOWLEDGMENTS

The work described here was funded through a grant from the National Science Foundation. The authors would also like to thank all those who have and continue to work in the COOLRoom, the operations center for the Coastal Observatory off New Jersey.

REFERENCES

[1] Kohut, J. T. and S. M. Glenn, 2003. Calibration of HF radar surface current measurements using measured antenna beam patterns. *J. Atmos. Ocean. Tech.*, 1303-1316.

[2] Kohut, J. T., Glenn, S. M., Chant, R. J. 2004. Seasonal current variability on the New Jersey inner shelf. *Journal of Geophysical Research*. 109, C07S07, DOI: 10.1029/2003JC001963.

[3] Stewart, R.H. and J.W. Joy, 1974: HF radio measurement of surface currents. *Deep-Sea Res.*, 21, 1039-1049.

Surface current response of Hudson River plume to wind forcing

Josh T. Kohut
Rutgers University, Institute of Marine and Coastal Sciences

Hugh J. Roarty
Rutgers University, Institute of Marine and Coastal Sciences

Scott M. Glenn
Rutgers University, Institute of Marine and Coastal Sciences

Robert J. Chant
Rutgers University, Institute of Marine and Coastal Sciences

Abstract - **One objective of the Lagrangian Transport and Transformation Experiment (LaTTE) is to determine the relative advantages of studying the Hudson River plume within the spatial and temporal context provided by an operational research observatory. Towards this end, a shelf-wide observational backbone was locally enhanced with high-resolution relocatable systems in the New York Bight apex. The permanent backbone includes local acquisition of international satellite ocean color imagery, a network of long-range High Frequency radars, and a cross-shelf Endurance line occupied by an autonomous underwater glider. The high resolution systems, including higher resolution HF Radar, glider and mooring networks, were moved to the New York Bight Apex to support the specific interdisciplinary process study. During the LaTTE field effort, datasets from the nested observation network, including a triple nested HF Radar array, were assembled in real-time at a shore-based acquisition center, and high-resolution atmospheric forecasts were performed. Surface current observations will be reviewed, with specific emphasis placed on the observed response of the Hudson River plume to local winds. The observatory results provide a spatial and temporal context for viewing the LaTTE dye release, chemical and biological results.**

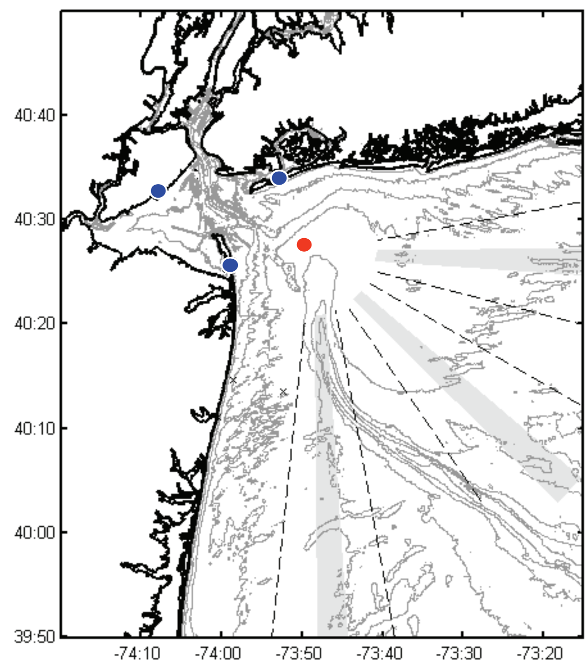

Fig. 1. Map of the Hudson River Estuary. CODAR Sites are shown as blue dots, wind measurement from a NOAA NDBC station at Ambrose Light is shown as a red dot.

I. INTRODUCTION

The Lagrangian Transport and Transformation Experiment (LaTTE) is a coordinated program of field and numerical experiments to examine processes that control the fate and transport of nutrients and chemical contaminants in the Hudson River plume, a plume that emanates from one of the United States' most urban estuaries -- the New York/New Jersey Harbor complex (Fig. 1). Urban estuarine plumes represent a major pathway for the transport of nutrients and chemical contaminants to the coastal ocean. However, the fate and transport of this material is controlled not only by the plumes dynamics but also by biological and chemical processes that are coupled to the dynamics of the plume. By conducting a series of dye experiments featuring continuous underway chemical and biological sampling with a state-of-the-art towed vehicle within the well sampled framework of an operational ocean observatory, we are able to distinguish between physical processes that transport/mix material in a buoyant plume from biological and chemical transformation processes. This allows us to quantify biological and chemical interactions in a Lagrangian perspective, and provide a means to assess their importance in determining the fate and transport of nutrients and chemical contaminants in a buoyant plume.

An ocean observatory facilitated interpretation of the dye study by placing the Lagrangian surveys in context with shelf-wide observations from satellite imagery, surface currents from a nested High Frequency (HF) radar array and far-field subsurface hydrography. The observatory was augmented with a cross shelf array of moored instruments that provided detailed estimates of subtidal circulation, stratification and Reynold stresses. Finally, data-assimilative numerical simulations provided high resolution and realistic hindcasts of the coastal ocean during the field experiments. This paper will focus on preliminary results from an intensive field effort in April of 2005. Specifically, we will discus the utility of the HF Radar nested network as an adaptive sampling tool.

II. HF RADAR NESTED ARRAY

Rutgers University operates an array of 10 CODAR-type HF radar systems [1],[2]. Six of these are lower resolution long-range sites. With an operating frequency around 5 MHz, these sites measure surface currents within the upper 1.6 meters of the water column [3]. Typical spatial resolutions are on the order of 6 km with maximum ranges exceeding 200 km. Four sites along the coast of New Jersey from Wildwood to Sandy Hook provide hourly surface current

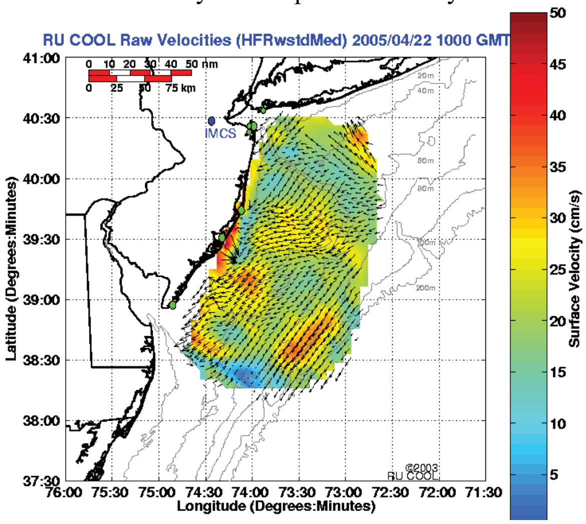

Fig. 2. Sample Hourly surface current vector map over the Mid-Atlantic Bight. Site locations are shown as green circles on the coast.

maps over the entire New Jersey Shelf (Fig. 2.). These four sites form one cluster of systems within the NorthEast Observing System (NEOS). A second cluster of systems include one site owned and operated by Rutgers in Nantucket MA, another owned by the UMaine and operated by Rutgers and the URI in Block Island and a third owned and operated by UMass on Cape Cod. These three sites provide similar hourly maps from east of Cape Cod to south of Block Island. Both the New Jersey and New England clusters are using GPS synchronization so that each site is operating at the same frequency and bistatically linked to the other sites within the cluster.

Two standard range systems, currently deployed on opposite sides of the entrance to New York Harbor, are nested within the New Jersey long-range cluster. With an operating frequency of 25 MHz, these systems measure the current within the upper 30 cm of the water column. Typical spatial resolutions are on the order of 1 km with maximum ranges out to 40 km. A third sight owned and operated by Stevens Institute of Technology was deployed on Staten Island, NY. Through this collaboration, a three site total vector product covering the mouth of the estuary was produced every 30 minutes (Fig. 3.)

The first medium range system for the New York Bight has just been funded by CNTPO. This site will be deployed in Sandy Hook NJ to compliment the existing long and standard range systems already operating at Sandy Hook.

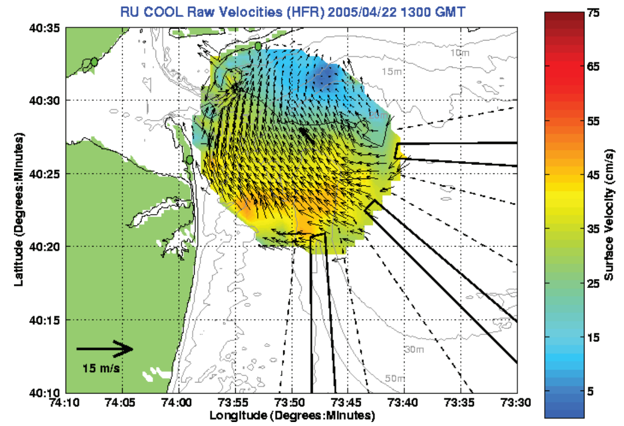

Fig. 3. Sample 30-minute surface current map at the mouth of the Hudson River estuary, nested within the long-range coverage shown in fig. 2. Site locations are shown as green circles along the coast.

The addition of this 13 MHz site makes Sandy Hook the only triple nested multi-static HF radar test bed for ship tracking in the world. While the primary use will be for ship-tracking applications, the site will be dual-use and also produce hourly medium resolution radial currents. With an operating frequency of 13 MHz, the measured surface current is the average over the upper 60 cm of the water column. Typical spatial resolutions are on the order of 3 km with maximum ranges out to 65 km.

III. THE PULSING PLUME

Prior to the first injection, HF radar data was used to determine the spatial and temporal variability of the surface current associated with the freshwater outflow. These data showed that instead of a steady outflow from the harbor

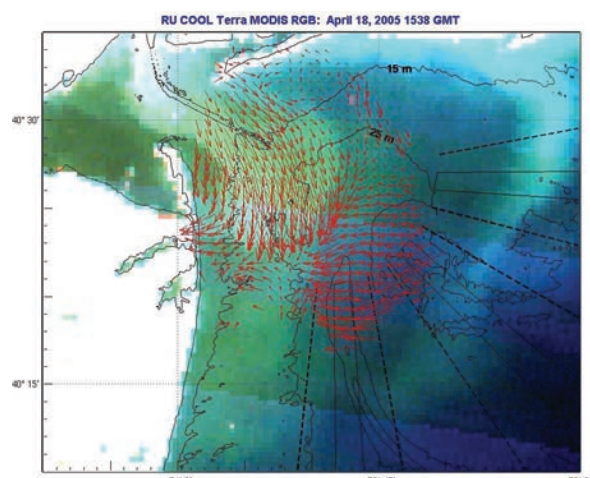

Fig. 4. A freshwater pulse moving on the shelf beyond the mouth of the estuary. The surface currents are shown as red vectors overlaid on a MODIS RGB Satellite image.

mouth, there was a series of strong pulses. These pulses were linked to the tide and local wind forcing. An example of the surface currents associated with on these pulses is shown in Fig. 4 Preceding each pulse was a region of very high convergence. Satellite RGB imagery clearly shows the

Fig. 5. Photograph taken aboard the R/V Cape Hatteras showing the surface signature of the freshwater bore.

increased sediment load within this pulse as it makes its way into the coastal ocean.

These data were sent to the researchers aboard the R/V Cape Hatteras and R/V Oceanus so that they could view the conditions in real-time for more strategic sampling. Based on the map shown in Fig. 4., the dye was injected right into the head of the freshwater plume. The region of convergence was so strong, that researchers aboard the boat could see the bore approach the ship (Fig. 5.). The ship shuttered as the bore propagated by. The ensuing injection was tracked for the next two days.

IV. THE TRANSPORT HIGHWAY

In addition to aiding in the adaptive sampling strategy on board the vessel, the HF radar data provided a shelf wide context for the shipboard data. Long-term averages of surface currents in the MAB indicate two transport pathways to the outer shelf. One originates near the mouth of New York Harbor and moves out along the Hudson Canyon. The second, originating upshelf, enters the field from the north and moves slowly toward the south. The flow along the Hudson Canyon is an alternative pathway that is a more direct transport to the shelf/slope region of the MAB. This cross-shelf pathway is also evident in the annual and seasonal means. While the general mechanism exists over these scales, the location, width, and strength does vary.

During the last dye injection, both the satellite and long range data showed that the transport highway was present and a possible pathway for freshwater out beyond the shelf (Fig. 6). The currents associated with this highway move south along the Hudson Canyon out to the shelf edge. The sea surface temperature clearly shows the warm water along the coast associated with the Hudson River plume. One can also see the warmer water heading across the shelf.

V. SUMMARY

The HF Radar array was a critical component of the LaTTE experiment The real-time high resolution maps near the mouth of the estuary and the lower respolution maps across

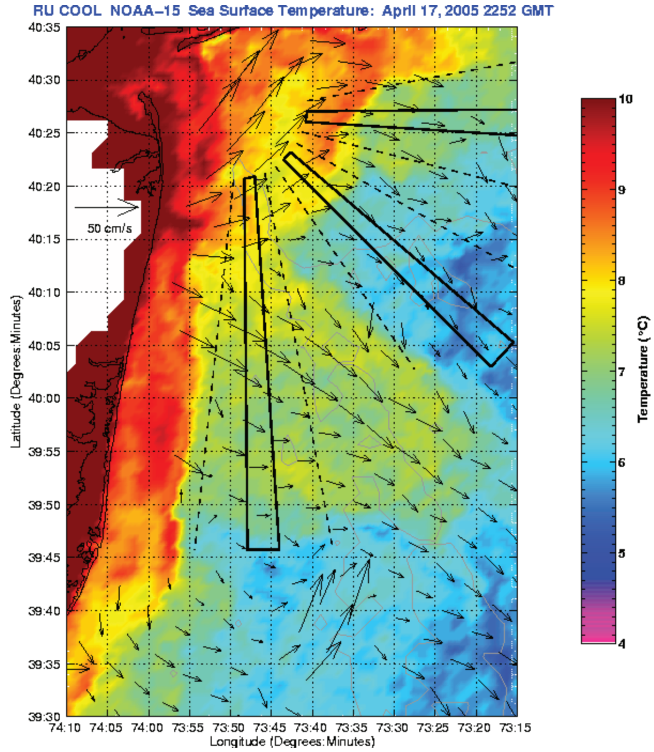

Fig. 6. Long range surface currents overlaid on satellite Sea Surface Temperatures (SST).

the entire shelf were used by the researchers on baord so that the dye could be injected in the head of a freshwater bore. Without these data and the real-time lionk to the ships, this would not have been possible. The Observatory data has also shown a possible cross-shelf pathway for the freshwater and all that it carries. The spatial surface data sustained through the observatory provides an unprecedented look at the coastal ocean. For the first time we are able to observe a transport pathway from the bight apex near the mouth of New York Harbor out to the deep ocean beyond the shelf break. This mechanism has significant implications on the transport of materials across the shelf over many different time scales.

Acknowledgments

The work described here was funded through a grant from the National Science Foundation. The authors would also like to thank all those who have and continue to work in the COOLRoom, the operations center for the Coastal Observatory off New Jersey.

References

[1] Kohut, J. T. and S. M. Glenn, 2003. Calibration of HF radar surface current measurements using measured antenna beam patterns. *J. Atmos. Ocean. Tech.*, 1303-1316.

[2] Kohut, J. T., Glenn, S. M., Chant, R. J. 2004. Seasonal current variability on the New Jersey inner shelf. *Journal of Geophysical Research*. 109, C07S07, DOI: 10.1029/2003JC001963.

[3] Stewart, R.H. and J.W. Joy, 1974: Hf radio measurement of surface currents. *Deep-Sea Res.*, 21,

PHASED IMPLEMENTATION OF THE MID-ATLANTIC REGIONAL HF RADAR SYSTEM

J. Kohut, S. Glenn, O. Schofield
Rutgers, The State University of New Jersey
Institute of Marine and Coastal Sciences
New Brunswick, NJ 08901
kohut@marine.rutgers.edu

ABSTRACT

Surface currents are an integral component of the Integrated Ocean Observing System (IOOS) and High Frequency (HF) radar technologies provide the means to measure these data across regional scales. A national committee on surface current mapping, supported by OCEAN.US, has outlined an organizational structure for a national HF radar system. This plan separates the national system into regional centers responsible for the operation and maintenance of the network. Recently MACOORA, the Mid-Atlantic Coastal Ocean Observing Regional Association, identified HF radar as an important component of the coastal observatory. In the context of MACOORA and the regional landscape outlined in the IOOS plan, the HF radar operators from Cape Cod to Cape Hatteras have formed a consortium for the operation and maintenance of the HF radar network, including system hardware, data management, and product delivery. Through this consortium the existing pockets of systems can be operated as part of one regional network. This network consists of 11 long-range sites providing total vector coverage across a large majority of the region. Additional sites are proposed in Moriches, NY, Block Island, RI, and Martha's Vineyard, MA to completely fill in the shelf-wide coverage from Cape Cod, MA to Cape Hatteras, NC. In addition there are three higher resolution systems made up of 13 sites in operation in the Chesapeake Bay, New York Harbor, and Long Island Sound estuaries with plans for 2 more sites in Delaware Bay. This nested network makes the Mid-Atlantic Bight the most heavily HF radar instrumented region in the world. In addition to scientific research and education applications, the data has already been ingested into United States Coast Guard Search and Rescue planning tools. An overview of the network including existing products and system infrastructure will be discussed as well as plans for the continued operation and reliable product delivery supporting the regional IOOS mission. By leveraging off national efforts like the Radiowave Oceanography Working Group (ROWG) for operation and maintenance and ROADNET for data management, the Mid-Atlantic HF radar consortium has moved from small groups of systems to a single integrated regional system, a model that could be scaled nationally and internationally. The coastal geometry surrounding the Baltic Sea is particularly well suited for a similar system with continuous coverage across the entire sea. A preliminary analysis of this system will also be presented in collaboration with existing HF radar work in the area.

1. INTRODUCTION

High Frequency (HF) radar derived real-time surface current maps are envisioned to be an integral component of the Integrated Ocean Observing System (IOOS). A national committee on surface current mapping, supported by OCEAN.US, has already outlined a structural plan to implement a national HF radar network. This plan separates the national network into regional centers responsible for the operation and maintenance of the systems. Recently MACOORA, the Mid-Atlantic Coastal Ocean Observing Regional Association, identified HF radar as an important integrating component of their envisioned Regional Coastal Ocean

Observing System (R-COOS). A Mid-Atlantic HF Radar network would be capable of providing high resolution nested coverage within the five sub-regions while simultaneously linking the sub-regions together in one coastal network that covers the full range of the Mid-Atlantic coastal ecosystem. To implement a regional HF Radar network for the MACOORA R-COOS, radar operators in the region have formed the Middle Atlantic High Frequency Radar Consortium (MAHFRC).

2. PAST ACCOMPLISHMENTS

The first continuously operated systems in the Mid-Atlantic Bight (MAB) were deployed in 1998. Since that time the MAB has become the most heavily instrumented HF radar network in the world (Table 1). Academic and government groups currently operate 19 radar systems and have 7 funded systems with deployments planned over the next 6 months.

Table 1. Existing sites in the Mid-Atlantic Bight.

Site Location	**Site Operator**	**Site Frequency**
Nauset, MA	U. Mass., Dartmouth	5 MHz
Nantucket, MA	Rutgers University	5 MHz
Block Island, RI	URI/UConn	25 MHz
Misquamicut, RI	URI/UConn	25 MHz
Montauk, NY	URI/UConn	25 MHz
Great Captain Is, NY	UConn	25 MHz
Bayville, NY	UConn	25 MHz
Staten Island, NY	Stevens Institute	25 MHz
Breezy Point, NY	Rutgers University	25 MHz
Sandy Hook, NJ	Rutgers University	25 MHz
Sandy Hook, NJ	Rutgers University	13 MHz
Sandy Hook, NJ	Rutgers University	5 MHz
Loveladies, NJ	Rutgers University	5 MHz
Tuckerton, NJ	Rutgers University	5 MHz
Wildwood, NJ	Rutgers University	5 MHz
Chesapeake BBT, VA	NOAA, Chesapeake Bay	25 MHz
Norfolk, VA	NOAA, Chesapeake Bay	25 MHz
Duck, NC	UNC-CH	5 MHz
Buxton, NC	UNC-CH	5 MHz

There are proposals pending for 7 additional systems. Site permission has already been granted for 5 of the proposed systems. Individual radars are operated at one of three different frequencies that can be used to adjust range and resolution to provide both regional and nested sub-regional coverage. At present there are 8 long-range sites that provide shelf-wide coverage in three distinct clusters, New England, New Jersey, and North Carolina. These

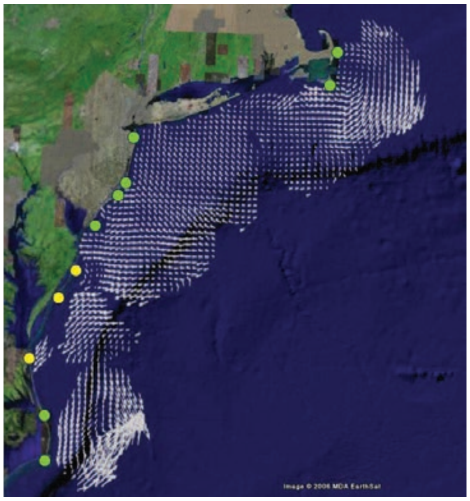

Figure 1. Coverage of the MAB Long range network. Green indicates operating sites, yellow indicates funded sites.

systems are in various levels of operation and development (Figure 1). A recent effort through NASA Wallops will provide three additional long-range sites in Virginia and Maryland. These new sites will fill the gap between North Carolina and New Jersey. Nested within this long-range network are several higher resolution systems strategically placed at the entrances to the largest estuaries within the region (Figure 2). These include the eastern and western Long Island Sound, New York Harbor, and Chesapeake Bay totaling 11 high resolution sites. There is currently an effort at the University of Delaware to instrument Delaware Bay with an additional 2 sites and at the University of Maryland to extend the Chesapeake Bay coverage north with 4 additional sites. In addition there are three sites in Block Island, RI, Moriches, NY, and Fire Island, NY that have permission granted with a Rutgers/Stevens collaborative proposal pending for the equipment.

Completed installation, validation and operation of the above radars has already resulted in over 50 person-years of local HF radar experience in the Mid-Atlantic. The experience covers the full range of skills from installation to product delivery. Every piece of an end-to-end system has been individually demonstrated in the Mid-Atlantic. Leveraging this experience and the above infrastructure investment, the HF Radar operators in the Mid-Atlantic have outlined an efficient route to demonstrate a regional capability within the structure of an R-COOS for MACOORA.

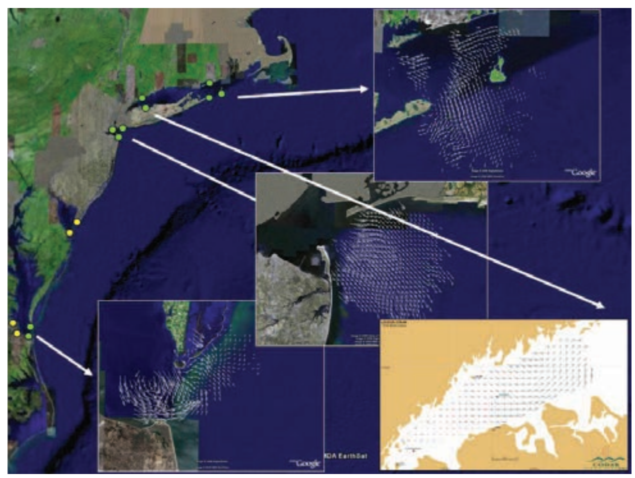

Figure 2. Nested high resolution coverage near the estuaries. Green indicates operating sites, yellow indicates funded sites.

3. PROPOSED EFFORT

The MAHFRC proposes a phased implementation of a regional scale HF Radar network that is scaleable to both the national and international level. The Mid-Atlantic Bight is an excellent test-bed for this because most of the HF radar systems are already in place but are operated in small clusters at different resolutions by a variety of groups, each with different funding profiles and different interests. MACOORA already provides a forum for this distributed group of HF radar operators to set priorities with users. The HF Radar Consortium Pilot will enable these operators to provide MACOORA a regional product in response. The proposed phased approach will extensively leverage the existing radar infrastructure, including a NOAA investment in a HF radar regional computer server. It immediately demonstrates interactions with SECOORA to our south through the North Carolina sites and GoMOOS to our north through the Massachusetts sites. The phased approach enables a product to be generated now on a regular basis with radars of opportunity. This will jumpstart the process of building a full scale regional network by making a demonstration product available now for users to evaluate, identifying the key needs and gaps, and using this experience to direct further investment. To ensure future growth, the ONR-sponsored Radiowave Oceanography Workshop (ROW) provides an international forum for new HF Radar technology developers to interact with scientists. Similarly, the NOAA-sponsored Radar Operators Working Group (ROWG) provides an international forum for HF radar operators to share ideas and distribute workloads.

4. DATA MANAGEMENT

Radial Data Archive: The radial data from each site will be fed into a prototype data management system already funded through NOAA. A surface current mapping network is characterized by a tiered structure that extends from the individual field installations of HF radar equipment (a site), a local regional operations center which maintains multiple installations (a node), and centralized locations which aggregate data from multiple regions (portal). This data system development effort focuses on building robust node to node communications with centralized data repositories that are updated in real-time. Through the NOAA funding, Rutgers was selected as a repository for east coast radial data. NASA Wallops will also serve as a radial data node to mirror the system at Rutgers. Radial data collected during this pilot could easily be ingested into this structure to facilitate radial data combination over the entire region.

Total Vector Combination and Distribution: A prototype server for providing HF radar vector current fields has been developed through a collaboration between the University of Rhode Island (URI) and the Open source Project for a Network Data Access Protocol (OPeNDAP) organization (Holloway and Ullman, 2005). The OPeNDAP HF radar combining server directly will access the archived radials from the regional archive housed at Rutgers. Through this pilot, vector combination throughout the region will be calculated using an OPeNDAP radial server that will be installed at the HF radar archive that is proposed for the region. To facilitate use of the OPeNDAP combining server, a web-site will be constructed to provide a simple user-interface to define the user's desired spatial and temporal extent, as well as optional parameters available in the processing algorithms. In addition to the user-selectable archived data retrieval, real-time maps will be created over fixed regions within the Mid-Atlantic Bight. This vector combination and distribution system would be implemented in phase two of this project with a more consistent data stream.

Short Term Forecast Products: To allow the US Coast Guard and other users to begin incorporating HF radar based surface current forecasts in their operational procedures, in Phase 2 of this project we will implement the prediction system described by Ullman et al (2003) and O'Donnell et al (2005) throughout the Mid-Atlantic Bight and provide open access to the product in a format compatible with the USCG software. These data have already been incorporated into Coast Guard planning tools as part of a Coast Guard R&D center funded project.

4. SERVING NATIONAL IOOS NEEDS

Data products from the Mid-Atlantic network have already supported many applications including Coast Guard Search and Rescue, NOAA NWS forecasts, and scientific research. Data from this network would support all seven of the national IOOS needs. A brief presented by Josh Kohut is available on the web for more information (http://marine.rutgers.edu/cool/coolresults/2005/KohutOS22F_03.ppt).

Specifically:

Detecting and forecasting oceanic components of climate variability

Surf Zone Forecasts, NOAA National Weather Service

Presently, several NOAA National Weather Service (NWS) Weather Forecast Offices (WFOs) around the country issue rip current warnings as part of a daily surf zone forecast. Within each forecast is a three tiered rip current outlook. Forecasters at the Mount Holly WFO indicate that the model is data limited and more near-shore wave and current observations are needed to improve the daily rip current outlooks (James Ebberwine, NWS; personal communications). Data from existing components of the regional system are already being used in this near-shore forecast. The regional scale of the HF radar system proposed here would provide additional data to support similar effort along the entire coastline from Cape Cod, MA to Cape Hatteras, NC.

Facilitating safe and efficient marine operations

Safe Harbor Operations, NOAA PORTS

The NOAA National Ocean Service has a Physical Oceanographic Real-Time System (PORTS) program supports safe operations in and out of major ports along the coasts of the United States. Each PORT program provides nowcast and forecast information based on available in situ data. With new technology, real-time data can be sent to operator aboard the ships for more informed decision making. Five of the thirteen currently operating PORTS are located within the Mid-Atlantic Region. These include Narragansett Bay, New Haven, New York/New Jersey Harbor, Delaware River and Bay, and Chesapeake Bay. Data from this pilot would be available to the existing PORTS programs for full surface current coverage in and around the approaches to these estuaries. These data could provide near real-time surface current maps and be assimilated into the existing forecasts models for improved predictions.

Ensuring national security

Vessel Tracking, Department of Homeland Security

Recently the DHS completed its external review of over-the-horizon HF radar technology and determined that it is a cost-effective surveillance gap-filler between satellites with global coverage but low revisit intervals and line-of-sight microwave radars deployed near-shore. The cost effectiveness is achieved by deploying a distributed network of compact HF radars that are linked in a multi-static network. The Office of Naval Research (ONR), the Department of Defense (DoD) Counter NarcoTerrorism Project Office (CNTPO) and the Department of Homeland Security (DHS), through a continuing series of research grants, have established the Mid-Atlantic as the U.S. testbed for over-the-horizon vessel tracking technology development. The approach is to expand CODAR compact HF Radar technologies for dual-use current mapping and vessel tracking applications.

Managing resources for sustainable use

Adaptive Sampling Strategies, NOAA Fisheries

Traditional fisheries or plankton surveys, based on fixed grid or stratified random designs, may not adequately describe conditions in the coastal ocean. These environments are driven by dynamic and episodic processes which can intensify, relax, or translate important features (fronts for instance) during a survey. Field studies should be aware of changes in the study area and should adapt to evolving conditions. Recent bioacoustic surveys in the New York Bight have made use of the near real-time surface current product to target specific features of interest. Remotely sensed CODAR, SST, chlorophyll and suspended sediment maps were relayed to the survey vessel from the Rutgers Coastal Ocean Observation Laboratory. Shipboard bioacoustics and hydrographic measurements augmented the remotely sensed data and enabled tracking and targeting of fronts, eddies, convergence/divergence zones during various sea states (high/low Hudson River discharge, coastal up/downwelling). Surface current products delivered in real-time have changed the way NOAA fisheries samples the coastal ocean. With these new data, sampling is more strategic and adaptable to the We argue that IOOS hold the promise for a new generation of fisheries surveys.

Preserving and restoring healthy marine ecosystems

Pollution Spill Response, NOAA OR&R/HAZMAT

Thousands of incidents occur each year in which oil or chemicals are released into the environment as a result of accidents or natural disasters. Spills into our coastal waters, whether accidental or intentional, can harm people and the environment and cause substantial disruption of marine transportation with potential widespread economic impacts. NOAA's Office of Response and Restoration (OR&R) Hazardous Materials Response Division (HAZMAT) provides scientific expertise to support an incident response and initiates natural resource damage assessment. Through this pilot, high resolution surface current maps near the estuary mouths and shelf-wide regional scale surface current map will be available to operators and scientists for incorporation into operational tools used during spill response. These data have been and could be incorporated into existing forecast systems (GNOME).

Mitigating natural hazards

Storm Response, NOAA National Hurricane Center & National Weather Service

Throughout the year significant storms including tropical storms, Hurricanes and Nor'easters impact the Mid-Atlantic region. These storms have the potential to cause significant coastal flooding and erosion. The surface current response to these storms as mapped by a fully nested CODAR network would provide data for both analysis and assimilation into numerical models for improved prediction. Data from existing systems in this network have already supported scientists of the NWS during the passage of a strong nor'easter in 200? And a tropical storm in 1999. Through this pilot the coverage area would be extended to include the entire area with more complete representation of the ocean response to these significant atmospheric systems.

Ensuring public health

Search and Rescue, United States Coast Guard, Office of Search and Rescue

In 2002, the USCG Research and Development center sponsored an investigation of the utility of HF radio sensed of coastal circulation to improve the prediction of target drift in search and rescue operations. That project (see Ullman et al, 2003) developed an operational algorithm to transform observations from Block Island Sound and the adjacent continental shelf into forecasts of the circulation. The forecasts exploit the periodicity of the tide and the serial correlation in the residual motion to forecast the current 24 hours into the future. These forecasts were then used to predict the drift of search and rescue targets. In a subsequent project, (O'Donnell et al, 2005) demonstrated that the prediction algorithm could readily be applied to data from new area, a section of the Middle Atlantic Bight where Rutgers University operate a CODAR network. Forecasts and uncertainties were then provided to the developers of the USCG's new search planning tool (SAROPS) so that the new capabilities could be rapidly integrated to their operations. Tests were conducted using drifters deployed in Block Island Sound and demonstrated to search planners at USCG Group Moriches. Demonstrations have already shown that the observations and short term statistical forecasts can be injected directly into current Coast Guard search planning tools. Results indicated that this infrastructure has the potential to be a valuable asset to the USCG search and rescue mission. Operational use of this technology awaits the development of a sustainable infrastructure for the observation and prediction system.

6. LITERATURE

1. Holloway, D. and D. Ullman, 2005. Seamless access to surface current vectors from the IOOS HF radar backbone, *OCEANS 2005*, MTS/IEEE Conference proceedings. (in press).
2. O'Donnell, J., D. Ullman, M. Spaulding, E. Howlett, T. Fake, P. Hall, I. Tatsu, C. Edwards, E. Anderson, T. McClay, J. Kohut, A. Allen, S. Lester, and M. Lewandowski (2005). Integration of Coastal Ocean Dynamics Application Radar (CODAR) and Short-Term Predictive System (STPS) Surface Current Estimates into the Search and Rescue Optimal Planning System (SAROPS). U.S. Coast Guard Technical Report DTCG39-00-D-R00008/HSCG32-04-J-100052
3. Ullman, D., J. O'Donnell, C. Edwards, T. Fake, D. Morschauser, M. Sprague, A. Allen, LCDR B. Krenzien, (2003). Use of Coastal Ocean Dynamics Application Radar (CODAR) Technology in U. S. Coast Guard Search and Rescue Planning, US Coast Guard report CG-D-09-03.

A Nested Multi-static HF Radar Testbed for the New York Bight and Beyond

Josh T. Kohut, Scott M. Glenn, Hugh J. Roarty, and Oscar M. Schofield

Abstract— **Surface currents are envisioned to be an integral component of the Integrated Ocean Observing System (IOOS) and High Frequency (HF) radar technologies provide the means to measure these data across multiple scales. The Rutgers University Coastal Ocean Observation Lab (COOL) has continuously operated a nested network of HF radars since 1998 as part of a sustained coastal observatory centered on the New York Bight. Components of this network include 25 MHz, 13MHz, and 5 MHz Tx /Rx shore stations and offshore buoy mounted Tx stations. These components are linked through GPS synchronization technology to provide fully nested multi-static surface current coverage. Data from these systems are supporting a growing number testbed activities and large science campaigns. Testbed activities focus on extending the present surface current mapping coverage closer to the beach with the development of new nearshore wave and current applications. Additional software and hardware modifications are beginning to extend the environmental monitoring to full maritime domain awareness by transitioning the sites to a dual-use mode that include hard target detection and tracking.**

The HF radar data has most recently supports two science campaigns, the Shallow Water 2006 (SW06) Joint Experiment supported by the Office of Naval Research and the Mid-shelf Front Experiment supported by the National Science Foundation (NSF). Both campaigns have used the HF radar as a resource for adaptive sampling. During the SW06 experiment, HF radar data was incorporated into daily reports along with other observation and forecast data to support the science fleet offshore. In addition to the adaptive sampling application, the mid-shelf front experiment takes advantage of the 5.5 year dataset within the study site. Long term means show a significant cross-shelf transport pathway south of the Hudson Shelf Valley that could possibly feed the mid-shelf front.

These Rutgers systems fit into a larger effort across the entire Mid-Atlantic Bight (MAB) region from Cape Hatteras, NC to Cape Code, MA. HF radar groups across this region have now formed a consortium for the operation and maintenance of the entire network, including system hardware, data management, and product delivery. Through this consortium the existing pockets of systems, of which Rutgers is one, can be operated as one regional system that spans over 1000 km of coastline. This network consists of 11 long-range sites providing total vector coverage across a large portion of the region from Cape Hatteras NC to the apex of the New York Bight. Additional funded sites for Moriches, NY and Block Island, RI, will extend the coverage north to Cape Cod, MA and Nantucket MA. In addition there are four higher resolution sub-systems made up of 15 sites in operation in the Chesapeake Bay, New York Harbor, the Long Island Sound and the Delaware Bay estuaries. In addition to scientific research and education applications, the United States Coast Guard Research and Development Center has identified the Mid-Atlantic Bight as a testbed for the new search and rescue planning tool, SAROPS.

Index Terms—**Coastal Ocean Processes, HF Radar, Ocean Observing Systems, Remote Sensing.**

I. Introduction

High Frequency (HF) radar derived real-time surface current maps are envisioned to be an integral component of the Integrated Ocean Observing System (IOOS). A national committee on surface current mapping, supported by OCEAN.US, has already outlined a structural plan to implement a national HF radar network. This plan separates the national network into regional centers responsible for the operation and maintenance of the systems. Recently MACOORA, the Mid-Atlantic Coastal Ocean Observing Regional Association, identified HF radar as an important integrating component of their envisioned Regional Coastal Ocean Observing System (R-COOS). A Mid-Atlantic HF Radar network would be capable of providing high resolution nested coverage within the five sub-regions while simultaneously linking the sub-regions together in one coastal network that covers the full range of the Mid-Atlantic coastal ecosystem. To implement a regional HF Radar network for the MACOORA R-COOS, radar operators in the region have formed the Middle Atlantic High Frequency Radar Consortium (MAHFRC).

II. Past Accomplishments

The first continuously operated systems in the Mid-Atlantic Bight (MAB) were deployed in 1998. Since that time the MAB has become the most heavily instrumented HF radar network in the world (Table 1). Academic and government groups currently operate 26 radar systems. Individual radars are operated at one of three different frequencies that can be used to adjust range and resolution to provide both regional and nested sub-regional coverage. At present there are 13 long-range sites that provide shelf-wide coverage across the shelf from Cape Cod, MA to Cpae Hatteras, NC (Figure 1). Nested within this long-range network are 13 higher resolution systems strategically placed at the entrances to the largest estuaries within the region (Figure 2). These include the

All authors are part of the the Rutgers University Coastal Ocean Observation Lab Team. Josh T. Kohut is the corresponding author (phone: 732-932-6555 x542; fax: 732-932-8578; e-mail: kohut@marine.rutgers.edu).

1-4244-0635-8/07/$20.00 ©2007 IEEE

TABLE I
EXISTING SITES IN THE MID-ATLANTIC BIGHT

Site Location	Site Operator	Site Frequency
Nauset, MA	U. Mass., Dartmouth	5 MHz
Nantucket, MA	Rutgers University	5 MHz
B lock Island, RI	Rutgers University	5 MHz
Block Island, RI	URI/UConn	25 MHz
Misquamicut, RI	URI/UConn	25 MHz
Montauk, NY	URI/UConn	25 MHz
Moriches, NY	Rutgers University	5 MHz
Great Captain Is, NY	UConn	25 MHz
Bayville, NY	UConn	25 MHz
Staten Island, NY	Stevens Institute	25 MHz
Breezy Point, NY	Rutgers University	25 MHz
Sandy Hook, NJ	Rutgers University	25 MHz
Sandy Hook, NJ	Rutgers University	13 MHz
Sandy Hook, NJ	Rutgers University	5 MHz
Loveladies, NJ	Rutgers University	5 MHz
Tuckerton, NJ	Rutgers University	5 MHz
Wildwood, NJ	Rutgers University	5 MHz
Cape May, NJ	U. Delaware	25 MHz
Cape Henlopen, DE	U. Delaware	25 MHz
Assateague, MD	CIT/NASA Wallops	5 MHz
Cedar Island, VA	CIT/NASA Wallops	5 MHz
Chesapeake BBT, VA	CIT/ODU	25 MHz
Norfolk, VA	CIT/ODU	25 MHz
Virginia Beach, VA	CIT/NASA Wallops	5 MHz
Duck, NC	UNC-CH	5 MHz
Buxton, NC	UNC-CH	5 MHz

eastern and western Long Island Sound, New York Harbor, Chesapeake Bay, Delaware Bay, and Block Island Sound. Completed installation, validation and operation of the above radars has already resulted in over 50 person-years of local HF radar experience in the Mid-Atlantic. The experience covers the full range of skills from installation to product delivery. Every piece of an end-to-end system has been individually demonstrated in the Mid-Atlantic. Leveraging this experience and the above infrastructure investment, the HF Radar operators in the Mid- Atlantic have outlined an efficient route to demonstrate a regional capability within the structure of an R-COOS for MACOORA.

III. APPLICATIONS

The major MARCOOS (Figure 1) products for Maritime Safety are the 2D surface current fields observed by the HF Radar network and predicted by the statistical and dynamical forecasts. The primary users are the USCG and NOAA HAZMAT. Both require surface current products to be delivered into centralized operation centers and loaded into tactical decision aids. USCG SAR users are the operational

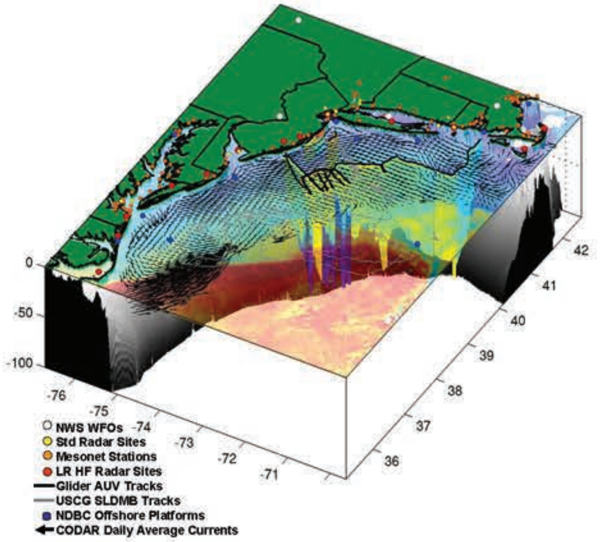

Fig. 1. The observing components of MARCOOS including the long range HF Radar coverage between Cape Cod and Cape Hatteras.

controllers that direct deployment of aircraft and vessels using an operational decision aid called SAROPS. SAROPS uses observed or predicted surface wind and surface current fields from the USCG's EDS to predict the trajectories of floating objects. During an actual event, or test, a cluster of a few hundred virtual objects is deployed in surface wind and current fields downloaded from EDS and allowed to drift over time. The cluster disperses based on the uncertainty estimates in the winds and currents. If SAROPS data has lower uncertainties there is lower dispersion in the cluster, a smaller search area, and greater likelihood for success. Coast Guard operational SAR controllers are trained in how to use SAROPS and get data from the EDS. No new training is required once the MARCOOS products are in EDS. NOAA HAZMAT operations have similar decision aids. HAZMAT is collaborating with the USCG to link EDS and HAZMAT oil

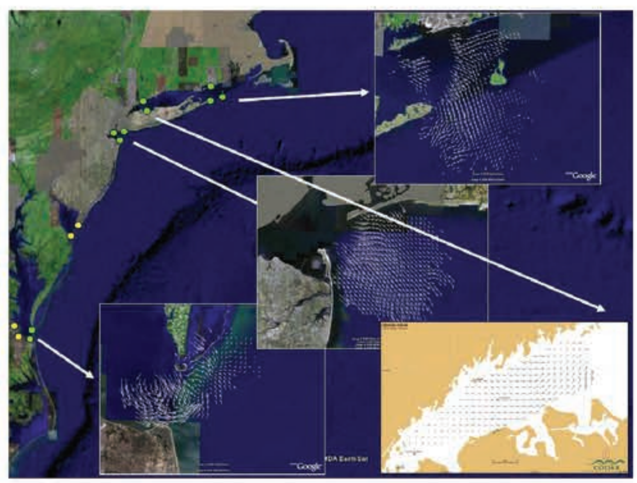

Fig. 2. Nested high resolution coverage near the estuaries.

spill drift models.

Other Maritime Safety products enabled by the HF Radar network are nearshore waves and alongshore currents being developed with SeaGrant. Where available, these products are *already* used by the Mount Holly WFO. The WFOs presently use observed and forecast surface waves to predict the probability of rip currents as low, medium or high. In the event of a nearshore search emergency, the direction of the alongshore drift is then the key unknown. Providing WFO forecasts currents will be a big step forward but will require outreach and training about wave and current products, and their relationship to rip current characteristics.

IV. Data Management

A. Radial Data Archive

The radial data from each site will be fed into a prototype data management system already funded through NOAA. A surface current mapping network is characterized by a tiered structure that extends from the individual field installations of HF radar equipment (a site), a local regional operations center which maintains multiple installations (a node), and centralized locations which aggregate data from multiple regions (portal). This data system development effort focuses on building robust node to node communications with centralized data repositories that are updated in real-time. Through the NOAA funding, Rutgers was selected as a repository for east coast radial data. NASA Wallops will also serve as a radial data node to mirror the system at Rutgers. Radial data collected during this pilot could easily be ingested into this structure to facilitate radial data combination over the entire region.

B. Total Vector Combination and Distribution

A prototype server for providing HF radar vector current fields has been developed through collaboration between the University of Rhode Island (URI) and the Open source Project for a Network Data Access Protocol (OPeNDAP) organization [1]. The OPeNDAP HF radar combining server directly will access the archived radials from the regional archive housed at Rutgers. Through this pilot, vector combination throughout the region will be calculated using an OPeNDAP radial server that will be installed at the HF radar archive that is proposed for the region. To facilitate use of the OPeNDAP combining server, a web-site will be constructed to provide a simple user-interface to define the user's desired spatial and temporal extent, as well as optional parameters available in the processing algorithms. In addition to the user-selectable archived data retrieval, real-time maps will be created over fixed regions within the Mid-Atlantic Bight. This vector combination and distribution system would be implemented in phase two of this project with a more consistent data stream.

Acknowledgment

The authors would like to acknowledge the efforts off all the participants in the Mid-Atlantic HF Radar Consortium stretching from Cape Cod, MA to Cape Hatteras, MA.

References

[1] Holloway, D. and D. Ullman, 2005. Seamless access to surface current vectors from the IOOS HF radar backbone, *OCEANS 2005*, MTS/IEEE Conference proceedings.

Surface current and wave validation of a nested regional HF radar Network in the Mid-Atlantic Bight

Josh Kohut, Hugh Roarty, Sage Licthenwalner, and Scott Glenn
Rutgers University
71 Dudley Rd.
New Brunswick, NJ 08901

Don Barrick and Belinda Lipa
Codar Ocean Sensors
1914 Plymouth Street,
Mountain View, CA 94043

Arthur Allen
United States Coast Guard
Office of Search And Rescue
1082 Shennecossett Road
Groton, CT, 06340-6096

Abstract— **The National High Frequency Surface Current Mapping Radar Network is being developed as a backbone system within the Integrated Ocean Observing System (IOOS). Of the core variables recognized in the IOOS Development Plan, two can be measured by High Frequency Radar (HFR): ocean surface currents and ocean surface waves. Rutgers University operates a nested multi-frequency network of HF Radar systems along the coast of New Jersey. The network provides near real-time current observations with varying coverage from the coast to the shelf break. This is a subset of the larger regional coverage of the 26 site Mid-Atlantic HF Radar Consortium. The primary goal of this consortium is to operate the regional system in a coordinated way to guarantee the delivery of quality ocean current and wave data.**

In this paper we present the validation of both wave and current observations measured with this nested network. Particular emphasis is placed on surface current comparisons with Coast Guard deployed surface drifters (SLDMBs) and nearshore wave comparisons with moorings. The Coast Guard comparisons have a specific focus on quantifying the uncertainty in the HF radar surface current estimates as applied to search and rescue operations. These metrics will be used to ensure that quality data is going to the Coast Guard and that this information is properly incorporated into existing search planning tools. The nearshore measurements focus on algorithm development projects to incorporate shallow water effects into the estimates of nearshore waves.

Index Terms—**Coastal Ocean Processes, HF Radar, Ocean Observing Systems, Remote Sensing.**

I. Introduction

Saving lives at sea and on beaches is a national IOOS priority that is supported by Memoranda of Understanding (MOU's) between NOAA and the USCG to collaborate in the establishment of a national HF Radar network. The nation's oldest & largest triple nested HF Radar network is in the 26-site MA HF Radar Consortium (MAHFRC). The Mid-Atlantic coverage is distinguished by its nested coverage of important bays and sounds. The MAHFRC network is a testbed for the (1) NOAA HF radar research for bistatic operations, which will improve surface current mapping in complicated coastal regions, (2) USCG for evaluation of new products for SAROPS, and (3) DHS/Counter NarcoTerrorism for development of dual-use vessel tracking capabilities. Best practices developed in the MA can be spread nationwide through the NFRA, NOAA QARTOD, and ROWG. In this paper we present validation of HF radar derived surface current and wave fields to improve offshore Search and Rescue (SAR) and nearshore rip current warnings.

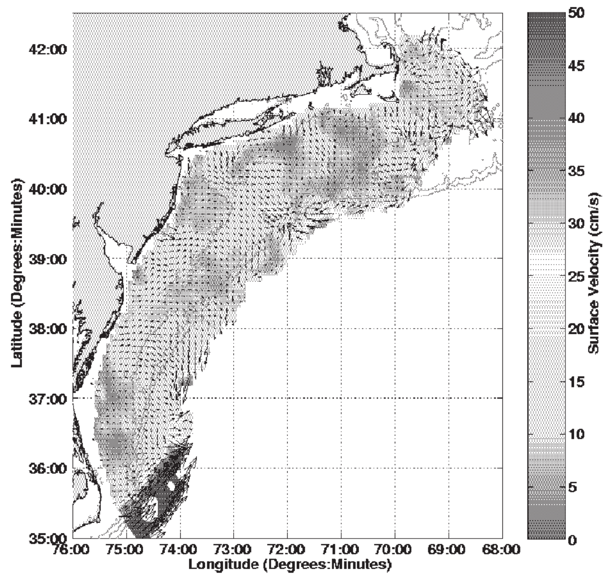

Figure 1. 24 hour average surface current map from the Long-Range MARCOOS CODAR Network.

Nationally, the Coast Guard receives an average of 13 SAR calls per day, of which 10 are successful rescues. To reduce the lives lost, the critical USCG need is to optimize SAR operations to minimize search time. SAROPS uses observed or predicted surface wind and surface current fields from the USCG's Environmental Data Server (EDS) to predict the trajectories of floating objects. During an actual event, or test, a cluster of a few hundred virtual objects is deployed in surface wind and current fields downloaded from EDS and allowed to drift over time. The cluster disperses based on the uncertainty estimates in the winds and currents. If SAROPS data has lower uncertainties there is lower dispersion in the cluster, a smaller search area, and greater likelihood for success. The analysis presented here is the result of a partnership with the U.S. Coast Guard R&D center in which expired SLDMBs were deployed in a series of targeted experiments to evaluate the growing data coverage of the HF radar network off the coast of the Mid-Atlantic Bight.

Rip currents are the number one cause of ocean drowning and rescue incidents along the coasts of the United States. According to the United States Lifesaving Association (USLA), 71% of the total surf zone rescues, 12,137 incidents, in 2003 were due to rip currents. Rip currents are strong near-shore features with cross-shore velocities on the order of 1 m/s and along-shore scales of tens of meters. Presently, several NOAA National Weather Service (NWS) Weather Forecast Offices (WFOs) around the country issue rip current warnings as part of a daily surf zone forecast. Within each forecast is a three tiered rip current outlook. The local WFO in Mount Holly New Jersey utilizes a linear regression wave model and local winds to categorize rip current risk as low, moderate, or high. Forecasters at the Mount Holly WFO indicate that the model is data limited and more near-shore wave and current observations are needed to improve the daily rip current outlooks (James Ebberwine, NWS; personal communications).

II. Background

A. HF Radar Surface Current Processing

High Frequency (HF) radar systems, typically deployed along the coast use Bragg peaks within a signal (3 ~ 30 MHz) scattered off the ocean surface to calculate radial components of the total surface velocity at a given location [1]. Crombie recognized that these peaks were the result of an amplification of a transmitted wave by surface gravity waves with a wavelength equal to half that of the transmitted signal [2]. A signal scattered off a wave and back toward the antenna will be in phase with a signal that traveled to the next surface wave (1/2 transmit wavelength further) and returned to the original wave (another 1/2 transmit wavelength). The frequency of the backscattered signal will be shifted depending on the velocity of the scattering surface. Using linear wave theory the phase speed of the surface waves can be separated from the total frequency shift, leaving only that shift due to the surface current. Over a given time period, sites along the coast generate radial component maps of the surface current with typical resolutions on the order of 1-6km in range and 5 degrees in azimuth. The CODAR-type systems discussed here are direction finding systems that use a three element receive antenna mounted on a single post to determine the direction of the incoming signals. The angular resolution, set in the processing, is typically 5 degrees. Since the Doppler shift can only resolve the component of the current moving toward or away from the site, information from at least two sites must be geometrically combined to generate total surface current maps. For the purpose of this paper, all surface current comparisons will focus on the long-range (5 MHz) component of the network.

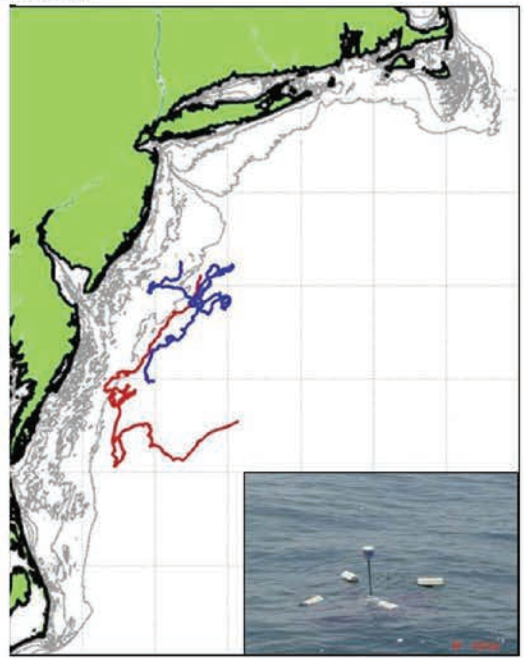

Figure 2. Tracks of the SLDMB deployment in February, 2007. A picture of a SLDMB just after deployment is shown in the lower right.

Every hour the available radial vector maps are combined into a single total vector map (Figure 1). All radial component vectors within 10 km of each grid point were used in the combination. A total vector was only generated if at least 3 radial vectors from at least two remote sites were used in the combination. The uncertainty of the combined totals can be separated into radial vector uncertainty and geometric uncertainty. The geometric uncertainty is based on the angles of the radial component vectors. The further the radials are from orthogonal, the larger the uncertainty. This is described by Chapman et. al. [3] as Geometric Dilution Of Precision (GDOP). These uncertainties increase along the baseline between the coastal sites as well as well offshore. In these regions the radial component vectors are resolving the along-shore and cross-shore velocity components, respectfully. Without a better representation of the orthogonal velocity component, error is introduced in the total vector estimate at the combine step. The relative magnitude of the geometric uncertainty was calculated at each grid point for every current map [4]. Using this scalar as an indicator of the magnitude of the geometric contribution to the uncertainty, data subject to poor geometry were eliminated. All data below a threshold of 1.25 was included in the analysis. This threshold was chosen based on qualitative analysis of previous data.

B. HF Radar Wave Processing

Waves are measured with HF radars from the second-order portion of the echo spectrum. This is distinctly separated from the first-order Bragg peaks used for current mapping. The derivation of the classic model presently employed by several groups for HF wave measurements was done 35 years ago [1]. Lipa first showed how this echo could be inverted to give wave spectral information, and it was first applied to narrow-beam phased array systems [5]. The methods were next extended to the CODAR compact crossed-loop antenna [6]. Since these data are derived from the second order spectrum, the lower signal to noise ratio limits data closer to the coast. The CODAR operational software is based on fitting the radar data with a model of the ocean wave spectrum. Second-order data is collected from the four second-order sidebands of hourly averaged cross spectra. Least-squares fitting of the Pierson-Moskowitz model for the ocean wave spectrum to the radar Fourier coefficients are used to derive estimates of the significant wave height, centroid period and direction. An advantage of this method is that it uses all available data above the noise, including cases where only one sideband is usable. Depending on the operating frequency of the HF radar site, the second order region of the Doppler spectrum becomes saturated for given wave conditions. For the 25 MHz system, any sea state over 4 m significant wave height will saturate the second order spectrum. For the longer range 5 MHz system, this saturation occurs at wave heights over 20m. It is important to note that the waves observed by the CODAR system are limited to those felt by the Bragg waves. As a result, the shortest period wave included in the HF radar data is 5 seconds. This lower bound will increase with increased noise. Additionally, because these are direction finding systems, the wave measurements are an average of the wave field over a measurement arc. The CODAR system has and continues to provide wave spectra, significant wave height, peak period, and direction from the range cells within several kilometers of the coast.

III. Results

A. Surface Current Validation

Self Locating Data Marker Buoy (SLDMB) position data was used to evaluate the CODAR observations. The SLDMBs are surface drifters drogued to one meter depth. Throughout the deployment, velocities based on two SLDMB positions one hour apart were calculated every half hour. These surface velocity estimates were compared to the radial and total vector estimates of the Long Range CODAR network off the New Jersey coast [7],[8]. For both the radial and total vector comparisons, the velocity average was set to match the sampling of the CODAR. The SLDMB data discussed here are from two SLDMBs deployed on opposite sides of the mid-shelf front off the southern coast of New Jersey in February 2007. Horizontal shears associated with the mid-shelf front lead to a large separation between the two with the offshore SLDMB moving quickly to the southwest toward North Carolina (Figure 2). The inshore SLDMB, on the other hand, spent over 40 days within the footprint of 4 remote CODAR sites including Loveladies, NJ, Tuckerton, NJ, Wildwood, NJ, and Assateague, MD. This offers a unique opportunity to look at relatively long time series of surface current data to compare to radial data from a series of sites along the Mid-Atlantic coast. For much of the comparisons discussed here, the sample of concurrent velocity pairs between the SLDMB and CODAR exceeds 900.

For the purpose of this paper we focus on the radial component vectors measured at the Loveladies, Tuckerton and Wildwood NJ CODAR sites as they had the longest data coverage overlap with the SLDMB. For all three sites the SLDMB spent almost the entire period in the 50% or greater coverage area. For each time step the velocity estimates from the SLDMB track was rotated into a coordinate system aligned with the radial direction of each remote site. The rotated SLDMB velocity was then directly compared to the observed CODAR radial current vector. Care was taken to ensure that the averaging time of both the CODAR and SLDMB current estimate matched. For all three sites, the number of comparison points in the sample exceeded 860. Each site shows a strong correlation between the SLDMB and CODAR with an RMS (r^2) ranging from 11.5 (0.62) to the north and 10.2 (0.79) to the south. A time series shows that both are resolving both the larger scale tidal and sub tidal variability throughout the 40-day deployment (Figure 3).

The east (U) and north (V) components of the SLDMB

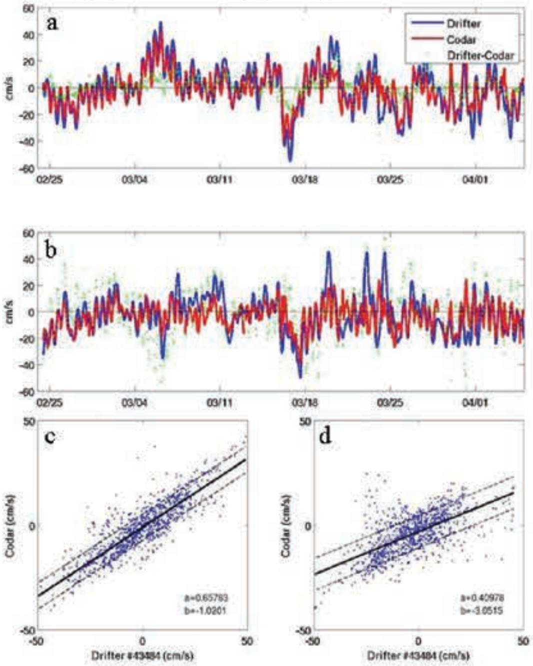

Figure 3. Radial vector time series (split between panel a & b) and (c) scatter of the radial component vector relative to Wildwood New Jersey

velocity estimates are directly compared to the geometrically combined radials from CODAR sites along the New Jersey and Maryland coasts. The radials were combined using the community toolbox with an averaging radius of 10 km. Vectors with a mapping error of greater than 1.25 were excluded from the analysis [4]. Again the data coverage was excellent with 929 velocity pairs throughout the deployment. As with the radial comparisons we see consistency in both the tidal and sub-tidal velocities, (Figure 4) with RMS (r^2) of 8.5 (0.87) and 11.7 (0.63) for the east and north components respectively. The disparity between the east and north component vectors comes for the geometry of the CODAR combination. Since the sites are all oriented along a roughly north/south coastline, the radial component vectors better resolve the east component of the total velocity compared to the north component.

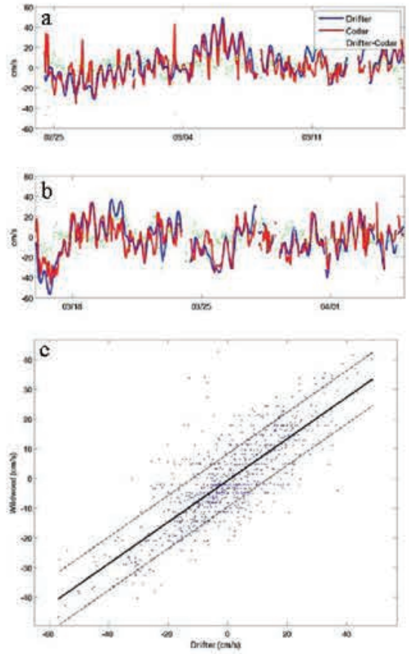

Figure 4. Total vector time series and scatter for the East (a,c) and North (b,d) components

B. Nearshore Wave Validation

The direct comparison results presented here focus on the 25 MHz site in Breezy Point, NY. Time periods were selected that provided simultaneous far-field and near-field observations between December 22, 2005 and January 12, 2006. This time was selected because far-field measurements from the NOAA NDBC buoy 44205 and a bottom mounted AWAC were both available (Figure 5). The NOAA buoy, located 70 km southeast of Breezy Point provided the far field observations and the AWAC deployed within the Breezy Point measurement cell provided the near field measurements. All data were averaged to match the hourly sampling of the HF radar observations.

All three sensors show a mean significant wave height on the order of 1m, with slightly higher waves offshore and smaller waves inshore. The CODAR wave heights compared to the far-field and near-field sensors show significant correlation on the order of 0.65 and 0.71 with an RMS on the order or 0.50-0.75 m (Figure 6). The time series shows that all three sensors are capturing the events with the CODAR observed wave heights falling somewhere between the smaller nearshore waves and the higher offshore waves. The correlation between the CODAR wave period and those of the two in situ sensors is not as strong as seen in the significant wave height. With a mean of 9.25s, the CODAR measurement is biased toward longer period waves. Since the CODAR measurement is based on second order region of the spectrum, it is limited to longer period waves modulating the surface Bragg waves. For that reason, the CODAR measurement is restricted to waves with a period of at least 5 seconds. In direction, the CODAR mean is biased toward waves coming from the southeast. This is likely related to the location of the in situ sensors. Both sensors deployed off the coast, have opportunities to sample waves from a full 360 degree swath. The CODAR, on the other hand, is deployed along the coast and limited to onshore waves only. As the waves approach the coast, shallow water refracts the waves normal to the coast (i.e. southeast).

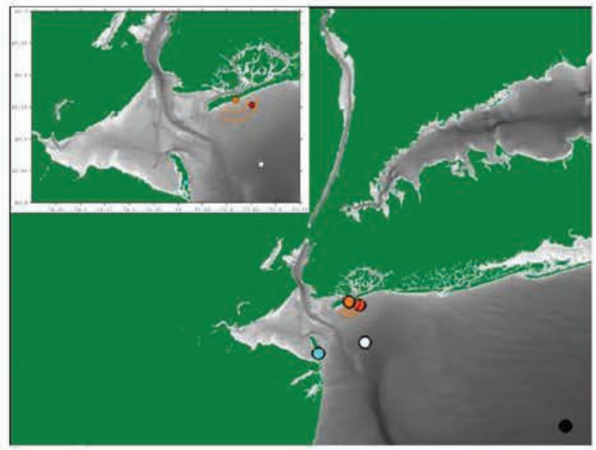

Figure 5. Map showing the locations of the measurement sites, including NOAA NDBC buoy 44205 (black), 25 MHz at Breezy Point (orange), and the AWAC (red). Range cells are also shown for Breezy Point.

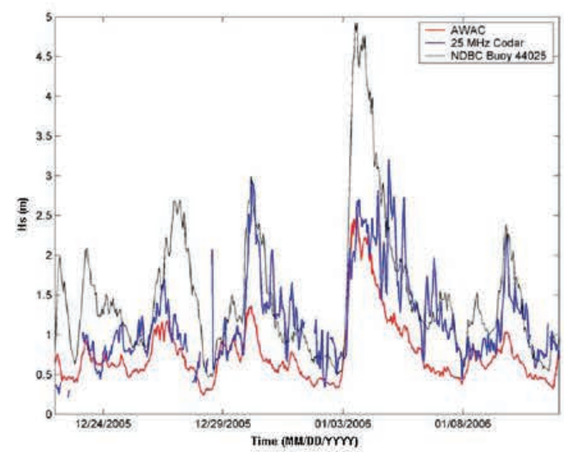

Figure 6. Time series of significant wave height measurements from the 25 MHz CODAR (blue), buoy 44025 (black), and the AWAC (red).

IV. Summary

The SLDMBs have offered an excellent opportunity to better understand both the subgrid scale variability and the uncertainty in the radial and total vector component surface current estimates from an HF radar system. Direct comparisons to CODAR show RMS differences on scales ranging from 8-11 cm/s. Through these deployments and others like them we can properly evaluate these new data streams so that they can be properly integrated into the new search and rescue tool (SAROPS). As part of a recently funded NOAA project (MARCOOS), an even larger HF radar footprint will be made available to the Coast Guard stretching from Cape Cod, MA in the North to Cape Hatteras, NC in the south (Figure 1). In addition these data will be incorporated into four forecast systems. These forecasts will be evaluated against future SLDMB deployments so that they too can be incorporated into SAROPS.

For the near-shore wave observations, the effect of shallow water is to (i) increase the wave height, (ii) affect the wave period, and (iii) to refract the long waves to move more perpendicular to the depth contours. We see evidence of these effects in these baseline comparisons. The RMS waveheight at 25 MHz falls between the nearshore AWAC and the far offshore NOAA buoy. This makes sense physically; one would expect higher waves (all directions) on average, further offshore. We also see a tendency for the mean wave direction to be aligned more perpendicular to the coast in the CODAR data compared to the offshore and nearshore in situ data. These results and others have prompted a focused project to incorporate these bottom effects into the CODAR wave processing software. A project funded by New Jersey Sea Grant will test these new algorithms with a similar multi-frequency approach discussed here including near-field and far-field wave measurements. The baseline evaluation discussed here will be used to evaluate these new algorithms that account for shallow water properly in extracting waves from the 2nd-order echo.

Acknowledgment

The authors would like to acknowledge the efforts off all the participants in the Mid-Atlantic HF Radar Consortium stretching from Cape Cod, MA to Cape Hatteras, MA. We would also like to thank the U.S. Coast Guard R&D Center and Office of Search and Rescue who provided their SLDMBs and expertise in the experiment setup and analysis. Dave Ullman (URI) provided valuable input in the SLDMB deployment design and interpretation of the track data compared to the HF Radar fields. We would also like to thank the crews of the R/V Endeavor and Sorenson Miller for their help with the deployments. The wave validation work is supported by two separate projects funded through NOAA.

References

[1] Barrick, D.E. , M.W. Evens and B.L. Weber, 1977: Ocean surface currents mapped by radar. *Science*, 198, 138-144.

[2] Crombie, D.D., 1955: Doppler spectrum of sea echo at 13.56 Mc/s. *Nature*, 175, 681-682.

[3] Chapman, R.D. and H.C. Graber, 1997: Validation of hf radar measurements. *Oceanography*, 10, 76-79.

[4] Gurgel, K. W., 1994. Shipborne measurement of surface current fields by HF radar. *L'Onde Electrique*. 74, 54-59.

[5] Lipa, B.J. and D.E. Barrick. 1983: Least-squares methods for the extraction of surface currents from CODAR cross-loop data: application at ARSLOE. IEEE J. Ocean. Engr, OE-8, 226-253.

[6] Lipa, B.J. and D.E. Barrick, 1986: Extraction of sea state from hf-radar sea echo: mathematical theory and modeling. Radio Sci, 21, 81-100.

[7] Kohut, J. T. and S. M. Glenn, 2003. Calibration of HF radar surface current measurements using measured antenna beam patterns. J. Atmos. Ocean. Tech., 1303-1316.

[8] Kohut, J. T., Glenn, S. M., Chant, R. J. 2004. Seasonal current variability on the New Jersey inner shelf. Journal of Geophysical Research. 109, C07S07, doi: 10.1029/2003JC001963.

The Mid-Atlantic Regional Coastal Ocean Observing System: Serving Coast Guard and Fisheries Needs in the Mid-Atlantic Bight

Hugh Roarty, Josh Kohut and Scott Glenn
Rutgers University
71 Dudley Road
New Brunswick, NJ 08901 USA

MARCOOS Principal Investigators
University of Delaware
700 Pilottown Road
Lewes, DE 19958

***Abstract*- High Frequency (HF) Radar is an established central component of Mid-Atlantic Regional Coastal Ocean Observing System (MARCOOS). The HF Radar network currently consists of 26-sites with multistatic and nested coverage from Cape Hatteras to Cape Cod with high-resolution coverage of the four major estuaries in the region. This network provides regional surface current maps to improve United States Coast Guard search and rescue operations, mitigate hazardous material spills as well as improve rip current forecasting. The radial current files are aggregated into the national data archival system. Specific applications include assimilation into a statistical model and three dynamical models with the goal of improving surface current forecasts for search and rescue. Test bed activities will routinely compare these forecasts with drifters released into the coverage area to determine the parameters necessary for inclusion into the Coast Guard search-planning tool, SAROPS. The MARCOOS HF Radar network has moved from small isolated systems to a single integrated regional system, a model that is being scaled around the world.**

I. INTRODUCTION

High Frequency (HF) Radar derived real-time surface current maps are envisioned to be an integral component of the Integrated Ocean Observing System (IOOS). A national committee on surface current mapping, supported by OCEAN.US, has already outlined a structural plan to implement a national HF Surface Current Mapping (SCM) network. This plan separates the national network into regional centers responsible for the operation and maintenance of the systems. Recently MACOORA, the Mid-Atlantic Coastal Ocean Observing Regional Association, identified HF radar as an important integrating component of their envisioned Regional Coastal Ocean Observing System (R-COOS). A Mid-Atlantic HF Radar network is now capable of providing high resolution nested coverage within the five sub-regions (Chesapeake Bay, Delaware Bay, New York Bight, Long Island Sound and Massachusetts and Rhode Island Bays) while simultaneously linking the sub-regions together in one coastal network that covers the full range of the Mid-Atlantic coastal ecosystem (Figure 1).

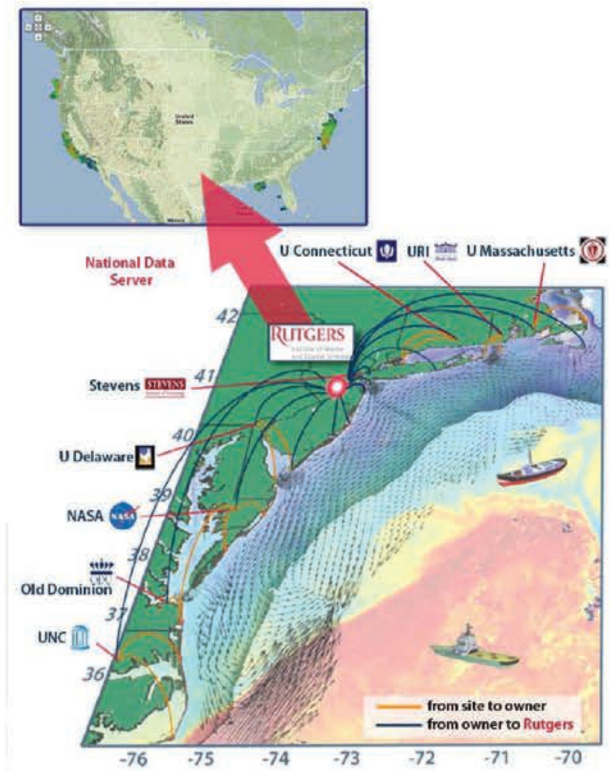

Figure 1: Map of MARCOOS HF Radar Network. The data flow is demonstrated as the movement of the radial data file from the radar site to node (orange line) and from node to central hub (blue). The radials are combined at the central hub and then displayed on the National Network.

MACOORA formed the Mid-Atlantic Regional Coastal Ocean Observing System (MARCOOS) to generate quality controlled and sustained ocean observation and forecast products that fulfill user needs. MARCOOS products will support the two priority regional themes and provide critical regional-scale input to MACOORA's nested sub regional efforts on Coastal Inundation and on Water Quality. MARCOOS will accomplish this by coordinating an extensive array of existing observational, data management, and modeling assets to generate and disseminate real-time

1-4244-1486-5/08/$25.00 ©2008 IEEE

data, nowcasts and forecasts of the ocean extending from Cape Cod to Cape Hatteras.

This first implementation phase of MARCOOS will be an end-to-end regional ocean data acquisition, management, modeling and product-generation system in response to region-wide user needs in the thematic areas of Maritime Safety and Ecological Decision-Support. MARCOOS regional products will support the production of higher-resolution products that are being proposed by MACOORA sub-regional groups in response to the thematic areas of Coastal Inundation and Water Quality. MARCOOS will augment existing federal backbone products by leveraging its extensive existing assets. By coordinating, sustaining, and expanding ongoing ocean observing and forecasting activities, regional-scale data and products will be available in real time across the full Mid-Atlantic (MA) region and extending into the Bays and Sounds. The data will be assimilated into 2D statistical and 3D dynamical ocean forecast models, driven by NOAA NCEP (National Center for Environmental Prediction) standard atmospheric forecasts that include a dedicated NOAA-WRF (Weather Research and Forecasting) regional Sea breeze resolving forecast. Datasets and forecasts will be delivered into operational decision making systems, such as USCG Environmental Data Server (EDS) and Search and Rescue Optimal Planning System (SAROPS), through IOOS-compatible automated data servers for forecasting applications and a MARCOOS website. Outreach activities will extend products to support ongoing NWS rip current forecasting projects and refine products for the fishing community.

II. History of National SCM System

Ocean.US created the Surface Current Mapping Initiative (SCMI) in September 2003. A steering committee was established to identify the technical and managerial challenges associated with the creation of a national SCM network. The SCMI report recommends 2 technicians to maintain and operate every 5 HF radar stations. The committee also recommended a ratio of 5 sites per node where a node is used to designate the collection of sites operated by a group. The committee further recommended that pilot projects would be a good vehicle for the development of operational systems and standards. [1]

The Alliance for Coastal Technologies convened a national meeting in March 2004 to further discuss the application of SCMs to an Integrated Ocean Observing System. One recommendation of the workshop was to embark on a regional large-scale pilot study integrating existing HF radar systems to demonstrate the challenges involved in data exchange and reliability. [2]

In response to these national level meetings, and the resulting call for regional scale demonstration projects, the Mid-Atlantic High Frequency Radar Consortium (MAHFRC) was formed. As the initial coordinating body for the numerous independent HF Radar owners and operators in the Mid-Atlantic, a three-Phased plan was developed to implement a regional network that met SCMI standards. Phase 1 assumed that the many HF radars in the region would remain independent in their operation and funding, but that we would agree to share radial level data with a central facility to produce a regional-scale surface current product and provide it to users as available. Phase 2 assumed that an initial multi-year demonstration period could be funded to provide the equivalent of 1 full time regional coordinator, 3 full time field technicians supporting operations in the northern, central and southern portions of the region, provide \$10,000 in annual support for each site to cover utilities, communications, and basic maintenance, and to maintain a regional spares fund to respond to outages such as the inevitable lightening strikes. After the initial demonstration period and the potential reevaluation of SCMI standards based on lessons learned, Phase 3 operations would be proposed at the regional level required for a sustained national network.

III. MARCOOS HF Radar Network Management

MACOORA was formed in 2005 as one of 11 Regional Associations making up the regional component of the U.S. Integrated Ocean Observing System. MACOORA initially identified over 20 independent and ongoing local or subregional ocean observing system efforts across their region. The MAHFRC plan to coordinate the HF Radar component of many of these individual programs and construct a regional-level system was presented to MACOORA and endorsed as having a high probability of successfully demonstrating the added-value of the regional approach, providing a pathfinder mechanism for more complicated regional coordination in the future. Numerous MACOORA user meeting break out sessions were used to identify potential end-to-end applications for future implementation with the regional-scale HF Radar network, including Coast Guard Search and Rescue, oil spill response, water quality, coastal flooding, and fisheries.

MARCOOS was MACOORA's response to the first national competitive merit-based call for the development of Regional Coastal Ocean Observing Systems (RCOOS). Funding of MARCOOS by NOAA IOOS in 2007 enabled MAHFRQ to jump from its Phase 1 voluntary level to the intermediate Phase 2 level of regional coordination (Figure 1). To produce regional scale products, the MARCOOS effort relies heavily on the existing infrastructure previously acquired and deployed at various times since 1996 as part of the subregional ocean observing systems.

For the first three-year increment of IOOS funding MARCOOS has sectioned the Mid-Atlantic HF Radar Network into 3 regions a northern, central and southern region. There is one fully funded operator responsible for the sites in their respective region. The operators are geographically separated. How can this separation be overcome? Several tools have been implemented to bridge this geographic divide. A monthly conference call has been set for operators to communicate and share pressing issues. A collaborative development web site was created for the sharing of documents and as an archive of communications during the project. An advanced HF radar operator training course was conducted by Codar Ocean Sensors from February 18-22, 2008. The agenda was user driven developed in collaboration with the manufacturer of the HF radar. A database was created where critical information on each site was centrally accessible and stored for a unified regional system. Best practices documents on radar antenna patterns and quality assurance and quality control of radial data were created to be shared among the HF radar operators.

IV. MARCOOS HF Radar Data Aggregation and Products Development

At present 26 radar sites are operating in the MARCOOS region. Radial current data from each site is first collected at the local central computer sites for each of the 9 operators. The radial data is then aggregated at Rutgers as part of the National HF Radar data server supplied by NOAA. Locally, the radial data is used to produce a regional scale product that covers coastal waters from Cape Cod to Cape Hatteras, and to produce local high resolution products in each of the bays (Figure 2). This data is currently displayed on the Rutgers Coastal Ocean Observation Lab website (http://marine.rutgers.edu/cool) to provide users a quick look at the datasets. The total vector fields are then made available for assimilation by the University of Connecticut's Short Term Prediction System (STPS) and via OPeNDAP servers for assimilation into an ensemble of 3 dynamical forecast models run by Rutgers, Stevens Institute of Technology, and U. Massachusetts – Dartmouth. Statistical and dynamical forecasts also can be viewed on the originator's websites, but more importantly are then transferred to the US Coast Guards Environmental Data Server (EDS) by Applied Science Associates. Once in EDS, the data and forecasts undergo a year test phase within the Coast Guard's new Search and Rescue Optimal Planning System (SAROPS). After the demonstration period at the Coast Guard office of Search and Rescue, the accepted data and model forecasts are available in the field offices that have access to SAROPS.

V. Success Stories

The ACT workshop [2] listed 13 different applications of SCMs. MARCOOS has utilized the existing HF radar network for 6 of those 13, Search and Rescue, Sewage

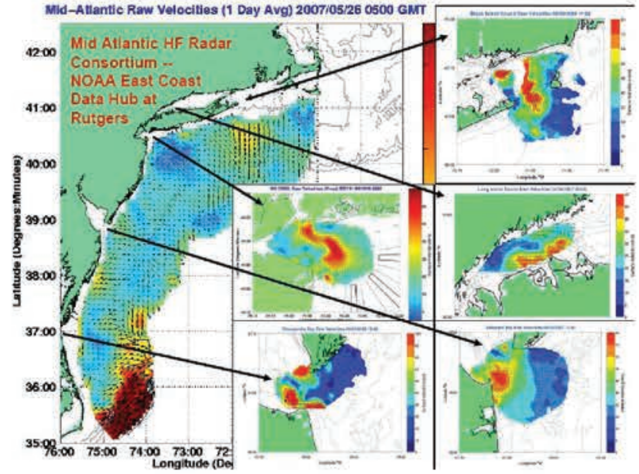

Figure 2: Initial data products from the MARCOOS HF Radar Network. Aggregated radial data is assembled into total vector products on a low resolution 6 km regional grid covering the full continental shelf between Cape Hatteras and Cape Cod. Total vector products on high resolution 1 km grids are produced in 5 nested subdomains.

Spills, River Discharge Plumes, Rip Currents, Fish Survival Recovery and Larval Invasive Species. Two stories of these applications are shared here.

A Webb Slocum Electric Glider was deployed as part of the NSF funded Lagrangian Transport and Transformation Experiment in 2004. While the glider was on the surface a software malfunction disabled the glider causing it to drift on the surface with no means of communicating and no ARGOS broadcasts of its location. The Civil Air Patrol offered to donate one tank of gas to a Glider search for use as a training mission. The days following the last glider communication, the wind and currents oscillated between upwelling and downwelling conditions. One hundred simulated drifters were released at the last known position of the glider in the surface current fields as measured by the high resolution HF radar network. A random ±5cm/s current was overlaid on the measured current field to predict the glider's drift (Figure 3). A 220 mi^2 search area was defined for the glider's probable location 10 days after communication was lost. Using this search area the Civil Air Patrol was able to locate the glider after their seventh pass through the search area, resulting in the successful recovery of the $100,000 robot by a rescue vessel that was standing by.

Tropical Storm Ernesto had weakened to a tropical depression after it made land fall in North Carolina. However a large high pressure system to the north combined with Ernesto's transition to an extratropical frontal structure to produce gale force winds over much of the coast from Virginia to New York. The strong winds from offshore caused significant transport of water towards the coast as Ernesto's newly developed extratopical front and rain bands propagated northward along the coast. Figure 4 illustrates Ernesto's forecast frontal structure just before (4a) and just after (4c) the front passed New York Harbor. The ocean response before the frontal passage (4b) shows the final hours of shoreward transport into New York Harbor, followed by rapid flushing of the system (4d) after the storm front passed. The model wind fields and observed surface currents are now providing a test case for coastal inundation models for MACOORA. The wind fields provide surface forcing for coastal inundation models, and the surface currents assimilated into regional forecast models provide offshore boundary conditions.

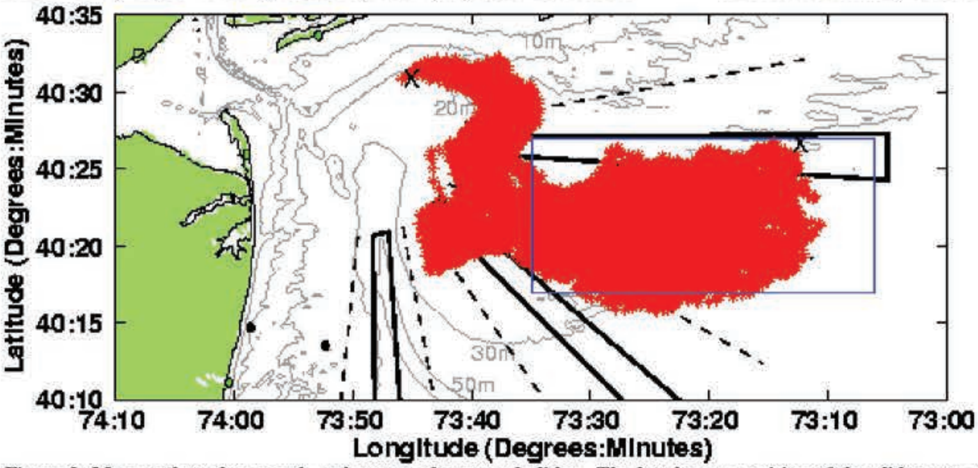

Figure 3: Map used to plan search and rescue of wayward glider. The last known position of the glider was at 40:30 N and 73:45 W. The search area was defined as the blue box. The glider was recovered at 40:25 N and 73:10 W.

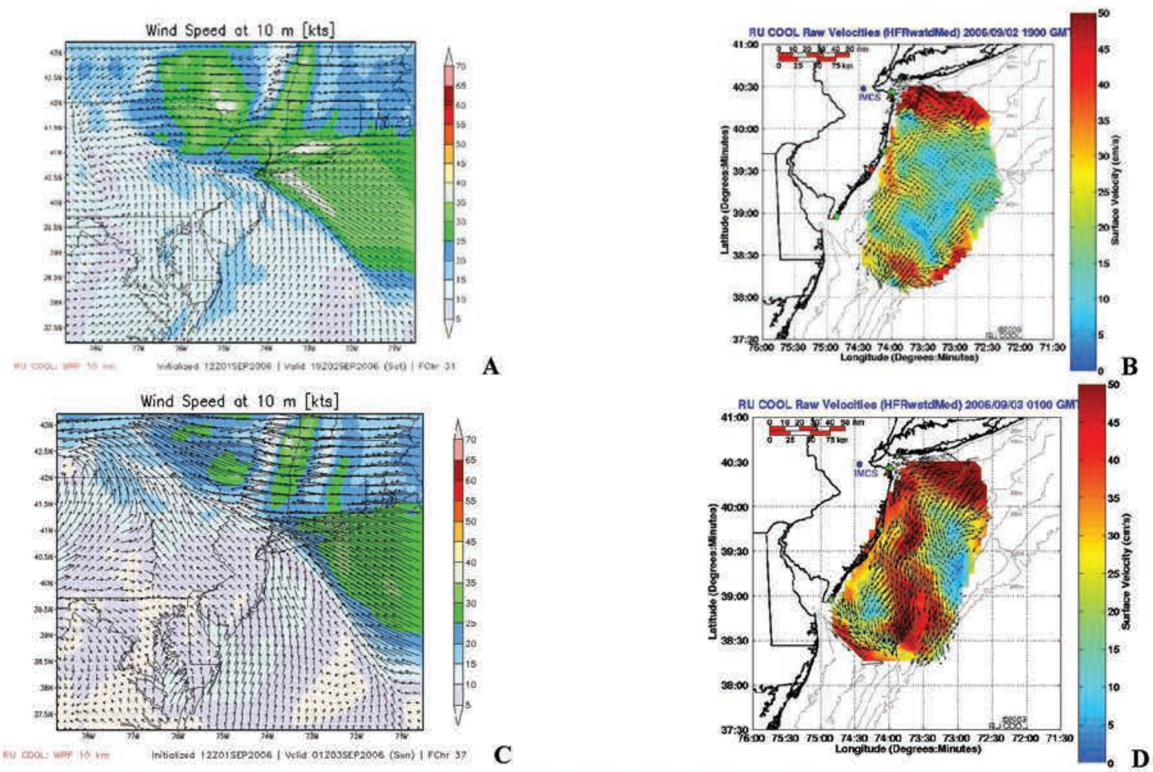

Figure 4: Slides showing the passage of Tropical Storm Ernesto. The top 2 panels are September 2, 2006 at 19:00 GMT. The bottom 2 panels show the conditions at September 3, 2006 at 01:00 GMT. The panels on the left are output from the Rutgers WRF model. The panels on the right are measured surface currents from the HF radar. The front of the storm can be seen progressing NE across the state of New Jersey. The storm surge that had accumulated at the NY Bight apex broke after the passage of the front and flowed south. This can be seen in panel D.

VI. Conclusions

MARCOOS has established an end-to-end system for operating a regional scale HF Radar network, aggregating the data in a central location, producing quality controlled total vector maps, distributing the maps to statistical and dynamical modelers for assimilation, bringing the data nowcasts and bringing the model forecasts into the USCG's Environmental Data Server so that it can be accessed through Search And Rescue decision-makers through SAROPS. The system is operating at the MAHFRC Phase 2 level during this initial three-year demonstration of MARCOOS.

One operational challenge for the Phase 2 level is that MARCOOS is currently using only 3 fully funded technicians and a regional coordinator to maintain 26 systems, well below the 2003 SCMI recommendation of 10 technicians for this level of network. Significant leveraging is still reducing costs. However, the present 3-year MARCOOS pilot project may ultimately result in an upward revision of the number of radar sites 2 technicians can cover. Advances in the reliability and speed of cell-phone communications, remotely controllable backup power systems, and larger computer disc storage over the last 5 years are extending the required revisit intervals at remote shore sites. The SCMI workforce numbers also were based on the operation of a long-range network, with one constraint being that a technician must be able to drive to a site, repair it, and drive home all in one day to be cost effective. The SCMI report did not anticipate that the actual network would evolve as a nested system of long range systems driven mainly by offshore Search and Rescue needs combined with an inner nest of high resolution systems driven mainly by water quality needs. The result is that many more than 5 sites are now expected to be located within a ½ day drive of each technician's home base. Ultimately new support technologies and revised designs of the national network may lead to a revision in the estimated workforce requirements.

VII. Acknowledgments

This work was supported by the National Oceanic and Atmospheric Administration.

References

[1] J. Paduan, J. O'Donnell, A. Allen, P.M. Kosro, S. Glenn, M. Bushnell, D. Musgrave, N. Shay, L. Washburn, M. Luther, 2004. *Surface Current Mapping in U.S. Coastal Waters: Implementation of a National System*. Ocean.US, Arlington, VA, 22 pp.

[2] Radar Technologies for Surface Current Mapping, Alliance for Coastal Technologies No. ACT-04-03

National IOOS High Frequency Radar Search and Rescue Project

Jack Harlan, NOAA IOOS Program, Silver Spring, MD
Arthur Allen, US Coast Guard, New London, CT
Mr. Eoin Howlett, Applied Science Associates, South Kingstown, RI
Eric Terrill, Scripps Institution of Oceanography, Coastal Observing R&D Center, La Jolla, CA
Sung Yong Kim, Scripps Institution of Oceanography, Coastal Observing R&D Center, La Jolla, CA
Mark Otero, Scripps Institution of Oceanography, Coastal Observing R&D Center, La Jolla, CA
Scott Glenn, Rutgers University, New Brunswick, NJ
Hugh Roarty, Rutgers University, New Brunswick, NJ
Josh Kohut, Rutgers University, New Brunswick, NJ
James O'Donnell, University of Connecticut, Groton, CT
Todd Fake, University of Connecticut, Groton, CT

Abstract

The U.S. Integrated Ocean Observing System (IOOS®) partners have begun an effort to extend the use of high frequency (HF) radar for U.S. Coast Guard (USCG) search and rescue operations to all U.S. coastal areas with HF radar coverage. This project builds on the success of an IOOS and USCG-supported regional USCG search and rescue product created by Applied Science Associates (ASA), Rutgers University and University of Connecticut for the mid-Atlantic region. We describe the regional product and the expanded national product's two main components: optimally-interpolated velocity fields and a predicted velocity field.

The regional product uses optimally-interpolated fields of HF radar-derived ocean surface current component estimates and then an extrapolation in time using local estimates of the autocorrelation function. The forecast fields are the result of a suite of applications known as the Short Term Prediction System (STPS). STPS, originally developed by the University of Connecticut for the USCG, uses a Gauss-Markov approach to compute forecasts of the surface velocity field. The USCG search and rescue operations center began operational access to the regional product in May 2009.

Presently, the IOOS national HF radar network is composed of 128 radars covering most of the coastal waters of the U.S. The data from each radar are ingested by a trio of national servers, providing data redundancy and failover capability. To provide further robustness, these servers are widely separated geographically, being located at Scripps Institution of Oceanography in California, Rutgers University in New Jersey and the NOAA National Data Buoy Center in Mississippi.

The current project, extending the optimal interpolation and STPS products to all coastal areas, began in FY2011 with the original partners, mentioned above, as well as Scripps Institution of Oceanography which is implementing nationwide the optimal interpolation code (originally developed at SIO) and providing near-real-time HF radar data to ASA, developers of the USCG's data server system. Rutgers University originally implemented, tested and hardened the optimal interpolation software code for the mid-Atlantic region and will test and validate the new code

0-933957-39-8 ©2011 MTS

for the entire East and Gulf coasts. Testing will involve comparisons of the optimally interpolated HF radar data fields with USCG Self-Locating Data Marker Buoys (SLDMB), similar to the well-known Davis drifters and other conventional current measurement sensor data provided by IOOS regional partners. Meanwhile, STPS will be tested throughout those U.S. coastal waters monitored by HF radars. STPS parameters are optimized to ensure realistic regional coastal ocean dynamics are represented in the forecasts.

The optimal interpolation software (also known as an objective mapping technique) is applied to the HF radar surface velocity vector field using both observed and idealized covariance matrices. This mapping results in a smoothed vector field and fills in spatial gaps as well. This is in contrast to the conventional widely-used unweighted least squares technique. A further benefit is that the method provides an improved uncertainty estimate of the velocity vector field. Both the gap-filling and the uncertainty estimates will be beneficial for the ingest of HF radar data into the NOAA Office of Response and Restoration's General NOAA Operational Modeling Environment (GNOME). GNOME provides its own prediction algorithms so would not need to use the the STPS.

By providing both the optimally-interpolated HF radar-derived surface current velocity fields and the STPS-derived predictions, we will enhance the information available for both USCG coastal search and rescue operations and NOAA's oil spill response operations.

Background

The Integrated Ocean Observing System (IOOS®) is a federal-regional partnership working to provide new tools and forecasts to improve safety, enhance the economy, and protect our environment. Once complete, IOOS will be a nationally important infrastructure enabling many different users to monitor and predict changes in coastal and ocean environments and ecosystems. This infrastructure is critical to understand, respond, and adapt to the effects of severe weather, global-to-regional climate variability, and natural hazards. One of the key networks within this infrastructure is a high frequency (HF) radar network, designed to bring ocean surface current velocity information to decision-makers and the broader public.

Nationally, the IOOS Program has been supporting the operations and maintenance of partner-owned HF radars throughout US coastal area. Additionally, IOOS has continued to facilitate the development of a national data management and distribution system for all US HF radars as well as radars operated by the Canadian Coast Guard in Nova Scotia. Presently, 128 HF radars and 30 institutions are part of the network and their data are delivered by IOOS national data servers. The development server resides at Scripps Institution of Oceanography's Coastal Observing R&D Center (http://cordc.ucsd.edu/projects/mapping/) and its mirror is at the NOAA National Data Buoy Center (http://hfradar.ndbc.noaa.gov/). Data file management and distribution follow internationally accepted standards, for example, netCDF-CF file and metadata formats and OpenGIS® Web Coverage Service Interface Standard (WCS) for interoperable delivery of gridded data.

For fiscal year 2010, NOAA IOOS and its regional partners and USCG search and rescue experts conferred on a design for national scale use of HF radar in the USCG Search and Rescue

Optimal Planning System (SAROPS) (Harlan et al, 2010). On a national scale, two important applications of HF radar are: 1) US Coast Guard (USCG) Search and Rescue (SAR) operations and 2) NOAA oil spill response operations. These applications use ocean surface current data to track and predict the flow of the uppermost layer of the ocean and IOOS is providing resources to bring new capabilities to both of them. Each of them requires reliable two-dimensional fields of surface currents. A schematic representation of the components and data pathways of the enhancements being undertaken with the IOOS community is shown in Figure 1.

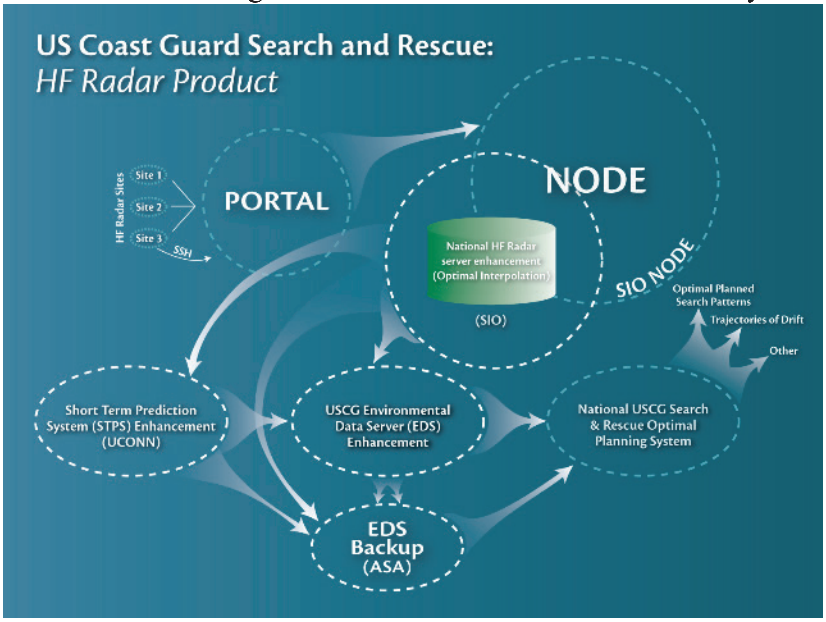

Figure 1. Schematic of the data pathways and components of the IOOS enhancements to the HF radar component of USCG SAROPS. The blue dotted lines enclose components that existed prior to the project. The enhancements are shown within the white dotted lines.

A description of the national HF radar network data management and delivery (Harlan et al, 2010) illustrated the ingest and distribution of radial surface current velocity data from the 128 HF radars presently in the national network. Here we present discussion of a project to enhance the IOOS HF radar component of SAROPS and for NOAA oil spill response.

Application of Optimal Interpolation

Once the HF radar radial velocity data are ingested, the data are combined to form total velocity vectors in two-dimensional grids. An un-weighted least-squares fitting (UWLS) method has been used by many authors to extract the vector currents from the radial velocities, e.g., Lipa and Barrick (1983), Gurgel (1994), Graber et al.(1997). Implicit in this approach is an assumption of a uniform vector velocity producing the radial velocities within the search radius for a given vector grid point. In other words, the correlation of the vector current is assumed to be one everywhere within the search radius and zero outside. The optimal interpolation (OI) method is a biased estimator and assumes a (continuous) spatial covariance function, derived from the observed spatial scale and structure. It improves both baseline consistency (the direct over-water line between two separate HF radar sites) and the uncertainty definition in the estimates, e.g.,Kim et al.(2008), Kim (2010).

The vector current field computed using UWLS has sparse spatial coverage due to the assumption of finite correlation function (e.g, step function) and the baseline inconsistency. However, the OI approach reduces the outlier near the baselines and offshore area and provides a unified uncertainty information.

These OI-derived two-dimensional grids of surface current velocity are the input to the Short-term Prediction System (STPS), the predictive portion of the HF radar component of SAROPS, which creates provides a 24-h forecast of surface currents based on the statistics of the previous 30 days of HF-radar-derived surface current data. Figures 2 and 3 show separate examples of one-hour-averaged vector fields in the vicinity of San Diego, California. Note that the UWLS approach (Figures 2 and 3, upper left) can yield physically inconsistent vectors in regions of fewer radial velocities. In these cases, the OI approach provides a more realistic solution as it tapers the solutions toward zero (Figures 2 and 3, upper right) where there are insufficient data. The OI approach also yields 30-40% more vector current solutions than the UWLS method when using the same input HF radar radial velocity data fields (Kim et al, 2008).

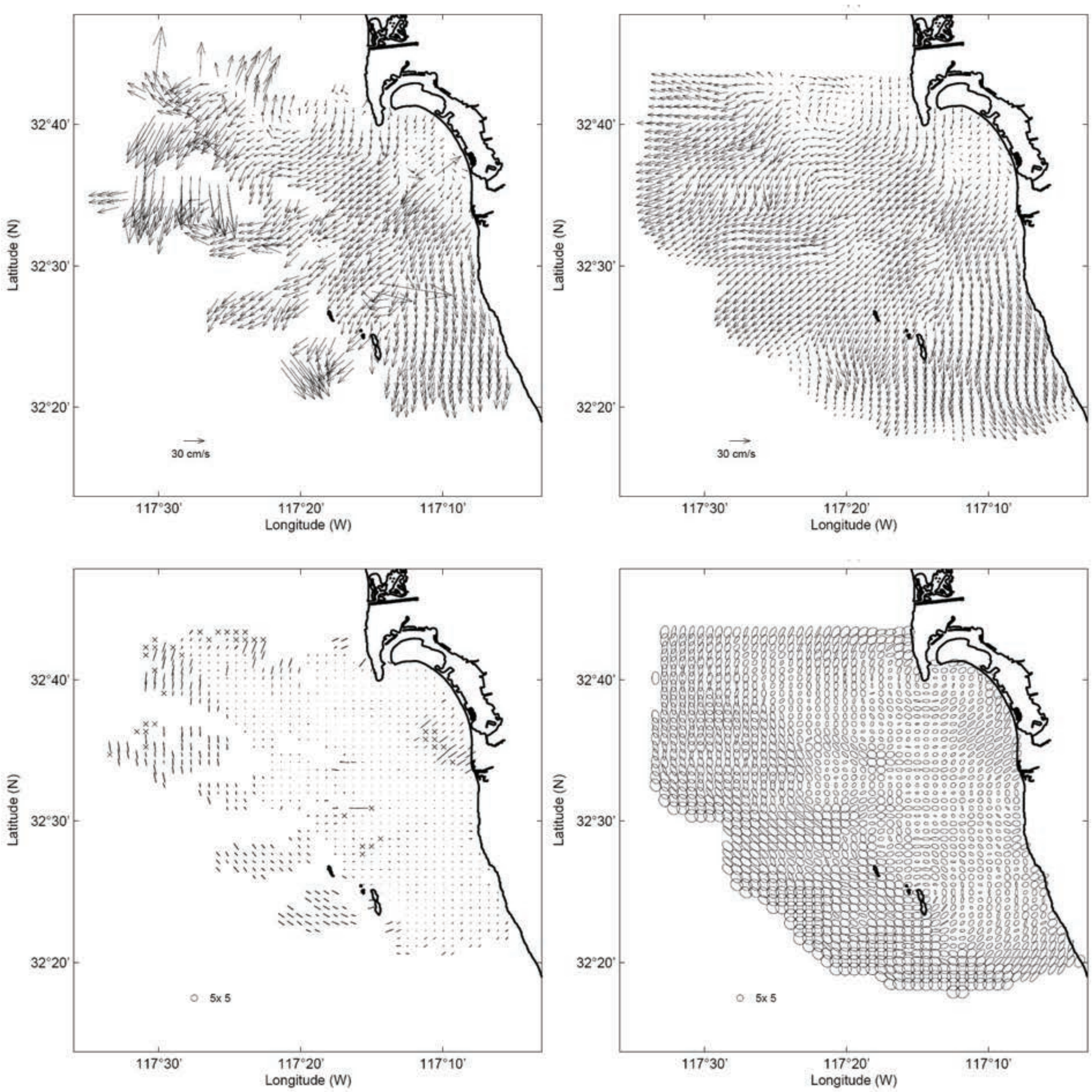

Figure 2: An example of the surface current vector fields for UWLS and OI and a posteriori uncertainty ellipses normalized by the observational error variance: UWLS (top left), OI (top right), UWLS normalized uncertainty ($\boldsymbol{\varphi}$) (bottom left), OI normalized uncertainty ($\boldsymbol{\varphi}$) (bottom right) for San Diego, California region.

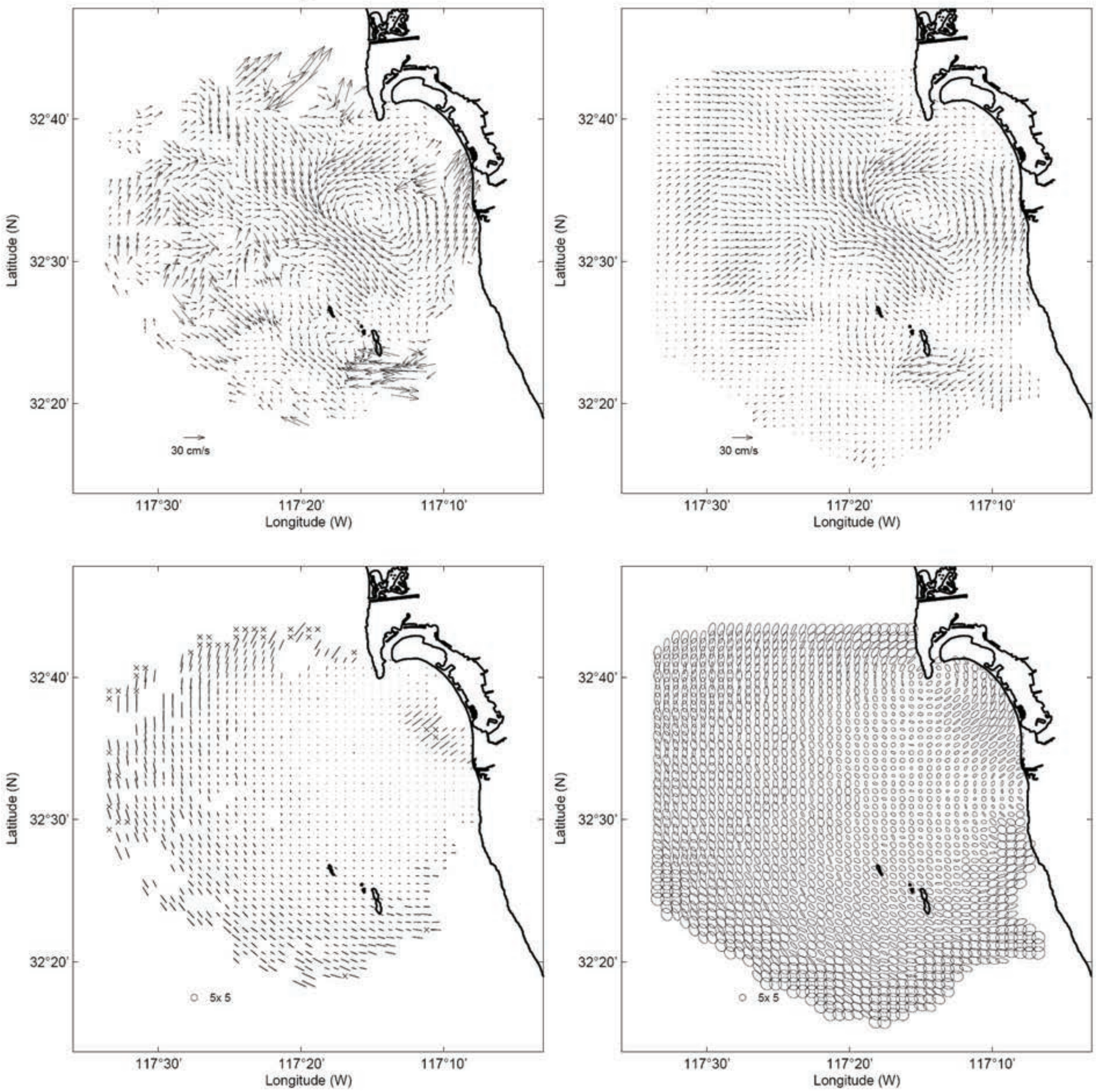

Figure 3: An example of the surface current vector for UWLS and OI and a posteriori uncertainty ellipses normalized by the observational error variance: UWLS (top left), OI (top right), UWLS normalized uncertainty ($\boldsymbol{\varphi}$) (bottom left), OI normalized uncertainty ($\boldsymbol{\varphi}$) (bottom right) for San Diego, California region.

Summary of mid-Atlantic development and use of HF radar for search and rescue

The USCG, for its SAR mission, responds to over 28,000 incidents with over 5,000 lives saved each year. The Search and Rescue Optimal Planning System (SAROPS) is the tool used to respond to these incidents. The effectiveness of SAROPS to define search areas depends critically on the observed real-time and forecasted surface current data that is delivered through their Environmental Data Server (EDS). The USCG SAR operators are trained in SAROPS and educated in modern ocean observation and regional current conditions.

High frequency radars were first operated in the Mid-Atlantic beginning in 1998. Today there are thirty five systems operated by eight different universities under the Mid Atlantic Regional Association Coastal Ocean Observing System (MARACOOS). The USCG Office of Search and Rescue and MARACOOS partners first demonstrated the effectiveness of measured surface currents in aiding search and rescue planning in 1998 (Figure 4). A series of projects then investigated the effectiveness of HF radar currents in SAR planning first using the 25 MHz network operated by the University of Connecticut and University of Rhode Island (Ullman et al., 2003) then expanding to use the long range network operated by Rutgers University (O'Donnell et al., 2005). This set the stage for the initiation of the MARACOOS effort in 2007 (Roarty et al., 2010). Maritime safety has been the highest priority theme within MARACOOS during its initial years.

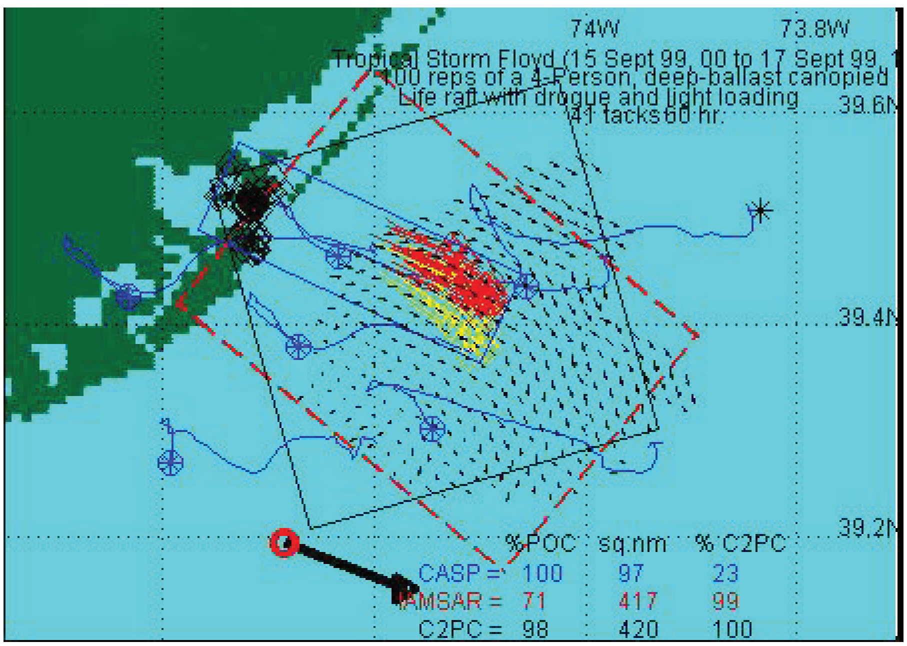

Figure 4: Graphic showing that the use of a field of surface current measurements can reduce the search area by a factor of 4 over a point measurement.

The USCG Office of Search and Rescue and MARACOOS have jointly demonstrated that surface current maps improve the effectiveness of SAROPS. In a simulated search case, using a USCG surface drifter released south of Long Island, the USCG used surface currents from an operational HYCOM model and the MARACOOS HF radar respectively with their SAROPS. The HF radar surface current-derived search area (Figure 5, right) was (a) centered on the drifter and (b) 3 times smaller than that derived from the HYCOM simulation. Thus, in Spring 2009, HF radar surface current data was installed on the USCG EDS for use as an operational component of SAROPS, an important first step toward a national capability. The USCG estimates that 50 additional lives will be saved each year after the national implementation of the HF radar surface current network. The indirect benefit is that USCG assets, which are typically redirected to SAR missions, will spend more time on their law enforcement and homeland security missions.

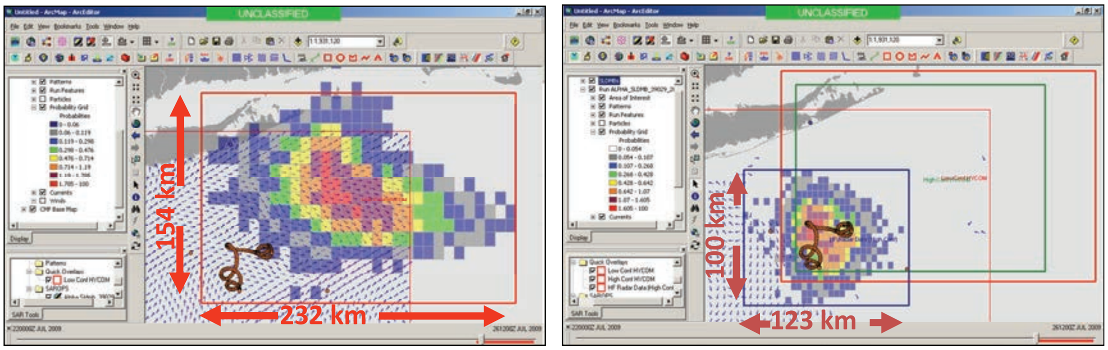

Figure 5: SAROPS search area using HYCOM model (left) and HF Radar data (right). The 4 day drifter path (brown inverted "V") is shown.

Graber, H. C., B. K. Haus, R. D. Chapman, and L. K. Shay (1997), HF radar comparisons with moored estimates of current speed and direction: Expected differences and implications, *J.Geophys.Res.*, *102*(C8), 18,749–18,766.

Gurgel, K.-W. (1994), Shipborne measurements of surface current fields by HF radar, L*'Onde Electr.*, *74*(5), 54–59.

Harlan, J., E. Terrill, L. Hazard, C. Keen, D. Barrick, C. Whelan, S. Howden and J. Kohut (2010). "The Integrated Ocean Observing System High Frequency Radar Network: Status and Local, Regional and National Applications." Marine Technology Society Journal 44(6): 122-132.

Kim, S. Y. (2010), Observations of submesoscale eddies using high-frequency radar-derived kinematic and dynamic quantities, *Cont. Shelf Res.*, *30*, 1639–1655, doi: 10.1016/j.csr.2010.06.011.

Kim, S. Y., E. J. Terrill, and B. D. Cornuelle (2008), Mapping surface currents from HF radar radial velocity measurements using optimal interpolation, *J.Geophys.Res.*, *113*, C10023, doi:10.1029/2007JC004244.

Lipa, B. J., and D. E. Barrick (1983), Least-squares methods for the extraction of surface currents from CODAR crossed-loop data: Application at ARSLOE, *IEEEJ.OceanicEng.*, *OE-8*(4), 226–253.

O'Donnell, J., D. Ullman, M. Spaulding, E. Howlett, T. Fake, P. Hall, T. Isaji, C. Edwards, E. Anderson, T. McClay, J. Kohut, A. Allen, S. Lester, C. Turner, and M. Lewandowski (2005). "Integration of Coastal Ocean Dynamics Application Radar (CODAR) and Short-Term Predictive System (STPS) Surface Current Estimates into the Search and Rescue Optimal Planning System (SAROPS)" U. S. Coast Guard Rep., CG-D-01-2006

Roarty, H. J., S. M. Glenn, J. T. Kohut, D. Gong, E. Handel, E. Rivera Lemus, T. Garner, L. Atkinson, C. Jakubiak, W. Brown, M. Muglia, S. Haines and H. Seim (2010). "Operation and Application of a Regional High Frequency Radar Network in the Mid Atlantic Bight." Marine Technology Society Journal 44(6): 133-145.

Ullman, D., J. O'Donnell, C. Edwards, T. Fake, D. Morschauser, M. Sprague, A. Allen, and B. Krenzien (2003). "Use of Coastal Ocean Dynamics Application Radar (CODAR) technology in U. S. Coast Guard search and rescue planning", U. S. Coast Guard Rep., CG-D-09-03.

Extended-Range RiverSonde Operation on the Hudson River

Calvin C. Teague, Donald E. Barrick, Peter M. Lilleboe, Hugh Roarty, Danielle Holden and Dakota Goldinger
CODAR Ocean Sensors, Ltd.
1914 Plymouth Street
Mountain View, CA 94303
Email: cal@codar.com,
don@codar.com, pete@codar.com

Rutgers University
71 Dudley Road
New Brunswick, NJ 08901
Email: hroarty@marine.rutgers.edu,
dbholden@eden.rutgers.edu, dakotag@eden.rutgers.edu

***Abstract*—A RiverSonde was operated during June–August 2010 along the Hudson River in New Jersey at a location about 140 m from the water's edge with the antenna about 40 m above the water level. With this configuration, usable signals were obtained all the way across the river, out to a range of 1400 m from the radar. This was considerably greater than the 300 m which had been observed in previous experiments. Initial data processing shows that the along-channel velocity had the expected tidal signature with a maximum value of approximately 1 m/s and was nearly in phase with the stage measured about 5 km downstream at a NOAA gaging station.**

I. Introduction

The RiverSonde® is a UHF radar system operating at 70-cm radar wavelength which measures the surface water velocity of a river using resonant Bragg scattering from 35-cm-wavelength water waves. It uses many of the same components as the HF SeaSonde®. It uses a swept-frequency waveform to determine range to the scattering patch, and direction finding with a 3-yagi antenna array to determine bearing. Normally it is installed on one bank of a river, a few meters from the water's edge, with the antenna a few meters above the water surface. In order to limit the power consumption and interference to other users, the average radiated power is limited to 1 W.

As part of a student grant program sponsored by CODAR Ocean Sensors, during June–August 2010 it was operated along the Hudson River between New York and New Jersey, at a location approximately 140 m from the water's edge where the river is approximately 1200 m wide.

II. Previous Experiments

In past experiments in Washington [1], [2], California [3] and South Carolina [4], [5], with the RiverSonde antenna placed on one bank a few meters from the water's edge and a few meters above the water surface, usable signals were observed out to a maximum range of 300 m. In some cases, two RiverSondes were operated simultaneously, separated by about 200 m, in order to measure the full two-dimensional flow patterns [6], [7]. The proposed location for this experiment involved a substantially greater range.

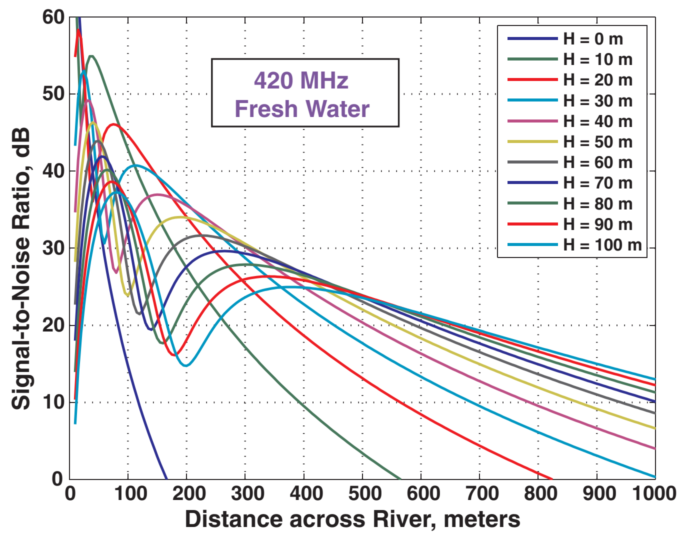

Fig. 1. Predicted Signal-to-Noise Ratio for a 1-W RiverSonde at various elevations as a function of range, assuming fully-developed 35-cm water waves.

III. SNR Predictions

In contrast to the ground-wave propagation over salt water utilized by the SeaSonde, the RiverSonde uses free-space propagation over fresh water. Previous studies suggested that operation was feasible at the proposed site provided that the antenna was sufficiently high.

The SNR was predicted by calculating the propagation loss and calibrating the results against observed performance of the RiverSonde in previous experiments. The propagation loss was predicted using the Numerical Electromagnetics Code (NEC) program [8], for various antenna elevations and ranges to the scattering patch. The one-way propagation loss was calculated as an exact solution to the Sommerfeld equation assuming a dipole at the scattering location and the dielectric properties of fresh water, and the loss was doubled to account for the two-way propagation, and modified by a term proportional to range to account for the increase in the area of the scattering patch as the range increases. This was converted to a signal-to-noise ratio estimate by forcing the curve corresponding to 6 m

978-1-4577-0022-4/10/$26.00©2010 IEEE

Fig. 2. RiverSonde after installation on the roof of the Stevens Institute building. The Hudson River and Manhattan are in the background. The view is toward the southeast.

antenna height and a range of 200 m to match the 10 dB SNR observed at Threemile Slough in previous experiments with similar parameters. This procedure accounts for the transmitter power (1 W), receiver noise, and the losses in the cables and transmit-receive switch, all of which are the same in this experiment. The resulting SNR predictions are shown in Fig. 1. These curves indicate that an antenna height of approximately 40 m would provide a signal-to-noise ratio of 5 dB at a range of 1000 m. (The dips in the SNR estimates at ranges of 50–200 m in Fig. 1 are caused by Brewster-angle effects, which arise naturally in the NEC calculations.)

IV. Installation

Normally, the RiverSonde is installed by an engineer from CODAR. However, the staff and students at Rutgers University had extensive experience in the installation and operation of SeaSondes, so the RiverSonde was installed by the students involved in the summer project, with guidance from CODAR. In June 2010, the RiverSonde was installed on the Stevens Institute of Technology's Maritime Systems building, a 6-story building directly across the Hudson River from Manhattan. The antenna location (40.74255°N, 74.02662°W) was about 140 m from the water's edge, and about 40 m above the water surface. The water channel was about 1200 m wide in front of the antenna. Figure 2 shows the installation on the rooftop and the Hudson River and Manhattan in the background.

V. Antenna Calibration

As with any ocean or river HF or UHF radar system, it is necessary to measure the antenna pattern in order to account for the influence of structures near the antenna. In previous experiments, the RiverSonde antenna pattern was measured using a target consisting of a 6-element yagi with a diode across the driven element, switched at a 512-Hz rate to provide a signal which could be distinguished from the naturally-occurring Bragg energy. This has the advantage of not requiring independent highly stable oscillators, since the same oscillator is used for transmitting and receiving, and the transponder provides range information as well as amplitude

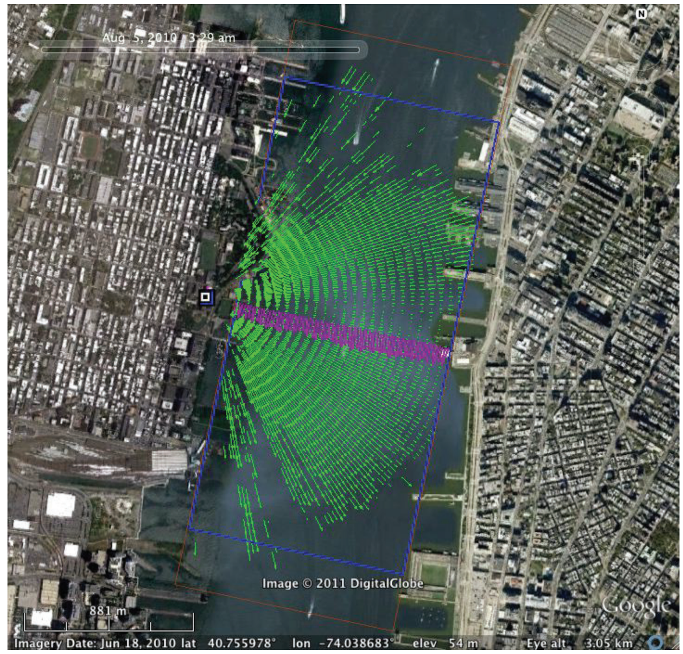

Fig. 3. RiverSonde radial vectors measured at 2010-08-05T03:30 UTC. The radar location on the Stevens Institute building is shown as the blue square. The outer red rectangle defines the area used in calculating the radials and the blue rectangle defines the area used for the profile calculations. The green arrows are individual radial vectors and the magenta arrows are the computed profile vectors. The river is approximately 1200 m wide in front of the radar, and the radar is about 140 m from the near bank.

and phase vs. bearing, but the radar cross section is quite low so the transponder is usable at a maximum range of only about 30 m. Clearly, this transponder would not work from a boat in the water at a range of several hundred meters. An alternative procedure was developed using an active signal source. The source was configured to sweep over several tens of kilohertz, while the radar receiver was tuned to a single frequency, and the resulting noise-like signal was sufficiently strong to provide a usable signal. The source was carried on a small boat which traversed several arcs in the river. A GPS receiver on the boat provided time and location information. The standard SeaSonde antenna pattern processing software was used to create the antenna pattern file.

VI. Results

After optimizing the radar parameters for this configuration, usable radar echoes were received from at least 1400 m, which extended all the way across the channel. Thus the resulting performance of the system was somewhat better than initially expected. Figure 3 shows the radial vectors obtained at 03:30 UTC on 2010-08-05. The green vectors represent the individual radial velocity measurements, and the magenta vectors show a calculated velocity profile as a function of distance across the channel. The profile vectors are computed as a least-squares fit of the radial projections of along- and cross-channel models to the measured radials within a 5-m strip parallel to the channel at various positions across the channel [9], [10].

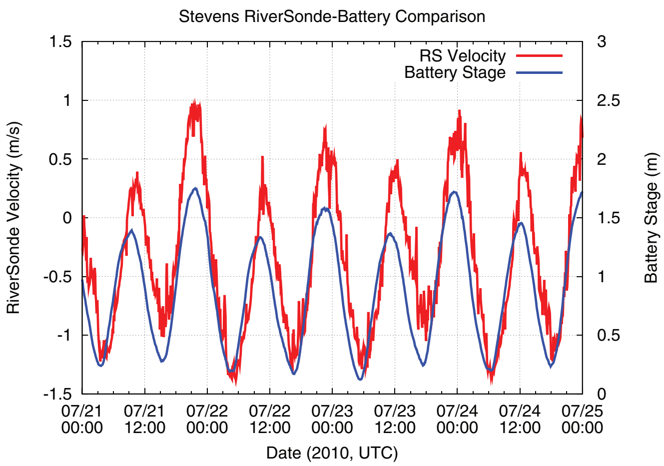

Fig. 4. RiverSonde along-channel velocity (red, left scale) and observed stage at NOAA station 8518750 at The Battery, NY (blue, right scale). Positive RiverSonde velocity is upstream, to the north.

The RiverSonde system was operated at this location for about 3 months. The water velocity here is dominated by tidal effects, and the tidal signature is the main feature in the radar data. In the lower Hudson River, the dominant tidal component is the semidiurnal, principal lunar component (the M_2 tide, with a period of 12.42 h) and the semidiurnal, solar constituent (the S_2 tide, with a period of 12.0 h) [11]. Extensive comparison with in-situ observations and assimilation into water circulation models is planned and will be the subject of future papers, but initial comparisons with NOAA stage measurements and predictions show that the RiverSonde velocity closely tracks the stage and that the two are nearly in phase.

Figure 4 shows the RiverSonde along-channel velocity for 4 days in July 2010, and the stage measured at the NOAA station 8518750 at The Battery, NY (40.700°N, 74.015°W, at the southern tip of Manhattan Island); this is about 5 km south of the radar location. Ship traffic is heavy in this area, but no attempt has been made yet to remove any signals due to ships. For this plot, positive RiverSonde velocity is upstream (to the north). The dominant tidal components are evident for both the RiverSonde velocity and stage at the Battery. The plot shows that the along-channel velocity and the stage a few kilometers away are nearly in-phase. From the figure, the Battery stage appears to lead the RiverSonde velocity by approximately one hour, particularly when the water level is falling.

VII. Summary

A RiverSonde was successfully installed and operated by students at Rutgers University during June–August 2010 at a site on the Hudson River between New Jersey and New York. With the antenna about 40 m above the water surface and 140 m from the near bank, usable echoes were obtained out to at least 1400 m. This was consistent with propagation predictions provided by the NEC program. The observed water surface velocity was nearly in phase with the stage measurements made about 5 km away at a NOAA gaging station.

Acknowledgment

The authors would like to thank the staff and students at Rutgers University and Stevens Institute of Technology for their support. This material is based upon work supported by the U. S. Department of Homeland Security under Award Number 2008-ST-061-ML0001 Rutgers would like to acknowledge CODAR for the equipment grant.

References

[1] Calvin C. Teague, Donald E. Barrick, and Peter M. Lilleboe, "UHF RiverSonde observations of Cowlitz River flow velocity at Castle Rock, Washington," in *Proc. of the 2004 International Geoscience and Remote Sensing Symposium*, New York, September 2004, pp. 1164–1166, IEEE.

[2] J. E. Costa, R. T. Cheng, F. P. Hacni, N. Melcher, K. R. Spicer, E. Hayes, W. Plant, K. Hayes, C. Teague, and D. Barrick, "Use of radars to monitor stream discharge by noncontact methods," *Water Resources Research*, vol. 42, no. W07422, pp. 1–14, 2006.

[3] Calvin C. Teague, Donald E. Barrick, Peter M. Lilleboe, Ralph T. Cheng, and Catherine A. Ruhl, "Long-term UHF RiverSonde river velocity observations at Castle Rock, Washington and Threemile Slough, California," in *Proceedings of the IEEE/OES 8th Working Conference on Current Measurement Technology*, New York, June 2005, pp. 85–89, IEEE.

[4] C. C. Teague, D. E. Barrick, P. M. Lilleboe, and R. Styles, "UHF RiverSonde operation in a tidal marsh," in *Proc. of the 2006 International Geoscience and Remote Sensing Symposium*, New York, July 2006, pp. 3665–3667, IEEE.

[5] Richard Styles and Calvin Teague, "Evaluation of a UHF radar surface current mapping system in an intertidal salt marsh," *Journal of Atmospheric & Oceanic Technology*, vol. 24, pp. 2120–2127, December 2007.

[6] Calvin C. Teague, Donald E. Barrick, Peter M. Lilleboe, Ralph T. Cheng, Paul Stumpner, and Jon R. Burau, "Dual-RiverSonde measurements of two-dimensional river flow patterns," in *Proceedings of the IEEE/OES/CMTC Ninth Working Conference on Current Measurement Technology*. 2008, pp. 258–263, IEEE.

[7] Calvin C. Teague, Donald E. Barrick, Peter M. Lilleboe, and Ralph T. Cheng, "Two-dimensional surface river flow patterns measured with paired RiverSondes," in *Proc. of the 2007 International Geoscience and Remote Sensing Symposium*. 2007, IEEE.

[8] G. J. Burke, E. K. Miller, and A. J. Poggio, "The Numerical Electromagnetics Code (NEC) – A Brief History," in *Proc. of the 2004 IEEE AP-S International Symposium and USNC / URSI National Radio Science*. IEEE, June 2004.

[9] C. C. Teague, D. E. Barrick, P. M. Lilleboe, R. T. Cheng, and C. A. Ruhl, "UHF RiverSonde observations of water surface velocity at Threemile Slough, California," in *Proc. of the 2005 International Geoscience and Remote Sensing Symposium*, New York, July 2005, pp. 4383–4386, IEEE.

[10] Calvin C. Teague, Donald E. Barrick, Peter M. Lilleboe, and Ralph T. Cheng, "RiverSonde: Measuring river surface velocity with UHF radar," in *Proceedings of the Hydraulics Measurement and Experimental Methods 2007 Conference*, New York, 2007, EWRI/ASCE.

[11] Alan F. Blumberg and Ferdi L. Hellweger, "Hydrodynamics of the Hudson River Estuary," in *Proc. of the American Fisheries Society Symposium*, 2006, pp. 51:9–28.

Examination of the SeaSonde Wave Processing Settings and the Effects of Shallow Water on Wave Measurements

Colin W. Evans
Hugh J. Roarty
Josh T. Kohut
Scott M. Glenn
Coastal Ocean Observation
Laboratory, Rutgers University IMCS
New Brunswick, United States of America

Abstract – **Derivation of wave measurements from the SeaSonde high frequency (HF) radar software is challenging when applied to the U.S. East Coast continental shelf. Shallow water depths have the capability of saturating the 1st and 2nd order Bragg, inevitably leading to imprecise estimates of the wave height conditions. This paper looks to examine the settings defined in the SeaSonde in an environment where water depth is less than 30 m within the first few range cells off of the coast of New Jersey. Wave measurements were taken from a 13 MHz standard range CODAR (Coastal Ocean Dynamics Applications Radar) antenna and compared with NDBC (National Data Buoy Center) 3-meter discuss buoys located outside New York Harbor and Delaware Bay.**

Index Terms – **HF (high-frequency) radar, wave measurements, shallow water, SeaSonde**

I. INTRODUCTION

The SeaSonde High-Frequency radar is utilized by the Rutgers University Coastal Ocean Observation Laboratory (RUCOOL) to measure coastal currents and waves. A potential application of the wave data set is for coastal zone management and bottom roughness estimation for input to a weather model. In order to clearly understand the effects that waves have on local shorelines, thirteen CODAR (Coastal Ocean Dynamics Applications Radar) systems operating at three different frequencies (5 MHz, 13 MHz, 25 MHz) have been installed along the New Jersey coast measuring wave activity every half hour at different spatial resolutions; a standard 13 MHz HF radar system was used for this study which operates at ~ 3 km range cell resolution.

The SeaSonde measures surface currents and wave parameters with the use of three elements [1]. Two of the elements are cross-looped in a directional figure-8 pattern (Loops 1 and 2) while the third element (monopole) is omnidirectional. When the signal is returned from a certain angle, the ratio of voltage magnitudes within the two elements with respect to the monopole outputs a directional bearing on the received signal [3]. A traditional CODAR site has one antenna transmitting and a separate receive antenna (installed at least 1 wavelength from the transmit antenna) listening for the incoming signal. A newer design places the transmit and receive function into a single antenna; this style antenna was used for this examination.

Since the slope of the continental shelf on the East Coast of the United States is more gradual when compared to the U.S. West Coast, shallow water depths play a pivotal role in near-shore wave measurements contained within the 2nd order Bragg spectra. The 2nd order Bragg peaks within the spectra are derived from the interaction between the short, 1st order Bragg-scattering waves with the dominant wave periods of the ocean [2]. Due to the variability in water depths with respect to the first five range cells along the New Jersey coast, the SeaSonde software is written to a) store the depth in the radar coverage area as opposed to position; b) allow the coupling coefficient to change with position according to water depth; c) use Snell's law for wave refraction to relate angular changes in wave energy to depth [1]. The coupling coefficient is derived from a series of equations and integrations in order to accurately change with varying shallow water depths. It becomes even more complicated when the coupling coefficient is site specific, which will be assessed further in sections IV and V. The underlying focus of this study was to determine if the wave processing algorithms in the SeaSonde deep-water software are optimal for operation along the coast of New Jersey with its distinct continental shelf features and to determine how much, if at all, shallow water depths affect the accuracy of wave measurements from shore-based radars compared with off-shore buoys. Section II provides the approach to comparing wave measurements recorded by the CODARs with the

978-1-4673-0831-1/12/$31.00 ©2012 IEEE

buoy wave measurements for the entire month of February, 2012. Section III provides the results of the examination period that shows the precision of the radars with the buoy measurements. Sections IV and V discuss in more detail how well the two remote sensing instruments correlate with each other and whether the shallow water depths induced a significant impact on the CODAR's capability to produce credible wave height measurements.

II. APPROACH

Simulations have been performed showing the potential of shallow water depths to induce inaccurate wave height measurements in SeaSonde systems [4]; Shallow water thresholds are 30 m for a 13 MHz SeaSonde.

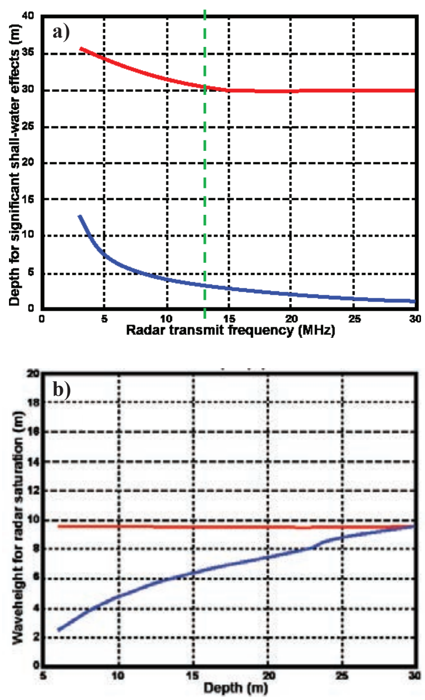

Figure 1: Figure showing the estimation of depth thresholds where (a) saturation can effect as a function of transmit frequency and (b) the wave height saturation limits for a 25 MHz radar system.

As seen in Figure 1a, the green dashed line represents a 13 MHz transmit frequency with saturation depths for both first-order Bragg (blue) and second-order Bragg (red), along with wave height saturation limits for a 25 MHz system (Figure 1b) with a wave period of 11 seconds. For a 13 MHz operating frequency, the wave height saturation limits are lower. Although we don't focus on a distinct wave period for this examination study, it was concluded in [4] that shallow water effects are more influential when the wave periods are longer.

We include results that compare wave heights and wave periods for each range cell that processed wave measurements from the second-order sea-echo during the study period but the primary objective of this paper is to examine the accuracy of the wave height measurements from four different 13 MHz radar systems with respect to the unique bathymetry defined by the shelf.

A. Study Area

Figure 2 shows the study area with the radar range cells highlighted to show the locations where waves are being processed with an overlaid bathymetry map. NDBC station 44065 had a watch radius of 90 yards and station 44009 covered a radius 0f 70 yards. Both

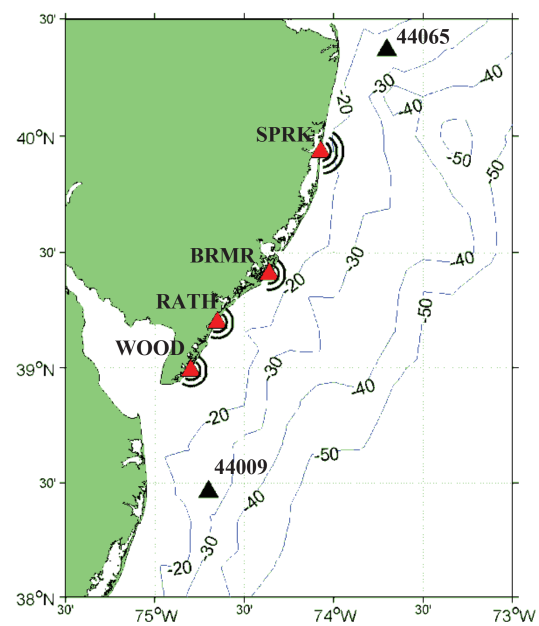

Figure 2: Map of the study area showing the location of the CODAR stations at Seaside Park (SPRK), Brigantine (BRMR), Strathmere (RATH), and North Wildwood (WOOD) along with NDBC buoys 44065 and 44009. The bathymetry contours(meters) are shown as blue lines and the range cells processing wave measurements are shown as black rings.

of the locations were within 30 m isobaths which means that the buoys were within the maximum shallow water depth limit (the depth threshold set by the 13 MHz operating frequency) that is considered to have the ability to inflate wave height measurements detected by the on-shore radars.

The CODAR site SPRK, located in Seaside Park, NJ, was evaluated with the buoy station 44065 and the remaining radar sites (BRMR, RATH, WOOD) were analyzed against the measurements from the Delaware Bay buoy 44009. The three southern CODAR sites in Figure 1 are currently involved in a program studying the off-shore wind resource for future off-shore wind turbines. The wave measurements by these systems can provide sea surface roughness estimates which serves as boundary conditions for the atmospheric models being run as part of the program.

B. Data Filtering Techniques

The SeaSonde was configured to measure ocean waves on the hour and 30 minutes past the hour, leading to a maximum 48 measurements per day. The NDBC buoys output a wave measurement at 50 minutes past the hour. The SeaSonde wave measurements on the hour were compared to the buoy measurements. Ideally, we would have 696 total wave measurements (1 for every hour in the entire month of February for 2012) if no data were absent. No interpolation or data filling techniques were applied to the data records.

III. RESULTS

A. Buoy Product

The purpose of this paper was to understand if and how shallow water can contribute to the overestimation of wave heights measured by the deep-water software in the SeaSonde. Before we evaluated the CODAR, the NDBC buoy stations were plotted against each other to form a foundation of what could be expected from the radar measurements.

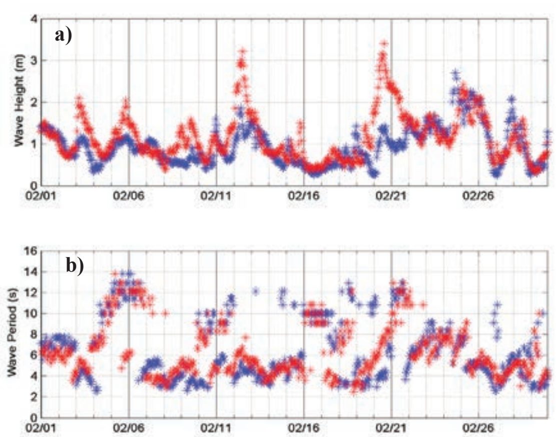

Figure 3: Comparison of (a) wave height measurements and (b) wave period measurements between NDBC station 44065 (blue) and 44009 (red) during the month of February, 2012.

Figure 3a shows the wave heights of the two buoys overlaid on top of each other. Overall, the wave heights track each other but there are instances of disagreement by as much as 2 m between the buoy wave height measurements, most notably in the second and third weeks of February. There are slight variations between the two wave period measurements (Figure 3b) but not as much as the wave heights. There are a number of reasons as to why there are defined differences between the two measurements and we present these explanations in the next section.

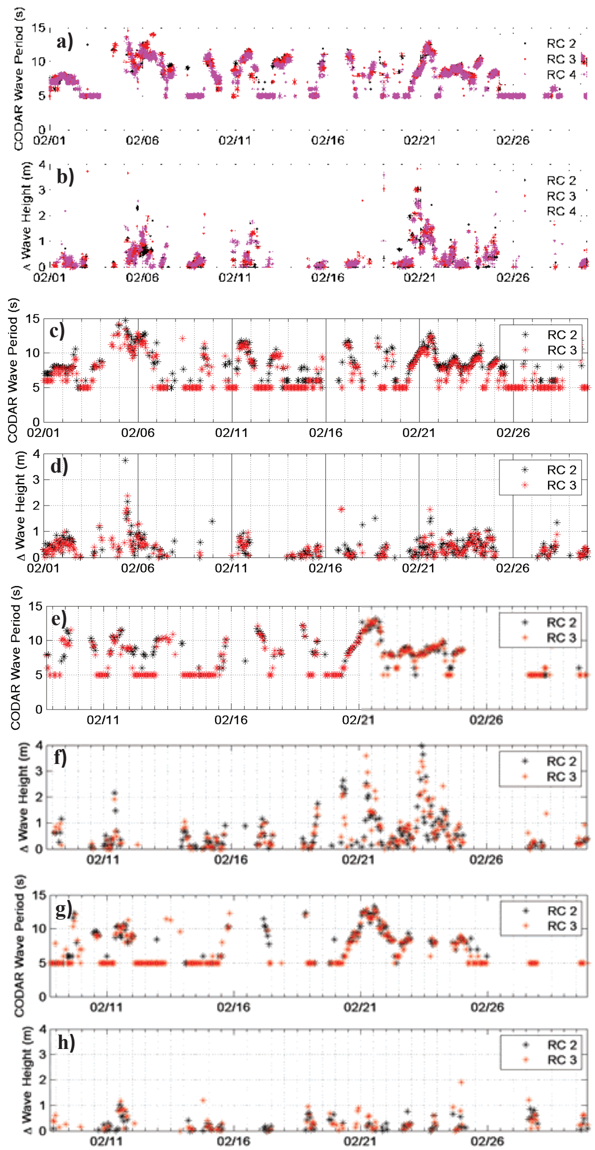

Figure 4: Subplots showing the wave period for each range cell and the wave height difference between the range cells and the buoy measurements for SPRK (a-b), BRMR (c-d), RATH (e-f), WOOD (g-h).

The wave height differences were plotted against the wave periods to analyze any potential correlations. If there is evidence of high wave height differences between the buoys and the radars, there is a possibility that the shallow water is influencing the wave height measurements. For a large majority of the study period, there are only a few occasions where the wave height differences exceed 2 m for each CODAR site.

IV. ANALYSIS

Figure 3 presents a solid basis of the measurements that should be detected from the on-shore radars compared with wave sensing instruments well off-shore. The buoy stations show intermittent deviations which could be due to distinct surrounding wave environments since buoy 44009 is located outside of the bay and the buoy 44065 is positioned outside of the New York Harbor. However, there is strong evidence that the measurements agree with each other for the bulk of February, 2012. Figure 4 presents wave height and wave period comparison plots for each radar site along the New Jersey coast. Few wave height differences greater than 2 m were found between SPRK and NDBC station 44065 and also between the remaining CODARs and NDBC station 44009. This suggests that the algorithms used in the SeaSonde software are accurately reading second-order energy for the majority of February, 2012. There appears to be a correlation between an increase in wave period and wave height differences, which could be due to changes in wind directions. Figure 5 shows the comparison of wind direction measurements between station 44065 and station 44009. One suggestion as to why there were occasional anomalies in the wave height differences and wave periods is wind energy transfer due to frictional drag of the air on the sea surface from a direct push of the wind [5]. When the wave height difference exceeded more than 2 meters on February 21st, 2012, the winds were moving out of the northeast. As the wind direction rotates clockwise to the southwest, the wave height differences decreased significantly between each CODAR station and each buoy location. This is presented as a reason for the sudden increase in wave height differences, due to an increase in energy transfer from the winds traveling in a certain direction off the coast of New Jersey.

Another potential cause of the wave height variations could be due to the broad signal return due to the enhanced wave breaking [6]. However, the same pattern in wave height differences is seen between the two buoys and is not presented in just the radars.

Figure 6 presents a histogram displaying the percentages of wave height measurements that are within four different ranges of the NDBC buoys. More than half of the amount of wave measurements determined from the SeaSonde shows a deviation from the buoy measurements of .5 m. For each of the examined radars, less than 8% of the measurements showed a difference of greater than 2 m. There was no evidence of second-order saturation in the spectra, which is an indication that shallow water did not play a significant role in the influence on the SeaSonde.

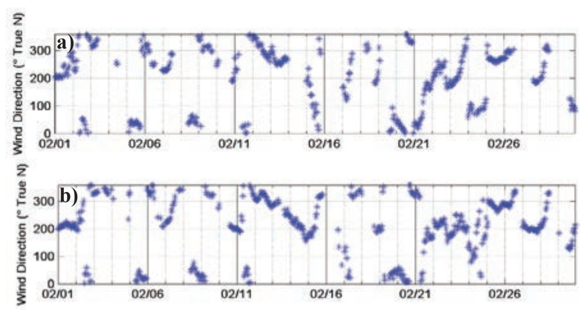

Figure 5: Wind direction comparison plots between (a) NDBC station 44065 and (b) 44009.

Site	Cell	Measured	Max	Percentage
SPRK	2	425	696	.61
	3	480	696	.69
	4	482	696	.69
BRMR	2	508	696	.73
	3	543	696	.78
RATH	2	291	511	.57
	3	305	511	.60
WOOD	2	271	511	.53
	3	269	511	.53

Table 1: Percentages of valid wave height mesurements after filtration for each range cell depicted from each of the four CODAR sites for February, 2012.

Site	R.C.	R Value
SPRK	2	.87
	3	.86
	4	.87
BRMR	2	.91
	3	.87
RATH	2	.90
	3	.89
WOOD	2	.91
	3	.89

Table 2: Table showing the correlation coefficients between each range cell compared with the NDBC stations when the wave height difference is within .5 m.

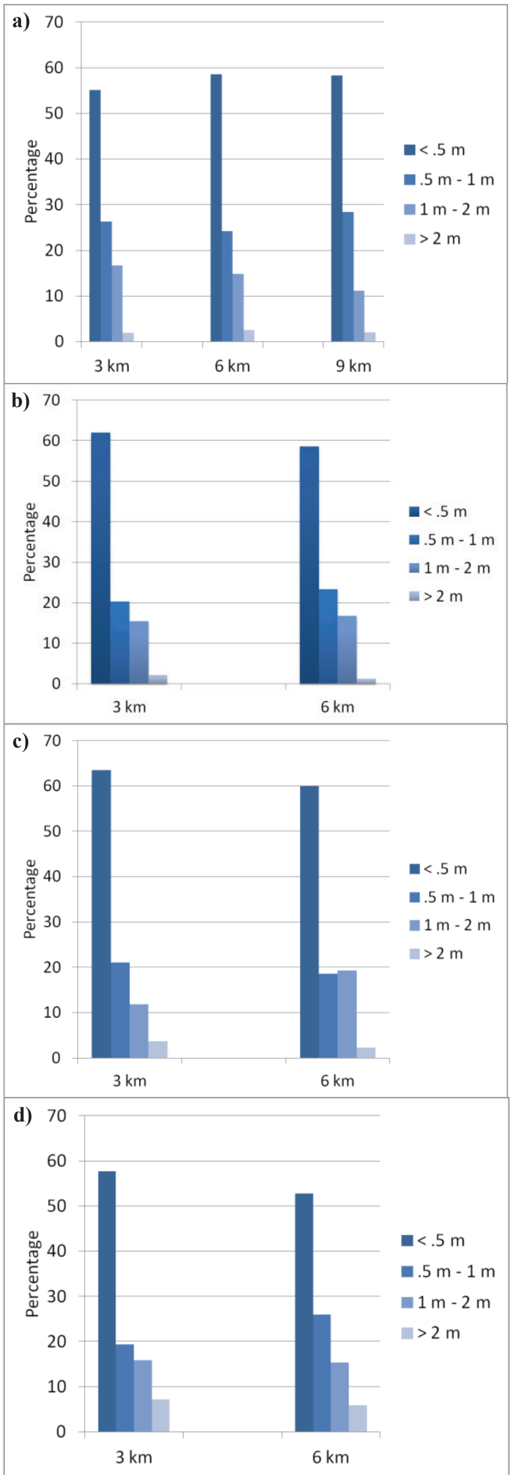

Figure 6: Histogram showing the percentages of wave height measurements within four different ranges of the buoy measurements. SPRK is compared with station 44065 (a). BRMR (b), RATH (c), and WOOD (d) were evaluated with wave measurements from buoy 44009.

Table 1 shows the consistency of the SeaSonde when measuring second-order energy. BRMR shows stability as the SeaSonde was able to measure the sea state 70% of February after filtering the data for every hour. This is particularly worth noting because extracting second-order energy information is much more difficult than first-order due to its higher probability of being contaminated by noise [4].Table 2 shows the correlation coefficients for wave height differences below 0.5 m for each range cell per CODAR with the corresponding NDBC buoys. Strong correlations are shown for each range cell; BRMR and WOOD showed the highest R values at 0.91. The accuracy of the radars for this study has shown that even with the use of deep-water software, the algorithms show the capability of using a correlation coefficient specifically for each site as a way to take into account shallow water depths. However, improvements on the SeaSonde can certainly eliminate the occasional anomalies in the data measurements. CODAR is currently working on shallow-water software to measure wave activity with more accuracy than the current deep-water software.

V. CONCLUSION

We discussed the potential of shallow water depths having the ability to negatively impact the accuracy of wave height measurements from the SeaSonde when compared to two NDBC buoy stations located near the New York Harbor (44065) and the Delaware Bay (44009). In theory, water depths below 30 m should cause the second-order Bragg to increase relative to the first-order Bragg resulting in spectral saturation when the wave height exceeds a limit of ~7.2 meters for a13 MHz radar [4]. When we examined the wave files for the entire month of February, 2012, there was no presence of wave heights exceeding the limit set by the radars, but there were occasions where the difference in measurements reached more than 2 m between the CODAR and the NDBC buoys. When the wave height differences were less than 0.5 m, the R values were within a 0.86 - 0.91 correlation range for all of the CODAR sites examined. Table 2 shows a clear indication that even when the water depths are below 30 m for a 13 MHz CODAR site, there is a strong potential of measuring wave heights accurately within 0.5 m of other in situ instruments. These systems provide a means for measuring ocean waves for the wide area along the New Jersey coast where there are no buoys present. The close correlation between the radars and the buoys suggest the abilities of the SeaSonde to fill in the gap between the station 44065 and station 44009 in terms of measuring wave heights accurately. However, there were short periods where the wave heights differences were more than 2 m. The current algorithm used by the SeaSonde software uses a coupling coefficient as a way to determine more accurate wave measurements with a change in water depth to compensate for the deep-water approach.

The 13 MHz systems showed no evidence of second-order saturation within the spectra during February, 2012 but the occasions where there were wave height differences more than 2 m suggest the complexity of deriving accurate wave measurements from the sea-state using the deep-water SeaSonde software. The shallow-water algorithm is currently in the works with a means to potentially eliminate instances where the wave height differences exceed more than 0.5 m between the SeaSonde and off-shore in situ buoy stations, along with other remote sensing technologies.

ACKNOWLEDGEMENTS

We want to thank the National Data Buoy Center and CODAR for providing the data necessary to calculate the accuracy and precision of our remote sensing instruments along the New Jersey coast. We also would like to acknowledge the Board of Public Utilities (B.P.U.) for the funding provided for the SeaSonde radars par-taking in the off-shore wind energy project.

REFERENCES

[1] Barrick, D.E., Lipa, B.J. (1986). "The Second-Order Shallow-Water Hydrodynamic Coupling Coefficient in Interpretation of HF Radar Sea Echo," *Journal of Oceanic Engineering*, Vol. OE-11, NO. 2, pg. 310-315.

[2] Lipa, B.J., Barrick, D.E. (1986). "Extraction of sea state from HF radar sea echo: Mathermatical theory and modeling," *Radio Science*, Vol. 21, NO. 1, pg. 81-100.

[3] Lipa, B., Nyden, B. (2005). "Directional Wave Information from the SeaSonde," *Journal of Oceanic Engineering*, Vol. 30, NO. 1.

[4] Lipa, B., Nyden, B., Barrick, D., Kohut, J. (2008). "HF Radar Sea-echo from Shallow Water," *Sensors*, Vol. 8, pg. 4611-4635.

[5] Kinsman, B. (1965). "Wind Waves," Englewood Cliffs, NJ: Prentice-Hall.

[6] Grabner H.C., Heron, M.L. (1997). "Wave Height Measurements from HF Radar," *Oceanography*, Vol. 10, No. 2, pg. 90-92.

Impact of Ocean Observations on Hurricane Forecasts in the Mid-Atlantic

Forecasting Lessons Learned from Hurricane Irene

Scott Glenn, Oscar Schofield, Josh Kohut, Louis Bowers, Michael Crowley, Rich Dunk, John Kerfoot, Travis Miles, Laura Palamara, Hugh Roarty, Greg Seroka and Yi Xu
Rutgers University
New Brunswick, NJ, USA
glenn@marine.rutgers.edu

Jay Titlow
Weatherflow, Inc
Poquoson, VA

Wendell Brown
University of Massachusetts
New Bedford, MA 02744

William Boicourt
University of Maryland
Cambridge, MD 21613

Larry Atkinson
Old Dominion University
Norfolk, VA 23529

Harvey Seim
University of North Carolina
Chappel Hill, NC 27599

Abstract—**Hurricane Irene followed a track that curved northward over the Bahamas and ran directly over the U.S. east coast from Cape Hatteras to New England in August of 2011, causing severe storm surges, intense inland flooding, loss of life and over $8 billon in storm damage. While the ensemble of atmospheric forecast models accurately predicted the hurricane timing and track, the hurricane intensity was consistently over-predicted. Data from the U.S. Integrated Ocean Observing System (IOOS) were used to better understand the potential impact of the Mid-Atlantic Bight's coastal ocean on the Hurricane Irene intensity forecast.**

***Index Terms*—Hurricane Forecasting, U.S. IOOS, Underwater Gliders, HF Radar, Air-Sea Interaction, Coastal Processes.**

I. Introduction

The Mid-Atlantic Regional Association Coastal Ocean Observing System (MARACOOS), one of eleven Regional Associations comprising the regional component of the U.S. Integrated Ocean Observing System (IOOS), operates a Regional-Scale Coastal Ocean Observatory that includes coastal weather mesonets, satellite data ground stations, a 1000 km long High Frequency (HF) Radar network (Roarty et al., 2010), and a distributed fleet of autonomous underwater gliders (Schofield et al., 2010). The Regional-Scale Coastal Ocean Observatory was fully operating when Hurricane Irene (Fig. 1) tracked along the U.S. East Coast over Labor Day weekend in 2011 (Glenn et al, 2011). Irene was the first hurricane to threaten New York City since Gloria in 1985. Intense rain from Irene broke flooding records on 26 rivers, causing at least 56 deaths and $8 billion in property damage. Power outages along the flood path lasted from days to weeks.

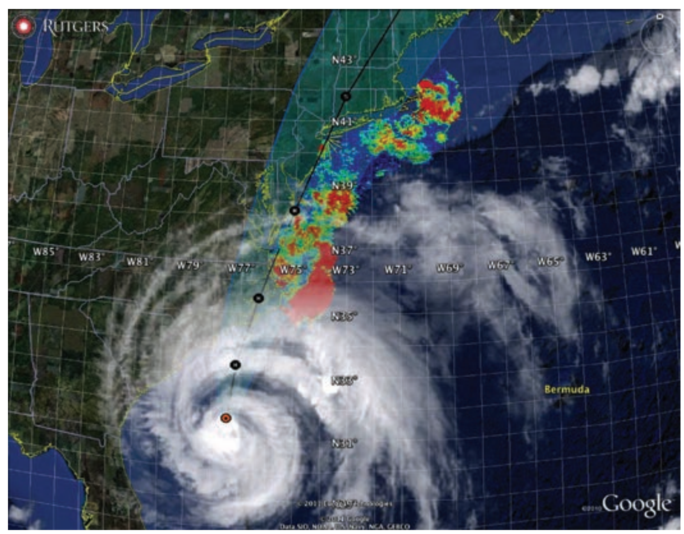

Fig. 1. Hurricane Irene in the South Atlantic Bight and forecast track as it approaches the Mid-Atlantic Regional HF Radar network.

Forecasts of Hurricane Irene's track (Fig. 1) derived by the National Hurricane Center (NHC) from the ensemble of forecast models were highly accurate. Surprisingly, much less damage than expected was caused by the hurricane winds, waves and storm surge along the beach. One reason for this was the consistent overestimate of Irene's intensity by the ensemble of atmospheric forecast models (Fig. 2). This led to numerous newspaper articles and television reports publicly reaffirming that "Intensity remains a big gap in storm science".

978-1-4673-0831-1/12/$31.00 ©2012 IEEE

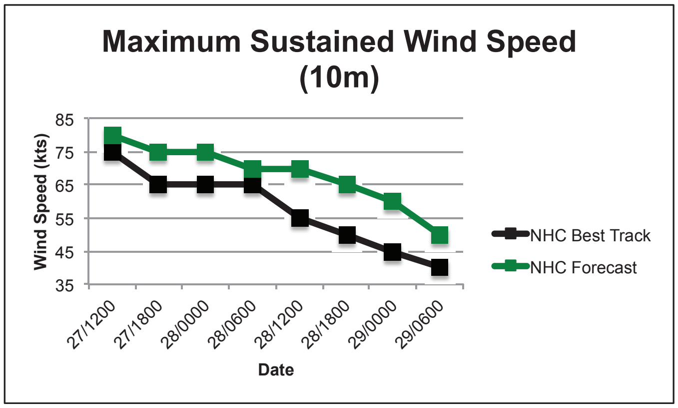

Fig. 2. Maximum sustained wind forecast (green) and best track reanalysis (black) showing the forecast overestimate of Irene's intensity.

In this paper, we discuss selected highlights of real-time ocean data acquired by the MARACOOS regional-scale network during Irene. Through a series of atmospheric model sensitivity studies, the potential impact of real-time ocean data on hurricane intensity forecasts in the Mid-Atlantic is demonstrated.

II. HF Radar Observations

The MARACOOS HF Radar network captured the shelf-wide surface current response to the intense hurricane forcing at the spatial scale of the storm. The direct wind forcing includes a rapid shift from intense onshore, to alongshore, and finally to offshore currents over the time scale of a day (Fig 3). As the eye of Hurricane Irene enters the Mid Atlantic Bight (MAB) on August 27 at 17:00 GMT, strong winds from offshore that precede the eye are forcing onshore currents and increasing the storm surge over much of the southern MAB (Fig 3a). Fifteen hours later on August 28 at 8:00 GMT, the eye of Hurricane Irene is offshore Delaware Bay, and the outer edge on the northeast side is reaching Cape Cod. Currents in the northern portion of the MAB are onshore, currents in the middle are alongshore, and currents in the southern portion have switched to offshore. By 14:00 GMT on August 28, the eye of Irene passes over New York City and the storm heads inland. Surface currents directly east of the eye are now onshore, and surface currents on the trailing side of the storm in the southern MAB are now diminishing and are beginning to turn in inertial circles.

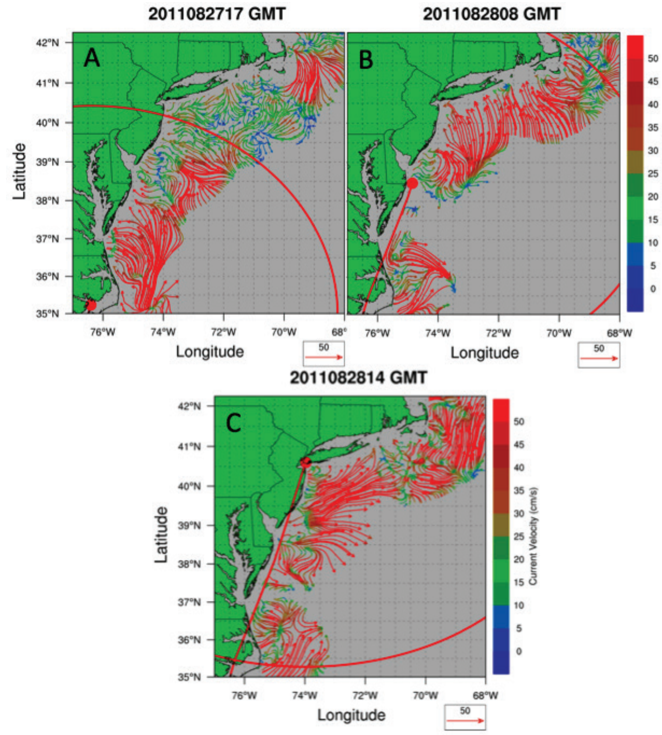

Fig. 3. Surface current response due to Hurricane Irene winds as (a) the eye enters the MAB near Cape Hatteras, (b) the eye crosses Delaware Bay, and (c) as the eye crosses over New York City and heads inland.

Observations of the lingering inertial current response to hurricanes are numerous in deepwater. Kohut et al. (200?) found the inertial response to Tropical Storm Floyd was quickly diminished in very shallow water as the stratification was eroded. The MAB HF Radar network provides the first look at the inertial tail of a hurricane over the full scale of the MAB shelf over a range of water depths and stratification. Starting with a single point at midshelf where an autonomous underwater glider was located (see Section III), a time series of the observed total currents along with the inertial component of the current derived from a least-squares fit to the current data is plotted for a 1 week period starting on August 26 before Hurricane Irene entered the MAB (Fig. 4). The peak in the direct wind forcing occurs on the scale of 1 day on August 28 (Fig. 4, top). The amplitude of the inertial component of the current (Fig. 4, bottom) increases until it peaks on August 29 as the back side of the storm crosses onto land in New England and New York. The inertial amplitude remains high for much of the day on August 29, then slowly decays at a linear rate over several days from August 29 through September 1.

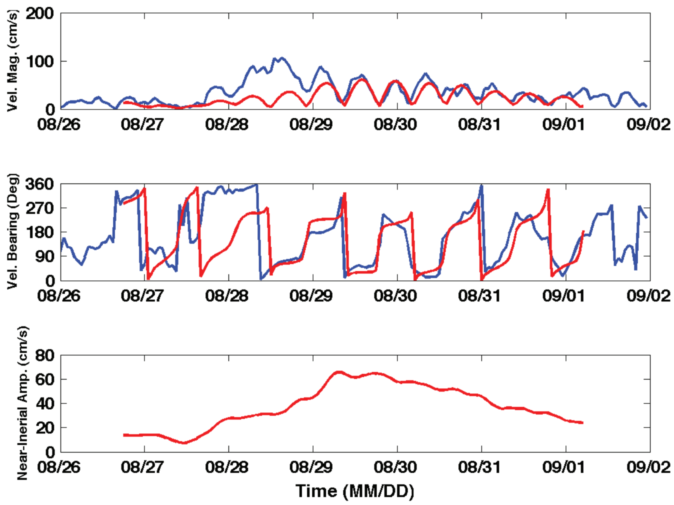

Fig. 4. Time series of total current (blue) and near-inertial current (red) calculated for a point on the outer shelf of NJ.

Spatial maps of the energy content in the diurnal and near-inertial frequency bands derived from a wavelet analysis of the surface currents are shown in Fig. 5. As the eye of Hurricane Irene moves into southern New England (Fig. 5a), the large amount of energy in both the diurnal and near-inertial frequency bands on the outer half of the shelf in the central MAB is visible. Two days later (Fig. 5b), the energy level in the diurnal band is reduced over the full MAB, while the energy in the near-inertial band persists.

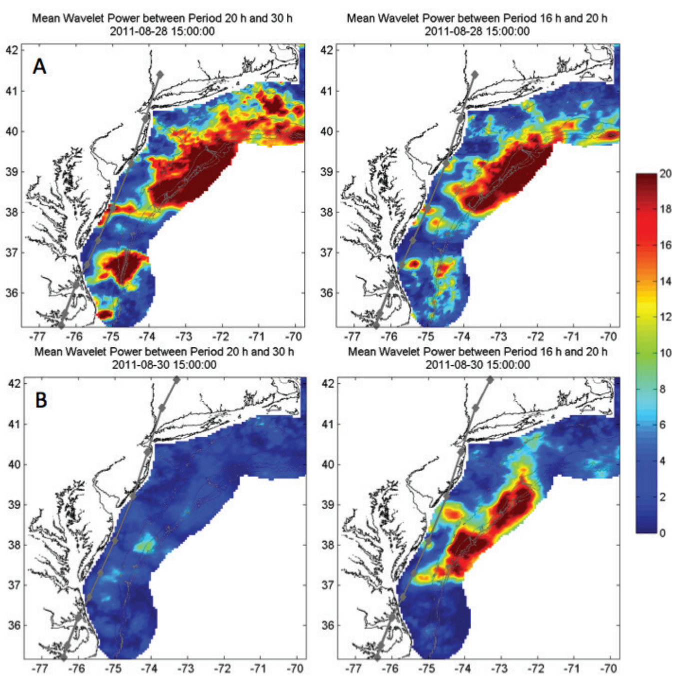

Fig. 5. Spatial maps of the diurnal (left) and near-inertial energy (right) as (a) the eye passes over NJ, and (b) 2 days later.

III. Glider Observations

Two autonomous underwater gliders were operating in the MAB when Hurricane Irene transited the region (Fig. 6). RU23 was deployed on a regional MARACOOS mission by UMass Dartmouth to map the subsurface temperature and salinity structure of the MAB during the decay phase of the Cold Pool to support ocean modeling activities for fisheries applications. RU23 was damaged early in the storm and was purposely kept at the surface through the storm to prevent its loss. Its track as a surface drifter illustrates the combination of the initial direct and persistent inertial forcing. RU23 was recovered after the storm by a sport-fishing vessel before it entered the shipping lanes as a drifter. RU16 was deployed on a New Jersey state mission to monitor dissolved oxygen concentrations for the Environmental Protection Agency. As Irene approached, RU16 was moved offshore to a mid-shelf point where it rode out the storm. This glider provides information on the magnitude and timing of the subsurface mixing that occurred during Irene.

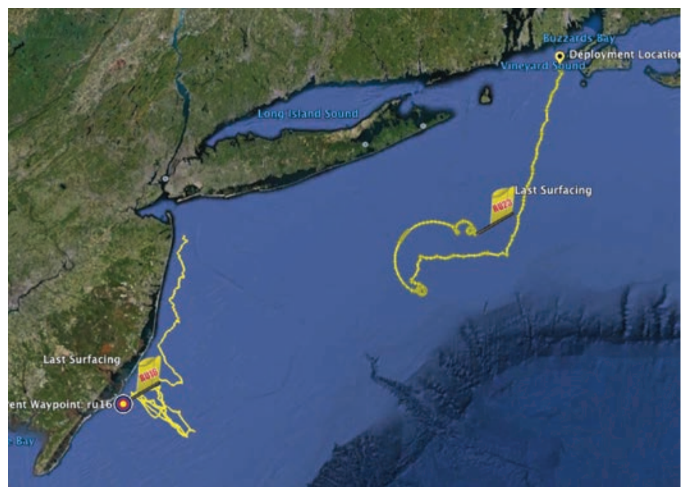

Fig. 6. Tracks for Gliders RU23 (deployed from Martha's Vineyard by UMass) and RU16 (deployed from New York Harbor by Rutgers).

The vertical sections of temperature, salinity and dissolved oxygen from the full RU16 EPA deployment are shown in Fig. 7. Initially in the deployment, as RU16 zig-zags along the New Jersey coast, the T,S and DO profiles illustrate the two distinct surface and bottom layers with the sharp interface typical of the New Jersey shelf in summertime. The surface layer is warmed by the sun, freshened by the riverine outflows from the MAB watersheds, and is oxygenated through its atmospheric interface. The bottom layer is known as the Cold Pool. It is what remains of the cold and salty winter water slowly flowing to the south along the shelf. Isolated from the surface waters by an intense pycnocline that inhibits mixing, dissolved oxygen values in the lower layer often plummet to values that can stress or even kill benthic organisms.

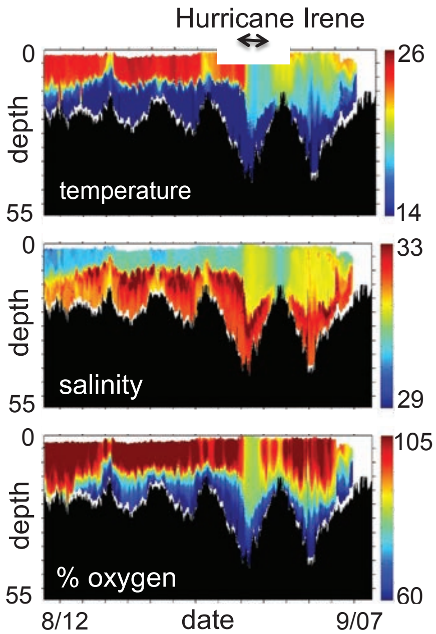

Fig. 7. Temperature, Salinity and Dissolved Oxygen sections from the full deployment of RU16.

Fig. 7 further illustrates the significant impact of Irene on the T, S and DO structure as it passes over the glider on August 28. The response is rapid. The interface between the two layers deepens and the surface layer gets cooler and saltier while the dissolved oxygen level decreases. Oxygen levels in the upper layer quickly recover after the storm, but the surface layer temperature never returns to its summertime pre-storm values. Zooming into the storm mixing period in the temperature section (Fig. 8), the transition from pre-storm to post-storm conditions occurs during the short time period between 00:00 GMT and 14:00 GMT as the eye of Irene passes the glider on August 28.

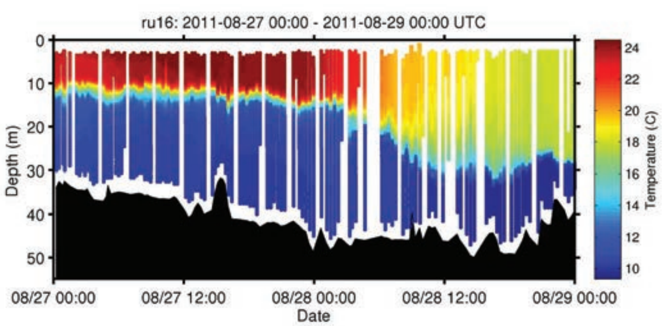

Fig. 8. Detailed plot of the temperature section showing the rapid mixing and cooling of the surface layer that occurred during Irene.

IV. Satellite Observations

V. Atmospheric forecasts over oceanic domains require a boundary condition for sea surface temperature. Numerous sea surface temperature products from a variety of sources are available for this purpose. The major difference between the products is how the cold pixels contaminated by clouds are removed and the resulting data gaps filled. Most commonly used methods include warmest pixel composites that combine multiple images in time, or by interpolating in space across pixels flagged as clouds.

VI. The existing product used to forecast Hurricane Irene's transit through the region is the Real-Time Global High Resolution Sea Surface Temperature product shown (Fig. 9a). For this product, the mixing that occurs during Hurricane Irene is not picked up by this product for several days after Irene left the region.

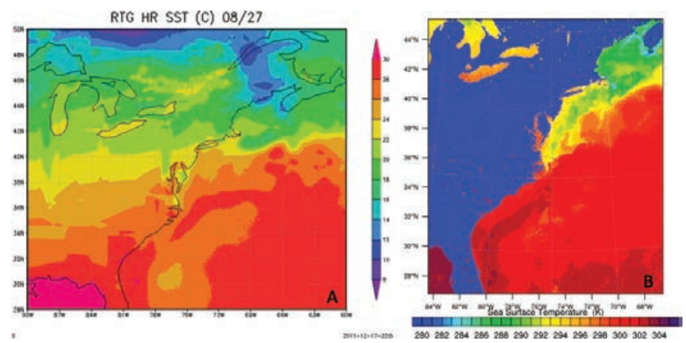

Fig. 9. Sea surface temperature maps (a) used in real time weather forecasts and (b) observed immediately after the clouds cleared from Irene.

To explore the impact of surface cooling during Irene, a new satellite SST product was produced that does not rely on warmest pixel compositing to remove clouds. Instead, daytime images of sea surface temperature where checked for their reflectivity in the visible part of the spectrum. High reflectivity pixels were flagged as clouds, and cooler pixels with low reflectivity were considered ocean pixels cooled by the storm. Retaining these cold but dark pixels observed after the storm produces the image in Fig. 9b. Significant cooling of order 5C-8C is observed on the MAB shelf, with the greatest cooling occurring in the middle of the shelf above the core of the Cold Pool.

VII. Atmospheric Forecast Sensitivities

The Rutgers University implementation of the Weather Research and Forecast (WRF) atmospheric model was used in a series of sensitivity studies to examine the impact of the cooler sea surface temperatures on the Hurricane Irene forecasts. Two endpoints of the sensitivity matrix are illustrated in Fig. 10 where the windfields are plotted at 18:00 GMT after the eye has propagated onto land. In all cases, the track of Hurricane Irene was reproduce, but the intensity of the forecast winds varied. The wind forecast on the left is the run with the standard sea surface temperature product that was available to the real-time forecast models (Fig. 9a). Maximum winds are located over the ocean and are in the 45-55 knot range. The wind forecast on the right is for the same time period but using the cooler sea surface temperature map of Fig. 9b assembled after the event. When this cooler sea surface temperature is used as a boundary condition, the forecast overwater winds are reduced to the 35-45 knot range.

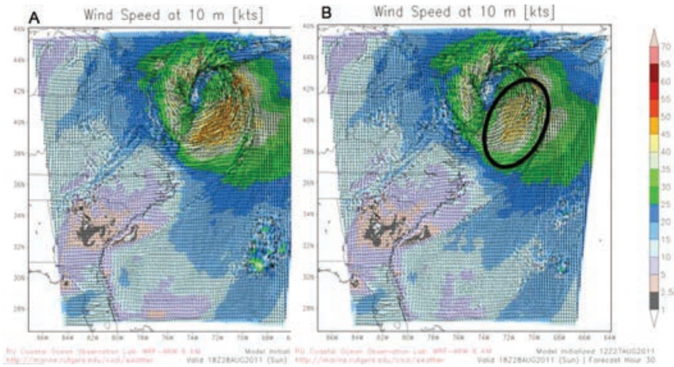

Fig. 10. Wind forecast from RU-WRF (a) using the warm sea surface temperature in figure 9a, and (b) applying the cold sea surface temperature in figure 9b at the time of the mixing observed by glider RU16.

The following table compares the Root Mean Square Error of the National Hurricane Center's best track estimates of Irene's intensity with their real time forecast, two runs of the RU-WRF model run with the warm SST from Fig. 9a, and one run of the RU-WRF model with the cold SST from Fig. 9b. The RSME of the RU-WRF model run using the warm sea surface temperature is similar to the RMSE of the real-time NHC forecast. The difference between the regular WRF model run and the "Hurricane WRF" with the attached Ocean Mixed Layer model is negligible. The WRF model run with the cold SST reduces the RMSE by a factor of 2-3.

TABLE I. MAXIMUM WIND SPEED FORECAST ERROR (KNOTS)

Date/Time (UTC)	*NHC Intensity Forecast*	*RU-WRF Warm SST (RTG) only*	*RU-WRF Warm SST (RTG) + OML Model*	*RU-WRF Cold SST (RTG+SPoRT+ AVHRR)*
27/1200	5	-17.22	-17.23	-6.17
27/1800	10	4.1	4.2	5.88
28/0000	10	1.39	-2.14	3.96
28/0600	5	-1.2	-1.04	-1.21
28/1200	15	2.39	4.79	0.5
28/1800	15	4.97	3.51	-2.67
29/0000	15	3.62	1.93	-0.89
29/0600	10	10.48	9.84	4.52
Sum of Squares	800	457	452	118
RMSE	9.43	7.13	7.09	3.61

VIII. CONCLUSIONS

Sensitivity studies of Hurricane Irene were conducted using the ensemble of MARACOOS atmospheric forecast models. The impact of a variety of Sea Surface Temperature (SST) boundary conditions were studied, ranging from persistence of the warm pre-storm SST to applying the cold post-storm SST at the time mixing was observed by the autonomous underwater gliders. The resulting timing and track are consistent with the real-time forecast ensemble. The composite SST developed using the observed variation in sea surface temperature was found to reduce the intensity of the storm, in some cases by 15 knots, bringing the hindcasts in line with offshore buoy and onshore mesonet observations.

The sensitivity matrix results indicate the potential importance of a coupled atmosphere-ocean model to hurricane intensity forecasting in the Mid Atlantic Bight. The coupled model will be required to produce realistic forecasts of sea surface temperature fields during intense mixing events before the clouds clear after the storm. This will require improved understanding of subsurface mixing processes during intense coastal storms, and sufficient subsurface data from autonomous gliders for assimilation into the ocean model to provide the proper initial state.

ACKNOWLEDGMENT

Support for this research was provided by the U.S. Integrated Ocean Observing System (IOOS) through the Mid-Atlantic Regional Association Coastal Ocean Observing System (MARACOOS). The deployment and operation of Glider RU16 was funded by the Environmental Protection Agency and the New Jersey Department of Environmental Protection.

REFERENCES

[1] S. Glenn, O. Schofield and J. Kohut, "Hurricane Irene 2011: Mid-Atlantic IOOS response to the hurricane", http://maracoos.org/sites/macoora/files/downloads/Hurricane_Irene_blog_2011.pdf, pp. 65, 2011.

[2] H. Roarty, S. Glenn, J. Kohut, D. Gong, E. Handel, E. Rivera, T. Garner, L. Atkinson, W. Brown, C. Jakubiak, M. Muglia, S. Haines, H. Seim, "Operation and Application of a Regional High-Frequency Radar Network in the Mid-Atlantic Bight" Marine Technology Society Journal, 44 (6), 2010.

[3] O. Schofield, J. Kohut, S. Glenn, J. Morell, J. Capella, J. Corredor, J. Orcutt, M. Arrott, I. Krueger, M. Meisinger, C. Peach, F. Vernon, A. Chave, Y. Chao, S. Chien, D. Thompson, W. Brown, M. Oliver, W. Boicourt, "A regional Slocum glider network in the Mid-Atlantic coastal waters leverages broad community engagement." Marine Technology Society 44(6): 64-74, 2010.

Analysis of the Wind Resource off New Jersey for Offshore Wind Energy Development

Hugh Roarty, Joe Riscica, Laura Palamara, Louis Bowers, Greg Seroka, Josh Kohut, Scott Glenn, Rich Dunk
Coastal Ocean Observation Laboratory
Rutgers University
New Brunswick, NJ USA
hroarty@marine.rutgers.edu

***Abstract*—The state of New Jersey has the goal of producing 23% of its energy from renewable sources by 2021. Offshore wind is envisioned as being part of that renewable portfolio. To meet this goal New Jersey passed the nation's first offshore wind renewable energy standard which requires that at least 1,100 megawatts (MW) by 2021. Currently NJ has 0 MW of offshore wind energy. In order to reduce the risk associated with installing these turbines, the Rutgers University Coastal Ocean Observation Laboratory has undertaken a two year study of the ocean winds and currents to provide insight to the wind farm developers to the best locations for siting the wind turbines. A 13 MHz HF radar network was installed to measure the surface currents every 2 km out to a range of 60 km from the coast. These surface current measurements were validated against surface wind measurements from available meteorological stations. The surface currents will then be used to validate the surface winds from a weather model that has been created for this program.**

***Index Terms*—HF radar, offshore wind, forecasting**

I. Introduction

The Rutgers University Coastal Ocean Observation Laboratory (RU-COOL), part of the Institute of Marine and Coastal Sciences (IMCS), is proposing to provide a detailed analysis of the wind resource and sea surface conditions over the area designated for potential wind energy development as defined by the NJ Energy Master Plan and the NJ Offshore Wind (OSW) Economic Development Act. The results of the previous offshore wind resource analysis conducted by RU-COOL for the New Jersey Board of Public Utilities (NJBPU) will be used as the basis for the proposed study. That study used the Rutgers University version of the Weather Research and Forecast model (RU-WRF). We propose to further enhance and verify the RU-WRF model, and run it over the 2-year study period, to enable further refinements in the estimates of the spatial and temporal variability of the offshore wind resource. Enhancements include nesting to resolutions better than 1 km, and use of a newly available sea surface temperature product generated at Rutgers for the Integrated Ocean Observing System (IOOS). Sea surface conditions and near surface winds for the entire study domain will be derived by Coastal Radar (CODAR) and high-resolution infrared satellite detection. Available data from coastal/offshore meteorological monitoring systems will be used to validate the vertical wind structure, and data from a surface current mapping radar network will be used to validate the complex horizontal structure. These remote sensing systems not only will provide necessary data for the wind resource assessment, they also will be used to support the coastal and offshore ecological studies being conducted under the supervision of the New Jersey Department of Environmental Protection (NJDEP). Specifically, the shore sites for each CODAR HF radar site are preferred locations for inexpensive Automatic Information System (AIS) transceivers to collect data on existing vessel traffic in the development area. Site variability and local wind resource perturbations, such as the sea breeze circulation, that affect wind power production will be resolved. Results of the proposed project can then be used to determine optimum, good, and poor locations for wind energy development. This will contribute to the risk reduction associated with achieving the objectives of the NJ Energy Master Plan and the NJ OSW Economic Development Act. The proposed wind resource and sea surface analysis program using a combination of advanced and adaptive monitoring and modeling systems that account for the dynamic interactions of the coast, sea, and atmosphere, which define the offshore wind resource, should prove to be cost-effective for assisting decision makers and other stakeholders involved in offshore wind energy development.

Additionally, the ocean monitoring systems will become part of the IOOS network thus increasing the coverage for weather forecasting, homeland security activities, water quality, fisheries, and the safety of life at sea. Furthermore, the proposed assessment program, which has both diagnostic and predictive capabilities, can support forthcoming forecasting efforts associated wind turbine installation and operational applications. At the conclusion of this 2-year study, technology that will be in place to continue supporting offshore wind development include (a) a fully validated high-resolution nested atmospheric forecast model (RU-WRF) that can be run daily, (b) a nested CODAR HF Radar network that provides hourly high resolution surface current maps in near-real time, (c) a collocated AIS transceiver network to monitor all reporting vessel traffic in the region, and (d) the satellite data analysis and model coupling routines to provide locally constructed and verified boundary conditions for area-specific wind resource and sea breeze forecasting.

II. Methods

A thirteen MHZ HF radar network was installed as part of this project. The CODAR SeaSonde type HF radars were installed in Brant Beach (BRNT), Brigantine (BRMR), Strathmere (RATH) and North Wildwood (WOOD) New Jersey. The average spacing between the systems was 29 km. The first system was installed in December 2011 and the last system was installed in January 2012. The radial data from three other thirteen MHz systems at Sea Bright [1], Belmar and Seaside Park, NJ was also used in this study. The radial data from these seven stations was combined on the 2km National grid [2] to produce surface current measurements once an hour.

The HF radar data collected for this study spanned from January to June 2012. A representative temporal and spatial coverage for the HF radar data is shown in Figure 1. The surface current data was compared with the wind measurements at six other locations. Three of the locations were National Data Buoy Center (NDBC) station 44025 Long Island 33 nautical miles south of Islip, NY, station 44065 entrance to New York Harbor and station 44009 Delaware Bay 26 nmi southeast of Cape May, NJ. The other three wind measurements were from MARACOOS partner WeatherFlow. Their stations were located in Tuckerton (station 37558), Barnegat Inlet (station 45247) and Atlantic City (station 1103) New Jersey. The wind data was binned to every hour to match the HF radar data.

The closest surface current grid point with at least 70% temporal coverage over the study period was used to compare with the wind measurements. The surface current data was first detided using a least squares technique that accounted for the 5 major constituents in the region (M2, S2, N2, K1 and O1). The currents were then passed through a 30-hour low pass filter. An example of this analysis is shown in Figure 2 for the east/west velocity u and Figure 3 shows the analysis for the north/south velocity v.

Then the complex correlation between the surface currents and surface wind were computed on a monthly basis (Figure 4). The complex correlation outputs a magnitude and bearing of the surface current most correlated with the wind. If the bearing is positive, it indicates that the surface currents are shifted to the right of the wind as should be the case in the northern hemisphere [3]. Then the currents were rotated based on the bearing to match the angle of the wind data (Figure 5). This methodology follows the work of previous research on the comparison between surface currents and winds [4]. The correlation between the rotated surface currents and one of the wind measurements for the entire study period is shown in Figure 6.

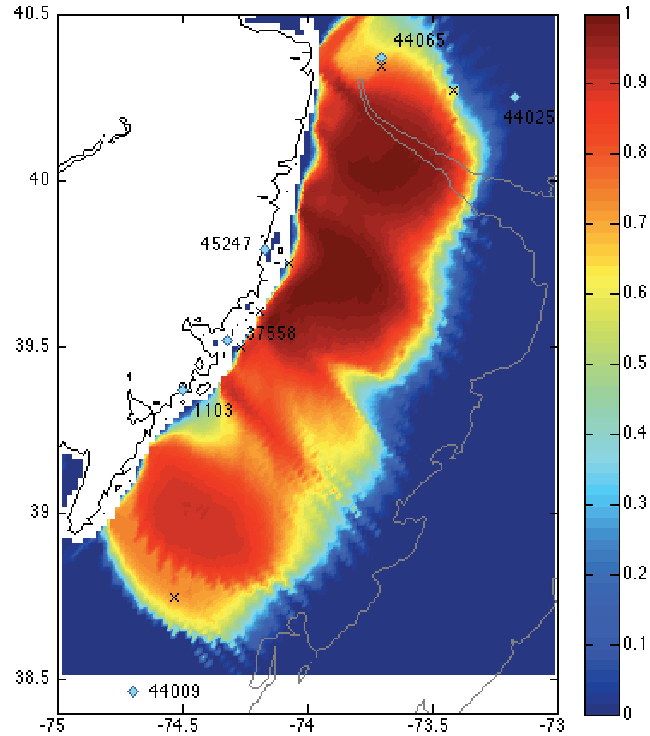

Figure 1: Spatial data coverage of the HF radar network from January 23 to May 7, 2012. The location of other data sampling locations are also depicted: NDBC buoys 44009 and 44025 and WeatherFlow wind stations 1103, 37558 and 45247. The x's mark the closest point to the wind measurements where there was HF radar surface current data for 70% of the study period. Bathymetry contours are shown as the gray lines.

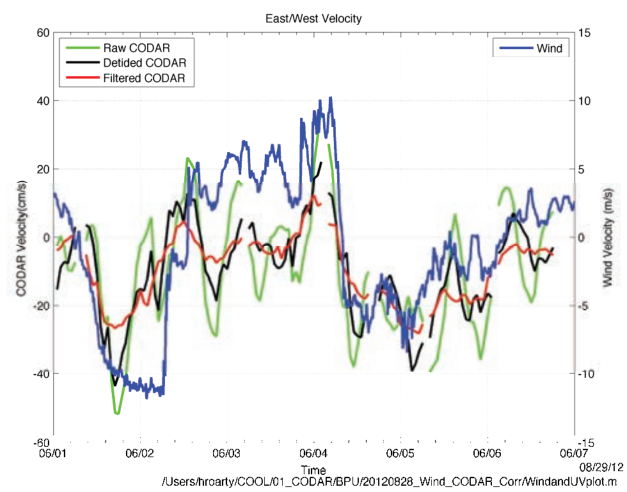

Figure 2: Time series plot from June 1-7, 2012 of the u velocity of the CODAR surface currents (green), detided surface currents (black), low pass filtered currents (red) and wind from station 44025 (blue).

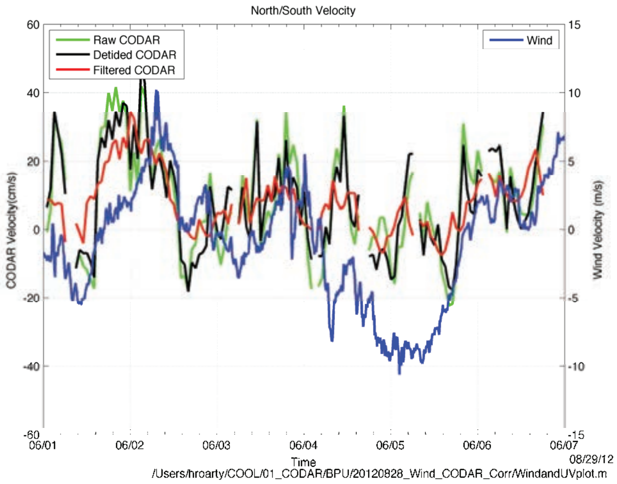

Figure 3: Time series plot from June 1-7, 2012 of the v velocity of the CODAR surface currents (green), detided surface currents (black), low pass filtered currents (red) and wind from station 44025 (blue).

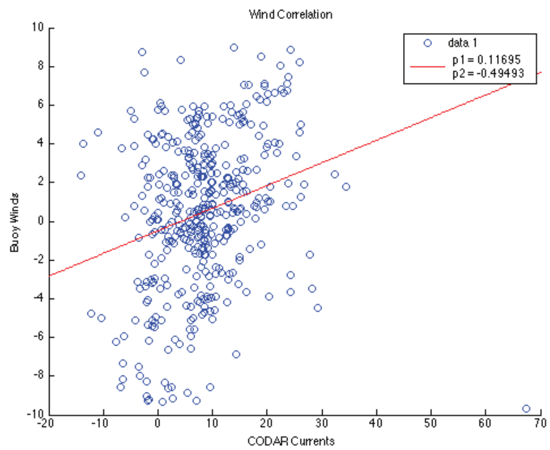

Figure 4: Scatter plot of u velocity for CODAR surface currents (cm/s) vs. u Winds from buoy 44025 (m/s) for June 2012.

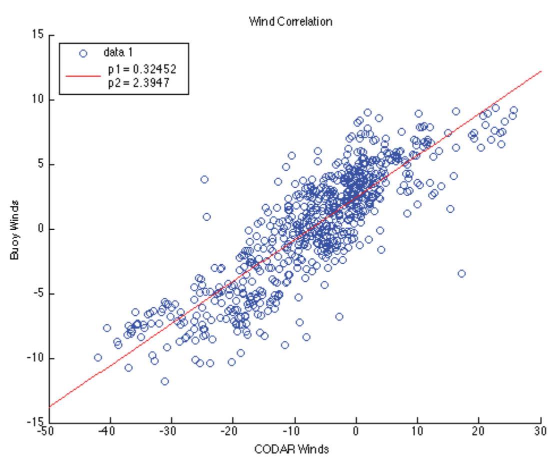

Figure 5: Scatter plot of rotated u velocity for CODAR surface currents (cm/s) vs. u Winds from buoy 44025 (m/s) for June 2012.

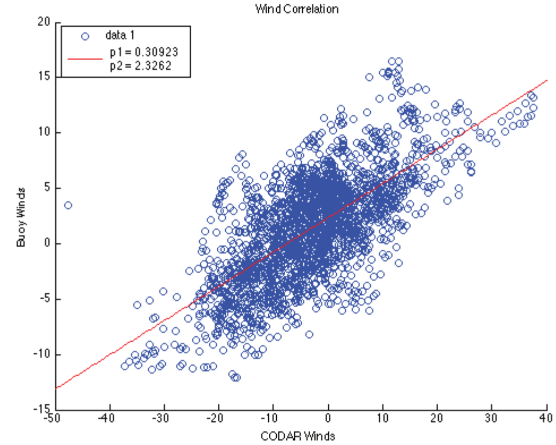

Figure 6: Scatter plot of rotated u velocity for CODAR surface currents (cm/s) vs. u Winds from buoy 44025 (m/s) for January to June 2012.

III. Results

The process, as described in the previous section, of comparing the surface current to the wind was repeated for each of the six wind sensors in the study area. The correlation between the surface currents and the wind were computed on a monthly basis. These six monthly measurements were then averaged to compute a spatial average over the study area of the surface currents with the wind as shown in Figure 7. This was done with the raw, detided and low pass filtered surface current records. The filtered product consistently produced the highest correlation of the surface currents with the wind.

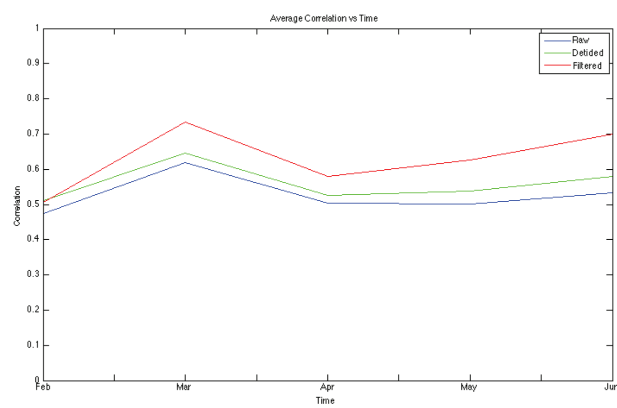

Figure 7: Average correlation between the CODAR surface currents (raw, detided and filtered) and the six wind measurements as a function of time. The x axis spans from February to June 2012.

IV. Conclusions

A weather model and 13 MHz HF radar network have been constructed to study the offshore wind resource off New Jersey for the potential construction of offshore wind turbines. The HF radar network is being utilized to assess the surface currents off New Jersey and to validate the weather model. The surface wind data from the model will be compared with the data from the HF radar network. Before this can take place the surface currents from the HF radar network were compared with point measurements of six meteorological stations in the study area. The HF radar surface currents showed moderate to strong correlation with each of the wind measurements throughout the study period. Therefore we conclude that the HF radar surface currents will be a valid method to evaluate the spatial variability of the surface winds in the weather model.

ACKNOWLEDGEMENTS

This work was funded by a grant from the New Jersey Board of Public Utilities "An Advanced Atmospheric/Ocean Assessment Program Designed to Reduce the Risks Associated with Offshore Wind Energy Development Defined by the NJ Energy Master Plan and the NJ Offshore Wind Energy Economic Development Act".

References

[1] H. Roarty, E. Lemus, E. Handel, S. Glenn, D. E. Barrick, and J. Isaacson, "Performance Evaluation of SeaSonde High-Frequency Radar for Vessel Detection," *Marine Technology Society Journal,* vol. 45, pp. 14-24, 2011.

[2] E. Temll, M. Otero, L. Hazard, D. Conlee, J. Harlan, J. Kohut, P. Reuter, T. Cook, T. Harris, and K. Lindquist, "Data Management and Real-time Distribution in the HF-Radar National Network," in *OCEANS 2006*, 2006, pp. 1-6.

[3] V. W. Ekman, "On the Influence of the Earth's Rotation on Ocean Currents," *Arkiv. Mat. Astron. Fysik,* vol. 2, 1905.

[4] J. T. Kohut, S. M. Glenn, and R. J. Chant, "Seasonal current variability on the New Jersey inner shelf," *J. Geophys. Res.,* vol. 109, p. C07S07, 2004.

Expanding the Coverage of HF Radar Through the Use of Wave Powered Buoys

Hugh J. Roarty, Michael Smith,
Ethan Handel, Scott M. Glenn
Coastal Ocean Observation Laboratory
Rutgers University
New Brunswick, NJ USA
hroarty@marine.rutgers.edu

Donald E. Barrick

CODAR Ocean Sensors
Mountain View, CA USA
don@codar.com

Abstract— **There are approximately 120 High Frequency (HF) radars deployed throughout the United States that are contributing to the Integrated Ocean Observing System (IOOS) National High Frequency Radar Network. The network is operational with the United States Coast Guard for search and rescue. These systems also posses a dual use capability for environmental monitoring with simultaneous detection of vessels at sea. These systems have ranges between 30 and 180 km offshore depending on the chosen frequency. These systems ability to measure the alongshore current is hampered by the geometry of the deployment locations. At the farthest ranges the radar can measure the cross-shore currents well while the alongshore current requires a scattering angle that is difficult to achieve with stations on land. We undertook a study to increase the coverage of HF radars through the use of an offshore transmitter. This bistatic signal increased the coverage of the HF radar network and also increased the number of look angles for current measurements. The signal was also used to extend the vessel detection capability of one of the radars. The placement of an offshore bistatic transmitter at key locations around the country can increase the accuracy and range of the National High Frequency radar network. The efficacy of the network's use in search and rescue, hazardous material spill response and homeland security can be increased through the use of offshore transmitters.**

Index Terms—**geoscience, remote sensing, multistatic radar, oceans**

I. Introduction

There are approximately 120 High Frequency (HF) radars deployed throughout the United States that are contributing to the Integrated Ocean Observing System (IOOS) National High Frequency Radar Network [1]. The network is operational with the United States Coast Guard for search and rescue. These systems also posses a dual use capability for environmental monitoring with simultaneous detection of vessels at sea [2].

These systems have ranges between 30 and 180 km offshore depending on the chosen frequency. These systems' ability to measure the alongshore current at offshore ranges of 70 to 150 km is hampered by the geometry of the deployment locations. The radar can measure the cross-shore currents at long distances well while the alongshore current requires a scattering angle that is difficult to achieve with stations on land. We undertook a study to increase the coverage of HF radars through the use of an offshore transmitter. The platform for the offshore transmitter was a wave powered buoy.

II. HF Radar Network

This experiment was conducted within the Mid Atlantic Regional Association Coastal Ocean Observing System (MARACOOS) [3]. A key component of this Observing System is a High Frequency radar network consisting of 36 radar sites. All the sites are equipped with SeaSonde HF radar systems from CODAR Ocean Sensors, Mountain View, CA. The radar sites used in this study were from north to south located in Sea Bright, Belmar and Seaside Park, NJ (Figure 1). The three shore stations were augmented with an at sea bistatic transmitter. An at sea bistatic transmitter has the capability to double or quadruple the coverage of an existing HF radar network [4].

The bistatic transmitter was designed and manufactured by CODAR Ocean Sensors. The transmitter designed to consume 80 watts and transmit 50 watts of power via the radio signal. The transmission signal from the bistatic transmitter is different from that of the SeaSonde where the signal from the bistatic transmitter is a continuous signal while the signal from the SeaSonde is pulsed with a 50% duty factor. The signal is pulsed from the SeaSonde due to the close proximity of the transmitter and receiver whereas this is not the case for the bistatic transmitter.

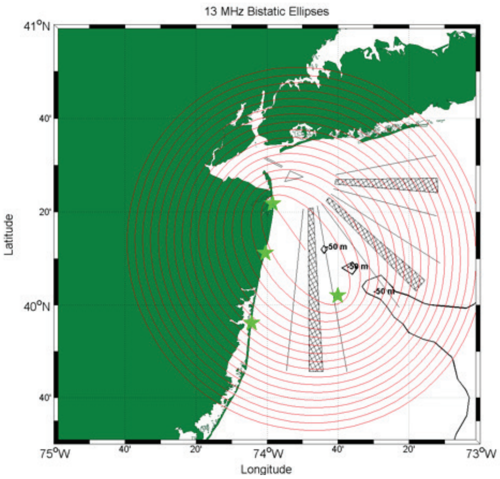

Figure 1: Location map for the experiment. The three HF radar stations are shown as the green stars on land. The LEAP buoy is the green star offshore. The bistatic time delay cells between the Sea Bright radar and LEAP buoy are shown as the red ellipses. The 50 m bathymetry contour and shipping lanes into New York Harbor are also shown on the map.

The theoretical coverage of a single 13 MHz HF radar is shown in Figure 2. This figure depicts the signal to noise ratio for the received radar signal. The theoretical coverage of a single 13 MHz radar paired with an at sea bistatic transmitter is shown in Figure 3. If you take the 20 dB contour as the range of the system, the coverage area for the single HF radar is 1,800 km2 while the coverage area for the system with the at sea bistatic transmitter is 4,600 km2, 2.5 times that of the single system.

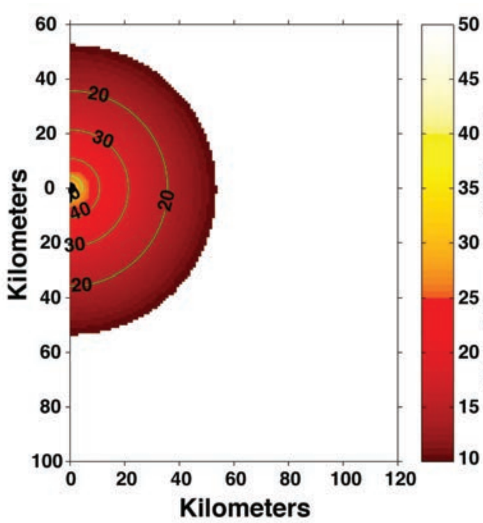

Figure 2: Theoretical coverage of a single 13 MHz HF radar in monostatic mode. The signal to noise ratio (dB) for the received signal is depicted by the color map and contours of equal signal strength are shown as the green lines.

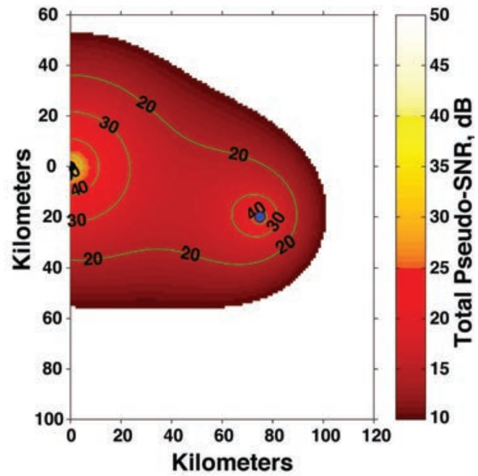

Figure 3: Theoretical coverage of a single 13 MHz HF radar paired with a bistatic transmitter 82 km offshore. The signal to noise ratio (dB) for the received signal is depicted by the color map and contours of equal signal strength are shown as the green lines.

III. Wave Powered Buoy

Ocean Power Technologies (OPT), Pennington NJ, manufactured the wave powered buoy, named the Littoral Expeditionary Autonomous PowerBuoy (LEAP). A drawing of the buoy is given in Figure 4. The three main parts of the buoy are the spar, float and heave plate. The spar section is designed to remain stationary while the float (yellow discus) is designed to move relative to the spar with the passage of each wave. The float is attached to a power take off (PTO) unit that converts the mechanical energy into electrical energy. Excess electrical power is stored in a bank of batteries located in the lower spar section that make power available to the payload during periods of flat calm seas.

The OPT PowerBuoy used during this test offered significant advantages as a platform for the HF bistatic transmitter. Firstly, the approximate 120W power requirement of the transmitter exceeds that which can be consistently produced from other at-sea power sources such as solar, small scale wind, or batteries alone. The alternative of using a diesel powered buoy would have brought its own challenges and risks. A spar buoy additionally provides a stable platform for sensors and communications, and is well adapted to provide a stable mounting platform for the HF radar antenna.

Figure 4: Schematic drawing of the OPT PowerBuoy. The three main sections are the float (yellow disk at top), spar (vertical cylinder) and heave plate (orange disk at the bottom).

IV. Installation and Operation

A 13 MHz bistatic transmitter and other instrument payloads were placed atop and in the upper section of the spar. The buoy was deployed on August 11, 2011 36 km offshore of Point Pleasant, NJ. We were conservative in placing the transmitter at this distance. The location of the transmitter that would optimize the spatial coverage of the HF radar network is 75 km offshore. However the closer distance to shore allowed for more frequent physical inspections of the buoy during this initial test period.

The buoy provided power to the transmitter on a continuous basis from August 11, 2011 till its recovery on October 31, 2011. The buoy even endured the passage of Hurricane Irene on August 28, 2011 (Figure 6). The signal transmitted from the buoy was received onshore by three SeaSonde systems.

Figure 5: The LEAP buoy being deployed off the coast of New Jersey by Coast Guard buoy tender. The white antenna on the left is the 13 MHz transmit antenna.

This bistatic signal increased the coverage of the HF radar network (Figure 7) and also increased the number of look angles for current measurements. The signal was also used to extend the vessel detection capability of one of the radars. A case study was made of the merchant vessel Amalthea as it was leaving NY harbor. The radar station at Sea Bright, NJ made monostatic detections of the vessel over a 1.5-hour period. The detections from the bistatic signal atop the buoy extended for 1.25 hours after the monostatic detections ceased essentially doubling the amount of detections.

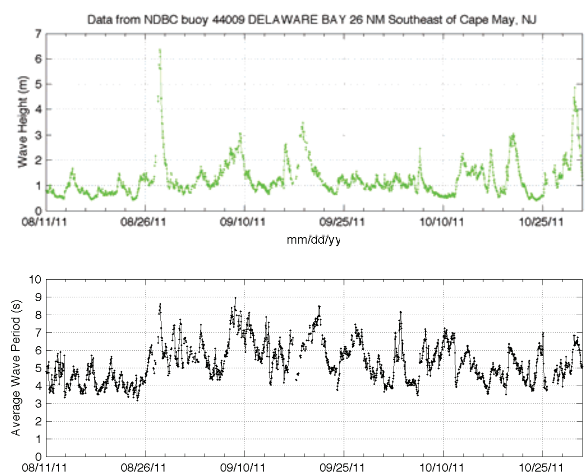

Figure 6: Wave environment during the deployment of the LEAP buoy. This is from NDBC buoy 44009 Delaware Bay.

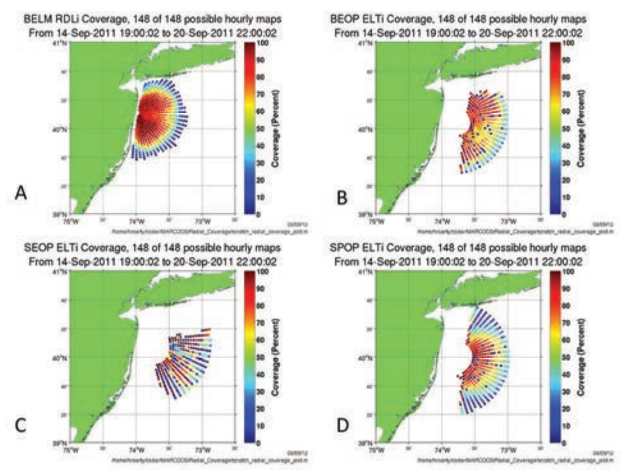

Figure 7: One week coverage density maps for A) Belmar radial site. Bistatic elliptical maps between the offshore transmitter and B) Belmar C) Sea Bright and D) Seaside Park. Red indicates 100% temporal coverage and dark blue shows 0% temporal coverage.

V. CONCLUSIONS

A bistatic HF radar transmitter was placed atop a wave-powered buoy. The transmitter and buoy both operated for a three-month test period. The signal from the bistatic transmitter was received at three radar stations along the northern coast of New Jersey. The bistatic signal increased the coverage of the HF radar network for surface currents and vessel detection.

The placement of an offshore bistatic transmitter at key locations around the country can increase the accuracy and range of the National High Frequency radar network. The efficacy of the network's use in search and rescue, hazardous material spill response and homeland security can be thus improved through the use of offshore transmitters.

ACKNOWLEDGMENT

This work was funded by the US Navy under contract N00253-09-D-0005 from Naval Undersea Warfare Center Keyport Division.

References

[1] J. Harlan, A. Allen, E. Howlett, E. Terrill, S. Y. Kim, M. Otero, S. Glenn, H. Roarty, J. Kohut, J. O'Donnell, and T. Fake, "National IOOS high frequency radar search and rescue project," in *OCEANS 2011*, 2011, pp. 1-9.

[2] H. J. Roarty, D. E. Barrick, J. T. Kohut, and S. M. Glenn, "Dual-Use Compact HF Radars for the Detection of Mid- and Large-Size Vessels," *Elektrik, Turkish Journal of Electrical Engineering and Computer Sciences,* vol. 18, pp. 373-388, 2010.

[3] H. J. Roarty, S. M. Glenn, J. T. Kohut, D. Gong, E. Handel, E. Rivera Lemus, T. Garner, L. Atkinson, C. Jakubiak, W. Brown, M. Muglia, S. Haines, and H. Seim, "Operation and Application of a Regional High Frequency Radar Network in the Mid Atlantic Bight," *Marine Technology Society Journal,* vol. 44, pp. 133-145, 2010.

[4] J. Harlan, P. Michael Kosro, Pete Barletto, "Next Generation Use of High Power and Bandwidth in the NE Pacific - A Component of the NSF Ocean Observing Initiative," in *Oceans 2009, MTS/IEEE Biloxi - Marine Technology for Our Future: Global and Local Challenges*, Biloxi, MS, 2009, pp. 1-8.

Automated Quality Control of High Frequency Radar Data

Hugh Roarty, Michael Smith, John Kerfoot, Josh Kohut, Scott Glenn
Coastal Ocean Observation Laboratory
Rutgers University
New Brunswick, NJ USA
hroarty@marine.rutgers.edu

Abstract*— There are approximately 300 High Frequency (HF) radars deployed around the globe making real time measurements of the surface currents in the coastal ocean. In the United States, the HF radar network within the Mid Atlantic Regional Association Coastal Ocean Observing System (MARACOOS) became operational with the United States Coast Guard in May 2009. This model was expanded nationally and the Integrated Ocean Observing System (IOOS) National HF Radar Network became operational with the Coast Guard in March 2011. Much of the quality control that is done with the data requires a person in the loop to be inspecting the data. We present several metrics and techniques to automate the quality control process to ensure that the radial and total velocity measurements are accurate. We have used average radial bearing, spectra merged count, radial count and data latency as measurements that are useful in assessing the performance of the network. Some of those techniques include real time comparisons with ADCPs and comparison of the detided total vector fields with nearby wind measurements. We also present metrics to gauge the performance of the network over seasonal and yearly time scales. The goal of the network is to provide surface currents to the Coast Guard over 80% of the spatial region of the Mid Atlantic over 80% of the time. The spatial grid that the network could realistically cover contained all grid points within 150 km of the coast and out beyond the 15 m isobath. We have also developed a user interface for the operators to control what radial sites contribute to the total vector generation. As discussed at the Radiowave Oceanography Working Group (ROWG) meetings it is the responsibility of the region to provide quality-controlled data to the National Network. Currently the National Network has only two checks for the radial data 1) that the radial measurement is over water and 2) that the magnitude of the radial measurement is below a certain threshold based on the region of the measurement. This model where radial data is inspected at the regional level before being sent onto the National Network can be expanded to the other 10 regions of the country. This also keeps the decision of what data is correct where the local knowledge of the current structure is best understood. We saw that these techniques can eliminate errors in the data stream. This also acts as a feedback mechanism to the operators to evaluate their performance in operating and maintaining the radars. The techniques discussed here can serve as data quality checks for the vast number of systems operating today. They will ensure that the data being produced is of the highest quality, which will in turn ensure that the products being generated with this data are sound and reliable.

***Index Terms*—HF radar, radar remote sensing, quality control**

I. Introduction

There are approximately 300 High Frequency (HF) radars deployed around the globe making real time measurements of the surface currents in the coastal ocean. In the United States, the HF radar network within the Mid Atlantic Regional Association Coastal Ocean Observing System (MARACOOS) became operational with the United States Coast Guard in May 2009. This model was expanded nationally and the Integrated Ocean Observing System (IOOS) National HF Radar Network became operational with the Coast Guard in March 2011. Much of the quality control that is done with the data requires a person in the loop to be inspecting the data.

We present several metrics and techniques to automate the quality control process to ensure that the radial and total velocity measurements are accurate. We have used average radial bearing, spectra merged count, radial count and data latency as measurements that are useful in assessing the performance of the network. Some of those techniques include real time comparisons with ADCPs and comparison of the detided total vector fields with nearby wind measurements. We also present metrics to gauge the performance of the network over seasonal and yearly time scales. The goal of the network is to provide surface currents to the Coast Guard over 80% of the spatial region of the Mid Atlantic over 80% of the time.

We have also developed a user interface for the operators to control what radial sites contribute to the total vector generation. As discussed at the Radiowave Oceanography Working Group (ROWG) meetings it is the responsibility of the region to provide quality-controlled data to the National Network. Currently the National Network has only two checks for the radial data 1) that the radial measurement is over water and 2) that the magnitude of the radial measurement is below a certain threshold based on the region of the measurement. This model where radial data is inspected at the regional level before being sent onto the National Network can be expanded to the other 10 regions of the country. This also keeps the decision of what data is correct where the local knowledge of the current structure is best understood.

We saw that these techniques can eliminate errors in the data stream. This also acts as a feedback mechanism to the operators to evaluate their performance in operating and maintaining the radars. The techniques discussed here can serve as data quality checks for the vast number of systems operating today. They will ensure that the data being produced is of the highest quality, which will in turn ensure that the products being generated with this data are sound and reliable.

II. Radial Quality Control

The NOAA National HF Radar Network has in place some quality control tests that are applied to the radial data before they are used to make total vector maps (Otero 2008). First the radial file is checked to make sure all required metadata is present and variables are within limits (e.g. -90≤ latitude ≤+90). Then the radial vectors are screened removing any that are above the magnitude threshold and over land. The magnitude threshold for the East and Gulf Coast of the United States is 3 m/s and 1 m/s for the West Coast. We present several additional tests that can be applied to the radial data to quality control it before it is used to make total vectors. We propose that these tests be performed at the regional level, as the technicians in the region are most familiar with the radial data. We also envision that these checks would be run on the portal [1] as the national network is accepting the radial data.

A majority of HF radars in the United States if not the world are located on straight shorelines with limited angular coverage. There are a few exceptions (25 MHz SeaSonde located on the Chesapeake Bay Bridge [2] where the radar is able to make measurements over 360 degrees of water. So in most instances the radar covers approximately 180 degrees of ocean (Figure 2).

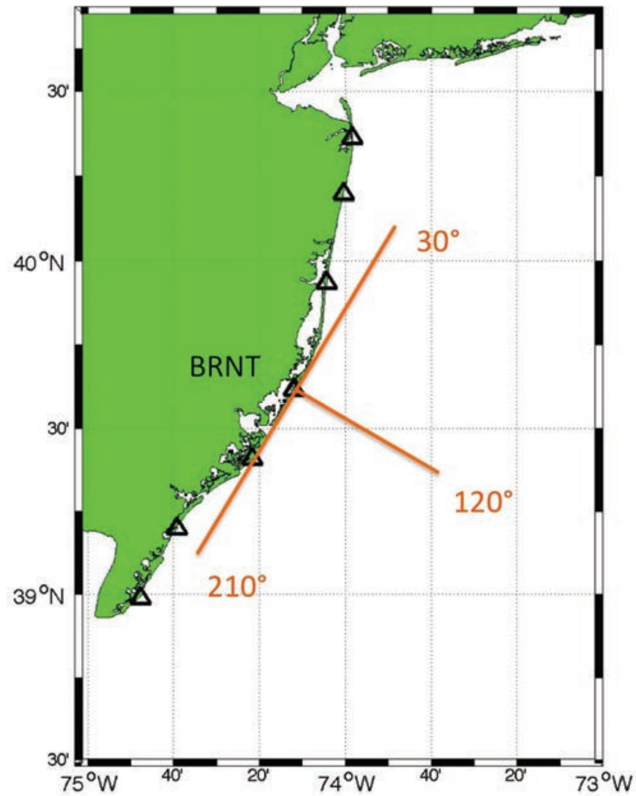

Figure 1: Map showing the location of HF radar stations (black triangles) along the coast of New Jersey. The shore normal and shore parallel bearing angles for the Brant Beach (BRNT) radar site are also shown.

As part of the diagnostic reporting the SeaSonde software calculates an average radial bearing. Most sites will have a bearing that is perpendicular to the shore. This shore normal bearing will serve as a reference and if the average bearing for the radial file is outside 1 standard deviation then the data is not admitted to the portal. The time over which to calculate the standard deviation will have to be researched further.

Another quality control metric is the comparison between the average radial bearing for the measured and ideal radials. Any metal in the near field of the antenna can distort the pattern of the receive antenna and produce errors in the bearing estimates of the vector measurements. This can be corrected for by performing an antenna calibration [3]. The radial vectors produced with the theoretical cosine antenna patterns are referred to as ideal radials. The radials produced with the calibrated antenna pattern are referred to as measured radials. If the distortion of the environment is low then these two measurements should be close to each other. Figure 3 shows the average radial bearing for the Brant Beach radar site from March 1 till August 18, 2012. The measured radials showed a consistent measurement of ~ 120 degrees while the ideal radials were more erratic with a mean of ~60 degrees and a standard deviation of ~ 60 degrees. It was discovered that the antenna had a coupling problem and this was causing the erratic vectors. The antenna was replaced on June 8, 2012 and the correlation between the ideal and measured radials average bearing increased after this. So if the difference between the measured and ideal radials is above some predetermined threshold then the radial data is flagged.

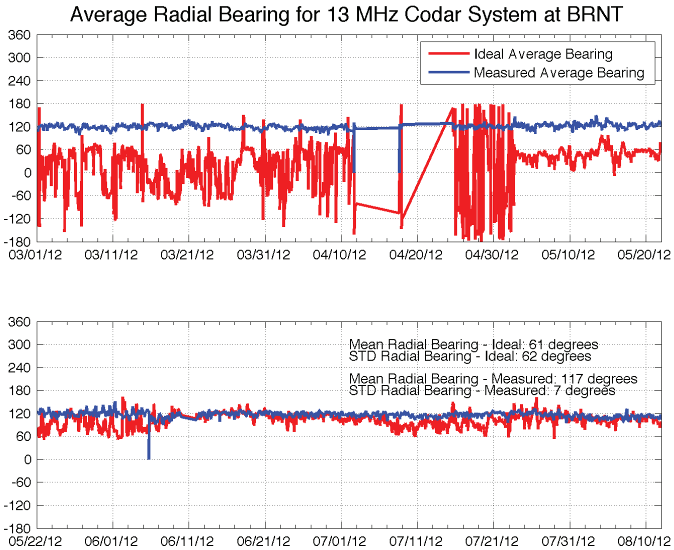

Figure 2: Average radial bearing plot for ideal radials (red) and measured radials (blue) for the Brant Beach radar site from March 25 to August 12, 2012.

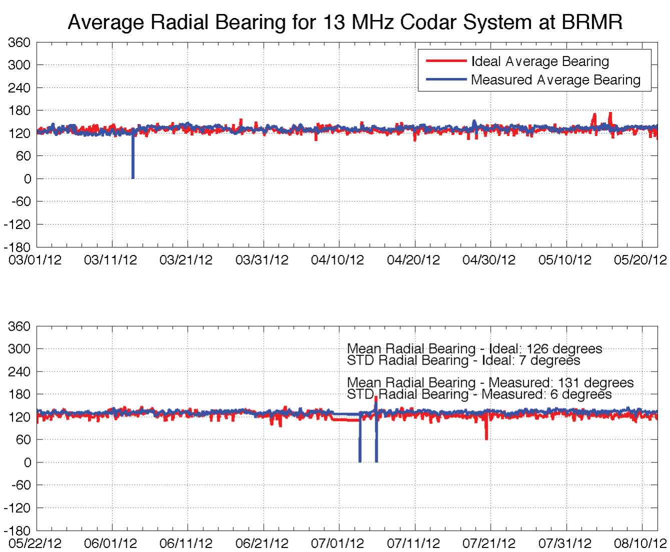

Figure 3: Average radial bearing plot for ideal radials (red) and measured radials (blue) for the Brigantine radar site from March 25 to August 12, 2012.

Lastly, we have analyzed the average radial velocity and compared it to the M2 principal lunar semidiurnal tidal constituent. The M2 is the strongest tidal constituent in the Mid Atlantic accounting for over 80% of the tidal variance [4]The entire radial data file was averaged each hour to create a time series of average radial velocity (Figure 5). The water level record from the tidal gauge at Atlantic City, NJ was also plotted along with the number of vectors per radial file. The number of radial vectors per file should accompany the interpretation of the average radial time series as a low number of vectors would decrease the confidence of the statistic. The 13 MHz data presented here does not exhibit the diurnal variability present in the 5 MHz systems [5]. Previous research on 13 MHz systems has suggested 520 radial vectors per file with a standard deviation of 310 [6]. That would match the results found here.

A fast Fourier transform (fft) was applied to each of the time series and is presented in Figure 6. All the systems display a peak near the 12.42-hour period, which coincides with the M2 tide. Based on this result we can say that the systems were operating properly over this time period. We analyzed another time period March 1-9, 2012 which is shown in Figure 7. Two of the systems (WOOD and RATH) do not show a peak near the M2 tidal period and the amplitude of the signal for BRNT is well below the other systems. The BRNT site was malfunctioning during this time period as mentioned earlier in this section. Each of these three systems should be flagged for low quality data during this time period.

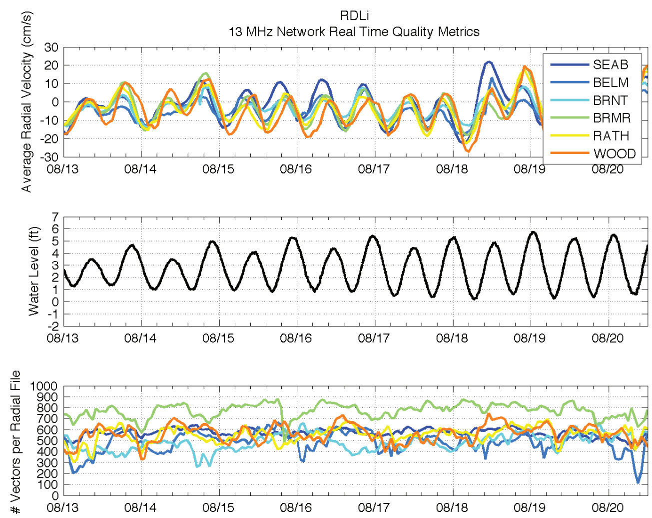

Figure 4: Plot of average radial velocity for six HF radar stations in New Jersey (top), plot of water level at Atlantic City, NJ (middle) and plot of the number of radial vectors per radial file (bottom). The X axes are month/day mm/dd for 2012.

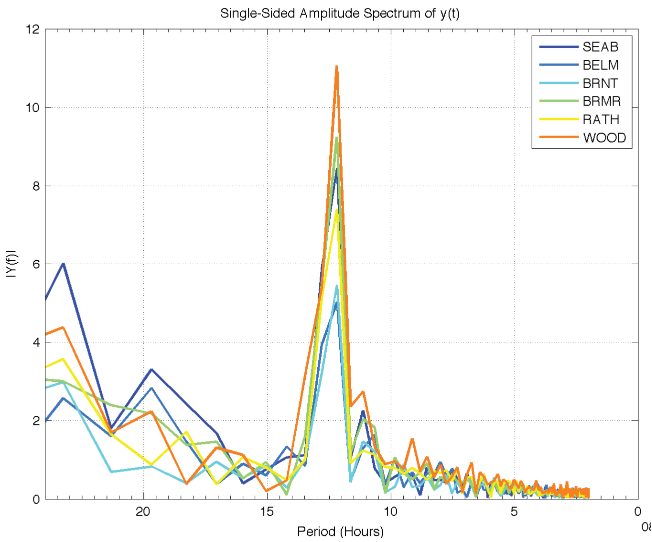

Figure 5: Fast Fourier transform of the average radial velocity for the 13 MHz HF radar sites in New Jersey. The data covers August 13-20, 2012.

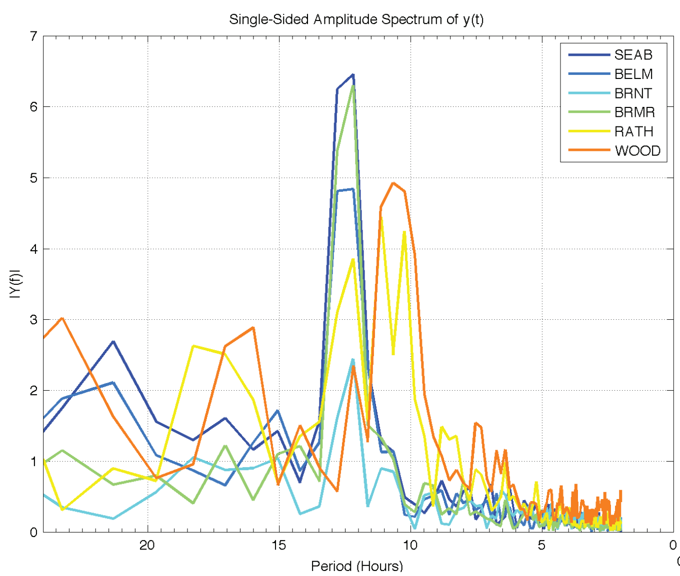

Figure 6: Fast Fourier transform of the average radial velocity for the 13 MHz HF radar sites in New Jersey. The data covers March 1-9, 2012.

III. RADIAL DATABASE

Once the data is retrieved from the radar site it must be stored in a central location for easy access and analysis. We have created a MySQL database to store the radial data for the sites within the region. The web display for the database can be found here (Figure 7): http://marine.rutgers.edu/cool/maracoos/codar/radials/.

The creation of the database allows for more robust processing of the radial to total data. The database provides an interface between the radial data and the Internet to make data management and visualization accessible from any web enabled device. If the communications are down to a particular radial site and the radial data is not retrieved in real time, the processing will detect when the communications are restored and reprocess any totals where the missing radial data is now present.

MARACOOS HF Radar Network Status: Active Systems

Network Home | LR Sites | MR Sites | SR Sites

Site Code	System Type	Tx Frequency(MHz)	Latitude	Longitude	Latest Radial	Site Link
ASSA	LR	4.55	38.205	-75.1529	RDLi_ASSA_2012_06_14_1800.ruv	
BLCK	LR	4.925	41.1527	-71.5509	RDLi_BLCK_2012_06_14_1800.ruv	
BRIG	LR	4.75	39.4074	-74.3621	RDLi_BRIG_2012_06_14_1800.ruv	
CEDR	LR	4.9795	37.6729	-75.5923	RDLi_CEDR_2012_06_14_1800.ruv	
DUCK	LR	4.537817	36.1803	-75.7501	RDLi_DUCK_2012_06_14_1800.ruv	
HATY	LR	4.537818	35.2572	-75.5199	RDLi_HATY_2012_06_14_1800.ruv	
HEMP	LR	4.513	40.586835	-73.590271	RDLi_HEMP_2012_06_14_1800.ruv	
HOOK	LR	4.537183	40.4332	-73.9838	RDLi_HOOK_2012_06_14_1800.ruv	
LISL	LR	4.55	36.6917	-75.9226	RDLi_LISL_2012_06_14_1800.ruv	
LOVE	LR	4.537183	39.7362	-74.1171	RDLi_LOVE_2012_05_22_1500.ruv	
MRCH	LR	4.78	40.7887	-72.7455	RDLi_MRCH_2012_06_14_1800.ruv	
MVCO	LR	5.6	41.3498	-70.5268	RDLi_MVCO_2012_06_14_1800.ruv	
NANT	LR	5.35	41.2498	-69.9719	RDLi_NANT_2012_06_14_1800.ruv	
NAUS	LR	4.78	41.8438	-69.9478	RDLi_NAUS_2012_06_14_1900.ruv	
WILD	LR	4.537183	38.9877	-74.7931	RDLi_WILD_2012_06_14_1900.ruv	
BELM	MR	13.449904	40.1961	-74.0052	RDLi_BELM_2012_06_14_1800.ruv	
BESE	MR	13.45			ELTi_BESE_2012_06_14_1800.euv	
BESP	MR	13.45			ELTi_BESP_2012_06_14_1800.euv	
BRMR	MR	13.449904	39.4074	-74.3621	RDLi_BRMR_2012_06_14_1900.ruv	
BRNT	MR	13.45	39.6156	-74.1983	RDLi_BRNT_2012_06_14_1900.ruv	
CDDO	MR	13.45	18.0998	-67.1907	RDLi_CDDO_2012_02_06_1100.ruv	
FURA	MR	13.45	18.2917	-67.1986	RDLi_FURA_2012_02_06_1400.ruv	
RATH	MR	13.45	39.1926	-74.6664	RDLi_RATH_2012_06_14_1900.ruv	
SEAB	MR	13.46	40.3617	-73.9727	RDLi_SEAB_2012_06_14_1700.ruv	
SESP	MR	13.45			ELTi_SESP_2012_06_14_1700.euv	
SPRK	MR	13.45	39.9352	-74.072	RDLi_SPRK_2012_06_14_1800.ruv	
WOOD	MR	13.45	38.9877	-74.7931	RDLi_WOOD_2012_06_14_1900.ruv	
BISL	SR	25.36	41.1526	-71.5518	RDLi_BISL_2012_06_14_1900.ruv	
CBBT	SR	25.4	37.0462	-76.0627	RDLm_CBBT_2012_04_12_1800.ruv	
CPHN	SR	25.6			RDLm_CPHN_2012_06_14_1400.ruv	
GCAP	SR	25.3	40.9826	-73.6238	RDLi_GCAP_2012_06_07_1400.ruv	
MISQ	SR		41.3229	-71.8042	RDLi_MISQ_2012_06_14_1900.ruv	
PORT	SR		40.4418	-74.0997	RDLi_PORT_2012_06_14_2030.ruv	
SILD	SR	25.500003	40.5436	-74.1245	RDLi_SILD_2012_06_14_2000.ruv	
SLTR	SR	25.8	38.9198	-75.3092	RDLi_SLTR_2012_04_04_1700.ruv	
STLI	SR	26.19	40.9087	-73.5873	RDLi_STLI_2012_06_14_2000.ruv	
SUNS	SR	25.6	37.1378	-75.9722	RDLi_SUNS_2012_06_14_2000.ruv	
VIEW	SR	25.4	36.9499	-76.2432	RDLm_VIEW_2012_06_14_2000.ruv	

Figure 7: Screen capture of the web display for the MARACOOS HF radar radial database. If a radial file is late by more than four hours it is colored yellow and if later than 12 hours it is colored red. The table lists site code, radar type, frequency, latest radial file name and link to radial web server.

We have also created a web based utility that will allow the operators to add new sites to the network (Figure 8) add and remove sites from the processing stream (Figure 9) and to assign site responsibility and contact information for the operators. It will also allow the operators to reprocess total files if a radial file(s) has been found to contain an error.

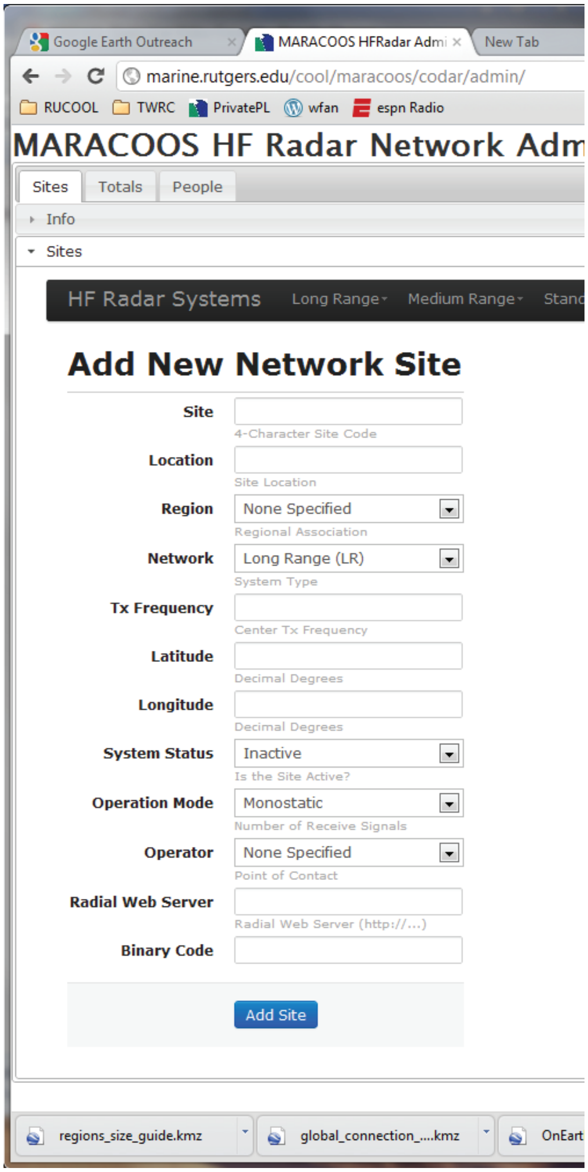

Figure 8: Screen capture of the web interface for HF radar operators to add new sites to the total processing stream.

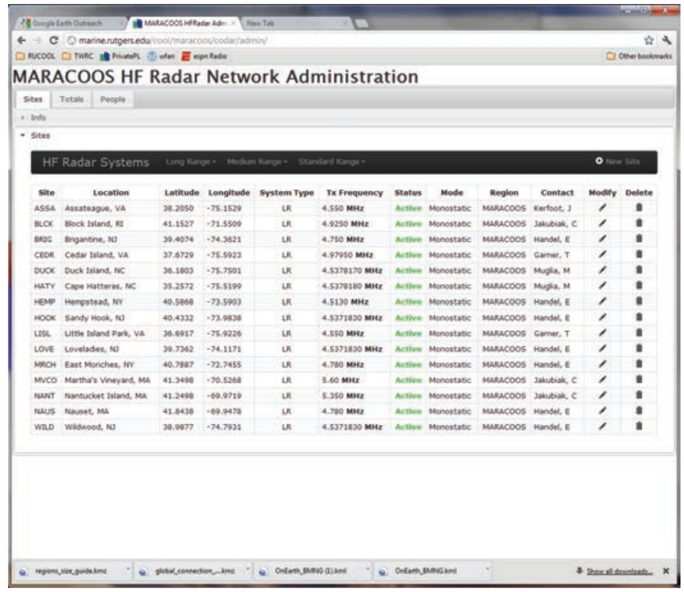

Figure 9: Screen capture of the web interface for HF radar operators to add and remove sites to the total processing stream.

IV. Total Metrics

In an effort to quantify the effort of the MARACOOS HF Radar group, we have analyzed the temporal and spatial coverage of the network over the calendar years of 2008-2010. The two radial vector-combining methods used in this study - Unweighted Least Squares (UWLS) and Optimal Interpolation (OI) - were compared. The national network 6 km grid is shown in Figure 10. We created a new grid with an inner cutoff using the 15 meters isobath and an outer cutoff using 150 km distance from shore. The 15-meter isobath is used as an inner cutoff. For shallower depths, the 30-m ocean waves that underlay Bragg scatter at 5 MHz for extracting currents no longer follow the deep-water dispersion relation needed to subtract out the wave-induced Doppler from the total shift, in order to get the current-induced shift and thence the current radial velocity.

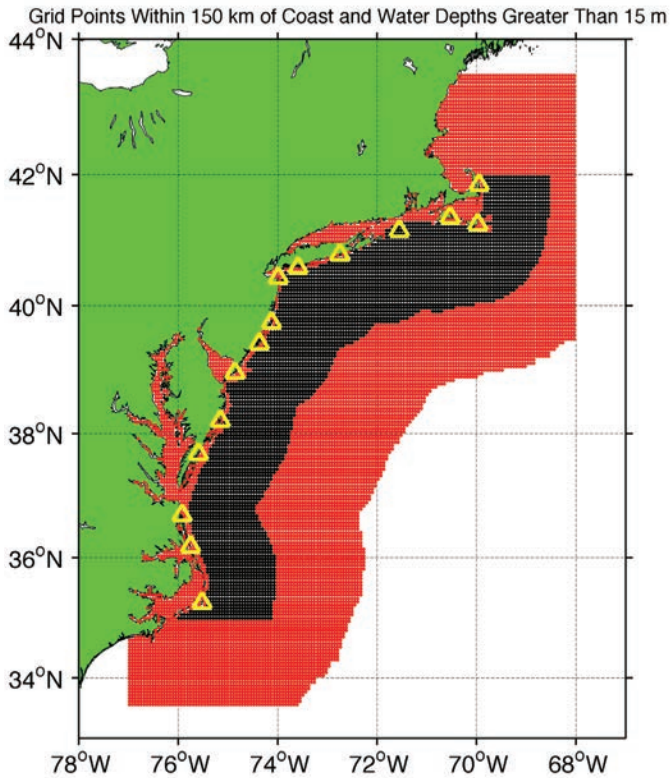

Figure 10: The MARACOOS sub-region of the national HF radar 6km grid (red). The filtered grid that represents points in water depths greater than 15 m and within 150 km of the coast (black). The location of the 5 MHz HF radar sites are shown as the yellow triangles.

There is no bathymetry associated with the HF Radar grid. We mapped the HF grid onto the bathymetry provided by the National Geophysical Data Center (NGDC). Using the national network 6 km grid and the 30 seconds resolution bathymetry map provided by NGDC we were able to merge both of them into one, using the function griddata from Matlab. The new grid has latitude and longitude with a corresponding depth. This will help us define the 15m water depth inner cutoff.

In addition, we wanted to know the distance to shore from each grid point, so that we could better define the outer cutoff. By knowing the latitude and longitude location of each grid point, we calculated the distance from each grid point to shore. This gave us the distance from shore and our cutoff of 150 km. This "filter" did not eliminate some grid points in Long Island and Block Island Sounds so these grid points that were eliminated using a simple coastline mask. The resulting grid in Figure 10 provides a potential spatial coverage area of 5,222 (black) grid points on the national grid.

Temporal coverage is defined by the ratio (x100%) of the number of hourly vectors obtained at a specific grid point in real time over the year and the maximum possible number of vectors or 24 x 365. We also computed the spatial coverage percentage at each temporal coverage percentage level - defined as the ratio (x 100%) of the total number of temporal coverage vectors that percentage level or greater and the 5,222 total number of green grid points. The temporal versus spatial coverage of the MARACOOS HF Radar Network in Figure 11 shows that the Optimal Interpolation method affords us an additional 10% spatial coverage at all times.

For example, Figure 11 shows that, based on the OI method for the 2009 operations year, the MARACOOS HF Radar Network covers 48% of the MARACOOS region 80% of the time. For the most recent progress period for MARACOOS we are near the recommended level of the US Coast Guard of 80% spatial coverage 80% of the time (Figure 12). There has been improvement in coverage with each year of MARACOOS.

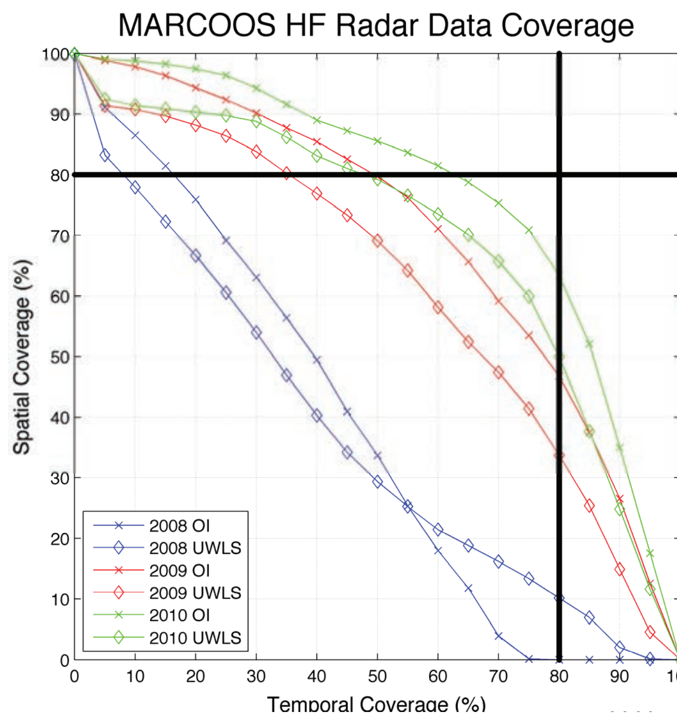

Figure 11: Temporal coverage versus spatial coverage computed for the MARCOOS HF Radar Network in 2008, 2009 and 2010.

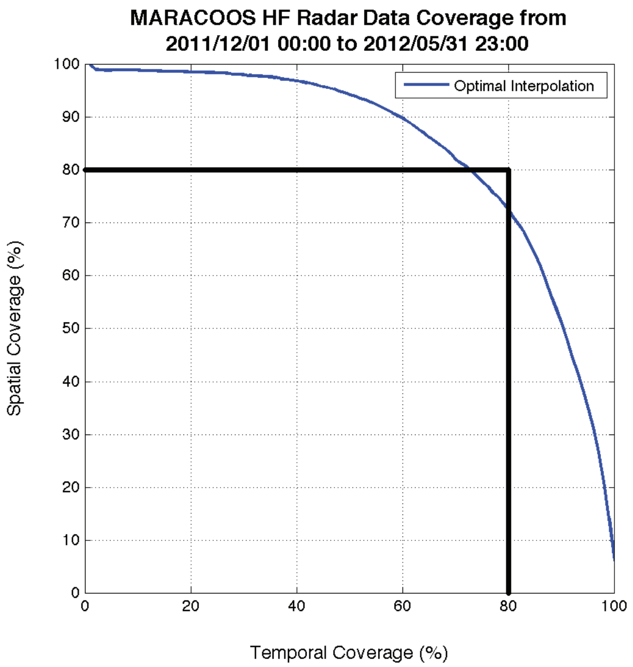

Figure 12: Temporal and spatial coverage of MARACOOS HF radar network for the most recent MARACOOS progress period December 1, 2011 to May 31, 2012.

V. Conclusions

Many High Frequency radar systems are in constant operation and the need to automate the quality control is paramount to the successful operation of the systems. We have presented several tools to automate this quality control. Within IOOS, we envision this quality control process being managed at the regional level with support from the national level. A database has been created to efficiently manage the radial and total data. A metric for the temporal and spatial coverage of the HF radar network has been created for the Mid Atlantic. This metric can easily be replicated at any number of the HF radar networks around the globe.

Acknowledgments

This work was funded by NOAA Award Number NA11NOS0120038 "Towards a Comprehensive Mid-Atlantic Regional Association Coastal Ocean Observing System (MARACOOS)". Sponsor: National Ocean Service (NOS), National Oceanic and Atmospheric Administration (NOAA) NOAA-NOS-IOOS-2011-2002515 / CFDA: 11.012, Integrated Ocean Observing System Topic Area 1: Continued Development of Regional Coastal Ocean Observing Systems

References

[1] E. Temll, M. Otero, L. Hazard, D. Conlee, J. Harlan, J. Kohut, P. Reuter, T. Cook, T. Harris, and K. Lindquist, "Data Management and Real-time Distribution in the HF-Radar National Network," in *OCEANS 2006*, 2006, pp. 1-6.

[2] L. P. Atkinson, T. Garner, and J. L. Blanco, "Surface current mapping in the lower Chesapeake," in *OCEANS 2008*, 2008, pp. 1-5.

[3] J. T. Kohut and S. M. Glenn, "Improving HF Radar Surface Current Measurements with Measured Antenna Beam Patterns," *Journal of Atmospheric and Oceanic Technology,* vol. 20, pp. 1303-1316, September 01, 2003 2003.

[4] J. A. Moody, B. Butman, R. C. Beardsley, W. S. Brown, P. Daifuku, J. D. Irish, D. A. Mayer, H. D. Mofjeld, B. Petrie, S. Ramp, P. Smith, and W. R. Wright, "Atlas of Tidal Elevation and Current Observations on the Northeast American Continental Shelf and Slope," *U.S. Geological Survey Bulletin 1611,* p. 122, 1984.

[5] D. Gong, J. T. Kohut, and S. M. Glenn, "Seasonal climatology of wind-driven circulation on the New Jersey Shelf," *J. Geophys. Res.,* vol. 115, p. 25, 2010.

[6] T. Cook, L. Hazard, M. Otero, and B. Zelenke, "Deployment and Maintenance of a High-Frequency Radar for Ocean Surface Current Mapping: Best Practices," Southern California Coastal Ocean Observing SystemFebruary 1, 2008 2008.

News for the Ocean Industry

www.ocean-news.com

Ocean News & Technology

June 2012

Worldwide Survey of Ocean Observing Activities

Technology Closes the Skills Gap

Feature Story – Page 10

Autonomous PowerBuoys: Wave Energy Converters as power sources for the next generation of ocean observatories

By Phil Hart, Chief Technology Officer, Ocean Power Technologies, Inc.
Scott Glenn, Hugh Roarty, Coastal Ocean Observation Lab., Rutgers University

The recent move in oceanographic academia to long-time series measurements at a specific location has been led by the introduction of cabled underwater observatories. Historically, an expedition was launched to monitor a location for perhaps a few weeks and a snapshot data set of the local environment was obtained. The cabled observatory, while still to some extent the new kid on the block in the world of oceanography, has changed the art of the possible by extending this snapshot from what used to be only a few weeks to many years. This is akin to the difference between a still image and a feature film!

Being able to access a long-time series of continuous data has allowed the formation of data trends that, until recently, were just not possible. However, this was achieved at a price – the old, nagging villain "Economics." Cabled observatories are not cheap, with the simplest installation (apart from local shoreline applications) costing millions of dollars, often tens or hundreds of millions of dollars. In some locations and economic environments, the payback in terms of achieved learning, basic research outcomes, and world-changing information makes the investment a justifiable proposition — see MARS, VENUS, NEPTUNE, and the Regional Scale Nodes as examples in the U.S. and Canada. However, as economic circumstances throughout the world have tightened, finding investments of this magnitude in an academic subject area that does not often generate huge cash paybacks has become extremely challenging. The future of large-scale cabled oceanography is, therefore, not as rosy as the more forward-looking and scientifically inquisitive among us might hope. A more cost-effective solution seems, therefore, to be required – one that for a much reduced cash cost offers at least matching performance – no challenge there then!

The Autonomous PowerBuoy® is a derivative of Ocean Power Technologies (OPT) core wave energy converter technology. After 15 years of development, these devices are now commercially available, offering applications in many industries that require long-term, cost effective monitoring of almost any marine location. This article discusses the technology and applications of the Autonomous PowerBuoy®, using the example of a deployment from 2011 in which HF RADAR was used to measure oceanographic parameters off the coast of New Jersey. In addition, other potential applications are discussed.

What is a PowerBuoy®?

OPT's PowerBuoy® technology fits into a category of wave energy converters referred to as a Point Absorber – defined in our industry as a device that presents a small projection in comparison to a wave. The device relies on the differential motion between two hull forms: one designed to react slowly and the other designed to act quickly when forced by a water wave. The differences in motion represent mechanical energy, which can be harnessed and transferred

Figure 1 *Photo of the PowerBuoy® after deployment in the foreground along with the USCG buoy tender that deployed it in the background*

onto any power producing mechanism (commonly referred to as a Power Take Off [PTO]). PTOs vary with device, but can be grouped into the predictable suspects of pneumatic, hydraulic, and direct mechanical machines. Regardless of the strengths and weaknesses of each PTO approach, it is typical to transmute into electrical energy at some point. Indeed, all of OPT's current wave energy converters export or deliver electrical energy from the buoy itself. The manner in which this change in energy type is performed has an extremely important influence on the overall efficiency of power delivery. After years of development, which continues, the efficiency of these devices is now very impressive.

While all of this sounds easy, the devil is incredibly well-embedded in this particular engineering challenge, as earlier papers and authors have testified. Suffice to say, necessary design details, hydrodynamic understanding, mechanical nuances and requirements, electrical finesse, and control theory on such devices is unexpectedly complex in order to get the maximum performance out of a device.

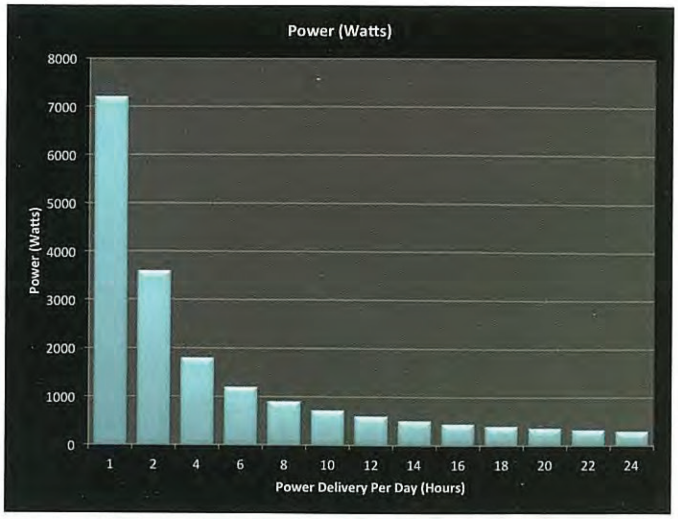

For the types of autonomous applications discussed here, where we seek to offer an alternative to a cable from shore, the governing design specifications include a requirement to deliver power to whatever sensor pack is utilized 100% of the time, regardless of prevailing wave conditions. Consider the case where (and the experimenters' frustration if) a unique oceanographic event occurs when the ocean was calm and no wave energy was being harvested to supply the payload. To avoid this, we must have access to power regardless of wave condition or the usefulness of the device is dramatically reduced. The PowerBuoy® must, therefore, harness power efficiently, store it effectively, and delivery it reliably. Happily, the defense provenance of these devices, which has extremely stringent and nearly identical availability and reliability requirements, has allowed this technology to be successfully developed and fully achieved. Current commercially available PowerBuoy® devices can deliver power to a payload even after a period of more than 7 days of flat calm seas and have built-in control algorithms that allow this period to be extended significantly by adaptive power management techniques.

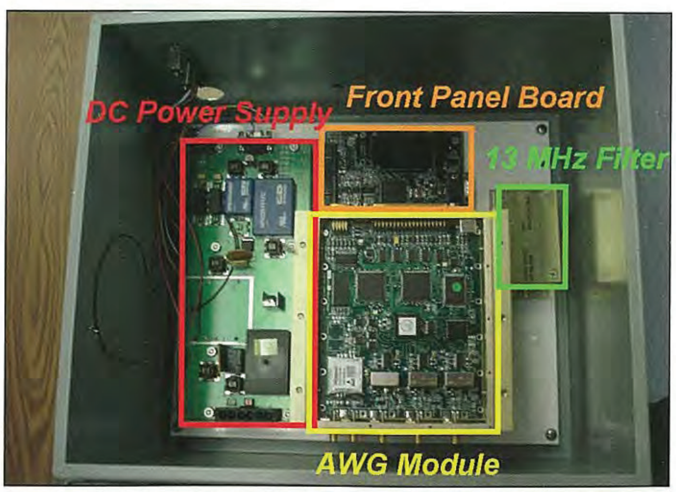

Figure 2 *Components of the bistatic transmitter DC power supply (red), front panel board (orange), advanced waveform generator (AWG) module (yellow), and 13MHz filter (green)*

Importantly, the whole suite of available autonomous PowerBuoy® devices has been designed to be a technology agnostic platform, in that they can power any (practically constrained) payload without foreknowledge of the purpose of any such payload. The practical considerations include how large and heavy the payload is, where the sensor is to be housed (internal or external to the buoy), and the power characteristics for the payload. For most intents and purposes, autonomous PowerBuoy® devices can be envisaged as a self recharging battery housed on a floating platform and capable of supporting, housing, or supplying a sensor suite selected by the customer. The way the power is used depends on customer requirements, constrained in exactly the same fashion as would be the case with a store-bought rechargeable battery. This gives the user the capability to draw on the available power in many different ways; for example, to have 100% power delivery 24 hrs/day (say 300 to 500W continuous), or take all the available energy over say 1 hr/day for a high-powered application (e.g., 4 to 5kW continuously over that hour), or to do any power draw intermediate of these approaches. The graph shows the power draw characteristics that might be applicable for a conservative wave energy site.

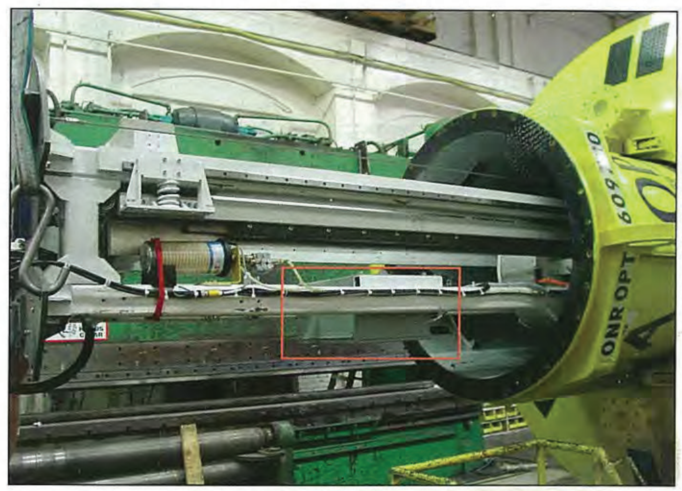

Figure 3 *Picture of the 13MHz bistatic transmitter package (outlined by the red rectangle) installed inside the LEAP buoy*

Similarly flexible is the physical system configuration for the payloads. Customer sensors can be housed within the PowerBuoy®, on the external surfaces (above and/or below the water) or remote to the device fed by an umbilical cable from the buoy. Hence, the power platform is extremely flexible and configurable and offers the chance to power today's known suite of payloads and any future requirements that might emerge as the applications expand.

Example application

In the summer of 2011, the first 500W continuous Autonomous PowerBuoy® was demonstrated off the coast of New Jersey. Developed under a U.S. Navy contract, the project was named the Littoral Expeditionary Autonomous PowerBuoy® (LEAP). The LEAP program sought to extend the range and provide additional directional capabilities to an existing shore-based High Frequency (HF) radar network by using a bistatic transmitter system augmented by an HF transmitter placed 35km offshore on the PowerBuoy®.

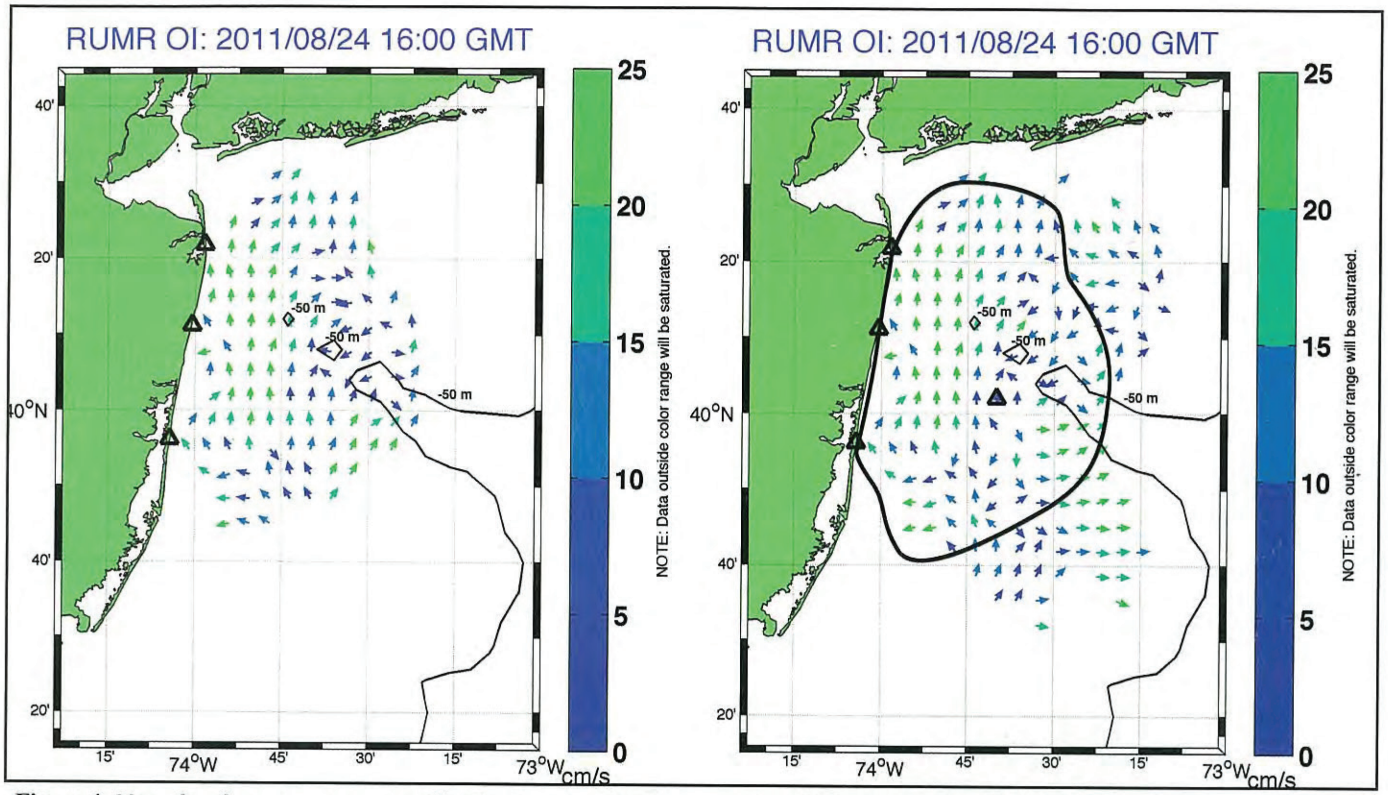

Figure 4 *Map of surface currents captured by the Rutgers HF radar network on 24 August 2011 at 16:00 GMT. The location of the radar sites and PowerBuoy® are shown as the black triangles. The figure on the left depicts the currents measured by the three radars in monostatic mode. The figure on the right show the currents measured by the three radars in bistatic mode (the three monostatic signals along with the signal from the bistatic buoy measured at all three radar shore stations). The thin black line is the 50m isobaths, and the thick, black line indicates the coverage in monostatic mode.*

Under the LEAP program, OPT integrated its autonomous PowerBuoy® with the HF radar network and communications infrastructure from Rutgers University's Coastal Ocean Observation Laboratory (RUCOOL). The LEAP system was deployed on 11 August 2011 (Figure 1) by a U.S. Coast Guard (USCG) vessel and was ocean-tested approximately 20mi off the coast of New Jersey until its recovery on 31 October 2011. It was integrated with the Rutgers University-operated, land-based radar network that provides ocean current mapping data for the National Oceanographic and Atmospheric Administration (NOAA) and USCG search and rescue operations. Rutgers is also developing the dual-use capability of the radar for environmental monitoring and vessel detection. The ocean test of the LEAP system enhanced the dual-use capability of the radar network.

The payload bay on this PowerBuoy® platform is modular, and the payload for this exercise was a bistatic transmitter manufactured by CODAR Ocean Sensors located in Mountain View, California. The payload consisted of a small enclosure that housed the radio transmitter, power supply, and radio filters (Figure 2) connected to a 20ft fiberglass antenna. The enclosure was placed inside of the spar section of the PowerBuoy® (Figure 3), and the antenna was placed atop the superstructure of the buoy. The enclosure had a volume of 1ft3 with a weight of 25lbs. The system had a continuous power draw of 120W, 45W being used for the signal generation.

HF radars are increasingly configured as distributed networks of multiple radars operating in monostatic mode, where the radar transmitter and receiver are collocated in space. Each monostatic radar site generates a map of the radial component of the ocean currents. By combining the radial current data from multiple radars with different look angles, a map of the total velocity vectors can be generated. Bistatic operation is an advance that enables the HF radar transmitter and receiver to be separated in space. In bistatic

Figure 5 *Communcations relay buoy - the Micro-Buoy*

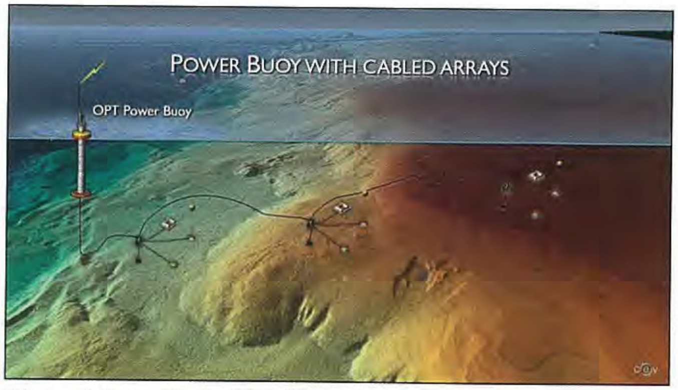

Figure 6 *PowerBuoy with cabled arrays*

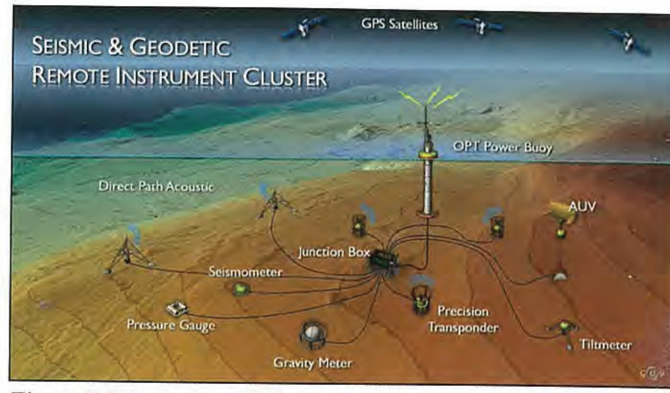

Figure 7 *Seismic & geodetic remote instrument cluster*

mode, a receiver can acquire radar signals from any transmitter within range. For this example, three shore stations in northern New Jersey received the signal from the PowerBuoy®. The bistatic data provide current component observations from additional look angles, increasing the range and robustness of the total vector maps. In this case, the PowerBuoy® increased the coverage of the HF radar network by 55% (see Figure 4).

Other ocean observatory application concepts

Autonomous PowerBuoys® have been constructed to be a payload platform. As such, while the HF radar application discussed above proves the concept and power performance characteristics, this is not a full picture of the offering. The table below represents some other potential uses.

Potential Payloads
Acoustics (passive and active)
CTD
Video (visible/IR) and lights
Seismometers
RADAR
Communications (satellite, VHF, acoustic, cellular, WiFi, etc.)
AUV docking
Mini-ROV power and communications
Environmental quality and chemistry sensors
Seafloor monitoring
Wave and current monitoring

For the majority of ocean-observing applications, a connection to the seabed is required. In the normal manner of a cabled observatory, a main connection interface center would link distributed to the power and communication feed. A wide variety of communication protocols can be supported, depending on customer preference, transmission distance, and data rates – although, DSL has been recognized as a cheap and effective solution in similar applications. In this circumstance, such a line would be fed directly from the PowerBuoy®, which as well as feeding power, provides the means of transmitting the data back to a central land site. Some example arrangements are shown in Figures 6 and 7.

Multiple LEAP-sized PowerBuoys® can be deployed in the same area, depending on the geographic spread and power requirements of the system. Distributed systems can be arranged with essentially any physical distance between main nodes being supported simply and easily.

One of the key benefits of this type of arrangement over a cabled system is scalability; the day one configuration can be enhanced or grown as required over time. In addition, if the demands change and the site is no longer of interest (perhaps the experiments have run their course), the equipment can be easily recovered and redeployed to a site of the customer's choice.

Therefore, the return on capital cost can be realized not only over many years, but potentially in many physical locations as well – offering the potential for a group of academic organizations to have access to a bank of resources, similar to what is achieved with the UNOLS vessel fleet.

Where high bandwidth transmission back to shore is required (i.e., beyond the range of the Iridium satellite system), a chain of wave energy-powered communications relays can be placed, providing a robust and cost-effective means of transmitting data at very high bandwidth. These "micro-buoys" (Figure 5) are designed to be deployed simply and easily from a small boat with a minimal anchoring system, and, thus, represent a very minor capital cost. They also offer the potential to communicate to multiple LEAP-style higher PowerBuoy® locations (nodes), which presents the option for deployment as a mesh-type communications network and supplying both maximum bandwidth and maximum redundancy/reliability. If only modest data bandwidth requirements exist, then Iridium or other satellite-based communications can suffice to fill the requirement directly from the main node. This becomes possible in many applications by making use of the in-buoy payload spaces to house data processing equipment to perform data processing and manipulation locally, reducing the data set by applying data-sifting or compacting algorithms prior to transmission.

Conclusions

As the economic climate tightens or, perhaps more accurately, remains prohibitively tight, ways must be sought to support oceanography professionals as they seek to push the knowledge set forward. The drive for long-time series measurement of the oceans is critical to the development of knowledge about the earth system as a whole. Therefore, cost-effective ways must be found to allow this critical knowledge to be gathered.

While the "A+" option has been seen as a cabled observatory, technology has advanced such that a PowerBuoy® system can now offer a very compelling alternative that can meet or, in some cases, exceed the performance of such systems. Wave energy-powered observatory systems, offering 90% of the functionality at a fraction of the cost of a cabled system, may provide a solution where research can continue and perhaps even expand – even within the current economic constraints.

Phytoplankton dynamics and bottom water oxygen during a large bloom in the summer of 2011

Oscar Schofield, Hugh Roarty, Grace Saba, Xu Yi, Josh Kohut, Scott Glenn
Coastal Ocean Observation Lab, Rutgers University, New Brunswick, NJ 08901
oscar@marine.rutgers.edu, roarty@marine.rutgers.edu, saba@marine.rutgers.edu, xuyi@marine.rutgers.edu, kohut@marine.rutgers.edu, glenn@marine.rutgers.edu

John Manderson
James J. Howard Marine Sciences Laboratory
Northeast Fisheries Science Center
74 Magruder Road, Sandy Hook, Highlands, NJ, 07732
John.Manderson@NOAA.gov

Matthew Oliver
School of Marine Science and Policy
College of Earth, Ocean and Environment,
University of Delaware,
700 Pilottown Rd. Lewes, DE, 19958
moliver@udel.edu

***Abstract*— During the summer of 2011 a large phytoplankton bloom occurred off the New Jersey coast, which was monitored using an existing ocean observatory. There was public concern about the root causes of the phytoplankton bloom and whether it reflected anthropogenic loading of nutrients from the Hudson River or whether it reflected coastal upwelling. We used the MARACOOS network to determine what were the likely drivers of the phytoplankton bloom. The bloom was studied using satellites, HF radar, a Hydroid REMUS and Webb Slocum gliders. Chlorophyll concentrations were over an order of magnitude larger than the decadal mean of ocean color data and the bloom was initiated by upwelling winds throughout the month of July that continued to dominate the wind patterns until the passage of Hurricane Irene. The high concentrations of phytoplankton resulted in the supersaturated oxygen values in the surface waters; however the flux of organic matter resulted in oxygen saturation values of <60% in the coastal bottom waters, which is sufficient to stress benthic communities in the MAB. Discrete samples identified the bloom was dominated by mixed assemblages of motile dinoflagellates. The passage of Hurricane Irene increased the oxygen saturation at depth by close to 20%, but was not sufficient to terminate the bloom. A re-analysis of the CODAR clearly indicated that the shelf wide bloom most likely originated from nearshore the New Jersey coast. Upwelling provided the source water that fueled the bloom. Alternating winds transported the bloom offshore and across the Mid-Atlantic Bight. This is consistent with past studies that observed regions of recurrent hypoxia on the New Jersey inner shelf are more related to coastal upwelling than riverine inputs.**

***Index Terms*—ocean observatories, hypoxia/anoxia, phytoplankton blooms**

I. INTRODUCTION

A widespread decline in bottom dissolved oxygen (DO) levels to hypoxic/anoxic conditions impacted nearly the entire New Jersey continental shelf in 1976, resulted in significant economic losses in shell-fishing and related industries [1, 2]. It was driven by a causal series of events that included large runoff during a warm winter resulting in early stratification of the shelf, followed by the development of a strong deep summer thermocline during an unusually hot summer, persistent southerly winds with fewer than usual storms, a large phytoplankton bloom with low grazing by zooplankton, and respiration and decomposition of the bloom below the seasonal thermocline. The source of the nutrients fueling the bloom was the major question. The initiation of coastal monitoring conducted in response to the 1976 event focused on the working hypothesis that the major source of nutrients was due to anthropogenic loading from urbanized riverine inputs [3]. An alternative hypothesis was posited by Glenn et al. [4], that regions of recurrent hypoxia on the New Jersey inner shelf were more related to coastal upwelling than riverine inputs of nutrients. The largest variations in ocean temperatures along the New Jersey coast, other than seasonal, are due to episodic summertime upwelling events driven by topographic variations associated with ancient river deltas that cause upwelled water to evolve into an alongshore line of recurrent upwelling centers [5]. These centers are co-located with historical regions of low dissolved oxygen [4].

In summer 2011, a series of visible images [Figure 1], indicated the presence of a large phytoplankton bloom off the coast of New Jersey. The dramatic imagery captured the

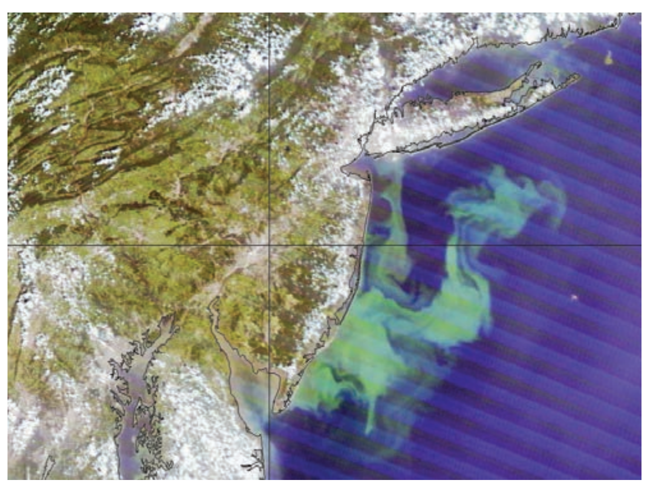

Figure 1. A visible image of a large phytoplankton bloom offshore the coast of New Jersey. The image resulted in a public debate about the causes.

978-1-4673-0831-1/12/$31.00 ©2012 IEEE

attention of the general public and the news media. The

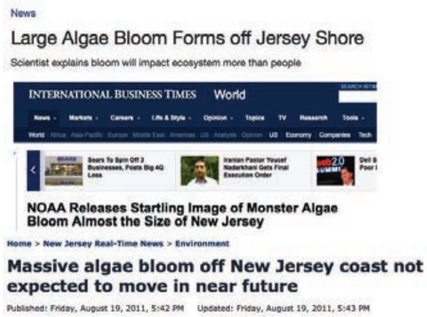

Figure 2. Headlines in response the release of the satellite imagery of the phytoplankton off the New Jersey coast.

resulting discourse resulted in a series of debates of the cause ranging from the bloom being fueled from anthropogenic loading of nutrients from the Hudson River estuary or that it reflected the upwelling processes. Having access to an existing ocean observatory [6], we conducted an analysis of the factors to assess the likely causes of the algal bloom, its potential impact on the coastal water quality and the response to Hurricane Irene. The multiple assets present in the waters reflected a range of projects funded by a range of sponsors that included National Oceanic and Atmospheric Administration, Environmental Protection Agency, Office of Naval Research, and Department of Homeland Security.

Analysis of the Bloom. For this analysis we will focus on the mid-July through Hurricane Irene in late August. Throughout early July wind were largely from the Southwest, which is upwelling favorable followed by a week with generally weak downwelling winds [Figure 3]. An analysis of the satellite imagery shows the bloom in late July or early August. Prevailing cloud cover unfortunately resulted in relatively poor coverage during this time. The sea surface temperatures prior to the passage of Hurricane Irene show the Mid-Atlantic Bight (MAB) bounded by the Gulf Stream offshore and cooler waters to the north [Figure 4]. In mid-July along the coast of New Jersey and Delaware, there were small zones of cooler water, which is indicative of coastal upwelling. The amount and spatial extent of the cooler water was variable and reflected the variability in the winds; however overall the amount of upwelling appeared to decline into the month of August prior to the arrival of Hurricane Irene. The ocean imagery showed low phytoplankton in the middle of July however little of the coastlines were visible given the prevailing cloud cover [Figure 5]. There was a significant increases in biomass by the second week of August. By Mid-August chlorophyll concentrations were well above 10 mg m^{-3}, which is significantly greater than climatological summer mean of chlorophyll which is ~0.5 mg m^{-3} for the MAB shelf [7]. The high concentrations of chlorophyll was confirmed with *in situ* fluorometery measurements made with a Hydroid REMUS system that surveyed the inner half of the bloom offshore Tuckerton New Jersey. Discrete surface samples were collected and were analyzed on a microscope and the dominant alga present within the bloom appeared to be *Gymnodinium*

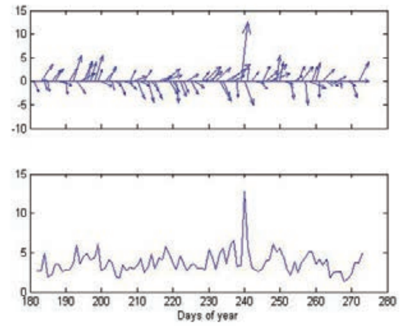

Figure 3. Prevailing wind speed for the month of July and August 2011 for the NODC buoy at Sandy Hook. The data stops upon the arrival of Hurricane Irene.

species. This is a motile dinoflagellate species, potentially allowing it access nutrients below the strong pyconcline and maintain themselves in the well lit euphotic zone.

The high concentration of phytoplankton had significant impacts on the biogeochemistry of the MAB which was documented by autonomous underwater vehicles. A Teledyne

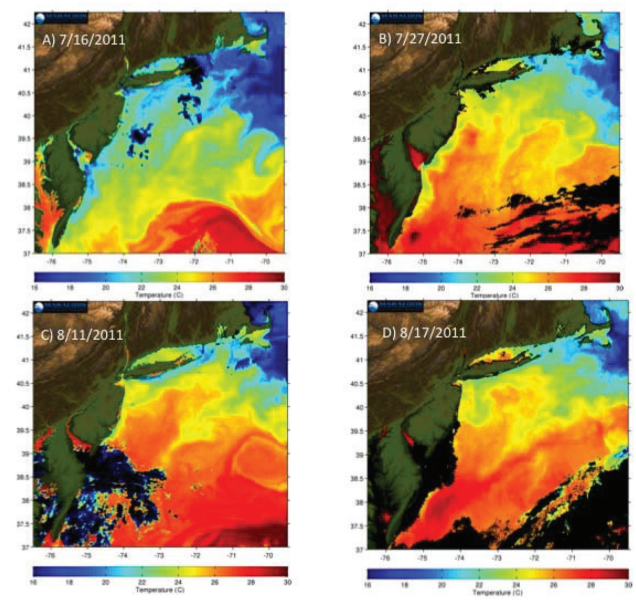

Figure 4. The sea surface temperatures for the Mid-Atlantic Bight (MAB) during the July and August in 2011. In mid-July there is evidence of upwelling new the New Jersey coast on July 16 through August 11th.

Webb glider had been deployed on the shelf and was outfitted with an Anderra Optode to provide measurements of oxygen concentrations for the New Jersey Department of Environmental Protection and the Environmental Protection Agency. The goal was to assess conduct a nearshore survey mapping if there were regions of low dissolved oxygen in bottom water offshore New Jersey. The glider conducted a southerly alongshore transect. The glider encountered super saturated oxygen concentrations in the upper mixed layer [Figure 6]. In contrast the bottom water show low dissolved oxygen concentrations with pre-Irene bottom water values heavily weighted to values lower then 5 mg L^{-1} [Figure 7]. These values were approaching values associated with potential animal mortality at 2.2 mg L^{-1} (indicated by the red arrow). The low values observed by the gliders prompted a series of adaptive surveys conducted by NOAA to confirm the presence of low bottom water oxygen levels. As part of those surveys, a Hydroid REMUS was utilized, outfitted with an Anderra Optode, and was deployed in low bottom water regions identified by the glider. The REMUS confirmed the low DO values during its high-resolution survey (inset in upper panel of Figure 7). The higher resolution surveys identified regions with low DO values close to the animal mortality concentrations. The passage of Hurricane and the associated mixing [Figure 6] significantly increased the oxygen concentration in the bottom water [Figure 7].

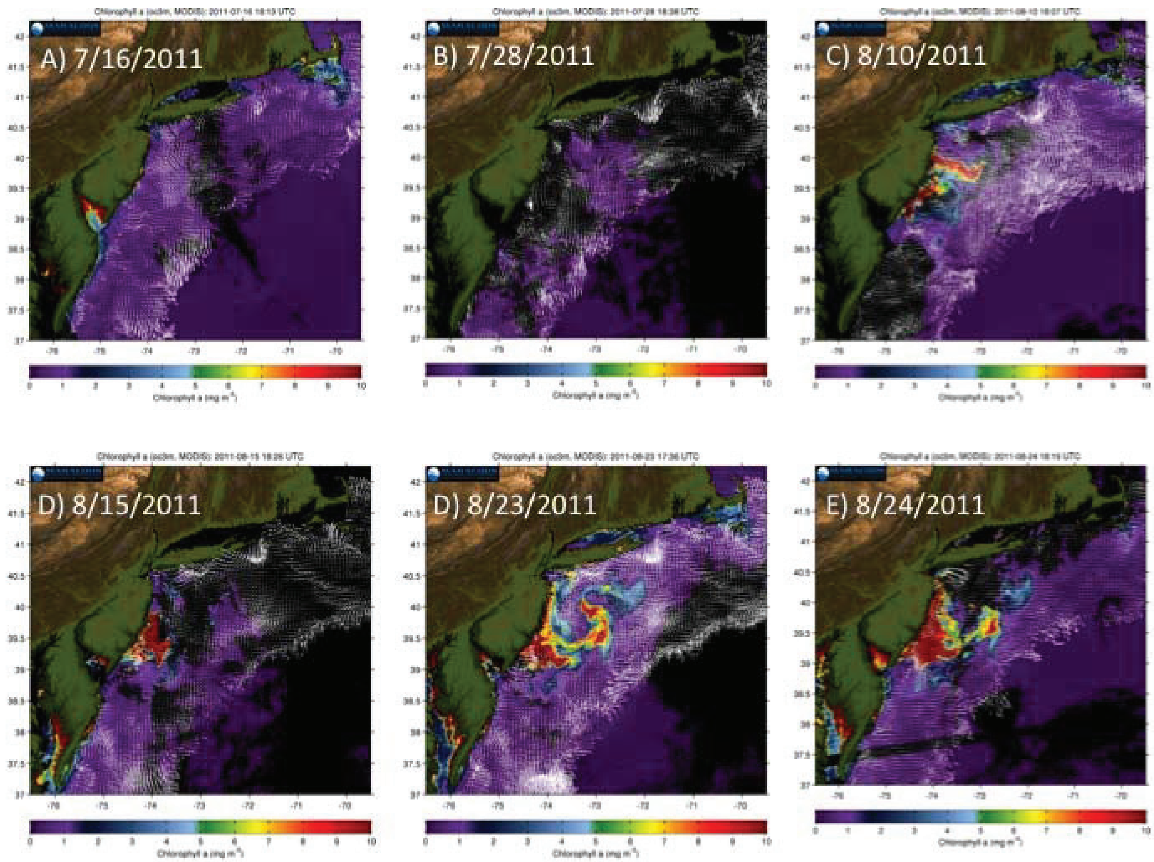

Figure 5. Ocean color estimates of chlorophyll a with the overlaid daily averaged surface currents measured by HF Radar.

The bloom was the result of nutrients provided by either riverine inputs, dominated by outflow from the Hudson river, and/or upwelling. So ultimately tracing the bloom back to its source waters is critical to understanding which processes fueled the bloom. At the start of the bloom and during the bloom, river outflow from the Hudson was low [Figure 8]. The impact of Irene is clearly visible, seen as a double peak in the river outflow [Figure 8], the first associated with the storm and the second to due the enhanced run-off associated with drainage of the water shed which received the majority of the rainfall associated with the storm. Therefore given the low river outflow, it is unlikely the bloom was caused by the Hudson river. This was in contrast to much of general media suggesting pollution run-off from the Hudson River estuary was to blame. To further assess the probable transport of the river and/or upwelled water we utilized the continuous record of data collected by the MARACOOS HF Radar array.

The HF radar surface currents maps were seeded with hypothetical passive particles, which were advected forward in time based on the measured currents. The trajectory of particles were tracked. Each day new particles were added, at three source locations [Figure 9]. The experiment was conducted for the month of July and up to the arrival of Hurricane Irene at the end of August. The final locations for all the drifters is shown in bottom panels in Figure 9. The left-handed panel is the trajectory of the particles released at the mouth of the Hudson river estuary. The majority of the particles are trapped at the mouth of the estuary, which reflects the bottom topographic

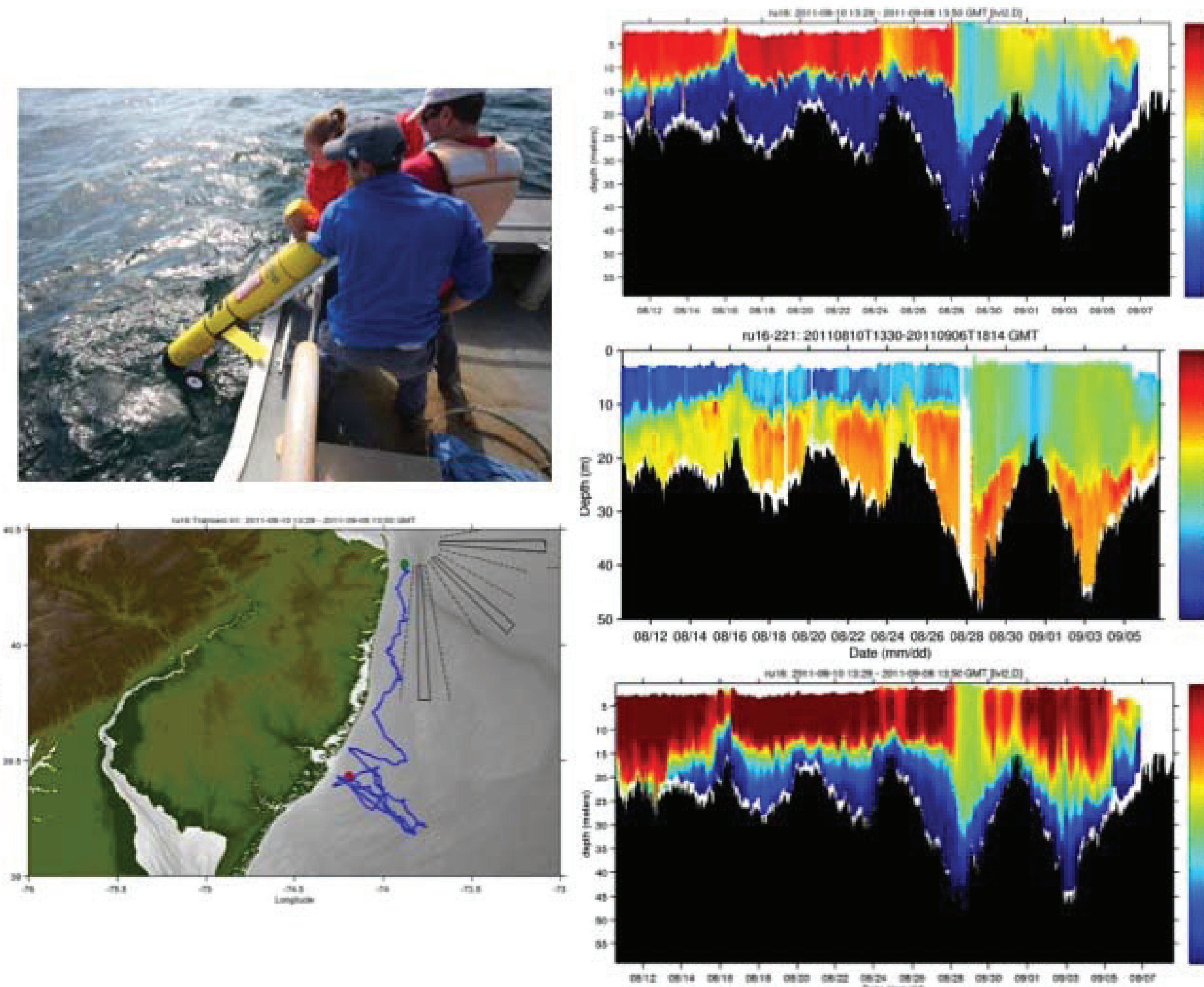

Figure 6. A Webb glider collected data offshore New Jersey in the summer of 2012. The glider, deployed by Rutgers collaborating with the New Jersey State of Environmental Protection (NJ DEP) and the EPA, was focused on measuring the water quality status in the New Jersey coastal waters. The mission consisted of a southerly transect "zig-zaging" inshore and offshore. Upon the approach of Hurricane Irene the glider was directed offshore and then was recovered after the conditions permitted boat operations. The right hand panels show glider data from the deployment. From top to bottom, the data is for temperature, salinity and the percent saturation of oxygen respectively. The passage of Hurricane Irene is clearly visible on August 28-29 as an immediate decline in surface water temperature. The mixing increased the salinity in the surface waters and increased the percent oxygen concentrations in the bottom water (see Figure 7).

affects on the river outflow circulation [8, 9]. The offshore boundary of the particles is associated with the edge of the Hudson Canyon. The majority of chlorophyll observed in the ocean color imagery is associated with the waters offshore and south of the river advection footprint. This combined with the overall low river outflow does not support hypothesis that the Hudson river is the source of chlorophyll (and/or nutrients promoting high growth) during the summer bloom in 2012. The right hand panel shows the advection footprint for the central New Jersey coast. The particles fan out over the broader shelf and high concentrations of advected particles are associated with the waters phytoplankton bloom. This is consistent with the hypothesis that the bloom is driven by upwelled water driven by the persistent Southwest winds found during the bloom. These maps represent a relatively

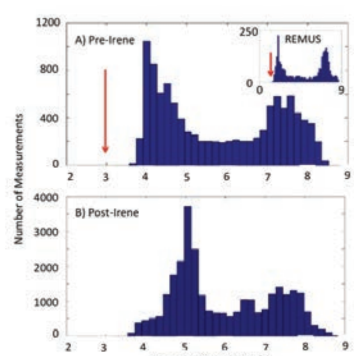

Figure 7. Dissolved oxygen measured pre and post Hurricane Irene. The inset is REMUS data flying in a similar location.

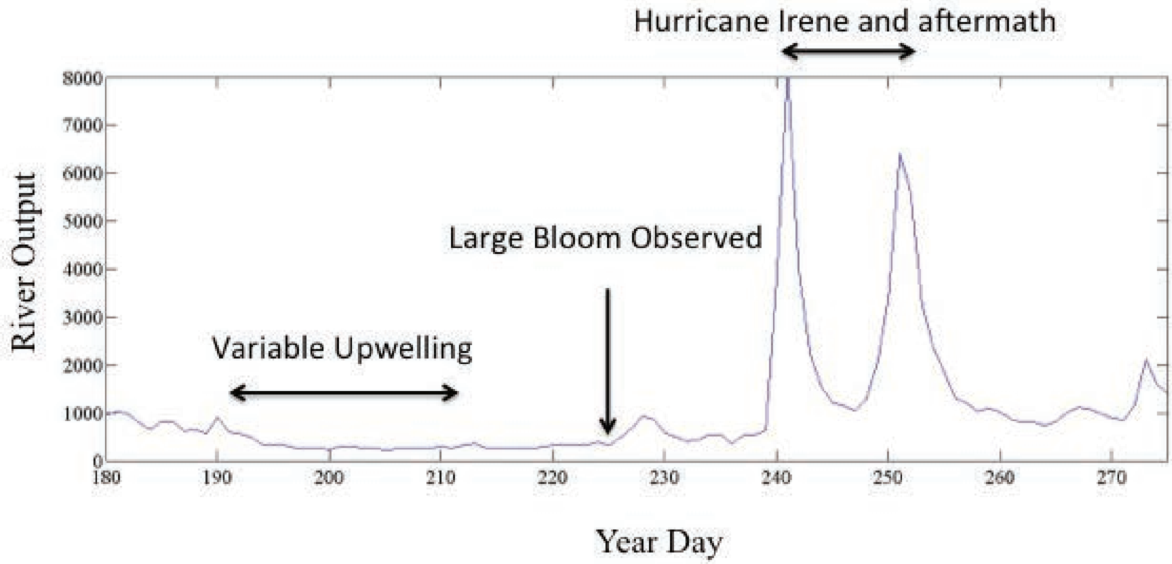

Figure 8. The outflow of the Hudson River during the summer bloom of 2012.

conservative estimate, as the phytoplankton biomass will be more dynamic given the variability in growth rates as well as the associated export to the sea floor.

CONCLUSIONS:

1) The phytoplankton bloom was most likely driven by upwelling, which induced the dinoflagellate bloom. The bloom was able to thrive given the ability of the cells to access nutrients in the subsurface waters.

2) The export of organic carbon associated with the bloom was likely the main culprit in driving the declines in the bottom water oxygen.

3) The availability of a existing ocean observatory allowed the bloom dynamics to be adaptively sampled in near real-time. This illustrates a unique tool for managing water quality of coastal waters.

ACKNOWLEDGMENT

This work represents the effort of the entire team of the Rutgers University Coastal Ocean Observation Lab (RU COOL). The work was supported by the IOOS MARACOOS program (NA11NOS0120038) and the ONR MURI program (N000140610739). Finally the support of Rutgers School of Environmental and Biological Sciences and the great state of New Jersey is acknowledged.

REFERENCES

[1] Figley, W., B. Pyle, and B. Halgren Oxygen depletion and associated benthic mortalities in New York Bight 1976. In Socioeconomic Imapcts, Swanson, R. L., and C. J. Sindermann, National Oceanic and Atmospheric Administration pp 315-335, 1979.

[2] Falkowski, P. G., T. S. Hopkin, and J. J. Walsh. An analysis of factors affecting oxygen depletion in the New York Bight, J. Mar. Res. 38, 479-506, 1980.

[3] Stoddard, A. J. E. O'Reilly, T. E. Whitledge, T. C. Malone and J. F. Malone. The application and development of a compatible historical data base for the analysis of water quality management issue in the New York Bight. IEEE Oceans, 18, 1030-1035, 1986.

[4] Glenn, S. M., R. Arnone, T. Bergmann, W. P. Bissett, M. Crowley, J. Cullen, J. Gryzmski, D. Haidvogel, J. Kohut, M. Moline, M. Oliver, C. Orrico, R. Sherrell, T. Song, A. Weidemann, R. Chant, and O. Schofield. The biogeochemical impact of summertime coastal upwelling on the New Jersey Shelf. J. Geophys. Res. Vol 109. C12S02, doi:10.1029/2003JC002265, 2004

[5] Song, T., D. B. Haidvogel, and S, M. Glenn. Effects of topography variability on the formation of upwelling centers off New Jersey: A theoretical model, Journal of Geophysical Research, Vol. 106, No. C5, pp. 9223-9240, 2001.
[6] Glenn, S. and O. Schofield. Growing a distributed ocean observatory: Our view from the COOL room. Oceanography 22(2): 78-92, 2009

[7] Xu, Y., R. C. Chant, R. Castaleo, D. Gong, S. M. Glenn, and O. Schofield,. Seasonal dynamics in the chlorophyll a in the Mid-Atlantic Bight. Cont. Sh. Res. 10.1016/j.csr.2011.05.019, 2011.

[8} Chant, R. J., S. M. Glenn, E. Hunter, J. Kohut, R. Chen, R. H. Houghton, J. Bosch, and O. Schofield. Bulge formation of a buoyant river outflow. J. Geophys Res. 113, C01017, DOI:10.1029/2007JC004100, 2008.

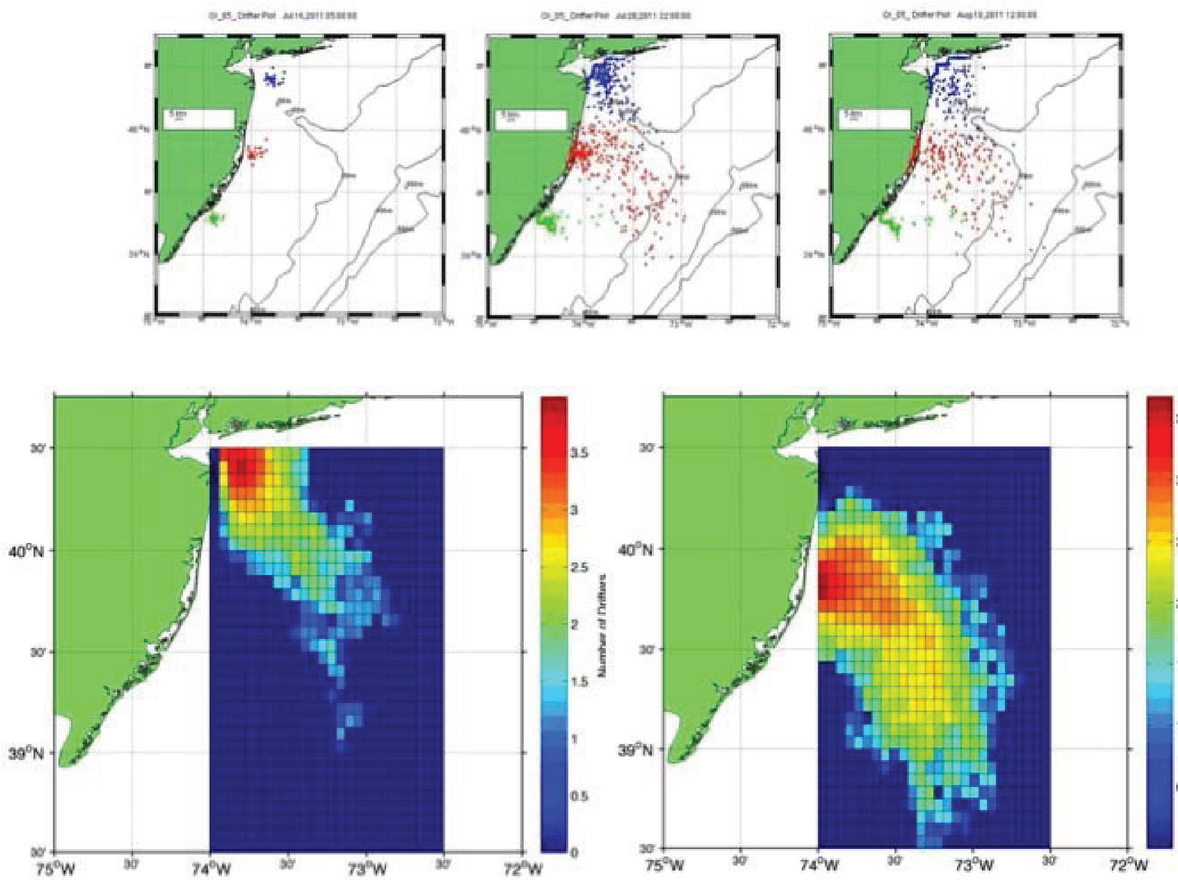

Figure 9. The utility of HF Radar in documenting surface particle transport for the month of July and August 2012. The upper three panels show three snapshots of particles being advected from three locations along the New Jersey coast. The upper left hand panel is the initial seeding location for particles on July 16th, and the subsequent transport for the particles on July 28th and August 10th are provided respectively. The lower two panels represent the final locations of all particles advected by the measured surface currents for the Hudson river estuary (left bottom panel) and from offshore the coast of New Jersey.

[9] Moline, M. A., T. K. Frazer, R. Chant, S. M. Glenn, C. A. Jacoby, J. R. Reinfelder, J. Yost, M. Zhou, and O. Schofield. Biological responses in a dynamic, buoyant river plume. Oceanography 21(4): 70-89, 2008.

.

Rutgers University Coastal Ocean Observation Laboratory (RU-COOL) Advanced Modeling System Developed to Cost-Effectively Support Offshore Wind Energy Development and Operational Applications

Greg Seroka, Rich Dunk, Scott Glenn, Louis Bowers, John Kerfoot, Michael Crowley, Hugh Roarty, Laura Palamara
Coastal Ocean Observation Laboratory
Rutgers University
New Brunswick, NJ USA
seroka@marine.rutgers.edu

***Abstract*—Studies are underway that are evaluating the offshore wind resource along the coast of New Jersey in an effort to determine the variability of the wind resource. One major source of variability is the sea-land breeze circulation that occurs during periods of peak energy demand. The sea breeze front, driven by the thermal difference between the warm land and relatively cooler ocean during hot summer afternoons, propagates inland and under weak atmospheric boundary layer wind conditions can affect much of the state. However, little is known about the offshore component of the sea breeze circulation. A large zone of subsidence over the coastal ocean, and subsequent divergence near the surface, is known to occur in unison with the inland-propagating sea breeze front. RU-COOL's unique monitoring and modeling endeavors are focused on exploring the details of these offshore dynamics of the sea breeze circulation and its development during both coastal upwelling and non-upwelling events.**

A case study from the August 13, 2012 is analyzed in this paper; coastal upwelling resulted from persistent south to southeasterly winds for days. In addition, a sea breeze front formed in the afternoon, propagating inland and producing a zone of weak winds offshore that coincides with the targeted area of offshore wind development. Model results, using unique declouded satellite sea surface temperature data, are validated inshore against weather radar and offshore against coastal ocean radar (CODAR). Small-scale offshore wind variability is resolved and verified in the model, which will be critical for producing accurate and reliable offshore wind resource assessments and precise operational forecasts for the future.

***Index Terms*—Offshore wind, atmospheric modeling, sea breeze, upwelling, HF radar, weather radar, satellite SST, WRF, air-sea interaction, coastal processes**

I. Introduction

Offshore wind energy has the potential for alleviating high energy supply and demand issues associated with the USA's heavily populated East Coast. A primary concern with offshore wind energy development along these highly populated centers is the high cost of implementing the construction and operation of wind turbines in an offshore environment. Although construction and subsequent power production costs will remain high in the near-term, a possible solution for providing significant cost reductions relevant to offshore wind energy development can be realized with accurate wind resource assessments and representative wind forecasts. The use of high-resolution numerical weather prediction (NWP) is a cost-effective means in which to study the wind resource prior to construction and provide precise operational forecasts that will enhance operational decisions related to the energy market and integration of wind power into the energy grid system.

Studies are underway that are evaluating the offshore wind resource along the coast of New Jersey in an effort to determine the variability of the wind resource. Once this variability is determined, the "risks" associated with offshore wind development, operations, and power supply into the affected energy grid will be minimized. Rutgers Institute of Marine and Coastal Sciences (IMCS) is integrating validated remote sensing technology and site-specific in-situ data into numerical modeling routines. The incorporation of this innovative monitoring data should significantly reduce the random error and systematic biases inherent in the resource assessment and NWP analyses.

It is well known that the offshore wind resource is influenced by synoptic weather patterns. Less is known about the effects of mesoscale and local influences of the sea breeze circulation. The sea breeze that forms along the New Jersey coast is one of the primary microclimate circulations that affect the offshore environment. The sea breeze front, driven by the thermal difference between the warm land and relatively cooler ocean during hot summer afternoons, propagates inland and under weak atmospheric boundary layer wind conditions can affect much of the state. Doppler weather radar, visible/infrared (IR) satellite imagery, and coastal ocean radar (CODAR) have detected the development of the sea breeze over offshore waters, along the coastline, and within adjacent inland areas.

However, little is known about the offshore component of the sea breeze circulation. A large zone of subsidence over the coastal ocean, and subsequent divergence near the surface, has been shown through NWP to occur in unison with the inland-propagating sea breeze front. Our unique monitoring and modeling endeavors are focused on exploring the details of these offshore dynamics of the sea breeze circulation and its development during both coastal upwelling and non-upwelling events. Consequently, accurate numerical simulation of the timing and intensity of the sea breeze circulation is crucial in accurately assessing and predicting offshore wind power potential and subsequent energy production during the times of peak energy demand along coastal communities and the adjacent densely populated areas.

II. Model Setup

To enhance understanding of the physics that control the sea breeze circulation and overall dynamics of the offshore wind resource, RU-COOL has developed and is currently running a high-resolution version of the Weather Research and Forecasting (WRF) model Advanced Research Core (ARW) [1]. Data from the operational 12-km North American Mesoscale (NAM) model are used as lateral initial conditions. Nested within the North American NAM domain is our operational 3-km RU-WRF domain, a mesoscale-resolving domain that stretches from south of Cape Hatteras to north of Cape Cod, with a focus on the coastal waters of New Jersey. Lateral boundary conditions after initialization are set using the new Rapid Refresh (RAP), which replaced the Rapid Update Cycle (RUC) on May 1, 2012 as the National Oceanic and Atmospheric Administration (NOAA) next-generation hourly-updated assimilation/modeling system.

Current operational NWP models (e.g. NAM and Global Forecast System, GFS) use relatively low resolution bottom boundary conditions over the ocean (i.e. sea surface temperatures, SST). Both NAM and GFS use the Real-Time Global SST High Resolution (RTG SST HR) product. This 1/12th degree (~9.25 km) composite incorporates the most recent 24 hours of in-situ (e.g. buoys, ships) and satellite (Advanced Very High Resolution Radiometer, AVHRR; MetOp) data.

Our RU-WRF model incorporates improved, higher resolution bottom boundary conditions that aim to more accurately represent the ocean thermal conditions (SST)—a critical driver of atmospheric winds. Because cloudy signals are usually colder than the ocean surface, warmest pixel composites of several satellite scans have frequently been used in the past to remove any data contaminated by clouds or cloudy edges. However, this technique is prone to also eliminate coastal upwelling and storm mixing, processes that produce cold SSTs. Therefore, RU-COOL "de-clouds" its satellite SST data by using various temperature and near IR thresholds which are empirically derived by season and location. Then, a 3-day *coldest* pixel composite of this de-clouded, 1-km resolution AVHRR data is performed, in order to preserve and resolve coastal upwelling and storm mixing. Finally, a coldest pixel composite is again performed with the 3-day AVHRR data and NASA's Short-term Prediction Research and Transition Center (SPoRT) SST Composite product [2] to fill in any remaining gaps due to persistent clouds. SPoRT's SST product is a 2-km, 7-day weighted blend of Moderate-Resolution Imaging Spectroradiometer (MODIS) and National Environmental Satellite, Data, and Information Service (NESDIS) data.

III. Case Study

To closely investigate the offshore dynamics and wind patterns within the sea breeze circulation, a unique case study was chosen. South to southeasterly winds over New Jersey persisted for several days prior to August 12-13, 2012, producing offshore Ekman transport at the ocean surface [3]. Cooler water from the winter's cold pool storage below upwelled to replace the departing warmer surface waters. The coastal upwelling event was not captured by the RTG SST HR product (Figure 1), but with skies beginning to clear on August 13, the RU-COOL enhanced de-clouded satellite product did (Figure 2).

Relatively quiescent synoptic conditions prevailed during the morning and afternoon of August 13. Solar daytime heating elevated land temperatures over inland NJ to 30ºC; strong terrestrial heating in conjunction with cool coastal upwelling created a land/sea temperature difference upwards of 9ºC. A sea breeze front, evident in the Doppler weather radar backscatter in clear-air mode at KDIX, began to form at about 15-16 UTC (11 am-noon local time) and dissipated at around 00 UTC the next day (8 pm local time). Figure 3 shows KDIX weather radar at time of initiation at about 16 UTC and also at a time in the middle of duration of the sea breeze front propagation inland.

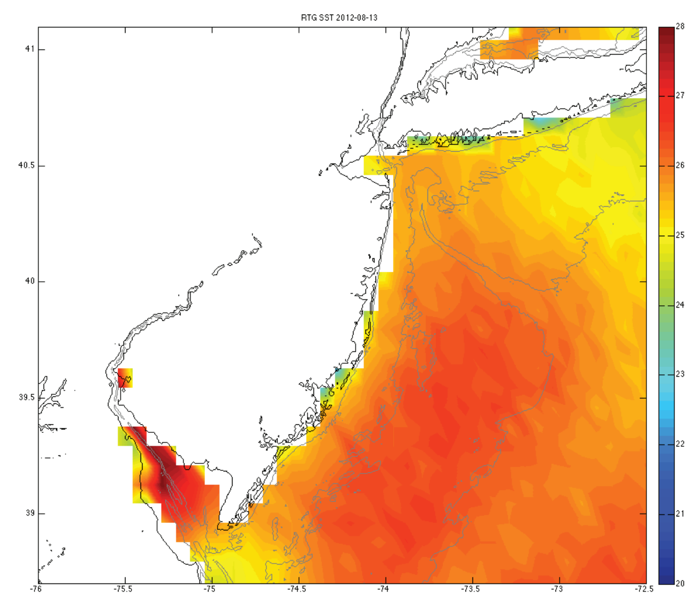

Fig. 1. RTG SST HR did not capture the coastal upwelling event on August 13, 2012. Note coastal waters of NJ are generally about 25-26ºC.

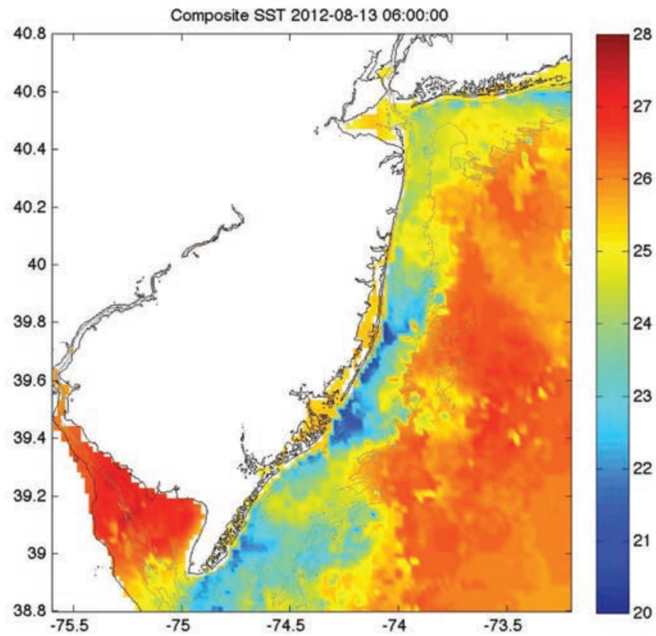

Fig. 2. RU-COOL 3-day coldest pixel composite (AVHRR + NASA SPoRT) captured the coastal upwelling (~21-23ºC) event. Upwelling temperatures were 3-4ºC cooler than surrounding coastal waters.

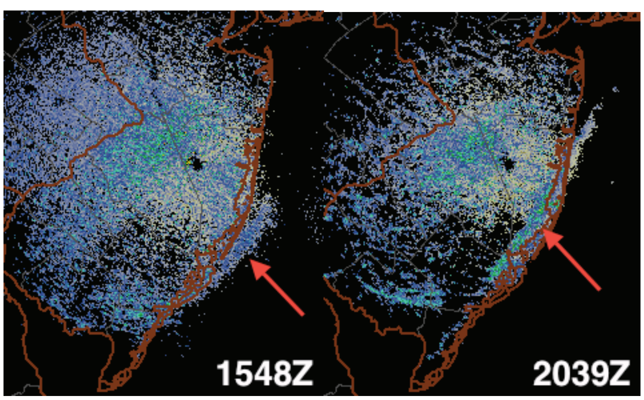

Fig. 3. KDIX weather radar in clear-air mode from 1548Z (left) and 2039Z (right). The sea breeze front is evident in the convergence of higher reflectivities at both times, indicated by the red arrows.

RU-WRF model results from that day, using the new RU-COOL composite SST product as bottom boundary conditions, are consistent with the general initiation time of the sea breeze front (~15 UTC) along the NJ coast (Figure 4). In addition, RU-WRF dissipates the sea breeze front at about 00 UTC on the 14th, which matches well with time of dissipation indicated by the KDIX weather radar. Therefore, our RU-WRF model run correctly validates inshore with the available KDIX Doppler weather radar.

Note the surface divergence of winds just offshore of the coast in Figure 4, extending from Long Beach Island south to Cape May. This general weak offshore zone of winds, common in similar sea breeze circulations, coincides with future offshore wind development areas. Thus, it is critical to validate the offshore component of this sea breeze case to ensure correct analysis of offshore wind variability.

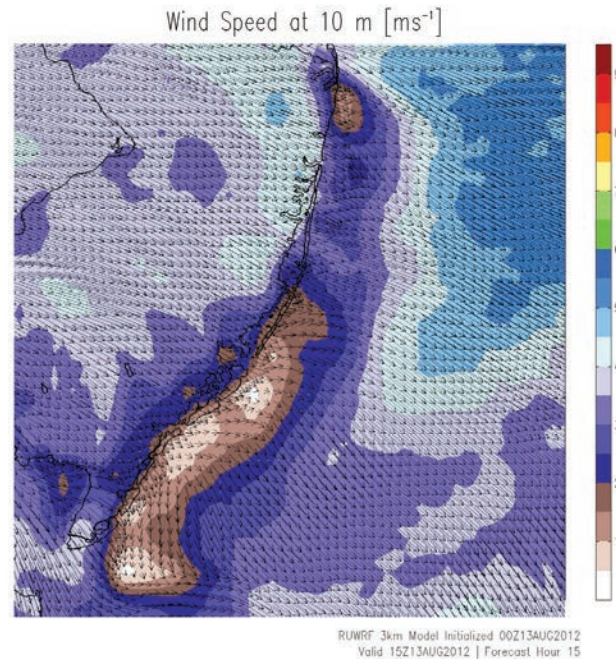

Fig. 4. RU-WRF model results from August 13, 2012 initiate the sea breeze front along the NJ coast at about 15 UTC.

To validate the model offshore for this case, high frequency (HF) coastal radar (CODAR) is used [4]. A thirteen MHZ HF radar network was installed as part of the current offshore wind assessment project for New Jersey as funded by the New Jersey Board of Public Utilities (NJBPU). This nested CODAR network provides hourly high-resolution surface current maps in near-real time. By monitoring the spatial patterns in the surface current data from the installed CODAR network, we can begin to resolve the spatial variability in surface winds offshore.

The elongated zone of surface divergence and weak winds apparent in the model just offshore, extending from southeast of Cape May north to Long Beach Island (Figure 4) is also apparent in the CODAR de-tided current velocities (Figure 5). These velocities are hourly-averaged, centered at 16 UTC. Furthermore, the area of higher wind speeds (approaching 6 m $s^{-1)}$ farther north and offshore in the model (Figure 4) can be seen in the stronger surface currents in the CODAR data south of Long Island and north of Long Beach Island (Figure 5). We can begin to validate these mesoscale details in the surface wind patterns offshore from the model against surface current data from the new CODAR system.

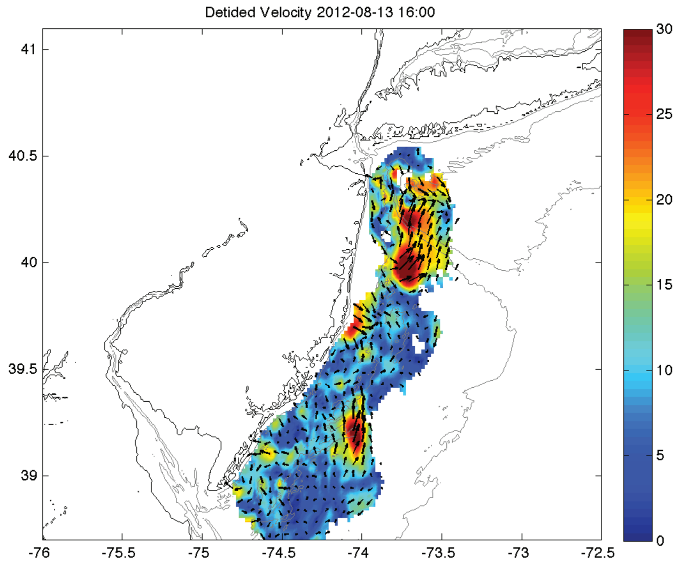

Fig. 5. CODAR hourly-averaged de-tided current velocities from August 13, 2012, centered at 16 UTC. Units contoured are cm/s.

IV. Conclusions

With a new and unique method of de-clouding and compositing SST from satellites, we can begin to preserve and resolve coastal upwelling as evidenced on August 13, 2012. Using this new satellite SST product as improved bottom boundary conditions over water for the RU-WRF atmospheric model, more reliable and accurate wind resource assessments and precise operational forecasts of winds can be achieved.

In the August 13, 2012 case study, the RU-WRF model validates inshore via the KDIX Doppler weather radar; the model's initiation timing and general propagation of the sea breeze front inland matches well with observed surface convergence of dust and other particulates along the sea breeze front apparent in the radar data. The RU-WRF model also validates for the case study offshore via CODAR surface current observations; small-scale variability in the modeled winds (surface divergence, weak wind zone) aligns well with observed de-tided current velocities from the installed CODAR system.

In this study, we have begun to resolve and understand the offshore properties of the sea breeze circulation, which are critical factors in determining accurate offshore wind resource assessments and analyses, especially during hot summer afternoons when energy demand is at its peak. Additional cases (e.g. upwelling vs. non-upwelling, RTG vs. SPoRT vs. RU-COOL SST runs, NAM and GFS vs. RU-WRF) will be analyzed and SST sensitivity runs will be conducted to further refine diagnoses and prognoses of the offshore component of the sea breeze.

Acknowledgments

This work was funded by a grant from the New Jersey Board of Public Utilities: "An Advanced Atmospheric/Ocean Assessment Program Designed to Reduce the Risks Associated with Offshore Wind Energy Development Defined by the NJ Energy Master Plan and the NJ Offshore Wind Energy Economic Development Act". Special thanks goes to NASA SPoRT for providing their SST composite data.

References

[1] Skamarock, W. C., J. B. Klemp, J. Dudhia, D. O. Gill, D. M. Barker, W. Wang and J. G. Powers, 2008: A Description of the Advanced Research WRF Version 3. NCAR Technical Note TN-468+STR. 113 pp.

[2] Jedlovec, G., F. LaFontaine, J. Shafer, M. Rigney, J. Vazquez, E. Armstrong, and M. Chin, 2010: Use of high resolution SST data for operational applications. Ocean Science Workshop, Portland.

[3] V. W. Ekman, "On the Influence of the Earth's Rotation on Ocean Currents," *Arkiv. Mat. Astron. Fysik,* vol. 2, 1905.

[4] Barrick, D.E., M.W. Evans, and B.L. Weber (1977), Ocean surface currents mapped by radar, Science, vol. 198, pp. 138–144.

Monostatic Vessel Detection Statistics from the CODAR SeaSonde

Collin Dobson, Kristen Holenstein, Michael Smith, Hugh Roarty, Scott Glenn
Coastal Ocean Observation Laboratory
Rutgers University
New Brunswick, NJ
Cdobs@eden.rutgers.edu

Chad Welan, Donald Barrick, James Isaacson
CODAR Ocean Sensors
Mountain View, CA
Chad@codar.com

***Abstract* - Rutgers University has begun to use their SeaSonde HF Radar coastal ocean current and wave-monitoring network for vessel detection purposes. This project aims to evaluate the effectiveness of using the HF Radar network for vessel detection in the New York Harbor. Two separate HF Radar sites were analyzed. The sites, Sea Bright and Seaside Park, are located along the New Jersey coast and are separated by approximately 48 km. The data from each of these sites was analyzed and compared to Automatic Identification System (AIS) data provided by ships entering and leaving the New York Harbor. This was done for a week (Sunday, October 21st through Sunday, October 28th) on a daily basis to determine the number of ships that were accurately detected by the HF Radar network. Sea Bright had an average detection rate of 72% for the week and Seaside Park had an average rate of 78%. Overall the HF radar network proved to be a quite accurate vessel detection resource during this one week case. At Sea Bright and Seaside Park, the radar detected an average of 6.375 and 5.75 vessels that were not reporting to the AIS network, respectively. The HF radar network's ability to detect vessels that do not report to the AIS network will be a great contribution to matters of homeland security.**

Keywords—vessel detection, high frequency radar, maritime safety, homeland security

I. Introduction

The Maritime Transportation Security Act (MTSA) was passed in the wake of the September 11, 2011 attacks. The MTSA creates a consistent security program for all the nation's ports to follow. Contributing to these efforts is a collaborative approach put forth by the National Center for Secure and Resilient Maritime Commerce and Coastal

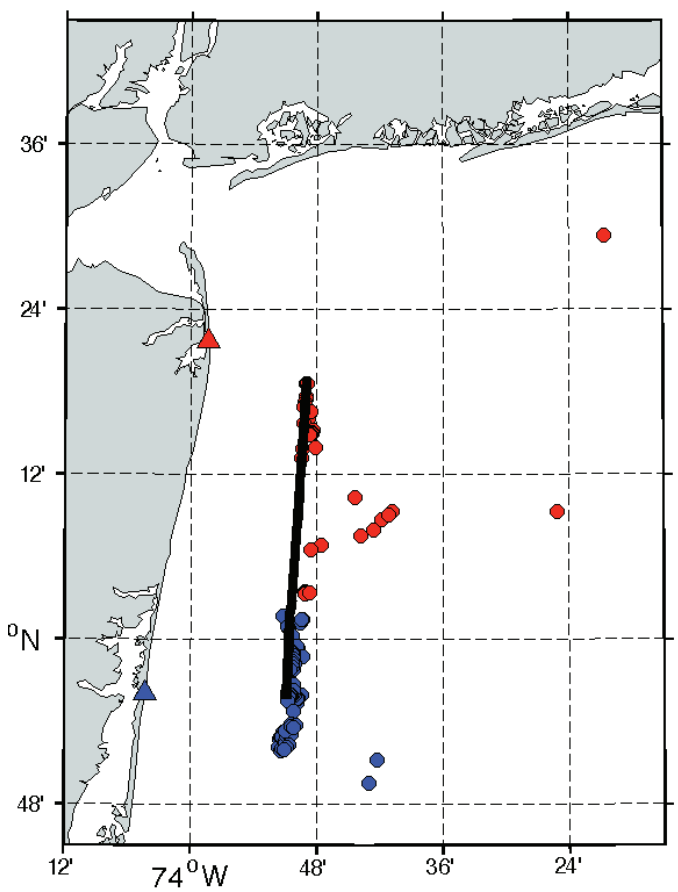

Figure 1. Map showing the location of the Sea Bright (red triangle) and Seaside Park (blue triangle) sites and the detections of a target vessel for Sea Bright (red circles) and Seaside Park (blue circles). The AIS track for the same vessel is shown as a black line.

Environments (CSR). The CSR is one of twelve centers of excellence established by the Department of Homeland Security. The goals of CSR aim to improve the security, emergency response, economic performance, and resiliency of the Maritime Transportation System (MTS). In an effort to contribute to the goals of the CSR, Rutgers University has begun to use their SeaSonde HF Radar coastal ocean current and wave-monitoring network for vessel detection purposes in over the approaches to the New York Harbor.

The implementation of HF Radar into the CSR collaboration will be extremely useful. With its ability to detect a large amount of ships that are leaving and entering the New York Harbor it can be used as an additional resource for maritime security measurements. Here we pair the HF radar detections with those reported with the Automatic Identification System to ground truth the remote detections fro the radar and to augment the total solution for maritime domain awareness in and around the approaches to New York Harbor.

This automatic system is successfully used to track marine traffic. AIS transponders aboard vessels automatically transmit information about the ship including speed, position, and navigational status. This information is received by transponders located on land and charted to give a depiction of the current state of marine traffic. The detections from the AIS network are limited to those vessels required to transmit AIS data. The HF radar detections are not limited to the participation of the vessels offshore. Instead these detections are based on signals scattered from the ship back to the receivers on shore. If the radar network can potentially detect vessels that do not report AIS, that could help fill a gap in monitoring and protecting New York Harbor.

This paper will concentrate on the validation of the HF radar based detections for vessels entering and exiting New York Harbor. We will use the existing AIS network to provide ground truth data for the evaluation. The raw HF radar data used as input into the detection algorithms are provided by two radial sites in Sea Bright and Seaside Park, NJ (Figure 1). These sites are part of a 41 site nested network for the MAB configured to map ocean currents from the beach to the shelf break between Cape Hatteras and Cape Cod [1].

II. METHODS

CODAR PeakPicker real-time vessel detection software was installed on the two different 13MHZ HF Radar Systems. These two SeaSonde sites, Sea Bright, NJ and Seaside Park, NJ, are located along the New Jersey coastline and are separated by about 48km (Figure 1). This vessel detection software was set up to run in unison with the already existing surface current mapping purpose of these radar sites. For our evaluation, Autonomous Identification System (AIS) receivers were also installed on these sites to record the GPS verified locations of ships entering/leaving the New York Harbor. [1]

The PeakPicker vessel detection software has the ability, via algorithms, to estimate the range, range rate, and bearing of potential offshore targets [2]. The range rate is the component of the vessel velocity directed toward the site. For each target we track these three variables in time (Figure 2). Overlapping these HF radar measurements, we calculate range, range rate and bearing relative to each site for each target from the AIS data. By plotting the output from the PeakPicker software over the same outputs provided by the AIS data, it can be determined if the HF radar was able to successfully detect a vessel or not (Figure 2). The detections from the HF radar and AIS were compared to determine if the HF radar detected the target.

Here we show results from a one week study between October 21st and October 28th, 2012. The accuracy of the HF radar was tested on a daily basis for this week. For each day, each individual vessel that reported AIS data was analyzed. Individual plots were made, using a series of MATLAB scripts, for every vessel that reported AIS data, and through the radar footprint (Figure 2 and Figure 3). For this analysis, each vessel from each day was considered separately. In some instances, the HF radar data associated with a certain vessel proved to be too noisy to get an accurate reading. This noise, result of environmental and man-made sources, was variable in time. These high noise cases were not considered in the analysis.

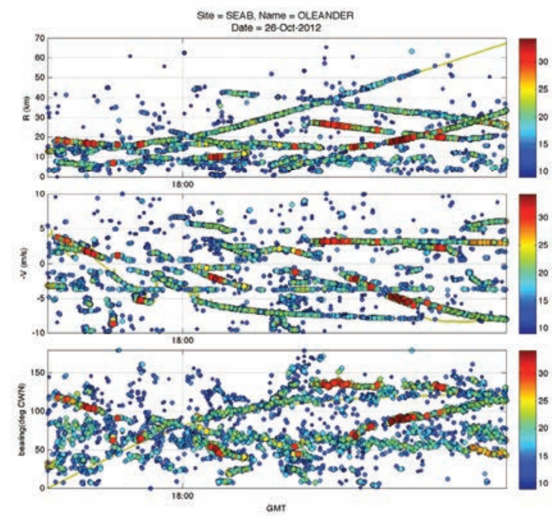

Figure 2: HF Radar data from Seabright (filled circles) overlaid onto the AIS reported track (yellow line) of the vessel Oleander for 10/26/12. The color of the detection indicates the Signal to Noise Ratio in dB. The HF radar data typically coincides with the AIS track for this vessel, showing that it was picked up by the radar.

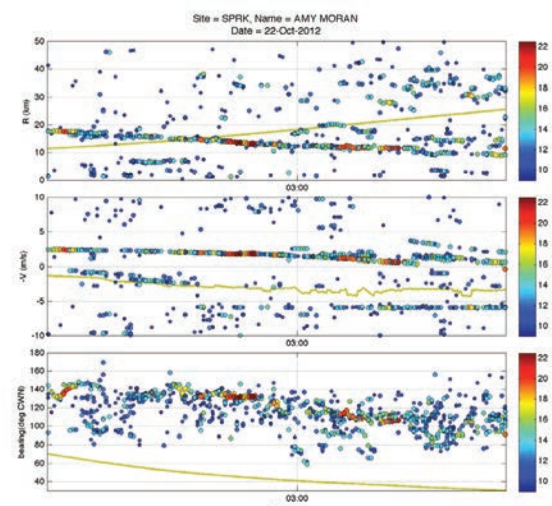

Figure 3: HF Radar data from Seaside Park (filled circles) data overlaid onto the AIS reported track of the vessel Amy Moran (yellow line) for 10/22/12. The color of the detection

indicates the Signal to Noise Ratio in dB. The HF radar data generally does not coincide with the AIS track for this vessel, indicating that this vessel was not picked up by the radar.

The number of vessels detected by each radar was determined each day over the study period. This was done by comparing each vessel's individual plot from each site, per day (Figure 4 and Figure 5). The purpose of this was to see if there was any overlap in the times during which the two different sites detected the same vessel.

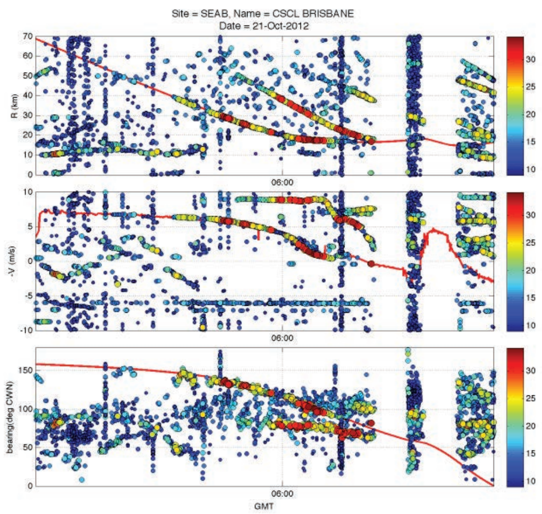

Figure 4: HF Radar data from Sea Bright (filled circles) overlaid onto the AIS track for the vessel CSCL Brisbane (red line) for 10/21/12. The color of the detection indicates the Signal to Noise Ratio in dB.

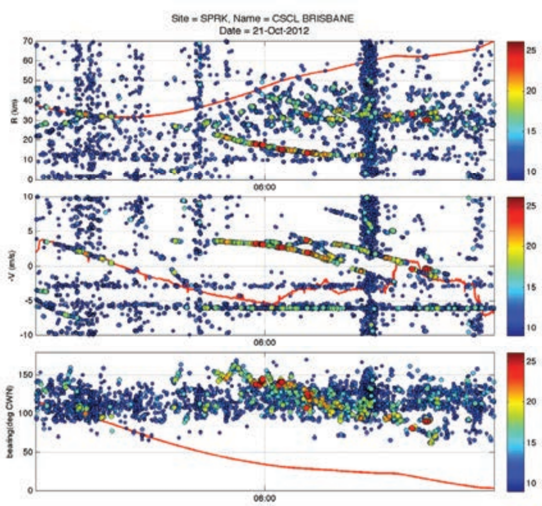

Figure 5: HF Radar from Seaside Park (filled circles) overlaid onto the AIS reported track of the vessel CSCL Brisbane (red line) for 10/21/12. The color of the detection indicates the Signal to Noise Ratio in dB.

To determine the number of vessels that were detected by the radars but did not report AIS data, eight plots were made for every day of the week, for each site. These plots covered an interval of 3 hours, per day, per site. For these plots, the collective HF radar data was overlaid on the collective AIS reported data for that time interval. Instances where the HF radar data indicated there should be a ship, but did not overlay an AIS track, were considered to be an unreported vessel passing by the radar sites (Figure 6).

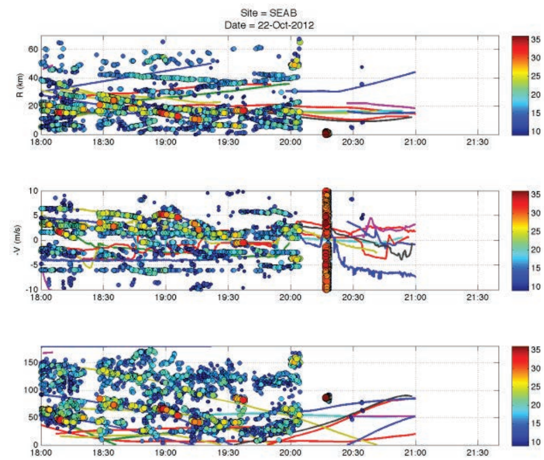

Figure 6: HF Radar data from a 3 hour interval on 10/22/12 at Seabright (filled circels) overlaid onto the AIS reported tracks of all of the vessels that past by the radar during that time frame (colored lines). The color of the detection indicates the Signal to Noise Ratio in dB.

III. RESULTS

For each site and each day, the total number of detectable vessels was recorded, as were the number of those that were detected and also those that were not. Also recorded were the number of additional vessels that were detected per day and the number of vessels that were detected by both sites at the same time. These numbers were used to determine the statistical accuracy of each site, as well as other trends.

Based on the methods outline above, it was determined that the HF radar in Sea Bright was able to accurately detect 308 vessels out of the 433 that were detectable, for an average detection rate of 72%. The Seaside Park radar detected 89 of the 112 detectable ships. The daily averages were also considered for both of these sites (Figure 7 and Figure 8). For Sea Bright, an average of 6.375, and Seaside Park an average of 5.75 vessels that did not report AIS data passed by the radar. There were a total of 13 instances when a single vessel was detected by both radar sites at the same time (Table 1).

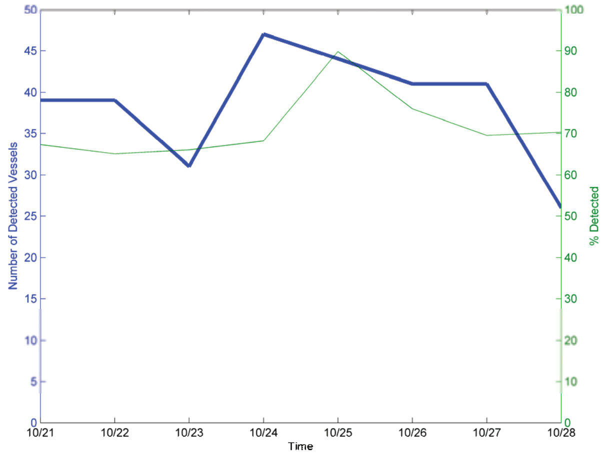

Figure 7: Number of detected vessels (blue) compared to the percentage of the total vessels detected (green) for Sea Bright (10/21/12-10/28/12)

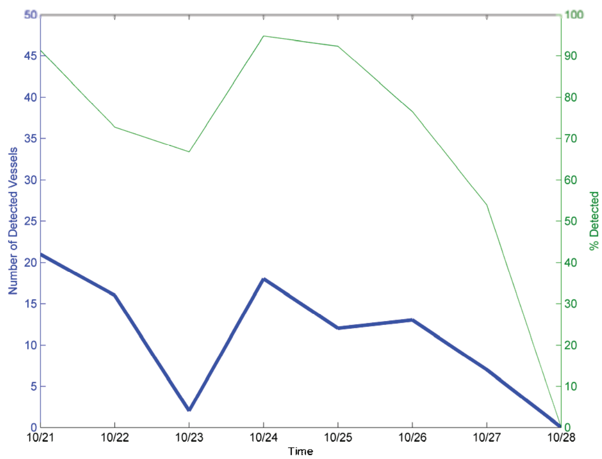

Figure 8: Number of detected vessels (blue) compared to the percentage of the total vessels detected (green) for Seaside Park (10/21/12-10/28/12)

Date	Additional Vessels Seabright	Additional Vessels Seaside Park	Detected by Both
10/21/2012	6	1	1
10/22/2012	10	10	2
10/23/2012	6	6	1
10/24/2012	9	3	2
10/25/2012	5	7	3
10/26/2012	8	8	3
10/27/2012	4	11	0
10/28/2012	3	0	0
Average	6.375	5.75	1.5

Table 1. The number of detected that did not report AIS at each site per day, and the number of vessels that were detected by both site each day.

IV. Discussion/Conclusion

The goal of this project was determine the effectiveness of the two different radar locations in their ability to detect vessels. Over the week long study period we determined a detection rate of 72% and 80 % for Sea Bright and Seaside Park, respectively. The PeakPicker algorithm was effective at mapping targets moving through the HF radar footprint of our two sites. In addition to the verification through vessels detected by both HF radar and AIS, there was an average of 5-6 vessels each day that were only detected by the HF radar. Therefore the sites, configured for their primary purpose of mapping currents, are shown to provide valuable detections of hard targets running through the radar footprints. For those targets not reporting AIS, this fills an important gap in the monitoring. We are continuing to evaluate and develop vessel detection algorithms that can be done in coordination with the current mapping to provide a dual-use capability for maritime domain awareness, from ocean currents to vessels. .

V. Acknowledgements

This material is based on work supported by the U.S. Department of Homeland Security under Award No. 2008-ST-061-ML0001. The views and conclusions contained in this document are those of the authors and should not be interpreted as necessarily representing the official policies, either expressed or implied, of the U.S. Department of Homeland Security. The current mapping and site maintenance was funded in part by NOAA Award Number NA11NOS0120038 “Towards a Comprehensive Mid-Atlantic Regional Association Coastal Ocean Observing System (MARACOOS)”.

VI. References

[1] Roarty HJ, Glenn SM, Kohut J.T., Gong D, Handel E, Rivera Lemus E, Garner T, Atkinson L, Jakubiak C, Brown W, Muglia M, Haines S, Seim H. 2010. Operation and Application of a Regional High Frequency Radar Network in the Mid Atlantic Bight. Marine Technology Society Journal 44 (6):133-145.

[2] Roarty, H. J., E. R. Lemus, E. Handel, S. M. Glenn, D. E. Barrick, and J. Isaacson. 2011. "Performance Evaluation of SeaSonde High-Frequency Radar for Vessel Detection." *Marine Technology Society Journal*, Vol. 45, 1-11.

Improvement of Surface Current Measurements with Spectra Reprocessing for 13 MHz SeaSonde Systems

Colin Evans
Hugh Roarty
Michael Smith
John Kerfoot
Scott Glenn
Coastal Ocean Observation Laboratory,
Rutgers University IMCS
New Brunswick, NJ United States of America

Hardik Parikh
Chad Whelan
CODAR Ocean Sensors
Mountain View, CA United States of America

***Abstract* - The demand for high-quality surface current measurements from High Frequency radar instrumentation is continuously increasing. To ensure that the CODAR (Coastal Ocean Dynamics Applications Radar) system is accurately mapping the surface current field, standards need to be met at the radial level. Limited radial coverage, flipped radial fields, and outlier vectors are a few signals indicating that there is a potential issue. This paper examines the results of the reprocessing methods for a 13 MHz SeaSonde located in Brant Beach, NJ (BRNT) between May 02, 2012 and May 09, 2012. After several test cases, it was determined that for that time period a signal above noise factor of 6.3 (~8 dB) and maximum radial velocity of 60 cm/s were the most ideal settings. Along with the altered radial configuration settings, a new batch application written by CODAR Ocean Sensors was utilized for reprocessing larger datasets at a quicker rate. The real time and reprocessed radial data was examined with neighboring CODAR sites operating at 13 MHz and the semi-diurnal (M2) tidal signal.**

Index terms—HF (High Frequency) radar, surface currents, reprocessing, radials, tides, SeaSonde.

I. Introduction

The importance of precise surface current measurements reflects in applications that include Coast Guard Search and Rescue (SAROPS) missions, input into weather models, and insight into understanding ocean physical processes. During 2012, seven 13 MHz radar systems were operated by Rutgers University Coastal Ocean Observation Laboratory (RUCOOL) between Sea Bright and North Wildwood, NJ. The higher resolution demands the task of ensuring that the radials from each site compliment each other in order to create a smooth, accurate representation of the surface current field.

The SeaSonde software creates radial files every hour on the hour as a result of spectral averaging. For a 13 MHz SeaSonde, Doppler spectra are averaged over 15 minutes and outputted every 10 minutes to produce radial current estimates [1]; seven spectra files cover a 15 minute period each, which means there is a 5 minute overlap between Doppler spectra computations. The short-term radials are created every 10 minutes from the individual spectra files and then averaged to create the hourly radial files utilized in total current estimates.

Ideally, analyzing every short-term radial would be beneficial for identifying whether first order line settings are suitable for the location and time of processing. However that can get extremely challenging when operating several High Frequency radars because it is time consuming to visually inspect each spectra file. So we rely on several quality control metrics for diagnosing radial accuracy. Average radial bearing between ideal and measured radials, spectra merged count, radial count, and data latency are a select few of the techniques that are applied for data inspection [2]. When one of the criteria for quality control is not met, spectra files need to be examined in order to determine whether the first order Bragg was properly processed.

This test case examines the week of May 02, 2012 for a 13 MHz SeaSonde in Brant Beach, NJ (BRNT) where interference was being processed as first order Bragg, leading to imprecise current measurements in that location. High noise or interference in the received signals is just one of the reasons for errors in the radial field. Other limitations for accurate radials include distortions in the measured antenna patterns and restrictions in the frequency resolution of the Doppler spectrum [3]. We present two considerations in the header settings when reprocessing the radials for this time period: 1) Max radial velocity limitation and 2) Noise factor (Signal above noise). The radial maps were then compared with two 13 MHz sites (Seaside Park, NJ and Brigantine, NJ), along with the semi-diurnal tidal constituent measurements from the NOAA gauge located in Atlantic City, NJ. We also present the description and results of a new batch processing application used during this case study.

II. Approach

Spectra files for the entire year of 2012 for the Rutgers University standard CODAR network were reprocessed with the new first order line settings. All of the header settings were replicated with the default settings with the exception of the noise factor and maximum radial velocity limit. The new settings were declared to be 6.3 (~8 dB) and 60 cm/s for the noise factor and maximum radial velocity limit, respectively. For the purposes of simplifying the analysis of the reprocessed data, we decided to focus on BRNT for the first week of May

978-0-933957-40-4 ©2013 MTS

2012 since most of the test cases were performed on this site with the altered first order line settings. We compared the real time and reprocessed results from BRNT with the nearest High Frequency radar sites operating at 13 MHz. These sites include Seaside Park (SPRK) North of Brant Beach and Brigantine (BRMR), the closest site to the South. Figure 1 shows a map of the SeaSonde locations along with the overlapping radial coverage. We also compared average radial velocities with the tidal data from Atlantic City, NJ.

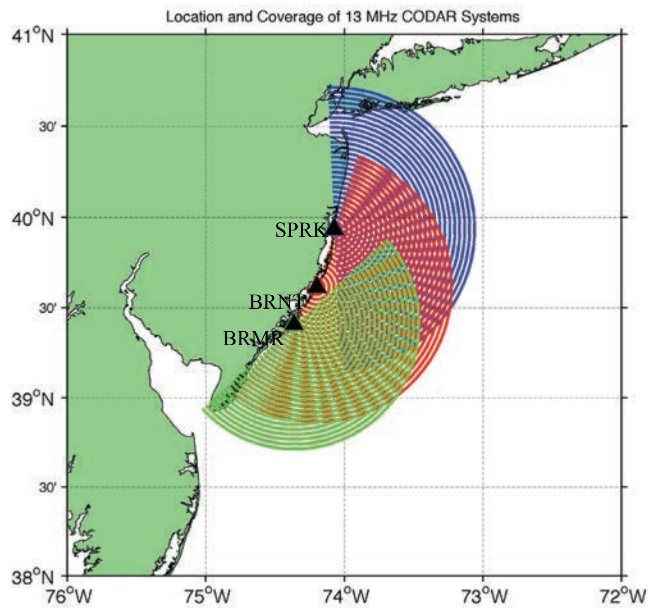

Figure 1. Map of study area. Seaside Park (SPRK), Brant Beach (BRNT), and Brigantine (BRMR) coverage areas shown in blue, red, and green, respectively.

A. Batch Reprocessing Application

A recently developed application written by CODAR Ocean Sensors allows for a very efficient method of reprocessing large datasets. In the past, and still in practice, spectra files had to manually be transferred to a specific directory with the new changes implemented in the radial configuration files. This approach became complicated when attempting to reprocess spectra files over the course of months to a year.

The new batch reprocessing function eliminated the need to transfer files, which makes working with an extensive amount of spectra files simpler. The application allows the user to input the following as variables: 1) Directory of spectra files to be reprocessed. 2) Time range. 3) Path of the radial configuration folder to be used. 4) Final reprocessed directory where a new folder is created with the new radials, spectra files, and radial configuration folder.

Another supportive feature includes the use of the console application, which displays messages as radials are being processed. If reprocessing discontinues at any point, console will present a log showing the spectra files processed and will be automatically saved in the new output folder. The new batch interface also allowed for performing several test cases with various first order line settings at an efficient rate.

B. SeaSonde Release 7 Software

We used CODAR'S Release 7 SeaSonde software during the examination with the first order lines. In order for this software to work, a SeaSonde radial or elliptical suite USB key is needed. This allows the SeaSonde Acquisition application to run which creates the cross spectra series files, time series files, and range series files. The CSPro application then averages and removes ship signals [4].

We had four available computers to reprocess all of the seven stations for 2012, all of which had Release 7 downloaded. Each computer was dedicated to reprocessing one of the four BPU (Board of Public Utilities) sites to limit confusion. Over time a log has been kept of APM dates, phase correction changes, hardware changes, antenna bearing alterations. All of this information was used to make the necessary changes to create the most accurate radials.

As opposed to Release 6, Release 7 allows the user to create AngSeg_SITE.txt files, which acts like a filter. This configuration file notifies the software to flag vectors that are over land and not within the site's coastal boundaries. The default AngSeg is 360 degrees, but we used a custom AngSeg for each site location, which is located within the radial configurations folder. Release 6 gives the user the option to specify how to mark vectors out of bounds in the Header.txt file. A custom AngSeg_SITE.txt file is only possible with the Release 7 software.

C. Spectra Files

It is habitual to collect spectra and range data throughout the entire year for each CODAR site. We have external hard drives installed for each site to maximize disk space. Over time, operators swap the external hard drives to ensure limited data loss. The spectra and range files are then transferred to a terabyte(s) hard drive in the lab with Level X RAID to have backup copies of the data. All of the 2012 spectra files were located on one hard drive, providing access from any machine for reprocessing.

III. DEFAULT FIRST ORDER LINE SETTINGS

The default noise factor set by the 13 MHz SeaSonde is set to 4, which translates to ~6 dB. The default maximum radial velocity limit is set to 180 cm/s. When noise and high interference saturate the first order Bragg, it often leads to uncharacteristicly strong vectors. In addition to interference, antenna phase corrections from the sea-echo are important for the [5] MUSIC algorithm to properly extract the bearing measurements of a given signal.

Figure 2 displays a radial map for BRNT during which the default first order parameters were used and also when improper phase corrections were set. Interference from an external source, along with the default first order line settings, resulted in many solutions placed over land and a gap in coverage to the South.

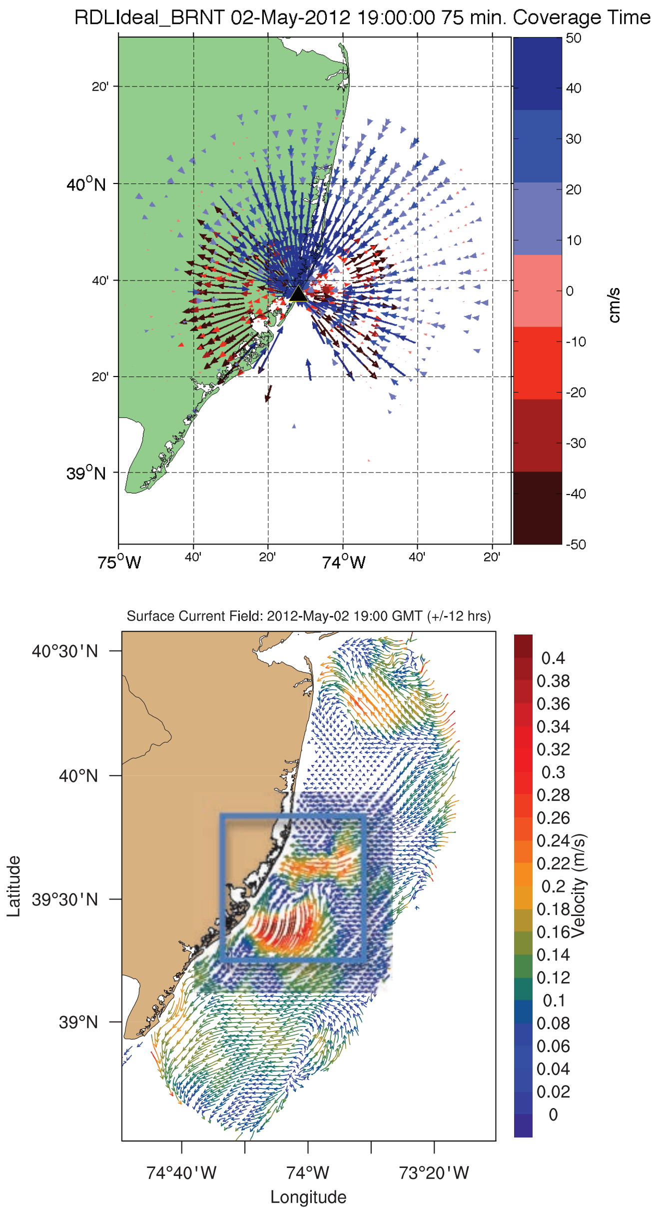

Figure 2. A radial map (top) for Brant Beach, NJ (BRNT) 13 MHz SeaSonde with default first order line settings. Blue vectors indicate a positive Doppler shift while red indicates a negative Doppler shift, or red shift. The bottom plot shows the 25 hour surface currents for that time period. The box highlights the large spatial variability in vector magnitudes due to interference.

IV. REPROCESSED FIRST ORDER LINE SETTINGS

After several small test cases with the BRNT radial configuration settings, it was decided that the most suitable factors for this time period were a noise factor of 6.3 and a maximum radial velocity of 60 cm/s. Switching the maximum velocity threshold significantly improved the radial qulaity by eliminating strong interference in the first order Bragg processing. Raising the noise factor by 2.3 dB also improved the boundary lines for first order processing in capturing very little noise without removing valid radial measurements. Figure 3 shows the reprocessed radial map with very few vector solutions over land and with no outlier radials due to interference; the bottom figure shows the 25 hour average currents for that time period. The reprocessed totals show much less spatial variability compared to the real time data, seen in Figure 2.

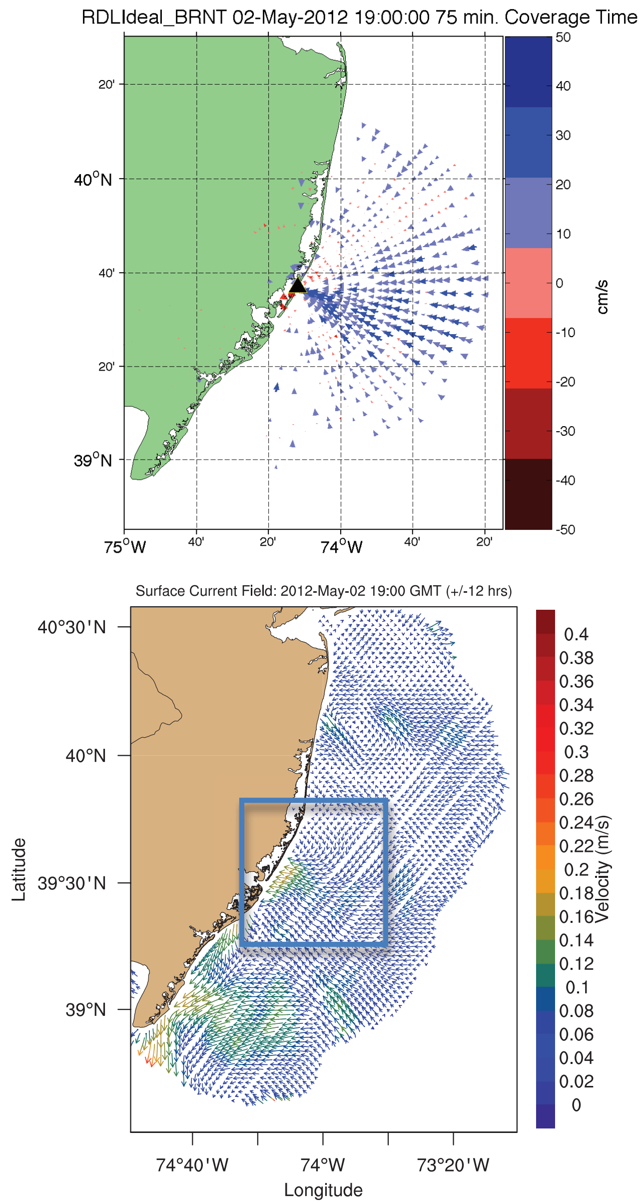

Figure 3. Reprocessed BRNT radial map (top) with the new first order line settings and phase corrections. On the bottom is a total map of the reprocessed surface currents for the 13 MHz CODAR network. Notice the difference in spatial variability in the box.

IV. ANALYSIS

Visually, the reprocessed radials and surface currents appear to be more realistic than the data processed in real time during the first week of May 2012. In this section, we relate the averaged radial velocities with the M2 tide measurements and also compare metric data to SPRK and BRMR.

A. M2 Tidal Constituent

The M2 tide is a strong, semi-diurnal tidal constituent caused by gravitational pull of the moon and is considered by [6] to be the strongest in the Mid-Atlantic, responsible for over 80% of the tidal variance [2]. Water level height should coincide with the average radial velocity directional change. Radial velocities depend on the backscattered signal due to ocean waves half the radar wavelength traveling towards or away from the site [7]. A negative velocity measurements indicates the Bragg waves are traveling away from the radar while a positive Doppler shift suggests that the waves are moving towards the receive antenna.

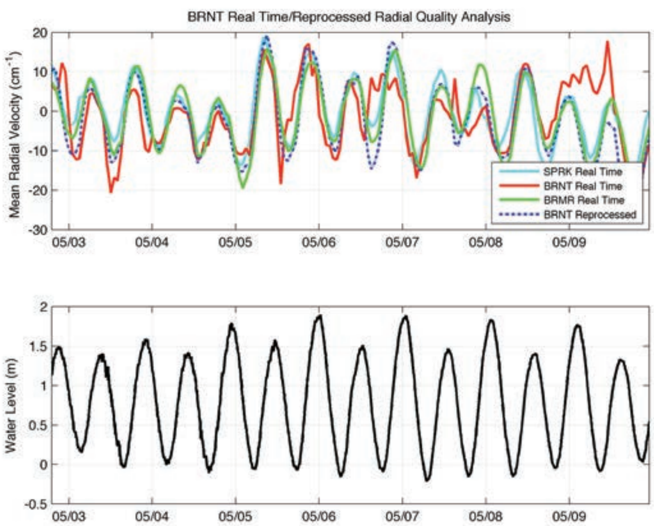

Figure 4. A subplot comparing the average radial velocities for 4 different datasets (top). The radial velocities are averaged every hour. The bottom plot shows the water level height from the NOAA Atlantic City tide gauge.

Figure 4 shows the comparison between the averaged radial velocities for each dataset with the water level at the nearest NOAA tide gauge. The datasets include the real time data during the study period from SPRK, BRNT, and BRMR along with the reprocessed data from BRNT with the altered first order line settings. There are multiple periods where the BRNT real time average radial velocity does not mirror the tidal peaks (May 9th for example), while the other datasets match up well with the water levels.

B. 13 MHz CODAR Data

Ideally, there should be a maximum peak in radial velocity every 12 hours. The default first order lines at SPRK and BRMR during that time period appear to capture the first order Bragg without any signs of interference. The BRNT real time data shows intermittent anomalies (Figure 4). The irregularities in the average velocity measurements are due to some source of interference that was processed as first order Bragg. Figure 5 displays the correlation between the average radial velocities for the BRNT real time and reprocessed datasets compared with the SPRK and BRMR real time average velocities.

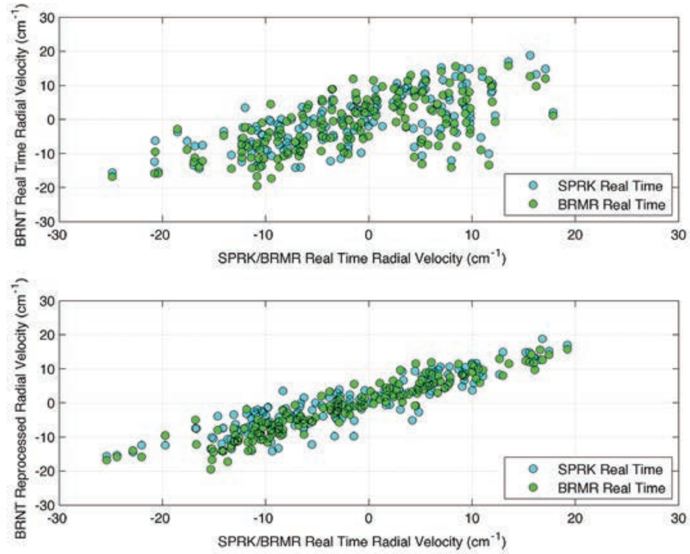

Figure 5. Scatter plot showing the comparison between BRNT real time radial velocities (y-axis) with SPRK and BRMR (x-axis) (top). The bottom plot shows the same comparisons with the BRNT reprocessed average velocities.

The correlation values between the BRNT real time velocities with the SPRK and BRMR real time velocities were 0.68 and 0.63, respectively. For the reprocessed BRNT data correlation values were caluclated to be 0.91 and 0.95 when compared with the SPRK and BRMR real time velocities, respectively. There was a much improved comparison with the reprocessed data set.

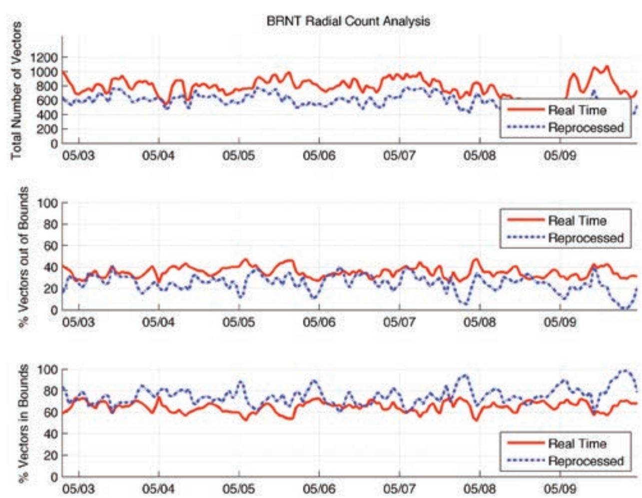

Figure 6. A subplot of the total amount of vectors for each radial file (top), the percentage of radials over land (middle), and the percentage of radials over water (bottom).

C. Radial Metrics

The quality of the reprocessed data correlates nicely with the other 13 MHz radar sites, as well as the M2 tidal signal. In this section we compare radial metric data. Figure 6 displays three plots showing the total amount of solutions witin the file, the percentage of vectors placed on land, and the percentage of vectors placed over water. The reprocessed BRNT files averaged approximately 600 vectors per file while the real time data recorded on average nearly 800 vectors per file. Though the real time files registered more vectors, the percentage of radials over land is much higher than the reprocessed, ultimately leading to less vectors MUSIC places over water with proper bearing measurements. Overall, radial metric analysis shows an improvement in radial coverage when reprocessing with a noise factor of 6.3 (~8 dB) and a maximum radial velocity threshold of 60 cm/s.

VI. CONCLUSIONS

First order line settings need to perform well during radial processing for any CODAR site. One of the major reasons they do not perform well is due to changing ionospheric conditions. The ionospheric conditions depend on solar radiation, leading to a day-night cyles, which attenuate and/or reflect the radio signals from the radar [8]. Other reasons for interference include other High Frequency radars operating within the same bandwidth, internal noise, and the environment (e.g. storms).

The default first order line settings are typically utilized within the Rutgers Univeristy CODAR network but there are occasions where the settings need to be changed. Often, the noise factor plays a role in eliminating contaminated spectra where first order processing becomes compromised. We saw strong interference contaminate the radial field in May 2012 for BRNT with the default settings. We found a 2.3 dB threshold increase in signal-to-noise and a lower maximum radial velocity allowed in the processing ensured the elimination of interference-induced radial velocities. These settings, or any first order line settings, will not always be suitable because there are too many factors that are constantly changing. For this reason, reprocessing is extremely important when it comes to operating high-frequency radars. The recently developed batch reprocessing application is a very efficient way to reprocess contaminated spectra to ensure the most accurate radial maps are being measured by the High Frequency radars.

REFERENCES

[1] Emery, B.M., Washburn, L., Harlan, J.A. (2004). "Evaluating Radial Current Measurements from CODAR High-Frequency Radars with Moored Current Meters," Journal of Atmoshperic and Oceanic Technology, Vol. 21-8, 1259-1271.

[2] Roarty, H., Smith, M., Kerfoot, J., Kohut, J., Glenn, S. (2012). "Automated Quality Control of High Frequency Radar Data," *Oceans*, 2012, 1-7.

[3] Laws, K., Paduan J.D., Vesecky, J. (2010). "Estimation and Assessment of Erros Related to Antenna Pattern Distortion in CODAR SeaSonde High-Frequency Radar Ocean Current Measurements," *American Meteorology Society*, Vol. 27, 1029-1043.

[4] CODAR Ocean Sensors. "Radial Processing Flow Diagram."

[5] Kohut, J.T., Glenn, S.M., (2003). "Improving HF Radar Surface Current Measurements with Measured Antenna Beam Patterns," *Journal of Atmospheric and Oceanic Technology*, Vol. 20, pg. 1303-1316.

[6] Moody, J.A, Butman, B., Beardsley, R.C., Brown, W.S., Daifuku, P., Irish, J.D., Mayer, D.A., Mofjeld, H.D, Petrie, B., Ramp, S., Smith, P., Wright, W.R. (1984). "Atlas of Tidal Elevation and Current Observations on the Northeast American Continental Shelf and Slope," *U.S. Geological Survey Bulletin* 1611, pg. 122.

[7] Essen, H., Gurgel, K., Schlick, T. (2000). "On the Accuracy of Current Measurements by Means of HF Radar," *Journal of Oceanic Engineering*, Vol. 25-4, pg. 472-480.

[8] Gurgel, K., Barbin, Y., Schlick, T. (2007). "Radio Frequency Interference Suppression Techniques in FMCW Modulated HF Radars," *Oceans 2007*, 1-4.

Process-Driven Improvements to Hurricane Intensity and Storm Surge Forecasts in the Mid-Atlantic Bight:

Lessons Learned from Hurricanes Irene and Sandy

Scott Glenn, Dave Aragon, Louis Bowers, Michael Crowley, Rich Dunk, Colin Evans, Chip Haldeman, Ethan Handel, Tina Haskins, John Kerfoot, Josh Kohut, Julia Levin, Travis Miles, Laura Palamara, Hugh Roarty, Oscar Schofield, Greg Seroka, Mike Smith, Nilsen Strandskov, John Wilkin, Yi Xu & Javier Zavala-Garay
Rutgers University
New Brunswick, NJ 08901, USA
glenn@marine.rutgers.edu

Carolyn Thoroughgood, Gerhard Kuska, Bruce Lipphardt, Matt Oliver, Matt Shatley
University of Delaware
Newark, DE 19711

Wendell Brown, Avijit Gongopadhyay, Chris Jakubiak & Andre Schmidt
University of Massachusetts
New Bedford, MA 02744

Eoin Howlett
Applied Science Associates
Kingston, RI 02879

David Ullman
University of Rhode Island
Narragansett, RI 02882

Jim O'Donnell & Todd Fake
University of Connecticut
Groton, CT 06340

Nickitas Georgas, Alan Blumberg, Michael Bruno & Tom Herrington
Stevens Institute of Technology
Hoboken, NJ 07030

William Boicourt & Tom Wazniak
University of Maryland
Cambridge, MD 21613

Jay Titlow
Weatherflow, Inc
Poquoson, VA 23662

Ray Toll
Computer Sciences Corporation
VA

Larry Atkinson & Teresa Updyke
Old Dominion University
Norfolk, VA 23529

Nancy Verona
Center for Innovative Technology
Herndon, VA 20170

Harvey Seim & Mike Muglia
University of North Carolina
Chapel Hill, NC 27599

***Abstract*— The coastal northeast United States was heavily impacted by hurricanes Irene and Sandy. Track forecasts for both hurricanes were quite accurate days in advance. Intensity forecasts, however, were less accurate, with the intensity of Irene significantly over-predicted, and the rapid acceleration and intensification of Sandy just before landfall under-predicted. By operating a regional component of the Integrated Ocean Observing System (IOOS), we observed each hurricane's impact on the ocean in real-time, and we studied the impacted ocean's influence on each hurricane's intensity.**

Summertime conditions on the wide Mid-Atlantic continental shelf consist of a stratified water column with a thin (10m-20m) warm surface layer (24-26C) covering bottom Cold Pool water (8-10C). As the leading edge of Irene tracked along the coast, real-time temperature profiles from an underwater glider documented the mixing and broadening of the thermocline that rapidly cooled the surface by up to 8C, well before the eye passed over. Atmospheric forecast sensitivity studies indicate that the over prediction of intensity in Irene could be eliminated using the observed colder surface waters. In contrast, Hurricane Sandy arrived in the late Fall of 2012 after seasonal cooling had already deepened and decreased surface layer ocean temperatures by 8C. The thinner layer of cold bottom water still remaining before Sandy was

978-1-4799-0002-2/13/$31.00 ©2013 IEEE

forced offshore by downwelling favorable winds, resulting in little change in ocean surface temperature as Sandy crossed and mixed the shelf waters. Atmospheric sensitivity studies indicate that because there was little ocean cooling, there was little reduction in hurricane intensity as Sandy came ashore. Results from Irene and Sandy illustrate the important role of the U.S. IOOS in providing the best estimate of the rapidly evolving ocean conditions to atmospheric modelers forecasting the intensity of hurricanes. Data from IOOS may enable improved hurricane forecasting in the future.

***Index Terms*—Hurricane Forecasting, U.S. IOOS, Underwater Gliders, HF Radar, Ocean Modeling, Atmospheric Modeling.**

I. INTRODUCTION

Tropical storms are some of the most destructive and deadly weather phenomena on Earth, and have killed more people than any other natural catastrophe (Keim et al. 2006). For example, in the United States during the 20th-century, ten times as many deaths and >three times as much damage occurred from these extreme weather events as compared with earthquakes (Gray, 2003). The impacts are magnified given the human population density found along the coastlines that are prone to hurricanes. Despite the potential devastation, advances in technology, communication, and forecasting have resulted in significant declines in hurricane-related mortalities between 1900 and present day (Walker et al. 2006). Most recently these declines reflect the developments in global atmospheric models and an ensemble forecasting approach that have successfully reduced hurricane track forecast errors by factors of 2-3 over the last two decades, allowing communities sufficient time to proactively prepare for the storms and evacuate prior to their arrival. Despite the progress in predicting hurricane tracks, the predictive skill for hurricane intensity forecasts has remained "flat" over the last twenty years (Pasch & Blake, 2012).

This current state of the science was illustrated by the two recent hurricanes Irene and Sandy that devastated many communities along the Mid-Atlantic coastline spread over dozen states. Hurricanes Irene and Sandy struck dense population centers, and as a result, the National Hurricane Center's list of costliest hurricanes in United States history ranks Sandy second with over $60 billion and Irene eighth with over $15 billion in damages. Despite the epic scale of devastation, the loss of life was greatly minimized due to accurate forecasts of the hurricane tracks days in advance. Unfortunately, forecasts of hurricane wind intensity were less accurate, impacting efforts to proactively mitigate the damage. For Irene, the wind intensity was significantly over predicted, and for Sandy, the rapid acceleration and wind intensification just before landfall were under predicted. The over prediction of Irene's intensity in 2011 led to skepticism of the storm surge warnings for Sandy in 2012. To further complicate matters, the under predicted intensity of Sandy resulted in an under predicted storm surge that in some cases led to insufficient preparation.

The Mid-Atlantic Regional Association Coastal Ocean Observing System (MARACOOS), one of eleven Regional Associations comprising the regional component of the U.S. Integrated Ocean Observing System (IOOS), operates a Regional-Scale Coastal Ocean Observatory that includes coastal weather mesonets, satellite data ground stations, a 1000 km long High Frequency (HF) Radar network (Roarty et al., 2010), and a distributed fleet of autonomous underwater gliders (Schofield et al., 2010). Observatory data is assimilated into global and regional-scale ocean models, and an ensemble of regional atmospheric models beginning to use the ocean surface conditions as a boundary condition. The Regional-Scale Coastal Ocean Observatory was fully operating during both hurricanes. In this paper, we discuss selected highlights of real-time ocean data acquired by the MARACOOS regional-scale network during Irene and Sandy, and how the ocean forecasts faired. Through a series of atmospheric model sensitivity studies, the potential impact of accurate real-time ocean data and forecasts on hurricane intensity forecasts in the Mid-Atlantic is demonstrated.

II. HURRICANES IRENE & SANDY

The Mid Atlantic Bight of North America was recently struck by two hurricane landfalls that devastated dense population centers and communities spread over a dozen neighboring states (Figure 1). Hurricane Irene, a category 1 storm offshore, tracked rapidly northward along the eastern seaboard in August of 2011, resulting in significant flooding on inland waterways due to torrential rains. Fourteen months later, Hurricane Sandy, a much larger category 2 storm offshore, made an uncharacteristic left turn and approached perpendicular to the coast in October of 2012, causing significant damage to coastal communities due to the extreme storm surge.

Fig. 1. National Weather Service tracks for hurricanes Irene (purple) and Sandy (orange).

Data from the Mid-Atlantic Regional Association Coastal Ocean Observing System (MARACOOS), one of eleven regional associations in the U.S. Integrated Ocean Observing System (IOOS), monitored the ocean response, and used that data to study the influence of the ocean on the intensity of both hurricanes.

Hurricane Irene approached the Mid Atlantic's regional ocean observatory from the south. The real-time observations of the evolving ocean are described in the MARACOOS blog (Glenn et al., 2011). Irene's size was similar to the 1,000 km length scale of the region's HF Radar network (Figure 2) Strong storm-related winds were experienced for only 1 day. Winds initially came from offshore, turned to an alongshore direction as the eye passed, and continued turning to come from the coast after the eye moved north into New England. Most atmospheric models in the ensemble converged on the track forecast days in advance, but unfortunately, the wind intensity was over-predicted by the ensemble. Because of the short duration of hurricane-forced winds, the relative timing between the high tide and the time of the most severe onshore currents for this rapidly moving storm were critical to determine the severity and location of the maximum storm surge. The severe damage from Irene instead occurred inland, where winds that picked up moisture over the warm ocean resulted in heavy rains and flood conditions along the Delaware, Hudson and Connecticut Rivers.

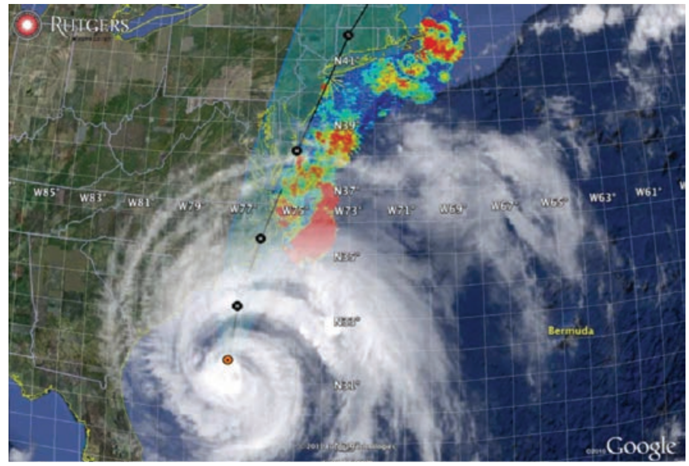

Fig. 2. Spatial extent of Hurricane Irene, August 27, 2011.

Hurricane Sandy approached the Mid-Atlantic's ocean observatory from offshore, perpendicular to the alongshore track of Irene. Real-time ocean observations were again described in the MARACOOS blog. The diameter of Sandy was twice as large as Irene, larger than the scale of the observatory (Figure 3). The approach direction had a significant impact on the areas with severe storm surge damage. North of the eye on the right hand side of the track, the counterclockwise circulation is in the same direction as the propagation. Here sustained winds from offshore that transported water towards the coast were experienced for multiple tidal cycles. South of the eye, winds blew from the coast and water was transported offshore. Compared to Irene, the relative timing between hurricane forcing and high tide was much less important for determining damage. More important for Sandy was your location north or south of the eye.

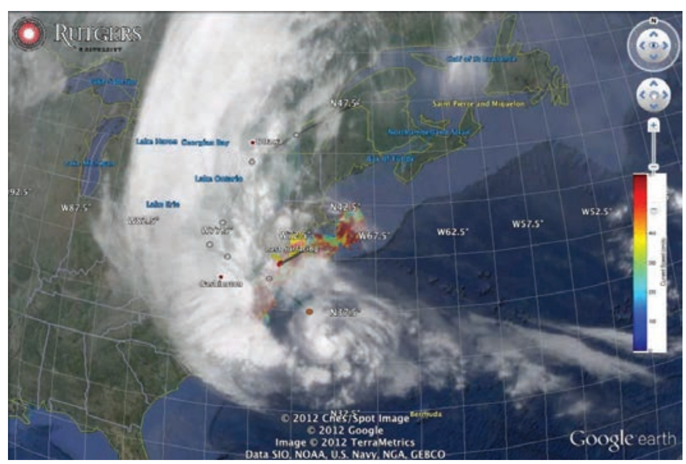

Fig. 3. Spatial extent of Hurricane Sandy, October 28, 2012.

III. Water Column Mixing in IRENE

The eye of Hurricane Irene made landfall in southern New Jersey near Atlantic City at 0900 UTC on August 28, 2011. Irene was moving rapidly northward, fully crossing the state of

New Jersey in about 6 hours. The rapidly evolving surface current response as Irene propagated along the New Jersey coast was observed (Figure 4) using the Mid-Atlantic's High Frequency (HF) Radar network (Roarty et al., 2010). At 0600 GMT, Irene's eye is still over water, with its location observed in the CODAR currents offshore southern New Jersey. Strong onshore currents over the entire width of the shelf are observed north of the eye. At 1200 GMT, the eye is over land in central New Jersey. The ocean currents have rotated to be along the coast to the northeast, and are reduced in speed. By 1800 GMT, the eye is over northern New Jersey. Currents behind the eye are again strong and offshore. The transition from strong onshore flow to strong offshore flow occurred over a short 6 hour period.

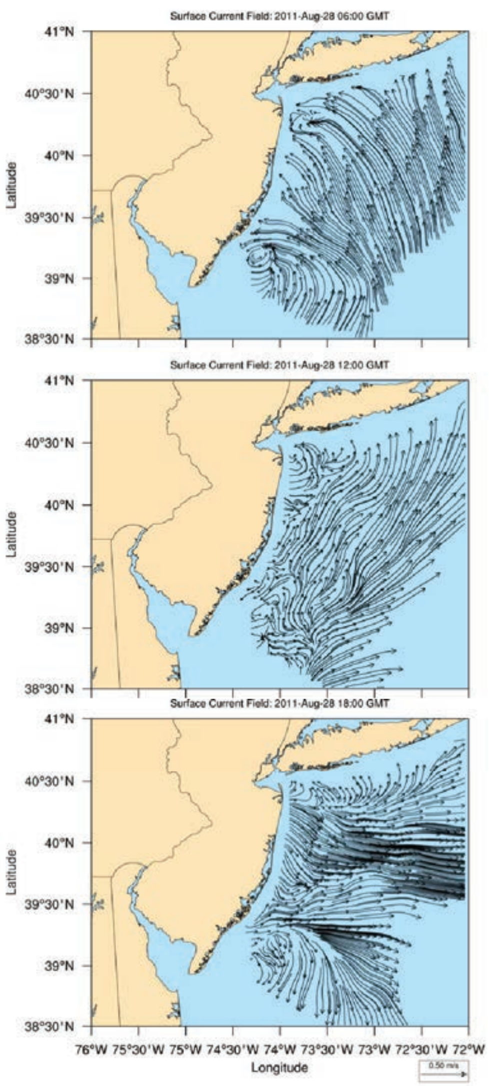

Fig. 4. CODAR-derived surface current spatial response as Irene tracks along the New Jersey coast.

Glider RU16 was deployed on the New Jersey shelf on a coastal survey mission well ahead of and independent of the hurricane. As Irene approached, the glider was purposely left at sea, but was moved offshore to the 40 m isobath to ride out the storm (Figure 5a) The 40 m isobath is an area of relatively uniform sandy sediment, and was considered far enough offshore that even strong hurricane currents faster than the glider's flight speed would not blow the glider onto the beach.

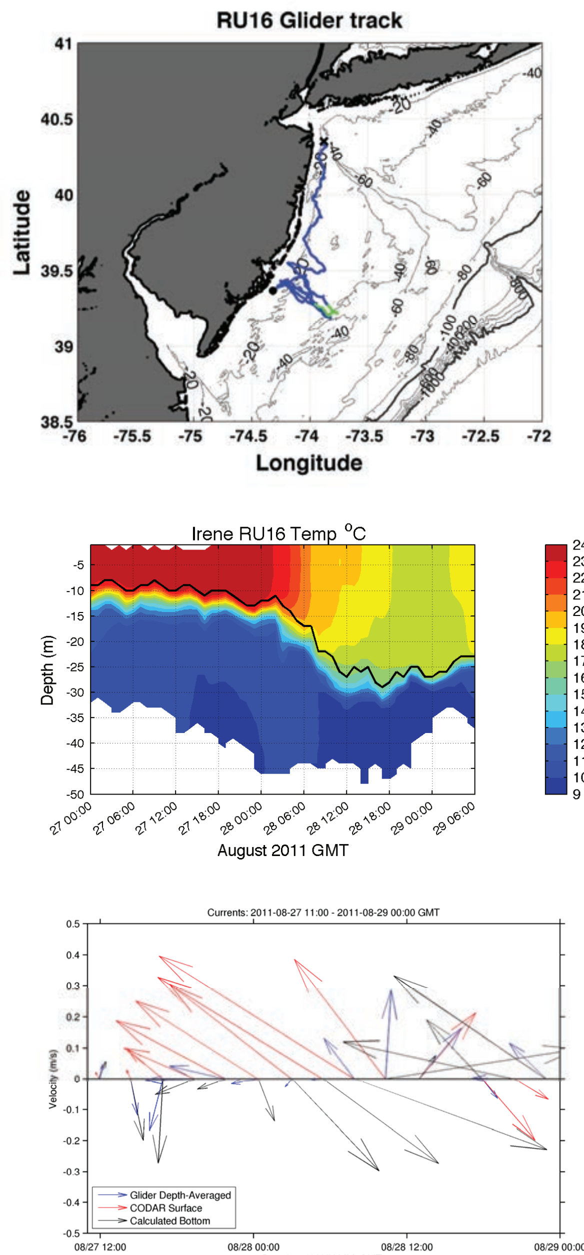

Fig. 5. (a) Glider track in Hurricane Irene. (b) Glider temperature section for the portion of the glider track marked in green. Black line is the depth of the surface mixed layer. (c) Glider depth averaged currents (blue), CODAR surface currents along the glider track (red), and inferred bottom layer currents (black).

The temperature section collected by the glider near the 40 m isobath during Irene (Figure 5b) indicates that on

August 27, the Mid Atlantic shelf was near its peak summer stratification, with a thin 10 m thick layer of warm surface water near 22-25C, and a thicker layer of bottom "Cold Pool" water near 8-10C. The summer thermocline was typically sharp, with the transition from warm surface waters to bottom Cold Pool waters occuring in a few meters. As Irene approached, mixing within each of the surface and bottom layers made each layer more uniform and tightened the thermocline. On August 28, between 0000 GMT and 1200 GMT, as the northern edge of Irene passed over the location of the glider, the thermocline broadened (from less than 5 m to over 15 m) and deepened (from 10 m to 28 m), and the surface layer cooled (from 24C to 18C). After 1200 GMT, as the backside of the hurricane passed over the glider, the deeper thermocline remained near 25 m. Both the surface and bottom layers continued to cool independent of each other as the thermocline reintensified.

Gliders report the depth averaged current over the previous segment with each surfacing. The depth averaged current is estimated by comparing the dead reckoned surface location with the actual surfacing location, and assuming the difference is due to advection of the glider by the depth averaged current. During the hurricane, depth averaged currents are initially southward at 20 cm/sec before the storm, drop to near zero during the approach of the storm, and transition to northward at 30 cm/sec on the backside of the storm (Figure 5c). The important observation is that the depth averaged current is near zero between 0000 GMT and 1200 GMT on August 28 when the thermocline deepening and surface layer cooling is observed. Plotting the CODAR surface currents at the location of the glider, shows how the surface layer is being forced directly onshore to the northwest by the hurricane winds starting on August 27 and peaking during the deepening event. After 1200 GMT on August 28, the CODAR surface currents rotate clockwise to alongshore and then to offshore as noted in the spatial maps (Figure 4). Using the observed CODAR surface current to represent the average current above the thermocline, the average current below the thermocline was estimated based on the requirement that the weighted average of the surface and bottom layers equal the observed glider depth averaged current. Based on the estimated bottom layer current, the onshore transport in the surface layer begins midday on August 27 and for the first 12 hours, there is little response in the bottom layer. During this time the storm surge is expected to grow. Between 0600 GMT and 1200 GMT, as the onshore currents in the surface peak, the offshore currents in the bottom layer accelerate, resulting in zero net transport towards the coast. This time interval when the greatest shear between the surface and bottom layers is expected is precisely the time when the thermocline is observed to deepen. The zero net transport also implies that the storm surge that would have resulted from the shoreward transport of surface water is compensated by the offshore transport of bottom water.

The Regional Ocean Modeling System (ROMS) was operated in forecast mode during the storm. The model was rerun here using the same forecast parameters for more in depth studies. The ROMS forecast/hindcast of the ocean response has several features consistent with these observations that enable further definition of the physical processes responsible for the surface layer cooling. But there are also several differences between the observations and the model. The initial state of the ocean in the ROMS model (Figure 6a) has a 10 m thick surface warm surface layer near 24 C, and bottom Cold Pool layer near 9C, but the initial thermocline is wider than observed, extending over 15 m thick instead of less than 5 m. So the initial condition has a less extreme thermocline that would be more easily mixed than observed. The model was driven by the North American Mesoscale (NAM) model winds. Despite the weaker thermocline, significant mixing does not begin in the model until 6 hours later than the observations. The initial response is an acceleration of the alongshore currents to over 60 cm/sec to the northwest at 0000 GMT on August 28 (Figure 6c). The cross-shore currents, in the onshore direction at the surface and the offshore direction in the bottom, spin up simultaneously and peak at 0600 GMT. At this peak in shear, the thermocline starts deepening and the surface water starts cooling. In the model, this process ends in 6 hours, with the surface water cooling 5C and the bottom water warming 1C. At 1200 GMT, the alongshore surface current reverses direction consistent with the CODAR observations, the bottom jet relaxes in the cross-shore current but remains present in the alongshore current. The glider observations indicate that the bottom jet should have remained in the cross-shore direction.

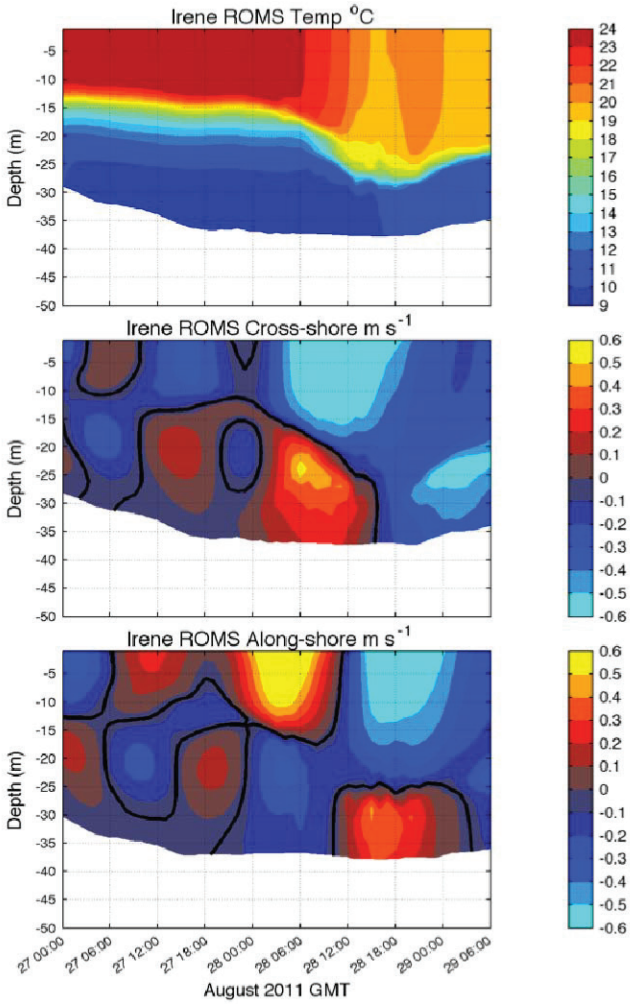

Fig. 6. Regional Ocean Modeling System (ROMS) hindcast of temperature, cross-shore (+offshore) and alongshore (+northeast) current sections along the green portion of the glider track in Figure 5a. Black lines indicate 0 cross and alongshore currents.

While the exact details of the deepening of the thermocline and the cooling of the surface layer do not exactly match those observered, model diagnostics indicate that the vertical diffusion in the surface layer dominate advective changes in the model. This points to improvements in the mixing parameterizations as a place to look to improve the model. Even with a weaker thermocline and stronger winds, the mixing is insufficient to cool the upper layer as much as observed.

Satellite-derived Sea Surface Temperature (SST) maps of the Mid-Atlantic Bight just after Irene indicate that the cooling was widespread (Figure 7). The locally generated SST product (Figure 7a) indicates that surface temperatures dropped to as low as 14C on the shelf, with the greatest cooling observed over the historical location of the Cold Pool and concentrated on the mid to outer shelf, shoreward of the shelfbreak. The cooling was so significant, even though skies were clear after the storm, the cloud detection algorithms rejected the data as being too cold, removing it from the Real Time Global (RTG) SST updates (Figure 7b). As a result, the RTG SST map is essentially unchanged before and after Irene. Since the RTG map is the SST used by several atmospheric forecast models as a bottom boundary condition, the ocean used in the Irene forecasts was too warm. The difference between the RTG and the actual sea surface temperatures after the storm is as large as 10C (Figure 7c).

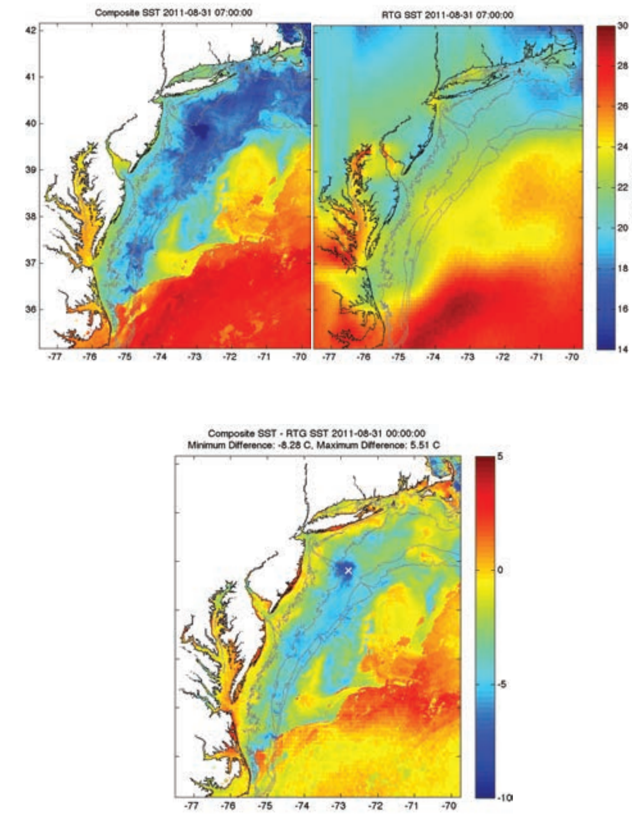

Fig. 7. Post-Hurricane Irene Satellite-derived Sea Surface Temperature (SST) products for August 31, 2011. (a) Locally composited SST showing the surface cooling. (b) Operational global SST product with the cool pixels incorrectly identified as clouds. (c) Difference.

The impact of the rapidly cooling SST on the Weather Research and Forecasting (WRF) model hindcast sensitivity studies of Hurricane Irene illustrates the significant impact of the cooler water. The glider data indicates that the cooling occurred ahead of the eye as the high winds of the outer wind bands approached. Thus the eye of the hurricane passed over cool water as it propagated northward. Since the RTG SST does not cool, it was used as the base case for comparison (Figure 8a). At the time of landfall, the hurricane intensity is over predicted. Since the ROMS model cools late and insufficiently, the locally composited SST product was used to simulate the change in SST as the storm passed. Starting with the warm pre-storm SST, the cold post-storm SST was applied everywhere at the time of peak mixing observed in the glider transect. The resulting WRF forecast is lower by 5-10 knots. (Figure 8b).

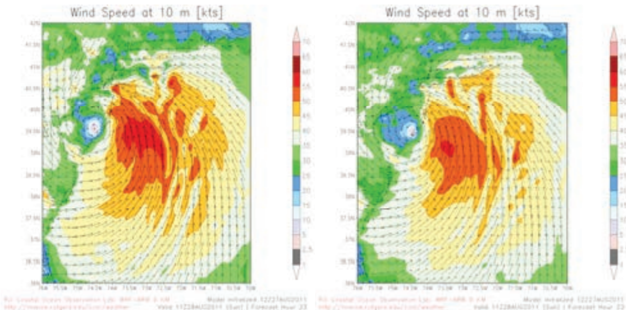

Fig. 8. Weather Research Forecast (WRF) atmospheric hindcasts of Hurricane Irene with different ocean boundary conditions. (a) Using the warm SST throughout the run. (b) Switching to the cold SST in Figure 7a when the cooling is observed in the glider data.

IV. SANDY

Hurricane Sandy followed Hurricane Irene by 14 months. Forecasts made by the European Center for Medium-range Weather Forecasting (ECMWF) alerted researchers to the possibility of a signficant storm hitting New Jersey a full week in advance. The importance of the glider observations in Irene prompted the deployment of glider RU23. Based on the lessons learned in Irene, the glider payload bay with its standard CTD was further equiped with optical sensors to look at the sediment concentrations as a tracer for mixing. A Nortek Aquadopp Acoustic Doppler Current Profiler (ADCP) was attached externally to examine the shear across the thermocline during the event. The glider was deployed nearshore with a small boat, and, as in Irene, was directed to fly to the 40 m isobath to ride out the storm (Figure 9).

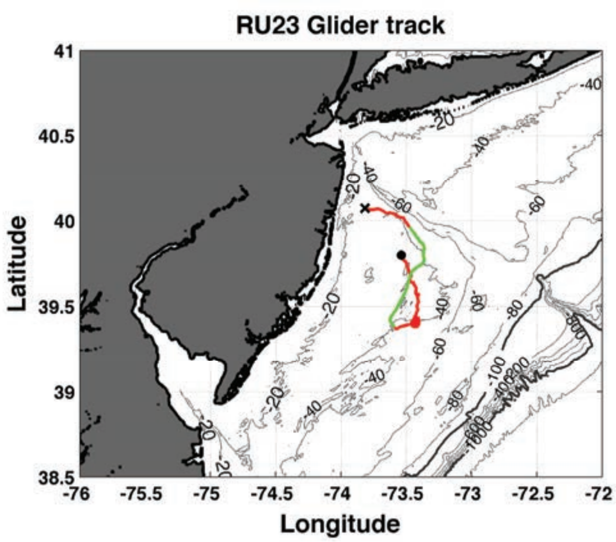

Fig. 9. Glider track during Hurricane Sandy.

Glider RU23 revealed that the initial ocean conditions for Hurricane Sandy were quite different than 14 months ago before Irene (Figure 10). The peak summer thermocline intensity observed in Irene was already 2 months into the fall transition. The two-layer structure was still present, but the surface layer had already cooled to 16C-17C, and thickened to a depth of 30 m. As usual, the bottom Cold Pool temperatures where observed to be around 9C-10C. Like Irene, the thermocline is again observed to be only a few meters thick. As Sandy approaches the coast, the increase in the thermocline depth is even more rapid than Irene, occuring within a few hours near 0600 GMT on October 29. After the deepening event, the water column is filled with a single surface layer, but the layer cooling is only 1 C from 16 C to 15 C. The glider data indicated that Sandy was going to make landfall propogating over SSTs that changed little from the pre-storm conditions. No ohterwise unobserved cooling to reduce intensity was expected.

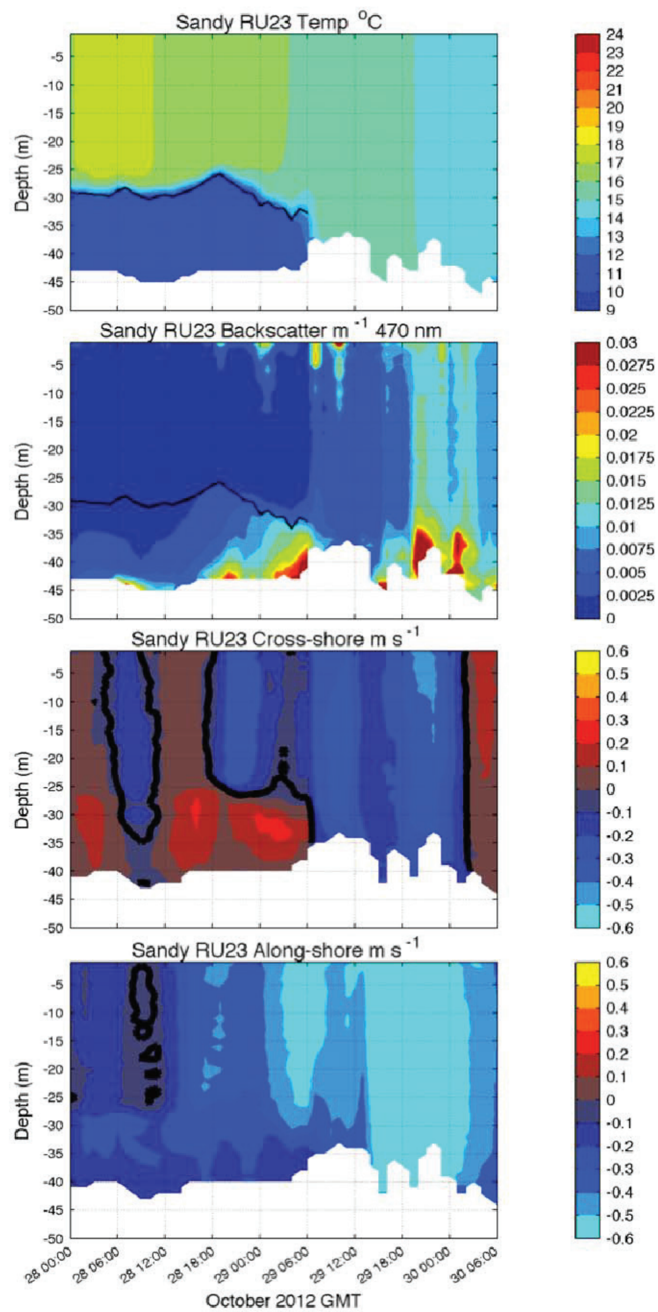

Fig. 10. Glider-derived temperature, backscatter, cross-shore (+offshore) and alongshore (+northeast currents for Hurricane Sandy.

The ocean model in Irene indicated the deepening and cooling of the surface layer, while inadequate, was dominated by a mixing processes. More extensive glider observations in Sandy indicate the layer deepening was likely dominated by an advective processes. Optical backscatter in Sandy indicates that before the transition to a fully mixed water column, sediment suspended from the bottom did not cross the thermocline. After the transition to one layer, optical sensors indicate that sediment resuspension filled the water column, with a single mixed layer going from surface to bottom. Currents measured by the glider-mounted ADCP indicate that before the transition, a two layer flow was observed, especially in the cross-shore direction. A strong offshore jet formed in the bottom layer and persisted for over 18 hours before the transition as the water in the bottom layer thinned and moved offshore. Once the transition was complete, the water column responded as a single layer. Most significantly, the cross-shore current was onshore throughout the water column and persisted for two tidal cycles as the alongshore current accelerated to the southwest.

The same two SST products used in Irene were also examined in Sandy for August 27 (Figure 11). There is little pre-storm difference between the two SSTs, both maps have shelf temperatures in the 16C-18C range before the storm. Because Sandy was so extensive, and it was followed several days later by a northeaster that dropped snow on the damaged area, new SST products were not available for 11 days after the storm.

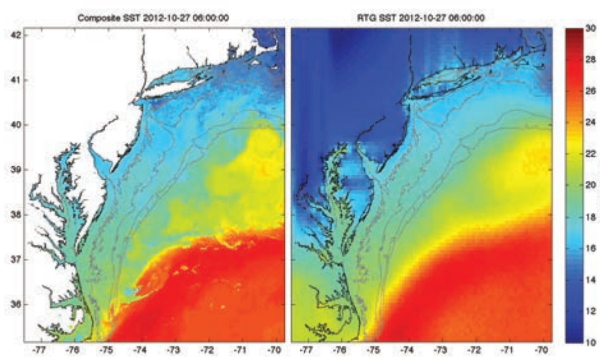

Fig. 11. Pre-Hurricane Sandy Satellite-derived Sea Surface Temperature (SST) products for October 27, 2012. (a) Locally composited SST. (b) Operational global SST product.

The Sandy observations indicated that there would be no significant cooling of the ocean surface layer as Sandy propagated shoreward. The WRF winds based on the conditions used in the real-time WRF forecasts, with atmospheric boundary conditions supplied by NCEP and ocean boundary conditions supplied by the locally composited SST are in Figure 12a. There is little sensitivity to the source of the SST, either the RTG or composite. Both result in an intensification of the storm as it makes landfall. The main sensitivity is the timing of landfall that is adjusted based on which NCEP atmospheric model is used for boundary conditions. WRF embedded within the North American Mesoscale (NAM) model captures the acceleration of Sandy during the last 6 hours before landfall better than WRF embedded in the Global Forecast System (GFS) model. The acceleration and intensification is significant, since the mean storm surge using operational products was under-predicted by 1 m in the hardest hit areas. Using the WRF model run in Figure 12a with the proper intensification and acceleration gains back the missing meter in the mean storm surge as predicted by the New York Harbor Ocean Prediction System (NYHOPS) run by Stevens Institute of Technology.

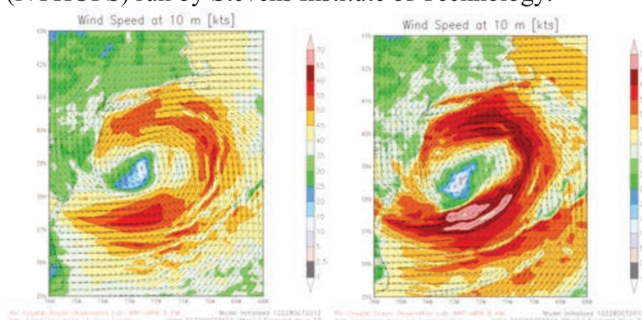

Fig. 12. Weather Research Forecast (WRF) atmospheric hindcasts of Hurricane Sandy with different ocean boundary conditions. (a) Using the cold SST from Figure 11a. (b) Using a warm SST characteristic of August conditions on the Mid-Atlantic continental shelf.

This series of model runs, while producing a hindcast that accurately recreates the observed storm surge, leaves unanswered the question of forecast sensitivity to SST in Sandy. If Sandy had hit earlier in the hurricane season during the peak summer stratification, would the forecast be sensitive to rapid changes in SST? As a test case, Sandy was rerun with typical August SSTs where, as in reality, it was assumed that no satellite updates to SST were available for over a week. The increase in forecast intensity at landfall is evident in Figure 12 b. Using these higher winds to force the NYHOPS storm surge model results in another meter increase in the predicted storm surge.

V. CONCLUSIONS

The back-to-back landfalls of hurricanes Irene and Sandy along the coast of New Jersey have hightened awareness of hurricanes and their potential impacts in the Mid-Atlantic. Irene’s alongshelf track was accurately forecast but the intensity was over-predicted. Ocean observations by U.S. IOOS provide guidance as to why. Operational SST products did not pick up the 8-10C cooling caused by Irene even several days after the weather had cleared. An autonomous underwater glider that flew through the storm indicated that the cooling occurred rapidly as the leading edge of the hurricane approached and well ahead of the eye. Even if the operational SST products were reconfigured to pick up the cooling after the storm, they could not be applied in time to impact Irene. A more useful SST mapping product that accurately captures the timing and spatial extent of the cooling can only be supplied by an ocean forecast model. The ocean observations indicate what processes the ocean model must capture. Specifically, the initial thermocline must be better represented as the starting point. Second, the model must be 3-D, with a coast and a bottom. An infinitely deep 1-D model, one potential option for coupled atmosphere-ocean modes, will not capture the processes observed here. These include the initial onshore transport in the surface layer towards the coast, and the delayed response of the bottom layer to produce an offshore transport that limits the net shoreward transport. When there are two layers, the water transported onshore has an escape route through the bottom layer that appears to limit the storm surge. It also appears that the bottom layer also should be sufficiently thin for the offshore transport to produce a large shear across the interface. It is when this large shear is present that the mixing and cooling occurs.

Sandy occurred later in the year than Irene, after the fall transition was well on its way. Real time ocean observations during Sandy provided different guidance on what to expect when Sandy came ashore. The surface layer was already much thicker and cooler, so significant additional cooling was not expected. Advection moved what remained of the bottom Cold Pool offshore, removing the midshelf source of cool water. The water column responded as a single layer as Sandy came ashore, with mixing from surface to bottom, no cooling to reduce the intensity, and no bottom layer for the water in the growing storm surge to escape offshore.

The U.S. IOOS observations of hurricanes Irene and Sandy as implemented by MARACOOS for the Mid-Atlantic provided unprecedented real-time views of the evolving coastal ocean as the hurricanes made landfall in New Jersey. The observations led to new process studies in the ocean using numerical ocean models to examine the role of shallow topography, stratification and mixing that ultimately will lead to better ocean forecasts in extreme forcing conditions. New atmospheric sensitifivity studies further indicate that the rapid evolution of the ocean's surface layer temperature can have a significant impact on hurricane intensity. These results provide further evidence that one step towards inrpoving hurricane intensity forecasting is to provide atmospheric modelers a better forecast of the rapidly changing coastal ocean beneath hurricanes.

ACKNOWLEDGMENT

Base support for this research was provided by the U.S. Integrated Ocean Observing System (IOOS) through the Mid-Atlantic Regional Association Coastal Ocean Observing System (MARACOOS). The Department of Homeland Security National Center for Secure and Resilient Maritime Commerce provided additional support for the HF Radar network. New Jersey Board of Public Utilities further augmented the satellite data products, the HF Radar network, and the atmospheric forecasting. The deployment and operation of Glider RU16 in Irene was funded by the Environmental Protection Agency and the New Jersey Department of Environmental Protection. The deployment and operation of Glider RU23 in Sandy was funded by graduate student grants from Teledyne Webb Research and Nortek.

REFERENCES

[1] S. Glenn, O. Schofield and J. Kohut, "Hurricane Irene 2011: Mid-Atlantic IOOS response to the hurricane", http://maracoos.org/sites/macoora/files/downloads/Hurricane_Irene_blog_2011.pdf, pp. 65, 2011.

[2] W. Gray, 2003. Twentieth century challenges and milestones. In: Hurricanes! Coping with Disaster, R. Simpson, ed., American Geophysical Union, Washington, DC. 10.1029/055SP02.

[3] B. Keim, R. Muller and G. Stone, Spatiotemporal patterns and return periods of tropical storm and hurricane strikes from Texas to Maine, Journal of Climate, 20, 3498-3509, 2007.

[4] H. Roarty, S. Glenn, J. Kohut, D. Gong, E. Handel, E. Rivera, T. Garner, L. Atkinson, W. Brown, C. Jakubiak, M. Muglia, S. Haines, H. Seim, "Operation and Application of a Regional High-Frequency Radar Network in the Mid-Atlantic Bight" Marine Technology Society Journal, 44 (6), 2010.

[5] Pasch, R. and E. Blake, 2012. 2012 Review of the NCEP Production Suite: Report from NHC, National Centers for Environmental Predictions, Maryland, December 4, 2012,

[6] O. Schofield, J. Kohut, S. Glenn, J. Morell, J. Capella, J. Corredor, J. Orcutt, M. Arrott, I. Krueger, M. Meisinger, C. Peach, F. Vernon, A. Chave, Y. Chao, S. Chien, D. Thompson, W. Brown, M. Oliver, W. Boicourt, "A regional Slocum glider network in the Mid-Atlantic coastal waters leverages broad community engagement." Marine Technology Society 44(6): 64-74, 2010.

[7] N. Walker, A. Haag, S. Balasubramanian, R. Leben, I. van Heerden, P. Kemp and H. Mashriqui, 2006. Hurricane prediction: A century of advances, Oceanography, 19(2), 24-36.

Bistatic Vessel Detection from the CODAR SeaSonde

Kristen Holenstein, Collin Dobson, Michael Smith, Hugh Roarty, Scott Glenn
Coastal Ocean Observation Laboratory
Rutgers University
New Brunswick, NJ USA
kmholenstein51190@gmail.com

Donald E. Barrick
CODAR Ocean Sensors
Mountain View, CA USA
don@codar.com

***Abstract*— Large numbers of ships travel up and down the East Coast of the United States daily, ranging from recreational vessels to cargo vessels. Especially busy areas are the approaches to New York Harbor. New York currently is the third-busiest port in the United States and it is growing rapidly [1]. The large number of vessels that travel in and around New York, and the expectation of increased numbers, makes Maritime Domain Awareness important for this region.**

To increase Maritime Domain Awareness, Rutgers University is now using their SeaSonde® HF Radar coastal ocean current and wave monitoring network for vessel detection. The vessel detection system focuses on the approaches to New York Harbor, where ship traffic is greatest. The capability of this system was tested along the New Jersey coastline in October 2012.

The vessel detection software, developed by CODAR Ocean Sensors and Rutgers University, was installed on two 13 MHz HF Radar sites. The data analysis for this paper focused on the period from October 22, 2012 to October 26, 2012. The three sites utilized were located in Belmar, Sea Bright and Seaside Park, New Jersey. The network was run in multistatic mode, which is a combination of monostatic and bistatic transmitters and receivers. A transmitter and receiver were located at the Sea Bright and Seaside Park stations. Each of these stations operated in monostatic mode where the transmitter and receiver are geographically collocated. A transmitter was placed at the Belmar site and acted as a bistatic transmitter where its signal was received at the Sea Bright and Seaside Park stations. So a total of four signals were processed using the three stations. The stations were able to operate in bistatic mode by synchronizing their signals through the use of the Global Positioning System (GPS) time signal. The bistatic data vessel detection data obtained from the two sites were compared against the Automatic Identification System (AIS) for verification. The use of bistatic vessel detection data will increase the number of detections on a single vessel by increasing the range of the system as well as adding different look angles when the vessel passes through the Bragg or zero Doppler clutter regions.

Maritime Domain Awareness is vital for areas with heavy ship traffic, such as New York Harbor. The Automatic Identification System (AIS) is a self-reporting system, and may not always be used. The vessel detection capability of the HF Radar system will provide information on ships that are not reporting on AIS. The use of vessel detection from HF Radar will provide a valuable layer that the US Coast Guard can utilize to increase its Maritime Domain Awareness.

Keywords—HF radar, MARACOOS, vessel detection, bistatics, maritime domain awareness

I. INTRODUCTION

Maritime Domain Awareness (MDA) is the effective understanding of anything associated with the maritime domain that could impact the security, safety, economy, or environment of the United States [2]. High Frequency radar is an effective tool to achieve MDA. HF radar has been assimilated into models for effective oil spill response [3-5], utilized in the planning of Coast Guard Search and Rescue (SAR) cases [6, 7] and used to determine the fate of coastal plumes [8, 9]. All of these applications will increase maritime domain awareness for personnel in the US Coast Guard (USCG) responsible for Search and Rescue activities and National Oceanic and Atmospheric Administration (NOAA) Office of Response and Restoration responsible for providing scientific support for hazardous material spills. A more recent application of coastal HF radar systems is the detection of vessels passing the radar [10, 11]. Currently the USCG relies upon the Automatic Identification System (AIS) to track vessels in coastal areas. One drawback of this method is that AIS is a self-reporting system [12]. The National High Frequency Radar Network [13] has the potential to provide another layer to MDA with the vessel detections from the coastal radars.

One obstacle to overcome with HF radar for vessel detection is the clutter from the sea. Any target with a radial velocity close to the Bragg velocity will be difficult to detect due to the large echo of the sea. Figure 1 shows the spectra from a 13 MHz surface wave HF radar. The Bragg speed for 13 MHz is ±4 m/s (±8 knots). Any vessel travelling with this radial velocity will produce an echo that will fall within the Bragg scatter and prove difficult to discern against the echo of the ocean. This sea-clutter problem can be overcome through sea-clutter cancellation

978-0-933957-40-4 ©2013 MTS

algorithms [14]. Another method to overcome this deficit is through the use of bistatic vessel detections. The transmit signal from another radar station or at sea buoy [15] can illuminate a vessel at sea. The echo from the target can be received at a shore radar station. The echo from the bistatic signal would not be masked by the sea-clutter as compared to the backscatter signal from the radar due to the different geometry.

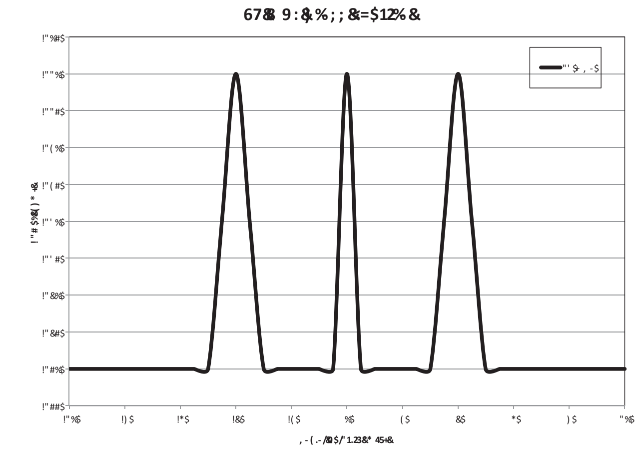

Figure 1: Diagram of the Bragg spectra from a 13 MHz HF radar with a. The x-axis is radial velocity (m/s) and the y-axis is signal power (dBm).

II. Methods

A 13 MHz network was established in New Jersey for the study of the offshore wind energy resource [16] and vessel detection [17]. Radar stations were located in Sea Bright, Belmar and Seaside Park, New Jersey (Figure 2). A CODAR SeaSonde was located at the stations in Sea Bright and Seaside Park. A CODAR bistatic transmitter (Model SSBT-100-0012) was located at the station in Belmar. All three systems were equipped with the SeaSonde SHARE-enabled transmitter. This allowed the systems to operate on the same frequency conserving bandwidth while also allowing for multiple transmit signals to be received on a single receive station. The stations at Sea Bright and Seaside Park received their own transmit signal (monostatic mode) and the transmit signal from the bistatic transmitter located in Belmar (bistatic mode). The combination of monostatic and bistatic operations is described as a multistatic network [18, 19].

This configuration was operated from October 22-25, 2012. The radar stations were equipped with CODAR Ocean Sensor's real-time vessel detection software. That meant the vessel detection data would be generated every 32 seconds and could be transferred back to an aggregation center. The file size for each detection file was on the order of 10 kB. So the detection file could easily be transferred back over the communication mode for the station (cable internet for Sea Bright and cellular modem for Belmar).

The systems officially transmitted on 13.45 MHz with 50 kHz of bandwidth. This equates to a range resolution of 3 km for currents. The signal from hard targets like ships will be seen in several range cells so an interpolation scheme is used within the vessel detection software to increase the range resoltion to approximately 0.5 km.

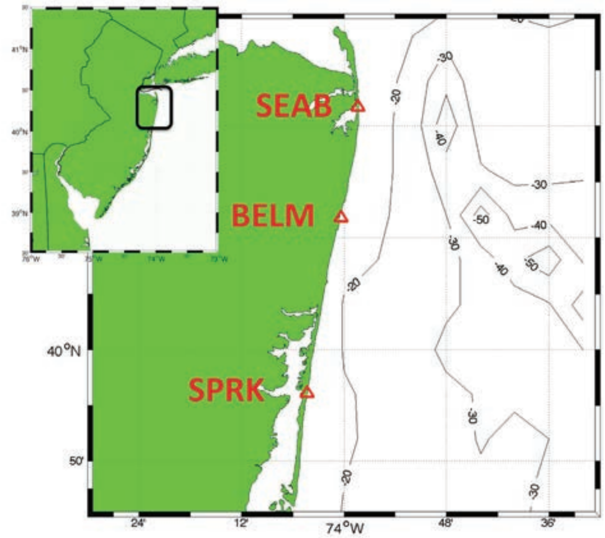

Figure 2: Study area off the northern coast of New Jersey. The locations of the radar stations are indicated by the red triangles with the four-letter site code. Bathymetry contours in meters are also shown. The inset shows the general location of the experiment.

Measured beam patterns [20] were used at each of the receive stations in order to obtain the most accurate bearing measurements of the target. Range and radial velocity measurements of the radar are not affected by beam patterns, only the bearing estimate is affected by the beam patterns.

A. Vessel Information

The four vessels were used during this experiment were the CMA CGM Dalila, CSAV Laja and Ever Radiant which are all large cargo containers and the Eagle Beaumont which is a crude oil tanker. Basic information on the vessels is provided in Table 1.

Table 1: Particulars of the vessels used in this experiment.

Vessel Name	Length (m)	Breadth (m)	Gross Tonnage
CSAV Laja	261	32	39906
CMA CGM Dalila	334	43	89787
Ever Radiant	293	32	53103
Eagle Beaumont	253	44	57456

Automatic Identification System (AIS) receivers were located at the Sea Bright and Belmar stations. The receivers were model SM161R-2 manufactured by Shine Micro. The receivers were outfitted with omnidirectional Very High Frequency (VHF) antennas to receive the AIS signal. The data from the receivers were transferred in real time over the Internet and recorded and time stamped at the aggregation center at Rutgers University. The time, latitude and longitude from the AIS data were converted to range, velocity and bearing relative to the particular radar station.

B. Vessel Detections

Vessel detections were generated at both the Sea Bright and Seaside Park radar stations. The detection data included range, radial velocity and bearing measurements of possible targets. Each of these measurements is accompanied with the corresponding uncertainty. The detection signal to noise ratio (SNR) on each of the three receive channels is also reported along with a radar cross-section estimate for the vessel. An example plot of the monostatic detections is given in Figure 3 and the bistatic detections are shown in Figure 4.

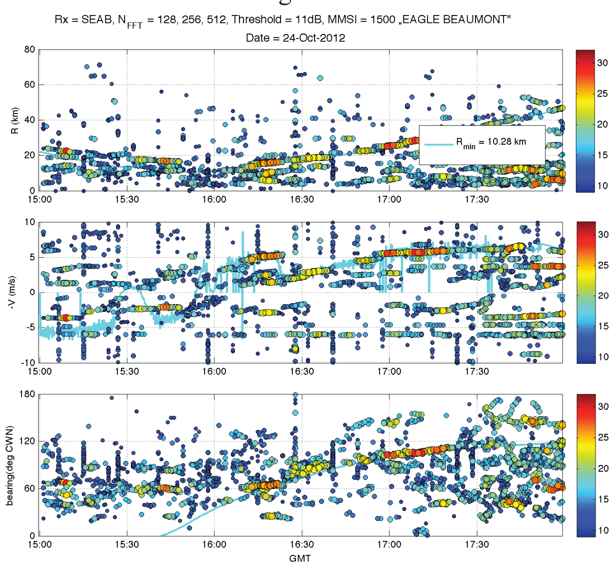

Figure 3: Monostatic Detections from the Sea Bright radar station from 15:00 to 18:00 GMT on October 24, 2012. The panels from top to bottom are range (km), radial velocity (m/s) and bearing (degrees CWN). The track of the Eagle Beaumont is shown as the aqua line in each of the panels. The color of the dot represents SNR on channel 3 of the radar.

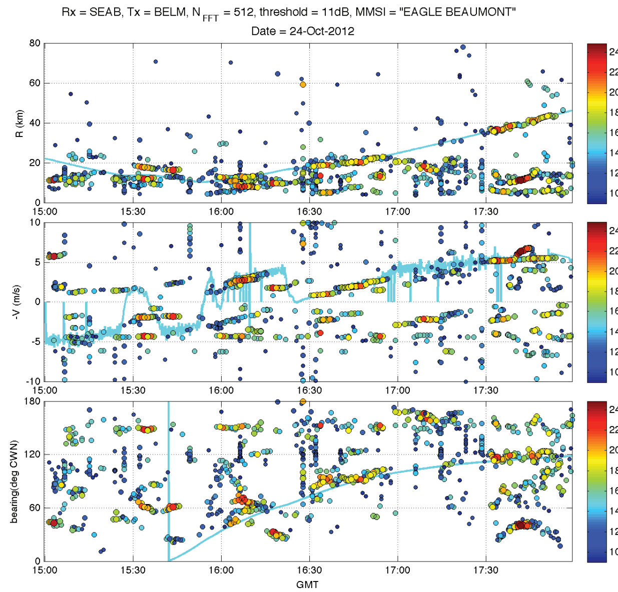

Figure 4: Bistatic Detections from the Sea Bright radar station from 15:00 to 18:00 GMT on October 24, 2012. The radar at Sea Bright acted as the receiver and the radar at Belmar was the transmitter. The plot description matches that of Figure 3.

III. RESULTS

The range, velocity and bearing data from the AIS is used to validate the detections by the radar. This also helps elliminate any false alarms in the radar data. Taking the plot of the monostatic detections from Figure 3 and only keeping the detections that are close in range and bearing to the Eagle Beaumont yields Figure 5. The same process was repeated for bistatic detections in Figure 4 to yield only the associated data in Figure 6.

The benefit of the two data streams is that targets that are hidden in the Bragg or zero Doppler region of one radar can not simultaneously be hidden in the second radar. For example in Figure 6, the Eagle Beaumont is travelling at the Bragg speed of the bistatic signal between 17:00 and 17:30. This leads to no detections of the vessel by the bistatic signal. However the monostatic detections by the radar at Sea Bright have good coverage during this time period as the vessel was just outside the Bragg region. The Bragg region is denoted by the yellow horizontal lines at ±4 m/s in the middle panel of Figure 5 and Figure 6.

And again there was a lack of monostatic detections at 16:07 in Figure 5. This deficit was overcome by the bistatic detections at the same time period in Figure 6. For the rest of the time period there were consistent detections by both the monostatic and bistatic signals. This highlights the second benefit of the bistatic data source which is multiple observations of the same target. This will increase the probability of detection and also lowering the false alarm rate.

Another example comes from the Ever Radiant. It was leaving New York Harbor at 18:30 on October 24, 2012.

National Oceanic and Atmospheric Administration, United States Department of Homeland Security

At 19:15 the vessel passes through zero Doppler relative to the radar at Sea Bright as it travels along the coast. So the radar at Sea Bright was not able to make any detections of the vessel due to the zero Doppler clutter region. However, the bistatic signal transmitted from Belmar and received at Sea Bright did make detections on the vessel during this time period.

All the detections that match the Ever Radiant are plotted on a map in Figure 7. The Belmar station (black circle) acted as a bistatic transmitter and the signal from that station was received at both the Sea Bright and Seaside Park station. The bistatic detections doubled the number of measurements on the vessel. The scatter of the detections around the track increases between 40° and 40° 10’ latitude. The bearing uncertainty increase from the detections at Sea Bright were due a drop in the signal to noise ratio [21]. This causes a scatter when the detections are placed on a map even though the radar makes an accurate measurement of target range and radial velocity.

One way to over come this scatter is through the use of a tracker to smooth out the target track. One other way to make more accurate position estimates of the target is to make use of the detections from another radar. At 40° N latitude, just as the errors in the bearing estimates from the radar at Sea Bright are starting to increase, the radar at Seaside Park is starting to detect the vessel with low bearing and position error. Combining these multiple datasets to form a more accurate track of the vessels path will be for future work.

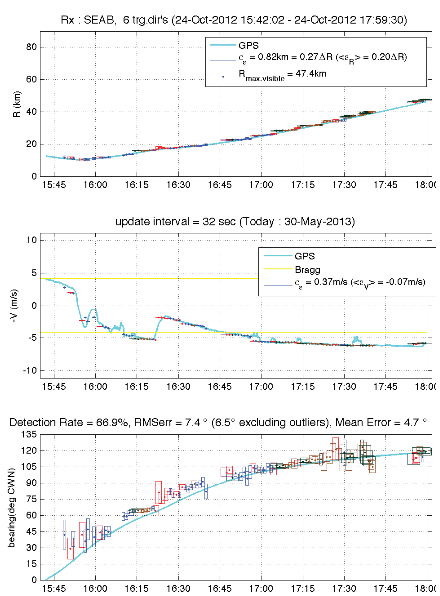

Figure 5: Monostatic detections by the radar at Sea Bright associated with the track of the Eagle Beaumont from AIS. The dots represent the detections while the boxes surrounding them represent the length of the FFT (width) and the uncertainty of the measurement (height). The different colors represent the type of background and fft length used for the detection.

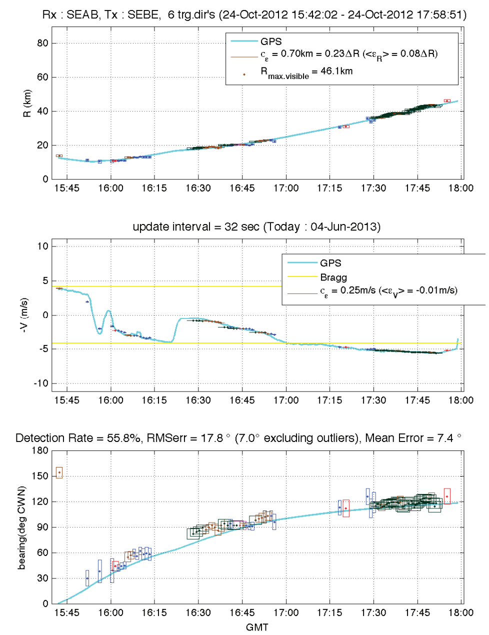

Figure 6: Bistatic detections by the radar at Sea Bright associated with the track of the Eagle Beaumont from AIS. The plot description matches that of Figure 5.

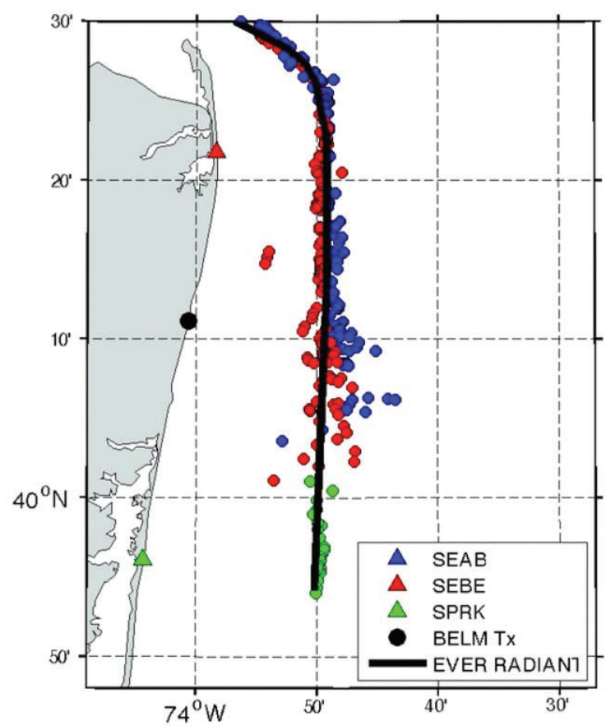

Figure 7: Detections from multiple sources of the Ever Radiant. The monostatic detections from Sea Bright are shown in blue, the monostatic detections from Seaside Park are in green and the bistatic detections (Belmar is the transmitter and Sea Bright is the receiver) are shown in red. The radar stations are shown as the icons on land and the track of the vessel is in black.

IV. CONCLUSIONS

The bistatic vessel detection capability has been demonstrated for the SeaSonde HF radar. This was accomplished by synchronizing the transmit signal between the shore stations through the use of GPS timing. This capability can reveal targets that are hiding in the zero Doppler or Bragg region of a monostatic radar. It also provides an additional measurement of the vessel position or velocity, thereby reducing the error of the measurement. Future work will focus on developing algorithms to combine these multiple data streams for a more refined end product.

ACKNOWLEDGMENTS

This material is based on work supported by the U.S. Department of Homeland Security under Award No. 2008-ST-061-ML0001. The views and conclusions contained in this document are those of the authors and should not be interpreted as necessarily representing the official policies, either expressed or implied, of the U.S. Department of Homeland Security.

This work was funded by NOAA Award Number NA11NOS0120038 “Towards a Comprehensive Mid-Atlantic Regional Association Coastal Ocean Observing System (MARACOOS)”. Sponsor: National Ocean Service (NOS), National Oceanic and Atmospheric Administration (NOAA) NOAA-NOS-IOOS-2011-2002515 / CFDA: 11.012, Integrated Ocean Observing System Topic Area 1: Continued Development of Regional Coastal Ocean Observing Systems.

REFERENCES

[1] A. J. Hawkins, "Surge in shipping has New York hot on L.A.'s heels," *Crain's New York Business,* vol. XXVIII, p. 36, August 6-12, 2012.

[2] National Plan to Acheive Maritime Domain Awareness, U. S. Department of Homeland Security, 1-33, 2005

[3] M. Yaremchuk, P. Spence, M. Wei, and G. Jacobs, "Lagrangian predictability in the DWH region from HF radar observations and model output," *Deep Sea Research Part II: Topical Studies in Oceanography,* 2013.

[4] A. J. Abascal, S. Castanedo, R. Medina, I. J. Losada, and E. Alvarez-Fanjul, "Application of HF radar currents to oil spill modelling," *Marine Pollution Bulletin,* vol. 58, pp. 238-248, 2009.

[5] S. W. Tinis, D. O. Hodgins, and M. Fingas, "Assimilation of radar measured surface current fields into a numerical model for oil spill modelling," *Spill Science & Technology Bulletin,* vol. 3, pp. 247-251, 1996.

[6] D. S. Ullman, J. O'Donnell, J. Kohut, T. Fake, and A. Allen, "Trajectory prediction using HF radar surface currents: Monte Carlo simulations of prediction uncertainties," *J. Geophys. Res.,* vol. 111, p. C12005, 2006.

[7] J. Harlan, A. Allen, E. Howlett, E. Terrill, S. Y. Kim, M. Otero, S. Glenn, H. Roarty, J. Kohut, J. O'Donnell, and T. Fake, "National IOOS high frequency radar search and rescue project," in *OCEANS 2011*, 2011, pp. 1-9.

[8] S. Y. Kim, E. J. Terrill, and B. D. Cornuelle, "Assessing Coastal Plumes in a Region of Multiple Discharges: The U.S.‚àíMexico Border," *Environmental Science & Technology,* vol. 43, pp. 7450-7457, 2009/10/01 2009.

[9] P. M. DiGiacomo, L. Washburn, B. Holt, and B. H. Jones, "Coastal pollution hazards in southern California observed by SAR imagery: stormwater plumes, wastewater plumes, and natural hydrocarbon seeps," *Marine Pollution Bulletin,* vol. 49, pp. 1013-1024, 2004.

[10] H. J. Roarty, M. Smith, S. M. Glenn, and D. E. Barrick, "Real-time beyond the horizon vessel detection," *Proc. SPIE 8714, Radar Sensor Technology XVII,* pp. 87140Z-87140Z, 2013.

[11] H. J. Roarty, D. E. Barrick, J. T. Kohut, and S. M. Glenn, "Dual-Use Compact HF Radars for the Detection of Mid- and Large-Size Vessels," *Elektrik, Turkish Journal of Electrical Engineering and Computer Sciences,* vol. 18, pp. 373-388, 2010.

[12] T. Hammond, M. McIntyre, D. Chapman, and A.-L. Lapinski, "The Implications of Self-Reporting Systems for Maritime Domain Awareness," *DRDC Atlantic TM 2006-232,* pp. 1-40, 2006.

[13] J. Harlan, "A Plan to Meet the Nation's Needs for Surface Current Mapping," *NOAA IOOS,* p. 64, September, 2009 2009.

[14] B. T. Root, "HF-over-the-horizon radar ship detection with short dwells using clutter cancelation," *Radio Science,* vol. 33, pp. 1095-1111, 1998.

[15] H. J. Roarty, M. Smith, E. Handel, S. M. Glenn, and D. E. Barrick, "Expanding the coverage of HF radar through the use of wave powered buoys," in *Oceans, 2012*, 2012, pp. 1-4.

[16] H. Roarty, J. Riscica, L. Palamara, L. Bowers, G. Seroka, J. Kohut, S. Glenn, and R. Dunk, "Analysis of the wind resource off New Jersey for offshore wind energy development," in *Oceans, 2012*, 2012, pp. 1-4.

[17] H. Roarty, E. Lemus, E. Handel, S. Glenn, D. E. Barrick, and J. Isaacson, "Performance Evaluation of SeaSonde High-Frequency Radar for Vessel Detection," *Marine Technology Society Journal,* vol. 45, pp. 14-24, 2011.

[18] J. I. Glaser, "Fifty years of bistatic and multistatic radar," *Communications, Radar and Signal Processing, IEE Proceedings F,* vol. 133, pp. 596-603, 1986.

[19] E. Hanle, "Survey of bistatic and multistatic radar," *Communications, Radar and Signal Processing, IEE Proceedings F,* vol. 133, pp. 587-595, 1986.

[20] J. T. Kohut and S. M. Glenn, "Improving HF Radar Surface Current Measurements with Measured Antenna Beam Patterns," *Journal of Atmospheric and Oceanic Technology,* vol. 20, pp. 1303-1316, September 01, 2003 2003.

[21] S. M. Glenn, D. E. Barrick, and W. J. Browning, "Development and Demonstration of Shiptracking Capabilities for a Dual-Use Multi-Static Long-Range HF Radar Network," *Office of Naval Research,* pp. 1-95, 2004.

Geophysical Research Abstracts
Vol. 15, EGU2013-7665, 2013
EGU General Assembly 2013

Uncertainty analysis of numerical model simulations and HFR measurements during high energy events

Fearghal O Donncha (1), Emanuele Ragnoli (1), Frank Suits (1), Teresa Updyke (2), and Hugh Roarty (3)

(1) IBM Research, IBM Smarter Cities, Ireland (feardonn@ie.ibm.com), (2) Center for Coastal Physical Oceanography, Old Dominion University, (3) Coastal Ocean Observation Laboratory, Rutgers University

The identification and decomposition of sensor and model shortcomings is a fundamental component of any coastal monitoring and predictive system. In this research, numerical model simulations are combined with high-frequency radar (HFR) measurements to provide insights into the statistical accuracy of the remote sensing unit. A combination of classical tidal analysis and quantitative measures of correlation evaluate the performance of both across the bay.

A network of high frequency radars is deployed within the Chesapeake study site, on the East coast of the United States, as a backbone component of the Integrated Ocean Observing System (IOOS). This system provides real-time synoptic measurements of surface currents in the zonal and meridional direction at hourly intervals in areas where at least two stations overlap, and radial components elsewhere. In conjunction with this numerical simulations using EFDC (Environmental Fluid Dynamics Code), an advanced three-dimensional model, provide additional details on flows, encompassing both surface dynamics and volumetric transports, while eliminating certain fundamental error inherent in the HFR system such as geometric dilution of precision (GDOP) and range dependencies. The aim of this research is an uncertainty estimate of both these datasets allowing for a degree of inaccuracy in both.

The analysis focuses on comparisons between both the vector and radial component of flows returned by the HFR relative to numerical predictions. The analysis provides insight into the reported accuracy of both the raw radial data and the post-processed vector current data computed from combining the radial data. Of interest is any loss of accuracy due to this post-processing. Linear regression techniques decompose the surface currents based on dominant flow processes (tide and wind); statistical analysis and cross-correlation techniques measure agreement between the processed signal and dominant forcing parameters. The tidal signal extracted from HFR measurements is cross-correlated against numerical simulations driven by tidal forcing alone. Results demonstrate a close statistical relationship, diminishing with distance from the HFR unit. To further analyse the relative performance of both, correlation statistics are computed during two different sampling periods: a seven day period of relatively calm conditions and a subsequent seven day period encompassing the highly dynamic effects of “Hurricane Sandy” on the region. During both these periods complex correlation coefficients between surface currents and measured wind speeds are computed and the data adopted to evaluate the performance of both. Of particular interest is the relative performance of the HFR during periods of both high and low-energy forcing, and the ability of a technically advanced model to mathematically simulate these complex flow features.

Expanding Maritime Domain Awareness Capabilities in the Arctic: High Frequency Radar Vessel-tracking

Hugh J. Roarty,
Michael Smith,
Scott M. Glenn
Coastal Ocean Observation Lab
Rutgers University
New Brunswick, NJ USA
hroarty@marine.rutgers.edu

Donald E. Barrick,
Chad Whelan
CODAR Ocean Sensors
Mountain View, CA USA
don@codar.com

Ed Page
Executive Director
Marine Exchange of Alaska
ed@mxak.org

Hank Statscewich,
Tom Weingartner
University of Alaska
Fairbanks, AK USA
hank.stats@alaska.edu

***Abstract*— The arctic could be ice free during the summer by as early as 2040 [1]. This could alter the dominant shipping routes between Europe and Asia. The ability to monitor this traffic is hindered by lack of sensors, communication and power for the sensors. SeaSonde High Frequency radars were installed along the northwest corner of Alaska from July to December 2012. These radars were able to make simultaneous measurements of ocean surface currents as well as measure the position and velocity of vessels passing by the radar. This successful demonstration proves that High Frequency radar can be a valuable tool for providing maritime domain awareness and persistent surveillance capabilities in the arctic.**

***Index Terms*—geoscience, remote sensing, High Frequency, radar, oceans, vessel detection, surveillance, Arctic, polar region**

I. Introduction

Rutgers University, as a partner in the U.S. Department of Homeland Security's (DHS) Center for Secure and Resilient Maritime Commerce (CSR), has demonstrated vessel detection as a dual-use capability for their SeaSonde® HF Radar (HFR) coastal ocean current and wave monitoring network [2]. Real-time HF Radar current maps are being used for Search and Rescue (SAR), oil spill response, among other uses on over 130 systems around the U.S. and now Rutgers is providing real-time detections for the approaches to New York Harbor. These detections are supplied to the Naval Research Lab's (NRL) Open Mongoose data fusion engine. In a collaborative effort between Rutgers and the University of Alaska, Fairbanks (UAF), a partner in the DHS National Center for Islands, Maritime, and Extreme Environments Security (CIMES), this dual-use capability was demonstrated in the Arctic region, near Barrow, Alaska in the summer and autumn of 2012.

With longer periods and larger areas of ice-free and broken ice floes in the Beaufort and Chukchi Seas during the summer and autumn ice free seasons, there is increasing vessel activity from cargo ships, cruise lines, fishing vessels and those taking advantage of the opening of the Northwest Passage and Northern Sea Route[3]. In addition, 2012 marked the beginning of offshore oil exploration in the Chukchi Sea. With increased activity from both foreign and domestic vessels, the U.S. Coast Guard has increased its presence in Arctic Alaska [4] and, as such, there is a need for increased Maritime Domain Awareness (MDA) in this area as well. UAF deployed and maintained three Long Range SeaSondes and two High Resolution SeaSondes from June through November to monitor 2-D surface currents in the Chukchi Sea during the summer ice-free season. The SeaSonde (Figure 1) is a High Frequency radar system that has been traditionally been used for measuring ocean surface currents [5] and ocean wave parameters [6]. Having observed vessel echoes in prior deployments in the Chukchi, vessel detection software from CODAR Ocean Sensors was installed and run in real–time in parallel with current mapping software on the local SeaSondes.

The vessel detection capability of the SeaSonde was observed off the coast of California [7] and then demonstrated for a year long test study off the coast of New Jersey [8]. The SeaSonde is a compact direction finding radar system. Vessel detections with phased array HF radar have also been observed [9, 10]. The study presented here is one of the first demonstrations of the real time capability of the SeaSonde. All previous studies were performed by bringing archived spectra data to the laboratory and post-processing it for vessel detections. In order to demonstrate multi-use capability, the offline vessel detection software was translated into the C programming language to run in parallel with current mapping software on the SeaSonde system.

The Arctic region poses challenges to HF Radar vessel detection including: remote locations requiring specialized shelter, power and communications; extreme weather; the presence of ice floes, which have their own Doppler echoes in addition to sea clutter; and a different radio frequency environment with auroral influences[11]. These challenges and their affects on HF vessel detections as a dual-use capability in the Arctic are discussed and vessel detections in the Chukchi Sea are shown.

Figure 1: Receive antenna for the SeaSonde system on the right. A person atop an all terrain vehicle is on the left for scale

II. METHODS

Three 5MHz (long range) SeaSondes were installed at Point Barrow, Wainwright and Point Lay Alaska (Figure 3). Two 25MHz (high resolution) SeaSondes were installed along the northern slope of Alaska in June 2012 (Figure 4). The radars were operated from July to December 2012. Four of the radars were powered with electricity from the power grid. The 25MHz radar at Point Barrow was powered with a remote power module (RPM) [12]. The RPM was equipped with solar panels and wind turbines, which charged a bank of 36 batteries with a total capacity of 3000 amp hours. The radars were configured to produce radial measurements of surface currents hourly.

The real time vessel detection software was installed at the 5 and 25 radars at Point Barrow. The vessel detection software utilizes two backgrounds and 6 combinations of coherent integration time and threshold level to produce detections [8]. The first background is a median type that averages in Doppler and range space. The second background is an infinite impulse response (IIR) filter that averages in time. So then any signal that is above the background by a certain threshold is counted as a detection, the classical constant false alarm rate (CFAR) detection

Vessel tracking, in its simplest form, takes place in three steps: (1) detection, (2) association, and (3) tracking. Detection uses different data processing algorithms to define peaks in the radar returns above a highly variable background of noise and clutter. The result, referred to as a pepper plot, produces a time-series of all the observed peaks (real or not) identified by their range, range-rate towards or away from the radar, and bearing. The association process decides which detections in the pepper plots of range, range rate and bearing are associated with a specific ship, clustering them for input to a tracker. The tracker then fits specific models for ship behavior (e.g. constant course and speed followed by a turning maneuver to a new constant course and speed) that enables both the past best fit and the projected track to be plotted on a computer screen.

Previous Department of Defense (DoD) sponsored research has confirmed that HFR are capable of detecting ships, and that given a known ship track for the association process, the resulting time series of range, range-rate and bearing could be used by a variety of trackers to produce accurate vessel tracks on a user's computer screen.

Figure 2: The remote power module (RPM) that powered the 25 MHz SeaSonde at Point Barrow.

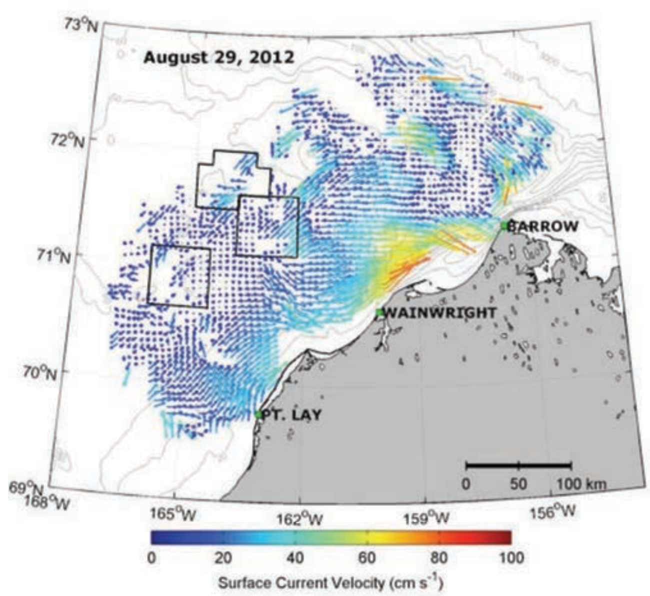

Figure 3: Map of the 25-hour average surface currents along the northern slope of Alaska for August 29, 2012. The magnitude of the surface current velocity is displayed by the colorbar along the bottom of the figure. The locations of the radars are shown as the green squares. Black boxes denote offshore regions slated for potential hydrocarbon development.

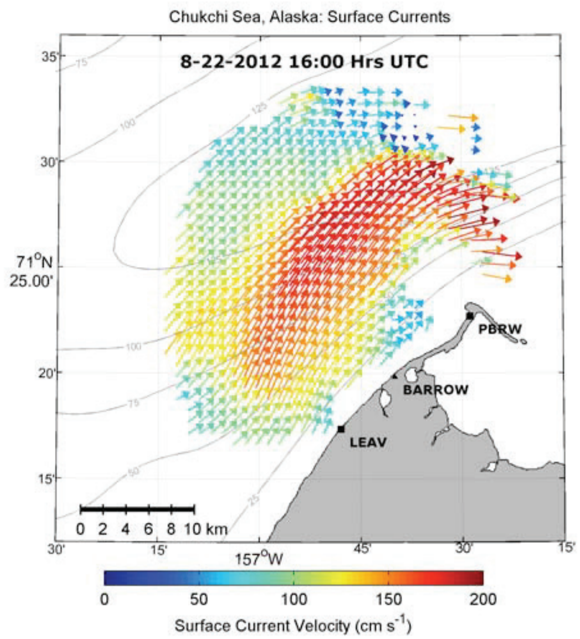

Figure 4: Map of the hourly average surface currents along the northern slope of Alaska using the 25 MHz HF radars. The locations of the radars are shown as the black squares.

III. RESULTS

The five radars made hourly measurements of radial surface currents. The radial currents were combined to produce total vector currents (Figure 3 and Figure 4).

The 5 MHz system in Barrow (BASC) operated continuously from July 9 to December 4, 2012. The real time vessel detections were transferred via satellite communications from Barrow, Alaska to New Brunswick, New Jersey every 5 minutes. There were no vessels detected by the radar from July 9 to August 14 as sea ice prevented safe passage of vessels through the region. Sea ice retreat commenced in early August and the first vessels were detected on August 15.

The BASC radar detected vessels daily from August 15 until September 30. The vessel traffic then diminished in early November as the sea ice encroached on the shore. The vessel detection data was plotted (Figure 5) as a function of time by range, range rate and bearing relative to the individual radars. The detection data from the radar showed several valid detections. These are shown as the dots with signal to noise ratios above 20 dB and that move in a coherent fashion (Figure 5)

The vessel detection data was compared against available Automatic Identification System (AIS) (Figure 6) and Global Positioning System (GPS) data from vessels in the area. The position data from each of the vessels was converted to range, range rate and bearing data relative to the radars so as to be compared with the vessel detection data (Figure 7). Detections that were within half a range bin and within two Doppler bins of the radial velocity from the AIS data were counted as valid detections.

The data from September 9th and 10th was further analyzed, as there were a large number of vessels present in the detection data. The data was also analyzed when the Coast Guard ice breaker Healy and Research Vessel Norseman II were within 100 km of the radar site as these were high value targets. The results of this analysis are summarized in Table 1. A summary of the physical characteristics of the vessels detected is presented in Table 2 with most of the vessels being tugboats with an average length of 30 m.

The maximum detection range for each vessel was averaged into a single number, which was 51 km. The maximum of all the maximum detection ranges was 82 km for the Aiviq on September 9th. The average detection time was 18 hours with a maximum of 24 hours for the four of the vessels, the Aiviq, Arctic Seal, Nokea and Warrior. The radar has a 32 second update rate. The percentage of time detected was calculated by dividing the total number of detections by the number of update cycles within the detection window. The average detection rate during the study period was 51% with a maximum of 88% for the Coast Guard Ice Breaker Healy on August 22nd.

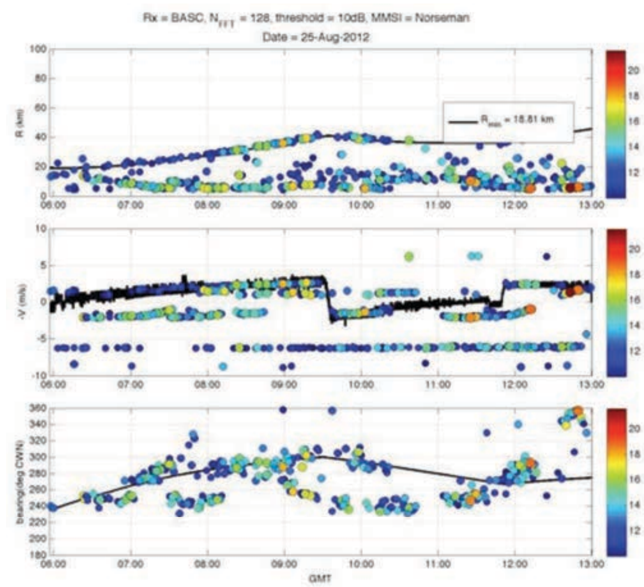

Figure 5: Time series plot of vessel detections from the 5 MHz radar at Point Barrow (BASC). The x-axis for all three plots is the hour of the day for September 1, 2012. The sub plots from top to bottom are vessel detection range, radial velocity (m/s) and bearing (degrees CWN). The color of the data points denotes the signal to noise ratio (dB) of the detection and is interpreted by the colorbar on the right. The ground truth information for one of the vessels is shown as the black line.

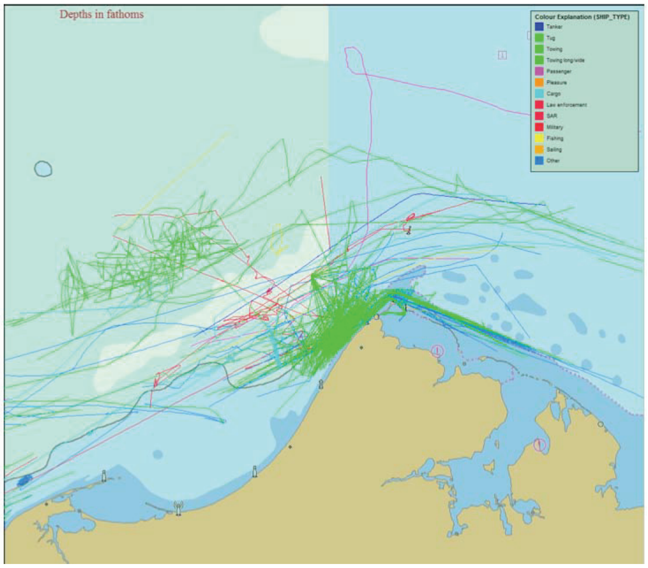

Figure 6: Tracks of vessels from the Automatic Identification System (AIS) from August 10 to September 10, 2012. The different colors denote the type of vessel.

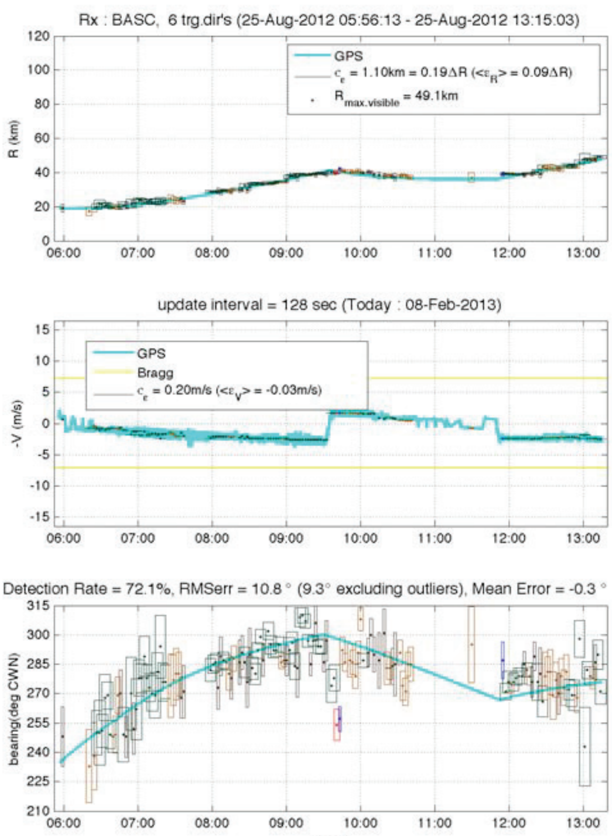

Figure 7: Range (top), radial velocity (middle) and bearing (bottom) of the research vessel Norseman II (aqua line) for August 25, 2012 from 06:00 to 13:30 GMT. The data was recorded via GPS and transmitted via AIS. The detections by the radar are shown as the dots with boxes around the detections that represent the error bars.

Table 1: Summary of vessel detections analyzed during the study period. The table presents the name of the detected vessel, the start and end time of the radar detections (Greenwich Mean Time), the percentage of time the vessel was detected, the maximum detection range (km) and the time of detection (hours).

Vessel Name	Start Time	End Time	Percentage of Time Detected	Maximum Detection Range (km)	Detection Time (hours)
Healy	8/22/12 10:00	8/22/12 21:00	88.3	71.1	11.00
Healy	8/22/12 21:00	8/23/12 18:37	35.9	70.8	21.62
Norseman II	8/25/12 5:56	8/25/12 13:15	72.1	49.1	7.32
Healy	8/26/12 23:00	8/27/12 2:22	81.2	16.3	3.37
Norseman II	8/29/12 9:00	8/29/12 19:00	58.1	53.2	10.00
Aiviq	9/9/12 0:00	9/10/12 0:00	26.1	81.9	24.00
Arctic Seal	9/9/12 0:00	9/10/12 0:00	21.6	52.4	24.00
Nachik	9/9/12 0:00	9/9/12 23:00	9.6	12.8	23.00
Nokea	9/9/12 0:00	9/10/12 0:00	68.5	23.2	24.00
Warrior	9/9/12 0:00	9/10/12 0:00	18.2	79.2	24.00
Lauren Foss	9/9/12 0:07	9/9/12 2:58	54.5	39.8	2.85
Sisuaq	9/9/12 9:05	9/9/12 17:12	70.8	74.8	8.12
Aiviq	9/10/12 0:00	9/11/12 0:00	48.5	72.1	24.00
Arctic Seal	9/10/12 0:00	9/11/12 0:00	53.6	45.8	24.00
Nokea	9/10/12 0:00	9/11/12 0:00	72	24.7	24.00
Sesok	9/10/12 0:00	9/10/12 23:44	49.2	17.2	23.73
Warrior	9/10/12 0:00	9/10/12 21:24	39.9	63.5	21.40
Pt.Oliktok	9/10/12 0:01	9/10/12 9:49	69.7	51.3	9.80
Pacific Raven	9/10/12 6:00	9/10/12 22:48	32.8	37.9	16.80
Healy	10/10/12 16:41	10/10/12 23:46	44.8	79.3	7.08
		Average	51	51	18
		Maximum	88.3	81.9	24

Table 2: Summary of the physical characteristics of the vessels detected during this study. The table presents the name of the vessel, the length (m), the breadth or the width (m) and the type of vessel.

Name	Length (m)	Breadth (m)	Type
Aiviq	109	24	Anchor Handling Vessel
Arctic Seal	37	10	Cargo
Healy	130	25	Coast Guard Ice Breaker
Lauren Foss	46	12	Tug
Nachik	23	10	Tug
Nokea	31	10	Tug
Norseman II	35	9	Research Vessel
Pacific Raven	31	10	Tug
Pt. Oliktok	30	10	Tug
Sesok	23	10	Tug
Sisuaq	90	19	Multi Purpose Offshore Vessel
Warrior	40	10	Tug

IV. Conclusions

SeaSonde HF radars were installed along the north slope of Alaska. They simultaneously generated measurements of ocean surface currents and vessel detections. The vessel detection data was compared against ground truth data transmitted via AIS or recorded on the vessel via GPS. The maximum detection range was 82 km with a maximum detection rate of 88 percent. The real-time dual use capability of the SeaSonde HF radar provides an ability to assess environmental security and shipping activity in a manner that reduces risk and enhances response.

The research advances of this study provide a tool to simultaneously maintain clear maritime domain awareness and conduct persistent surveillance activities over a large area. This information will be a valuable asset to the US Coast Guard, United States Northern Command (USNORTHCOM), the Alaska state Department of Emergency Management and Military Affairs, the Alaska Department of Environmental Conservation, the Alaska state Department of Natural Resources, and the Alaska North Slope Borough who all have a stake in keeping commercial activity in the Arctic safe and secure.

ACKNOWLEDGMENT

This material is based on work supported by the U.S. Department of Homeland Security under Award No. 2008-ST-061-ML0001.

The views and conclusions contained in this document are those of the authors and should not be interpreted as necessarily representing the official policies, either expressed or implied, of the U.S. Department of Homeland Security.

REFERENCES

[1] M. Wang and J. E. Overland, "A sea ice free summer Arctic within 30 years?," *Geophys. Res. Lett.,* vol. 36, p. L07502, 2009.

[2] H. Roarty, E. Lemus, E. Handel, S. Glenn, D. E. Barrick, and J. Isaacson, "Performance Evaluation of SeaSonde High-Frequency Radar for Vessel Detection," *Marine Technology Society Journal,* vol. 45, pp. 14-24, 2011.

[3] Arctic Council, "Arctic Marine Shipping Assesment 2009 Report," *Arctic Council,* vol. Norwegian Chairmanship, p. 190, 2009.

[4] K. Johnson, "For Coast Guard Patrol North of Alaska, Much to Learn in a Remote New Place," in *New York Times*, ed. New York, 2012.

[5] J. T. Kohut, S. M. Glenn, and R. J. Chant, "Seasonal current variability on the New Jersey inner shelf," *J. Geophys. Res.,* vol. 109, p. C07S07, 2004.

[6] R. Long, D. E. Barrick, J. L. Largier, and N. Garfield, "Wave Observations from Central California: SeaSonde Systems and In Situ Wave Buoys," *Journal of Sensors,* vol. 2011, pp. 1-18, 2011.

[7] D. M. Fernandez, J. F. Vesecky, C. C. Teague, J. D. Paduan, and K. E. Laws, "Ship detection with high-frequency phased-array and direction-finding radar systems," in *Geoscience and Remote Sensing Symposium Proceedings, 1998. IGARSS '98. 1998 IEEE International*, 1998, pp. 204-206 vol.1.

[8] H. J. Roarty, D. E. Barrick, J. T. Kohut, and S. M. Glenn, "Dual-Use Compact HF Radars for the Detection of Mid- and Large-Size Vessels," *Elektrik, Turkish Journal of Electrical Engineering and Computer Sciences,* vol. 18, pp. 373-388, 2010.

[9] A. L. Dzvonkovskaya and H. Rohling, "HF radar ship detection and tracking using WERA system," in *Radar Systems, 2007 IET International Conference on*, 2007, pp. 1-5.

[10] A. Dzvonkovskaya and H. Rohling, "HF radar performance analysis based on AIS ship information," in *Radar Conference, 2010 IEEE*, 2010, pp. 1239-1244.

[11] C. C. Teague, "Ionospheric Effects on Coastal Radar Systems," *Proceedings of the Radiowave Oceanography Workshop,* vol. Timberline, OR, 2001.

[12] H. Statcewich, T. Weingartner, S. Danielsen, B. Grinau, G. Egan, and J. Timm, "A High-Latitude Modular Autonomous Power, Control, and Communication System for Application to High-Frequency Surface Current Mapping Radars," *Marine Technology Society Journal,* vol. 45, pp. 59-68, 2011.

Improving the Measurements of High Frequency Radar: Reduced Averaging Times and Bistatics

Hugh Roarty, John Kerfoot, Josh Kohut, Scott Glenn
Coastal Ocean Observation Laboratory
Rutgers University
New Brunswick, NJ USA
hroarty@marine.rutgers.edu

Chad Whelan, Max Hubbard
CODAR Ocean Sensors
Mountain View, CA USA
chad@codar.com

***Abstract*— High Frequency radar has been operational with the US Coast Guard since May 2009. The long-range SeaSonde is a key component of the national HF radar network. Default SeaSonde processing on long-range systems only captures 92% of the M2 tidal current velocity and hence 85% of the tidal energy due to a 180-minute averaging time. Reducing this averaging time would help improve the surface current measurements of the SeaSonde system. A study was undertaken to analyze the radial processing of the long-range SeaSonde. Radial current files were generated using a sixty-minute radial averaging and compared with the default one hundred and eighty minute average. This was performed at five stations in the northern section of the Mid Atlantic Regional Association Coastal Ocean Observing System (MARACOOS) for a two-week period. This study has implications for the thirty-five long-range radars operating in the United States and the approximately eighty-six long-range radars operating around the globe. The hope being that the shorter averaging time will lead to increased accuracy of the measured surface currents. This in turn will lead to more effective search and rescue cases for the US Coast Guard.**

Another study was conducted to measure the impact that bistatic radar has on the measurements of surface currents. A 13 MHz radar network was used to test to see if elliptical current measurements would decrease the uncertainty of a total surface current measurement. A three-week record of hourly radial and elliptical measurements were used and combined in several configurations to test the impact of the elliptical currents. Initial findings show that the elliptical current measurements decreased the uncertainty of the total vector calculation and reduced gaps due to missing radial data.

***Index Terms*—HF radar, radar remote sensing, quality control, bistatic**

I. Shorter Averaging Time Theory

The SeaSonde is unique from other radars in that it uses a swept frequency modulation to determine range to target and not the time delay of received echo. Most radars measure the time delay from the signal transmission to the return of the echo to determine range. The SeaSonde sweeps the transmit frequency over the prescribed bandwidth in order to determine range to target. Range to target is the first calculation by the radar and this outputs what are called Range files. This is performed by the application SeaSonde Acquisition, which is part of the SeaSonde processing suite. Next the Doppler calculation is performed to determine the ensemble of radial velocities that are being measured by the system. Lastly the bearing of the radial velocity signals are determined using the MUSIC algorithm [1].

This processing results in a radial vector file from each Cross Spectra Short-time file (CSS). These files are not kept by default but can be with a modification the configurations settings of the system. The radials from each CSS file are then averaged based upon the radial coverage period and radial output period. Our first tests using the 5 MHz system entailed a 240 minute radial coverage period with a 180 minute radial output period [2]. Further studies showed that we could reduce the radial coverage period to 180 minutes with an output period of 60 minutes [3]. With this research we are investigating if a radial coverage period of 60 minutes and an output period of 30 minutes is sufficient to characterize the surface currents in the coastal ocean.

The focus of this study was on the 5 MHz model that provides surface current measurements out to 200 km from the coast. The systems that were used are part of the Mid Atlantic Regional Association Coastal Ocean Observing System (MARACOOS) [4]. The sites used were located in Nauset (NAUS) and Nantucket (NANT), Massachusetts, Block Island (BISL), Rhode Island, Moriches (MRCH), New York and Wildwood (WILD), New Jersey. Figure 1 shows the locations of these sites within the Mid Atlantic Bight. The data that was used spanned from November 19-28, 2012.

978-1-4799-0002-2/13/$31.00 ©2013 IEEE

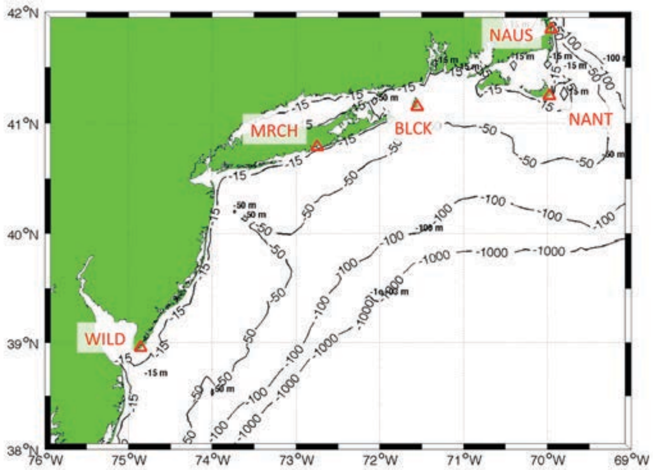

Figure 1: Location of the HF radar stations (red triangles) sites used in this study. The four-letter site code represents the name of each site.

The default settings for the SeaSonde HF radar are given in Table 1. The default radial output for all three frequencies is 60 minutes but there are differences in how the spectra are averaged to arrive at the final product. For instance the graphic in Figure 2 outlines the averaging that is performed with the default settings for a 5 MHz system. CSS files are generated every 30 minutes that encompass a 60-minute average. The radial coverage parameter, which is 180 minutes for this case, determines the number of CSS files that contribute to the radial file that is transferred back to the central location to be combined into a total vector file. With 180-minute radial coverage time, 5 CSS files contribute to an individual radial file. The signal that can be measured with this type of averaging is shown as the pink line in Figure 3. The system would only capture 92% of the amplitude of a current with a period of 12.42 hours, like the M2 tidal current.

If on the other hand, only 1 CSS was used to contribute to a radial file, then 98% of the potential current amplitude could be measured of the M2 tidal signal. This is shown as the red line in Figure 3.

Table 1: Default radio frequency and data acquisition parameters for the SeaSonde HF radar

Transmitted Signal			
Center Frequency (MHz)	5	13	25
Sweep (Sampling) Rate (Hz)	1	2	2
Data Acquisition			
Velocity Resolution (cm/s)	2.9	4.5	2.3
Range File Averaging Period (s)	1024	256	256
CSS File Averaging Period (minutes)	60	15	15
CSS Output Period (minutes)	30	10	10
Radial Coverage Period (minutes)	180	75	75
Radial Output Period (minutes)	60	60	60

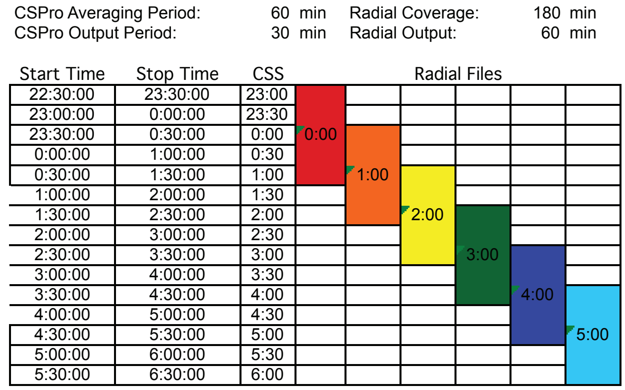

Figure 2: Graphic depicting the averaging of a 5 MHz SeaSonde.

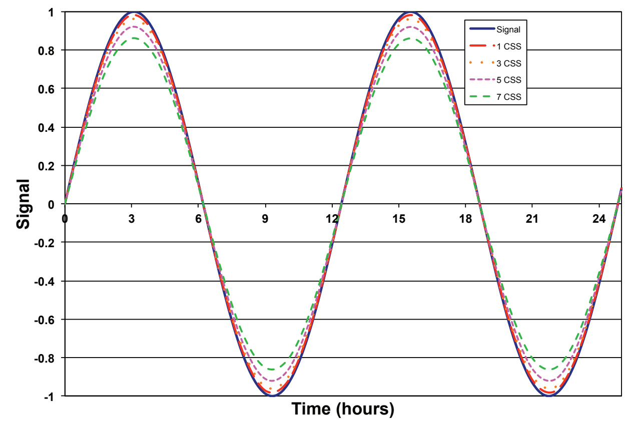

Figure 3: Graphic depicting the sampling result from different averaging techniques. The blue line represents a hypothetical tidal current with amplitude of 1 and period of 12.42 hours (M2 tidal constituent). The red, orange, pink and green lines represent the current that could be measured with a 1, 2, 3 and 4 hour moving average respectively.

II. Shorter Averaging Time Results

If all the radial vectors in a radial file are averaged and a time series is produced from this average then the M2 tidal signal becomes quite evident in the data for the sites used in this study. A plot of this processing technique using the default averaging times for the SeaSonde with a 180-minute radial coverage period for the five stations is shown in Figure 4. The NAUS site on Cape Cod has the strongest M2 signal in its data while the MRCH site has the lowest principal lunar semidiurnal tidal current.

These same processing techniques were applied to the radial files with the 60-minute radial coverage period. The signal that was generated for the NAUS site is shown as the green line in Figure 5. The reduction of the radial averaging time from 180 minutes down to 60 clearly increased the amplitude of the M2 tidal signal for this station. The green line has a larger peak for a majority of the local maxima and minima.

A least squares harmonic analysis was applied to the three-hour and one-hour current record for each of the five stations. The amplitude of the derived signal for each of the five stations is given in Table 2. Three of the stations (NAUS, MRCH and WILD) saw an increase in the tidal current amplitude when the averaging time was reduced to 60 minutes. The two other stations (NANT and BLCK) experienced a drop in the tidal amplitude when the 60-minute radial was utilized.

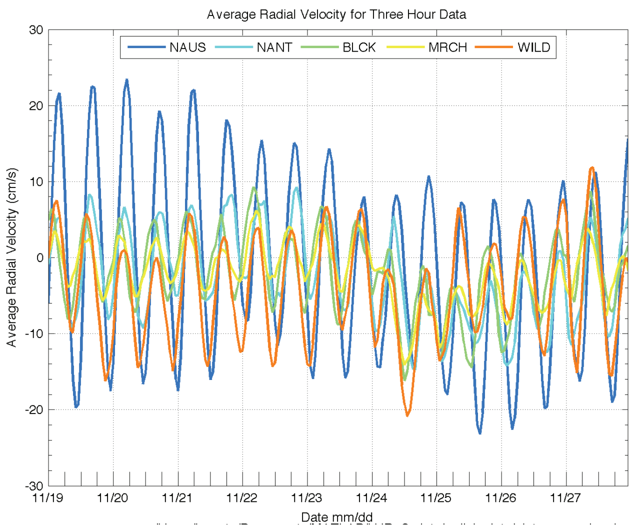

Figure 4: Plot of average radial velocity from five HF radar stations located along the Mid Atlantic coast of the United States. The X-axis is month/day (mm/dd) for 2012.

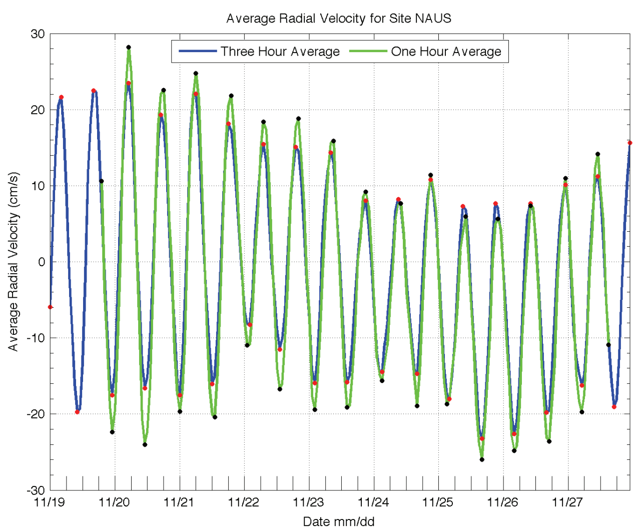

Figure 5: A time series plot of the average three hour radial in blue and the average one hour radial in green. The local maxima and minima are identified as the red and black dots.

Table 2: Amplitude from least squares harmonic analysis of average tidal current for the three-hour and one-hour radial averaging times along with the percent change from three to one hour averaging.

	NAUS	NANT	BLCK	MRCH	WILD
Three Hour Amplitude (cm/s)	15.4	6.23	5.62	3.37	8.42
One Hour Amplitude (cm/s)	17.2	5.64	4.52	3.91	8.89
Percent Change	12%	-9%	-20%	16%	6%

III. BISTATIC GEOMETRY

A 13 MHz multistatic High Frequency radar network was established along the coast of New Jersey in 2012. Multistatic [5, 6] describes a network that simultaneously operates in monostatic mode, where the transmitter and receiver are collocated, and bistatic mode, where the transmitter and receiver are geographically separated. The HF radar network in the Mid Atlantic has traditionally been operated in the monostatic mode[3, 4, 7]. A majority of the SeaSonde sites in the Mid Atlantic are equipped with the GPS-enabled frequency multiplexing feature that allows sites to operate on the same frequency. This prevents the sites from interfering with each other and allows the users to occupy a smaller bandwidth in that region of the HF band. It also allows the sites to operate bistatically where the signal transmitted from one station is received at multiple stations [8].

The sites used in this study are shown in *Figure 6*. Five sets of elliptical current files were generated during the experiment. The naming convention we have adopted for the elliptical file is the first two letters of the receive station are paired with the first two letters of the transmit site to generate the elliptical file name. Table 3 provides the list of receiver and transmitter pairs and the corresponding elliptical file name.

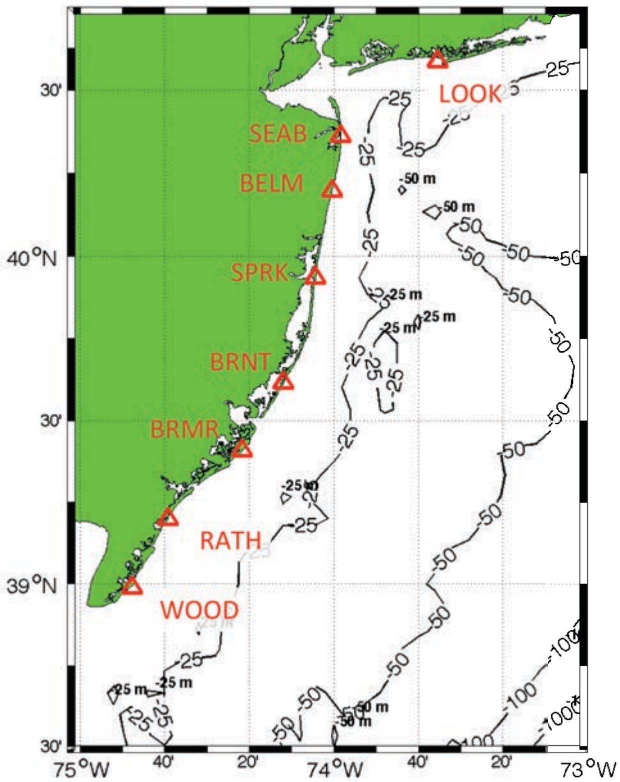

Figure 6: Map showing the location of the 13 MHz radar stations (red triangles) that were used in the experiment. The four-letter site code is next to each station. The 25, 50 and 100-meter isobaths are also shown.

Table 3: Receive and Transmit site pairs and the Elliptical file name designated from the pairing.

Receive Site	Transmit Site	Elliptical Site
BELM	SEAB	BESE
BELM	SPRK	BESP
SEAB	SPRK	SESP
RATH	WOOD	RAWO
RATH	BRNT	RABR

The four stations in the northern (LOOK, SEAB, BELM and SPRK) region were set to the same frequency and the four sites in the southern region (BRNT, BRMR, RATH and WOOD) were paired together. The SeaSonde is capable of synchronizing XX systems on a single frequency but it proved quite challenging to synchronize four systems on a single frequency. Offsetting the start of the frequency sweep between the stations synchronizes the stations. This is achieved by setting the alignment timing in the SeaSondeController application so each site is offset by a multiple on the order of 2000μs.

IV. Bistatic Results

A coverage example for one of the elliptical files is given in Figure 7. The elliptical files have a bearing and range resolution similar to the radial files for the station. For these stations the range resolution was 3 km and the bearing resolution was 5 degrees.

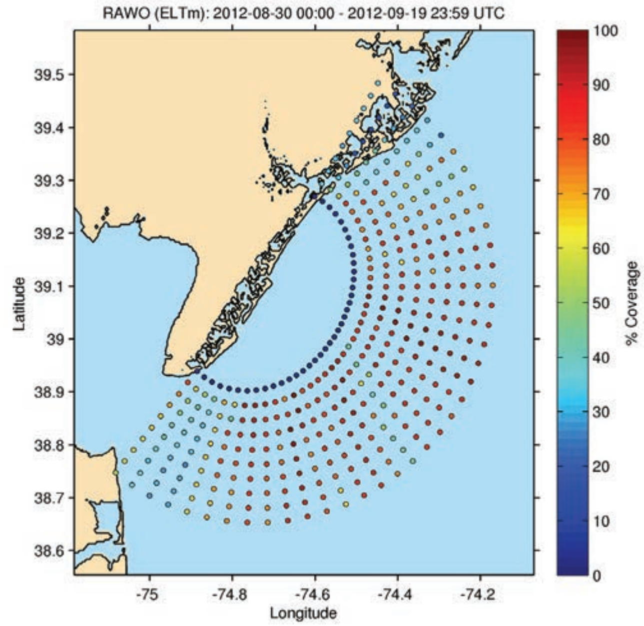

Figure 7: Spatial and temporal coverage map for the RAWO elliptical file from August 30, 2013 to September 20, 2013.

The SeaSonde Radial Suite 6 was used to process the monostatic spectra through to radial vectors. The SeaSonde Multi-Static Data Processing Software package was used to process the bistatic spectra through to elliptical current files. These radial and elliptical files were combined into total current vectors using the HFR_Progs version 2.1.3beta MATLAB toolbox. The optimal interpolation combining scheme [3, 9] was used to combine the radial and elliptical files into total files. Three sets of totals were generated 1) radials only 2) ellipticals only and 3) radials and ellipticals together. Radials and ellipticals using the measured antenna pattern [10] were combined into total vectors for all three sets. The totals were then filtered to only retain vectors where both the uncertainty in the east (Uerr) and north (Verr) component of the vector were below 0.6 [3].

A coverage map of the totals only using radials is shown in Figure 8. During this time period the radar station SPRK was down due to a hardware failure. This caused a large gap in coverage in the vicinity of 39.8 degrees north. Figure 9 shows the coverage using both radials and elliptical files. The use of the elliptical files results in increased coverage for the gap in front of the SPRK station as well as other regions that were sparse in the radials only total vector field.

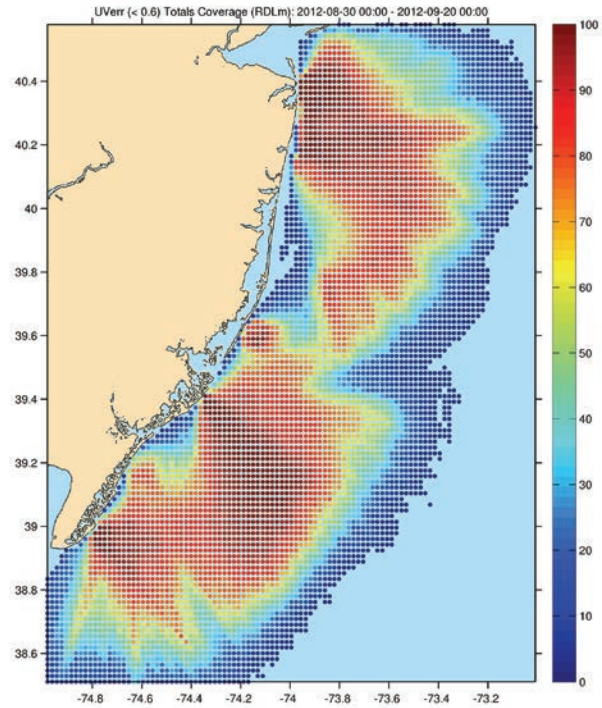

Figure 8: Temporal and spatial coverage of the 13 MHz network from August 30 to September 20, 2012 using only radial vector files. The image only shows percent coverage for grid points where both the Uerr and Verr were < 0.6.

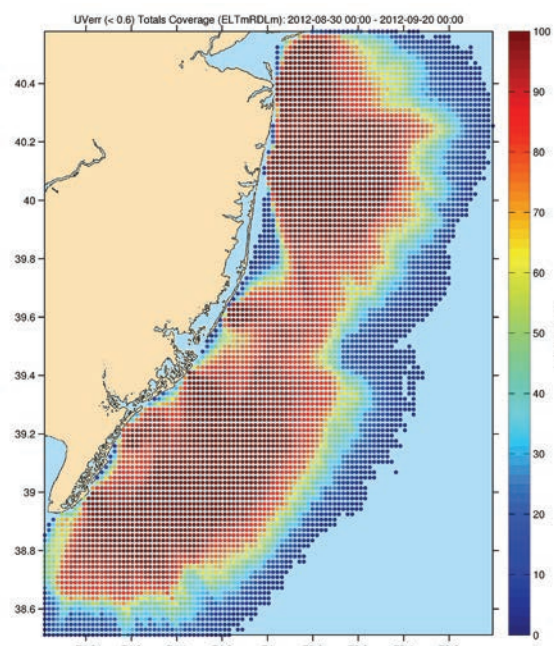

Figure 9: Temporal and spatial coverage of the 13 MHz network from August 30 to September 20, 2012 using radial and elliptical vector files. The image only shows percent coverage for grid points where both the Uerr and Verr were < 0.6.

V. CONCLUSIONS

Two experiments were conducted to improve the measurements of the SeaSonde High Frequency radar. The first involved decreasing the averaging time of the radial processing from 180 minutes down to 60 minutes. This increased the amplitude of the average radial velocity at three of the five stations examined. This is a good result, as it will lead to more accurate measurements of the surface currents in the coastal ocean. The next analysis will focus on the impact of the shorter averaging time on the total current calculations.

The second experiment used the bistatic capability of the SeaSonde to improve measurements and reduce gaps. Initial findings indicate that the elliptical vectors do reduce the uncertainty measurements of the radar. The elliptical files also provided measurements in areas where there were gaps due to lack of radial coverage because a radial site developed a hardware problem.

ACKNOWLEDGMENTS

This work was funded by NOAA Award Number NA11NOS0120038 "Towards a Comprehensive Mid-Atlantic Regional Association Coastal Ocean Observing System (MARACOOS)". Sponsor: National Ocean Service (NOS), National Oceanic and Atmospheric Administration (NOAA) NOAA-NOS-IOOS-2011-2002515 / CFDA: 11.012, Integrated Ocean Observing System Topic Area 1: Continued Development of Regional Coastal Ocean Observing Systems

REFERENCES

[1] T. de Paolo and E. Terrill, "Skill Assessment of Resolving Ocean Surface Current Structure Using Compact-Antenna-Style HF Radar and the MUSIC Direction-Finding Algorithm," *Journal of Atmospheric and Oceanic Technology,* vol. 24, pp. 1277-1300, 2007.

[2] J. T. Kohut, H. J. Roarty, and S. M. Glenn, "Characterizing Observed Environmental Variability With HF Doppler Radar Surface Current Mappers and Acoustic Doppler Current Profilers: Environmental Variability in the Coastal Ocean," *Oceanic Engineering, IEEE Journal of,* vol. 31, pp. 876-884, 2006.

[3] J. Kohut, H. Roarty, E. Randall-Goodwin, S. Glenn, and C. Lichtenwalner, "Evaluation of two algorithms for a network of coastal HF radars in the Mid-Atlantic Bight," *Ocean Dynamics,* vol. 62, pp. 953-968, 2012.

[4] H. J. Roarty, S. M. Glenn, J. T. Kohut, D. Gong, E. Handel, E. Rivera Lemus, T. Garner, L. Atkinson, C. Jakubiak, W. Brown, M. Muglia, S. Haines, and H. Seim, "Operation and Application of a Regional High Frequency Radar Network in the Mid Atlantic Bight," *Marine Technology Society Journal,* vol. 44, pp. 133-145, 2010.

[5] J. I. Glaser, "Fifty years of bistatic and multistatic radar," *Communications, Radar and Signal Processing, IEE Proceedings F,* vol. 133, pp. 596-603, 1986.

[6] E. Hanle, "Survey of bistatic and multistatic radar," *Communications, Radar and Signal Processing, IEE Proceedings F,* vol. 133, pp. 587-595, 1986.

[7] D. Gong, J. T. Kohut, and S. M. Glenn, "Seasonal climatology of wind-driven circulation on the New Jersey Shelf," *J. Geophys. Res.,* vol. 115, p. 25, 2010.

[8] B. Lipa, C. Whelan, B. Rector, and B. Nyden, "HF Radar Bistatic Measurement of Surface Current Velocities: Drifter Comparisons and Radar Consistency Checks," *Remote Sensing,* vol. 1, pp. 1190-1211, 2009.

[9] S. Y. Kim, E. J. Terrill, and B. D. Cornuelle, "Mapping surface currents from HF radar radial velocity measurements using

optimal interpolation," *J. Geophys. Res.,* vol. 113, p. C10023, 2008.

[10] J. T. Kohut and S. M. Glenn, "Improving HF Radar Surface Current Measurements with Measured Antenna Beam Patterns," *Journal of Atmospheric and Oceanic Technology,* vol. 20, pp. 1303-1316, September 01, 2003 2003.

Real-Time Beyond the Horizon Vessel Detection

Hugh J. Roarty[a], Michael Smith[a], Scott M. Glenn[a], Donald E. Barrick[b]
[a]Rutgers University Coastal Ocean Observation Laboratory, 71 Dudley Road, New Brunswick NJ, USA 08901; [b]CODAR Ocean Sensors, 1914 Plymouth Street, Mountain View, USA 94043

ABSTRACT

The marine transportation system (MTS) is a vital component of the United States Economy. Waterborne cargo accounts for more than $742 billion of the nation's economy and creates employment for 13 million citizens. A disruption in this system would have far reaching consequences to the security of the country.

The US National High Frequency radar network, which comprises 130 radar stations around the country, became operational in May 2009. It provides hourly measurements of surface currents to the US Coast Guard for search and rescue (SAR). This system has the capability of being a dual use system providing information for environmental monitoring as well as vessel position information for maritime security.

Real time vessel detection has been implemented at two of the radar stations outside New York Harbor. Several experiments were conducted to see the amount vessel traffic that the radar could capture. The radars were able to detect a majority of the vessels that are reporting via the Automatic Identification System (AIS) as well as 30 percent of mid to large size vessels that are not reporting via AIS. The radars were able to detect vessels out to 60 km from the coast.

The addition of a vessel detection capability to the National HF radar network will provide valuable information to maritime security sector. This dual use capability will fill a gap in the current surveillance of US coastal waters. It will also provide longer-range situational awareness necessary to detect and track smaller size vessels in the large vessel clutter.

Keywords: High Frequency radar, multistatic, bistatic, remote sensing, oceanography, detection

1. INTRODUCTION

The United States Coast Guard can protect the Marine Transportation System (MTS) by collecting and evaluating information about the MTS, an effort referred to as Maritime Domain Awareness (MDA). One component of MDA is the detection and tracking of vessels moving through the system. This has been deemed a vital component of MDA by the US government [1]. The US Coast Guard, the lead agency in charge of MDA, operates a land-based Nationwide Automatic Identification System (NAIS) as the primary tool for tracking vessels in coastal and inland waterways. The Automatic Identification System (AIS) was originally developed for collision avoidance where it would help vessels see each other when ship based radar was not able to detect other vessels. It has now been adopted as a maritime intelligence tool [2]. AIS is required equipment aboard tankers, passenger vessels that are over 150 gross tons and other vessels over 300 gross tons. AIS operates by transmitting a Very High Frequency (VHF) radio signal encoded with the vessel identity, position, speed and other safety related information.

One drawback of AIS is that it is a self-reporting system. The potential exists for human error when information is entered into the system, sensor failure in reporting position or speed information, switching off the signal at crucial times in transit [3] or even malicious intent of the operator to conceal or switch identities of the vessel.

The vessel detection capability of the SeaSonde High Frequency radar has the capability to augment the Nationwide Automatic Identification System as a tool for MDA. The SeaSonde has been used for the past two decades for the measurement of surface currents in the coastal ocean [4] [5] [6]. The dual use capability of the SeaSonde for current measurements with simultaneous vessel detection was introduced recently [7]. The benefit of HF radar is persistent surveillance with over the horizon detection capability. In this paper we test what are the optimal settings for the vessel detection system and apply that to a one-day test case.

Radar Sensor Technology XVII, edited by Kenneth I. Ranney, Armin Doerry, Proc. of SPIE Vol. 8714, 87140Z

2. METHODOLOGY

The 13 MHz High Frequency radar network deployed along the coast of New Jersey and New York consists of eight systems (Figure 1). All the radars are the SeaSonde models manufactured by CODAR Ocean Sensors, Mountain View CA. The SeaSonde is a solid state High Frequency radar. The northernmost radar was located in Hempstead, New York. The other radars were located in Sea Bright, Belmar, Seaside Park, Brant Beach, Brigantine, Strathmere and North Wildwood New Jersey. The average spacing between the radar sites was 26 km. A 13 MHz HF radar has a typical measurement range of 80 km for ocean currents.

Vessel detection tests with the radar in Sea Bright began in February 2009. Initial findings were summarized in a previous study [8]. At the time of that study, the vessel detection was non-real-time and run offsite of the radar. A technician would travel to the radar site to collect a copy of the raw spectra. This was brought back to the laboratory where it was processed for ship signals. This proved to be a laborious process.

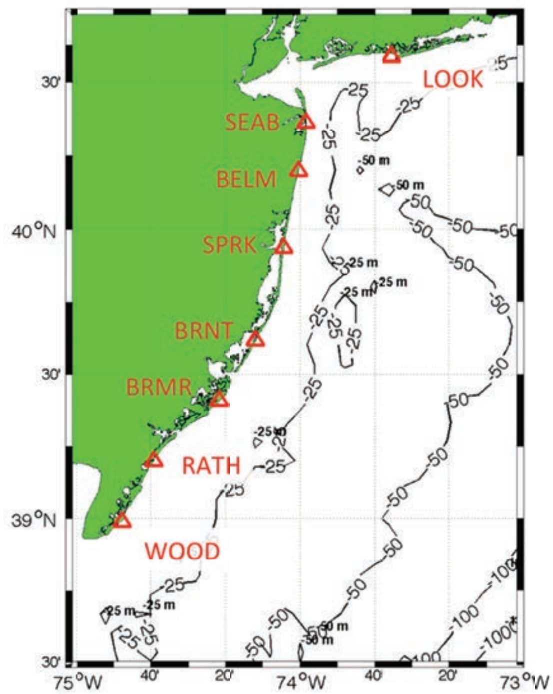

Figure 1: Map of New Jersey showing the location of the 13 MHz radar stations as red triangles. The sites from north to south are located in Hempstead, NY (LOOK), Sea Bright, NJ (SEAB), Belmar, NJ (BELM), Seaside Park, NJ (SPRK), Brant Beach, NJ (BRNT), Brigantine, NJ (BRMR), Strathmere, NJ (RATH) and North Wildwood (WOOD). The bathymetry contours in meters are also shown.

The real-time vessel detection software was installed on the Seaside Park from September 27, 2012 to October 29, 2012 and on the Sea Bright radar from April 5, 2011 to October 29, 2012. The radars at Seaside Park and Sea Bright were destroyed when Hurricane Sandy made landfall in New Jersey on October 29, 2012 [9]. The real-time software was moved to the Strathmere and North Wildwood stations and real time flow of the data commenced again on November 13, 2012 for Strathmere and November 26, 2012 for North Wildwood.

All the systems operated at 13.45 MHz center transmit frequency with 50 kHz of bandwidth. They are able to transmit on the same frequency through GPS synchronization which is unique to the SeaSonde[10]. The SeaSonde sweeps it's transmit frequency every 2 Hz over the specified bandwidth in order to determine range. Simultaneously it switches the transmit signal on and off with a period of 640 μs and only has the receiver on while the transmit signal is off. This prevents the receiver from being damaged by the transmit signal. The system requires 300 watts continuous and uses approximately 50 watts for the transmission of the radio signal [11]. A more detailed description of the waveform can be found here [7].

The detection data is generated every thirty two seconds and transferred back to a central processing center in New Brunswick, New Jersey every five minutes. The data is placed into a MySQL database and is then available to be plotted for quality control. An email is sent to notify the operators if the data is late by more than 10 minutes.

The radar uses a thresholding scheme and constant false alarm rate (CFAR) to determine if a signal should be considered a detection. After a signal peak in the spectra is identified it is compared against a background and if the peak is above the background by the specified threshold it is considered a detection. The detection algorithm uses two background types, a median background that averages in Doppler and range space and an infinite impulse response (IIR) filter that averages the spectra in time.

A series of AIS receivers were collocated at the radar stations to receive the transmissions emanating from passing ships. The AIS data served as a verification source for the radar detections. This data was transmitted back to the laboratory in New Brunswick, NJ where it was time stamped and stored and in a MySQL database. The vessel information that was critical for comparison with the radar data was the vessel's position in latitude and longitude as a function of time. This was then converted to range, radial velocity and bearing relative to the radar that was detecting the vessel.

3. RESULTS

In order to determine what the best settings would be for the real-time detection software, several case studies were conducted to see if there were optimal integration times, background types and detection thresholds. First a single ship was examined using the full processing matrix and then a series of tests were conducted with a variety of vessels using a subsampling of the processing matrix.

3.1 Los Angeles Test Case

In order to determine what settings should be used on the real time software we started with a single ship and explored the full matrix of fft lengths and thresholds that would yield optimal results. The shipping vessel Los Angeles (Figure 2) moved north past the radar in Sea Bright into New York Harbor on November 9 between 06:30 and 07:45 Coordinated Universal Time (UTC). The spectra from the radar were analyzed using the offline vessel detection software. The detection code was run with fast Fourier transform (fft) lengths on the Doppler spectra between 16 and 1024 and thresholds between 6 and 13 dB. The Doppler processing is also referred to as coherent integration time. Since the detection software is capable of three simultaneous fft lengths and corresponding thresholds, a total of 12 iterations were needed to fill out the test matrix.

Figure 2: Picture of the merchant vessel Los Angeles

The detection rate of the radar is the ratio of the number of detections to the number of update cycles for the radar. The update rate of the radar is 32 seconds, so there were 141 update cycles over this 75-minute period. A detection is verified using the AIS data as ground truth and is counted if the detection matches the AIS in range and radial velocity, the two most accurate measurements of the radar. The detection rate on the Los Angeles using the infinite impulse response background is given in Table 1 and Table 2 shows the detection rate for the median background method.

If multiple fft lengths and backgrounds are used then the probability of detection can be increased. For instance the detections from the 128, 256 and 512 point fft with both backgrounds were combined and the detection rate increased to 78% as shown in Figure 3. This figure shows detections from the radar that match the range and radial velocity of the Los Angeles from the AIS. The most accurate measurement of the radar is the radial velocity, followed by the range and lastly the bearing. This is evident by the small error bars on the radial velocity and range and larger ones on the bearing. Since the bearing measurement exhibits slightly larger error, it was not included in the verification scheme.

Table 1: Detection rates of the M/V Los Angeles on November 9, 2009 using the Infinite Impulse Response background method. The gray boxes indicate runs that were not performed and NSD stands for "no ship detected". The rows indicate the length of the fft used in the Doppler processing and the columns indicate the threshold used on the signal peaks.

		Threshold (dB)							
		6	7	8	9	10	11	12	13
FFT Length	16	NSD	NSD	NSD	NSD	NSD	NSD		
	32	6.6	6.1	4.1	1.7	0.8	NSD		
	64	21.7	20.2	17.8	16.2	13.7	10.6		
	128	41.8	41.1	39.7	37.4	36.0	34.3		
	256	42.7	41.6	39.9	39.2	37.9	35.5		
	512	33.7	32.3	30.9	29.8	28.4	26.0		
	1024								

Table 2: Detection rates of the M/V Los Angeles on November 9, 2009 using the Median background method. The gray boxes indicate runs that were not performed. The rows indicate the length of the fft used in the Doppler processing and the columns indicate the threshold used on the signal peaks.

		Threshold (dB)							
		6	7	8	9	10	11	12	13
FFT Length	16								
	32			11.8	9.0	5.8	3.0	1.4	0.3
	64			28.9	22.4	15.0	9.3	6.1	3.1
	128			50.3	48.6	46.6	43.0	39.0	36.1
	256			47.1	46.1	45.7	44.0	43.0	39.9
	512			36.5	34.0	32.6	30.5	29.5	28.8
	1024			29.7	28.6	26.1	25.0	22.1	19.6

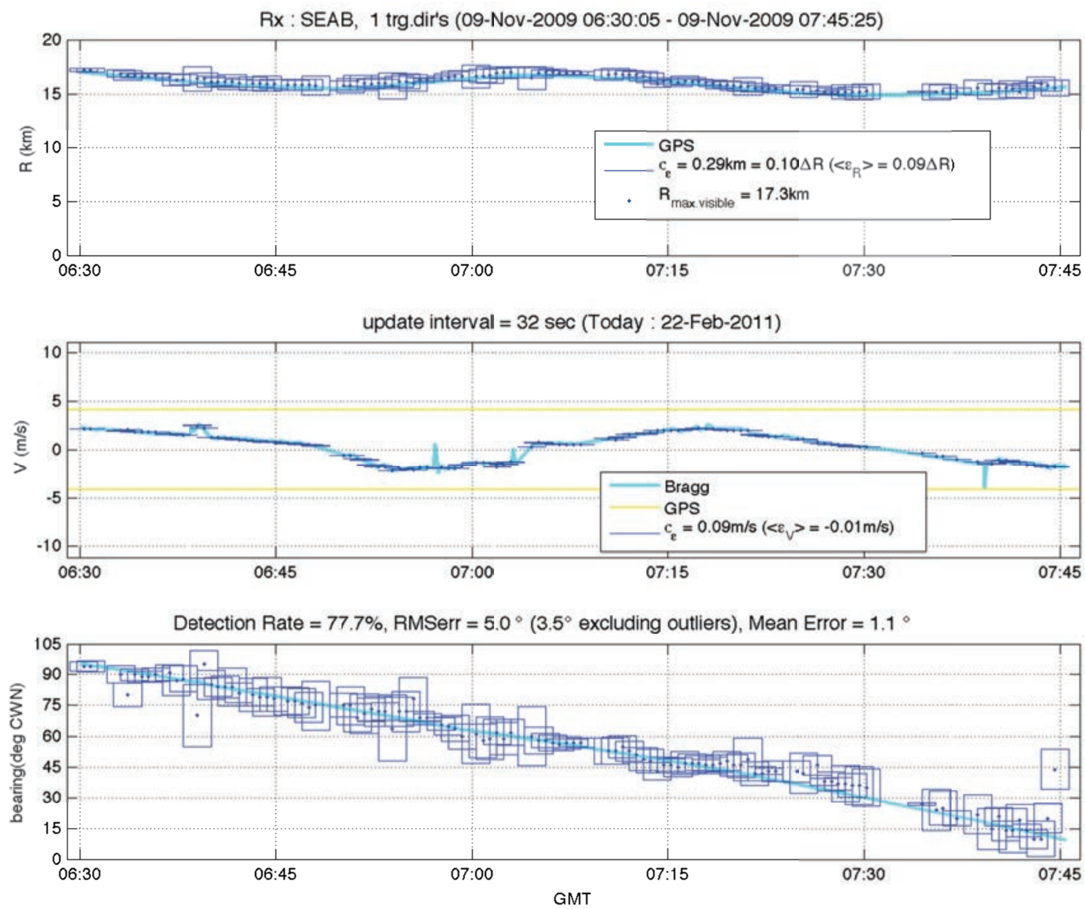

Figure 3: **Time series plot of vessel detections from the 13 MHz radar at Sea Bright (SEAB). The x-axis for all three plots is time of the day (UTC) for November 9, 2009. The sub plots from top to bottom are vessel detection range (kilometers), radial velocity (m/s) and bearing (degrees clockwise from north). The detections from the radar are shown as the blue dots and the associated uncertainty of the measurement is the height of the box around the detection and the width of the box is the fft length. The ground truth information from GPS for the Los Angeles is shown as the aqua line.**

3.2 Multiple Test Cases

Based upon the Los Angeles test case, we ran several more tests cases. We did not fill out the entire processing matrix; rather we completed the diagonal to of the matrix to most efficiently test the parameter space. The processing parameters used in this series of tests are summarized in Table 3. The yellow boxes represent the runs using the IIR background the orange boxes denote the runs for the median background. This test matrix was applied to the Los Angeles as well as another 16 vessels. The particulars (length and beam) of the vessels that were used in the consolidated test matrix are shown in Table 4. It is the height of the vessel that is critical for detection for the vertically polarized wave at HF [12] [13]. Unfortunately the authors have been unable to find sources that list the height of the vessels so the length and beam have been used as a proxy for height.

The detection rates for the 17 vessels using the infinite impulse response background are shown in Figure 4 and the median background results are shown in Figure 5.

Table 3: Processing matrix for the remaining test cases. The yellow boxes represent the runs using the IIR background the orange boxes denote the runs for the median background.

Threshold (dB)

FFT Length	6	7	8	9	10	11	12	13
16								
32								
64								
128								
256								
512								
1024								

Table 4: Summary of the vessels used in this study. The date that the vessel passed by the radar, the name of the ship its length and beam are given in the table.

#	Date	Ship Name	Ship Length (m)	Ship Beam (m)
1	2/26/09	Joel Mare	228	32
2	2/26/09	Maas Trader	139	23
3	2/26/09	Dolphin	41	6
4	5/30/10	Dace Reinauer	134	21
5	11/9/09	Sand Master	110	10
6	11/9/09	Punta Arenas	216	32
7	11/9/09	OOCL Thailand	277	40
8	11/9/09	Maersk Virginia	291	32
9	11/9/09	Los Angeles	294	32
10	11/9/09	Asphalt Seminole	108	19
11	11/9/09	Bow Tone	170	26
12	11/9/09	Barcarolle	177	32
13	11/9/09	Moscow Kremlin	242	42
14	11/9/09	NY Express	294	32
15	4/12/11	CFL Prospect	117	14
16	4/12/11	Jin Zhou	190	32
17	5/4/11	Cape Breton	210	32

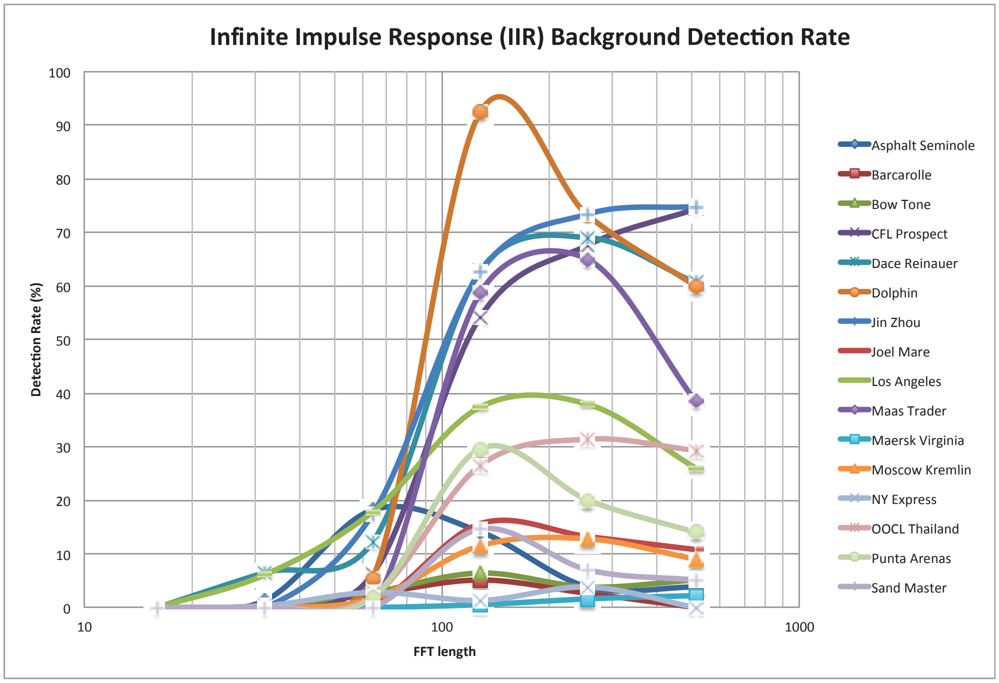

Figure 4: Vessel detection rates as a function of integration time using the infinite impulse response background for all 17 vessels in this study along the diagonal of Table 3.

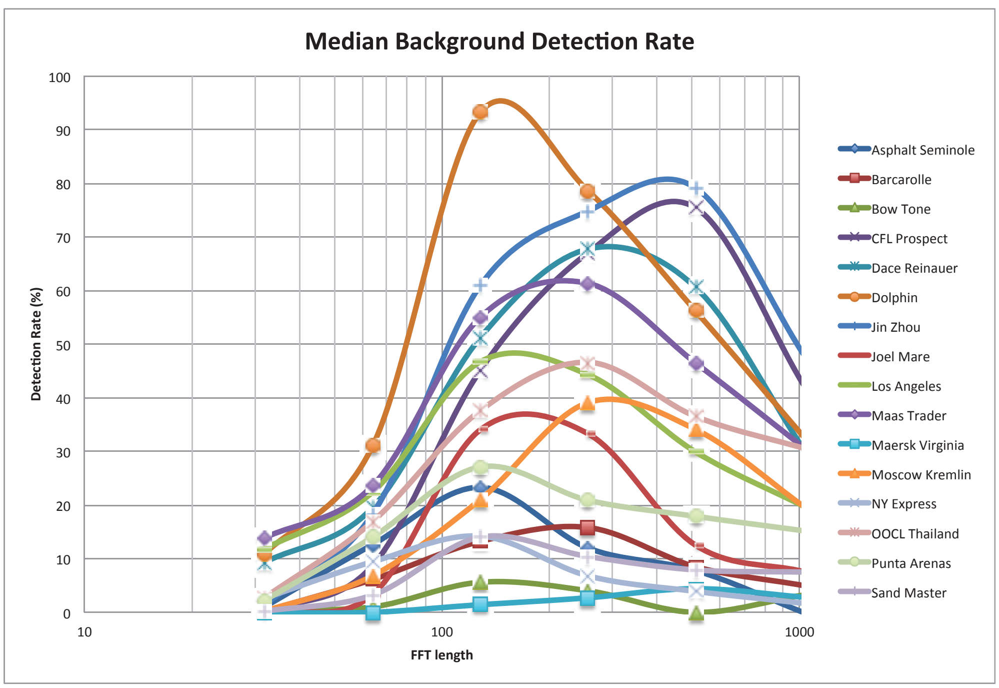

Figure 5: Vessel detection rates as a function of integration time using the median background for all 17 vessels in this study along the diagonal of Table 3.

4. DISCUSSION

From the Los Angeles test matrix, the optimal fft lengths were 128, 256 and 512. Since the radar sweeps at 2 Hz this equates to an optimal averaging time of between 1 and 4 minutes. The 1024-point fft was not run for the IIR background, but the detection rate was decreasing from the peak along the 256-point integration time so this case was not needed. The detection rate increases as the threshold is lowered but at the cost of introducing false alarms into the system.

From the diagonal test matrix applied to the other 16 vessels, 128, 256 and 512 were again found to be the optimal settings for the Doppler processing. If the results from all 17 vessels were averaged the 256-point fft was the optimal integration length. The median method was consistently better than the iir for the detection of vessels with the SeaSonde. This is shown in Figure 6.

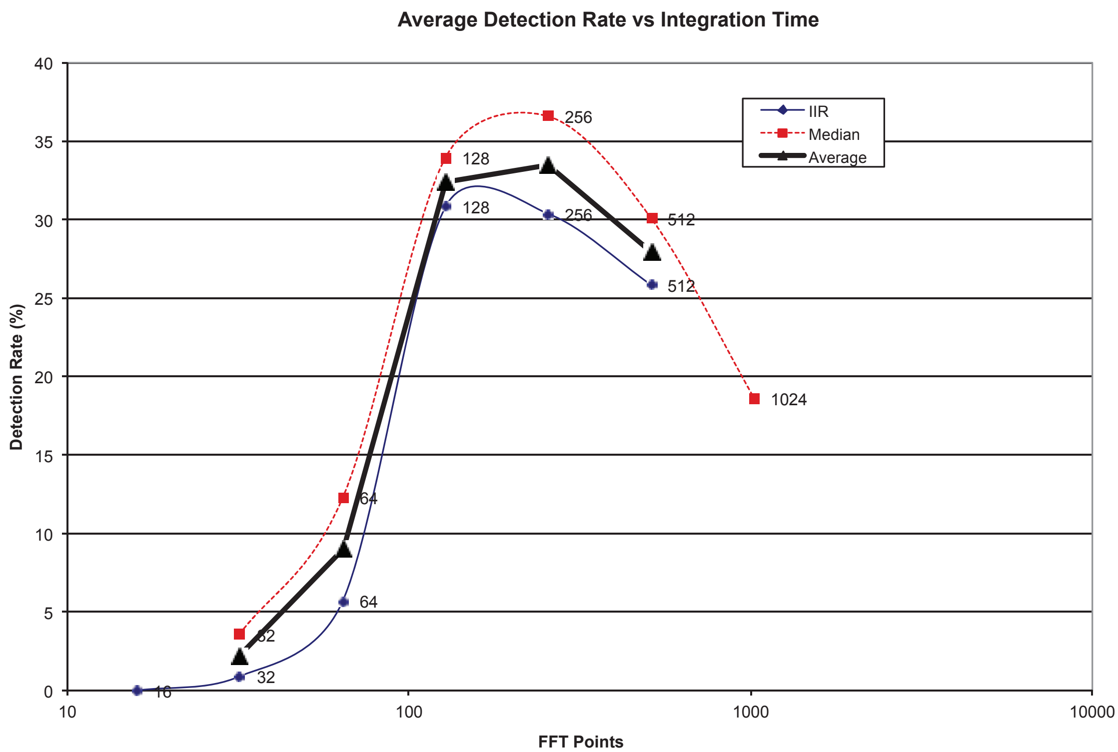

Figure 6: FFT length versus average detection rate for the 17 vessels used in this study. The IIR background, median background and the average of the two background types are shown.

5. APPLICATION TO JUNE 11, 2012

The optimal settings that were found in the 17 test cases discussed in the previous sections were applied to the real time software. One day of data from June 11, 2012 was processed to determine how well the radar was detecting vessels at sea. This day happened to coincide with a fake distress call that the Coast Guard was responding to in the coverage area of the radar [14]. The vessel detection from the radar can help a situation like the fake distress call where more information on the vessels in the area can help the Coast Guard with decision making.

The AIS data was used to determine the number of vessels that were within range of the radar. The initial query of the AIS database yielded 265 vessels for that day. The data was then filtered to only keep vessels within 100 km of the radar at Sea Bright, NJ. This reduced the data set down to 64 vessels. The data was further refined by removing any vessels with a bearing between 180 and 360 degrees, meaning the vessels were to the west of the radar site most likely in Raritan Bay or Upper New York Harbor. Another filter was added to remove any vessels where their radial velocity was zero meaning the vessels were at mooring for the period of the test. This yielded a total of 54 vessels that the radar at Sea Bright could realistically detect. Of those 54 vessels, the radar at Sea Bright was able to detect 51 of them. If the data is binned hourly, there were an average of 11 vessels on AIS in any given hour. The radar at Sea Bright detected 9 of them and there were an additional 4 vessels per hour that were detected by the radar with no AIS to corroborate against.

6. CONCLUSIONS

Vessel detection software has been transitioned from an offline tool into a real-time tool that is running on two SeaSondes along the coast of New Jersey. A sensitivity study was conducted to determine what were the optimal settings for the software. An integration time of 1-2 minutes was found to be optimal. This is consistent with previous studies [8]. The median background outperformed the iir background across all integration times. The radar is able to detect a majority of vessels that are reporting on the AIS network and the radar detects one third of the vessels in coastal waters that are not reporting on AIS.

6.1 Application to the US National Network

There are approximately 140 HF radars operating along the coast of the United States as part of the National High Frequency Radar Network. The coverage is very good in the northeast and west coasts. There is a plan [15] to expand the current number of radars out to 320 and have full coverage on the continental United States and good coverage in Alaska, Hawaii and Puerto Rico. The vessel detection algorithm that has been developed here can be implemented on these radar stations to provide another layer of data for maritime domain awareness. The capability to track a vessel transiting along the coast for several hundreds of kilometers is one benefit of this system.

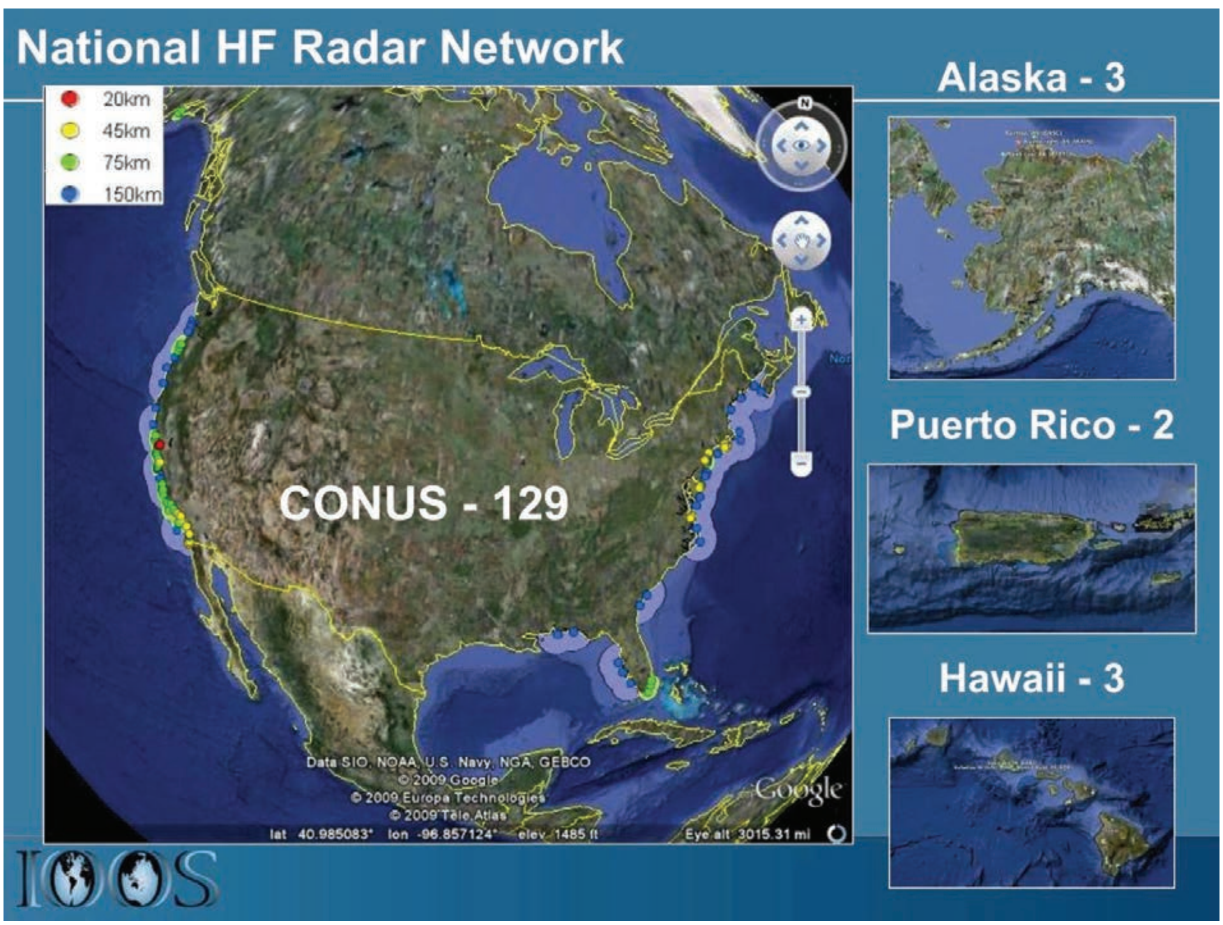

Figure 7: US HF Radar National Network. 5 MHz sites are shown as blue dots, 13 MHz sites are shown as green dots, 25 MHz sites are shown as yellow dots and 42 MHz sites are shown as red dots. The numbers of radars for each region are shown. (Image courtesy of the NOAA Integrated Ocean Observing System (IOOS) Program)

7. ACKNOWLEDGEMENTS

The US Navy under contract N00253-09-D-0005 from Naval Undersea Warfare Center Keyport Division funded this work. This material is based on work supported by the U.S. Department of Homeland Security under Award No. 2008-ST-061-ML0001. The views and conclusions contained in this document are those of the authors and should not be interpreted as necessarily representing the official policies, either expressed or implied, of the U.S. Department of Homeland Security.

REFERENCES

[1] Caldwell, S.L., "Vessel Tracking Systems Provide Key Information, but the Need for Duplicate Data Should Be Reviewed": p. 54 (2009)

[2] Tetreault, B.J. "Use of the Automatic Identification System (AIS) for maritime domain awareness (MDA)" in *OCEANS, 2005. Proceedings of MTS/IEEE*. (2005).

[3] Chang, S.J. "Development and analysis of AIS applications as an efficient tool for vessel traffic service" in *OCEANS '04. MTTS/IEEE TECHNO-OCEAN '04*. (2004).

[4] Kim, S.Y., Terrill, E.J., Cornuelle, B.D., Jones, B., Washburn, L., Moline, M.A., Paduan, J.D., Garfield, N., Largier, J.L., Crawford, G., and Kosro, P.M., "Mapping the U.S. West Coast surface circulation: A multiyear analysis of high-frequency radar observations″ Journal of Geophysical Research: Oceans. 116(C3): p. C03011 (2011)

[5] Roarty, H.J., Glenn, S.M., Kohut, J.T., Gong, D., Handel, E., Rivera Lemus, E., Garner, T., Atkinson, L., Jakubiak, C., Brown, W., Muglia, M., Haines, S., and Seim, H., "Operation and Application of a Regional High Frequency Radar Network in the Mid Atlantic Bight″ Marine Technology Society Journal. 44(6): p. 133-145 (2010)

[6] Glenn, S.M., Dickey, T.D., Parker, B., and Boicourt, W., "Long-term real-time coastal ocean observation networks. Oceanography″ Oceanography. 13(1): p. 24-34 (2000)

[7] Roarty, H.J., Barrick, D.E., Kohut, J.T., and Glenn, S.M., "Dual-Use Compact HF Radars for the Detection of Mid- and Large-Size Vessels″ Elektrik, Turkish Journal of Electrical Engineering and Computer Sciences. 18(3): p. 373-388 (2010)

[8] Roarty, H., Lemus, E., Handel, E., Glenn, S., Barrick, D.E., and Isaacson, J., "Performance Evaluation of SeaSonde High-Frequency Radar for Vessel Detection″ Marine Technology Society Journal. 45(3): p. 14-24 (2011)

[9] Malakoff, D., "Scientists Assess Damage From Sandy's Deadly Punch″ Science. 338(6108): p. 728-729 (2012)

[10] Barrick, D.E., Lilleboe, P.M., and Teague, C.C., *Multi-station HF FMCW radar frequency sharing with GPS time modulation multiplexing*, 2001.

[11] Cook, T., Hazard, L., Otero, M., and Zelenke, B., "Deployment and Maintenance of a High-Frequency Radar for Ocean Surface Current Mapping: Best Practices″ Southern California Coastal Ocean Observing System. p. 35 (2008)

[12] Leong, H. and Wilson, H., "An estimation and verification of vessel radar cross sections for high-frequency surface-wave radar″ Antennas and Propagation Magazine, IEEE. 48(2): p. 11-16 (2006)

[13] Ponsford, A.M. and Wang, J., "A Review of High Frequency Surface Wave Radar for Detection and Tracking of Ships″ Elektrik, Turkish Journal of Electrical Engineering and Computer Sciences. 18(3): p. 409-428 (2010)

[14] Rundquist, J. and DInges, T., "Seconds of Panic, Hours of Drama: N.J. Boat Explosion Call Investigated as Hoax″ Newark Star Ledger. p. 1-2 (2012)

[15] Harlan, J., "A Plan to Meet the Nation's Needs for Surface Current Mapping″ NOAA IOOS. p. 64 (2009)

Spatial evaluation of high-resolution modeled offshore winds using estimated winds derived from a network of HF radars

Greg Seroka, Josh Kohut, Laura Palamara, Scott Glenn, Hugh Roarty, Lou Bowers, Rich Dunk
Coastal Ocean Observation Laboratory
Rutgers University
New Brunswick, NJ USA
seroka@marine.rutgers.edu

***Abstract*—The temporal and spatial variability in the New Jersey offshore wind resource has large implications on the energy production for proposed offshore wind parks. The Rutgers University Weather Research and Forecasting (RU-WRF) mesoscale atmospheric modeling system can begin to diagnose as well as predict key sources of variability both in space and time, including sea and land breezes and frontal passages. While vertically validating model performance in coastal and offshore regions is readily achieved through the use of meteorological towers and approved remote sensing systems, horizontal evaluation of winds—especially at sufficiently high resolutions—can be difficult with pre-existing systems.**

We apply the high-resolution surface current mapping capabilities of a high frequency (HF) radar network to infer wind fields over the offshore domain of RU-WRF. Surface wind fields derived from the HF radar network are compared to 10m wind fields modeled by the RU-WRF; correlations are generally between 0.5 and 0.8 in the study domain.

Finally, to demonstrate the feature-tracking ability of the HF radar and RU-WRF model simulated offshore winds, we focus on a passing front and its associated thunderstorms. An area of divergence in RU-WRF modeled near-surface winds is evident as the thunderstorm line passes, likely caused by either a strong outflow boundary ahead of the thunderstorm front or directly from the cold downdraft in the core of the cold rain, which would reach the ocean's surface and diverge outwards. The forcing was so strong that the response was evident in both the HF radar currents and HF radar-inferred surface winds. The case warrants future analysis in surface ocean response to thunderstorm outflow boundaries and downdrafts, especially via the use of the HF radar-derived surface winds.

***Index Terms*—Offshore wind, atmospheric modeling, HF radar, CODAR, weather radar, WRF, air-sea interaction, coastal processes, complex correlation, coastal upwelling, surface ocean response**

I. Introduction

The temporal and spatial variability in the New Jersey offshore wind resource has large implications on the energy production for proposed offshore wind parks. The Rutgers University Weather Research and Forecasting (RU-WRF) mesoscale atmospheric modeling system can begin to diagnose as well as predict key sources of variability both in space and time, including sea and land breezes and frontal passages.

It is critical to evaluate the performance of RU-WRF not only in the vertical but also over the spatial horizontal study domain in order to identify areas for improvement and subsequently, if necessary, refine the model. Although vertical validation of winds can be performed with meteorological towers and approved remote sensing systems, horizontal spatial evaluation of winds, especially for offshore areas, can be difficult with pre-existing observational systems. Satellite-based scatterometers (e.g. QuikSCAT [1]) have historically provided wind measurements over the ocean. However, their relatively low spatial resolution of 25 km is not adequate for wind resource assessments associated with the spatial scale for most offshore wind turbine arrays. Furthermore, land contamination can occur within 25-37 km from the coast [2], precisely the development zone for non-floating offshore wind turbines.

II. Methods

We apply the high-resolution surface current mapping capabilities of a high frequency (HF) radar network (coastal radar, or CODAR) to infer wind fields over the offshore domain of the atmospheric model. The surface currents sampled by the shore-based CODAR system are forced by a combination of processes. In our study region the surface currents are largely driven by tides, buoyancy, and local winds [3,4]. The tides were extracted from the raw observed currents using standard least squares approaches [5]. We have found that in our region the relative importance of local winds in driving detided surface currents depends largely on stratification. During the winter season when the water column is mixed, bottom friction and pressure gradients drive the flow. During the summer, strong stratification isolates the slippery surface layer from the bottom leading to a surface current more dependent on the local wind forcing. Here we apply a regression model to estimate the offshore surface wind fields during this summer-stratified season at a resolution of 2 km across the designated study area.

We identified two sea breeze events during the summer-stratified season on which to focus our CODAR surface

978-0-933957-40-4 ©2013 MTS

current-based wind model: one without coastal upwelling (30 Aug-6 Sep 2012) and one with coastal upwelling (8-15 Sep 2012). We trained the model on one month of data spanning both events, 25 Aug to 25 Sep, while the water column was still stratified. We used measured wind from the Ocean City WeatherFlow site, which is on the coast centered on the study region and has good coverage over this time period. Wind observations were 75-minute center averaged to be consistent with the CODAR processing (Fig. 1).

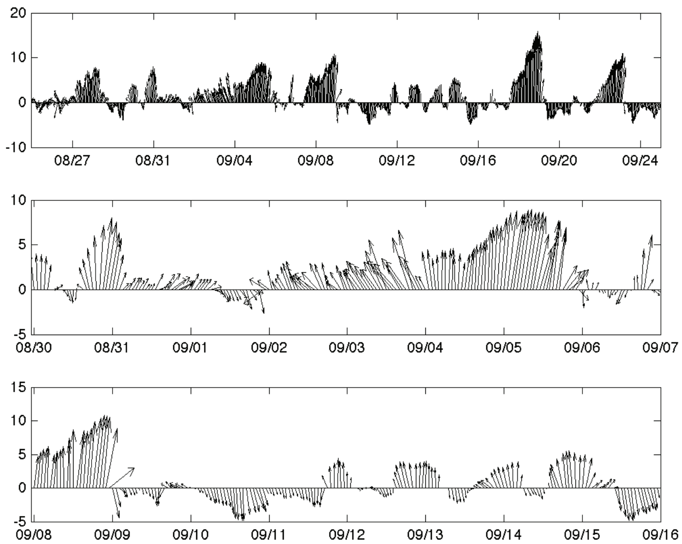

Fig. 1: Hourly 75-minute averaged wind measurements at the Ocean City WeatherFlow site for the time period used to train the surface current-based wind model. Top panel shows winds for the entire time period, middle panel shows the early September 2012 sea breeze case, and the bottom panel shows the mid-September 2012 sea breeze case. Tick marks are at 00:00 GMT for day noted.

The wind model is based on the correlation between the local wind observation in Ocean City, NJ and the surface current observations at each grid point in the survey region [5]. For each grid point we calculated the complex correlation between the local wind observation and the observed detided surface current. The magnitude across the field had a mean of 0.56 and a maximum of 0.73, and most of the region had a correlation higher than 0.4. The phase indicates that the highest correlated current was shifted to the right of the wind with an angle that ranged from about 0 to 60° across the field. These values are based on a zero time lag between the wind and current. Three points in regions of high correlation were used to determine the time lag that yielded the highest correlation between surface winds and currents. For each of these points we lagged the currents by 0 to 12 hours and recalculated the complex correlation. For each point, the highest correlation between wind and current peaked with a lag of about three hours. This indicates that the surface currents lag the wind forcing by approximately three hours (Fig. 2).

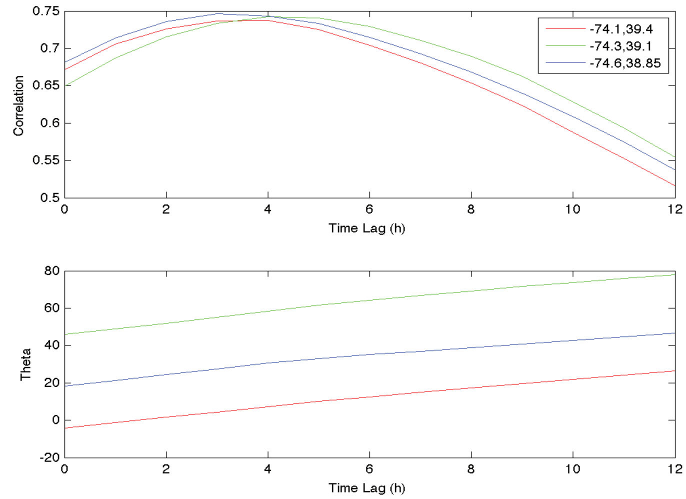

Fig. 2: Time-lag dependent complex correlation magnitude (top) and angle offset between highest correlated components of wind and surface current (bottom) for three points in regions of high correlation (red: northernmost, green: central, blue: southernmost). The correlation peaks at a time lag of around three hours, and offset angle steadily increases with increasing time lag.

The complex correlation was then recalculated with this lag across all grid points. The majority of the study region had a resulting a mean correlation of 0.62 and a maximum of 0.92, with over 50% of the region at a correlation above 0.6. The new correlation values increased with lowest values near the edges and the highest values again near the center of the CODAR coverage (Fig. 3). Surface currents were rotated based on the angles shown in the right panel of Fig. 3 and a best-fit line applied to the rotated surface u (v) current and measured u (v) wind three hours previous as in [5]. Estimated wind maps were then generated by rotating CODAR-measured surface currents and applying the best-fit equations to the rotated currents. The resulting surface current-based wind estimates were the basis for the spatial evaluation of the offshore wind fields predicted by the RU-WRF model. An example of the final suite of imagery that was used to spatially evaluate RU-WRF offshore winds is presented in Fig. 4, which includes CODAR detided currents, surface winds, and RU-WRF modeled 10m winds.

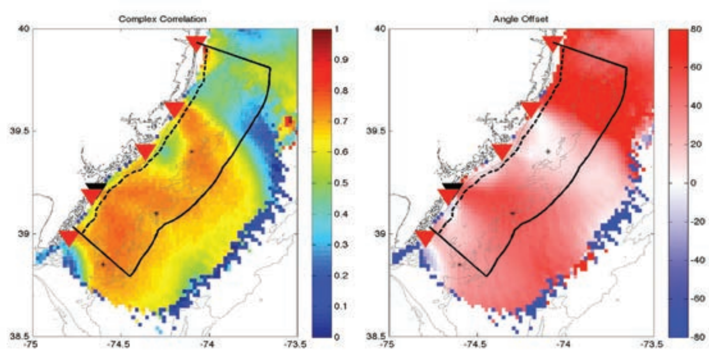

Fig. 3: Magnitude of complex correlation and angle offset between the highest correlated components of the wind and surface currents with a three-hour lag. Black triangle: location of the Ocean City WeatherFlow site, red triangles: 13 MHz CODAR sites, solid line: study area offshore wind (extending 20 nm offshore), dashed line: boundary between federal and state waters (3 nm offshore), asterisks: test locations for time lags shown in Fig. 2.

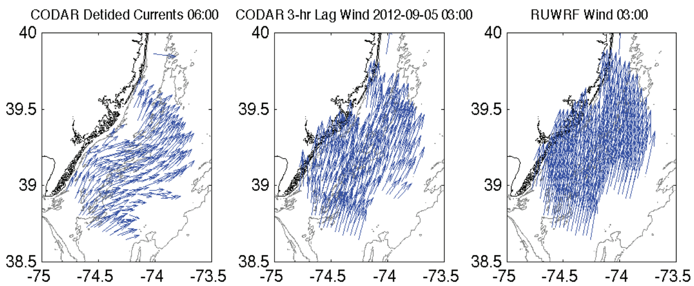

Fig. 4: Detided surface currents on 5 Sep 2012, 06:00 GMT (left), wind predicted for 03:00 based on those currents (center), and RU-WRF model 10m wind at 03:00 (right).

Because our surface wind estimates are derived directly from CODAR currents, any uncertainty in the current measurements would produce a subsequent uncertainty in the wind estimates. Several prior studies [6,7] using acoustic Doppler current profilers (ADCPs) to evaluate HF radar currents measurements found the intrinsic 5 MHz HF radar radial uncertainty to be of O(5 cm/s). We can assume an uncertainty of the same order or smaller for this study which uses the shorter range, higher-resolution measurements from a 13 MHz HF radar system. Accounting for this surface current uncertainty in our wind model produces O(0.75 to 1 m/s) uncertainty in our estimated winds.

III. Results

For the upwelling and non-upwelling case studies, we used the CODAR surface wind estimate to evaluate RU-WRF performance offshore throughout the study region. In this evaluation, we limited the comparison to those grid points in which the correlation between the CODAR currents and Ocean City WeatherFlow winds was at least 0.6. For these grid points, the comparison between CODAR winds and RU-WRF model winds were determined for the upwelling and non-upwelling cases. For the non-upwelling case between 30 Aug 2012 and 6 Sep 2012, the correlation coefficient was at least 0.5 across the study region, with a large area of 0.65 correlation near the center of the field. Angle offset values were consistently between 0° and about 20° across the study region indicating that the most correlated RU-WRF model wind vector is shifted to the right of the CODAR wind estimate (Fig. 5).

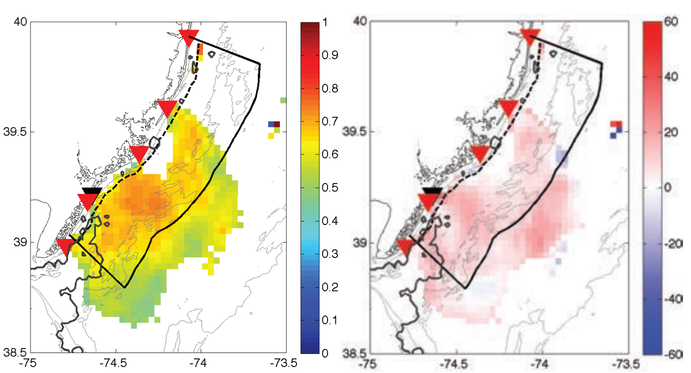

Fig. 5: Magnitude of complex correlation (left) and angle offset (right) between the CODAR-predicted surface wind (e.g. Fig. 4, center) and RUWRF modeled 10m wind (e.g. Fig. 4, right), for the non-upwelling case (30 Aug 2012-6 Sep 2012). Black triangle: location of the Ocean City WeatherFlow site, red triangles: 13 MHz CODAR sites, black solid line: study area coinciding with the study area for offshore wind (extending 20 nm offshore), dashed line: boundary between federal and state waters (3 nm offshore), dark gray solid contour: 24°C isotherm of SST, showing minimal to no coastal upwelling occurring in the study area.

The upwelling case, between 8 Sep 2012 and 15 Sep 2012, had a different spatial pattern in the comparison between CODAR wind estimates and RU-WRF model simulated offshore winds. For the upwelling case, there was a cross and along-shelf gradient in the correlation with the lowest values very near shore close to the center of the field. Farther offshore there is a faint banding pattern with the highest correlations centered on the middle of the field (Fig. 6). The region of low correlation near shore with values less than about 0.6, coincides with the core of coastal upwelling that occurred for much of the time period. This zone of upwelling is depicted by the gray contour of 22°C SST along the coast of Atlantic City. Inside the upwelling center the water column is well mixed [8]. Under these mixed conditions it has been shown the CODAR surface currents are less responsive to local winds. Therefore, the low correlation in this upwelling center is likely more a result of uncertain CODAR estimates of the winds rather than inaccuracies in the RU-WRF model winds.

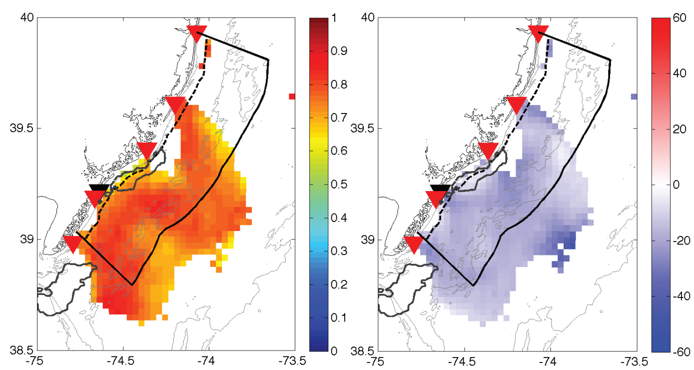

Fig. 6: Magnitude of complex correlation (left) and angle offset (right) between the CODAR-predicted surface wind and RUWRF modeled 10m wind, for the upwelling case. Black triangle: location of the Ocean City WeatherFlow site; Red triangles: 13 MHz CODAR sites; Black solid line: study area; Dashed line: boundary between federal and state waters: Gray solid contour: 22°C isotherm of SST, showing coastal upwelling.

The faint bands of lower correlation in the alongshore direction farther offshore are spaced approximately 30 km apart, matching the scale of the inshore upwelling center. It has been shown that these upwelling centers are characterized by an alongshore velocity jet running up the NJ coast along the offshore edge of the surface front [8]. A closer examination of the surface currents over this upwelling case show that the surface currents offshore tend to follow the shape of the upwelling center with a general flow along the coast near the southern boundary of our survey region that turns sharply offshore just south of the upwelling center before turning alongshore farther north. This spatially dependent perturbation in the flow around the upwelling center could bias the wind estimates from the CODAR systems. Furthermore, the banding that is evident over the upwelling case could also be in part due to the geometry of the CODAR sites.

CODAR derived wind field estimates were used to evaluate the RU-WRF model performance in resolving the spatial structure of the offshore wind field. Wind estimates derived from CODAR data appear to be influenced by the near-shore upwelling center, and perhaps the geometry of the CODAR sites during the upwelling case. Therefore, we chose to concentrate this analysis on the non-upwelling case. During the non-upwelling case the CODAR estimated winds were more uniformly correlated with the RU-WRF model results over most of the study region.

Fig. 7 depicts a subtle banding in convergence/divergence west to east in the RU-WRF modeled winds (Fig. 7, right) as well as the CODAR-derived surface wind field (Fig. 7, center) on 4 Sep 2012 at 19:00 GMT. A convergence band is evident on the southwestern edge of the study area in both the CODAR wind and RU-WRF wind fields. Just to the east, an area of lighter, more divergent winds is evident in both fields, and then farther east another area of higher, more convergent winds. In general, there is good overall correlation between wind direction in both the CODAR product and RU-WRF model (i.e. both from the south), while CODAR de-tided currents are more variable from the southwest, west, and south at that time as one moves north up the coast (Fig. 7, left).

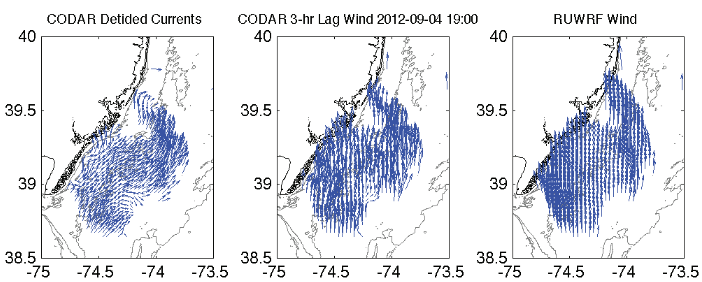

Fig. 7: Detided surface currents on 4 Sep 2012, 19:00 GMT (left), wind predicted for 19:00 based on the currents 3-hrs earlier (center), and RU-WRF modeled 10m wind at 19:00 (right).

Throughout the model study the RU-WRF model winds showed significant spatial variability associated with local processes including fronts associated with the sea breeze and passing thunderstorms. To demonstrate the feature tracking of the CODAR and RU-WRF model simulated offshore winds, we focused on a passing front between about 18:00 GMT on 5 Sep 2012 and 06:00 GMT on 6 Sep 2012. A strong line of thunderstorms developed along the front; at 23:00 GMT, the line of storms was directly over the northern section of the study area. At the same time, the near-surface wind response to the thunderstorms was evident in our RU-WRF model run with a distinct area of surface divergence located in the northeastern section of the study area, offshore of Tuckerton, NJ (Fig. 8, bottom left).

The surface divergence in the winds was likely caused by either a strong outflow boundary ahead of the thunderstorm front or directly from the cold downdraft in the core of the cold rain, which would reach the ocean's surface and diverge outwards. The forcing was so strong that the response was evident in both the CODAR detided ocean currents (Fig. 8, top left) that are directed offshore in the coincident area, and the CODAR-derived surface winds (Fig. 8, top right) that are directed outward from the thunderstorm core and offshore of Tuckerton. A time-series further indicates the slow progression of the thunderstorm line, and along with it the southeastward movement of the surface divergence in the winds as well as currents.

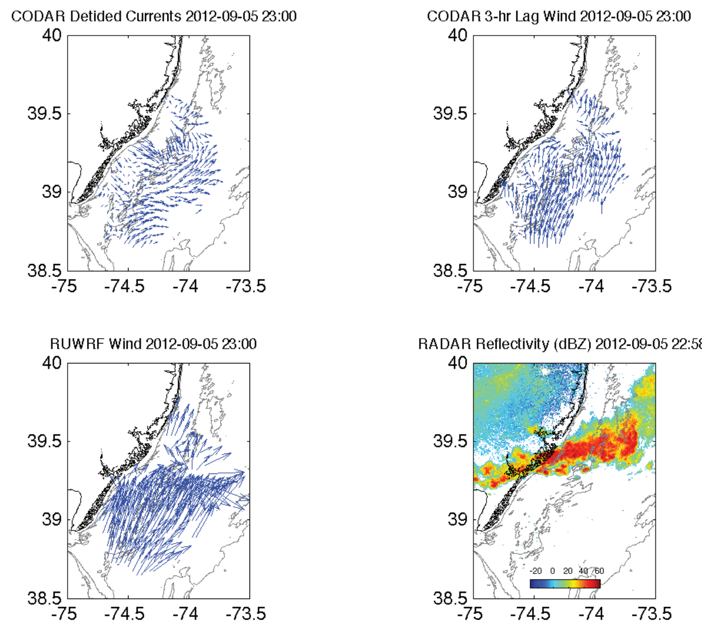

Fig. 8: Detided surface currents on 5 Sep 2012 23:00 GMT (top left), wind predicted for 23:00 GMT based on the currents 3 hrs earlier (top right), RU-WRF model 10m wind at 23:00 (bottom left), and weather radar reflectivity depicting a line of strong thunderstorms at 22:58 GMT (bottom right).

IV. Conclusions

A method for estimating surface winds using a network of HF radars has been developed, and the resulting wind estimates were used to spatially evaluate the performance of a high-resolution atmospheric model in the coastal regime. When pairing this spatial evaluation (i.e. in the xy-plane across time) with vertical validation (i.e. in the z direction, across time) we can begin to determine the accuracy of the model's depiction of mesoscale atmospheric processes in all four dimensions (i.e. in the x,y, and z directions across time).

The thunderstorm case study presented above provided a period of time that showed excellent correlation between modeled surface wind divergence and observed ocean response, possibly due to the slow-moving nature of the cold front. Because maximum correlation between currents and winds occurred at a three-hour lag, any phenomenon that has a lifetime in the study domain shorter than three hours may not be effectively captured. The case warrants future analysis in surface ocean response to thunderstorm outflow boundaries and downdrafts, especially via the use of the CODAR-derived surface winds. In addition, the methods developed above can be used to spatially evaluate the model's performance during sea/land breeze events, which potentially have a significant impact on the daily timing of offshore wind power production during the summer peak energy demand season.

ACKNOWLEDGMENTS

This work was funded by a grant from the New Jersey Board of Public Utilities: "An Advanced Atmospheric/Ocean Assessment Program Designed to Reduce the Risks Associated with Offshore Wind Energy Development Defined by the NJ Energy Master Plan and the NJ Offshore Wind Energy Economic Development Act".

REFERENCES

[1] Shirtliffe, G. M. (1999), QuikSCAT science data product user's manual, overview, and geophysical data products. Version 1.0. JPL D-18053, Jet Propulsion Laboratory, Pasadena, CA, 90 pp.

[2] Chao, Y., Z. Li, J. Kindle, J. Paduan, and F. Chavez (2003), A high-resolution surface vector wind product for coastal oceans: Blending satellite scatterometer measurements with regional mesoscale atmospheric model simulations, Geophys. Res. Lett., 30(1), 1013, doi:10.1029/2002GL015729.

[3] Beardsley, R. C., W. C. Boicourt, and D. V. Hansen (1976), Physical oceanography of the Middle Atlantic Bight, Limnol. Oceanogr. Spec. Symp., 2, 20 – 34.

[4] Beardsley, R. C., and D. B. Haidvogel (1981), Model studies of wind driven transient circulation in the Middle Atlantic Bight, part 1: Adiabatic boundary conditions, J. Phys. Oceanogr., 11, 355 – 375.

[5] Kohut, J. T., S. M. Glenn, and R. J. Chant (2004), Seasonal current variability on the New Jersey inner shelf, J. Geophys. Res., 109, C07S07, doi:10.1029/2003JC001963.

[6] Kohut, J., H. Roarty, and S. M. Glenn (2006), Characterizing observed environmental variability with HF Doppler radar surface current mappers and acoustic Doppler current profilers: Environmental variability in the coastal ocean, IEEE J. Oceanic Eng., 31, 876 – 884, doi:10.1109/ JOE.2006.886095.

[7] Chapman, R. D., and H. C. Graber (1997), Validation of HF radar measurements, Oceanography, 10, 76 – 79.

[8] Chant, R. J., S. M. Glenn, J. Kohut (2004), Flow reversals during upwelling conditions on the New Jersey inner shelf, J. Geophys. Res., Vol. 109, No. C12, C12S03. 10.1029/ 2003JC001941.

Methods of Associating CODAR SeaSonde Vessel Detection Data Into Unique Tracks

Michael Smith, Hugh Roarty, Scott Glenn
Coastal Ocean Observation Laboratory
Rutgers University
New Brunswick, NJ USA
michaesm@marine.rutgers.edu

Chad Whelan, Donald Barrick, James Isaacson
CODAR Ocean Sensors
Mountain View, CA USA
chad@codar.com

***Abstract*— Since 2011, Rutgers has been operating an over-the-horizon vessel detection software called 'PeakPicker' at two 13 MHz CODAR SeaSonde sites located in Sea Bright, NJ and Belmar, NJ. The challenge of vessel detection using High Frequency (HF) radar is dealing with false detection peaks and then associating multiple peaks derived from different coherent integration times and background filters at a single time step into one peak representing the best estimate. Association of distinct signal peaks derived from the CODAR SeaSonde high frequency (HF) radar PeakPicker software provides a challenge. Association of peaks occurs in two distinct phases. Level 1 Association will associate multiple detection peaks derived from different coherent integration times and background filters at a single time step into one 'best' peak while Level 2 Association will combine data from multiple sites representing different viewing angles. A Matlab script, plot_all_matches, finds matches target data in range and range rate (radial velocity) with AIS data providing a ground truth of our ship detection progress. Utilizing the output of the matching data from plot_all_matches, we present techniques that increase the accuracy and decrease the error of detections.**

Keywords— remote sensing; high frequency radar; vessel detection; maritime domain awareness; tracker; association

I. Introduction

Rutgers University, as a partner in the U.S. Department of Homeland Security's (DHS) Center for Secure and Resilient Maritime Commerce (CSR), has demonstrated over-the-horizon vessel detection as a multi-use capability for their SeaSonde® High Frequency (HF) Radar coastal ocean current and wave monitoring network [1] in New York Harbor and in Barrow, Alaska [2]. Real-time current maps are being used for Search and Rescue (SAR) [3], oil spill response [4], among other uses on over 130 systems around the U.S. and now Rutgers is providing real time detections for the approaches to New York Harbor and the Delaware Bay. These detections are supplied to the Naval Research Lab's (NRL) Open Mongoose data fusion engine where they are turned into vessel tracks using a combination of data from different sensors.

Since 2008, Rutgers has deployed and maintained three Mid Range SeaSonde high frequency radar systems operating in the 13 MHz band around the entrance to New York Harbor. In April 2011, Real–time vessel detection software, developed by CODAR Ocean Sensors and Rutgers University, was installed and run in parallel with current mapping software running locally at the radar sites. Since this time, thousands of vessels have been successfully detected entering and exiting the harbor ranging from smaller pleasure craft (15-20m) to large shipping vessels (100+m). Additionally, in order to provide ground truth of vessel detections, multiple Autonomous Identification System (AIS) receivers were installed in order to record GPS verified locations of ships in transit.

The three observable outputs (range, range rate, and bearing, See Figure 1) present a unique challenge when attempting to associate a series of unique vessel detections to multiple distinct tracks. While range rate and range give accurate measurements with low uncertainty, determining accurate bearing of a target has proved to be the most challenging with the compact SeaSonde HF Radar system. Tests indicate that the local environment, not system hardware, causes the most significant distortion of the pattern from the theoretical shape [5]. Thus, antenna patterns must be measured frequently in order to correct for bearing bias. If antenna patterns are not up to date, significant discrepancies in true bearing versus MUSIC-derived bearing may occur. To make up for any potential bearing inaccuracies, we are developing a series of algorithms that incorporates all three measurements into a single associated track. Whereas normal trackers utilize range and bearing in their calculations, we are attempting to utilize our most accurate measurement, range rate. This associated track is then compared to range, range rate, and bearing data derived from AIS data. Statistics on three observables are presented along with vessel tracks. The challenges of integrating the three observables into a tracker

978-0-933957-40-4 ©2013 MTS

are discussed and associated vessel detections are shown.

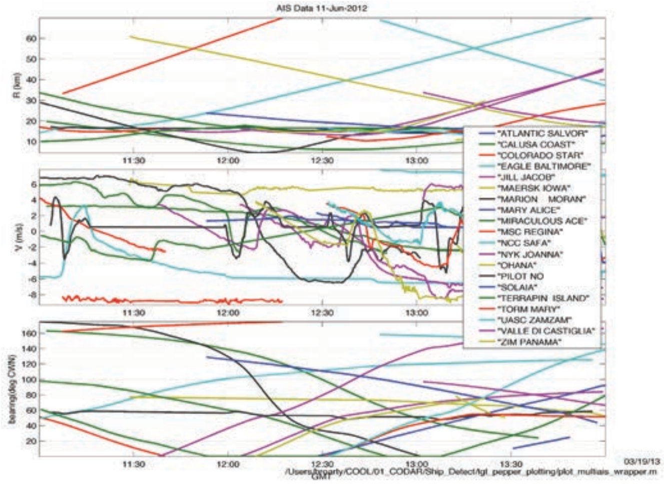

Figure 1: Vessel traffic on June 11, 2012 in the New York Bight Apex area. Range, range rate, and bearing of vessels were computed using the 13 MHz Sea Bright, NJ site as the receiver origin.

II. METHODS

A. CODAR SeaSonde Hardware/Software

CODAR PeakPicker real-time vessel detection software was installed at two existing 13MHz (mid range) SeaSonde sites located in Sea Bright, NJ (SEAB) and Belmar, NJ (BELM) in April 2011 and July 2011 respectively. These radars have been operating as surface current monitoring stations since their installations in January 2009 and July 2011. To provide ground truth data of ship locations, Autonomous Identification systems (AIS) receivers were installed at locations including Sea Bright, NJ, Belmar, NJ, and Hempstead, NY. These receivers provided location data for ships entering/exiting New York Harbor from every direction.

B. Vessel Tracking

Vessel tracking with HF radar takes place in three different steps: (1) detection, (2) association, and (3) tracking [2]. Detection uses different data processing algorithms to define peaks in the radar returns above a highly variable background of noise and clutter. The vessel detection software utilizes two background filters and 6 combinations of coherent processing (FFT) times and threshold level to produce detections [2]. The first background filter is the median type, which averages both in Doppler and range space. The second background filter is the Infinite Impulse Response (IIR) filter, which averages only in time. Any signal above the background by a certain signal-to-noise ratio (SNR) threshold is counted as a potential detection. This is known as the classical constant false alarm rate (CFAR) detection. The result produces a time-series of all the observed peaks (real or not) identified by their range, range-rate towards or away from the radar, and bearing [2].

The software, PeakPicker, developed jointly by CODAR/Rutgers is the detection step. Long coherent processing (FFT) times yield high signal-to-noise ratios (SNRs) if the target's radial velocity is constant. However, if the target is changing velocity during the processing time, then the echo will be spread and SNR reduced; in this case, short FFTs are preferred [6]. Therefore, PeakPicker is set to process multiple FFT lengths consisting of both long and short FFT lengths. The association process takes all of the detection output and decides which detections range, range rate, and bearing are associated with a specific ship, clustering them for input to a tracker. The tracker then fits specific models for ship behavior (e.g. constant course and speed followed by a turning maneuver to a new constant course and speed) that enables both the past best fit and the projected track to be plotted on a computer screen [2].

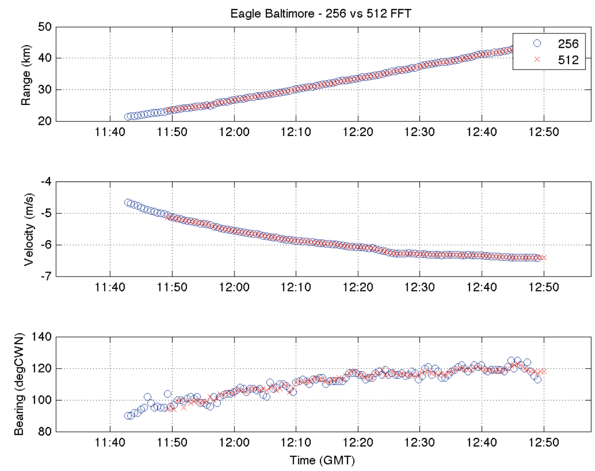

Figure 2: Detection data derived from CODAR SeaSonde Spectra data using separate FFT lengths of 256 and 512 seconds. These peaks were picked out because their SNR levels where above the pre-defined signal-to-noise ratio threshold.

III. RESULTS

A. Level I Association Algorithm

The first step of the association process is considered Level I association. In this process, detection data is sorted and combined as the detection files are created. This step eliminates the multiple looks at the same target and greatly reduces the number of false alarms, while providing more accurate target information and lower uncertainties. The two most accurate HF radar observables are range (backscatter or bistatic) and radial/elliptical target velocity. Suppose we have a high SNR peak at a given range/velocity from a given FFT/threshold/background at a given time. We define a search window in range/velocity space, and search through all combinations of FFT, threshold, and background at that time for the appearance of other detections within this window. The assumption is that these could be the same target. From this we have three aggregate samples of range, radial velocity, and bearing. Utilizing "maximum likelihood" methodology, all redundant, multiple looks of a single target are turned into a single "best estimate" [6]. Level I Association occurs in the CODAR software "ShipAssoc1" which outputs Level I Association ASCII (.asc1) files. Comparing Figure 3 and Figure 4, we can see that ShipAssoc1 reduced the total number of detections from 7115 to 2905**,** removing singular false detections and combining multiple detections of the same ship into one.

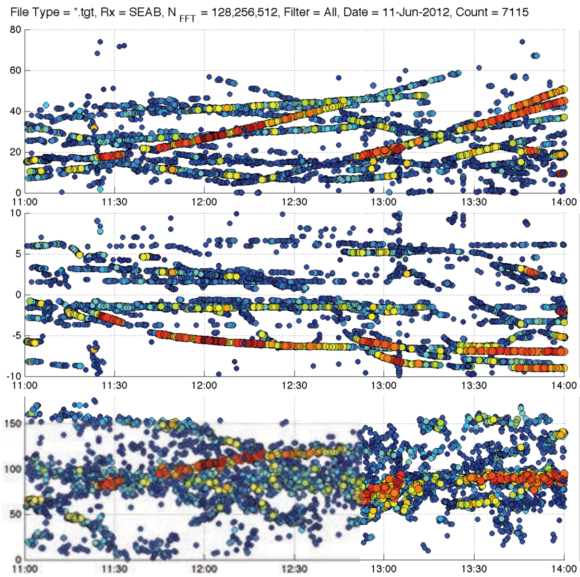

Figure 3: Raw PeakPicker data containing data derived from all FFT lengths using different SNR thresholds and background filters.

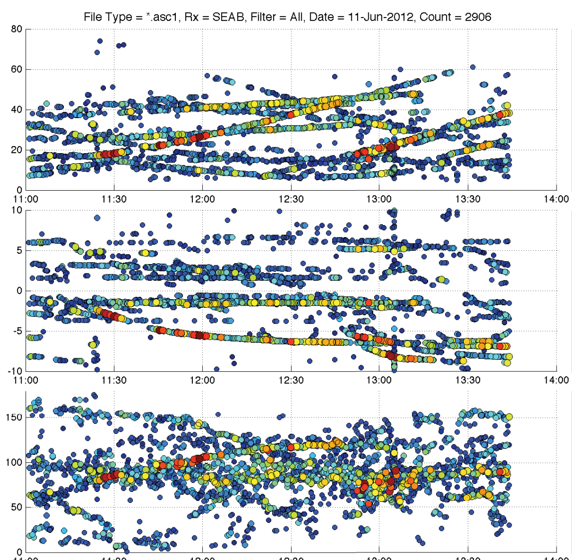

Figure 4: Level 1 Association Data. This data is the result of the input of PeakPicker TGT files into the ShipAssoc1 Level 1 Association Program.

B. Level II Association Algorithm

The Level I Associated ASCII files for each field site are sent to a central processing site, where Level II Association occurs. Level II Association combines multiple field sites, both backscatter and multi-static, to give Latitude/Longitude and x-y target velocity of the same targets as seen by multiple looks geometrically [6].

Currently, we are utilizing a Matlab script called “plot_all_matches” (PAM) which takes in both PeakPicker detection data and AIS data and correlates both of these datasets through time based on range and range rate to assist in our development of the Level II association algorithm. The output of PAM results in the range, range rate (velocity), and bearing plot in Figure 5. PAM can be run separately, one for each of the six background/FFT combination available, or all at once. Each time PAM is run it calculates an approximate percentage of time that PeakPicker successfully detected a given ship. If PAM is run with multiple background/FFT combinations, it calculates the ratio of each combinations contribution to the total detection percentage. This script creates text files that contain the peaks that were matched to ground truth AIS data. From these six text files, location data can be plotted on a map to show where certain background/FFT combinations detected the ship throughout its movement. The resulting text file from PAM is an important step allows us to know which peaks are confirmed to be ships.

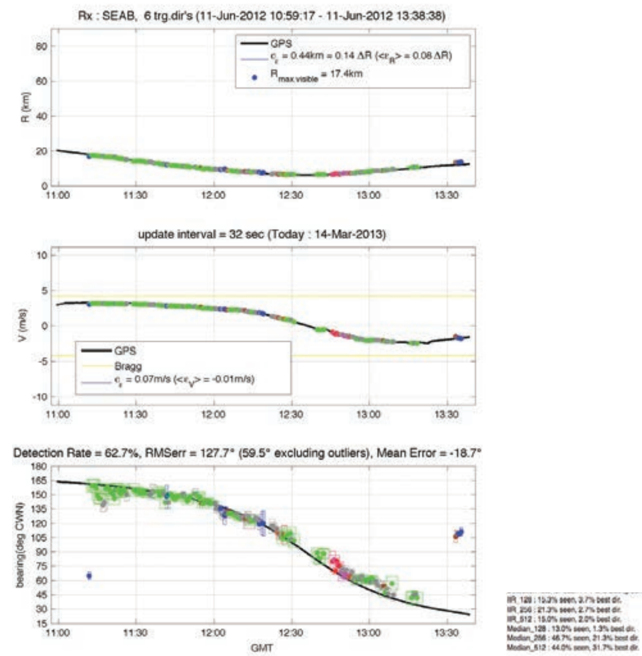

Figure 5: The result of plot_all_matches. Range and range rate derived from AIS data is correlated with vessel detection data. From this data, the percentage of time the PeakPicker software successfully detected a certain ship for each FFT length and background method can be calculated.

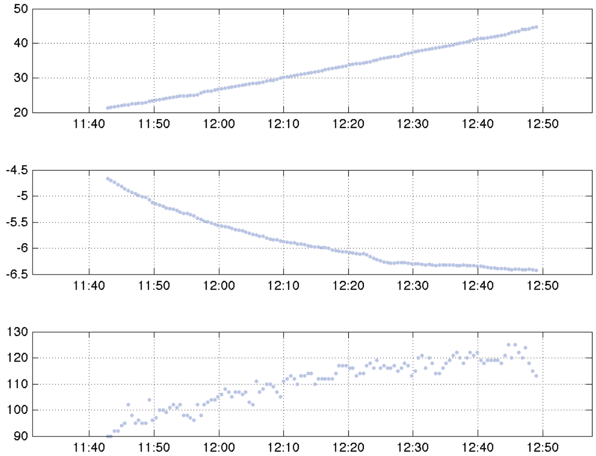

Figure 6: The text file output from plot_all_matches prints a file containing matching time, longitude, latitude, bearing, and error estimates.

The data output from PAM is extremely useful in developing new methods to implement in the Level II Association Algorithm. Our initial step towards Level II associations is by combining the results of PAM from different sites on a map. By combing all matched target detection data into one plot, we can see how each site performed when detecting a single ship and can calculate the ratio that each unique SeaSonde site contributed to the overall detection rate.

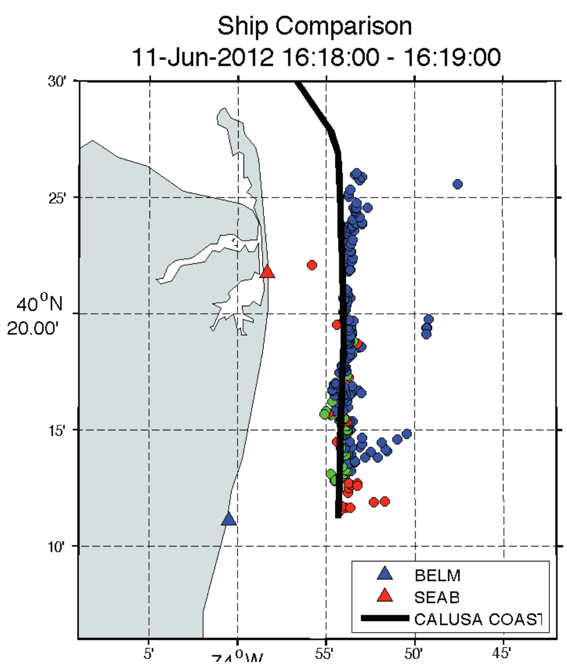

Figure 7: The Calusa Coast was detected on June 11, 2012 transiting from South Jersey and into New York Harbor. Multiple radar sites were able to successfully detect this ship as it moved along the coast.

When multiple HF radar sites are able to detect the same ship from different angles, we are able to estimate a third "overlap" location. In Figure 7, BELM detections are blue and SEAB detections are red. When both BELM and SEAB detect a specific ship at the same time, rings are drawn around the receiver site at the range where the detections are located. Where these two "range rings" overlap, a third "overlap" point is added to the map, shown as the green detection. This overlap point is typically closer to the actual location of the vessel at a given point in time, compared to each separate site. In Figure 8, the mean error of the overlap point locations is very low compared to the SEAB and BELM points. This shows that the overlap range ring points correlate well with the GPS locations.

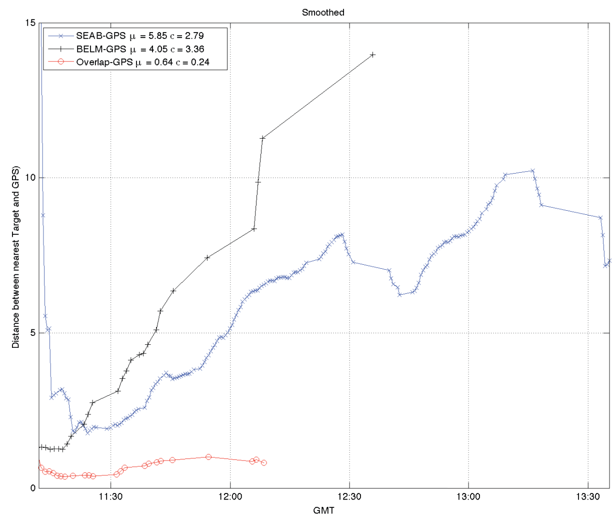

Figure 8: Distance between nearest PeakPicker Target and GPS location. The SEAB site (blue) had a mean error of 5.85 km and standard deviation of 2.79 km. The BELM site (black) had a mean error of 4.05 km and a standard deviation of 3.36 km. The overlap points (red) had a mean error of 0.64 km and a standard deviation of 0.24 km. The overlap points were considerably closer in distance to the GPS provided location of the vessel at a specific period in time than either sites detections.

We have investigated calculations utilizing the range error estimates contained in the PAM outputted text files in order to better define the area where a specific detection may be found. Our most promising work has been in creating a quadrilateral box around the center of detection (Figure 9). Four additional points are calculated from the initial point using the range errors in both the positive and negative directions. These four additional points create a quadrilateral box around the center of detection, giving us an area of detections rather than a specific location for a detection. The size of this quadrilateral changes based on the increase/decrease in range error. A smaller quadrilateral denotes more confidence in the data, while a large quadrilateral means less confidence. The quadrilateral points can be advantageous due the antenna pattern of the radars being frequently affected by the local environment around the radar. When an antenna pattern changes, the bearings that the system calculates become distorted, thus skewing the results.

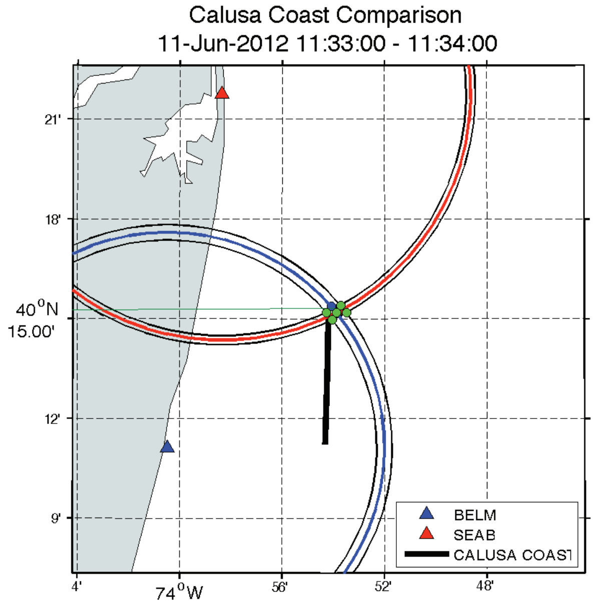

Figure 9: Quadrilateral box formed by intersecting range rings of Belmar (BELM) and Sea Bright (SEAB) sites. The black (range from receiver to target +/- range error) rings bordering both the red (SEAB) and blue (BELM) range rings intersect to create four green points that form the outline of the quadrilateral search box. The green point in the center of the box is the intersection point of the two colored range rings representing a detection from each site.

C. Future Level II Association Work

For future association work, we plan to investigate how well Probabilistic Data Association Filters (PDAF) and Kalman filters will work on PeakPicker vessel detection data. The PDAF will take all potential detections for association into a track and combine into a single statistically most probable update [7]. The Kalman filter takes the current known state (range, range rate, and bearing) of the target detections and predicts the new state of the target detections before the next radar measurement [8].

IV. Conclusion

The key to creating multiple unique vessel tracks lies not in the detection step, but rather the two subsequent association steps. The end goal is an algorithm that can quickly and efficiently sort through raw detection data while eliminating false detections. This occurs in two distinct steps. Level I association cuts down on false alarms and combines multiple targets into a "best estimate" target [6]. The algorithm for Level II associations is currently in development at Rutgers. At this time, Level II associations consist of running detection data through a Matlab script called plot_all_matches, which matches detection data to AIS locational data in range and range rate. The outputted matching data from PAM is then plotted on a map. As the plotting routine is running, new data points are created on the map where the "range rings" from two separate sites intersect. These new overlap data points are more accurate in location with respect to AIS data. The completed algorithm will build on our work presented in this paper.

Acknowledgements

This material is based on work supported by the U.S. Department of Homeland Security under Award No. 2008-ST-061-ML0001. The views and conclusions contained in this document are those of the authors and should not be interpreted as necessarily representing the official policies, either expressed or implied, of the U.S. Department of Homeland Security.

This work was funded by NOAA Award Number NA11NOS0120038 "Towards a Comprehensive Mid-Atlantic Regional Association Coastal Ocean Observing System (MARACOOS)". Sponsor: National Ocean Service (NOS), National Oceanic and Atmospheric Administration (NOAA) NOAA-NOS-IOOS-2011-2002515 / CFDA: 11.012, Integrated Ocean Observing System Topic Area 1: Continued Development of Regional Coastal Ocean Observing Systems.

References

[1] H.J. Roarty, E.R. Lemus, E. Handel, S.M. Glenn, D.E. Barrick, and J. Isaacson. "Performance evaluation of SeaSonde High-Frequency radar for vessel detection." *Marine Technology Society Journal*, Vol. 45, pp. 1-11, 2011

[2] H.J. Roarty, M.J. Smith, S.M. Glenn, D.E. Barrick, C. Whelan, E. Page, H. Statscewich, and T. Weingartner, "Expanding maritime domain awareness capabilities in the Arctic: High Frequency Radar Vessel Tracking, " in *Radar Conference, 2013. RADARCON 13. Proceedings of the 2013 IEEE,* 2013

[3] J. Harlan, A. Allen, E. Howlett, E. Terrill, S.Y. Kim, M. Otero, S. Glenn, H. Roarty, J. Kohut, J. O'Donnell, T. Fake, "National IOOS High Frequency radar search and rescue project," in OCEANS 2011, pp. 1-9, 2011

[4] A.J. Abascal, S. Castanedo, R. Media, I.J. Losada, and E. Alvarez-Fanjul, "Application of HF radar currents to oil spill modelling, " *Marine Pollution Bulletin*, vol. 58, pp. 238-248, 2009.

[5] J.T. Kohut, S.M. Glenn. "Improving HF Radar surface current measurements with measured antenna beam patterns." *J. Atmos. Oceanic Technol.*, Vol. 20, pp. 1303-1316, 2003

[6] H.J. Roarty, D.E. Barrick. "Requirements and recommendations for HF radar data association." Littoral Expeditionary Autonomous PowerBuoy Final Report 023

[7] Y. Bar-Shalom, E. Tse, "Tracking in a cluttered environment with probabilistic data association." *Automatica*, Vol. 11, Issue 5, pp. 451-460, 1975

[8] E. Brookner, Tracking and Kalman Filtering Made Easy. New York, NY: Wiley-Interscience, 1998.

The Role of Regional-Scale Ocean Observations for Improved Hurricane Intensity and Impact Forecasts in Coastal Regions

Scott Glenn, Greg Seroka, Travis Miles, Yi Xu, Hugh Roarty, Josh Kohut and Oscar Schofield
Rutgers University
New Brunswick, NJ 08901, USA
glenn@marine.rutgers.edu

***Abstract*— The coastal northeast United States was heavily impacted by hurricanes Irene and Sandy. Track forecasts for both hurricanes were quite accurate days in advance. Intensity forecasts, however, were less accurate, with the intensity of Irene significantly over-predicted, and the rapid acceleration and intensification of Sandy just before landfall under-predicted. By operating a regional component of the Integrated Ocean Observing System (IOOS), we observed each hurricane's impact on the ocean in real-time, and we studied the impacted ocean's influence on each hurricane's intensity.**

Summertime conditions on the wide Mid-Atlantic continental shelf consist of a stratified water column with a thin (10m-20m) warm surface layer (24-26C) covering bottom Cold Pool water (8-10C). As the leading edge of the Irene tracked along the coast, real-time temperature profiles from an underwater glider documented the mixing and broadening of the thermocline that rapidly cooled the surface by up to 8 C, well before the eye passed over. Atmospheric forecast sensitivity studies indicate that the over prediction of intensity in Irene could be reduced using the observed colder surface waters. In contrast, Hurricane Sandy arrived in the late Fall of 2012 after seasonal cooling had already deepened and decreased surface layer ocean temperatures by 8C. The thinner layer of cold bottom water still remaining before Sandy was forced offshore by downwelling favorable winds, resulting in little change in ocean surface temperature as Sandy crossed and mixed the shelf waters. Atmospheric sensitivity studies indicate that because there was little ocean cooling, there was little reduction in hurricane intensity as Sandy came ashore. Results from Irene and Sandy illustrate the important role of the U.S. IOOS in providing the best estimate of the rapidly evolving ocean conditions to atmospheric modelers forecasting the intensity of hurricanes. Data from IOOS may enable improved hurricane forecasting in the future.

***Index Terms*—Hurricane Forecasting, U.S. IOOS, Underwater Gliders, HF Radar, Ocean Modeling, Atmospheric Modeling.**

I. INTRODUCTION

Tropical storms are some of the most destructive and deadly weather phenomena on Earth, and have killed more people than any other natural catastrophe (Keim et al. 2006). For example, in the United States during the 20th-century, ten times as many deaths and >three times as much damage occurred from these extreme weather events as compared with earthquakes (Gray, 2003). The impacts are magnified given the human population density found along the coastlines that are prone to hurricanes. Despite the potential devastation, advances in technology, communication, and forecasting have resulted in significant declines in hurricane-related mortalities between 1900 and present day (Walker et al. 2006). Most recently these declines reflect the developments in global atmospheric models and an ensemble forecasting approach that have successfully reduced hurricane track forecast errors by factors of 2-3 over the last two decades, allowing communities sufficient time to proactively prepare for the storms and evacuate prior to their arrival. Despite the progress in predicting hurricane tracks, the predictive skill for hurricane intensity forecasts has remained "flat" over the last twenty years (Pasch & Blake, 2012).

This current state of the science was illustrated by the two recent hurricanes Irene and Sandy that devastated many communities along the Mid-Atlantic coastline spread over dozen states. Hurricanes Irene and Sandy struck dense population centers, and as a result, the National Hurricane Center's list of costliest hurricanes in United States history ranks Sandy second with over $60 billion and Irene eighth with over $15 billion in damages. Despite the epic scale of devastation, the loss of life was greatly minimized due to accurate forecasts of the hurricane tracks days in advance. Unfortunately, forecasts of hurricane intensity were less accurate, impacting efforts to proactively mitigate the damage. For Irene, the intensity was significantly over predicted by many operational hurricane models and overforecast by the National Hurricane Center, and for Sandy, the rapid acceleration and intensification just before landfall were under predicted. The over prediction of Irene's intensity in 2011 led to skepticism of the storm surge warnings for Sandy in 2012. To further complicate matters, the under predicted intensity of

978-1-4799-3646-5/14/$31.00 ©2014 IEEE

Sandy resulted in an under predicted storm surge that in some cases led to insufficient preparation.

The Mid-Atlantic Regional Association Coastal Ocean Observing System (MARACOOS), one of eleven Regional Associations comprising the regional component of the U.S. Integrated Ocean Observing System (IOOS), operates a Regional-Scale Coastal Ocean Observatory that includes coastal weather mesonets, satellite data ground stations, a 1000 km long High Frequency (HF) Radar network (Roarty et al., 2010), and a distributed fleet of autonomous underwater gliders (Schofield et al., 2010). Observatory data is assimilated into global and regional-scale ocean models, and an ensemble of regional atmospheric models beginning to use the ocean surface conditions as a boundary condition. The Regional-Scale Coastal Ocean Observatory was fully operating during both hurricanes. In this paper, we discuss selected highlights of real-time ocean data acquired by the MARACOOS regional-scale network during Irene and Sandy, and how the ocean forecasts faired. Through a series of atmospheric model sensitivity studies, the potential impact of accurate real-time ocean data and forecasts on hurricane intensity forecasts in the Mid-Atlantic is demonstrated.

II. Hurricanes Irene & Sandy

The Mid Atlantic Bight of North America was recently struck by two hurricane landfalls that devastated dense population centers and communities spread over a dozen neighboring states (Figure 1). Hurricane Irene, a category 1 storm offshore, tracked rapidly northward along the eastern seaboard in August of 2011, resulting in significant flooding on inland waterways due to torrential rains. Fourteen months later, Hurricane Sandy, a much larger category 2 storm offshore, made an uncharacteristic left turn and approached perpendicular to the coast in October of 2012, causing significant damage to coastal communities due to the extreme storm surge. Data from the Mid-Atlantic Regional Association Coastal Ocean Observing System (MARACOOS), one of eleven regional associations in the U.S. Integrated Ocean Observing System (IOOS), monitored the ocean response, and used that data to study the influence of the ocean on the intensity of both hurricanes.

Fig. 1. National Weather Service tracks for hurricanes Irene (purple) and Sandy (orange).

Hurricane Irene approached the Mid Atlantic's regional ocean observatory from the south. The real-time observations of the evolving ocean are described in the MARACOOS blog (Glenn et al., 2011). Irene's size was similar to the 1,000 km length scale of the region's HF Radar network (Figure 2) Strong storm-related winds were experienced for only 1 day. Winds initially came from offshore, turned to an alongshore direction as the eye passed, and continued turning to come from the coast after the eye moved north into New England. Most atmospheric hurricane models in the ensemble converged on the track forecast days in advance, but unfortunately, the intensity was over-predicted by the tropical model ensemble. Dire warnings of severe storm surges and damage at the beach were not realized. Because of the short duration of hurricane-forced winds, the relative timing between the high tide and the time of the most severe onshore currents for this rapidly moving storm were critical to determine the severity and location of the maximum storm surge. The severe damage from Irene instead occurred inland, where winds that picked up moisture over the warm ocean resulted in heavy rains and flood conditions along the Delaware, Hudson and Connecticut Rivers.

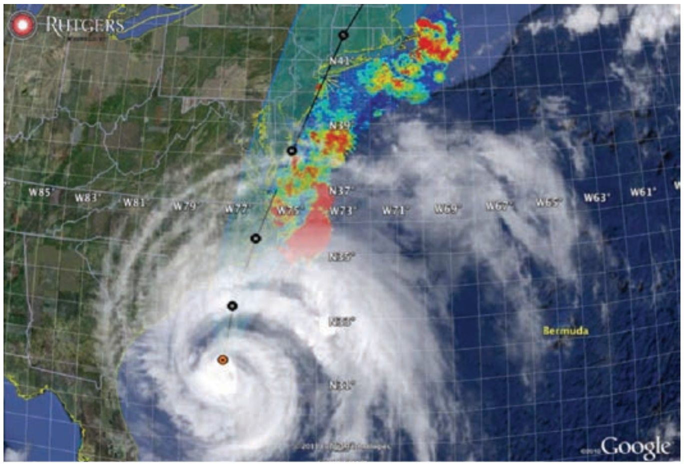

Fig. 2. Spatial extent of Hurricane Irene, August 27, 2011.

Hurricane Sandy approached the Mid-Atlantic's ocean observatory from offshore, perpendicular to the alongshore track of Irene. Real-time ocean observations were again described in the MARACOOS blog. The diameter of Sandy was twice as large as Irene, larger than the scale of the observatory (Figure 3). The approach direction had a significant impact on the areas with severe storm surge damage. North of the eye on the right hand side of the track, the counterclockwise circulation is in the same direction as the propagation. Here sustained winds from offshore that transported water towards the coast were experienced for multiple tidal cycles. South of the eye, winds blew from the coast and water was transported offshore. Compared to Irene, Sandy's size and slower movement over the continental shelf meant that several high tides were expected as Sandy came ashore. More important for Sandy was your location north or south of the eye, as damage was widespread in space and time.

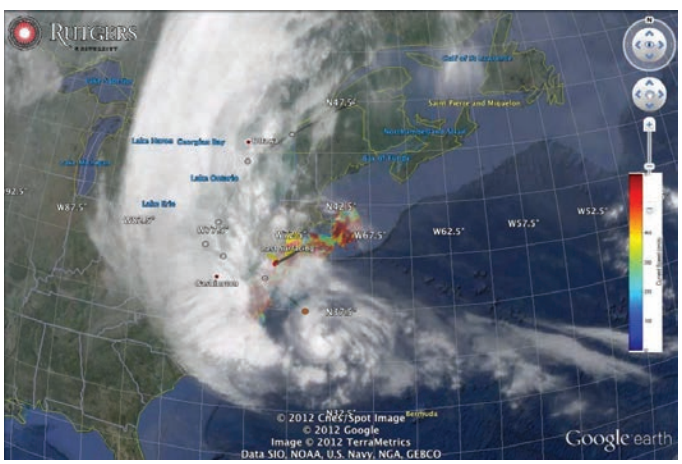

Fig. 3. Spatial extent of Hurricane Sandy, October 28, 2012.

III. WATER COLUMN MIXING IN IRENE

The eye of Hurricane Irene made landfall in southern New Jersey near Atlantic City about 0935 UTC on August 28, 2011. Irene was moving rapidly northward, fully crossing the state of New Jersey in about 6 hours. The rapidly evolving surface current response as Irene propagated along the New Jersey coast was observed (Figure 4) using the Mid-Atlantic's High Frequency (HF) Radar network (Roarty et al., 2010). At 0600 GMT, Irene's eye is still over water, with its location observed in the CODAR currents offshore southern New Jersey. Strong onshore currents over the entire width of the shelf are observed north of the eye. At 1200 GMT, the eye is over land in central New Jersey. The ocean currents have rotated to be along the coast to the northeast, and are reduced in speed. By 1800 GMT, the eye is over northern New Jersey. Currents behind the eye are again strong and offshore. The transition from strong onshore flow to strong offshore flow occurred over a short 6 hour period.

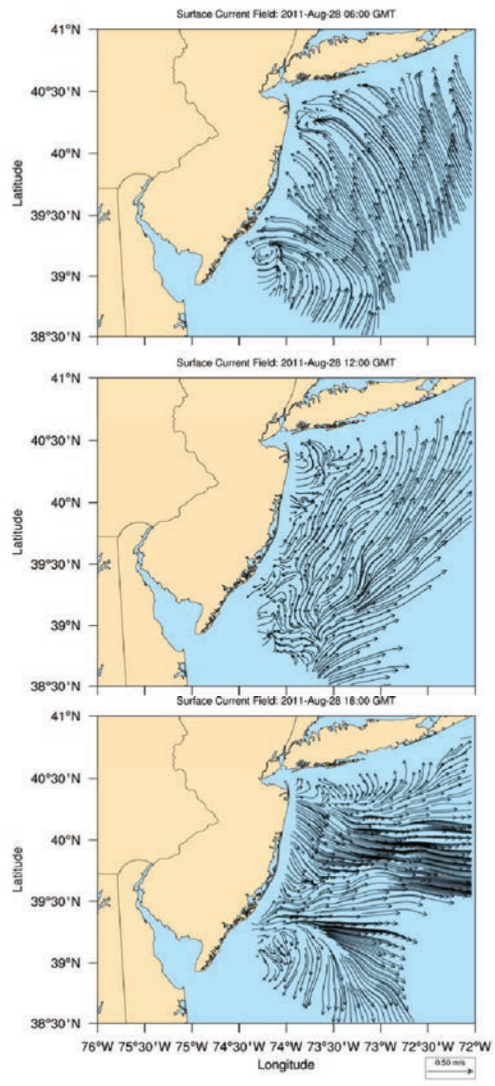

Fig. 4. CODAR-derived surface current spatial response as Irene tracks along the New Jersey coast.

Glider RU16 was deployed on the New Jersey shelf on a coastal survey mission well ahead of and independent of the hurricane. As Irene approached, the glider was purposely left at sea, but was moved offshore to the 40 m isobath to ride out the storm (Figure 5a) The 40 m isobath is an area of relatively uniform sandy sediment, and was considered far enough offshore that even strong hurricane currents faster than the glider's flight speed would not blow the glider onto the beach.

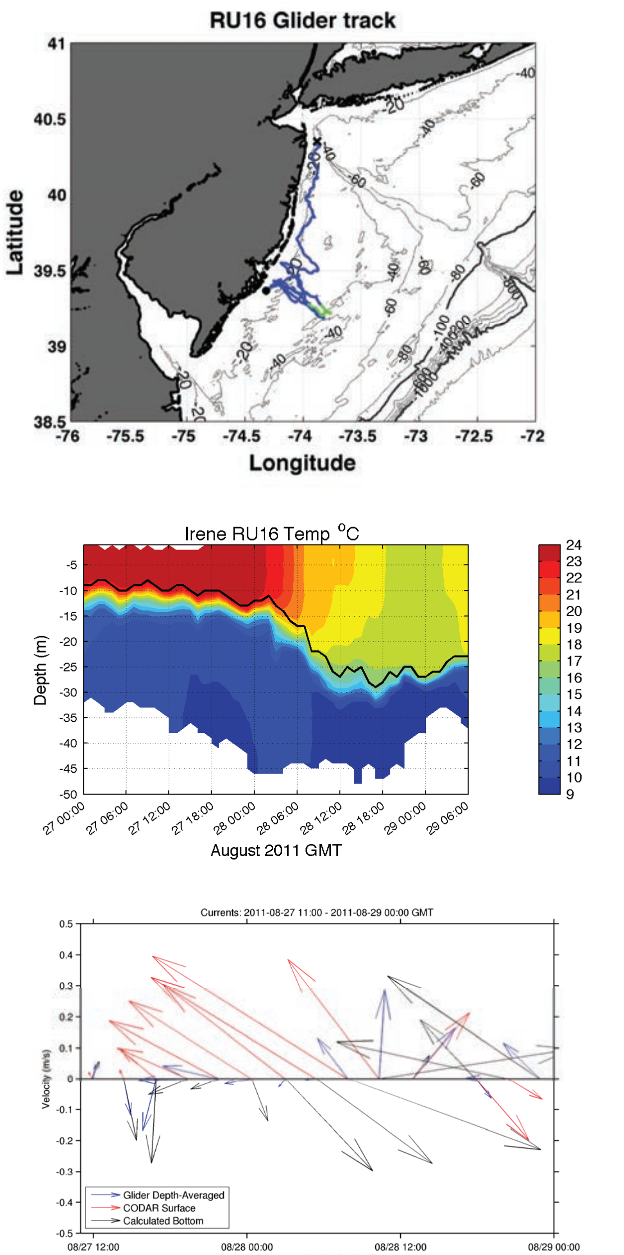

Fig. 5. (a) Glider track in Hurricane Irene. (b) Glider temperature section for the portion of the glider track marked in green. Black line is the depth of the surface mixed layer. (c) Glider depth averaged currents (blue), CODAR surface currents along the glider track (red), and inferred bottom layer currents (black).

The temperature section collected by the glider near the 40 m isobath during Irene (Figure 5b) indicates that on August 27, the Mid Atlantic shelf was near its peak summer stratification, with a thin 10 m thick layer of warm surface water near 22-25C, and a thicker layer of bottom "Cold Pool" water near 8-10C. The summer thermocline was typically sharp, with the transition from warm surface waters to bottom Cold Pool waters occuring in a few meters. As Irene approached, mixing within each of the surface and bottom layers made each layer more uniform and tightened the thermocline. On August 28, between 0000 GMT and 1200 GMT, as the northern edge of Irene passed over the location of the glider, the thermocline broadened (from less than 5 m to over 15 m) and deepened (from 10 m to 28 m), and the surface layer cooled (from 24C to 18C). After 1200 GMT, as the backside of the hurricane passed over the glider, the deeper thermocline remained near 25 m. Both the surface and bottom layers continued to cool independent of each other as the thermocline reintensified.

Gliders report the depth averaged current over the previous segment with each surfacing. The depth averaged current is estimated by comparing the dead reckoned surface location with the actual surfacing location, and assuming the difference is due to advection of the glider by the depth averaged current. During the hurricane, depth averaged currents are initially southward at 20 cm/sec before the storm, drop to near zero during the approach of the storm, and transition to northward at 30 cm/sec on the backside of the storm (Figure 5c). The important observation is that the depth averaged current is near zero between 0000 GMT and 1200 GMT on August 28 when the thermocline deepening and surface layer cooling is observed. Plotting the CODAR surface currents at the location of the glider, shows how the surface layer is being forced directly onshore to the northwest by the hurricane winds starting on August 27 and peaking during the deepening event. After 1200 GMT on August 28, the CODAR surface currents rotate clockwise to alongshore and then to offshore as noted in the spatial maps (Figure 4). Using the observed CODAR surface current to represent the average current above the thermocline, the average current below the thermocline was estimated based on the requirement that the weighted average of the surface and bottom layers equal the observed glider depth averaged current. Based on the estimated bottom layer current, the onshore transport in the surface layer begins midday on August 27 and for the first 12 hours, there is little response in the bottom layer. During this time the storm surge is expected to grow. Between 0600 GMT and 1200 GMT, as the onshore currents in the surface peak, the offshore currents in the bottom layer accelerate, resulting in zero net transport towards the coast. This time interval when the greatest shear between the surface and bottom layers is expected is precisely the time when the thermocline is observed to deepen. The zero net transport also implies that the storm surge that would have resulted from the shoreward transport of surface water is compensated by the offshore transport of bottom water.

The Regional Ocean Modeling System (ROMS) was operated in forecast mode during the storm. The model was rerun here using the same forecast parameters for more in depth studies. The ROMS forecast/hindcast of the ocean response has several features consistent with these observations that enable further definition of the physical processes responsible for the surface layer cooling. But there are also several differences between the observations and the model. The initial state of the ocean in the ROMS model (Figure 6a) has a 10 m thick surface warm surface layer near 24 C, and bottom Cold Pool layer near 9C, but the initial thermocline is wider than observed, extending over 15 m thick instead of less than 5 m. So the initial condition has a less extreme thermocline that would be more easily mixed than observed. Despite the weaker thermocline, significant mixing does not begin in the model until 6 hours later than the observations. The initial response is an acceleration of the alongshore currents to over 60 cm/sec to the northwest at 0000 GMT on August 28 (Figure 6c). The cross-shore currents, in the onshore direction at the surface and the offshore direction in the bottom, spin up simultaneously and peak at 0600 GMT. At this peak in shear, the thermocline starts deepening and the surface water starts cooling. In the model, this process ends in 6 hours, with the surface water cooling 5C and the bottom water warming 1C. At 1200 GMT, the alongshore surface current reverses direction consistent with the CODAR observations, the bottom jet relaxes in the cross-shore current but remains present in the alongshore current. The glider observations indicate that the bottom jet should have remained in the cross-shore direction.

While the exact details of the deepening of the thermocline and the cooling of the surface layer do not exactly match those observed, model diagnostics indicate that the vertical diffusion in the surface layer dominate advective changes in the model. This points to improvements in the mixing parameterizations as a place to look to improve the model. Even with a weaker thermocline, the mixing is insufficient to cool the upper layer as much as observed.

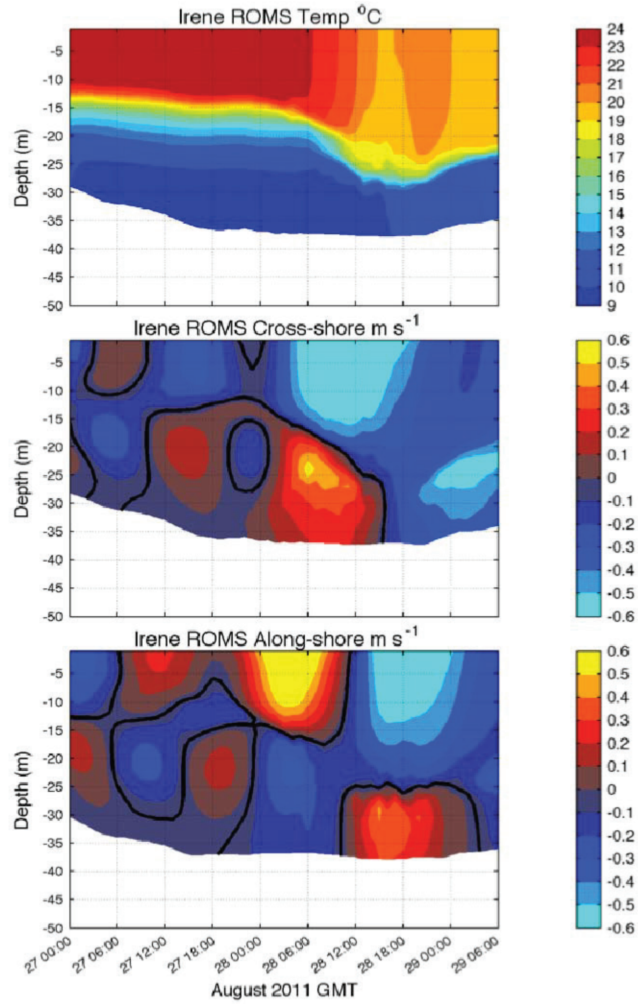

Fig. 6. Regional Ocean Modeling System (ROMS) hindcast of temperature, cross-shore (+offshore) and alongshore (+northeast) current sections along the green portion of the glider track in Figure 5a. Black lines indicate 0 cross and alongshore currents.

Satellite-derived Sea Surface Temperature (SST) maps of the Mid-Atlantic Bight just after Irene indicate that the cooling was widespread (Figure 7). The locally generated SST product (Figure 7a) indicates that surface temperatures dropped to as low as 14C on the shelf, with the greatest cooling observed over the historical location of the Cold Pool and concentrated on the mid to outer shelf, shoreward of the shelfbreak. The cooling was so significant, even though skies were clear after the storm, the cloud detection algorithms rejected the data as being too cold, removing it from the Real Time Global (RTG) SST updates (Figure 7b). As a result, the RTG SST map is essentially unchanged before and after Irene. Since the RTG map is the SST used by several atmospheric forecast models as a bottom boundary condition, the ocean used in the Irene forecasts was too warm. The difference between the RTG and the actual sea surface temperatures after the storm is as large as 10C (Figure 7c).

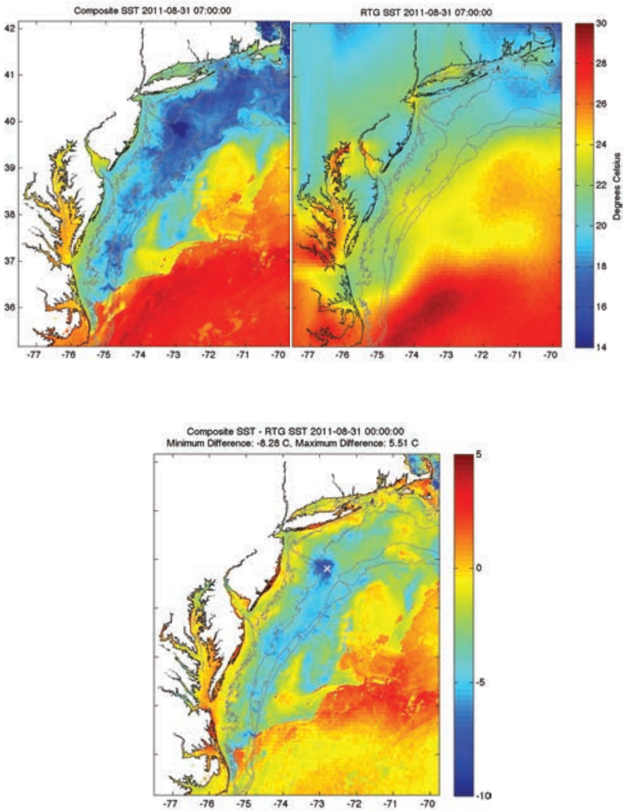

Fig. 7. Post-Hurricane Irene Satellite-derived Sea Surface Temperature (SST) products for August 31, 2011. (a) Locally composited SST showing the surface cooling. (b) Operational global SST product with the cool pixels incorrectly identified as clouds. (c) Difference.

The impact of the rapidly cooling SST on the Weather Research and Forecasting (WRF) model hindcast sensitivity studies of Hurricane Irene illustrates the significant impact of the cooler water. The glider data indicates that the cooling occurred ahead of the eye as the high winds of the outer wind bands approached. Thus the eye of the hurricane passed over cool water as it propagated northward. Since the RTG SST does not cool, it was used as the base case for comparison (Figure 8a). Since the ROMS model cools late and insufficiently, the locally composited SST product was used to simulate the change in SST as the storm passed. Starting with the warm pre-storm SST, the cold post-storm SST was applied everywhere at the time of peak mixing observed in the glider transect. The resulting WRF forecast is lower by 5-10 knots. (Figure 8b).

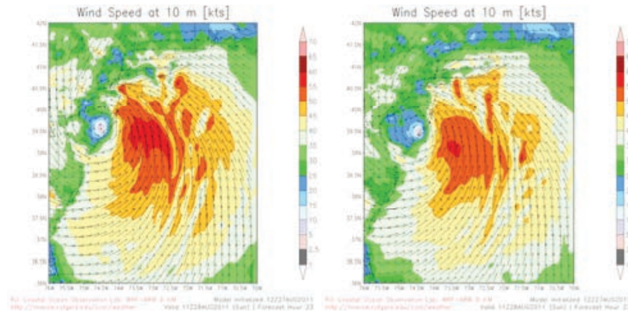

Fig. 8. Weather Research Forecast (WRF) atmospheric hindcasts of Hurricane Irene with different ocean boundary conditions. (a) Using the warm SST throughout the run. (b) Switching to the cold SST in Figure 7a when the cooling is observed in the glider data.

IV. Sandy

Hurricane Sandy followed Hurricane Irene by 14 months. Forecasts made by the European Center for Medium-range Weather Forecasting (ECMWF) alerted researchers to the possibility of a signficant storm hitting New Jersey a full week in advance. The importance of the glider observations in Irene prompted the deployment of glider RU23. Based on the lessons learned in Irene, the glider payload bay with its standard CTD was further equiped with optical sensors to look at the sediment concentrations as a tracer for mixing. A Nortek Aquadopp Acoustic Doppler Current Profiler (ADCP) was attached externally to examine the shear across the thermocline during the event. The glider was deployed nearshore with a small boat, and, as in Irene, was directed to fly to the 40 m isobath to ride out the storm (Figure 9).

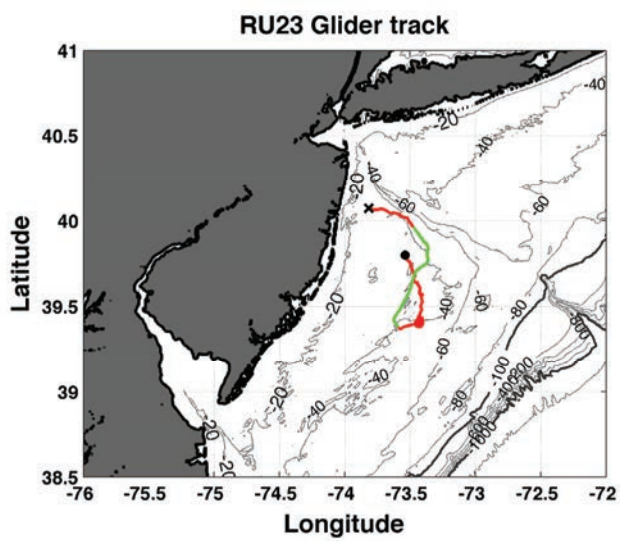

Fig. 9. Glider track during Hurricane Sandy.

Glider RU23 revealed that the initial ocean conditions for Hurricane Sandy were quite different than 14 months ago before Irene (Figure 10). The peak summer thermocline intensity observed in Irene was already 2 months into the fall transition. The two-layer structure was still present, but the surface layer had already cooled to 16C-17C, and thickened to a depth of 30 m. As usual, the bottom Cold Pool temperatures where observed to be around 9C-10C. Like Irene, the thermocline is again observed to be only a few meters thick. As Sandy approaches the coast, the increase in the thermocline depth is even more rapid than Irene, occuring within a few hours near 0600 GMT on October 29. After the deepening event, the water column is filled with a single surface layer, but the layer cooling is only 1 C from 16 C to 15 C. The glider data indicated that Sandy was going to make landfall propogating over SSTs that changed little from the pre-storm conditions. No ohterwise unobserved cooling to reduce intensity was expected.

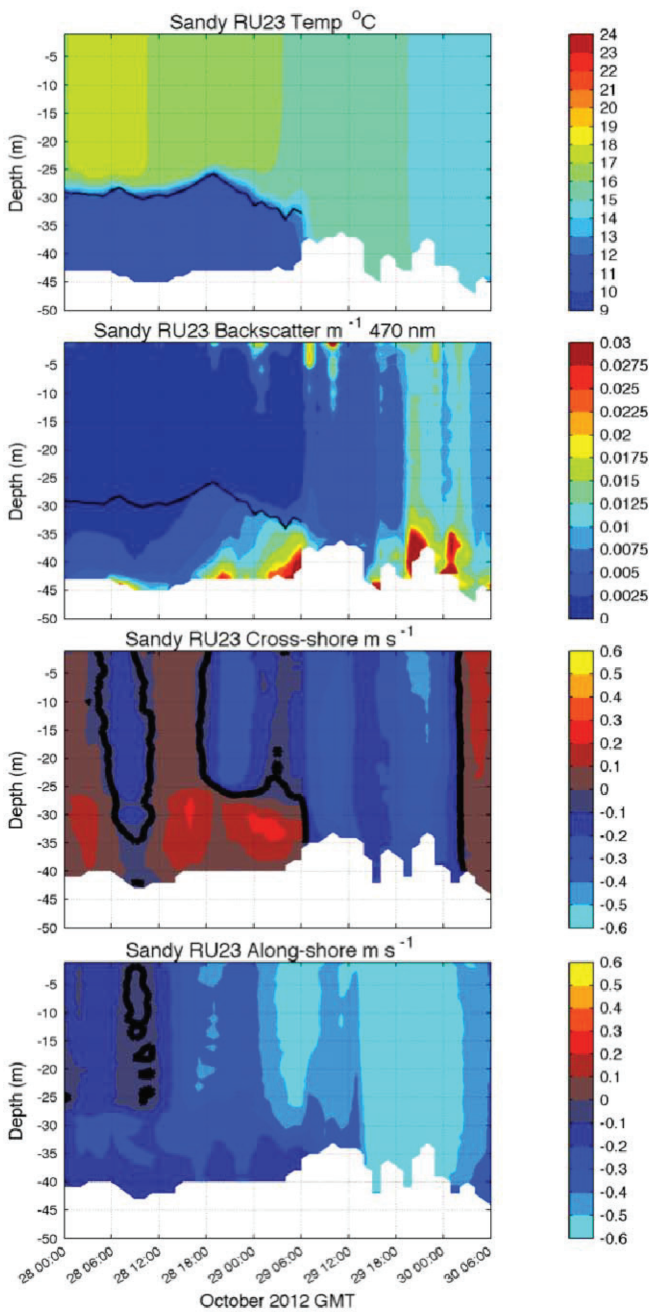

Fig. 10. Glider-derived temperature, backscatter, cross-shore (+offshore) and alongshore (+northeast currents for Hurricane Sandy.

The ocean model in Irene indicated the deepening and cooling of the surface layer, while inadequate, was dominated by a mixing processes. More extensive glider observations in Sandy indicate the layer deepening was likely dominated by an advective process. Optical backscatter in Sandy indicates that before the transition to a fully mixed water column, sediment suspended from the bottom did not cross the thermocline. After the transition to one layer, optical sensors indicate that sediment resuspension filled the water column, with a single mixed layer going from surface to bottom. Currents measured by the glider-mounted ADCP indicate that before the transition, a two layer flow was observed, especially in the cross-shore direction. A strong offshore jet formed in the bottom layer and persisted for over 18 hours before the transition as the water in the bottom layer thinned and moved offshore. Once the transition was complete, the water column responded as a single layer. Most significantly, the cross-shore current was onshore throughout the water column and persisted for two tidal cycles as the alongshore current accelerated to the southwest.

The same two SST products used in Irene were also examined in Sandy for August 27 (Figure 11). There is little pre-storm difference between the two SSTs, both maps have shelf temperatures in the 16C-18C range before the storm. Because Sandy was so extensive, and it was followed several days later by a northeaster that dropped snow on the damaged area, new SST products were not available for 11 days after the storm.

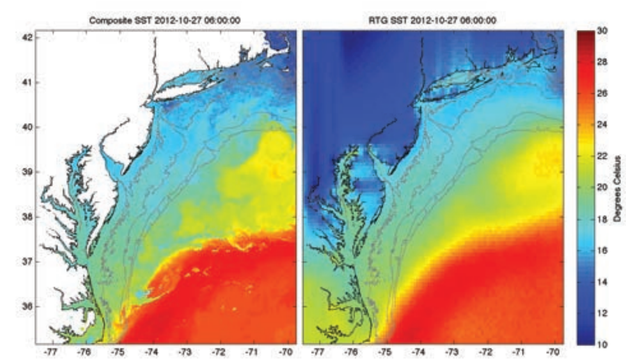

Fig. 11. Pre-Hurricane Sandy Satellite-derived Sea Surface Temperature (SST) products for October 27, 2012. (a) Locally composited SST. (b) Operational global SST product.

The Sandy observations indicated that there would be no significant cooling of the ocean surface layer as Sandy propagated shoreward. The WRF winds based on the conditions used in the real-time WRF forecasts, with atmospheric boundary conditions supplied by the National Centers for Atmospheric Prediction (NCEP) and ocean boundary conditions supplied by the locally composited SST are in Figure 12a. There is little sensitivity to the source of the SST, either the RTG or composite. Both result in an intensification of the storm as it makes landfall. The acceleration and intensification is significant, since the mean storm surge using operational products was under-predicted by 1 m in the hardest hit areas. Using the WRF model run in Figure 12a with the proper intensification and acceleration gains back significant portions of the missing meter in the mean storm surge as predicted by the New York Harbor Ocean Prediction System (NYHOPS) run by Stevens Institute of Technology.

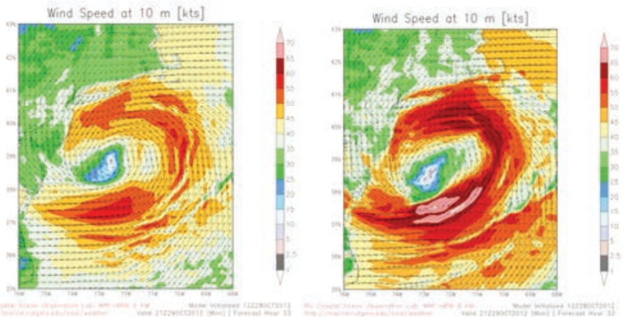

Fig. 12. Weather Research Forecast (WRF) atmospheric hindcasts of Hurricane Sandy with different ocean boundary conditions. (a) Using the cold SST from Figure 11a. (b) Using a warm SST characteristic of August conditions on the Mid-Atlantic continental shelf.

This series of model runs, while producing a hindcast that accurately recreates the observed storm surge, leaves unanswered the question of forecast sensitivity to SST in Sandy. If Sandy had hit earlier in the hurricane season during the peak summer stratification, would the forecast be sensitive to rapid changes in SST? As a test case, Sandy was rerun with typical August SSTs where, as in reality, it was assumed that no satellite updates to SST were available for over a week. The increase in forecast intensity at landfall is evident in Figure 12 b. Using these higher winds to force the NYHOPS storm surge model results in further increases in the predicted storm surge.

V. CONCLUSIONS

The back-to-back landfalls of hurricanes Irene and Sandy along the coast of New Jersey have hightened awareness of hurricanes and their potential impacts in the Mid-Atlantic. Irene's alongshelf track was accurately forecast but the intensity was over-predicted. Ocean observations by U.S. IOOS provide guidance as to why. Operational SST products did not pick up the 8-10C cooling caused by Irene even several days after the weather had cleared. An autonomous underwater glider that flew through the storm indicated that the cooling occurred rapidly as the leading edge of the hurricane approached and well ahead of the eye. Even if the operational SST products were reconfigured to pick up the cooling after the storm, they could not be applied in time to impact Irene. A more useful SST mapping product that accurately captures the timing and spatial extent of the cooling can only be supplied by an ocean forecast model. The ocean observations indicate what processes the ocean model must capture. Specifically, the initial thermocline must be better represented as the starting point. Second, the model must be 3-D, with a coast and a bottom. An infinitely deep 1-D model, one potential option for coupled atmosphere-ocean modes, will not capture the processes observed here. These include the initial onshore transport in the surface layer towards the coast, and the delayed response of the bottom layer to produce an offshore transport that limits the net shoreward transport. When there are two layers, the water transported onshore has an escape route through the bottom layer that appears to limit the storm surge. It also appears that the bottom layer also should be sufficiently thin for the offshore transport to produce a large shear across the interface. It is when this large shear is present that the mixing and cooling occurs.

Sandy occurred later in the year than Irene, after the fall transition was well on its way. Real time ocean observations during Sandy provided different guidance on what to expect when Sandy came ashore. The surface layer was already much thicker and cooler, so significant additional cooling was not expected. Advection moved what remained of the bottom Cold Pool offshore, removing the midshelf source of cool water. The water column responded as a single layer as Sandy came ashore, with mixing from surface to bottom, no cooling to reduce the intensity, and no bottom layer for the water in the growing storm surge to escape offshore.

The U.S. IOOS observations of hurricanes Irene and Sandy as implemented by MARACOOS for the Mid-Atlantic provided unprecedented real-time views of the evolving coastal ocean as the hurricanes made landfall in New Jersey. The observations led to new process studies in the ocean using numerical ocean models to examine the role of shallow topography, stratification and mixing that ultimately will lead to better ocean forecasts in extreme forcing conditions. New atmospheric sensitifivity studies further indicate that the rapid evolution of the ocean's surface layer temperature can have a significant impact on hurricane intensity. These results provide further evidence that one step towards improving hurricane intensity forecasting is to provide atmospheric modelers a better forecast of the rapidly changing coastal ocean beneath hurricanes.

ACKNOWLEDGMENT

Base support for this research was provided by the U.S. Integrated Ocean Observing System (IOOS) through the Mid-Atlantic Regional Association Coastal Ocean Observing System (MARACOOS). The Department of Homeland Security National Center for Secure and Resilient Maritime Commerce provided additional support for the HF Radar network. New Jersey Board of Public Utilities further augmented the satellite data products, the HF Radar network, and the atmospheric forecasting. The deployment and operation of Glider RU16 in Irene was funded by the Environmental Protection Agency and the New Jersey Department of Environmental Protection. The deployment and operation of Glider RU23 in Sandy was funded by graduate student grants from Teledyne Webb Research and Nortek.

REFERENCES

[1] S. Glenn, O. Schofield and J. Kohut, “Hurricane Irene 2011: Mid-Atlantic IOOS response to the hurricane”, http://maracoos.org/sites/macoora/files/downloads/Hurricane_Irene_blog_2011.pdf, pp. 65, 2011.

[2] W. Gray, 2003. Twentieth century challenges and milestones. In: Hurricanes! Coping with Disaster, R. Simpson, ed., American Geophysical Union, Washington, DC. 10.1029/055SP02.

[3] B. Keim, R. Muller and G. Stone, Spatiotemporal patterns and return periods of tropical storm and hurricane strikes from Texas to Maine, Journal of Climate, 20, 3498-3509, 2007.

[4] H. Roarty, S. Glenn, J. Kohut, D. Gong, E. Handel, E. Rivera, T. Garner, L. Atkinson, W. Brown, C. Jakubiak, M. Muglia, S. Haines, H. Seim, "Operation and Application of a Regional High-Frequency Radar Network in the Mid-Atlantic Bight" Marine Technology Society Journal, 44 (6), 2010.

[5] Pasch, R. and E. Blake, 2012. 2012 Review of the NCEP Production Suite: Report from NHC, National Centers for Environmental Predictions, Maryland, December 4, 2012,

[6] O. Schofield, J. Kohut, S. Glenn, J. Morell, J. Capella, J. Corredor, J. Orcutt, M. Arrott, I. Krueger, M. Meisinger, C. Peach, F. Vernon, A. Chave, Y. Chao, S. Chien, D. Thompson, W. Brown, M. Oliver, W. Boicourt, “A regional Slocum glider network in the Mid-Atlantic coastal waters leverages broad community engagement.” Marine Technology Society 44(6): 64-74, 2010.

[7] N. Walker, A. Haag, S. Balasubramanian, R. Leben, I. van Heerden, P. Kemp and H. Mashriqui, 2006. Hurricane prediction: A century of advances, Oceanography, 19(2), 24-36.

Assessment and quantification of HF radar uncertainty

Fearghal O'Donncha*, Sean McKenna*, Teresa Updyke†, Hugh Roarty‡ and Emanuele Ragnoli*
*IBM Research - Ireland
Email: feardonn@ie.ibm.com
†Old Dominion University
‡Rutgers University

***Abstract*—A large body of work exists concerning uncertainty in ocean current measuring high-frequency radar (HFR) systems. This study investigates the magnitude of uncertainty present in a HFR system in the lower Chesapeake Bay region of Virginia. A method of assessing the fundamental performance of the HFR is comparing the radial velocities measured by two facing HF radars at the centre point of their baseline. In an error-free network, radial vectors from the two sites would be equal and opposite at a point on the baseline, so the magnitude of their sum represents a measure of imperfection in the data. Often essential information lies not in any individual process variable but in how the variables change with respect to one another, i.e. how they co-vary. PCA is a data-driven modelling technique that transforms a set of correlated variables into a smaller set of uncorrelated variables while retaining most of the original information. This paper adopts PCA to detect anomalies in data coming from the individual HF stations. A PCA model is developed based on a calibration set of historical data. The model is used with new process data to detect changes in the system by application of PCA in combination with multivariate statistical techniques. Based on a comprehensive analysis the study presents an objective preconditioning methodology for preprocessing of HFR data prior to assimilation into coastal ocean models or other uses sensitive to the divergence of the flow.**

I. Introduction

The technology of measuring surface current by high frequency radar (HFR) has been rapidly expanding over the last decade [1], having been used to study nearshore circulation in a large variety of environmental conditions [2]–[6]. HFR allows measurement along the conductive sea surface for distances of up to 200km offshore at time intervals of 0.2-1h [7]. HFR systems have a number of unique advantages in terms of the observation of coastal ocean dynamics. These include: providing real-time data over large ocean areas at relatively low cost; enabling two-dimensional mapping of surface currents at resolutions that capture the complex structure related to coastal bathymetry and the intrinsic instability scales of the coastal circulation; as systematic input to operational ocean models via data assimilation [8]; while HFR systems can also play a role in environmental monitoring and event response systems.

A large body of work exists concerning uncertainty in ocean current measuring HFR systems. A study by Emery et al. (2004) [9] comparing HFR and moored current meters in the Santa Barbara basin indicated rms differences of $7-19cm/s$. In a similar study by Essen at al. (2000) [10], the accuracy of HFR was assessed by comparison with in situ current meters. RMSD were in the range of $10-20cm/s$; however, the theoretical error of the HFR based on the sea state was estimated to only be in the range $3-10cm/s$. The rest was assumed to be due to differences in the quantities measured, e.g. the spatial averaging, point in water column at which measurement recorded, etc.

Much of this work, however, focuses on direct comparisons of radar observation versus an alternate sensor measurement, be it ADCP, drifters or other current measuring instruments. However, these comparisons introduce inherent complexities due to additional errors being introduced from the second sensor and also what is termed target difference: discrepancies between both sensors due to the HFR typically measuring different spatial and temporal scales. This study aims to isolate individual errors in a HFR system; quantify the magnitude of the error in a historical dataset; and finally, develop a transportable algorithm that can be used to establish the uncertainty in a real-time measuring system.

This paper describes research conducted by the authors in assessing HFR uncertainty and the definition of a preconditioning technique to lessen the impact of potential errors on operational applications. A detailed dataset of HFR observed currents was collected at 60 minute intervals for a 12 month period (2012) encompassing a wide range of environmental conditions. This dataset is used to provide insight into error magnitudes associated with HFR systems. A multivariate analysis procedure, Principal Component Analysis (PCA) is used to detect anomalous measurements and reconstruct the data with a reduced number of modes.

The approach adopted by the authors is presented in the section on methodology; this section includes a description of both the HFR system and the PCA methodology. The process of reconstructing the data is described and the validation of the technique against new data discussed. The section on results presents a quantitative investigation of HFR error ranges; the viability of using PCA to identify and reduce anomalous data measurements is discussed. Finally, conclusions from this research are drawn and the recommendations for future research made.

978-1-4799-4918-2/14/$31.00 ©2014 IEEE

II. METHODOLOGY

High frequency (HF) radar surface current data were provided by three radar systems located in the lower Chesapeake Bay region of Virginia. Figure 1 presents the geometric configuration of the three sites. These radar stations operate at 25 MHz and are a part of the Mid-Atlantic Regional Association Coastal Ocean Observing System (MARACOOS). At each site, radial current velocities were determined following the method described in Lipa et. al. (2006) [11]. Radial maps were generated with velocity vectors placed in 1.5 kilometre range bins and 5 degree directional bins. Radial processing algorithms utilized antenna response patterns measured at VIEW and CPHN stations. An ideal antenna response pattern was assumed at SUNS. Hourly surface current maps were produced by a standard un-weighted least squares method of combining radial data from individual radar sites onto a defined grid [12]. The grid in this case was a nominally 2 kilometer spaced grid developed by the U.S. National HF radar network [13]. Vector measurements returned hourly data and the data covered a one year period, January - December 2012 (8784 hours).

The study investigates a number of techniques to elucidate the inherent uncertainty of the system. As a means of assessing the fundamental performance of the HFR, analysis compares the radial velocities measured by two facing HF radars along their baseline. This serves to localise data uncertainty as the target difference is negligible if, both, the comparison is made at the middle of the baseline and the electromagnetic wave frequencies of the two sensors are the same. In an error-free network, radial vectors from the two sites would be equal and opposite at a point on the baseline, so the magnitude of their sum represents a measure of imperfection in the data.

Often essential information lies not in any individual process variable but in how the variables change with respect to one another, i.e. how they co-vary. PCA is a data-driven modelling technique that transforms a set of correlated variables into a smaller set of uncorrelated variables while retaining most of the original information. The first principal component accounts for as much of the variability in the data as possible, and each succeeding component accounts for as much of the remaining variability as possible.

In computational terms the principal components are found by calculating the eigenvectors and eigenvalues of the data covariance matrix. In the case of vector observation (HFR velocities in the horizontal plane), it is convenient to represent the flow as complex number $\vec{u} = u + iv$, where u and v are the zonal and meridional components of flow respectively. The data matrix (X) is constructed where each row is one map of HFR measurements and each column is a time series of observations for a given location. The data are detrended so that each column has zero mean, the covariance matrix computed by calculating $R = X^T X$, and then we solve the eigenvalue problem

$$RP = P\lambda \tag{1}$$

λ is a real diagonal matrix containing the eigenvalues λ_i of R. The p_i column vectors of P are the eigenvectors of R corresponding to the eigenvalues of λ_i.

For each eigenvalue λ_i chosen we find the corresponding complex eigenvector p_i. Each of these eigenvectors can be regarded as a map. These eigenvectors are the principal components (PC) of the data. Each eigenvalue λ_i gives a measure of the fraction of the total variance explained by the mode. This fraction is found by dividing the λ_i by the sum of all the other eigenvalues.

The pattern obtained when an eigenvector is plotted as a map represents a standing oscillation. The time evolution of an eigenvector shows how this pattern oscillates in time. To see how PC_1 'evolves' in time we calculate

$$\overrightarrow{t_1} = X\overrightarrow{p_1} \tag{2}$$

The n components of the vector $\overrightarrow{t_1}$ are the projections of the maps in X on PC_1, and the vector is a time series for the evolution of PC_1. In general for each calculated PC_j, we can find a corresponding $\overrightarrow{a_j}$. These are the *principal component time series* or the *expansion coefficients* of the PCs. Just as the PCs were uncorrelated in space, the expansion coefficients are uncorrelated in time. We can reconstruct the data from the PCs and the expansion coefficients:

$$X = \sum_{j=1}^{p} \overrightarrow{a_j}(p_j) \tag{3}$$

A common use of PCA is to reconstruct a cleaner version of the data by truncating this sum at some $j = N << p$, that is, we only use the PCs of the few largest eigenvalues. The rationale is that the first N eigenvectors are capturing the dynamical behaviour of the system.

III. RESULTS

A. Baseline Comparisons

Prior to more detailed comparisons, a direct comparison of the radial velocity measured by the individual radar station along the baseline between sites is investigated. Previous studies have demonstrated significant differentials when baseline radial values are compared away from the central region due to disparate horizontal averaging scales within the radial cells [14], [15]. In this study, a midpoint between the two radars is selected and all radial measurement within a 1km radius of that point gathered from both sites.

Figure 1 presents the geometry of the radar sites and baselines. Figure 2 shows scatterplots of hourly radial velocities at the midpoint of SUNS–CPHN (top), SUNS–VIEW (middle) and CPHN–VIEW (bottom). All statistics were computed for a one month period in December 2012. The solid line is the regression line obtained from the principal component analysis (PCA) which minimizes the sum of the square distance from the point (x, y) to the regression line $(y = Ax + B)$. PCA is particularly suitable for this analysis because it provides the symmetric regression line with respect to the two variables in scatterplots, as opposed to other measures of regression such

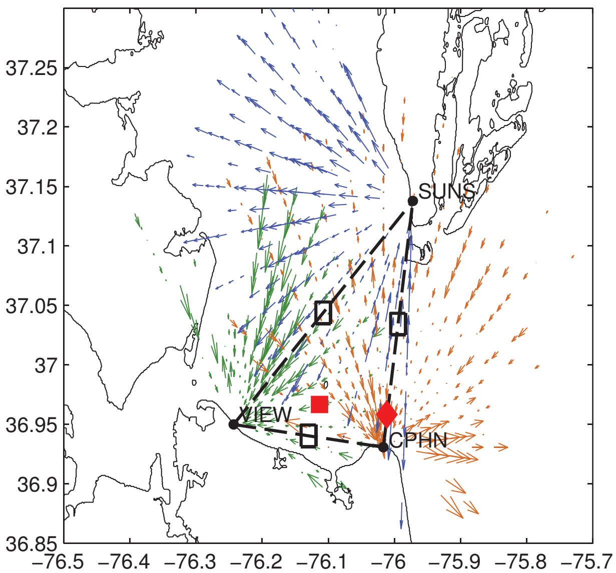

Fig. 1: Radial current synoptic vector map along with the baseline between HF radar sites along and the mid-point sampling region where radial values were compared (black rectangle). The red diamond and rectangle denotes the location of ADCP and weather station, respectively, used for the study.

as ordinary least squares which are more suitable for predictor-observed comparisons. In addition, rms distances from the regression line can be readily computed as an estimate of the uncertainty in the radar. The regression coefficients (A and B), correlation (COR), root-mean-square differentials (RMS), and number of samples (NUM) are also presented.

Good agreement is observed between two of the radar pairs (namely, SUNS–CPHN and SUNS–VIEW) reflected in correlation scores of 0.81 and 0.84 respectively. The baseline between SUNS–VIEW demonstrates very high agreement with regression coefficients of $(A = 0.91, B = -3.23cm/s)$. Regression line coefficients from the SUNS-CPHN site $(A = 0.61, B = 2.46cm/s)$ suggests that the variance from the SUNS site is almost 40% greater than the CPHN site. The relatively high rms figures between these sites further illustrates this. These agreement metrics are similar to comparable studies in other HFR systems. In comparisons of four baseline geometries in the Monterey Bay region, Paduan et al. [16] observed a linear regression relationship ranging in slope from 0.63 to 0.98, while correlation coefficients ranged from $0.6 - 0.8$. Similar analysis of HFR accuracy in the Tsushima Strait [15], observed correlation in the range of 0.63 - 0.88 was returned while the RMS varied between $5.75 - 13.71cm/s$.

Baseline comparisons between CPHN–VIEW provides an interesting contrast. There is no evident agreement between values measured by the facing radar stations. Further investigation of this identified the cause to be a thin strip of land approximately 600m long beside the CPHN station over which the baseline HFR signal travels before reaching open water. This serves to distort the signal in this direction and result in contaminated data measurement.

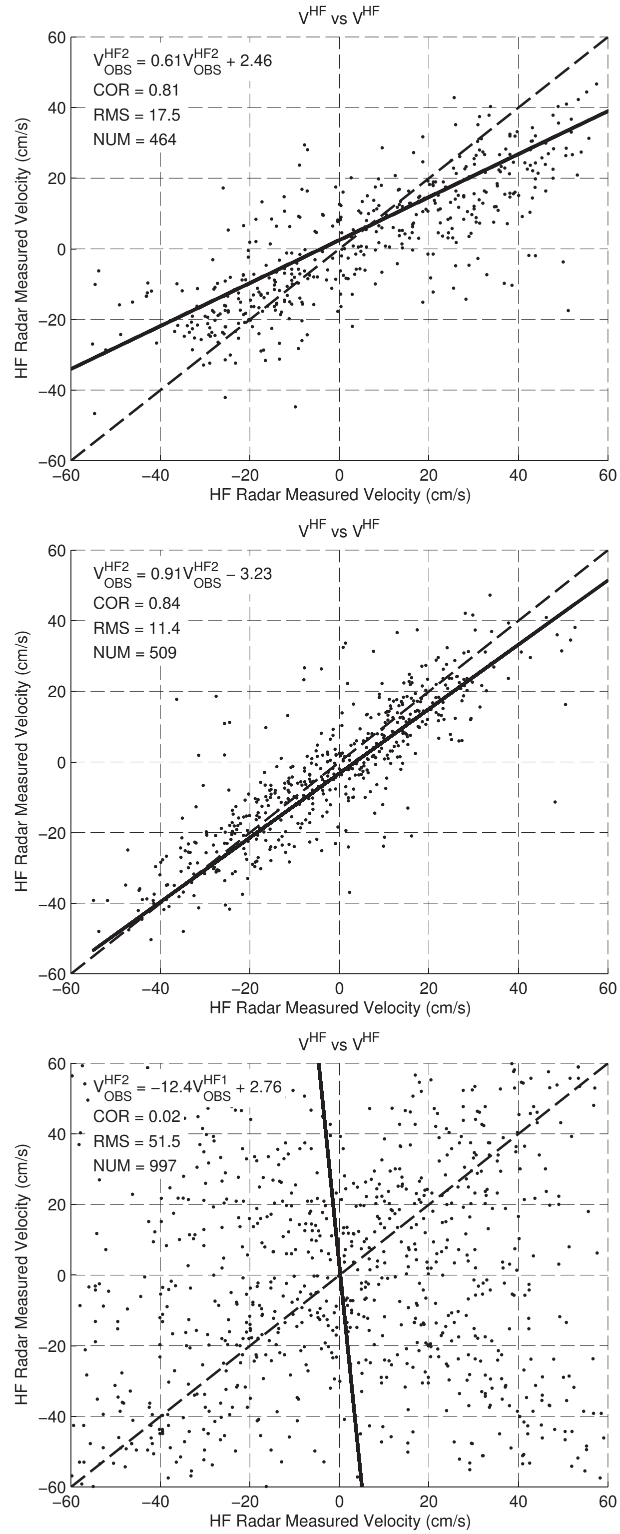

Fig. 2: Scatter plot of radial measurements from the three radar sites, SUNS–CPHN (top), SUNS–VIEW (middle) and CPHN–VIEW (bottom) (see Figure 1) along their baseline are presented. The solid line denotes the linear regression computed from Principal Component Analysis. Radial measurements returned at 30 minute intervals from the CPHN and VIEW stations while SUNS operated at 60 minute intervals.

This analysis highlights the inherent uncertainty present in HFR systems. In addition the CPHN–VIEW comparison demonstrates the additional complexities involved and one of the many factors that may impact on measurement accuracy of a remote sensing installation. The next section investigates this uncertainty further and discusses techniques to identify and eliminate these measurement errors.

B. PCA

First analysis of HFR data focused on a two month period June-July 2012. This time window was chosen since it was hypothesised that flows would be at their most stationary during this period avoiding both energetic winter storm events and high river outflows during spring ice melts. As common with sensor data percent coverage varies considerably over the course of the study period. Gaps in the data need to be accounted for prior to the application of PCA. Two approaches were adopted:

- Only data from grid cells that returned data $> 60\%$ of the time was used.
- Missing data in remainder of cells are interpolated from neighbouring grids using standard linear interpolation technique.

The PCA method was then applied to the data as described in section II.

Figure 3 presents the spatial patterns of the first three PCs for the time period June-July 2012 while Figure 4 displays the associated time expansion coefficients. Cumulatively, these 3 PCs account for 74% of the total variance. Mode I is the most dominant mode accounting for 54% with mode II and III accounting for 13% and 7% respectively.

The consistent direction of flows in PC_1 along with the high proportion of variance explained suggests it to be connected with tidal flows in the region. To investigate this hypothesis further, PC_1 was compared with an independent estimate of the tidal signal. To estimate the tidal signal, data from an Acoustic Doppler Current Profiler (ADCP) located in the Southern Region of the inner-Bay was used (red diamond in Figure 1). The ADCP data were processed via the t_tide software [17]; this decomposed the data into its harmonic (tidal) and residual component. In conjunction with this the HFR flow was reconstructed using PC_1 only from the grid cell nearest the ADCP location. Figure 6 presents time series plot comparing the two datasets. The tidal signal is clearly evident within the reconstructed data displaying close agreement with the extracted tidal signal.

It is reasonable to expect subsequent PCs to be closely related to wind forcing in the bay. Correlation coefficients between PC_2 and measured wind speeds from a weather station located at the Chesapeake Bay Bridge Tunnel (Figure 1) however, did not provide significant correlation. Computing a complex correlation coefficient [18] between the two vector time series (wind speed and flows reconstructed with PC_2 only) returned a correlation of 0.28 (where 0 indicates no correlation and 1 represents perfect agreement) with higher

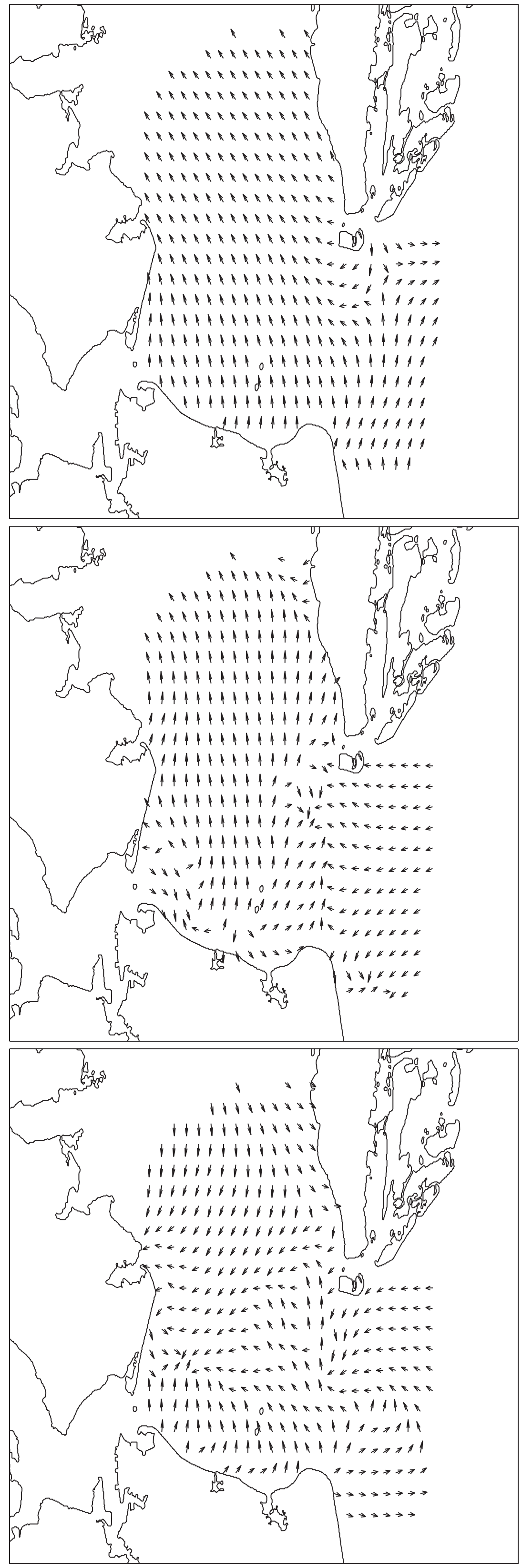

Fig. 3: PC spatial map patterns for modes I(top), II(middle) and III(bottom)

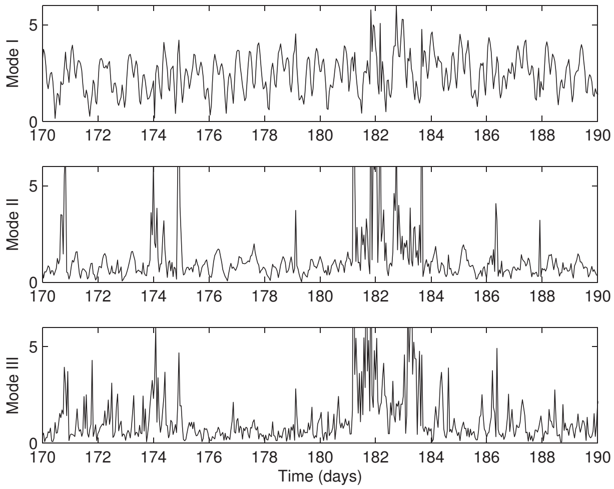

Fig. 4: First three principal component expansion coefficients computed for June-July period (20 day window presented for display purposes). The modal amplitudes are normalized by their respective standard deviations.

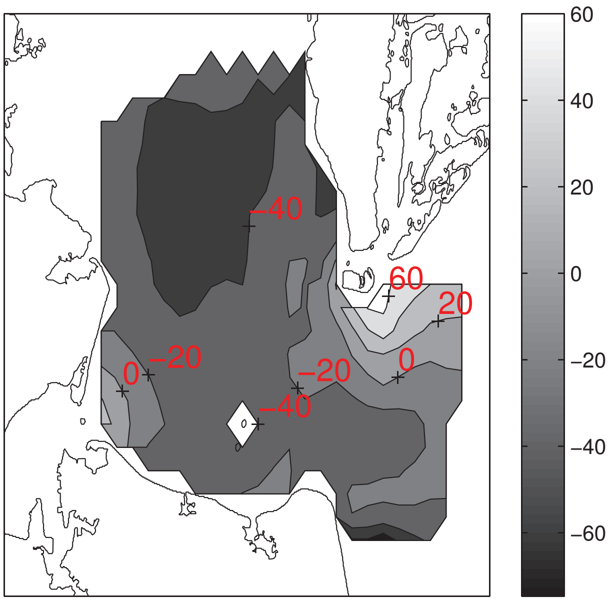

Fig. 5: Average counterclockwise angle derived from correlation computations between wind speed and PC_1 of the low pass filtered HFR dataset.

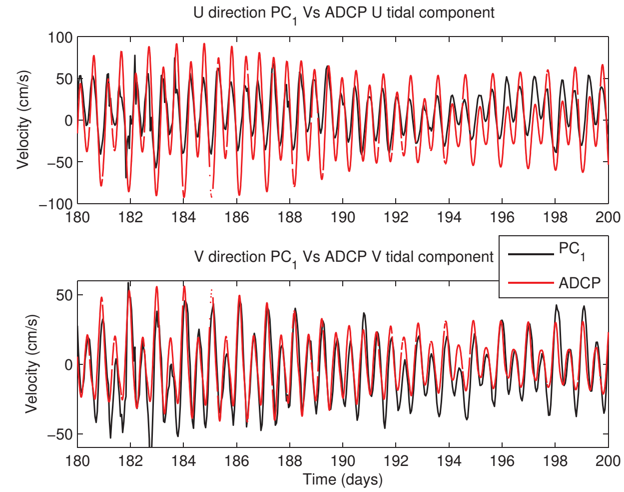

Fig. 6: Plotting flows reconstructed from the first principal component only against the estimated tidal signal in the bay. Flows reconstructed for the HFR grid cell closest to the ADCP probe. The tidal signal is computed by applying a harmonic analysis to the near-surface ADCP data from the Chesapeake Bay Bridge Tunnel.

agreement observed in the North-South direction when investigating correlation independently in the zonal and meridional direction.

Analysis of the temporal evolution of the principal components (Figure 4) indicates this to be a result of the residual presence of tidal signal in this PC. To permit analysis of the signal distinct from the tidal component we returned to the original HFR data and low-pass filtered using a cosine-Lanczos filter with a 40-hr halfpower point [19] to remove the tidal signal from the data. Applying PCA to the filtered data gives insight into variability in the bay excluding the dominant tidal signal. The expectation in this case was that PC_1 would be primarily a result of wind effects. Recomputing complex correlation between PC_1 and measured wind speeds returned a value of 0.73 with this mode accounting for 50% of the total variance of the filtered data. The PC pattern associated with this mode is presented in Figure 7. The phase angle of the complex correlation coefficient, by definition, gives a measure of the average counterclockwise angle of the second vector (wind speed) with respect the first. Figure 5 presents the phase angle of correlation. Analysing the figure suggests reasonable agreement between angle of flows and wind forcing. In the outer bay, the angle is quite close to zero while in the inner bay the discrepancy is plausibly a result of topographical steering of the flow as it enters the bay and is directed Northwards into the bay.

The development of a PCA model that is representative of the raw data while excluding high frequency "noise" has two important considerations

- the number of PCs to include in the reconstruction
- the choice of temporal window width to which to apply the linear technique

The choice of number of PCs to retain is often times empirical and case specific. The simplest criterion is to retain enough PCs to represent a sufficient fraction of the total variance. Jolliffe [20] suggests the range of fractional variance between 0.7 and 0.9 may be a reasonable range. Applying total variance explained cut off points of 70, 90 and 95% results in retaining 2, 12, and 29 PCs respectively

Another subjective approach is based on the shape of the graph of the eigenvalues. The method looks for a "knee point" in the residual percent variance (RPV) plotted against the

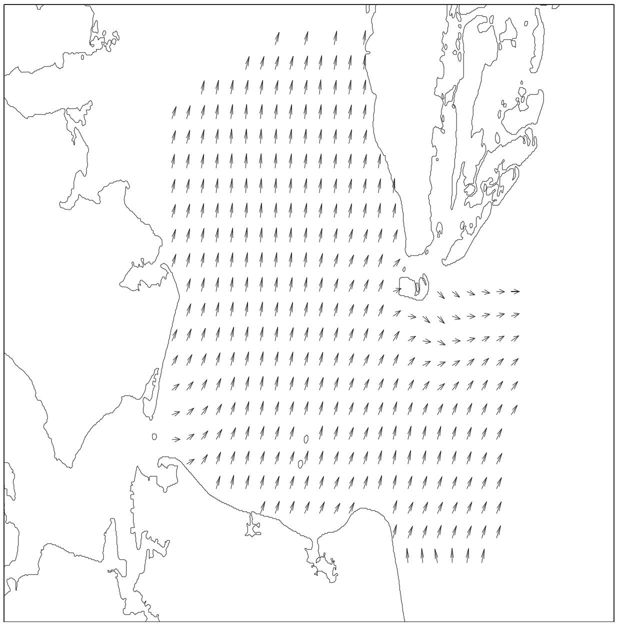

Fig. 7: PC spatial map patterns for modes PC_1 when the raw data is low-pass filtered prior to the application of PCA.

number of principal components. The method is based on the idea that the residual variance should reach a steady state when the factors begin to account for random errors. When a break point is found or when the plot stabilizes that corresponds to the number of principal components to represent the process. The RPV is computed based on residual eigenvalue:

$$RPV(k) = 100 \left[\frac{\sum\limits_{j=k+1}^{m} \lambda_j}{\sum\limits_{j=1}^{m} \lambda_j} \right] \% \qquad (4)$$

Analysing graph of the RPV (not presented) suggests that steady state develops after 7 PCs.

An alternative criterion dictating which principal components to retain is the Guttman-Kaiser criterion [21]: Principal components associated with eigenvalues that are larger in magnitude than the average, $\overline{\lambda}$, of the eigenvalues or, better, a somewhat lower cut-off such as $\lambda^* = 0.7\overline{\lambda}$, are retained. Applying these criterion to this dataset would retain 20 and 25 of the principal components respectively. North et al. [22] argue that a set of principal components with similar eigenvalues should either be all retained or all excluded. The size of gaps between successive eigenvalues is thus an important consideration for any decision rule, and North et al. (1982) [22] provide a rule-of-thumb for deciding whether gaps are too small to split the principal components on either side. The rule states that if the sampling error of a particular eigenvalue $\lambda \left[\partial\lambda - \lambda \left(\frac{2}{N}\right)^{1/2} \right]$ is larger than the spacing between λ and a neighbouring eigenvalue, then the associated PCs will have comparable sampling errors. This implies that these eigenvectors are a random mixture of the

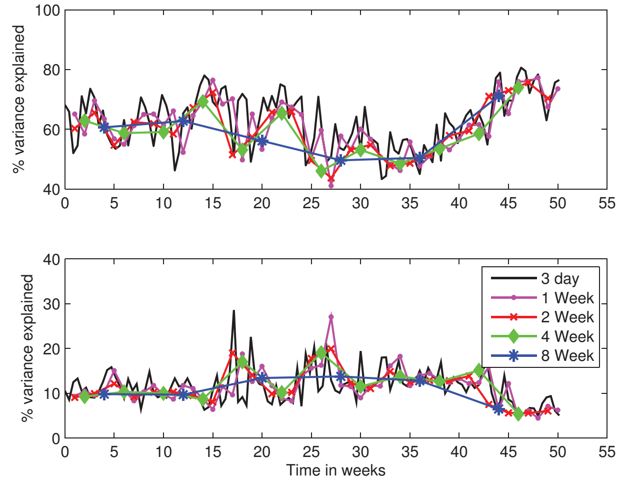

Fig. 8: Time evolution of fraction of variance explained by PC_1 (top) and PC_2 (bottom) for a range of window width. The window width used are of three days (72 time points), one, two, four and eight weeks.

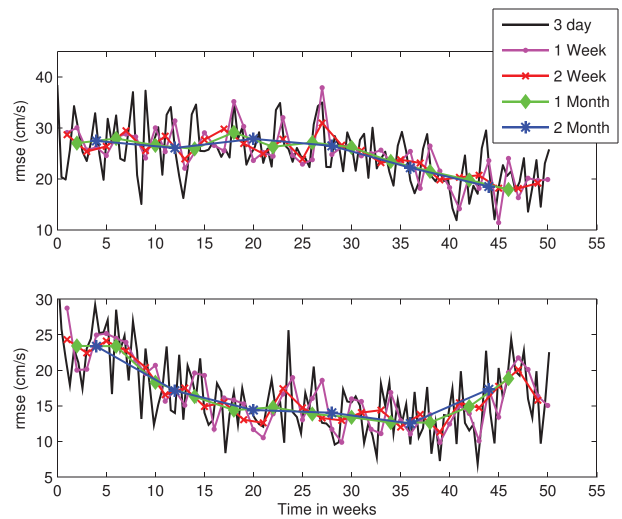

Fig. 9: RMSE computed between flows reconstructed from PC_1 (only) and the harmonic component of ADCP data for zonal (top) and meridional (bottom) components. The flows are reconstructed for the yearly dataset using five different PCA window widths of three days (72 time points), one, two, four and eight weeks.

true eigenvectors and could be excluded from the set. Applied to this data results in retention of 9 PCs.

The second point demanding attention is the window width of the PCA model. Up to now, we adopted a two month window and assumed the data had near-stationary mean and covariance structure for this time period. However, in such a dynamic system as ocean surface currents, this assumption is an area that requires further investigation.

To investigate how the process drifts with time we returned to the original one year dataset and applied PCA to the entire

TABLE I: Mean and standard deviation (σ) of RMSE computed between PC_1 and harmonic component of Cape Henry ADCP for a range of PCA window widths. Results are presented decomposed into their zonal and meridional components

Window Width	Zonal rmse	Merid rmse	Zonal σ	Merid. σ
1 day	25.04	16.96	7.84	6.91
3 day	24.71	16.99	5.57	7.20
1 week	24.74	16.46	4.89	4.47
2 week	24.72	16.48	3.72	3.82
1 month	24.89	16.41	3.48	3.81
2 month	24.75	16.46	3.68	3.85
3 month	24.67	16.53	3.75	3.56
6 month	24.77	16.07	2.02	3.55
1 year	26.61	16.49	-	-

year with a range of window widths, namely: one day, three day, and 1, 2, 4, 8, 12, 24, and 48 weeks.

Of interest was both the evolution in time of the PCs with different time windows and also the degree of compression provided by PCA as a function of time. As a preliminary step the degree of compression was investigated by evaluating how much of the total variance was explained by the first modes. Figure 8 presents the variance explained by different PCA models for the duration of the 48 week period. Analysing the figure indicates that while the 4 and 8 week sampling windows captures the general trend of the data, the linearity of the technique results in a considerable amount of information relevant to shorter time scales being neglected.

As a further measure of the amount of relevant information extracted by the different applications we returned to the information on the tidal signal gleaned from Figure 6. Considering that the information contained in the PC_1 is strongly correlated with tide, it is reasonable to associate the optimum compression of the data to that which best represents the tidal signal extracted from the ADCP. Again, the flows were reconstructed using PC_1 only, at the grid cell nearest the ADCP location at a range of window widths. To quantify performance, root-mean-square-error (RMSE), was computed between the reconstructed data and the tidal component and the progression in time analysed. Figure 9 plots the resultant differential.

As expected the general trend of the tidal signal is captured with large sampling times (two months). Table I presents the mean and standard deviation computed for the RMSE for the year. While the means are in very close agreement, there is considerable differences in standard deviation as would be expected from a visual inspection of Figure 9. Apparent is that with a high frequency sampling time, there are short periods when the RMSE is considerably higher. This may be a result of dynamicity present in the flow that cannot be captured by PC_1 or alternatively "noise" in the signal that a larger window width effectively averages out.

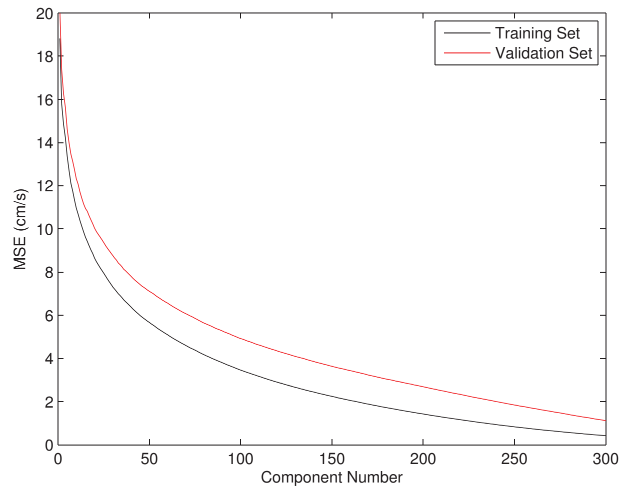

Fig. 10: MSE computed between reconstructed data for training and validation datasets

C. Application of model to validation set

Cross-validating the PCA model using new data is a means of providing further objective insight into PCA model performance. The basic idea of cross-validation is the use of different datasets for estimation and validation of each PC model [23]. For all applications the data was split into two equal time partitions: the training set used to construct the PCA model and the validation set to assess performance of the model with new data. PC models were determined using the training data and then evaluated on the validation data. The application of the method to new data involves making use of the scores of the PCA model. The scores of the model are the projections of the samples in the new coordinate system defined by the PCs. Projecting the validation data X_{val} onto the same PCs gives a reconstruction of the validation dataset $\tilde{X}_{val} = X_{val} P^T P^T$ which can be used to monitor changes in the system. The skill of the model (as function of window width and mode truncation) was evaluated with regards to optimum model selection. The skill of the model in returning the raw data can be represented by the mean squared reconstruction error (MSE) defined as:

$$MSE = \frac{1}{nm} ||X - \tilde{X}||_F^2 \tag{5}$$

where X is the raw data, $\tilde{X}$ is the data reconstructed from PCA, n, m the dimensions of the matrix and $||X||_F$ is the Frobenius (or matrix) norm.

Figure 10 presents a comparison of the MSE computed for both the training set and the validation set. Apparent is the equivalent trend evident in both training and validation data MSE. This suggests that the signal of the HFR contains such similarities that prevent a simple decomposition of the noise from the distinct signal. It also does not provide any useful insight into the number of components required to describe the process. To further the usefulness of the PCA model in noise reduction a choice on number of PCs to retain must be

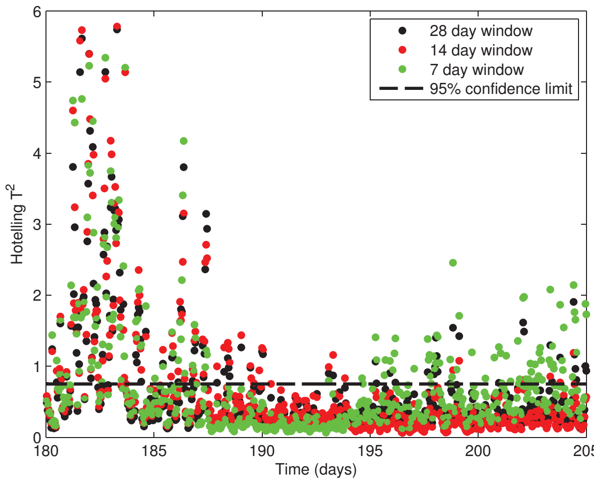

Fig. 11: Hotelling's T^2 statistic computed for a validation set of 28 days. The PCA model was computed using a window width of 7, 14 and 28 days and the validation set reconstructed. For the 7 and 14 day window widths, the PCA model was applied repeatedly using the previous dataset to best capture the evolution of the mean of the dataset. The dashed line represents the computed 95% confidence limit above which the dataset is considered an "outlier"

made. Considering the similarities with other cutoff choices and to permit for automated applications, the Guttman-Kaiser criterion [21] discussed earlier, that retains all eigenvalues, q, where $\lambda > 0.7\overline{\lambda}$ was adopted. The validation set was then reconstructed as $\tilde{X}_{val} = X_{val} P_q^T P_q^T$

To provide further insight into outliers in the dataset and their origins, Hotelling's T^2-test which is a multivariate representation of Student's t-test is adopted. It gives a measure of the variation *not* captured by the model and can be expressed as:

$$T_i^2 = t_i^T \Lambda^{-1} t_i \tag{6}$$

where $\lambda = diag(\lambda_1, \lambda_2 ... \lambda_k)$ are PC eigenvalues. A range of PCA models was constructed using different window widths as described earlier and deviations from the model computed using the T^2 measure. A multivariate process is considered to be anomalous at the i_{th} sampling time if T_i^2 exceeds an upper control limit. A limit for the 95% confidence level can be expressed as:

$$T_{lim}^2 = \frac{K(N-1)}{N-K} F(K, N-K, \alpha) \tag{7}$$

where$F(K, N-K, \alpha)$ corresponds to the probability point on the F-distribution with (K,N-K) degrees of freedom and confidence level α, K is the number of principal components, and N is the number of observations.

Figure 11 presents the Hotelling's T^2 statistic computed for validation set of 28 days. The PCA model was computed using a window width of 7, 14 and 28 days and the validation set reconstructed. For the 7 and 14 day window widths, the PCA model was applied repeatedly using the previous dataset to best capture the evolution of the mean of the dataset. The 95% confidence limit is also denoted. Apparent is the considerable number of returns that exceed the computed confidence intervals. In itself, the metric is of limited value as it only provides a measure for the entire dataset at each time return. To provide meaningful insight, the contribution of each HFR grid cell to the total is more practical. A spatial representation of the contribution can be computed as

$$t_{con,i} = t_i \lambda_i^{-1/2} P_k^T \tag{8}$$

From Figure 11, it is apparent that the earlier portion of the time window contains a number of points that exceed the confidence limit by multiple orders of magnitude. For illustration purposes we adopted the time return that corresponds to the largest T^2 value (day 181 at 05:00am); i.e. the time when the model performs poorest in capturing the variation of the data.

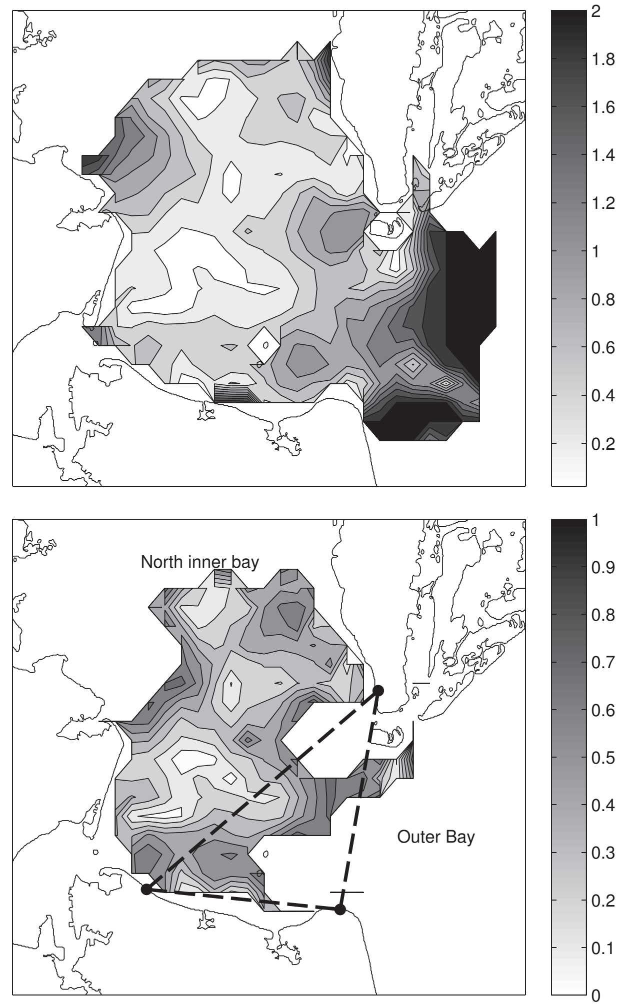

Fig. 12: Spatial maps of T2 contributions to (a) total and (b) eliminating cells that exceed limit until confidence interval met corresponding to HFR measurements for julian day 181 at 05:00am (selected due high volume of anomalous returns for representative purposes)

Figure 12 presents the spatial contribution of each grid cell to the T2 score for this time.

It is evident that a region in the outer bay contributes a large proportion of the total variation computed. The methodology adopted for this study is the iterative elimination of cells with maximum T^2 contribution until the confidence interval of the dataset is met. Figure 12b presents the spatial map of T^2 after the data is processed as described. For this particular case, the elimination of outlier data reduces the number of return by 40%. Analysis of the map of processed data suggests that the data identified by the PCA model as being anomalous is physically meaningful. Known issues exist regarding the performance of the HFR in the outer Bay. The SUNS station does not return radial measurements in this region due to no direct over water line of sight (see Figure 1). Hence, the meridional component of velocity is not well resolved in the region resulting in an uncertain reconstruction of the flow. Monitoring the incoming data with process control metrics identify and eliminate measurements from this region. Other areas with potential issues that are successfully identified include the North inner Bay where distance from radar station plausibly impacts performance and beside the headland in the Northern Bay where the signal is distorted by the nearby land.

It is important to note that this data return represents the most extreme outlier of all the data analysed. Hence, the exclusion ratio of 40% can be considered a worst case scenario. It also requires stressing that no pre-processing of the data was conducted prior to analysis. Typically in HFR applications, the data is pre-processed to eliminate particular cells based on known performance issues such as low signal-to-noise ratio, areas of high geometric dilution of precision [9], extreme distance from radar measuring site, etc. No pre-processing was performed in this study as the goal was an objective analysis that would identify and eliminate outlier data in an automated manner.

IV. Conclusions

This paper presents the application of multivariate process control techniques to the analysis of surface current flows collected by HFR system in the Chesapeake Bay area. To better understand flows in the region. PCA de-constructs the data based on the amount of variance present. Analysis shows that this data-driven approach inherently links measured flows to physical processes in the bay. The decomposition into distinct spatial and temporal patterns serves as a means to better understand and describe flow patterns and further relate synoptic patterns to local environmental variables. It also supports the viability of adopting PCA to partition the physically driven signal present in the HFR measurement from underlying noise.

Application of the technique to the validation dataset correctly identifies area that have known performance issues. In this study we chose to remove these cells thereby reducing the measurement area; an alternative option is to filter these anomalous cells by truncating the reconstruction at fewer PCs or applying a weighting coefficient to reflect the increased uncertainty of these cells.

The research also highlights challenges in the application of PCA to HFR data that requires further investigation. The high spatial and temporal variability of the data makes a distinct decomposition of flows into uncorrelated variables in space and time difficult. The relative close proximity in time of the measurements (hourly) imply that there is likely to be correlation between measurements at adjacent time points, resulting in non-independence between observations. Several techniques exist that take account of correlation between observations such as Singular Spectrum Analysis (SSA) or frequency domain PCA [20]. Future work will focus on a more detailed investigation of these relationships and combination with multivariate process control metrics.

References

[1] M. Yaremchuk and A. Sentchev, "A combined EOF\variational approach for mapping radar-derived sea surface currents," Stennis Space Center, MS, 39529, Naval Research Laboratory, Tech. Rep., 2011.

[2] D. Prandle, S. G. Loch, and R. Player, "Tidal flow through the Straits of Dover," *J. Phys. Oceanogr.*, vol. 23, no. 1, 1993.

[3] J. T. Kohut, H. J. Roarty, and S. M. Glenn, "Characterizing observed environmental variability with HF radar surface current mappers and acoustic Doppler current profilers: Environmental variability in the coastal ocean," *IEEE J. Oceanic. Eng.*, vol. 31, no. 4, pp. 876–884, Oct. 2006.

[4] D. S. Ullman, J. O'Donnell, J. Kohut, T. Fake, and A. Allen, "Trajectory prediction using HF radar surface currents: Monte Carlo simulations of prediction uncertainties," *J. Geophys. Res.*, vol. 111, p. 14 PP., Dec. 2006.

[5] J. Kohut, H. Roarty, S. Licthenwalner, S. Glenn, D. Barrick, B. Lipa, and A. Allen, "Surface current and wave validation of a nested regional HF radar network in the Mid-Atlantic bight," in *IEEE/OES 9th Working Conference on Current Measurement Technology, 2008. CMTC 2008.* IEEE, Mar. 2008, pp. 203–207.

[6] B. Lipa, C. Whelan, B. Rector, and B. Nyden, "HF radar bistatic measurement of surface current velocities: Drifter comparisons and radar consistency checks," *Remote Sensing*, vol. 1, no. 4, pp. 1190–1211, Dec. 2009.

[7] M. Yaremchuk and A. Sentchev, "Mapping radar-derived sea surface currents with a variational method," *Cont. Shelf Res.*, vol. 29, no. 14, pp. 1711–1722, Jul. 2009.

[8] J. D. Paduan and L. Washburn, "High-frequency radar observations of ocean surface currents," *Annual Review of Marine Science*, vol. 5, pp. 115–136, 2013.

[9] B. M. Emery, L. Washburn, and J. A. Harlan, "Evaluating radial current measurements from CODAR high-frequency radars with moored current meters," *J. Atmos. Ocean. Tech.*, vol. 21, pp. 1259–1271, 2004.

[10] H. H. Essen, K. Gurgel, and T. Schlick, "On the accuracy of current measurements by means of HF radar," *IEEE J. Oceanic. Eng.*, vol. 25, no. 4, pp. 472–480, 2000.

[11] B. Lipa, B. Nyden, D. S. Ullman, and E. Terrill, "Seasonde radial velocities: derivation and internal consistency," *Oceanic Engineering, IEEE Journal of*, vol. 31, no. 4, pp. 850–861, 2006.

[12] B. Lipa and D. Barrick, "Least-squares methods for the extraction of surface currents from codar crossed-loop data: Application at arsloe," *Oceanic Engineering, IEEE Journal of*, vol. 8, no. 4, pp. 226–253, 1983.

[13] J. Harlan, A. Allen, E. Howlett, E. Terrill, S. Kim, M. Otero, S. Glenn, H. Roarty, J. Kohut, J. O'Donnell *et al.*, "National ioos high frequency radar search and rescue project," in *OCEANS 2011*. IEEE, 2011, pp. 1–9.

[14] B. Lipa, "Uncertainties in seasonde current velocities," in *Current Measurement Technology, 2003. Proceedings of the IEEE/OES Seventh Working Conference on*. IEEE, 2003, pp. 95–100.

[15] Y. Yoshikawa, A. Masuda, K. Marubayashi, M. Ishibashi, and A. Okuno, "On the accuracy of hf radar measurement in the tsushima strait," *Journal of Geophysical Research: Oceans (1978–2012)*, vol. 111, no. C4, 2006.

[16] J. D. Paduan, K. C. Kim, M. S. Cook, and F. P. Chavez, "Calibration and validation of direction-finding high-frequency radar ocean surface current observations," *Oceanic Engineering, IEEE Journal of*, vol. 31, no. 4, pp. 862–875, 2006.
[17] R. Pawlowicz, B. Beardsley, and S. Lentz, "Classical tidal harmonic analysis including error estimates in matlab using t_tide," *Comput. Geosci.*, vol. 28, no. 8, pp. 929–937, 2002.
[18] P. Kundu, "Ekman veering observed near the ocean bottom," *J. Phys. Oceanogr.*, vol. 6, pp. 238–242, 1976.
[19] W. J. Emery and R. E. Thomson, *Data analysis methods in physical oceanography*. Elsevier Science, 2001.
[20] I. Jolliffe, *Principal component analysis*. Wiley Online Library, 2005.
[21] J. E. Jackson, *A user's guide to principal components*. John Wiley & Sons, 2005, vol. 587.
[22] G. R. North, T. L. Bell, R. F. Cahalan, and F. J. Moeng, "Sampling errors in the estimation of empirical orthogonal functions," *Monthly Weather Review*, vol. 110, no. 7, pp. 699–706, 1982.
[23] G. Diana and C. Tommasi, "Cross-validation methods in principal component analysis: a comparison," *Statistical Methods and Applications*, vol. 11, no. 1, pp. 71–82, 2002.

Reduced Averaging Times in the Long Range SeaSonde

Hugh Roarty, Chloe Baskin, Michael Smith, Scott Glenn
Coastal Ocean Observation Laboratory
Rutgers University
New Brunswick, NJ USA
hroarty@marine.rutgers.edu

***Abstract*—High frequency (HF) radar systems are useful for measuring the velocity of sea surface currents. Besides the ecological and economic importance of being able to accurately measure currents, the US Coast Guard uses HF radar to make decisions involved in search and rescue operations. Currently, 5 MHz or long-range HF radar systems output radial vector files that are calculated using a 180-minute averaging interval. Reducing the averaging interval to 60 minutes could improve accuracy in areas where the current changes significantly over this 3 hour averaging interval. To test this, the track of a real drifter was compared to the track of two virtual drifters over a 48-hour period. One virtual drifter was tracked using HF radar total surface currents derived from radial measurements averaged over the default 180-minute interval and the other using HF radar data averaged over the 60-minute interval. Distance between real drifter and virtual was determined for both cases. For the first 24-hour period, both HR radar intervals had similar differences between the real drifter and the virtual. The largest difference was approximately 5 km, and the smallest was less than 2 km. The next 24 hours were less similar with the HF radar for the 60-minute interval being more accurate. For example, the 180 minute interval, the distances between the virtual and real drifter reached a maximum of approximately 12 km while the maximum difference for the HF radar averaged over 60 minute intervals was only 7km. The improvement of accuracy when switching the HF radar over to 60 minute intervals has implications in the broad sense for studies looking at biological and ecological species as well as for transportation at sea but where this difference maybe most important is in the ability to narrow a search area during US Coast Guard Search and Rescue missions.**

***Index Terms*—HF radar, radar remote sensing**

I. INTRODUCTION

The Mid Atlantic 5 MHz Radar Network [1] (Figure 1) is coordinated through a central office at Rutgers University with sub-regional technology centers at the University of Connecticut, University of Massachusetts Dartmouth and Old Dominion University. The hardware workforce consists of a part time regional coordinator with one full time radar operator stationed at each of the three sub-regions all within a days drive of any shore station in the sub-region. Technical expertise and hardware resources are shared during regular conference calls. Quality assurance measures are enacted during weekly remote site inspections. Radial data is collected and quality controlled before further processing. The radial data is aggregated and combined into totals. The performance metric for the network is 80% spatial coverage of the 190,000 km^2 of continental shelf at 80% temporal coverage. These totals are made available on a Thematic Real-time Environmental Distributed Data Services (THREDDS) Data Server (TDS) that are then accessible for assimilation into the statistical and dynamic models operated in the region. The totals are also retrieved by Applied Science Associates who make the data available on the US Coast Guard Environmental Data Server (EDS) for use in the Search and Rescue Optimal Planning System (SAROPS).

It was introduced in [2] that if the averaging time for the long-range SeaSonde was reduced from 180 minutes down to 60 minutes then 98% of the M2 tidal signal could be captured with the shorter averaging time compared to 92% for the longer averaging time. The analysis in that paper focused on the radial level of data. For the analysis in this paper we focus on the total vector data. Radial data was generated using 60 and 180-minute span. Each set of radial data was combined to make total surface vectors. The position of virtual drifters was compared against in situ drifters after a period of 48 hours.

978-1-4799-3646-5/14/$31.00 ©2014 IEEE

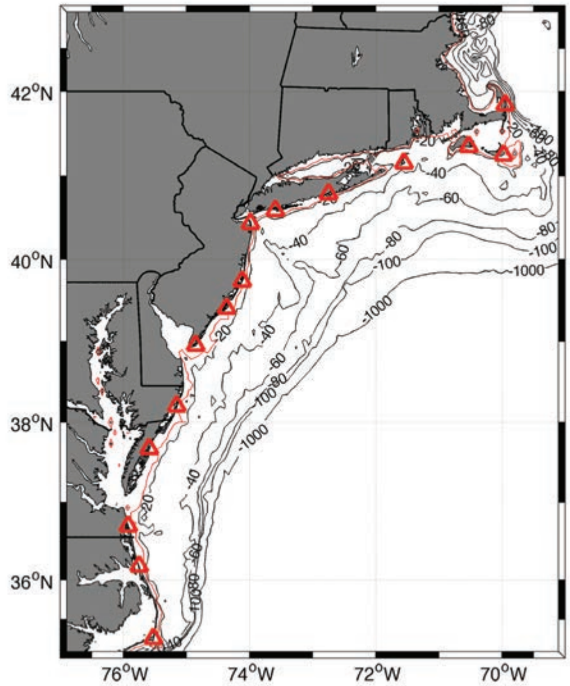

Figure 1: Location of the HF radar stations (red triangles) sites used in this study. The sites from north to south are Nauset, MA (NAUS), Nantucket, MA (NANT), Martha's Vineyard, MA (MVCO), Block Island, RI (BLCK), Moriches, NY (MRCH), Hempstead, NY (HEMP), Sandy Hook, NJ (HOOK), Loveladies, NJ (LOVE), Brigantine, NJ (BRIG), Wildwood, NJ (WILD), Assateague, MD (ASSA), Cedar Island, VA (CEDR), Little Island, VA (LISL), Duck, NC (DUCK) and Cape Hatteras, NC (HATY).

II. METHODS

The radar systems used here include the 15 long-range (5 MHz) SeaSonde systems that are one component of the Mid Atlantic Bight HF radar network. Two different averaging schemes were used on the radial data. The first scheme is what is currently used operationally in the Mid Atlantic Bight. We will refer to this as averaging scheme 1. A 60-minute average Cross Spectra file is generated every 30 minutes. A short time radial is generated from each Cross Spectra file. Five short time radials are then averaged to produce a radial file once an hour. This radial file represents 180 minutes of averaging time. The radials from each radar station are then combined to produce a total vector map once an hour.

The second averaging scheme utilizes the short time radials in the vector combination. This is referred to as averaging scheme 2. These short time radials represent 60 minutes of averaging time. These radials are combined to produce a total vector map once every 30 minutes. The optimal interpolation combining method [3, 4] was used in both cases to combine radials into totals.

Drifters from the National Oceanic and Atmospheric Administration (NOAA) Northeast Fisheries Science Center (NEFSC) Drifter Program were used to compare with the two data sets from the HF radar. The Drifter Program [5] provides instruction and materials to schools to construct passive drifters that will be deployed in the ocean. Two drifters were utilized in this study. Drifter 138410701 was deployed on August 25, 2013 in Nantucket Sound by undergraduate students from Harvard (Figure 2) and reported positions till November 1, 2013. Drifter 138410722 was deployed on August 21, 2013 by students from the University of Connecticut in Long Island Sound and reported positions till September 9, 2013. The drifters were of similar form to a Self Locating Data Marker Buoy (SLDMB), the type of drifter that the Coast Guard uses in search and rescue cases [6]. The surface drifter has been a popular device to ground truth HF radar measurements [4, 7, 8]. The position data of the drifters were linearly interpolated to match the time of the HF radar data and to also fill any gaps in the position history. Both drifters were deployed in areas not covered by the HF radar network. We began the comparison when the drifters made it into the open ocean.

Figure 2: Picture of drifter 138410701 being deployed.

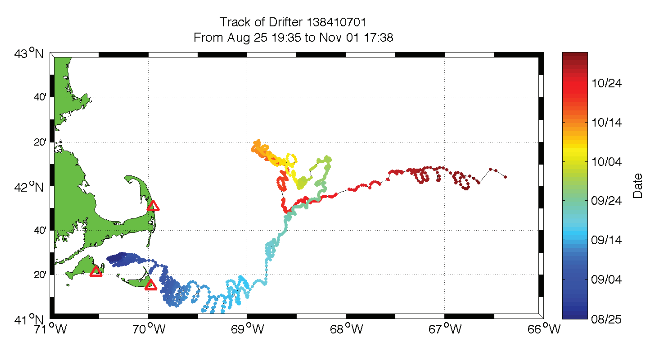

Figure 3: Track of drifter 138410701 off the coast of Cape Cod. The colorbar denotes the time of the drifter position.

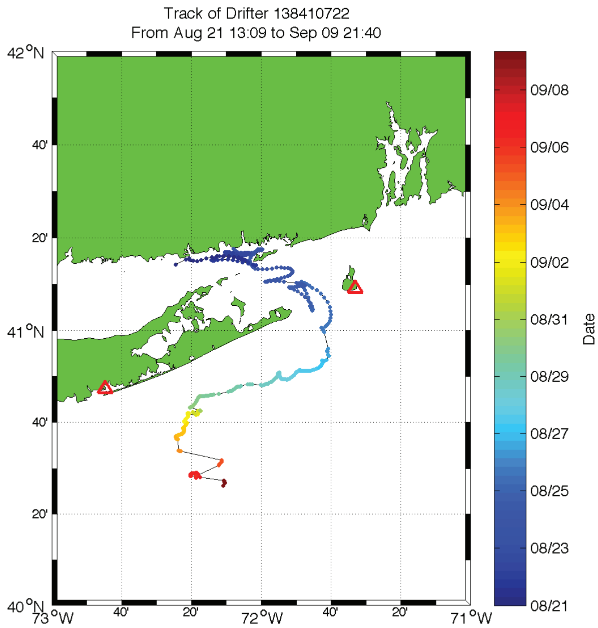

Figure 4: Track of drifter 138410722 off the coast of Long Island. The colorbar denotes the time of the drifter position.

III. Preliminary Results

Drifter trajectories based on averaging scheme 1 and 2 were compared to the actual track of drifter 138410701. For each simulation 1,000 simulated particles were advected from the position of the actual drifter using the surface current field from the HF radar data. Included in this motion was a dispersion term that was estimated using a Markovian random flight model [9, 10]. The simulation was run for 48 hours then stopped. The process was repeated from the next time step (60 minutes later for averaging scheme 1 and 30 minutes later for averaging scheme 2) and next position of the actual drifter. This was carried out till the data from the in situ drifter was exhausted.

An example of this simulation is shown in Figure 5. This shows the path of the drifter 138410701 from September 15-17, 3013 off the coast of Cape Cod. The strong tidal currents over Nantucket Shoals are evident in the large corkscrew pattern of the actual drifter (red) and virtual drifter (green) paths. The 1,000 virtual particles have disprsed to an area of 1,400 km^2 over the 48 hours. The separation between the virtual and actual drifter was calculated as a function of time and is shown in Figure 6. The separation of the particles advected by averaging scheme 1 is shown as the red circles and that of averaging scheme 2 are the black circles. The shorter averaging time gave a consistently closer approximation to the in situ drifter than the longer averaging time. The error after 48 hours of simulation was 10 km with averaging scheme 1 while it was only 5 km with averaging scheme 2. Based on these promising results we increased the number of simulations to see if this improvement still held.

We replicated the simulation with the drifter deployed in Long Island Sound (138410722). The simulations were run from August 27, 2013 00:00 UTC to September 4, 2013 04:00 UTC. There were a total 197 simulations for averaging scheme 1 and the results are shown in Figure 7. Since averaging scheme 2 updated every 30 minutes there were double the number of simulations or 394 and the results are shown in Figure 8. The mean for all the simulations is shown as the black line in each figure.

The mean separation between drifter 138410722 and the virtual particles was 19 km after 48 hours using averaging scheme 1. The shorter time avergaing of scheme 2 showed a slight improvement with the separation only being 16 km after 48 hours. However the variance of shorter averaging interval was increased when compared to the longer averaging time of 180 minutes. This could be due to the larger sample size or that the shorter averaging interval yields more uncertainty in the measurement of the surface currents. Further analysis will be required to determine this.

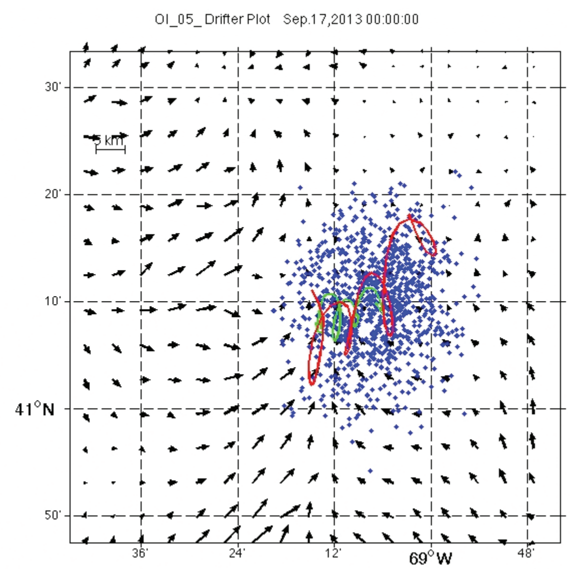

Figure 5: Predicted particle locations (blue dots) using averaging scheme 1 after 48 hours of simulation. The path of the centroid of the blue particles is the green line. The path of in situ drifter 138410701 is the red line. The simulation was run from September 15, 2013 00:00 UTC to September 17, 2013 00:00 UTC. The instantaneous surface currents from the HF radar are shown as the black vectors.

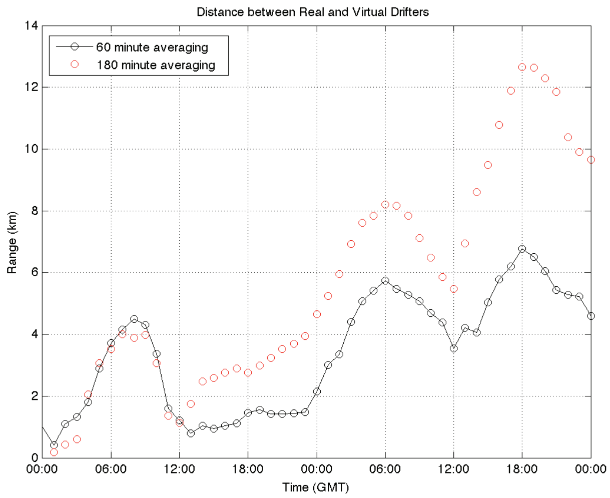

Figure 6: One realization of the Separation between drifter 138410701 and centroid of virtual particles advected using averaging scheme 1 (red dots) and averaging scheme 2 (black line). The x axis is time from 0 to 48 hours.

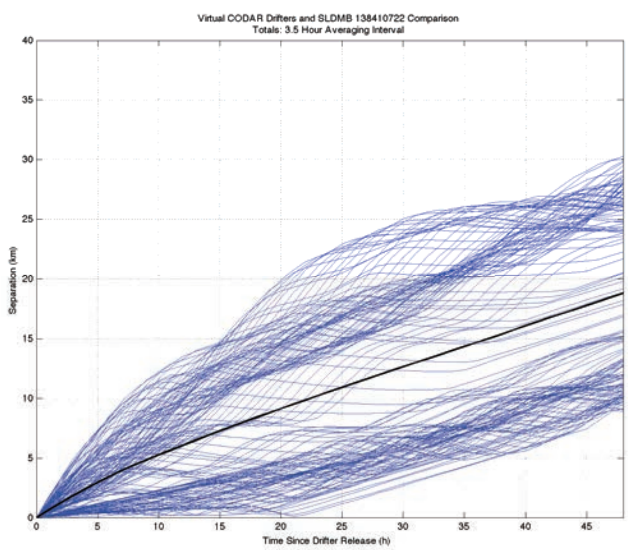

Figure 7: Separation between drifter 138410722 and centroid of virtual particles advected using averaging scheme 1 (blue lines). The black line is the average of all the drifter simulations. The x axis is time from 0 to 48 hours.

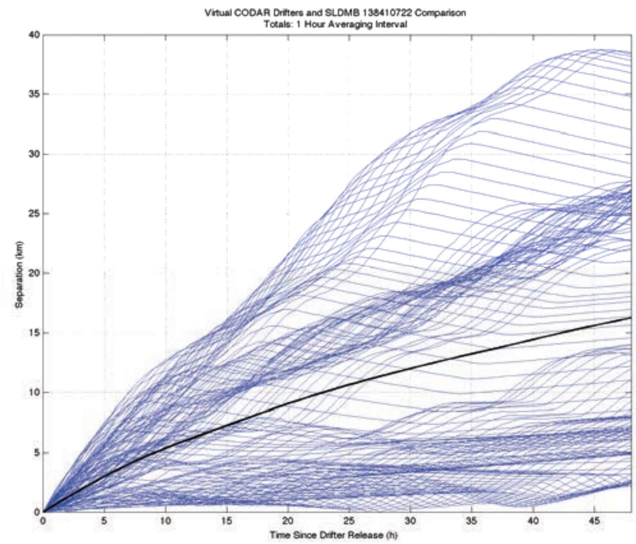

Figure 8: Separation between drifter 138410722 and centroid of virtual particles advected using averaging scheme 2 (blue lines). The black line is the average of all the drifter simulations. The x axis is time from 0 to 48 hours.

IV. CONCLUSIONS

An experiment was conducted to improve the measurements of the SeaSonde High Frequency radar. This first involved decreasing the averaging time of the radial processing from 180 minutes down to 60 minutes. Total surface currents were produced with the two data sets. Comparisons were then made between drifters released in the ocean and virtual drifters released in the HF radar surface currents. The mean separation between the two data sets was compared after 48 hours. The surface currents with the 60-minute averaging time showed a slight improvement over the longer averaging time of 180 minutes but with higher uncertainty. We will continue this research by making additional comparisons with in situ drifters in a variety of flow regimes in the Mid Atlantic Bight.

ACKNOWLEDGMENTS

This work was funded by NOAA Award Number NA11NOS0120038 "Towards a Comprehensive Mid-Atlantic Regional Association Coastal Ocean Observing System (MARACOOS)". Sponsor: National Ocean Service (NOS), National Oceanic and Atmospheric Administration (NOAA) NOAA-NOS-IOOS-2011-2002515 / CFDA: 11.012, Integrated Ocean Observing System Topic Area 1: Continued Development of Regional Coastal Ocean Observing Systems.

Thanks to Jim Manning from the NOAA Northeast Fisheries Science Center for providing the drifter data.

References

[1] H. J. Roarty, S. M. Glenn, J. T. Kohut, D. Gong, E. Handel, E. Rivera Lemus, T. Garner, L. Atkinson, C. Jakubiak, W. Brown,

M. Muglia, S. Haines, and H. Seim, "Operation and Application of a Regional High Frequency Radar Network in the Mid Atlantic Bight," *Marine Technology Society Journal,* vol. 44, pp. 133-145, 2010.

[2] H. Roarty, J. Kerfoot, J. Kohut, S. Glenn, C. Whelan, and M. Hubbard, "Improving the measurements of high frequency radar: Reduced averaging times and bistatics," in *OCEANS - Bergen, 2013 MTS/IEEE*, 2013, pp. 1-6.

[3] S. Y. Kim, E. J. Terrill, and B. D. Cornuelle, "Mapping surface currents from HF radar radial velocity measurements using optimal interpolation," *J. Geophys. Res.,* vol. 113, p. C10023, 2008.

[4] J. Kohut, H. Roarty, E. Randall-Goodwin, S. Glenn, and C. Lichtenwalner, "Evaluation of two algorithms for a network of coastal HF radars in the Mid-Atlantic Bight," *Ocean Dynamics,* vol. 62, pp. 953-968, 2012.

[5] J. P. Manning, D. J. McGillicuddy Jr, N. R. Pettigrew, J. H. Churchill, and L. S. Incze, "Drifter observations of the Gulf of Maine Coastal Current," *Continental shelf research,* vol. 29, pp. 835-845, 2009.

[6] A. Allen, "Performance of GPS/Argos self-locating datum marker buoys (SLDMBs)," in *OCEANS '96. MTS/IEEE. 'Prospects for the 21st Century'. Conference Proceedings*, 1996, pp. 857-861 vol.2.

[7] C. Ohlmann, P. White, L. Washburn, B. Emery, E. Terrill, and M. Otero, "Interpretation of Coastal HF Radar‚ÄìDerived Surface Currents with High-Resolution Drifter Data," *Journal of Atmospheric and Oceanic Technology,* vol. 24, pp. 666-680, 2007/04/01 2007.

[8] J. D. Paduan and L. K. Rosenfeld, "Remotely sensed surface currents in Monterey Bay from shore-based HF-radar (CODAR)," *Journal of Geophysical Research,* vol. 101, pp. 20669-20686, 1996.

[9] D. Gong, J. T. Kohut, and S. M. Glenn, "Seasonal climatology of wind-driven circulation on the New Jersey Shelf," *J. Geophys. Res.,* vol. 115, p. 25, 2010.

[10] D. S. Ullman, J. O'Donnell, J. Kohut, T. Fake, and A. Allen, "Trajectory prediction using HF radar surface currents: Monte Carlo simulations of prediction uncertainties," *J. Geophys. Res.,* vol. 111, p. C12005, 2006.

Quality Control for a Network of SeaSonde HF Radars

Hugh Roarty, Michael Smith, Colin Evans, Ethan Handel, Josh Kohut, Scott Glenn
Coastal Ocean Observation Laboratory
Rutgers University
New Brunswick, NJ USA
hroarty@marine.rutgers.edu

***Abstract*—The proliferation of HF radar networks around the globe has made them a vital component of the ocean observing endeavor. There are approximately thirty-four nations with oceanographic HF radar networks, eight of which have over 10 radar stations in their network. Providing high quality measurements for sustained periods of time is of the utmost importance. The global HF radar network has been established to meet this goal. The network was established in 2012 with the goal of increasing the number of coastal radars, develop emerging applications of the data and to deliver a set of easy to use standard products. The network was established under the Group on Earth Observations (GEO) work plan for 2012-2015. The work plan endorses a task to plan a Global HF Radar Network for data sharing and data delivery and to promote the proliferation of HF radar surface current velocity measurements. The goal of this paper is to propose quality standards for this global network.**

In this paper we will take inventory of the existing quality assurance and quality control measures that have been proposed at the radial level and offer measures to manage the systems on a network level. We have developed a best practices checklist for validating and operating a HF radar stations in the Mid Atlantic – a checklist that can be transferred to other regions nationally and internationally. Some of these techniques include the comparison of radials from measured and ideal beam patterns. We have also performed beam pattern sensitivity tests, first order line settings tests, angular segmentation tests and different time averaging schemes on the radial data. We share the results of those tests here so that they may be replicated by other operators to strengthen the methodology. We propose best practices for the operation of a High Frequency radar network.

The techniques outlined in this paper have shown an increased accuracy of the measured radial currents and a better understanding of the data processing stream associated with the particular HF radar system. The other networks around the globe can adopt the methods and best practices outlined in this paper. The other networks can also provide input to these methods and best practices which will result in an improved surface current measurement.

***Index Terms*—HF radar, radar remote sensing, quality control**

I. INTRODUCTION

Rutgers installed their first HF Radar station in 1998 and currently operates 23 stations in the Mid Atlantic Bight and Puerto Rico and coordinates 45 stations as part of the Mid-Atlantic Regional Association Coastal Ocean Observing System (MARACOOS). See Figure 1 for the location of the 42 stations in the radar network. Rutgers, in cooperation with the United States Coast Guard, developed the use of HF Radar data for search and rescue planning. The MARACOOS HF radar network became operational with the U.S. Coast Guard on May 4, 2009. Rutgers has also applied the use of HF Radar surface current data in oil spill response and mitigation. This work was highlighted in the response to the Deepwater Horizon oil spill in the Gulf of Mexico. Rutgers data and analysis that was central to the federal government's coordinated response to the oil spill.

Rutgers supports the U.S. National HF Radar Network through participation on its Technical Steering Committee, the Group on Earth Observations (GEO) HF Radar task through the developing Global HF Radar Network's Applications Working Group. The goals of this effort are to increase the number of coastal radars, ensure the HF Radar data is available in a single standardized format in near-real-time, develop worldwide quality standards, a set of easy to use standard products, assimilate the data into ocean and ecosystem modeling and develop the emerging uses of HF Radar. This paper will be a first step in developing worldwide quality standards.

The automated quality control of HF radar data is another area where Rutgers is looking to make improvements. Up until now the quality control of HF radar data has been labor intensive. This is becoming increasingly unattainable as the number of radars around the country increases. Developing algorithms that will take the person out of the loop to perform this quality control is of the utmost importance. In this paper we will take inventory of the existing methods for oceanographic data quality control, the existing methods specific for HF radar data and propose some new methods.

978-1-4799-3646-5/14/$31.00 ©2014 IEEE

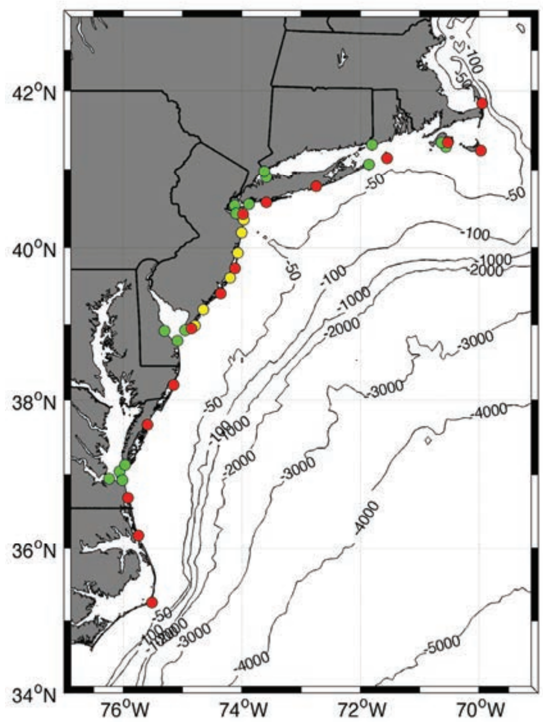

Figure 1: The Mid Atlantic Bight High Frequency Radar Network. The long-range 5 MHz systems are shown in red, the standard range 13 MHz systems are shown in yellow and the high-resolution 25 MHz systems are shown in green.

II. OCEANOGRAPHIC QA/QC METHODS

The Quality Assurance of Real Time Oceanographic Data (QARTOD) workshops have been held over the past two decades to develop standards for the quality assurance (QA) and quality control (QC) of oceanographic data. There have been five national meetings to discuss the quality control of oceanographic data. Reports are now starting to emerge for the quality control of different sensor types and variable measurements. For instance reports have recently been released for the quality control of in-situ temperature, salinity, dissolved oxygen, surface waves and currents. Quality control of High Frequency radar surface current mapping was discussed at QARTOD I, II and III. The development of QA/QC techniques for HF radar data then shifted to the Radiowave Operators Working Group (ROWG) as it was established in 2005.

The National Data Buoy Center (NDBC) has maintained a technical document for the quality control of sensor data aboard their payloads since 2009 [1].

The European Global Ocean Observing System (EuroGOOS) has created a document for the real time quality control of temperature, salinity, currents and sea level [2].

III. HF RADAR QA/QC METHODS

The Mid Atlantic High Frequency Radar Network [3] is coordinated through a central office at Rutgers University with sub-regional technology centers at the University of Connecticut, University of Massachusetts Dartmouth and Old Dominion University. The hardware workforce consists of a part time regional coordinator with one full time radar operator stationed at each of the three sub-regions all within a days drive of any shore station in the sub-region. Technical expertise and hardware resources are shared during regular conference calls. Quality assurance measures are enacted during weekly remote site inspections. Radial data is collected and quality controlled before further processing. The radial data is aggregated and combined into totals. The performance metric for the network is 80% spatial coverage of the 190,000 km^2 of continental shelf at 80% temporal coverage. These totals are made available on a Thematic Real-time Environmental Distributed Data Services (THREDDS) Data Server (TDS) that are then accessible for assimilation into the statistical and dynamic models operated in the region. The totals are also retrieved by Applied Science Associates who make the data available on the US Coast Guard Environmental Data Server (EDS) for use in the Search and Rescue Optimal Planning System (SAROPS).

The Southern California Coastal Ocean Observing System (SCOOS) in conjunction with the Radiowave Operators Working Group (ROWG) created a best practices document for the installation and operation of High Frequency radar systems [4]. This serves as a quality assurance manual for any operator to utilize when installing or maintaining a radar system. We have found this document to be very useful and look forward to additions from other operators.

The Mid Atlantic Bight HF Radar Network is divided into the northern, central and sub-region. There is a full time technician responsible for each sub-region. The current ratio of technicians to radar stations is 1:10, below the recommended 1:3.5 [5]. The technicians ensure on a daily basis that their radial stations are reporting back to the central aggregation system. We utilize a radial database [6] that displays information on the most recent radial file and color codes the table to indicate data latency. Green represents a file that is current and red represents a file that is older than 12 hours.

One of the tasks for these technicians is to remotely inspect the radar system once a week and follow a 17-point inspection process. A sample of that inspection sheet is shown in Figure 2. Some of the inspection points include examining the signal to noise ratio and noise floor on each of the three channels, the amplitude and phases of the receive antenna and visually inspect the radial coverage over the past 24 hours. If a problem is identified then the technician determines if can be remedied by a change to the software settings. If this is unsuccessful then a trip is scheduled to the site and a physical inspection is made of the system to determine the cause of the error. The weekly inspections serve as a quality assurance measure for future radials and a quality control measure for the radials that were produced in the previous week.

Site Code	Frequency (MHz)	Alignment (µ)	Date & Time OK	GPS OK?	Visible Bragg?	Interference	Rx Chassis Temperature (C)	TX Amplifier Temperature (C)
NAUS	4.512035	100	yes	yes	yes	no	26.6	NA
NANT	4.513	8000	yes	yes	yes	no	27.3	34
MVCO	4.513	14500	yes	yes	yes	no	28	30
BLCK	4.513	24000	yes	yes	yes	yes	18	27
BISL	25.36	3.2	yes		yes	no	23	31
MISQ	25.44	3.2	yes		yes	no	17	23
MNTK	25.6	3	yes		yes	no	16	20
STLI	26.19	10	yes		yes	no	13	18
GCAP	25.3	1635.2	yes		yes	no	16	19
MRCH	4.513	32000	Y	Y	Y	N	19	29
HEMP	offline							
HOOK	4.89995	100	Y	Y	Y	N	24	30
LOVE	4.513	56000	Y	Y	Y	N	13	18
BRIG	4.89995	30000	Y	Y	Y	N	23	26
WILD	4.513	63000	Y	Y	Y	N	19	27
SILD	25.85	10000	Y	Y	Y	N	9	19
PORT	25.85	9700	Y	Y	Y	N	18	23
LOCK	13.449081	3370	Y	Y	Y, L1/2 weak	N	26	29
HOMR	13.45	2184	Y	Y	Y	N	27	29
SEAB	offline							
BELM	offline							
SPRK	offline							
BRNT	13.45	1187	Y	Y	Y	moderate	25	29
BRMR	offline							
RATH	13.45	100	Y	Y	Y	moderate vertical	21	25
WOOD	offline							
ASSA	4.575	6710	Y	Y	Y	N	19	
CEDR	4.575	4400	Y	Y	Y	iono	17	
LISL	4.537183	200	Y	Y	Y	iono	20	
DUCK	4.537183	3300	Y	Y	Y	iono	26	
HATY	4.575	2600	Y	Y	Y	N	23	
CBBT	25.4	100	Y	Y	Y	N	26	
VIEW	25.4	600	Y	Y	Y	N	23	
CPHN	25.6	600	Y	Y	Y	N	31	
SUNS	25.6	100	Y	Y	Y	N	17	
HLPN	25.4	-	Y	-	Y	noise	20	
CMPT								
SLTR								

Figure 2: Screen shot of the weekly technician inspection sheet. The inspection categories are the columns. Each row is a different radar station. The sub-regions are shown as north (blue), central (yellow) and green (southern).

The regional coordinator oversees the work of the technician in each sub-region. We have constructed several visualization images and web sites for the coordinator to utilize to inspect the quality of the network as a whole. Some of the visualization images include a 24-hour plot of data coverage (Figure 3), a 24-hour average vector map of the surface currents (Figure 4). These products are inspected on a daily basis by the regional coordinator and if the coverage drops or a region of vectors looks suspicious then a dialogue is begun between the regional coordinator and technician responsible for that area to formulate a solution.

Automated tests for radial quality control that examine average radial bearing and energy in the M2 tidal band have been proposed [6]. We propose a new visualization method to quality control the data that represent a 24-hour average radial map. Figure 5 shows the average radial velocity for the Sandy Hook, NJ 5 MHz system on February 22-23, 2014 using the ideal antenna pattern [7]. Figure 6 is similar except in that it uses the measured antenna pattern, which is also plotted on the map. The figures follow the color convention borrowed from astronomy that red represents currents moving away from the radar and blue towards the radar. For this day, both figures show an average velocity away from the radar. A consistent picture between ideal and measured radial maps would indicate to the authors that this station is functioning properly. One area for further inspection would be the five bins in Figure 5 that show flow towards the radar and the variance is large compared to the surrounding measurements. It would be the job of the technician to determine from which radial file and hence which spectra file the errant radial vectors originated. It is also useful to make comparisons of these images among adjoining radar stations. Figure 7 shows the average radial velocity of the radar stations at Loveladies, NJ, the next station south of the Sandy Hook radar. This figure also shows a general trend of currents away from the radar for this particular time period. The next step for this research will be to develop an algorithm that can detect and remove these outliers.

The remote current working group at QARTOD II defined a hierarchy of HF radar data:

- Level 1 – refers to radial vectors
- Level 2– refers to total vectors
- Level 3– refers to higher order data products e.g. trajectory estimates, climatology products

This structure is identical to a hierarchy that has been proposed by Puertos del Estado, a Spanish institution within the Ministry of Development and a long time operator of HF radar systems [8]. The authors propose an additional layer, Level 0 which would cover spectra level data from the radar. Developing quality control algorithms for each level of data is an area of research that the HF radar community should embrace.

The U.S. National HF Radar Network proposed a radial performance metric in June 2013. An example of this is given in Figure 8. An optimal grid would be constructed at each radar station that would take into account system range based on frequency, land obstructions, coastline shape and offshore island construction. All radials produced at this station would be measured against this optimal grid. This would determine if a radial site was operating properly and provides an indication on overall network performance. The time period over which the site will be measured and the number of solutions against the optimal grid have yet to be defined.

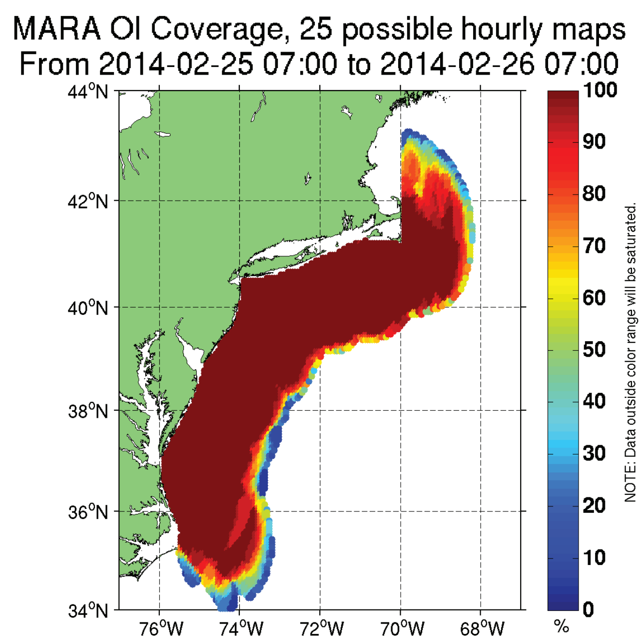

Figure 3: 24-hour coverage map of the long-range network. The colorbar on the right shows 100% coverage as red and 0% coverage as blue.

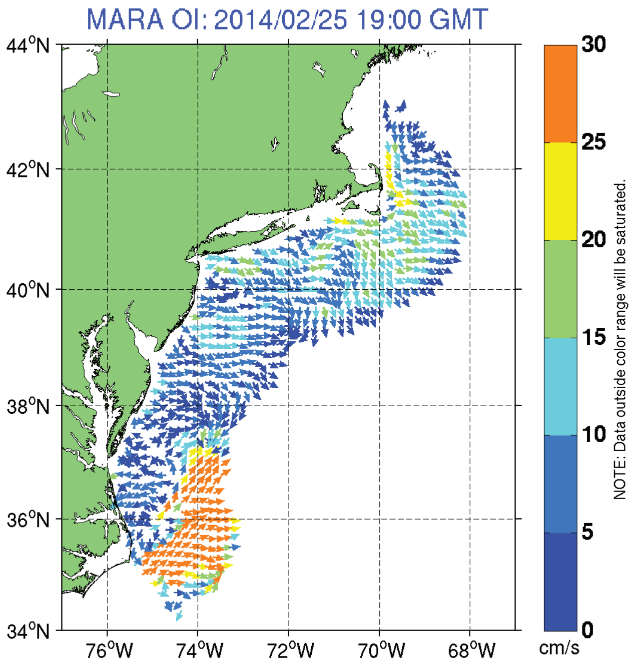

Figure 4: 24-hour mean vector map of the long-range network. The colorbar on the right denotes velocity from 0 to 30 cm/s.

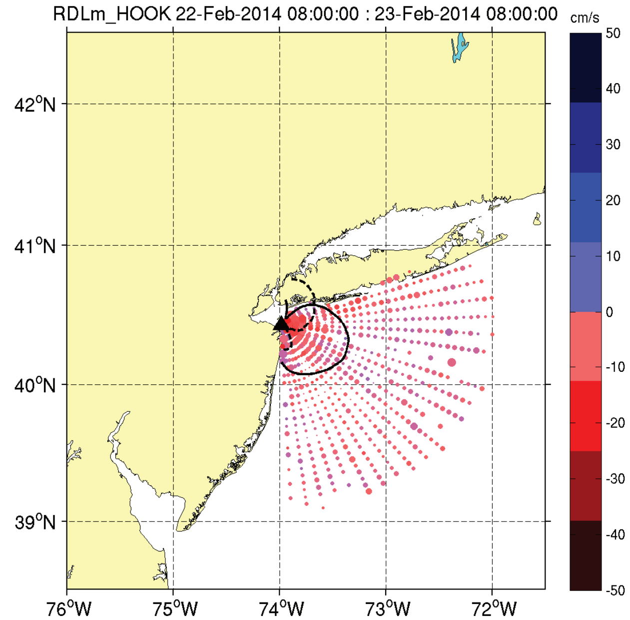

Figure 6: 24-hour average radial plot from the radar at Sandy Hook, NJ (black triangle) for the measured radial file. . The colorbar denotes radial velocity with red signifying currents away from the radar and blue denotes currents towards the radar. The color of the dot shows average velocity and the size of the dot represents the variance over the 24-hour period. The most recent antenna pattern is shown as the black circles.

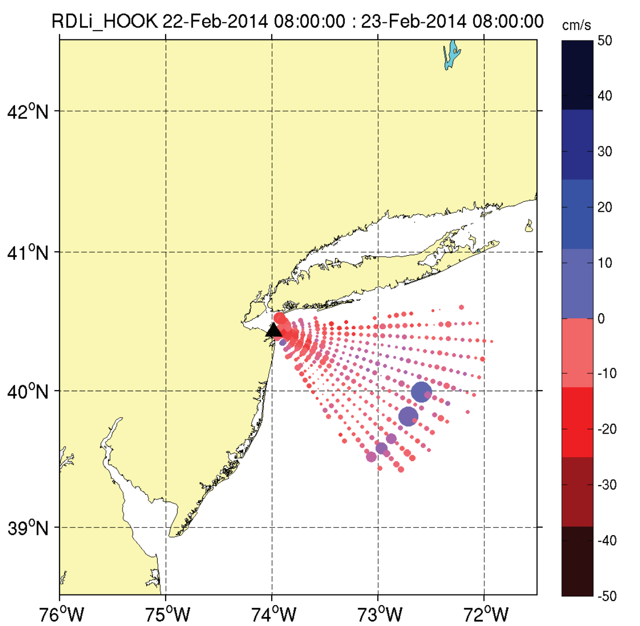

Figure 5: 24-hour average radial plot from the radar at Sandy Hook, NJ (black triangle) for the ideal radial file. The colorbar denotes radial velocity with red signifying currents away from the radar and blue denotes currents towards the radar. The color of the dot shows average velocity and the size of the dot represents the variance over the 24-hour period.

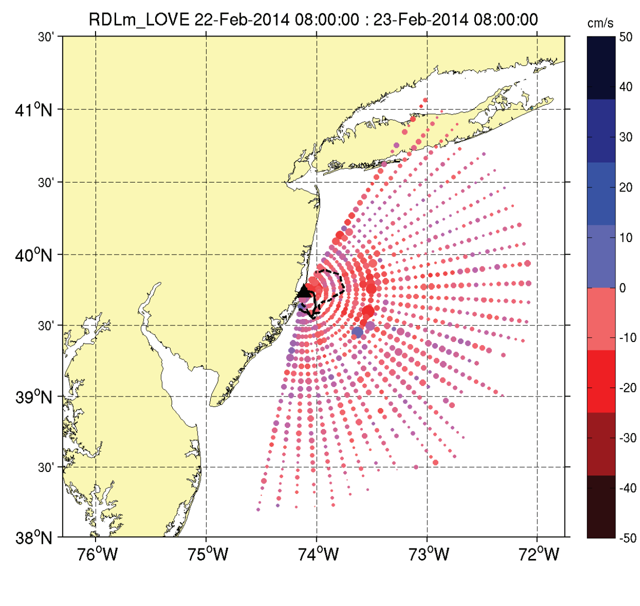

Figure 7: 24-hour average radial plot from the radar at Loveladies, NJ (black triangle) for the measured radial file. . The colorbar denotes radial velocity with red signifying currents away from the radar and blue denotes currents towards the radar. The color of the dot shows average velocity and the size of the dot represents the variance over the 24-hour period. The most recent antenna pattern is shown as the black circles.

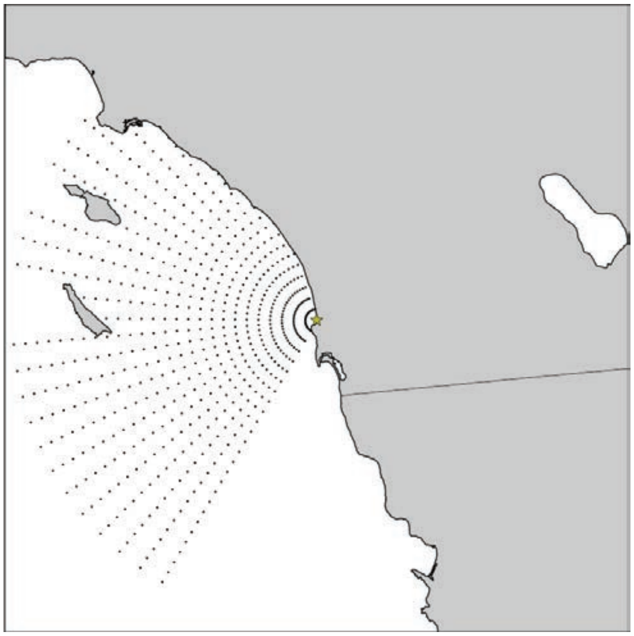

Figure 8: Example of optimal radial grid. Points shadowed by the coast and offshore islands have been removed.

IV. Conclusions

The quality control for a network of High Frequency radars was discussed. The operations and management structure of the radar network in the Mid Atlantic Bight was explained. The existing quality assurance and quality control methods utilized by the technicians and regional coordinator were discussed. We have proposed existing and new methods that can possibly be adopted by other operators around the world. Future work will be to develop algorithms that can take the place of humans inspecting the data at each level.

Acknowledgments

This work was funded by NOAA Award Number NA11NOS0120038 “Towards a Comprehensive Mid-Atlantic Regional Association Coastal Ocean Observing System (MARACOOS)”. Sponsor: National Ocean Service (NOS), National Oceanic and Atmospheric Administration (NOAA) NOAA-NOS-IOOS-2011-2002515 / CFDA: 11.012, Integrated Ocean Observing System Topic Area 1: Continued Development of Regional Coastal Ocean Observing Systems.

References

[1] "Handbook of Automated Data Quality Control Checks and Procedures," *NDBC Technical Document 09-02,* pp. 1-78, 2009.

[2] S. Pouliquen and D.-M. w. Group, "Recommendations for in-situ data Real Time Quality Control," *EuroGOOS Publication No. 27, EuroGOOS Office, SMHI, 601 76 Norrkoping, Sweden,* 2011.

[3] H. J. Roarty, S. M. Glenn, J. T. Kohut, D. Gong, E. Handel, E. Rivera Lemus, T. Garner, L. Atkinson, C. Jakubiak, W. Brown, M. Muglia, S. Haines, and H. Seim, "Operation and Application of a Regional High Frequency Radar Network in the Mid Atlantic Bight," *Marine Technology Society Journal,* vol. 44, pp. 133-145, 2010.

[4] T. Cook, L. Hazard, M. Otero, and B. Zelenke, "Deployment and Maintenance of a High-Frequency Radar for Ocean Surface Current Mapping: Best Practices," *Southern California Coastal Ocean Observing System,* p. 35, February 1, 2008 2008.

[5] J. Harlan, "A Plan to Meet the Nation's Needs for Surface Current Mapping," *NOAA IOOS,* p. 64, September, 2009 2009.

[6] H. Roarty, M. Smith, J. Kerfoot, J. Kohut, and S. Glenn, "Automated quality control of High Frequency radar data," in *Oceans, 2012*, 2012, pp. 1-7.

[7] J. T. Kohut and S. M. Glenn, "Improving HF Radar Surface Current Measurements with Measured Antenna Beam Patterns," *Journal of Atmospheric and Oceanic Technology,* vol. 20, pp. 1303-1316, September 01, 2003 2003.

[8] A. J. Abascal, S. Castanedo, R. Medina, I. J. Losada, and E. Alvarez-Fanjul, "Application of HF radar currents to oil spill modelling," *Marine Pollution Bulletin,* vol. 58, pp. 238-248, 2009.

High Frequency Radar Measurement Resiliency with Bistatics

Chloe Baskin, Hugh Roarty,
Lucas Marxen, Scott Glenn
Center for Ocean Observing Leadership
Rutgers University
New Brunswick, NJ USA
chloe.baskin@rutgers.edu

Chad Whelan, Don Barrick
CODAR Ocean Sensors
Mountain View, CA USA
chad@codar.com

Abstract— **Increasing the resiliency of High Frequency radar measurements has been a priority within the community for the past several years. One method to increase resiliency is through the use of a bistatic radar configuration, which is unique to the SeaSonde HF radar. This is achieved by separating the transmit and receive stations and then linking them through the Global Positioning System (GPS) reference time signal. A study was undertaken to determine the impact of bistatic data on the surface current measurements of the Mid Atlantic Bight. Simulation software was used to model different permutations of transmit and receive stations to determine if there was an optimal configuration. The software modeled the Geometric Dilution of Statistical Accuracy (GDOSA) of the HF radar coverage area. GDOSA describes regions where combination from radials to totals is of high accuracy because the crossing angle between measurements from two different radars is orthogonal. The converse to this are regions where the total vector measurement are of low accuracy because the measurements from two different radars are nearly parallel. The scenarios tested included the bistatic measurements from the adjacent two, three and four stations on either side of a receive station. The simulation was applied to the 5, 13 and 25 MHz networks that are operated as part of the Mid Atlantic Regional Association Coastal Ocean Observing System (MARACOOS). We also simulated radars being offline to determine if any were more critical than others. Initial findings indicate that the area of highest data quality can be increased by a factor of five when the network is fully bistatic. The use of three or four adjacent radars did not increase the coverage compared to the adjacent two radars. The results of the site outage tests indicated that the loss of certain sites could reduce the coverage of the network by as much as 55%. The results found here have implications for the approximately 300 High Frequency radars that are in operation around the globe. With the addition of a hardware and software to make the network bistatic the coverage area with the highest accuracy can be increased by a dramatic amount.**

Index Terms—HF radar, remote sensing, quality control, bistatic, MARACOOS, Ocean Observing

I. Monostatic, Bistatic, and Multistatic

The Mid-Atlantic Regional Association Coastal Ocean Observing System (MARACOOS) is a regional association of the US Integrated Ocean Observing System (IOOS). It has pushed for increasing the quality and resilience of its High-Frequency radar network (Figure 1). Increasing the quality and resiliency of the HF radar network is important not only for an improved understanding of the movement of organic and inorganic material through the coastal ocean, but also for the United States Coast Guard search and rescue. The United States Coast Guard uses the real time surface currents to help reduce the search area of rescue missions [1]. Increasing the quality of the measurements and the resiliency of the radars, especially in storms, can potentially save lives.

Currently the Mid-Atlantic HF Radar Network has a total of 45 HF radars, which is composed of 17 long-range (5MHz), 7 standard range (13MHz), and 21 high-resolution radars (25MHz). The long-range radars provide coverage of the entire Mid-Atlantic Bight (MAB) and have a range of 200 km offshore. The standard range radars cover the coast of New Jersey to study offshore wind resource [2]. The high-resolution radars measure the currents of the five major estuaries in the region. Currently all the radars in the region run in a monostatic mode.

A monostatic configuration, sometimes referred to as a backscatter, is when the HF radar transmits and receives from the same site resulting in a radial measurement of current. A bistatic configuration [3] can be accomplished by using a GPS reference time signal to link separated transmit and receive stations. The geographical separation of transmit and receive sites leads to an elliptical geometry for current measurements. A multistatic configuration is a network that is run in monostatic and bistatic mode. Using a bistatic or multistatic system can increase the quality of the radar signal.

The bistatic configuration will allow for a higher quality of coverage as it will increase the number vector solutions for the total vector combination as well as adding solutions with different bearing angles to reduce the geometric error. Additionally a bistatic system can result in higher resiliency since during storms or hurricanes if a monostatic system stops reporting, then a coverage gap can develop. In a bistatic configuration, the surrounding radars

978-0-933957-43-5 ©2015 MTS

will be able to provide coverage in the area of the malfunctioning radar.

The combination of radial velocities into a total vector measurement carries with it a position dependent error on the vector solution. For instance, the total vector measurement along the baseline between two radars will be poor as both radars are incapable of measuring the component of the current perpendicular to the baseline. This is described as the Geometrical Dilution of Precision (GDOP) [4, 5]. The concept of GDOP has been expanded upon to be described as the Geometric Dilution of Statistical Accuracy (GDOSA) [6]. The GDOSA is not meant to be used with measured data. It is meant as a tool to estimate total vector quality based on the number and location of radar stations in the network.

This specific study will be conducted with radars covering the MAB and radars that cover the Lower Bay portion of the New York Harbor. There will be two scenarios on the MAB comparing the effectiveness of bistatics with the current monostatic system. In the New York Harbor, there were five scenarios tested, three of which are comparing the current monostatic situation with a bistatic configuration. The last two situations deal with the addition of a new station at either Old Bridge, NJ or Union Beach, NJ.

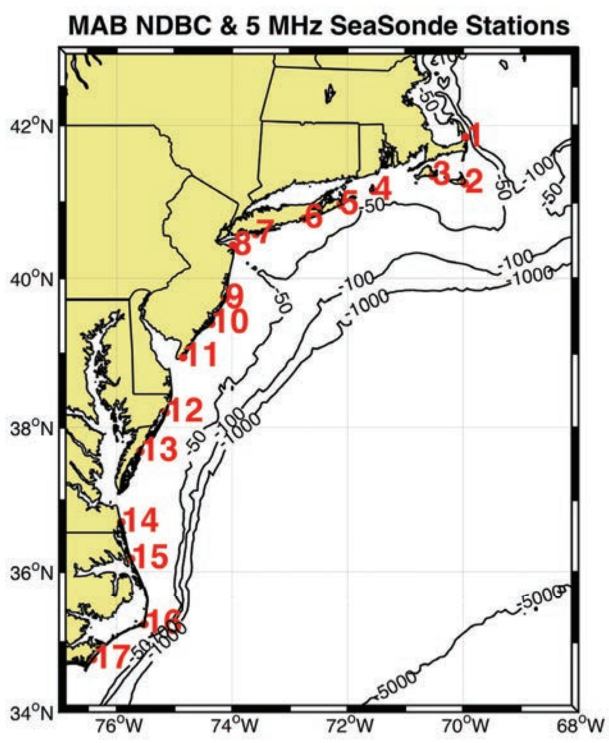

Figure 1: Location of the HF radar stations (red triangles) sites used in this study. The four-letter site code represents the name of each site.

II. Methods

CODAR Ocean Sensors provided the GDOSA code that was used. GDOSA was used to estimate the quality of proposed radar sites. GDOSA calculates the inaccuracies in the 'u', 'v', and 'w' [4]. The 'w' is equivalent to the total velocity and is derived from the vector components 'u' and 'v'. The 'u' component is the horizontal movement and the 'v' is the vertical movement. Inaccuracies are calculated using a series of formulae that determine when the radial measurements are orthogonal. As the angles between the radial measurements approach being orthogonal the accuracy increases.

The GDOSA code utilizes a pair of configuration files as input, a site file and a pairing file. The site file stores the coordinates for the station, along with the range, frequency and coverage bearing angles. Each site is also assigned a site identification number. The pairing file lists which stations are bistically linked to one another. The GDOSA code then combines the monostatic and bistatic configuration to assess the multistatic configuration.

A. The Mid-Atlantic Bight

There are a total of 17 long-range radar sites in the Mid Atlantic (Figure 1, Table 1). GDOSA code was run where each station was in monostatic and then the pairing file was modified to put the network in a multistatic mode. Figure 2 outlines the bistatic pairings that were established. The MAB was divided into north, central and southern sub-regions [1]. In each sub-region, a station was selected to receive the bistatic signals from all other stations in the sub-region. The next station in the list would receive the remaining bistatic signals and so forth. For example, the five stations in the north combine to form 11 bistatic pairings.

The GDOSA code delineates areas of good (low uncertainty) to poor (high uncertainty) total vector combination. The spatial coverage area for each uncertainty bin for the different pairings was calculated. The minimum uncertainty zone is a range between 0 - 0.25 (Table 2). There are 5 bins, including the maximum uncertainty zone, ending at 3. We also measured the coverage drop where each of the 17 stations was removed from the network to gauge the coverage loss in a monostatic and bistatic configuration.

Table 1: Each long-range site from north to south is numbered along with the 4-letter site code for the station. This table corresponds with each numbered stations in Figure 1.

Site #	Site Code
1	NAUS
2	NANT
3	MVCO
4	BLCK
5	AMAG
6	MRCH
7	HEMP
8	HOOK
9	LOVE
10	BRIG
11	WILD
12	ASSA
13	CEDR
14	LISL
15	DUCK
16	HATY
17	CORE

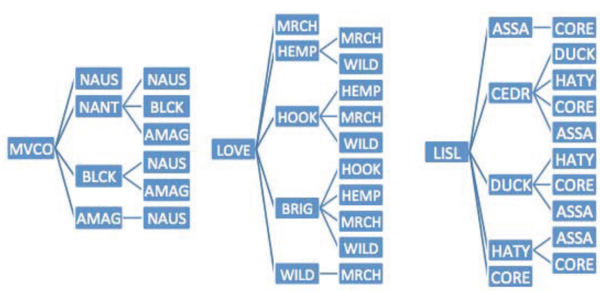

Figure 2: A chart that describes the bistatic pairing of the radars. It is to be read left to right and top to bottom. For example, MVCO recieves the reflected signal from NAUS, NANT, BLCK, and AMAG.

B. New York Harbor

In New York Harbor there are 2 sites, each 25MHz (Figure 6). One station is located in Port Monmouth, NJ (PORT) and the other is located in Great Kills, NY (SILD). Here we tested 5 different scenarios 1) both stations in monostatic mode 2) SILD as the bistatic transmitter 3) PORT as the bistatic transmitter 4) the addition of a third site in Old Bridge, NJ (Figure 9) and 5) the addition of a third site in Union Beach, NJ. The two new sites were tested to see which improved quality and resiliency of the system the most. Then each scenario was compared to one another in terms of area coverage area of each uncertainty bin.

III. Results

A. The Mid-Atlantic Bight

For the 5 MHz radars covering the MAB, the bistatic configuration (Figure 4) greatly improved the coverage along the coast when compared to the monostatic configuration (Figure 3). Table 2 shows the spatial coverage area of each uncertainty bin for the monostatic and bistatic scenario. The area of minimum uncertainty increased by 71,682 square kilometers in the bistatic pairing, an increase of 188%. Overall the total area increased approximately 40,000 km^2. These results suggest that a multistatic system would give the highest quality of signal along the East Coast. However the switch to a multistatic system adds an additional 40 elliptical files to be processed with 17 radial files. The number of files that to be processed would more than double, leading to potential strain on the operators to maintain 57 data streams over the current load of 17.

The impact of losing an individual radar station was also analyzed. Figure 5 shows the coverage area of the lowest uncertainty bin (0-0.25) for the monostatic network. Each column lists which station was removed from the network. The loss of Station 9 in Loveladies, NJ causes the largest decrease in coverage for the network. This helps inform our resiliency steps as to which stations are critical for operations.

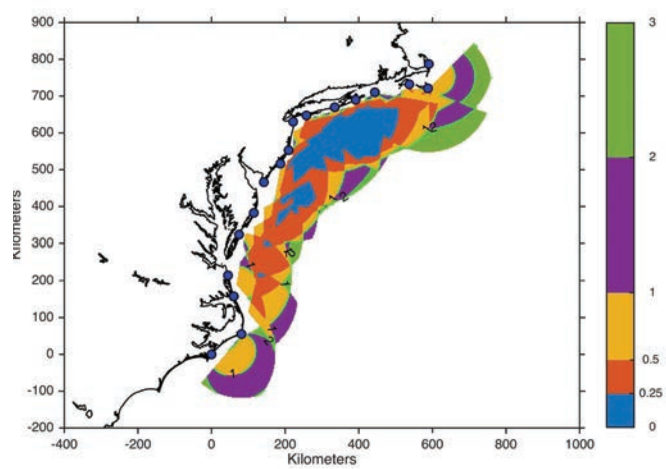

Figure 3: A graphic depicting the coverage of radars under a monostatic configuration. The blue area is the highest signal quality, as it has the lowest uncertainty.

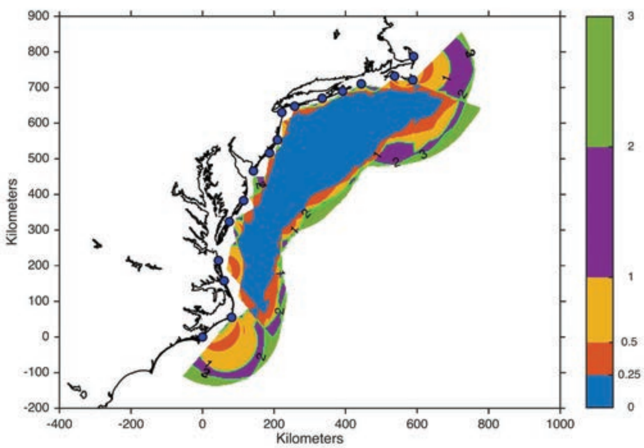

Figure 4: A graphic depicting the coverage of the radars under a multistatic system. The amount of high quality signal coverage has increased compared to the monostatic configuration.

Table 2: The signal quality range brackets and the area in square kilometers. The highlighted row is the "minimum uncertainty zone".

Signal Total vector coverage and uncertainty	Area (Sq. Km.)		Area gained/lost
0.0 – 0.25	38,138	109,820	71,682
0.25 - 0.5	46,444	28,725	-17,719
0.5 – 1.0	41,700	34,719	-6,981
1.0 – 2.0	40,444	33,669	6,775
2.0 – 3.0	24,600	24,756	156
TOTAL AREA	191,326	231,689	40,363

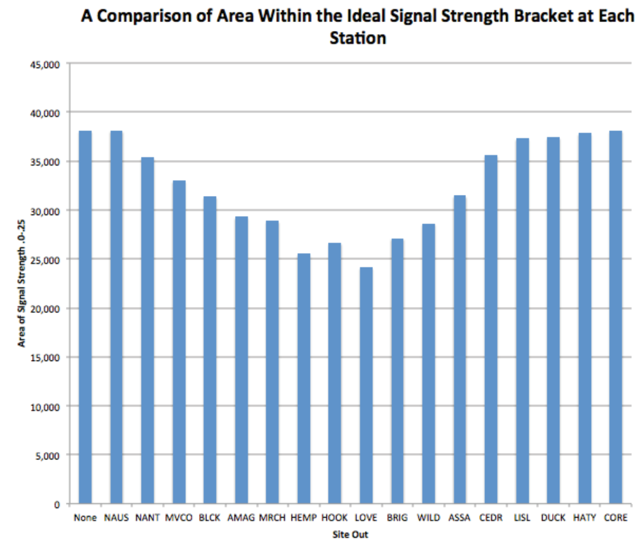

Figure 5: The impact on total coverage the when an individual site is offline. Each bar represents the station that is offline and the y-axis denotes the coverage area (km^2) of the 0-0.25 uncertainty bin.

B. New York Harbor

In New York Harbor, with the current sites SILD and PORT (Figure 6), the total area on a backscatter system is only 150 square kilometers (Table 3). With a multistatic system transmitting from SILD (Figure 7), the total area does not increase but the quality does. In the backscatter system there is no coverage in the first two signal quality bins (0.0 -0.5). In the multistatic system transmitting from SILD there is a 43.75 square kilometer increase in the second highest signal quality bracket. When the system is multistatic and transmitting from PORT (Figure 8) the total area increases by about 31 square kilometers. When compared to the existing backscatter only configuration, the multistatic system of transmitting from PORT results in higher quality.

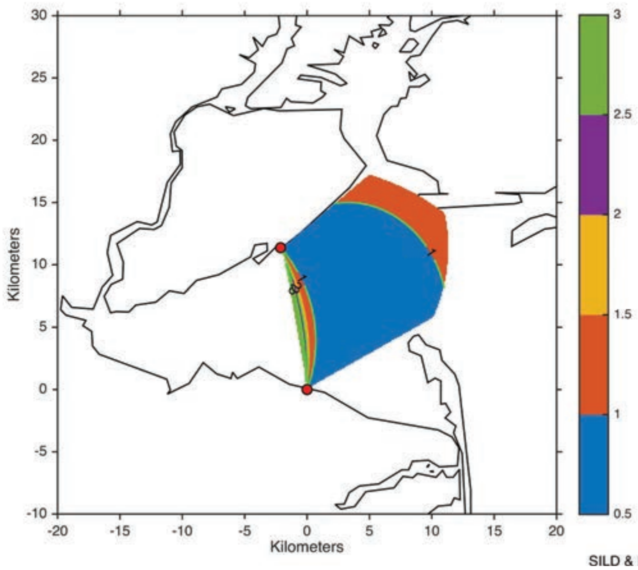

Figure 6: The coverage of the current radar sites in NY Harbor. This is a monostatic configuration with SILD and PORT. The resiliency of this configuration is low.

The addition of another site in Old Bridge, NJ increased the total area and the overall quality of the network (Figure 9). With the addition of Union Beach (Figure 10) the coverage area increased but not as much as with the addition of the Old Bridge site. The code in its current state does not allow for land masking so that explains the coverage on land. This is a drawback that will be addressed and fixed in a future release.

A graphical representation of Table 3 is shown in Figure 11. This confirms that scenario 4 is optimal for increasing the coverage in New York Harbor.

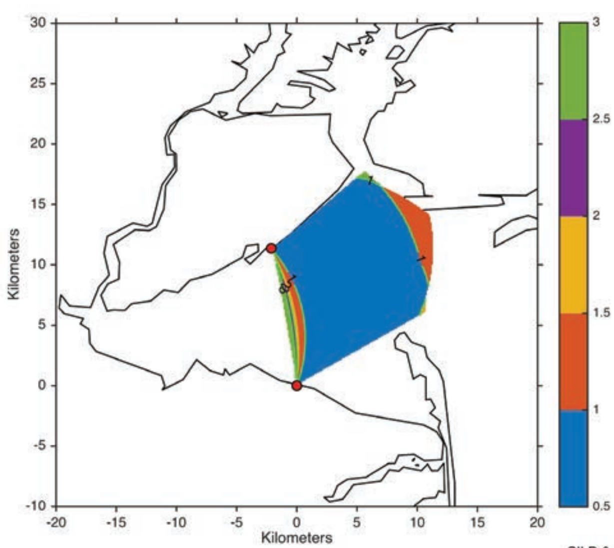

Figure 7: Coverage of the NY Harbor multistatically transmitting at SILD. This system has higher resiliency due to the bistatic pairing.

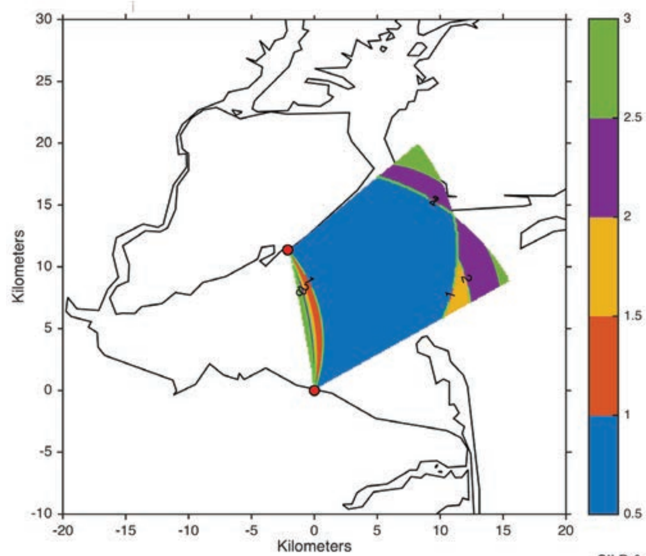

Figure 8: A graphical depiction of the NY Harbor sites in a multistatic configuration transmitting from PORT. This is more resilient due to the bistatic configuration.

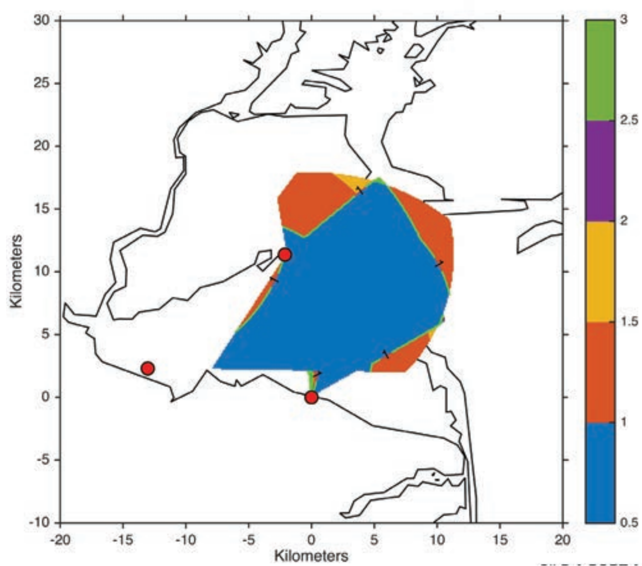

Figure 9: The NY Harbor sites in a monostatic configuration with the addition of a site in Old Bridge, NJ. Even though this is a monostatic configuration the resiliency has increased due to the additional site.

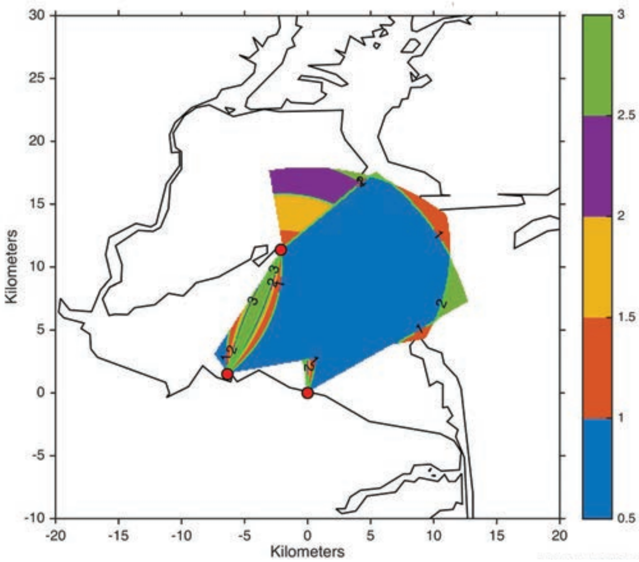

Figure 10: The NY Harbor sites in a monostatic configuration with the addition of the Union Beach site.

Table 3: The signal quality for each scenario in New York Harbor. Scenario 1 is the current status in NY Harbor. Scenario 2 is a multistatic configuration transmitting from SILD. Scenario 3 is a multistatic configuration transmitting from PORT. Scenario 4 is a monostatic configuration with the addition of Old Bridge, NJ site. Scenario 5 is a monostatic configuration with the addition of Union Beach, NJ site.

Scenario	1	2	3	4	5
Signal Total vector coverage and uncertainty	**Area (Sq. Km)**				
0.0 – 0.25	0	0	0	0	0
0.25 – 0.5	0	43.75	50	93.75	93.75
0.5 – 1.0	106.25	81.25	81.25	87.5	68.75
1.0 – 2.0	37.5	18.75	12.5	50	18.75
2.0 – 3.0	6.25	6.25	37.5	0	43.75
Total Area	150	150	181.25	231.25	225

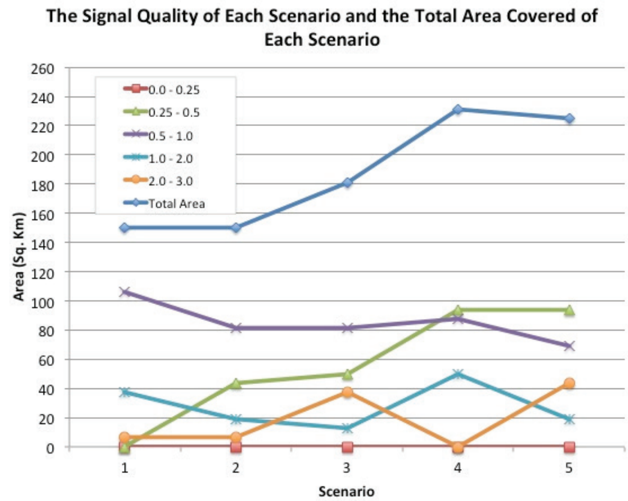

Figure 11: A graphical representation of each scenario for New York Harbor and the coverage area for each uncertainty bin.

IV. Conclusion

Increasing the resiliency and accuracy of HF radar through bistatics is possible. GDOSA is an effective tool to calculate if a multistatic configuration will decrease the uncertainty of the total vector measurement. As seen in the MAB, the uncertainty can drop drastically with the addition of bistatic pairings. The multistatic configuration in the MAB added 40 more elliptical files that need to be analyzed which could be a potential challenge for quality assurance and quality control measures.

In New York Harbor GDOSA predicted that transmitting from SILD will yield a higher quality than if the bistatic signal originated from PORT. It has also proved itself useful with predicting future CODAR sites. After comparing the addition of an Old Bridge or Union Beach site, Old Bridge provides more coverage. When the Old Bridge site is eventually installed tests will be run to compare the predicted coverage with the actual coverage.

V. Acknowledgments

This work was funded by NOAA Award Number NA14NOS4830003 “Repair and Hardening of Mid Atlantic Ocean Observing Assets After Hurricane Sandy”.

This work was funded by NOAA Award Number NA11NOS0120038 “Towards a Comprehensive Mid-Atlantic Regional Association Coastal Ocean Observing System (MARACOOS)”. Sponsor: National Ocean Service (NOS), National Oceanic and Atmospheric Administration (NOAA) NOAA-NOS-IOOS-2011-2002515 / CFDA: 11.012, Integrated Ocean Observing System Topic Area 1: Continued Development of Regional Coastal Ocean Observing Systems.

VI. REFERENCES

[1] H. J. Roarty, S. M. Glenn, J. T. Kohut, D. Gong, E. Handel, E. Rivera Lemus, T. Garner, L. Atkinson, C. Jakubiak, W. Brown, M. Muglia, S. Haines, and H. Seim, "Operation and Application of a Regional High Frequency Radar Network in the Mid Atlantic Bight," *Marine Technology Society Journal,* vol. 44, pp. 133-145, 2010.

[2] G. Seroka, J. Kohut, L. Palamara, S. Glenn, H. Roarty, L. Bowers, and R. Dunk, "Spatial evaluation of high-resolution modeled offshore winds using estimated winds derived from a network of HF radars," in *Oceans - San Diego, 2013*, 2013, pp. 1-5.

[3] J. I. Glaser, "Fifty years of bistatic and multistatic radar," *Communications, Radar and Signal Processing, IEE Proceedings F,* vol. 133, pp. 596-603, 1986.

[4] R. D. Chapman, L. K. Shay, H. C. Graber, J. B. Edson, A. Karachintsev, C. L. Trump, and D. B. Ross, "On the accuracy of HF radar surface current measurements: Intercomparisons with ship-based sensors," vol. 102, pp. 18737-18748, 1997.

[5] R. D. Chapman and H. C. Graber, "Validation of HF radar measurements," *Oceanography,* vol. 10, pp. 76-79, 1997.

[6] D. Barrick, *Geometrical Dilution of Statistical Accuracy (GDOSA) in Multi-Static HF Radar Networks*, 2006.

Evaluation of Three Antenna Pattern Measurements for a 25 MHz SeaSonde

Colin W. Evans, Hugh J. Roarty, Ethan M. Handel, Scott M. Glenn
Center for Ocean Observing Leadership
Rutgers University DMCS
New Brunswick, United States of America

***Abstract* – The need for reliable surface current measurements from the SeaSonde high-frequency radar network is essential for Coast Guard search and rescue missions, oil spill mapping, and algal bloom tracking. To ensure the advancement of accurate surface current maps, antenna calibrations need to be performed to correct for bearing errors at the radial level. Due to environmental interference, three different antenna pattern measurements were performed at a 25 MHz radar site located in Staten Island, NY (SILD). Spectra taken over a three-day period starting from Oct. 15, 2014 were reprocessed using the different pattern methods and analyzed with the ideal radial measurements from the same time period at three separate bearing locations 9 km offshore in the New York Harbor.**

***Index Terms* – HF (high-frequency) radar, antenna pattern measurements, SeaSonde**

I. INTRODUCTION

Antenna calibrations play a major role in correcting for bearing errors. At the radial level, bearing errors result from several known factors such as limitations resulting from noise and interference in the received signals, distortions in the antenna sensitivity patterns, limitations in the signal processing methods, and limitations in the frequency resolution [1]. This paper focuses on pattern sensitivity by analyzing different antenna pattern calibration methods.

Two 25 MHz direction-finding CODAR (Coastal Ocean Dynamics Applications Radar) systems are located in Port Monmouth, NJ and Staten Island, NY that measure surface currents within the New York Harbor. Each of these high-frequency radars within the network measure the scattered return radio signal off of a 6-meter-long surface gravity wave [2] and produce hourly radial maps of current velocities. When hourly radial files are inputted into the totals processing, a high-resolution (1-km range bin) current map is produced to get a velocity and directional component of the surface currents. Since there is no third high-frequency radar site operating within the harbor, it is important that the radial field from each site is as accurate as possible.

Three different antenna pattern calibrations were performed for the 25 MHz high-frequency radar site in Staten Island, NY. The first pattern generated from the site was processed through new software that takes AIS information and creates TRAK files to be inputted into the AIS-pattern generation algorithm. In order to measure an accurate pattern, the AIS system on site must run for an average of a few days. Daily loop files are created that are then processed through the application CrossLoopPatterner. Based on the file sizes, more than one loop file can be processed at one time. Through the AIS filter tab in CrossLoopPatterner, the loop files can be refined by altering the local and IIR signal to noise values, bearing hits, Doppler width, range width, and time of day.

The second and last antenna calibrations that were completed were walking and boat patterns, respectively. Both of these antenna pattern measurements are still much more common than AIS-generated patterns and are used for many CODAR sites. These calibrations are accomplished by completing a semi-circle path (equidistant) around the receive antenna with a small battery-operated transponder [3]. The magnified signal from the transponder is echoed off the surface gravity wave (typically between range cells 8-10) for each bearing value, which is every 5 degrees. In both the walking and boat patterns, one loop file is processed with the CrossLoopPatterner application and implemented in the configurations folder.

We examine all three of the discussed antenna calibration methods and analyze the quality of the radial and surface current data. The purpose of this examination is to determine limitations and accuracy of each pattern method. Future work includes combining different pattern calibration methods to limit bearing errors at the radial level, while increasing measured radial coverage.

II. METHODS

Pattern measurements were conducted for the 25 MHz CODAR site SILD. The pattern calibrations were performed and processed within less than two weeks of each other. The dates of the antenna pattern calibrations are displayed in table 1. No changes to the hardware or processing parameters were made during the duration between pattern calibrations.

Spectra files were reprocessed with each pattern between October 15, 2014 and October 18, 2014 with no changes in the first order line settings. Reprocessing was accomplished with an offline batch-reprocessing application written by CODAR Ocean Sensors [4]. The app outputs a folder containing the configuration settings and radial files.

Pattern Method	Date
Walking	August 26, 2014
Boat	August 28, 2014
AIS	August 20, 2014

Table 1. Dates when pattern calibrations were conducted.

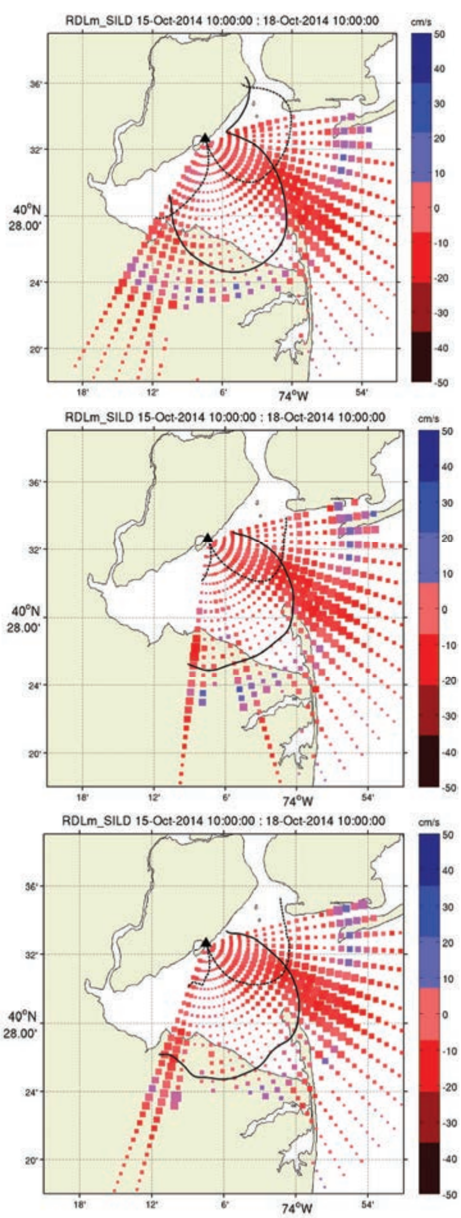

Figure 1. From top to bottom - patterns measured for 25 MHz CODAR SILD by walking, boat, and AIS, respectively averaged over 3-day examination period.

Figure 1 shows the processed patterns overlaid on top of an averaged radial velocity plot with an applied standard deviation. The color bar indicates whether the surface current is moving towards (blue) or away (red) from the radar and the size of the icon signifies the standard deviation value (large dot means higher standard deviation). Some locations within the channel will inevitably have higher standard deviation values with the M2 tide.

Three bearing locations were chosen 9-km offshore as a way of comparing temporal variability between each pattern method. The bearings chosen for the examination were 102, 132, and 167 (degrees true) with respect to the antenna location. Figure 2 shows the site and bearing locations within the harbor.

The bearing of loop 1 (loop 2 null) is 167 degrees, which was one of the bearings chosen for this study. A bearing of 132 degrees is nearly perpendicular to the coastline and is also close to where loop 1 and loop 2 intersect. The last bearing of 102 degrees was chosen because of the higher current velocity shifts in that area from the M2 tidal constituent. Range cell 9 was selected because the Bragg starts to split after range cell 10 and first order processing can be challenging, which would make it difficult to compare antenna pattern measurement methods.

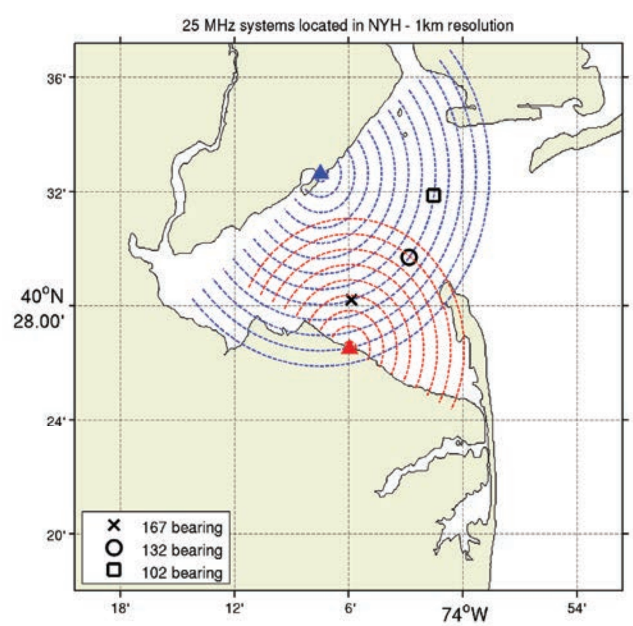

Figure 2 Location of the two 25 MHz site locations (blue - SILD, red - PORT) and bearings chosen 9-km offshore for the examination.

Radial velocities for each bearing were compared with the ideal measurements for each hour over the 3-day examination period. Correlation values were calculated between each pattern method and the ideal radial measurements. Surface current maps were then created with each pattern with the Port Monmouth 25 MHz CODAR site.

III. RESULTS

The radial velocities for each of the selected bearings within each pattern method were analyzed over the 3-day time period. No averaging was done since we are comparing hourly velocity measurements for each hourly radial file. Figure 3 shows the hourly radial measurements for bearings 102, 132, and 167. The variation in radial velocities differ greatly in the 167 bearing bin, which is related to the flow of the current and the radar's inability to depict a clear Doppler shift at that location. For a majority of the time-span, the radial velocities did not differ much at bearing locations 102 and 132, with the exception of a few outliers, which are evident mostly in the AIS-generated pattern.

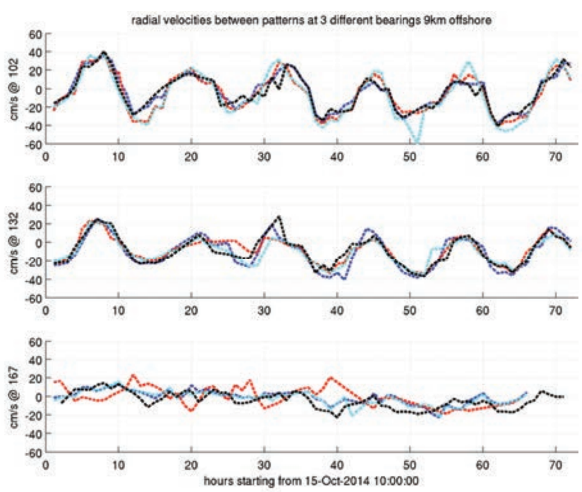

Figure 3. Radial velocities for each pattern (blue - walking, red - boat, cyan – AIS, black - ideal) at 3 different bearings.

Table 2 shows the associated correlation values (r) comparing each measured hourly measured radial velocity component with the ideal measurements at each bearing. The highest correlation was witnessed with the walking pattern measurement at 0.96 with a bearing of 102, 9-km offshore. The least amount of variation in the correlation values was seen in the 132 degree bearing location, which is nearly perpendicular to the coastline. The correlation values decreased by more than 20% for the walking and AIS patterns for the radial measurements recorded at 167 degrees. The boat pattern experienced a significant drop to the point where there is a slight negative correlation of 0.14. This bearing location is very close to the baseline between the two New York Harbor sites, which can validate the drop in correlation.

Figure 4 shows the correlation between the hourly radial velocities for each pattern at each bearing location with the ideal hourly radial velocity components. Each pattern showed a strong correlation with the ideal measurements at bearing locations 102 and 132, but the correlation drops for bearing 167. The walking and AIS antenna pattern measurements show a significant decline in correlation but the most notable is the boat-generated pattern, which actually shows a negative correlation.

Bearing	Walking	Boat	AIS
102	0.96	0.90	0.89
132	0.90	0.92	0.91
167	0.73	-0.14	0.70

Table 2. Correlation coefficients between measured and ideal radial velocities.

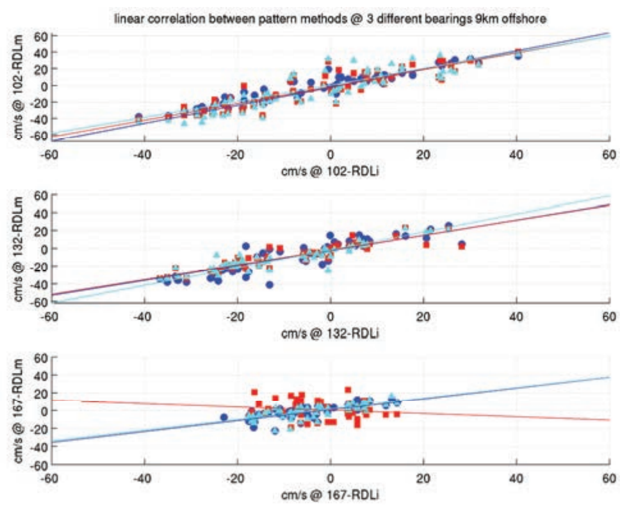

Figure 4. Correlation between ideal (x-axis) and measured (y-axis) radial velocities at each hour for different patterns (blue - walking, red - boat, cyan- AIS).

Figure 5 shows the 24-hourly averaged surface current maps between Oct 16, 2014 at 10:00 GMT and Oct 17, 2014 at 10:00 GMT. The spatial variability of the surface currents for each pattern differs minimally for each pattern method combined with the measured radials measured from PORT (Port Monmouth, NJ). On a temporal scale, there is small variability at bearings 102 and 132 (localized more in the center of the channel). Bearing 167 (max. of loop 1) shows a larger variance in the surface current velocities with respect to time. Without a third New York Harbor site operating at 25 MHz, baseline biases are inevitable which is near the location of the 167 bearing location. Rutgers is currently operating mobile test runs for a third 25 MHz radar site.

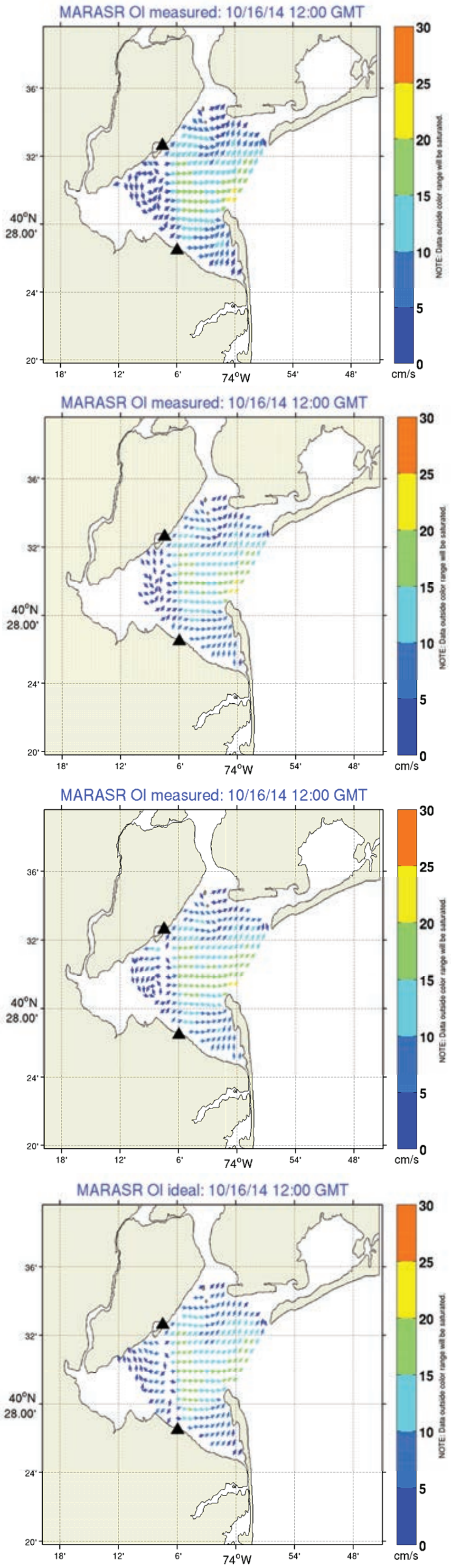

Figure 5. From top to bottom: Surface currents measured with walking, boat, AIS, and ideal patterns.

IV. CONCLUSIONS

Three different pattern calibration methods were examined for a 25 MHz CODAR system. The calibrations were performed with no changes in the hardware or spectra processing parameters. The correlation between ideal radial velocities and measured radial velocities was strong in the middle of the channel (bearing values of 102 and 132) with the lowest correlation being 0.89, seen in the AIS-generated pattern.

However, the correlation weakened at bearing 167. This bearing lies nearly along the baseline between the two 25 MHz systems, which proves to be challenging in depicting surface currents with two radar stations within the network as discussed in [5].

Measured radial coverage decreased most with the boat pattern, mostly due to our inability to complete a full semi-circle path with the shallow bathymetry. Radial and total coverage differed minimally between the walking and AIS-generated patterns. Further research includes combining different pattern methods to improve both coverage and surface current accuracy.

ACKNOWLEDGEMENTS

The authors would like to acknowledge MARACOOS – Mid-Atlantic Regional Association Coastal Ocean Observing System and NOAA Sandy Supplemental for funding this project.

REFERENCES

[1]. laws, K., Paduan, J.D., Vesecky, J., "Estimation and Assessment of Errors Related to Antenna Pattern Distortion in CODAR SeaSonde High-Frequency Radar Ocean Current Measurements," *American Meteorological Society,* Vol. 27, pp.1029-1043, 2010.

[2]. Kohut, J.T. and Glenn, S. M., "Improving HF Radar Surface Current Measurements with Measured Antenna Beam Patterns," *j. Atmospheric and Ocean Technology*, Vol. 20, pp.1303-1316, 2003.

[3] Barrick, D.E., Lipa, B. L., "Using Antenna Patterns to Improve the Quality of SeaSonde HF Radar Surface Current Maps," *Ocean Engineering*, Vol. 11-2, pp.304-309.

[4]. Evans, C., Roarty, H., Smith, M., Kerfoot, J., Glenn, S., Parikh, H., Whelan, C., "Improvement of Surface Current Measurements with Spectra Reprocessing for 13 MHz SeaSonde Systems," *Oceans – San Diego, 2013*, pp.1-5, 2013.

[5]. Atwater, D.P., Heron, M.L, “HF Radar Two-Station Baseline Bisector Comparisons of Radial Components,” *OCEANS 2010 IEEE – Sydney,* pp.1-4.

Measuring Waves with a Compact HF Radar

Robert Forney, Hugh Roarty, Scott Glenn
Center for Ocean Observing Leadership
Rutgers University
New Brunswick, NJ USA
robert.k.forney@gmail.com

Abstract— **Ocean wave conditions impact many ways in which humans interact with the ocean, from the safety of recreation at the beach to the viability of offshore operations. Wave conditions are also topical from a research perspective, controlling processes such as coastal erosion and ocean mixing. Therefore, being able to characterize wave conditions on broad spatiotemporal scales is extremely valuable. A network of High-Frequency (HF) radar systems can provide measurements of wave conditions in near-real time along the coast where better observations are needed. Measurement of wave parameters such as significant wave height, wave period and wave direction is a secondary function of the SeaSonde HF radar. Waves are measured with SeaSonde HF radars from the second-order portion of the echo spectrum. The Doppler shift of the radio transmission from the SeaSonde contains information about the orbital velocity of the primary Bragg waves and the larger waves that they ride on. Since the wave data is dependent upon the occurrence of both Bragg and larger surface gravity waves, there is a minimum threshold for sea states in which reliable wave parameters can be determined. There is also a limiting factor for the radar in large sea states as the first-order spectra merge with the second-order and interpretation of the spectra becomes impossible with existing methods. We have tested methods for wave extraction and will present the results here. Our analysis explores the frequency-dependent threshold wave conditions for reliable wave parameter measurements, and which systems provide the best measurements. We also tested different radio waveform parameters to see which performed best in different environmental conditions. The study focuses on in-situ wave measurements from National Data Buoy Center (NOAA) buoys within the domain of the HF radar network, deployed offshore of Long Island and Delaware Bay, as well as mooring deployments of opportunity closer to the coast. Measurements will also be evaluated within the context of larger scale wave models routinely run in the area by NOAA. The threshold conditions determined by this study will guide the application of HF radar-based wave estimates to surf zone conditions by local weather forecast offices.**

Keywords—radar, remote sensing, oceanography, waves, NOAA, MARACOOS, CINAR

I. Introduction

Ocean wave conditions impact practically many ways in which humans interact with the ocean, from the safety of recreation at the beach to the viability of offshore operations. Wave conditions are also topical from a research perspective, controlling processes such as coastal erosion and ocean mixing. Therefore, being able to characterize wave conditions on broad spatiotemporal scales is extremely valuable for stakeholders interested in making economic use of the ocean as well as researchers addressing larger questions that ultimately interest consumers. High-Frequency (HF) radar systems provide one potential means of measuring wave conditions in near-real time. The Mid-Atlantic HF radar network consists of a 5-MHz long-range network that provides ocean surface current coverage over the entire Mid-Atlantic Bight with a range of 200 km offshore, a 13-MHz mid-range network that provides mesoscale coverage along the coast of New Jersey, and a 25-MHz short-range network that provides high-resolution sampling of several major estuaries. There are 45 SeaSonde HF radars operating in the Mid-Atlantic Bight (MAB) in total; we have chosen the MAB as our study domain because of the extensive spatiotemporal coverage of the network there. The main purpose of the HF radars in the Mid-Atlantic HF radar network is to measure surface currents, which has been their principal function since their inception more than thirty years ago.

Measurement of wave parameters such as significant wave height, wave period and wave direction is a secondary function of the SeaSonde HF radar. Waves are measured with HF radars from the second-order portion of the echo spectrum. This is distinctly separated from the first-order Bragg peaks that make current mapping possible. The derivation of the classic model presently employed by several groups for HF wave measurements was done 43 years ago [1]. Lipa first showed how this echo could be inverted to give wave spectral information. The methods were next extended to the CODAR compact cross-loop antenna [2]. Since these data are derived from the weaker second-order spectrum, its lower signal to noise ratio limits these data closer to the coast. The Doppler shift of the radio transmission from the SeaSonde contains information about the orbital velocity of the primary Bragg waves as they ride on top of the larger waves.

Since the wave data is dependent upon the occurrence of both Bragg and larger surface gravity waves, there is a minimum threshold for sea states in which reliable wave parameters can be determined. There is also a limiting factor for the radar in large sea states as the first-order spectra

978-0-933957-43-5 ©2015 MTS

merge with the second-order and interpretation of the spectra becomes impossible with existing methods. Also, the perturbation theory on which the inversion model is based breaks down for higher sea states [3]. We have tested methods for wave extraction and will present the results here. Our analysis explores the frequency-dependent threshold wave conditions for reliable wave parameter measurements, and which systems provide the best measurements. We also tested different radio waveform parameters to see which performed best in different environmental conditions. The study focuses on in-situ wave measurements from National Data Buoy Center (NOAA) buoys within the domain of the HF radar network, deployed offshore of Long Island and Delaware Bay, as well as mooring deployments of opportunity closer to the coast. Measurements will also be evaluated within the context of larger scale wave models routinely run in the area by NOAA. The threshold conditions determined by this study will guide the application of HF radar-based wave estimates to surf zone conditions by local weather forecast offices.

II. Background

Radar was first developed for military applications. The development of radar systems was almost simultaneous across Europe as well as in the United States and Russia [4]. Since then, it has been used in the operation of semi-active missile seekers, experimental lunar surface mapping, grounded aircraft intruder detection (security), and ionosphere observation [5].

The SeaSonde Coastal Ocean Dynamics Applications Radar (CODAR) used in monitoring ocean surface currents is different from most radars in a few respects—it operates in the High-Frequency (HF) range, like amateur radio, as opposed to the microwave range that airplane detection and mapping applications use; it has low directivity as a result of the lower HF frequencies; and direction scanning is limited due to the fact that the radar units are limited to the azimuthal direction [4]. The fundamental measurements of the radar are range to target, direction to target relative to reference azimuth, Doppler frequency of target, and power returned from target.

The instrument consists of a transmit and receive antenna positioned on a coastline connected to a computer that stores the collected data and controls the antenna settings. The form of the SeaSonde antenna varies—in the past it was more common for receive antennas to have large "whips" but as of late an omnidirectional whipless configuration is favored—but the concept of its operation remains mostly unchanged. The transmit and receive antennas can be collocated (monostatic) or geographically separated (bistatic). The pulse can reflect off of or be deflected by conducting materials, which is why it is important to install the antennas in a relatively isolated place. Some fraction of the energy is reflected and received at the receive antenna, which carries with it information about the reflecting surface which can be made meaningful through spatial and temporal averaging and processing in the computer.

All stations (or sites) employ a linear frequency sweep to resolve range to target, and can be timed to begin their sweeps with high precision, of the order of ten nanoseconds. This enables backscattered echo to be discerned from background noise [6]. The SeaSonde stations emit radio waves, which go out a certain distance then bounce back off of wave fronts, and can be 'heard' at nearby stations. Dominant echoes appear in the radar spectra as peaks, often called 'Bragg peaks' in reference to the physical phenomenon that gives rise to the increased return from waves of the Bragg wavelength. The first-order peaks give information about the surface currents: the frequency shift of these peaks from the radar frequency belies a Doppler shift, and hence a velocity of the currents being observed relative to the radar. There are also second-order peaks that give information about the waves themselves: the Doppler shift of this second-order peak gives information about the orbital velocity of shorter gravity waves riding on the longest waves present, that are sea surface reflectors for SeaSonde-emitted radio waves. Wave theory provides a means of inferring other characteristics of the surface gravity waves.

III. Methods

Spectra files from the Bradley Beach (BRAD, Figure 1) site from February to June of 2015 were utilized for this study. These spectra files were reprocessed using different averaging schemes to test the hypothesis that poor temporal coverage and random echo noisiness in the data were caused by small number of observations going into the wave characteristic calculations. Previous studies analyzed the wave measurements from the SeaSonde with the default averaging time of 75 minutes [7, 8]. In this study several different averaging schemes were used. The 10-minute spectra files were reprocessed with wave averaging times of 30, 60, 100, 120 and 180 minutes. The resulting significant wave heights and average wave periods as measured by the BRAD SeaSonde in the second range cell were plotted alongside the same measured wave parameters from nearby NDBC buoy 44065. Since our analysis focuses on the quality of the data (presence or absence of gaps and spikes), the distance between BRAD and Buoy 44065 is not important, although it must be kept in mind that Buoy 44065 is in deeper water and hence experiencing wave conditions with somewhat greater heights and longer periods. 44065 is taken to represent wave conditions in the locality of the BRAD observations with only this caveat. We expect the correlation between wave height measurements to be on the order of 0.9 since the distance between the measurements is 30 km [8].

To study the effects of modifying the radar waveform on wave parameterization quality, the 5 MHz site BRIG was set to use enhanced blanking and compared with the nearby 5 MHz site LOVE, which utilized the conventional waveform. The conventional waveform is optimized to listen for echoes from the farthest range cell to maximize the signal-to-noise ratio in outer range bins where surface current measurements are desirable. Enhanced blanking is optimized to listen for echoes in the near range cells where wave parameterizations can be made. It is safe to assume that the wave field does not change significantly between BRIG and LOVE, so observed differences in wave estimates are mostly due to the change in the waveform.

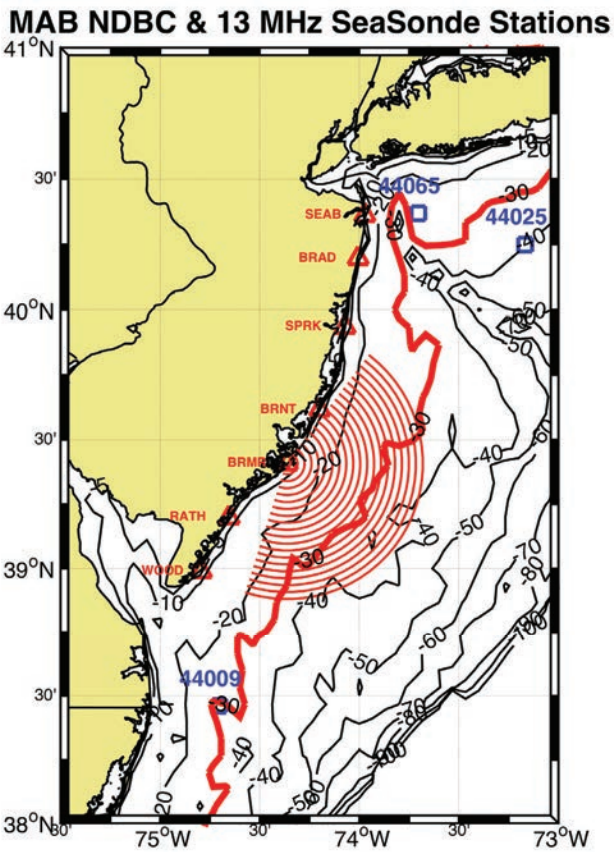

Figure 1: Map of the study area showing the location of the radar stations (red triangles) and buoys (blue squares). Each station is identified with a four-letter site code, and each buoy is identified with its serial number. The bathymetry is marked with the 30m contour as the thick red line. The range cells from the HF radar in Brigantine are the red semicircles.

IV. Results

We began our analysis with a comparison of wave real-time measurements from HF radars operating at different frequencies. Figure 2 shows wave estimates from the 25 MHz site SILD. 25 MHz sites provide higher spatiotemporal resolution wave and current observations over a relatively small region. Figure 3 shows wave estimates from the 13 MHz site BRAD, which provides measurements over a broader spatial range than the 25 MHz. In Figure 4, it is apparent that the long-range 5 MHz systems exhibit more gaps and spikes than the other systems—this is further emphasized by comparison with Figure 5, which is a 5 MHz system without enhanced blanking. The enhanced blanking waveform used at the BRIG site improved measurement quality by increasing temporal coverage. The enhanced blanking is not meant to remove spikes in the wave measurements.

Based on a qualitative comparison of data quality among sites of different frequencies, we decided to pursue improvements in the 13 MHz wave parameterizations first, and used BRAD as our test site. The five month record of reprocessed wave data is shown in Figure 6 along with the measurements from buoy 44065. A one month zoom in on the record is shown in Figure 7.

Time series of wave parameters using different averaging schemes demonstrate an improvement in temporal coverage with increased averaging scheme, with a maximum tradeoff between increase in coverage and loss of information around a two-hour average (Table 1). However, reduction in the number of spikes could not be definitively observed in any averaging scheme (Figures 6-7). Interesting is the observation that gaps could not be avoided for times during which the average wave periods were lower than 5-6 seconds. It is also possible that spikes are due to low wave height conditions. Both of these observations point to the possibility that additional processing techniques will need to be developed or adopted to make inferences about the wave conditions during these times.

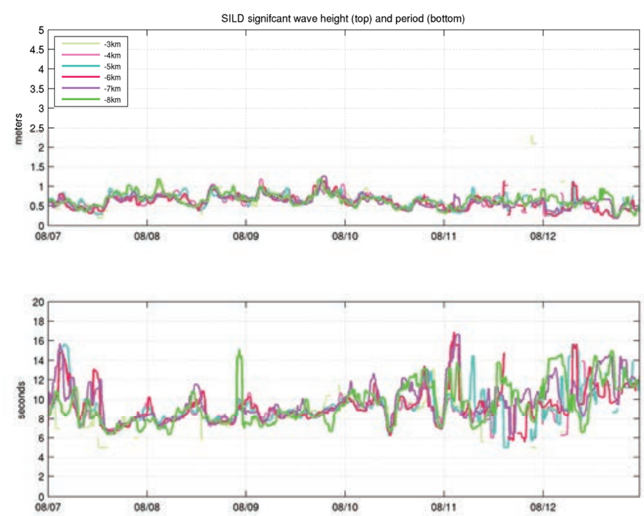

Figure 2: Wave estimates (top: wave height and bottom: wave period) from the SILD 25 MHz site from August 7-13, 2015. The different colors represent the range cell of the wave measurement.

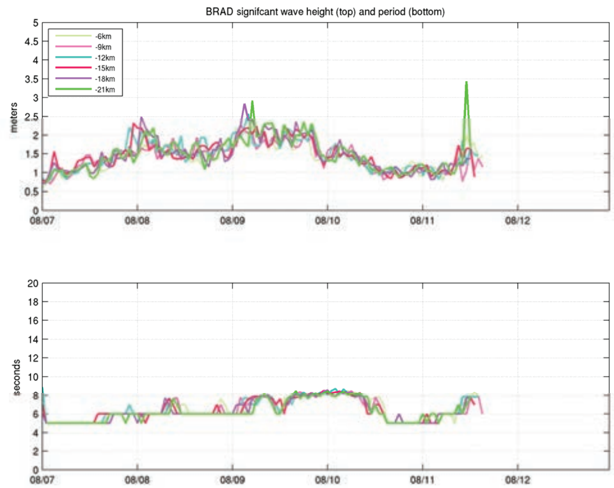

Figure 3: Wave estimates (top: wave height and bottom: wave period) from the BRAD 13 MHz site from August 7-13, 2015. The different colors represent the range cell of the wave measurement.

Figure 4: Wave estimates from the BRIG 5 MHz site, using enhanced blanking. Temporal coverage is improved relative to expected coverage based on the nearby LOVE site at the same time.

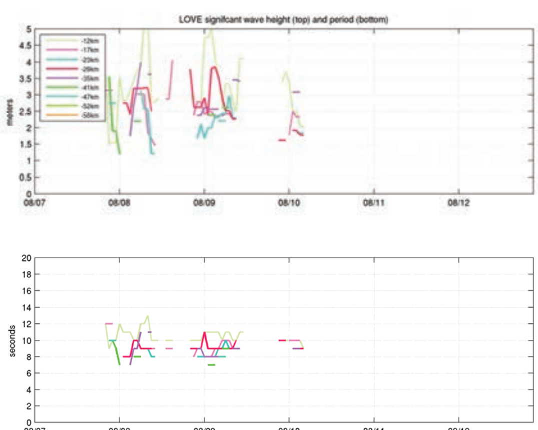

Figure 5: Wave estimates from the LOVE 5 MHz site, which does not use enhanced blanking. Serious gaps and many spikes are evident in the data.

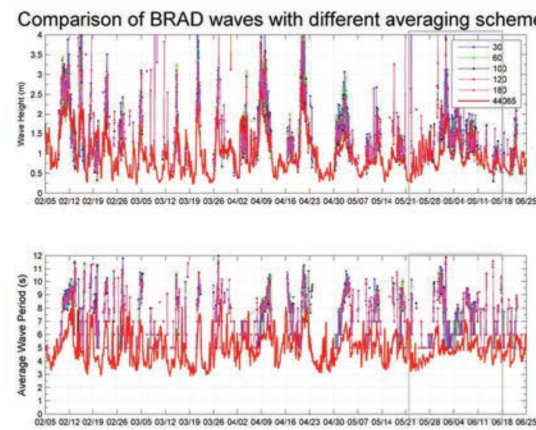

Figure 6: Plot of significant wave height (top) and average wave period (bottom) over time between February and June of 2015 as measured by BRAD in a variety of averaging schemes and compared to the nearest NDBC buoy, 44065 (see legend). The grey box is expanded in Figure 7.

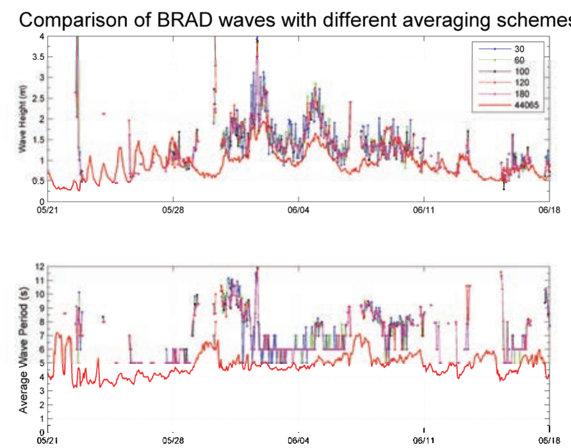

Figure 7: A close-up of the previous figure (grey box, Figure 5), exhibiting the decrease in number of gaps as averaging time goes up, and persistence of spikes.

Table 1: Temporal coverage from February to June 2015 for each averaging scheme. Coverage increases with averaging time, but there is a diminishing return with increase in averaging time.

Averaging Time	Temporal Coverage
30	32%
60	40%
100	43%
120	45%
180	49%

V. CONCLUSIONS

The averaging time used in generation of wave parameterizations from SeaSonde HF radar impacts temporal coverage. The default averaging time is 75 minutes; reduction of the averaging time to 30 minutes reduced temporal coverage, and with increasing averaging time temporal coverage increases. However, there is a diminishing return with increase in averaging time, and averaging over unnecessarily long periods of time is undesirable because it represents a loss of information. Reduction of frequency of spikes could not be definitively observed in any averaging scheme. However, outlier-removal techniques are under development and will be implemented soon, similar to those used by NDBC to clean up their raw buoy data outputs. Since gaps seem to correlate with low average wave periods and spikes seem to correlate with low significant wave heights, additional processing may be possible to fill in expected values in place of spikes and during periods of low wave periods. Use of enhanced blanking led to improvements in wave estimates at the BRIG site based on comparison with the nearby LOVE site.

During high sea states, the HF radar overestimated significant wave height because of the shallow 10 – 12 m depth in Range Cell 2 (6 km offshore); see Figure 7. This factor was studied in [9]. Second-order echo increases significantly, while wave height (e.g., measured by the buoy) does not. Improving operational techniques to handle shallow water (including enhanced blanking that allows observation farther out) is the subject of our continuing investigations.

SeaSonde HF radars in operation are presently optimized for measuring surface currents, since this is the primary and highest priority function of HF radars. In the future it may be practical to optimize some radars for measuring waves operationally.

VI. ACKNOWLEDGMENTS

This work was funded by NOAA award NA13OAR4830233 “Integrated Rapid-Response Observations and Ocean Ensemble Optimization to Improve Storm Intensity Forecasts in the Northeast US”. The radar measurements were supported by NOAA Award Number NA11NOS0120038 “Towards a Comprehensive Mid-Atlantic Regional Association Coastal Ocean Observing System (MARACOOS)”

REFERENCES

[1] B. Lipa, "Derivation of directional ocean-wave spectra by integral inversion of second-order radar echoes," vol. 12, pp. 425-434, 1977.

[2] D. E. Barrick and B. J. Lipa, "Correcting for distorted antenna patterns in CODAR ocean surface measurements," *IEEE J. Ocean. Eng,* vol. OE-11, pp. 304-309, 1986.

[3] B. Lipa and B. Nyden, "Directional wave information from the SeaSonde," *Oceanic Engineering, IEEE Journal of,* vol. 30, pp. 221-231, 2005.

[4] C. C. Teague, J. F. Vesecky, and D. M. Fernandez, " HF radar instruments, past to present.," *Oceanography,* vol. 10, pp. 40-44, 1997.

[5] J. P. Villain, R. A. Greenwald, K. B. Baker, and J. M. Ruohoniemi, "HF radar observations of E region plasma irregularities produced by oblique electron streaming," *Journal of Geophysical Research: Space Physics,* vol. 92, pp. 12327-12342, 1987.

[6] C. Whelan, B. Lipa, D. Barrick, B. Nyden, and B. Rector, "Improving Coverage and Accuracy of Coastal Current Maps Using SeaSonde Multi-Static® HF RADAR Operation," in *Ocean Sciences*, Portland, OR, 2010.

[7] C. W. Evans, H. J. Roarty, J. T. Kohut, and S. M. Glenn, "Examination of the SeaSonde wave processing settings and the effects of shallow water on wave measurements," in *Oceans, 2012*, 2012, pp. 1-6.

[8] H. Roarty, C. Evans, S. Glenn, and Z. Hao, "Evaluation of algorithms for wave height measurements with high frequency radar," in *Current, Waves and Turbulence Measurement (CWTM), 2015 IEEE/OES Eleventh*, 2015, pp. 1-4.

[9] B. Lipa, B. Nyden, D. Barrick, and J. Kohut, "HF Radar Sea-echo from Shallow Water," *Sensors,* vol. 8, pp. 4611-4635, 2008.

Assessing HF Radar Data in the New York Harbor: Comparisons with Wind, Stream Gauge and Ocean Model Data Sources

Joe Gradone
University of Colorado
Boulder, CO USA
joe@gradone.com

Hugh Roarty, Colin Evans,
Scott Glenn, Ethan Handel, Chloe Baskin
Rutgers University
New Brunswick, NJ USA
hroarty@marine.rutgers.edu

Gregory Dusek,
Christopher Paternostro
NOAA/NOS Center for Operational
Products and Services
gregory.dusek@noaa.gov

***Abstract*— The Physical Oceanographic Real-Time System (PORTS) is operated in 26 regions of the United States including New York/New Jersey Harbor. This system provides observations and predictions of water level, currents, salinity and meteorological parameters that are used by mariners to safely navigate the coastal waters. HF radar surface current measurements are a new data product available in three of the regions. A study was conducted to analyze this new data stream to ensure that is suitable for PORTS. The NOAA Center for Operational Oceanographic Products and Services (CO-OPS) using data from the U.S. Integrated Ocean Observing System (IOOS) has recently released a new HF Radar Surface Currents web product which provides near real time surface current observations and tidal current predictions in estuarine and coastal locations. Two High Frequency radar systems are providing surface current measurements over Lower Bay, just outside New York Harbor. A year long record of surface currents was used to generate tidal harmonics for the region. These harmonics are used to generate surface tidal current predictions along the 1 km grid in Lower Bay. The tidal harmonics were calculated for 37 constituents and analyzed in detail the five major constituents for the region (M2, S2, N2, K1 and O1). The tidal components matched those of previous studies. HF radar is now available in NOAA PORTS and surface current predictions cover approximately 50% of the bay. The use of HF radar in NY/NJ PORTS as well as other IOOS assets will improve navigation in NY Harbor and lead to economic growth for the region.**

Keywords—HF radar, remote sensing, ocean models

I. INTRODUCTION

The Mid-Atlantic Regional Association Coastal Ocean Observing System (MARACOOS) is operated as part of the Integrated Ocean Observing System (IOOS). A major component of MARACOOS is a High Frequency Radar Network. It is comprised of a total of 45 radars, 17 being long-range sites (5MHz), 7 standard-range sites (13 MHz), and 21 high resolution sites (25 MHz). This network has been in operation since 2007 and has expanded to have consistent coverage from Cape Cod to Cape Hatteras. The surface current data obtained from this radar network has a variety of important uses, including Coast Guard search and rescue, response to hazardous material spills, water quality monitoring, coastal inundation, and fisheries support [1].

This study assessed the HF radar network in New York Harbor and looked for correlations between the surface current measurements, other environmental measurements and an ocean model. Specifically, our study area (Figure 1) was Lower Bay, which will be referred to as New York Harbor in this manuscript. The 25 MHz radars in the New York Harbor were the focus of this study.

Seventeen High Frequency radars were damaged within MARACOOS when Hurricane Sandy passed through the region in October 2012 [2]. The radar at Staten Island (SILD) was damaged and the radar at Port Monmouth, NJ was submerged in salt water. We have been working to repair and harden the observing system assets that were damaged or lost during Hurricane Sandy. The aim of this study is to ensure accurate measurements by the repaired radar stations for use by NOAA PORTS and others.

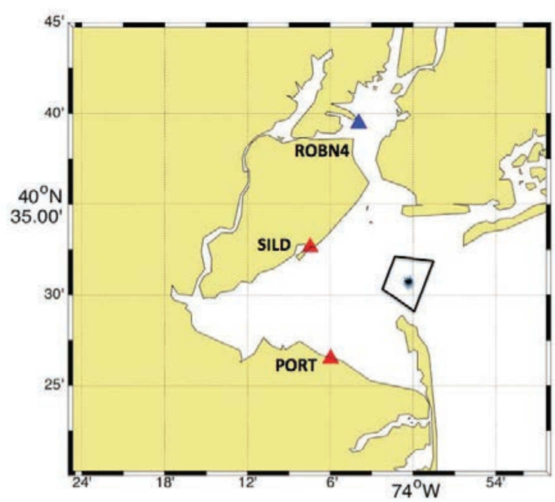

Figure 1- Map of the New York Harbor where Red triangles are HF radar sites SILD and PORT and blue triangle is NDBC Station ROBN4. Current measurements from SILD located inside the black polygon were averaged to create a radial velocity time series. The surface current data from ESPreSSO was located at the black star.

HF radar data was compared against wind measurements from the National Data Buoy Center (NDBC), river discharge measurements from the United

978-0-933957-43-5 ©2015 MTS

States Geological Survey's (USGS) stream gauges and Rutgers University's Experimental System for Predicting Shelf and Slope Optics Model (ESPreSSO).

NDBC, operated as a part of the National Weather Service, is an online portal where data from buoys from all over the world are logged and made available to the public and scientists alike. This data consists of wind direction, speed, and gusts, atmospheric pressure, air temperature, and water level among other measurements, which assist in meteorological predictions.

The USGS's stream gauges provided information on the discharge from the two main rivers that feed the New York Harbor, the Raritan River and the Hudson River. These two data sources served as comparison points for the HF radar measurements in the New York Harbor.

The HF radar data is now available through the National Oceanic and Atmospheric Administration's Physical Oceanographic Real-Time System (NOAA PORTS). NOAA PORTS is part of NOAA's Tides and Currents program where historical and real-time observations and predictions of water levels, coastal currents and other meteorological and oceanographic data for a dozen US estuaries is provided to the public and maritime industry [3]. This program utilized one year (July 14, 2013 to July 14, 2014) of measurements to perform a harmonic analysis of the surface current data in New York Harbor to generate the tidal predictions for the area. Currently, HF radar tidal predictions are available over approximately 50% of the bay. We examined the HF radar data to ensure the highest quality and most accurate data was being passed to NOAA PORTS.

Rutgers University's ESPreSSO model uses the Regional Ocean Modeling System (ROMS) [4] and spans the entire Mid-Atlantic Bight. The coverage of the ESPreSSO model is similar to that of the Mid Atlantic HF radar network. ESPreSSO also assimilates the 5 MHz HF radar measurements into its model.

Correlation of the radar data with several of the data sources was expected. This is due to the fact the ESPreSSO model assimilates the long-range HF radar data to make its forecast. The highest expectations for correlations with radar data were with the USGS's stream gauges and NDBC's wind measurements. Measurements from these data sources had the potential to provide information about discrepancies or important features of the radar data. By addressing the accuracy of the HF radar network, navigation in the region will improve and economic growth will be stimulated, along with a variety of other important uses for the network.

II. METHODOLOGY

This study utilized measurements from each data source from January 1, 2015 to June 1, 2015. The main radar used in this study was located in Staten Island, New York (SILD). There is also another radar in the New York Harbor in Port Monmouth, New Jersey (PORT) that, when combined with SILD, produces a total plot for the harbor. HF radars use a vertically polarized signal, which travels along the electrically conductive ocean water surface. These signals travel from the radar, reflect off of an ocean wave and travel back to the radar. These radars first measure signal range, then velocity, and finally the bearing of the scattering ocean waves. After subtracting the theoretical speed of the ocean waves from the received Bragg Scatter, the signal received at the radar can be used to determine a radial velocity measurement of surface current. The radar network reports data every hour at a resolution dependent on the frequency of the radar. The hourly radial map of surface currents measured at SILD can bee seen in Figure 2. The total map for New York Harbor can be seen in Figure 3.

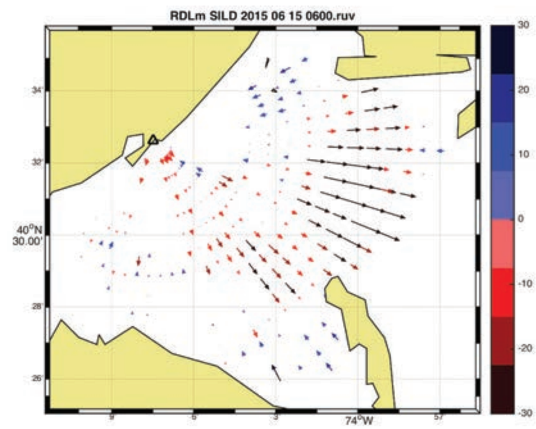

Figure 2- Radial map from HF radar station SILD. Red indicates currents moving away from the radar (negative) and blue indicates currents moving towards the radar (positive).

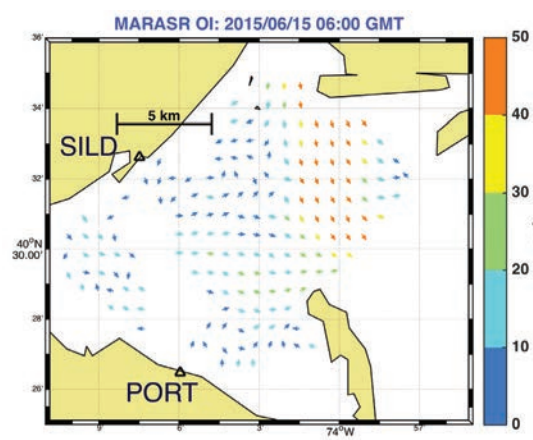

Figure 3- Map of total surface currents in the New York Harbor from HF radar stations SILD and PORT(black triangles). The colorbar on the right signifies current magnitude (0-50 cm/s).

Plots of radial surface current velocities at specific points in the New York Harbor were made from the SILD radar. The radial resolution of the radar was set to 1 km and the bearing resolution was set to 5 degrees. The radial measurements between bearing angles 97 and 113 degrees in range cells 10, 11 and 12 (a total of 9 radial vectors) were averaged to make a single surface current measurement in the vicinity of the harbor entrance. This averaging area is depicted as the black polygon in Figure 1 and an example of a surface current time series is shown as the blue line in Figure 7. A plot like the one in Figure 7 was generated for each month of the study, five in total. Positive flow is directed into the harbor and negative flow is out of the harbor. The radar surface current measurement is aligned parallel to the Ambrose channel and the entrance to the harbor. The M2 and K1 tidal constituents were calculated over each month to create the tidal component of the flow. Lastly, the surface currents were filtered with a Lancocz (low pass) filter with a cut-off period of 32 hours to remove the tidal variability. The low pass filtered data is shown as the green line. This low pass filtered record was utilized to compare the radar measurements with the wind and stream gauge measurements.

Stream gauges from the USGS record measurements consisting of discharge, gauge height, temperature, specific conductance, and turbidity among other parameters every 15 minutes. Gauge data from the Raritan and Hudson Rivers was compared against HF radar data. The stream gauge used from the Raritan River was located in Bound Brook, NJ (40°33'04", 74°32'54") while the stream gauge used from the Hudson River was located in Poughkeepsie, NY (41°39'03", 73°56'42"). One complication that arose was the proximity of the most downstream gauge in the Hudson River to the harbor. The furthest downstream gauge is 120 km north of the radar measurements. Therefore, in order to account for the full discharge from the Hudson river the data from Poughkeepsie were multiplied by a factor of 1.12 [5]. This factor was derived from the estimated additional discharge from the remaining watershed. This new value became the Hudson River discharge estimate. Another complication that arose was the strong tidal signature shown in the discharge data for the Hudson River. This signature was removed with a low pass (32-hour) filter in order to obtain a more representative, general description of how the water was moving. The results of the low pass filter can be seen as the green line in Figure 4. The stream gauge record from the Raritan was not modified as it was only 20 km from the radar measurements and did not exhibit the large tidal oscillations as seen in the Hudson.

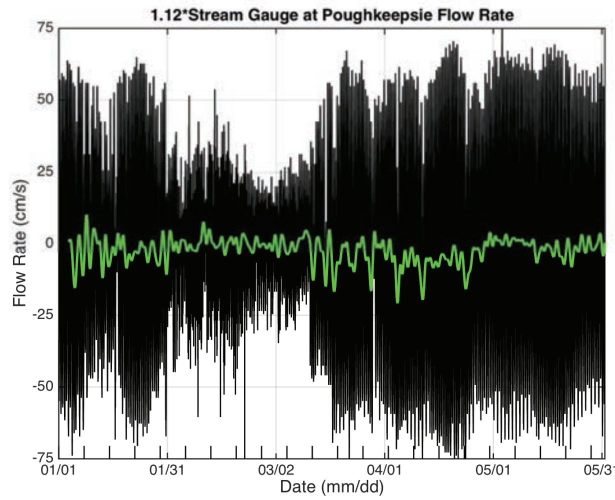

Figure 4: Graph of the raw (black) and low pass (green) Hudson River flow rate from January 1, 2015 to May 31, 2015. Positive flow is towards the north. General flow (green line) of the river downstream is indicated by the negative flow rate values.

Lastly, the discharge data from these stream gauges were converted to flow rate to be in comparable format of the radar surface current measurement. This conversion was done by dividing the rate of discharge by the average cross-sectional area of the river [6]. The final result of this alteration can be seen in Figure 4 for the Hudson and Figure 5 for the Raritan. From these modifications, signals seen in the stream gauge data could be compared to the low pass record of the HF radar.

NOAA's National Data Buoy Center also contributed significant data to this comparison. In particular, wind speed and direction measurements were utilized in order to make comparisons. A 5-month plot of wind data from buoy station ROBN4 (40°39'26" N 74°3'55" W) in Bayonne, New Jersey can be seen in Figure 6.

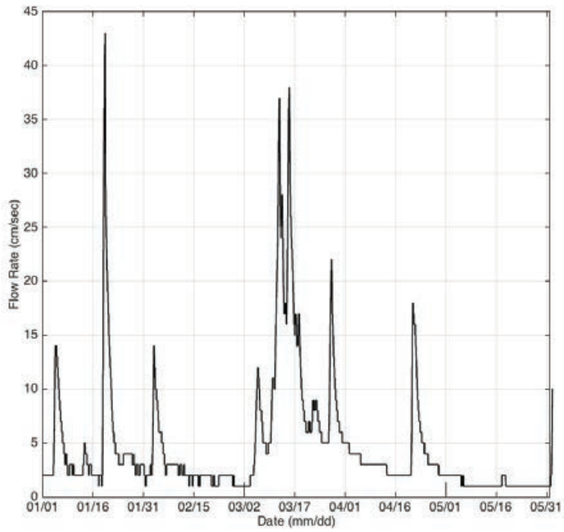

Figure 5: Graph of the flow rate from the Raritan River at Bound Brook from January 1 to May 31, 2015. Large flow rate events are attributed to large rainfall events.

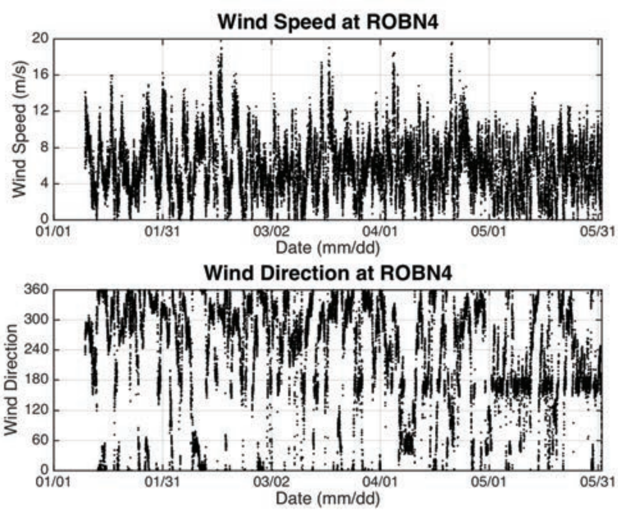

Figure 6: Graph of wind speed (top) and direction (bottom) from NDBC station ROBN4 from January 1, 2015 to May 31, 2015.

HF Radar data from NOAA's Physical Oceanographic Real-Time System is different from our other data sources because it provides a prediction for future oceanic conditions. This system produces an hourly harmonic prediction of oceanic conditions based on historical HF radar data. Therefore, any deviation of the radar data from the predictions suggested that other environmental data should be examined to explain the difference.

The last comparison point of this study was with an ocean model, Rutgers University's ESPreSSO model. ESPreSSO's goal is to develop an understanding of the coupled bio-optical and physical processes in the coastal zone [7]. Time-series plots and spatial coverage maps will enable this study to compare model's results with radar data and analyze inconsistencies. Through this comparison, the models' uncertainties were analyzed and the need for further assimilation with radar data was shown.

III. RESULTS

An interesting correlation was determined through comparisons of the HF radar data with wind data from ROBN4. This comparison analyzed the HF radar's ability to show the effects of wind on the currents in the New York Harbor. Utilizing the low pass filtered HF radar data, it was determined that any positive flow (into the harbor) or flow more negative than -20 cm/s (out of the harbor) would be considered a large event in terms of surface currents. In order to make this comparison, time-series plots of wind measurements from NDBC station ROBN4 were created for each of the large surface current events noticed on the HF radar record. As can be seen in Figure 1, this station is only 14 km from the HF radar surface current measurements so we assumed that the wind field was isotropic over this distance.

From January 1, 2015 to June 1, 2015 there were 7 large surface currents events in New York Harbor that were compared with wind data in this study. The results of this comparison can be seen in Table 1. From this comparison, the correlation between changing surface currents in the harbor and wind direction and speed was very obvious. An increased flow in or out of the New York Harbor consistently aligned with an increase in wind speed from the East/Northeast or West/Northwest respectively. The large surface current events occurred when speeds were above 12 m/s. This was further evidence for wind being the cause of this increased flow because the average wind speed over the 5-month study period was 6 m/s.

One particular instance when the radar and wind records lined up particularly well occurred from March 14-17, 2015 as seen in Figures 7 and 8. During this event, the winds were blowing at about 17 m/s from the West/Northwest for about a day. This wind event can be seen on the radar record on 3/15. Increased flows out of New York Harbor were not only attributed to large wind events but also large rainfall events, as seen in the USGS stream gauge record.

NDBC ROBN4 Wind Data vs HF Radar Data						
Event Date	General Wind Direction	Max Wind Speed (m/s)	Flow in or out of harbor on radar?	Event Low Pass Magnitude	Consistent with wind?	Comments
1/15/15-1/18/15	West/Northwest	16 m/s	Out	~ -30 cm/s	✓	Highest winds on 1/17
2/12/15-2/15/15	Northwest	16 m/s	Out	~ -30 cm/s	✓	Highest winds on 2/13
2/19/15-2/22/15	Northwest	16 m/s	Out	~ -30 cm/s	✓	Winds strong from 2/19-2/20 → visible on radar
3/14/15-3/17/15	West/Northwest	17 m/s	Out	~ -33 cm/s	✓	Highest winds on 3/15
4/10/15-4/13/15	West/Northwest	14 m/s	Out	~ -32 cm/s	✓	Highest winds on 4/11
4/18/15-4/21/15	East	20 m/s	In	~ 10 cm/s	✓	Highest winds on 4/20
4/22/15-4/25/15	West/Northwest	12 m/s	Out	~ -35 cm/s	✓	Highest winds on 4/23

Table 1: Large surface current events in NY Harbor and the corresponding wind measurements at ROBN4.

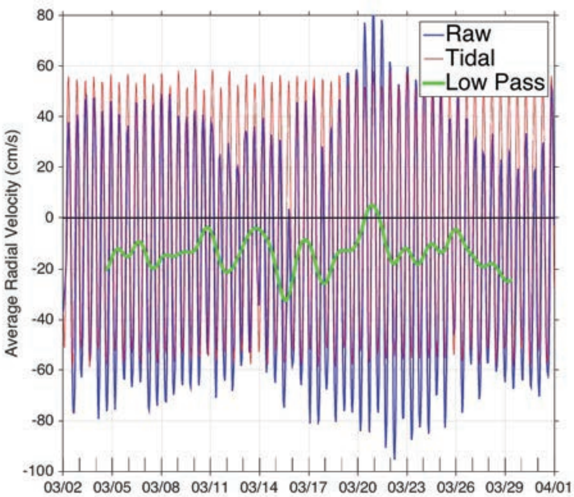

Figure 7- Graph of average radial velocity (blue) from HF radar station SILD for March 2015. The tidal component of the flow is in red and the low pass filtred flow is in green. Large flows out of harbor are indicated by values in green less than -20 cm/s while large flow events into the harbor are indicated by values greater than zero.

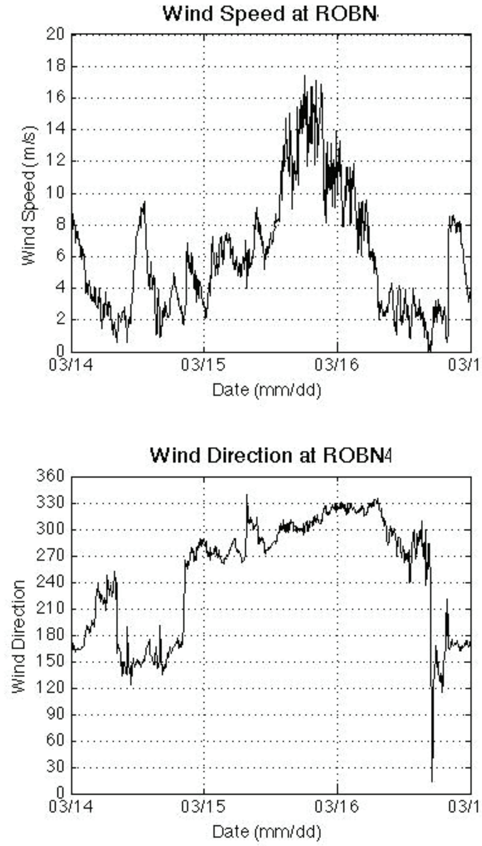

Figure 8: Graphs of wind speed (top) direction (bottom) from NDBC station ROBN4 from a large wind event from March 14-17, 2015.

Comparisons with the USGS stream gauges also showed a noteworthy relationship. For this analysis, we looked for large flow events in the stream gauge data and then examined the corresponding time period in the surface current data. There were four instances that stood out in the discharge record that were deemed worthy of comparison. The results of this comparison can be seen in Table 2. During these large rainfall events, the flow rate increased by about 5 to 10 times the average flow rate for each river. One particular instance when the radar and flow rate records lined up particularly well occurred from March 11-17, 2015. During this time there were two large rainfall events on March 12th and 15th in the Raritan River where the max flow rate increased to 40 cm/s from the average of 5 cm/s. This increased flow rate was visible on the radar record three days later on March 15th and 17th. There was about a three-day span between rainfall events, which is visible on the radar as well, as seen in Figures 7 and 9.

Table 2: Table of USGS stream gauge data from large rainfall events seen on HF radar record

Rainfall Event Data USGS Stream Gauges vs HF Radar Data						
Event Date	**Location**	**Max flow rate**	**Mean flow rate for location**	**When visible on radar?**	**Event Low Pass Magnitude**	**Time-lag**
1/19/15-1/22/15	Raritan River	44 cm/s	4.66 cm/s	1/25/15	~ -23 cm/s	Two day time-lag
3/11/15-3/14/15 & 3/15/15 3/17/15	Raritan River	40 cm/s	4.66 cm/s	3/15/15-3/18/15	~ -33 & -25 cm/s	One day time-lag and gap because of two storms
4/21/15-4/22/15	Raritan River	18 cm/s	4.66 cm/s	4/23/15	~ -35 cm/s	One-two day time-lag
4/4/15-4/6/15	Hudson River	21 cm/s	2.04 cm/s	4/11/15	~ -32 cm/s	Five day time-lag

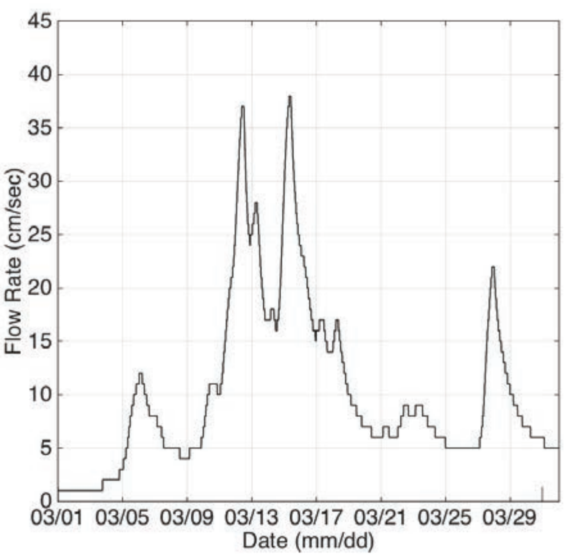

Figure 9: Graph of flow rate from the Raritan River for the month of March. Two large rainfall events on 3/12 and 3/15 were noticeable on HF radar record with a timelag.

These external wind and rain factors influencing the surface currents in the New York Harbor could very well be the key characteristics affecting surface current plots in NOAA PORTS. The NOAA PORTS HF radar product utilizes HF radar observations to calculate tidal current predictions. By performing a harmonic analysis of the observations, tidal constituents like the M2 (principal lunar semidiurnal; Figure 10) are calculated and enable indefinite predictions of tidal currents.

Tidal current predictions can be quite accurate for locations and time periods when tidal currents are the dominant forcing mechanism. However, in some cases tidal currents may be relatively weak or there may be strong non-tidal influences like wind and river flow, at which point tidal current predictions can be inaccurate since it is no longer a majority of the current energy. For example high non-tidal residual was found in the western extent of the harbor when performing the harmonic analysis (Figure 11).

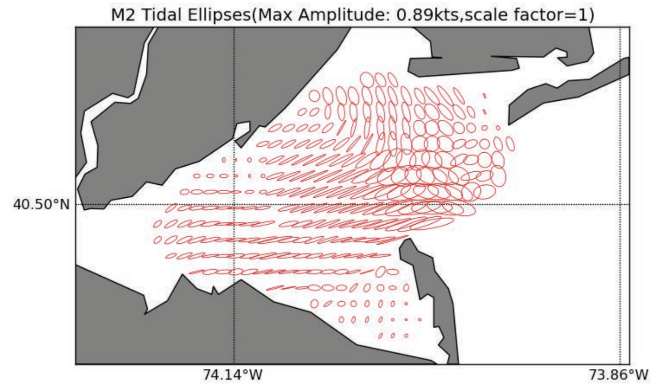

Figure 10: The M2 tidal ellipses resulting from the harmonic analysis of HF radar observations.

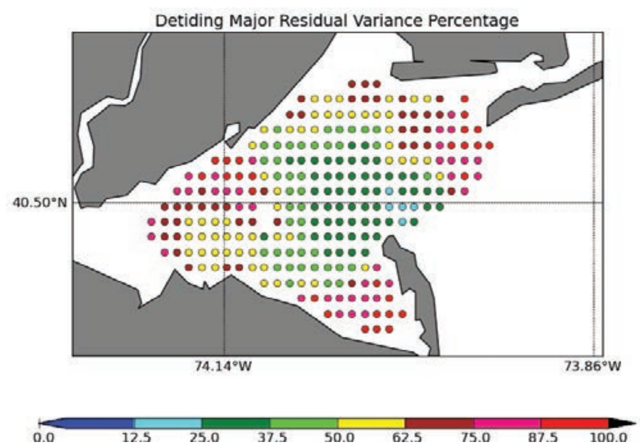

Figure 11: The percent of non-tidal residual variance observed at each point in the HF Radar domain. Note the high (> 50%) residual variance observed for many of the data points.

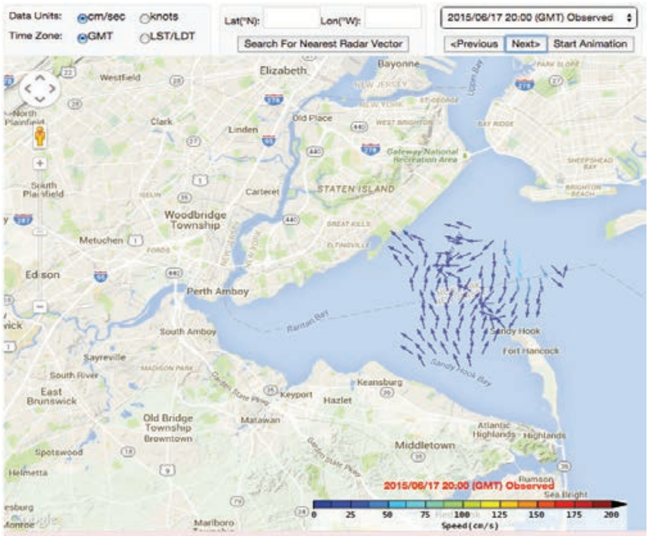

Figure 12- Map of NOAA PORTS HF radar data in the New York Harbor. The spatial coverage of the surface currents in NOAA PORTS is noticeably smaller when compared with the HF radar map in *Figure 13*.

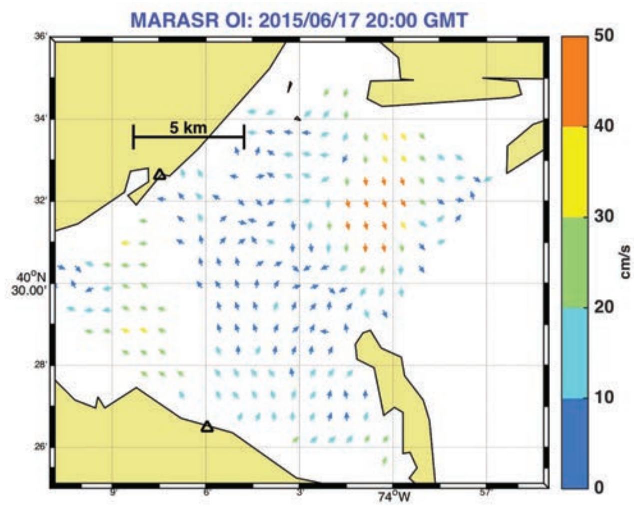

Figure 13: Map of total radials in the New York Harbor

These locations of high non-tidal residual were not utilized in the NOAA PORTS product (Figure 12), and because of this there is a significant spatial limitation when compared to the HF Radar observations (Figure 13). Part of the reason for the high non-tidal residual observed in the western extent of the harbor may be due to HF Radar data quality in these locations. Radar measurements are currently excluded along the baseline between SILD and PORT, as the system is unable to make an accurate measurement perpendicular to the baseline. Rutgers is experimenting with adding a third radar in the New York Harbor located near the mouth of the Raritan River in order to increase the quality and coverage of the radar measurements in the harbor.

Another interesting comparison with the HF radar record was through oceanographic models, and in particular, the Rutgers University's ESPreSSO model. We chose the closest ESPreSSO grid point to compare with the HF radar measurements (black star in Figure 1). The u and v components of ESPreSSO were combined and rotated to match the radial bearing line from SILD. A one-month plot of this time series for March 2015 is shown in Figure 14. The HF radar surface current velocities ranged between ±80 cm/s while the range for ESPreSSO was ±40 cm/s, half that of the radar. The low pass signature of ESPreSSO better matched the HF radar at approximately -20 cm/s, however ESPreSSO estimated two large flow events into the harbor while the radar measured one large event. These two factors are key points highlighting ESPreSSO's need to assimilate the high resolution HF radar data into its model for better estimation of New York Harbor currents.

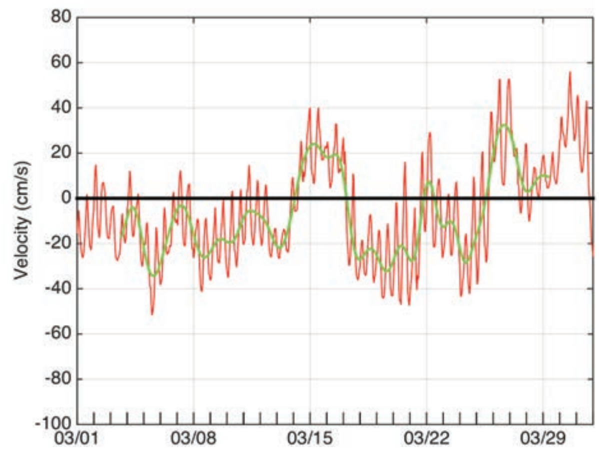

Figure 14: Graph of ESPreSSO surface velocity north of Sandy Hook, positive is into the harbor. When compared with the HF radar surface current velocity graph, ESPreSSO's range of surface currents is an underestimate.

IV. Conclusions

The results of this study indicate that the HF radar network in the New York Harbor has a variety of correlations with other oceanographic data sources. Furthermore, HF radar data can certainly be used to increase the accuracy of ocean models. As for comparison with other oceanographic data sources, the most striking correlation with HF radar data that this study discovered was with wind data from NDBC. Wind direction and speed proved to be a correlation with increased flows in the New York Harbor. In addition, discharge data from the USGS's stream gauges also proved to show interesting correlations. Mainly, when a large rainfall event was noticed by a stream gauge, more often that not, it was also noticed with a time lag by the HF radars in the harbor. Lastly, this comparison showed how ocean models, such as ESPreSSO, could benefit from the assimilation of HF radar data from the New York Harbor because of this regions complicated nature. Details from this study will be presented to the creators of ESPreSSO in order to increase the models accuracy in the New York Harbor as well as NOAA in order to increase their PORTS program's accuracy.

V. Acknowledgments

This work was funded by NOAA Award Number NA14NOS4830003 “Repair and Hardening of Mid Atlantic Ocean Observing Assets After Hurricane Sandy”.

VI. References

[1] H. J. Roarty, S. M. Glenn, J. T. Kohut, D. Gong, E. Handel, E. Rivera Lemus*, et al.*, "Operation and Application of a Regional High Frequency Radar Network in the Mid Atlantic Bight," *Marine Technology Society Journal,* vol. 44, pp. 133-145, 2010.

[2] D. Malakoff, "Scientists Assess Damage From Sandy's Deadly Punch," *Science,* vol. 338, pp. 728-729, 2012.

[3] M. E. J. Werner, and T. Bethem, "Real-time Narrative Summaries for NOAA's PORTS &#174," *Oceans, 2005,* vol. Proceedings of MTS/IEEE, pp. 1-3, 2005.

[4] D. B. Haidvogel, H. Arango, W. P. Budgell, B. D. Cornuelle, E. Curchitser, E. Di Lorenzo*, et al.*, "Ocean forecasting in terrain-following coordinates: Formulation and skill assessment of the Regional Ocean Modeling System," *Journal of Computational Physics,* vol. 227, pp. 3595-3624, 3/20/ 2008.

[5] S. M. G. R.J. Chant, E. Hunter, J. Kohut, R.F. Chen, R.W. Houghton, J. Bosch, and O. Schofield, "Bulge Formation of a Buoyant River Outflow," *Geophys. Rs,* vol. 113, p. C01017, 2008.

[6] G. Wall, "Email from USGS," J. Gradone, Ed., ed, 2015.

[7] R. A. I. Shulman, W. Teague, F. Chavez, O. Schofield, M. Moline, B. Penta, J. Ryan, R. Gould, S. Anderson, J.K. Jolliff, J.W. Book, S. Derada, and J.D. Paduan, "Modeling and Field Study of Coupled Bio-Optical Physical Processes in the Monterey Bay Area," *AGU Fall Meeting Abstracts,* p. C1303, 2008.

Increasing the Coverage of an Island-Based HF Radar Network

Ethan Handel, Hugh Roarty,
Scott Glenn
Rutgers University
New Brunswick, NJ USA
handel@marine.rutgers.edu

Carlos Garcia, Miguel Canals, Julio Morell, Jorge Corredor
University of Puerto Rico
Mayaguez, PR USA
carlos.garcia6@upr.edu

Abstract— **High frequency (HF) radar networks are operated in different regions around the world for use in monitoring ocean surface currents and coastal wind dynamics. These networks are individually composed of multiple HF radar surface current monitoring systems, each installed at a different coastal research site. The data derived from these networks is used to study coastal currents, offshore wind, oil spill response, algal bloom movements, and also used by the United States Coast Guard (USCG) as part of their Search and Rescue Optimal Planning System (SAROPS). We describe here the HF radar network that is part of the Caribbean Coastal Ocean Observing System (CariCOOS). The existing HF radar network covers parts of the southern and western coast of Puerto Rico, and is currently managed and operated by the University of Puerto Rico Mayaguez (UPRM). Rutgers University Center for Ocean Observing Leadership (RUCOOL) has been collaborating with UPRM on the Integrated Ocean Observing System (IOOS) program "Advancing the Caribbean Ocean Observing System". Increasing the coverage of the UPRM-CariCOOS HF radar network could be used to enhance the operational abilities of the USCG and other local and regional emergency response agencies.**

Keywords—HF radar, ocean currents, emergency response

I. INTRODUCTION

Rutgers University Center for Ocean Observing Leadership (RUCOOL) is a member of the Mid-Atlantic Regional Association of Coastal Ocean Observation Systems (MARACOOS), which itself is part of the Integrated Ocean Observing System (IOOS) program administered by the National Oceanic and Atmospheric Administration (NOAA). The University of Puerto Rico Mayaguez (UPRM) is a member of the Caribbean Coastal Ocean Observing (CariCOOS), which is also part of NOAA's IOOS program. RUCOOL has been working with UPRM to develop and enhance the High-Frequency Radar (HFR) Network around the coast of Puerto Rico. The HFR Network is a key component of the CariCOOS observational system, and the ocean surface current data provided by the HFR Network is currently being used by the United States Coast Guard (USCG) to assist in search-and rescue operations, as well as oceanographers studying coastal ocean dynamics.

The initial HFR network in Puerto Rico consisted of two 13 MHz Coastal Ocean Dynamic Application Radar (CODAR) sites located on the west coast if the island. The northern site, named FURA, was installed in September 2009, and is located at 18.2919N, -67.1983W, at the Forces United for Rapid Action (FURA) station in Anasco. The southern site, CDDO, was installed in February 2009, and is located at 18.0999 N, -67.1905 W, at the Club Deportivo del Oeste in Cabo Rojo. Both of these sites produce hourly surface current radial vector maps with approximately 3km range cell spacing, with coverage extending to approximately 100km offshore. The data from these sites have been used to create hourly surface current total maps using the Optimal Interpolation (OI) combining method, as seen in Figure 1.

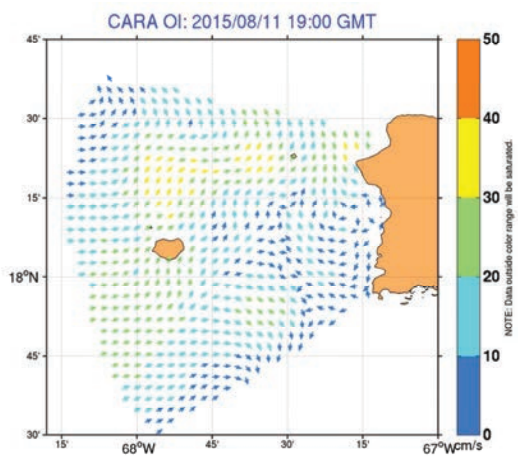

Figure 1- Map of OI surface currents with 3km resolution off the west coast of Puerto Rico, created from radial files from CDDO and FURA.

Over the last year, two additional HFR sites have been installed along the southern coast of Puerto Rico. The western site, which is named FARO, is located at 17.9334 N, -67.1920 W, at the Cabo Rojo Lighthouse in Cabo Rojo. The eastern site, named PYFC, is located at 17.9628 N,

978-0-933957-43-5 ©2015 MTS

-66.6183 W, at the Ponce Yacht and Fishing Club in Ponce. These sites are both 5 MHz systems with approximately 6 km range cell resolution and approximately 200 km range.

Using the unweighted least squares (UWLS) combining method, surface current total maps have been created using radial files from the FURA, CDDO, FARO and PYFC sites, as seen in Figure 2.

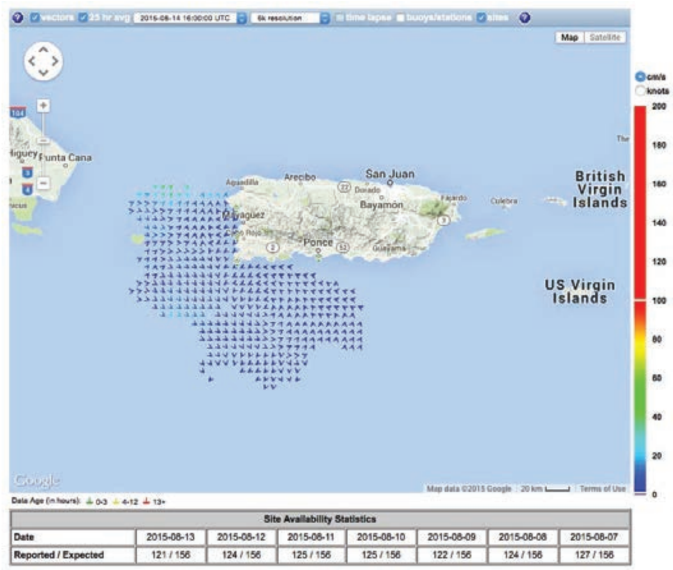

Figure 2- Surface current total map with 6km resolution, created by combining radial files from the CDDO, FURA, FARO, and PYFC sites.

In order to increase the HFR Network's total coverage area around the southern and eastern sides of Puerto Rico, one or two additional sites are potentially going to be installed at new locations in Emajagua, PR, and on St. Croix, British Virgin Islands. The placement of new HFR sites must take into account the location and coverage area of existing sites, as surface current total vectors can only be created in areas of ocean that have overlapping coverage from more than one HFR site.

II. Methodology

Using SeaDisplay and SeaDisplaySetup software developed by Codar Ocean Sensors, potential individual site coverage areas, as well as areas of overlapping coverage, can be estimated and plotted, as seen in Figure 3.

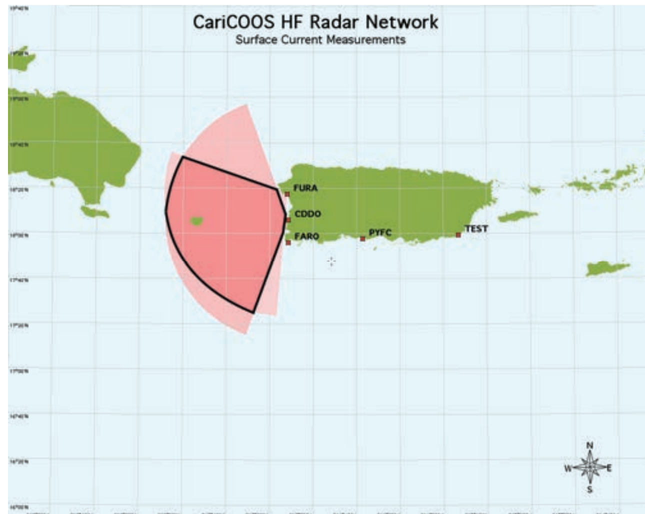

Figure 3- Potential coverage areas of the FURA and CDDO sites. Area of overlapping coverage/potential total current coverage is outlined in black.

Due to coastal geography, and the limitations of HFR sites to efficiently transmit and receive signals over land due to attenuation, the bearing range for the coverage area of the FURA site is limited to approximately 105 degrees. The bearing range for the coverage area of the CDDO is limited to approximately 140 degrees.

The first 5 MHz HFR site in Puerto Rico, FARO, was installed in February 2015 at the Cabo Rojo Lighthouse last year. The bearing range for is coverage area is limited to approximately 170 degrees. Although this site can produce radial vector files covering the majority of the coastal waters off the southern coast of Puerto Rico, the increase of coverage of surface current total generation is limited to the small areas that overlap with existing sites' radial coverage, as seen in Figure 4.

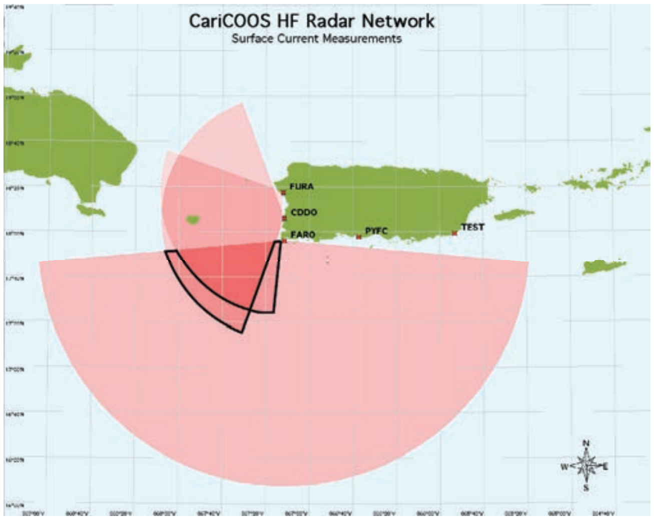

Figure 4- Approximate radial coverage of the FURA, CDDO, and FARO HFR sites. Areas outlined in black indicate the potential increase in total surface current coverage when combining data from FARO with data from CDDO and FURA.

The second 5MHz in Puerto Rico, PYFC, was installed in April 2015 at the Ponce Yacht and Fishing Club. This site has radial coverage out to approximately 200km, and has an approximate bearing coverage range from 160 degrees. When combined with radial files from FARO, CDDO, and FURA, the total surface current coverage area is greatly extended over the southern and south western waters off the coast of Puerto Rico, as seen in Figure 5.

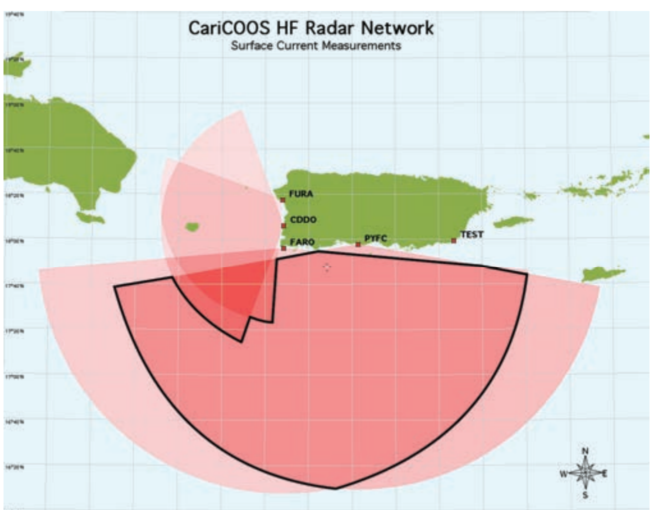

Figure 5- Approximate radial coverage of the FURA, CDDO, FARO, and PYFC HFR sites. Areas outlined in black indicate the potential increase in total surface current coverage when combining data from PYFC with data from FARO, CDDO, and FURA.

Future plans for the CariCOOS HFR Network include potential placement of a third 5 MHz site, named TEST, in Emajagua, at the Tuna Point Lighthouse. This site would have radial coverage out to approximately 200km, and an approximate bearing coverage range from 185 degrees, as seen in *Figure 6*.

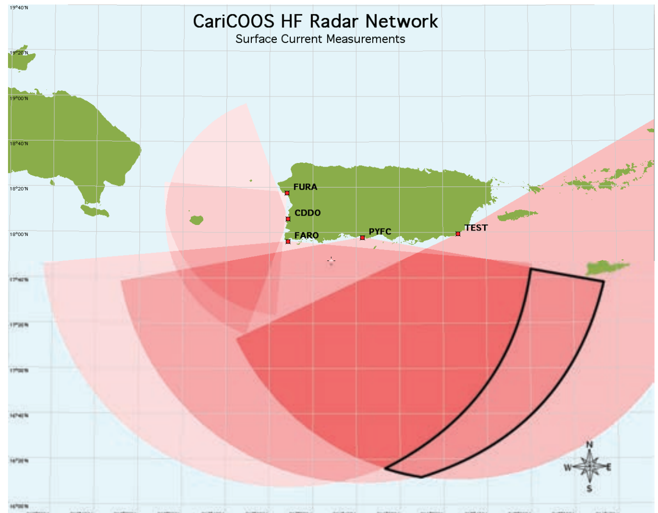

Figure 6- Approximate radial coverage of the FURA, CDDO, FARO, PYFC, and TEST HFR sites. Areas outlined in black indicate the potential increase in total surface current coverage when combining data from TEST with data FURA, CDDO, FARO, and PYFC.

In order to further increase the total surface current coverage areas around the eastern part of Puerto Rico, an additional 5 MHz or 13 MHz HFR site, named TEMP, may be installed on the western side of St. Croix, British Virgin Islands, as shown in Figure 7 and Figure 8, respectively. This area would cover the flow through the Virgin Passage.

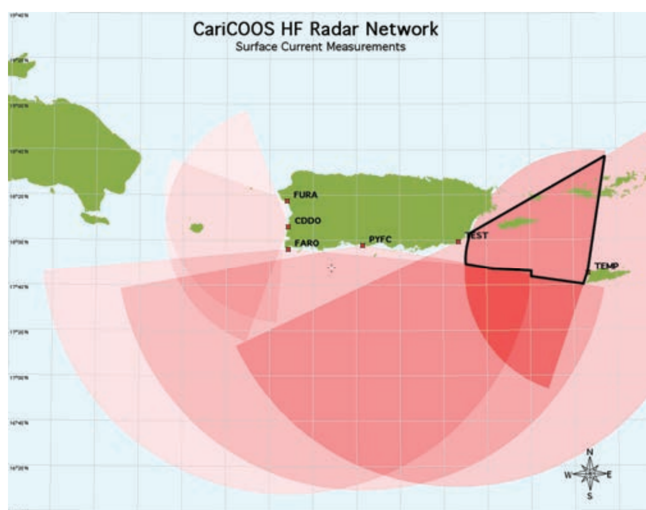

Figure 7- Approximate radial coverage of the FURA, CDDO, FARO, PYFC, TEST, and TEMP HFR sites. Areas outlined in black indicate the potential increase in total surface current coverage if TEMP is a 13 MHz site with an approximate coverage range of 100km.

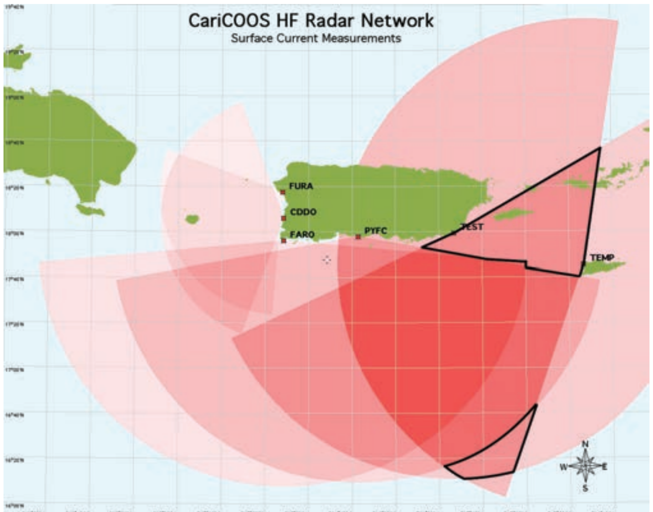

Figure 8- Approximate radial coverage of the FURA, CDDO, FARO, PYFC, TEST, and TEMP HFR sites. Areas outlined in black indicate the potential increase in total surface current coverage if TEMP is a 5 MHz site with an approximate coverage range of 200km.

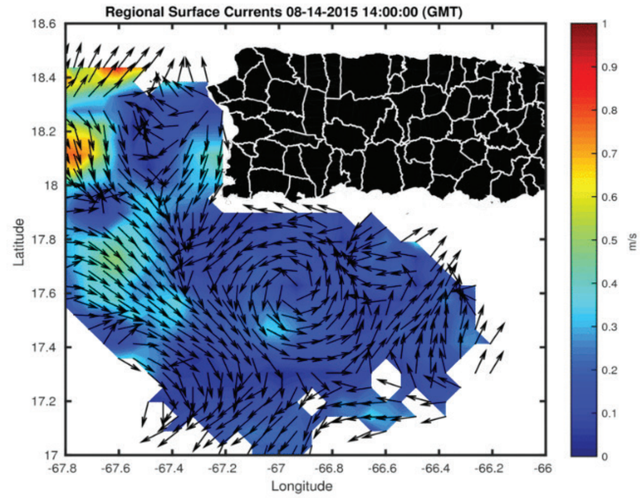

Figure 10- Hourly CariCOOS HFR Network total surface currents map, with 180min averaging and 6km resolution.

III. Results

Data from the two 13 MHz HFR sites, FURA and CDDO, as well as data from the two 5 MHz sites, FARO and PYFC, are currently being served to the United States National HFR Network. These data sets are being used to calculate ocean surface currents along the large parts of the southern and western coasts of Puerto Rico. An example 25hr averaged 6km resolution total current map is shown in Figure 9.

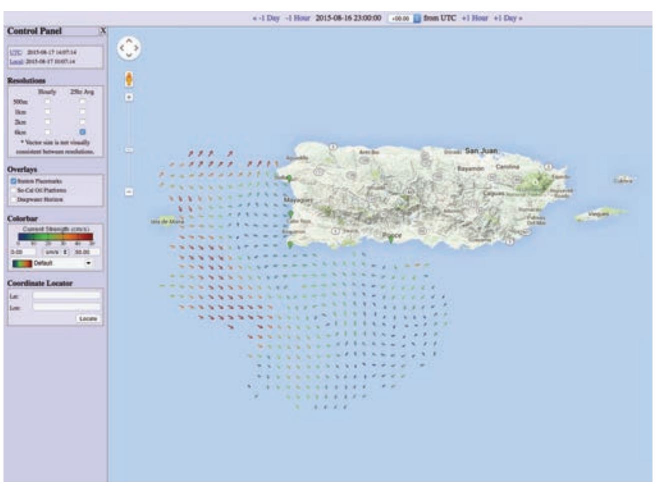

Figure 9- 25hr averaged 6 km resolution total surface currents from 08/16/2015 2300UTC.

These data are also being used by CariCOOS to generate hourly surface current total maps with 180min averaging, as seen in Figure 10.

An analysis of six months of data from the two 13 MHz sites covering the west coast of Puerto Rico and the waters in the Mona Passage was also conducted.

The past six months of data from the 13 MHz network were analyzed. The surface current data within 4 km of 67°30’ W and 18° 10’ was averaged to produce a north (U) and east (V) current time series. The results are shown in Figure 11 and Figure 12, respectively. The hourly surface current measurements were filtered with a Lancocz filter with a cut-off period of 32 hours to remove the tidal variability. The low pass filtered data is shown as the green line. We also calculated the monthly average with 95% confidence interval error bars. Those are shown as the black lines and error bars.

The hourly data varied between ±40 cm/s in the zonal direction and ±80 cm/s in the meridional direction. The monthly plots show a consistent flow that is towards the north and west. The monthly average transport to the north varied between 16.5 and 1.6 cm/s and was between 7.8 and 2.2 cm/s to the west.

The low pass data reveals several events in the record where the flow switched from the dominant mode towards the south or east. We are analyzing the wind data from the CariCOOS Mesonet for possible correlations between the currents and winds.

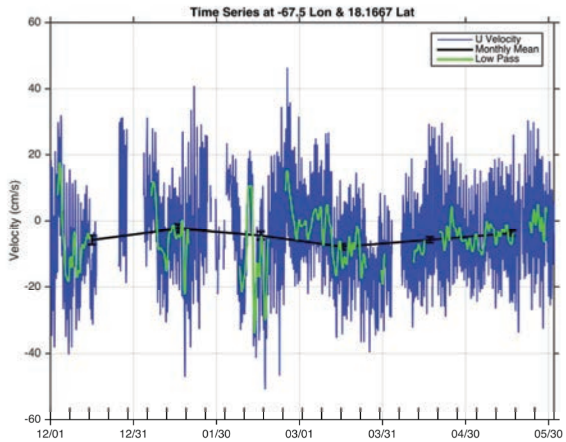

Figure 11- Six-month average of 13 MHz totals north (u) time series.

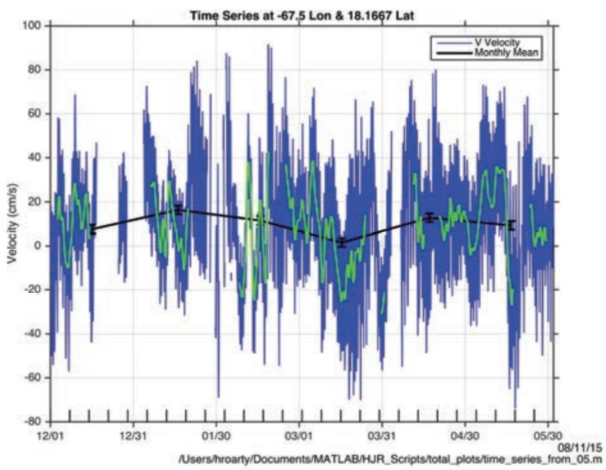

Figure 12- Six-month average of 13 MHz totals west (v) time series.

IV. Conclusions

To date, the CariCOOS HFR Network in Puerto Rico consists of two 13 MHz sites on the west coast of the island, and two 5 MHz sites on the southern coast. These sites have been running well and providing data to the IOOS National HFR Network, as well as the United States Coast Guard search-and-rescue operators in North America and the Caribbean. As the coverage of the network has grown, so has the desire to have ever-larger areas covered by this data. Choosing the most appropriate location for future HFR site installations requires taking the coverage of existing sites into consideration, as total surface current maps can only be created for areas that have overlapping data from at least two separate sites. In order for the CariCOOS HFR Network to be able to produce surface current total maps covering all the coastal waters around Puerto Rico, additional sites must be installed. These additional sites will most likely be located in the southeastern part of the island and on the island of St. Croix, BVI. Adding sites in these two locations would enable surface current totals to be calculated off all of the southern coast of the island, as well as well as off a large part of the eastern coast, too. If additional future funding becomes available to supplement growth of the Caribbean HFR Network, new locations will be analyzed, selected, and tested for additional HFR sites.

V. Acknowledgments

This work was funded by the NOAA IOOS Award "Advancing the Caribbean Ocean Observing System"

United States Integrated Ocean Observing Serving

National Data Buoy Center HF Radar National Server

National Oceanographic and Atmospheric Administration

Rutgers University Center for Ocean Observing Leadership

Mid-Atlantic Regional Association of Coastal Ocean Observing Systems

University of Puerto Rico Mayaguez

Caribbean Integrated Ocean Observing System

Scripps Institution of Oceanography Coastal Observing Research and Development Center

Codar Ocean Sensors

The Integrated Ocean Observing System HF Radar Network:

Ten Year Status

Jack Harlan
US Integrated Ocean Observing System
NOAA
Silver Spring, MD, USA
jack.harlan@noaa.gov

Eric Terrill, Lisa Hazard, Mark Otero
Scripps Institution of Oceanography
University of California-San Diego
La Jolla, CA, USA
eterrill@ucsd.edu, lhazard@ucsd.edu, motero@ucsd.edu

Hugh Roarty
Center for Ocean Observing Leadership (RUCOOL)
Rutgers University
New Brunswick, NJ, USA
hroarty@marine.rutgers.edu

***Abstract*— As the US Integrated Ocean Observing System (IOOS) high frequency (HF) radar network (HFRNet) approaches its tenth year of existence, we highlight the growth and enhancements that have occurred. High frequency radar systems measure the speed and direction of ocean surface currents in near real time. Starting with about 30 radars in 2005, the network has grown to over 130 radars with 33 participating organizations and approximately ten million radial files sent via the network. A key component of the network has been the data ingest, processing and distribution system that is the core of the national HF radar data servers. Due to the scalability that was designed into it, this IOOS HF radar data management system has kept pace with the network growth and continues to have high reliability. We will show how the gridded vector velocity data have repeatedly proven their value in a number of operational applications including offshore search and rescue, oil spill response and water quality monitoring.**

I. INTRODUCTION

The US Integrated Ocean Observing System (IOOS) high frequency (HF) radar network approaches its tenth year of existence, we highlight the growth and enhancements that have occurred during the last five years. A Marine Technology Society (MTS) IEEE 2006 paper [1] details the data management and near real-time distribution of the system with applications and updated status of the network published in a 2010 MTS journal. [2]

High frequency radar systems measure the speed and direction of ocean surface currents in near real time. These radars can measure currents over a large portion of the coastal ocean, from a few kilometers offshore up to 200 km,and can operate under any weather conditions. The antennas are located near the water's edge, and transmit a signal that is reflected back to the instrument by moving surface waves. The reflected signal is processed to remove the wave speed and determine the surface currents producing a radial vector map in reference to the antenna. Two, or more, receive antenna sites with overlapping coverage are necessary to extract the direction of the currents. The data from each instrument site are sent to central computers where the individual signals undergo quality control checks and then are combined to calculate the total vector currents. These near real-time total vectors (RTV) are visualized online, distributed via web services, and archived at the NOAA National Centers for Environmental Information (NCEI).

Starting with about 30 radars in 2005, the network has grown to over 130 radars and is often referred to as HFRNet. Approximately 33 IOOS partner institutions contribute their near real-time low-level radar data to the three IOOS national radar data servers housed at the National Data Buoy Center, Scripps Institution of Oceanography and Rutgers University. A key component of the network has been the data ingest, processing and distribution system that is the core of these national data servers. Due to the scalability that was designed into it, this IOOS HF radar data management system has kept pace with the network growth and continues to have high reliability. Every US state with a coastline, except New Hampshire and Louisiana, has at least one HF radar site. Also, Puerto Rico now has four HF radars in operation. The system has even enabled the ingest and distribution of radar sites outside of the US including Canada and Mexico. See http://cordc.ucsd.edu/projects/mapping/maps/ to view an interactive map of the radar sites and the near-real-time maps

978-0-933957-43-5 ©2015 MTS

of the gridded current vectors computed, assembled and displayed by the national data server and Scripps Institution of Oceanography's Coastal Observing Research and Development Center (CORDC). The growth of the network in terms of number of radars and amount of terabytes of radial velocity data are given in fig. 1 and 2.

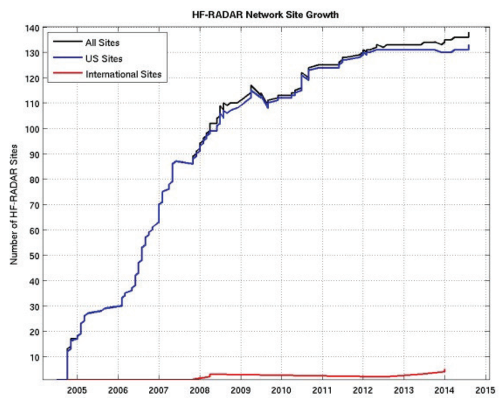

Figure 1. HFRNet site growth including Canada and Mexico sites

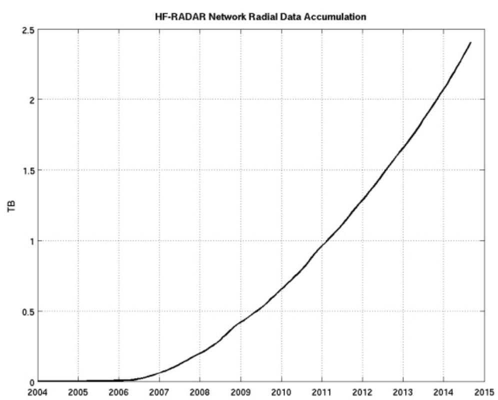

Figure 2. HFRNet data volume (TB) growth from 2005 through 2015

II. APPLICATIONS

A. Specific Events or Local/Regional Applications

IOOS funded HF radar derived surface currents have established data feeds to NOAA Office of Restoration and Response (OR&R), California State Office of Spill Prevention and Response (OSPR) and regional models such as Regional Ocean Model System (ROMS) for oil spill response within the California region. A recent operational example of HF radar derived surface currents usage occurred on May 19, 2015 with a ruptured oil pipeline just north of Refugio State Beach in Santa Barbara County, CA. Approximately 21,000 gallons of crude oil flowed to the coast and into the ocean triggering a response from participants within the Coast Guard led oil spill response area committee. These data were used to assist in analyzing and tracking the oil spill as it entered the region of coverage approximately 1km offshore. HF radar visualizations were used by local News Channel 3 in Santa Barbara for use during the weathercast in order to show circulation patterns in the area. In response to the Refugio oil spill, University of California, Santa Barbara (UCSB) HF radar operators from the Southern California Coastal Ocean Observing System (SCCOOS) established a temporary site at Gaviota in order to fill in coverage north of the spill and ran a local trajectory model advecting simulated particles through the current field to visualize the potential path of the slick. Scripps programmers integrated into HFRNet within an hour of being online to provide improved coverage to operational users within the region.

The Mandy Ness, a commercial fishing vessel, sank on Tuesday January 17, 2012. The Coast Guard had marked is position after sinking. When the Coast Guard attempted to locate the vessel for salvage it had moved from its original position. Rutgers University created drift scenarios with the 5 and 13 MHz radar network to aid the Coast Guard in their search for the vessel. One thousand virtual particles were released at the last known location for the Mandy Ness. The particles were advected using the HF radar surafce currents along with a random-flight model [5]. The drifter simulations showed a consistent drift towards the southeast that was utilized by the Coast Guard in the search efforts.

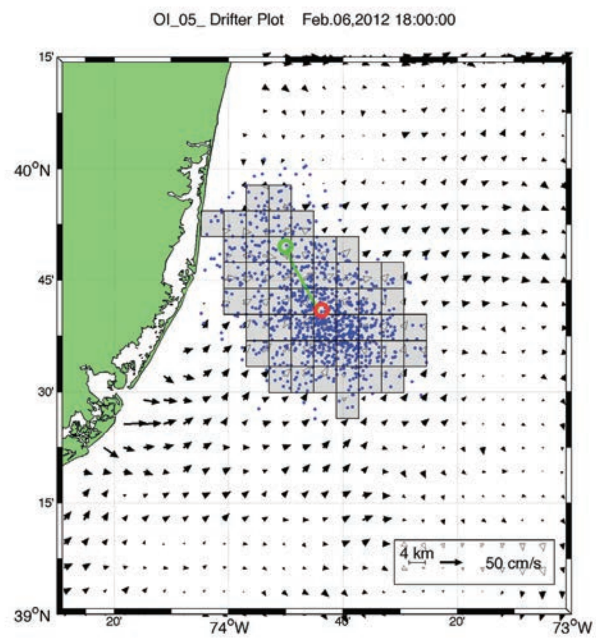

Figure 3: Drift scenario for the Mandy Ness fishing vessel. Surface currents showed a consistent drift towards the southeast. The 1,000 virtual particles are the blue dots, the path of the mean particle position is the green line with green circle indicating start and red circle showing end. The gray boxes encompass 95% of the virtual drifters.

Another regional application of the HF radar measurements was the detection of a meteotsunami off the coast of New Jersey on June 13, 2013 [6]. A derecho, which is a long-lived straight-line wind storm, had passed the area in the morning. The propogation speed of the weather front (40 knots, 25 m/s) matched the phase speed of a shallow water ocean wave to initiate the tsunami wave. The tsunami wave propogated east and then reflected off the shelf break and then made landfall later that afternoon. The 13 MHz HF radars detected the meteotsunami 23 km offshore, 47 minutes before it arrived at the coast.

Recently, the California Environmental Protection Agency (EPA) began efforts to create a marine debris tracking application and sought to use the HF radar api, adding the data layer combined with additional information for a holistic picture. These types of applications and requests continue to increase as the public, managers, and scientists use ocean observations to further our stewardship of ocean resources.

B. National Applications and Activities

Nationally, use of HF radar-derived currents continues with the US Coast Guard Search and Rescue Optimal Planning System (SAROPS) as well as NOAA's Office of Response and Restoration capability to react to offshore oil spills. Their GNOME Online Oceanographic Data Center (GOODS) routinely ingests HFR data. These efforts were discussed in [2].

Two new capabilities have been added recently. First, the NOAA National Weather Service's Automated Weather Information Processing System (NWS AWIPS) has been updated to ingest HF radar vector velocity gridded data in near-real-time. It is envisioned that HF radar will be useful to operational marine coastal forecasters and developers of numerical guidance. In some regions, the data will be compared to Real-Time Ocean Forecast System (RTOFS) output and, in the future, to the Extra-tropical Surge and Tide Ocean Forecast System (ESTOFS). A key prerequisite for this task was to convert the data from the NOAA National Data Buoy Center (NDBC) in its native network format to the GRIdded Binary (GRIB2) format. The data are then transmitted over the NWS Satellite Broadcast Network which provides access to the data for each AWIPS office. Since this is a new activity for AWIPS, at the time of this writing, we do not have specific weather events for which HF radar data have been used. Second, the HFR data have been ingested by the National Centers for Environmental Prediction (NCEP) for use in ocean circulation model development. Two levels of HFR data are being ingested in Binary Universal Form for the Representation of meteorological data (BUFR) format: radial velocities and vector velocity gridded data.

NOAA's Center for Operational Oceanographic Products and Services (CO-OPS) has released a product with national implications: an HF radar web product that provides near real-time surface current observations and tidal current predictions. The new web product is presently available in Chesapeake Bay, San Francisco Bay and New York Harbor (http://tidesandcurrents.noaa.gov/hfradar/) providing both near real-time HF radar surface current observations and tidal current predictions. The expectation is that the primary users of the new information provided by this product are the marine navigation community. Additional geographic locations where the product could be developed are being explored.

III. Data Management and Diagnostics

The HFRNet surface current mapping data management network is characterized by a tiered structure that extends from the individual field installations of HF radar equipment (a site), a local regional operations center which maintains multiple installations (an aggregator), and centralized locations which aggregate data from multiple regions (a node). This data system relies on robust aggregator to node communications with centralized data repositories that are updated in near real-time. Hourly Radial files are generated locally at the site and transmitted through the national network for inclusion in the total vector calculation which then produces a near real-time total vector (RTV). RTV's are generated on grids with multiple resolutions (500m, 1km, 2km, and 6km).

The backend processes require ongoing maintenance and updates to ensure processing speeds can keep up with near real-time in an environment of increasing site locations and expanding area of coverage. FY12-13 focused on a "tech refresh" effort, necessary to retain system consistency and reliability. CORDC replaced site aggregating systems operating for four years or more and deployed new centralized nodes at the three participating organizations to ensure processor speed and reliability was maintained for the growing network.

In 2013, a draft performance metric was defined to characterize the operational availability of data reporting from IOOS supported sites and contributing to HFRNet. The performance metric is based on the operation of the U.S. array over a 12 month fiscal cycle (October through September) or otherwise defined reporting cycles (e.g. quarterly cycle). The HF Radar IOOS metric is defined as the percentage of time NOAA IOOS funded radars are operational during a given reporting period. Operational radial files are considered to be a radial file where the number of observed radial solutions meets or exceeds a nominal number of radial solutions and the file was reported within twenty five hours of the observation. The number of operational radial files reported to the network are divided by the expected number of radial files and reported as a percentage of time the network was operational at full capacity.

The need to have a well-structured data archiving process for HF radar data was recognized and documented more than ten years ago [3]., This need was reiterated and described in more detail in [4]. Beginning in 2015, both gridded total vector velocity and radial velocity data types are being archived by the NOAA National Centers for Environmental Information (NCEI). Each month, the data files are transferred from the

NDBC data server to NCEI for archival. This effort will ensure data availability for future access and retrieval.

IV. GLOBAL EARTH OBSERVATION SYSTEM OF SYSTEMS (GEOSS)

GEOSS aims to coordinate and connect producers of environmental observations and information systems with end users to address global issues related to the Earth system. GEOSS is organized into nine "Societal Benefit Areas": disasters, health, energy, climate, water, weather, ecosystems, agriculture, and biodiversity. The Group on Earth Observations (GEO) is leading this effort with a focus on creating and managing a GEOPortal which allows access and discovery of relevant data sources, models, and decision making tools to promote and advance international cooperation. The Global Ocean Observing System (GOOS) is the oceanographic component of GEO and U.S. Integration Ocean Observing System (IOOS) is the U.S. contribution to GOOS. IOOS contributes ocean surface currents from HF radar to the GEOPortal enabling distribution of HFRNet data.

U.S. HFRNet has participated in the GEO Global HF Radar task since its inception in March 2012 at the first meeting held at Oceanology International in London, England. The goals of this task are to: 1.) Increase the number of coastal radars operating around the world; 2.) Ensure that HF radar data are available in a single standardized format in real-time; 3.) Establish worldwide quality standards; 4.) Distribute a set of easy-to-use standard products; 5.) Assimilate the data into ocean and ecosystem models. Subsequently, there have been international meetings held in Bergen, Norway (2013), Kaohsuing, Taiwan (2014) to promote these directives. Efforts have been focused on standardizing data management, cataloging applications and success stories, and promoting capacity building. The U.S. network efforts are being leveraged on a global level from a visualization and distribution perspective. Ideal data management standards include a standard gridded velocity format (e.g. Network Common Data Format (NetCDF), standard metadata naming conventions (e.g. Climate Forecast Interoperability), and a standard distribution service (e.g. THREDDS Data Server (TDS)). Scripps CORDC supports a global visualization http://cordc.ucsd.edu/projects/mapping/global/fullpage.php from distributed services that can be encapsulated into partnering visualizations and showcase international collaborations.

Increasing partnerships and data sharing globally promotes scientific and operational advances in coastal areas. The radiowave operators working group (ROWG) and GEO Global HF Radar Task promote national and international knowledge exchange and cooperation within the community.

V. REFERENCES

[1] E. Terrill, M. Otero, L. Hazard, D. Conlee, J. Harlan, J. Kohut, P. Reuter, T. Cook, T. Harris, K. Lindquist, Data Management and Real-time Distribution in the HF Radar National Network, Marine Technology Society Oceans 2006.

[2] J. Harlan, E. Terrill, L. Hazard, C. Keen, D. Barrick, C. Whelan, S. Howden, and J. Kohut, The Integrated Ocean Observing System High-Frequency Radar Network: Status and Local, Regional, and National Applications Marine Technology Society Journal, vol. 44, pp. 122-132, 2010.

[3] Paduan et al. Ocean.US document. Surface Current Mapping in U.S. Coastal Waters, 2004J. Clerk Maxwell, A Treatise on Electricity and Magnetism, 3rd ed., vol. 2. Oxford: Clarendon, 1892, pp.68–73.

[4] *A Plan to Meet the Nation's Needs for Surface Current Mapping* 2009, http://www.ioos.noaa.gov/library/national_surface_current_plan.pdf.

[5] D. S. Ullman, J. O'Donnell, J. Kohut, T. Fake, and A. Allen, "Trajectory prediction using HF radar surface currents: Monte Carlo simulations of prediction uncertainties," *J. Geophys. Res.,* vol. 111, p. C12005, 2006.

[6] [2] B. Lipa, H. Parikh, D. Barrick, H. Roarty, and S. Glenn, "High-frequency radar observations of the June 2013 US East Coast meteotsunami," *Natural Hazards,* pp. 1-14, 2013/12/17 2013.

Evaluation of Algorithms for Wave Height Measurements With High Frequency Radar

Hugh Roarty, Colin Evans, Scott Glenn
Center for Ocean Observing Leadership
Rutgers University
New Brunswick, NJ USA
hroarty@marine.rutgers.edu

Hao Zhou
School of Electronic Information
Wuhan University
Wuhan 430072, P.R. China
zhou.h@whu.edu.cn

Abstract*— Ocean wave conditions impact navigation, offshore operations, recreation, fisheries, safety of life at sea and hence the economic stability of any country's maritime sector. Making accurate measurements of wave conditions will help validate wave models and will help with forecasts of the wave conditions over the next few days. The United States has put forth "A National Operational Wave Observation Plan" to meet this need. It has called for 133 wave measurements in the coastal zone. High Frequency radar systems that are already in place can be one type of sensor to fill this measurement gap. Seven 13 MHz HF radars collected wave data along the coast of New Jersey from February 1, 2012 to June 1, 2012. The measurements from the radars utilizing existing algorithms were compared with wave measurements from accelerometer measurements aboard National Buoy Data Center platforms. Since there were large distances between the comparison points we first determined what the correlation was amongst the various buoy platforms to gauge the variability within the region. This provided a baseline for the comparison between the HF radar measurements and the nearby buoy measurements. We then evaluated three new wave measurement algorithms at one of the radar stations to see if that improved the measurements. The correlation of the radar wave measurements with that of the buoy varied considerably. We then chose one radar station that had good correlation with the buoy measurement and tested new algorithms to extract the wave information from the radar spectra. In each case, the comparison between the in situ record with the new algorithm showed improvement. The measurement of wave information with the radar showed moderate correlation with the in situ measurements. The four algorithms each showed improvement over the existing one. HF radar could be a sensor to play a role in the US national waves plan.

Keywords—radar, remote sensing, algorithm, wave, measurement, MARACOOS

I. Introduction

The Mid Atlantic High Frequency radar network consists of three components. The first is a 5 MHz long range network that covers from Cape Hatteras to Cape Cod with a 150 km range offshore. The second are five 25 MHz networks that provide high resolution sampling of the major estuaries in the region : Chesapeake Bay, Delaware Bay, New York Harbor, Western Long Island Sound and Block Island Sound. The third component of the HF radar network is a 13 MHz network that provides mesoscale coverage along the coast of New Jersey. See [1] for a detailed description of the network.

The main purpose for the Mid Atlantic radar network is measurment of ocean surface currents. These measurements have been used to characterize the climatology of the region [2, 3] and study flow events with shorter time scales[4, 5]. Wave height, period and wind direction are secondary measurements that can be made by each of the individiual radar stations. The method for wind and wave extraction is still has trailed that of the surface current measurement because of the complicated second order electromagnetic scattering that is utilized to extract the wind and wave information.

Each radar station in the Mid Atlantic is a SeaSonde HF radar manufactured by CODAR Ocean Sensors. CODAR provides a wave measurement package [6] as part of the software suite. This package has shown good results when applied off the California coast [7]. However the bathymetry off the coast of California deepens very quickly and is quite different from the East Coast of the United States that has a broad and shallow continental shelf. This is important as the existing CODAR wave software assume infinte water depth, which complicates the application of the wave software on the East Coast. Through this research paper we seek to determine if the existing wave software from CODAR can be applied to the radar stations in the Mid Atlantic.

II. Methods

A. In Situ Wave Measurements

Wave data from National Data Buoy Center (NDBC) for the time period between February 1, 2012 to June 1, 2012 was utilized as the reference measurement. Wave height measurements from buoy 44008, 44097, 44025, 44065. 44009 and 44014 were utilized in this study. The record for buoy 44066 only covered from February 1, 2012 to February 26, 2012 when the buoy broke free of its mooring, so it was removed from the analysis.

978-1-4799-8419-0/15/$31.00 ©2015 IEEE

B. High Frequency Radar

Wave data from seven High Frequency radar systems was collected and processed from February 1, 2012 to June 1, 2012. The radar network operated at the 13 MHz band and was established to study the offshore wind resource for the state of New Jersey [8]. The radar stations were located in munipalities of Sea Bright (SEAB), Belmar (BELM), Seaside Park (SPRK), Brant Beach (BRNT), Brigantine (BRMR), Strathmere (RATH) and North Wildwood (WOOD). The four letter site code for each radar station is given in the parenteses after the municipality.

The radar spectra from each station was processed with the software provided by the manufacturer. Table 1 provides the software version numbers for each of the tools used in the wave processing.

Table 1: Version numbers for the wave tools used in the SeaSonde software.

SeaSonde Wave Tool	Version
WaveModelForFive	10.6.4
SpectraToWavesModel	10.8.4
WaveModelSlider	11.2.6
WaveModelArchiver	11.2.5
AnalyzeSpectra	10.7.7

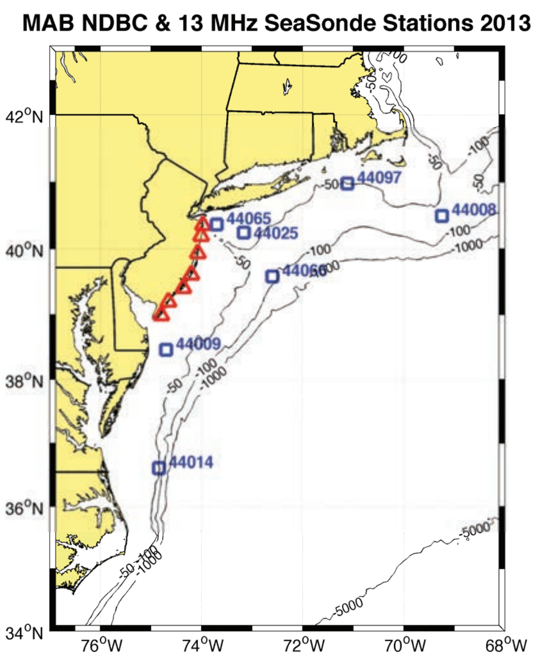

Figure 1: Study area of the Mid Atlantic Bight showing the location of the High Frequency radar stations (red triangle) and NDBC buoys (blue square).

III. Results

Since there was a large spacing between the HF radar and NDBC wave measurements, we first calculated the variability of the wave environment in the Mid Atlantic using all the NDBC buoy data. The correlation (Figure 2) and root mean square error (rmse) (Figure 3) was calcuated amongst the six wave buoys used in the study. These values were then plotted as a function of distance between the measurements to see how they vary spatially over the domain. This will be useful when comparisons are drawn between the HF radar and NDBC measurements as there is some distance between these measurements.

Figure 2 shows that correlation between the wave measurements of the NDBC buoys decreases as the distance between them increases. Figure 3 shows that the root mean square error between the wave measurements increases as the distance between the measurements increases.

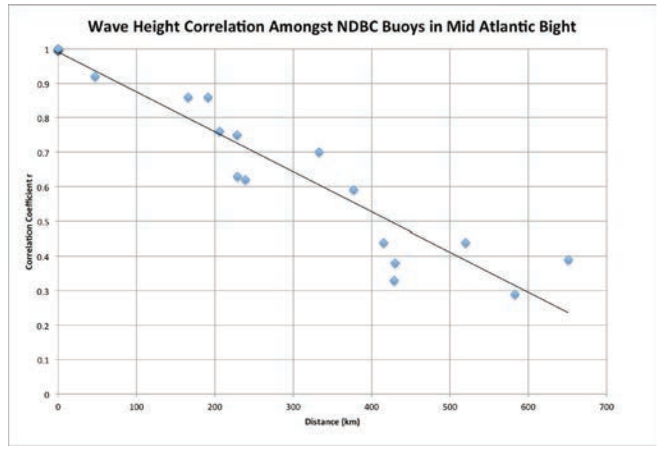

Figure 2: Wave height correlation between the NDBC buoys in the Mid Atlantic Bight as a function of distance (km) between the buoys.

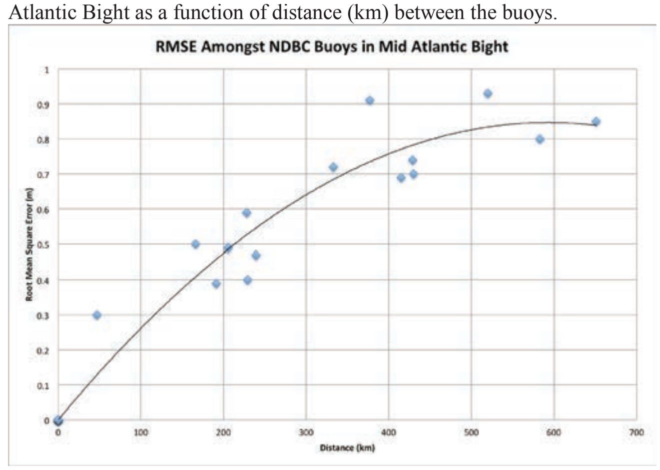

Figure 3: Root mean square error (m) between the NDBC buoys in the Mid Atlantic Bight as a function of distance (km) between the buoys.

Table 2 gives the distance in kilometers between the HF radar stations and each of the NDBC buoys. NDBC buoys 44065 and 44025 were used for comparison against the HF radar stations. The distance between the radar stations and buoy 44065 was 23-180 km and for buoy 44025 it was 69-198 km.

Based on Figure 2 we should expect the wave height correlation between the HF radar measurements and either buoy 44065, 44025 or 44009 to be between 0.9 and 0.7. We should also expect the root mean square error between the HF radar measurements and the three NDBC buoys to be between 0.1 and 0.5 m.

For the operational SeaSonde software the measurements did not meet these expectations. Table 2 gives the wave height correlation and rmse between NDBC buoy 44009 and 44025 and each of the seven HF radar stations. The table is ordered by lowest rmse at the top to highest at the bottom. The correlation was moderate to weak for each of the radar stations and did not meet the bounds of 0.7 to 0.9 that we expected. The lowest rmse was 0.56 m between buoy 44009 and radar station WOOD and was also outside the bounds of 0.1 to 0.5 m that we expected from the NDBC measurements.

One possible explanation for the low correlation and high rmse between the HF radar measurements and the in situ measurements is that radar measurements were made in water depths less than 30 m. The operational SeaSonde software assumes infinite water depth [9]. Shallow water effects become significant for the second-order spectra in water depths less than 30 m for the 13 MHz transmit frequency band used in this study. For instance, Figure 4 shows a time series plot for May 2012 of significant wave height from the radar station in Brigantine, NJ versus buoy 44025. On several occasions the radar measurements overestimate wave height. This is due to the failure of the operational SeaSonde algorithm to account for the increase of the radar coupling coefficient in shallow water [9].

The general trend of the wave environment is captured by the HF radar as seen in Figure 4. Some adjustments to the data processing steps or the radio wave form could improve the comparison between the two data sets. For this endeavor we utilized four algorithms to extract the wave height information from the radar spectra. The four algorithms are an 1) **Integration** - method similar to the Barrick method [10] without the weighting function 2) **Peak Ratio** - where the ratio of the first order Bragg peak to the second order Bragg peak gives wave height 3) **Peak Ratio Exclusion** – where the second order harmonic is excluded from the peak ratio algorithm and 4) **Integration With Beam Forming** where a beam is formed from the two loops of the SeaSonde and the data is processed with algorithm 1.

Each of the new algorithms was tested with the radar data from the Brigantine radar station for May 2012. Figure 5 shows a time series comparison of algorithm 4 with the wave buoy. It shows a marked improvement over the existing method. Table 4 gives the correlation coefficient between the different wave algorithms and the nearby wave buoys. Each of the new algorithms showed improved correlation with the in situ buoys. The algorithm that provided the highest correlation was the integration method after beam forming with the two cross loops.

Table 2: Distances (km) between the HF radar stations and the NDBC buoys.

	44008	44097	44025	44065	44009	44014	44066
SEAB	400	250	69	23	220	424	145
BELM	405	259	71	32	202	405	138
SPRK	414	276	85	58	173	376	132
BRNT	433	302	113	94	136	339	137
BRMR	453	326	139	121	109	314	152
RATH	484	360	173	153	82	288	182
WOOD	503	384	198	180	59	264	200

Table 3: Wave height correlation (r), root mean square error (RMSE) and number of data points (N) between NDBC buoys 44009 and 44025

NDBC Buoy	SeaSonde	r	RMSE (m)	N
44009	WOOD	0.41	0.56	1652
44009	SPRK	0.47	0.63	1978
44025	WOOD	0.29	0.67	1683
44025	SPRK	0.45	0.68	2009
44009	BRMR	0.39	0.71	2173
44009	RATH	0.42	0.75	2182
44025	BRMR	0.33	0.76	2204
44025	RATH	0.41	0.77	2213
44025	SEAB	0.46	1.12	2099
44009	BELM	0.14	1.15	1444
44025	BELM	0.16	1.18	1475
44009	SEAB	0.28	1.24	2068
44025	BRNT	0.22	1.54	1840
44009	BRNT	0.17	1.58	1809

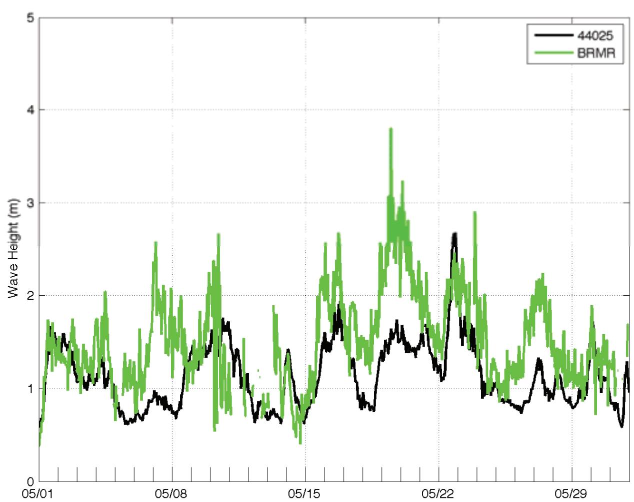

Figure 4: Time series plot of significant wave height as measured by the HF radar station with the SeaSonde operational algorithm at Brigantine (green) and NDBC buoy 44025 (black) for May 2012.

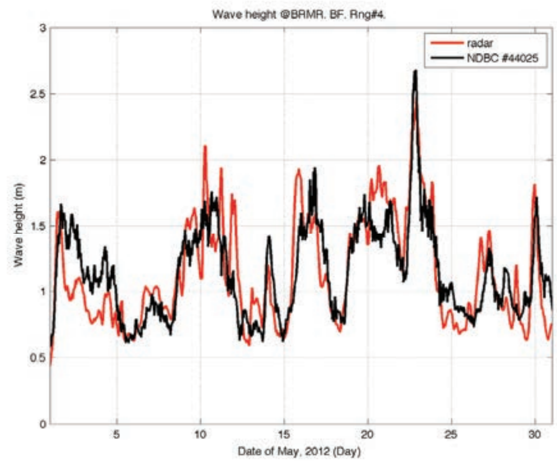

Figure 5: Time series plot of significant wave height as measured by the HF radar station with algorithm 4 integration with beam forming at Brigantine (red) and NDBC buoy 44025 (black) for May 2012

Table 4: Correlation coefficients between NDBC buoys and BRMR radar using different wave extraction algorithms. The time period of the comparison was for May 2012.

Method	NDBC Buoy	Correlation
SeaSonde Software	44025	0.53
SeaSonde Software	44065	0.50
Integration	44065	0.70
Peak Ratio	44065	0.74
Peak Ratio Second Harmonic Peak Excluded	44065	0.71
Integration after Beam Forming	44025	0.79

IV. CONCLUSIONS

Wave height comparisons were made between remotely sensed measurements with High Frequency radar and in situ wave buoys. The spatial variablility of the wave environment was provided by the wave buoys in the Mid Atlantic. This served as a backdrop for the comparisons between the radar measuremts and buoy measurements as the two were not colocated. The existing operational software for radar wave measurements showed moderate correlation with the wave buoys. Four new wave algorithms were tested on a month long data set and each showed an improvement over the exisiting method.

HF radar is a backbone technology of the United States Integrated Ocean Observing System (US IOOS). The surface current product from the HF radar network is widely used and operational with the US Coast Guard for search and rescue. The wave product from the individual radar stations shows good promise to becoming an operational product. These stations would fit well into the “National Operational Wave Observation Plan”.

ACKNOWLEDGMENT

This work was funded by NOAA Award Number NA11NOS0120038 “Towards a Comprehensive Mid-Atlantic Regional Association Coastal Ocean Observing System (MARACOOS)”. Sponsor: National Ocean Service (NOS), National Oceanic and Atmospheric Administration (NOAA) NOAA-NOS-IOOS-2011-2002515 / CFDA: 11.012, Integrated Ocean Observing System Topic Area 1: Continued Development of Regional Coastal Ocean Observing Systems.

REFERENCES

[1] H. J. Roarty, S. M. Glenn, J. T. Kohut, D. Gong, E. Handel, E. Rivera Lemus, T. Garner, L. Atkinson, C. Jakubiak, W. Brown, M. Muglia, S. Haines, and H. Seim, "Operation and Application of a Regional High Frequency Radar Network in the Mid Atlantic Bight," *Marine Technology Society Journal,* vol. 44, pp. 133-145, 2010.

[2] D. Gong, J. T. Kohut, and S. M. Glenn, "Seasonal climatology of wind-driven circulation on the New Jersey Shelf," *J. Geophys. Res.,* vol. 115, p. 25, 2010.

[3] B. Dzwonkowski, J. T. Kohut, and X.-H. Yan, "Seasonal differences in wind-driven across-shelf forcing and response relationships in the shelf surface layer of the central Mid-Atlantic Bight," *J. Geophys. Res.,* vol. 114, p. C08018, 2009.

[4] B. Dzwonkowski, B. L. Lipphardt Jr, J. T. Kohut, X.-H. Yan, and R. W. Garvine, "Synoptic measurements of episodic offshore flow events in the central mid-Atlantic Bight," *Continental Shelf Research,* vol. 30, pp. 1373-1386, 2010.

[5] E. Hunter, R. Chant, L. Bowers, S. Glenn, and J. Kohut, "Spatial and temporal variability of diurnal wind forcing in the coastal ocean," *Geophys. Res. Lett.,* vol. 34, p. L03607, 2007.

[6] B. Lipa and B. Nyden, "Directional wave information from the SeaSonde," *Oceanic Engineering, IEEE Journal of,* vol. 30, pp. 221-231, 2005.

[7] R. Long, D. E. Barrick, J. L. Largier, and N. Garfield, "Wave Observations from Central California: SeaSonde Systems and In Situ Wave Buoys," *Journal of Sensors,* vol. 2011, pp. 1-18, 2011.

[8] H. Roarty, J. Riscica, L. Palamara, L. Bowers, G. Seroka, J. Kohut, S. Glenn, and R. Dunk, "Analysis of the wind resource off New Jersey for offshore wind energy development," in *Oceans, 2012*, 2012, pp. 1-4.

[9] B. Lipa, B. Nyden, D. Barrick, and J. Kohut, "HF Radar Sea-echo from Shallow Water," *Sensors,* vol. 8, pp. 4611-4635, 2008.

[10] D. Barrick, "Extraction of wave parameters from measured HF radar sea-echo Doppler spectra," *Radio Science,* vol. 12, pp. 415-424, 1977.

Effectiveness of a Bistatic System on High Frequency Radar Resiliency

Chloe Baskin, Hugh Roarty, Josh Kohut, and Scott Glenn

Rutgers, The State University of New Jersey

Department of Marine and Coastal Sciences

Center for Ocean Observing Leadership

New Brunswick, New Jersey

chloe.baskin@rutgers.edu

***Abstract*— A paper was presented at OCEANS ’15 on a new way of increasing the resiliency of a High Frequency radar network through the use of bistatic measurements. This was modeled on the Mid Atlantic Regional Association Coastal Ocean Observing System (MARACOOS) High Frequency Radar network. The bistatic operating system is a recent feature of the SeaSonde HF radar. The bistatic capability is a viable way of increasing resiliency with out increasing the number of antennae. It involves the separation of the transmit and receive stations, as well as GPS timing to coordinate the time of the transmission signals. This results in a switch from a radial geometry and measurement to an elliptical geometry and measurement. This allows for higher percentage of overlapping coverage, which could potentially increase accuracy and resiliency.**

Using the configuration found through the previous models, bistatics were implemented along the MARACOOS network. Currently three radar stations are operating bistataically and generating elliptical current maps. They are stations located in North Wildwood (WOOD), Strathmere (RATH), and Brigantine (BRMR) New Jersey. The results have shown promise that the elliptical current measurements can become part of the operational data stream for the radar network. The bistatic systems are renamed using the first two letters of the four-letter station codes. For example the Strathmere-Brigantine bistatic system is called RABR. Initial findings suggest that the RABR is getting better coverage than the RAWO station. Using bistatics in RABR has widened the coverage area. Accuracy and coverage will be closely monitored during this time.

I. Introduction

Over the last five years, the East Coast of the United States has been hit with 3 major hurricanes: Irene, Sandy, and Arthur. Hurricane Sandy was the second costliest hurricane in US history [1]. The threat of storms initiated the push for increased coastal resiliency. The MARACOOS HF radar network has answered this push for increased coastal resiliency through bistatics.

The Mid-Atlantic Regional Association Coastal Ocean Observing system, (MARACOOS), has a network spanning most of the east coast of the United States (Figure 1). The MARACOOS HF radar network was one of the first to attempt to use a bistatic operating system to increase accuracy and resiliency [2]. The network is comprised of SeaSonde

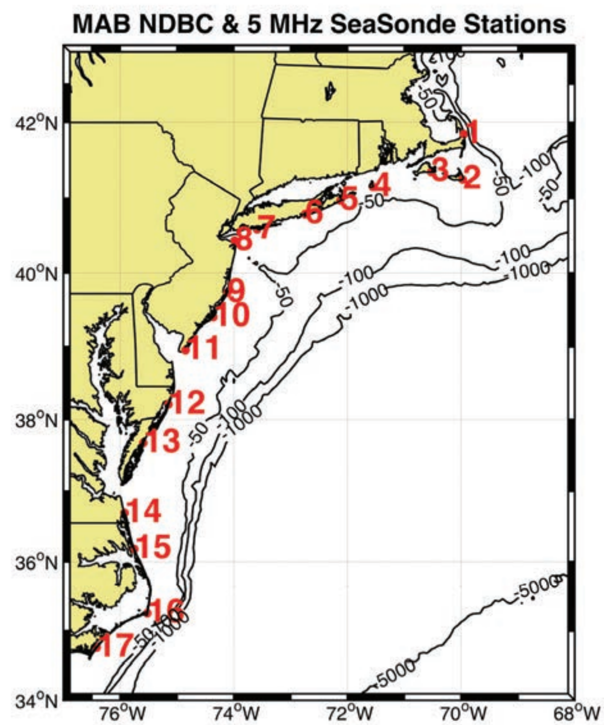

Figure 1: The locations of the 17 HF radar sites in the MARACOOS HF radar network. See table 1 for the corresponding site code and number.

radars, which use a unique sweeping frequency modulation to determine the range. The radars do not rely on the time delay of the signal echo.

978-1-5090-1537-5/16/$31.00 ©2016 IEEE

The unique operating system of SeaSonde, allowed for this network to operate multistatically. A multistatic system is one that runs both monostatically and bistatically. Monostatic systems receive and transmit a signal at a single site.. A bistatic system is accomplished by separating the transmit station and the receive station while using a GPS reference signal to link them [3].

A Multistatic system has the ability to increase accuracy because the combination of a bistatic and monostatic system increases the number of vector solutions for the total vector combinations [2,4]. It creates solutions with different bearing angles to help reduce the geometric error of the total surface current measurement. It also has the ability to increase resiliency during storms due to the capability of the system to provide additional coverage if an individual radar station stops reporting data.

The combination of radial velocities into total vector measurements carries along its position dependent error.. This error is described as the Geometric Dilution of Precision or GDOP. GDOP has expanded into GDOSA or the Geometric Dilution of Statistical Accuracy. Neither of these ideas was to be used with measured data. They are used to model the vector quality based on the radar network [2].

Table 1: Each long-range site from north to south is numbered along with the 4-letter site code for the station. This table corresponds with each numbered stations in Figure 1.

Site #	Site Code
1	NAUS
2	NANT
3	MVCO
4	BLCK
5	AMAG
6	MRCH
7	HEMP
8	HOOK
9	LOVE
10	BRIG
11	WILD
12	ASSA
13	CEDR
14	LISL
15	DUCK
16	HATY
17	CORE

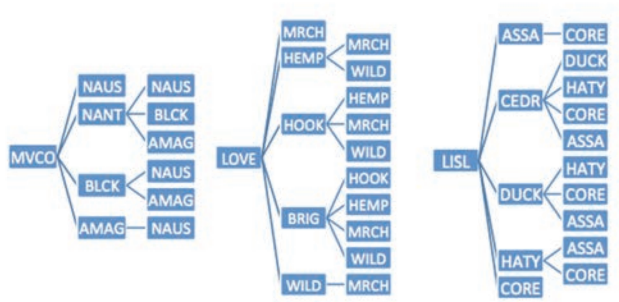

Figure 2: A chart that describes the proposed bistatic pairing of the radars. It is to be read left to right and top to bottom. For example, MVCO recieves signal from NAUS, NANT, BLCK, and AMAG

Using the original pairing, shown in Figure 2, the total coverage of a multistatic system was estimated. In these estimates, all 17 sites were paired and theoretically run bistatically. The results suggested that a multistatic system in the MARACOOS HF radar network would increase the accuracy. With such favorable estimates, the actual transition from monostatic to multistatic system seemed appropriate.

The initial goal was to implement bistatics in the long-range sites seen in Figure 2. The original pairing schema did not include the mid range radars so a new pairing map was created to accommodate for the mid range radar (Figure 3) Pairing five stations on a single frequency proved challenging, so the number of stations on a single frequency was reduced to three. Finding the exact timing that allows for a paired site to run properly is challenging and requires experimentation on the pat of the operator. However, when done properly the increase in coverage can be seen.

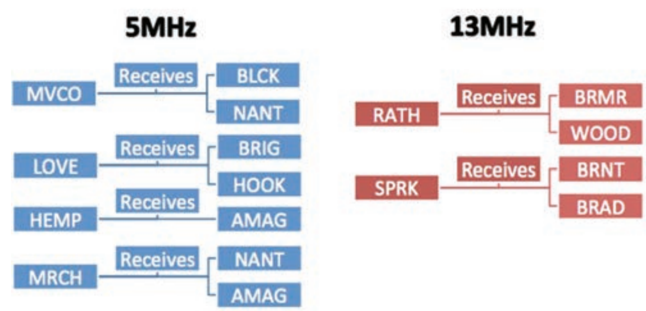

Figure 3: A chart of the new bistatic schema for the long-range radars (left) and mid range radars (right). It is also read left to right and top to bottom. For example, MVCO receives from BLCK and NANT.

II. Methods and Results

At each site elliptical velocity maps were used to measure surface current direction and velocity, as well as coverage of the area. These elliptical maps were then compared to the radial maps and analyzed for any discrepancies in coverage or average measurements.

The 13 MHz sites SPRK, SPAD, and RABR had the best coverage/consistency through out the multistatic network (Figure 4). The coverage over SPAD and SPRK along the coast is good. The coverage at RABR is not as good when compared to SPAD and SPRK. The sites have a wide blank area close to shore, which is to be expected with elliptical files. When compared to radial files the range of the coverage of the elliptical file is on par with the radial file.

Quality metrics for the 13MHz sites were created (Figure 5) where the top panel shows the average elliptical velocity in cm/s over the entire month of May 2016 and the bottom panel shows the number of vectors per elliptical file. Sites RAWO and RABR share anchor site RATH and are fairly consistent with each other in terms of the average velocity. RAWO had a few dips in the average velocity towards the end of the month. The number of vectors per file

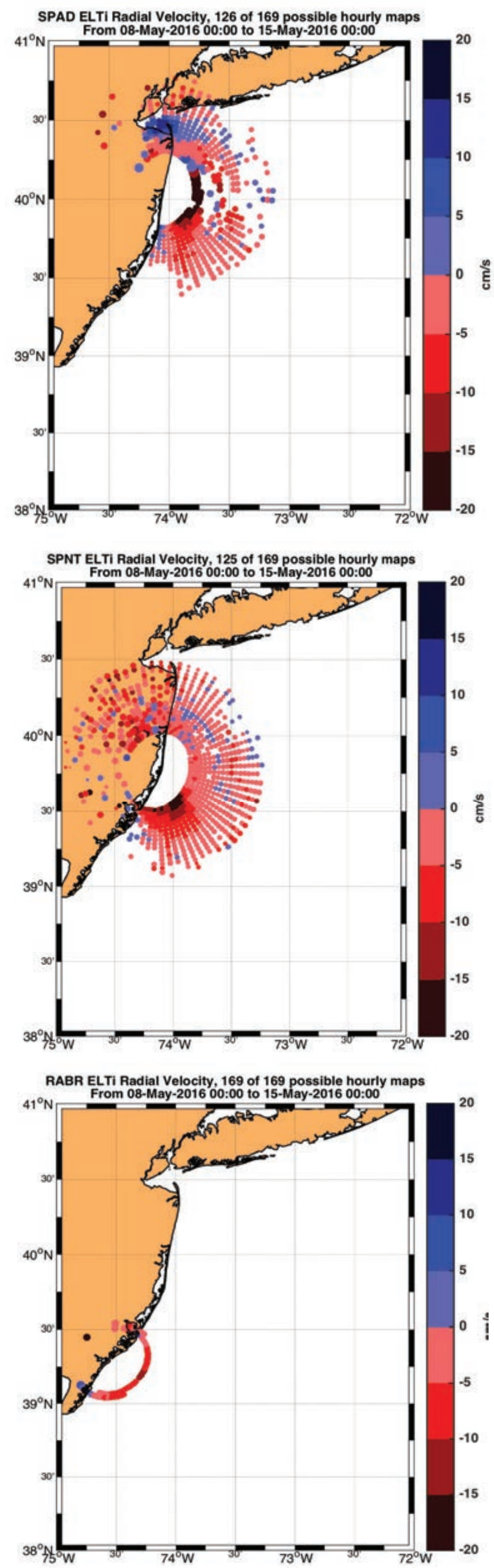

Figure 4: Average velocity maps for 13MHz sites SPAD, SPNT, and RABR for May 8-15, 2016. The coverage of these bistatic mid range radars spans the length of the NJ coast.

for RAWO tended to be more variable when compared to RABR.

Sites SPNT and SPAD share anchor site SPRK and were not generating elliptical files until the second week of May. They appear to be fairly consistent with one another in terms of velocity. However, SPAD experienced a malfunction near the 23rd of May had a large drop off in the number of vectors and that led to large negative spike in the average radial velocity.

SPNT and SPAD fluctuated largely in the number of

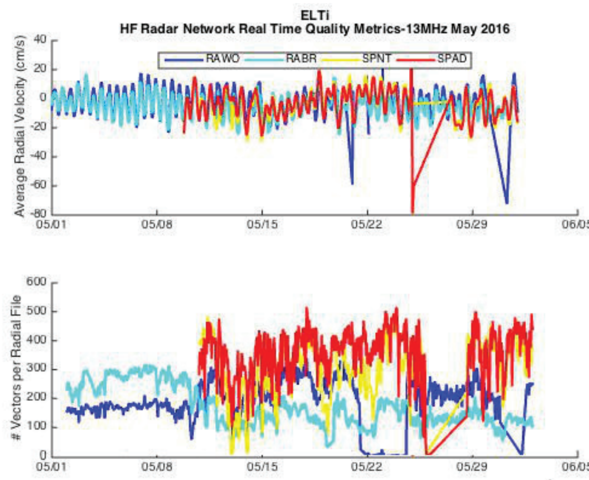

Figure 5: The quality metrics of the 13 MHz sites include average radial velocity (top) and the number of vectors per file (bottom).

vectors per radial file during May. Towards the 23rd of the month there was a large drop in the number of vectors almost to zero, which was caused by a power failure at the station.

Using the average radial velocities from the quality metrics, a power spectra was created. This power spectra, shown in Figure 6, indicates an accurate daily measurement of the M2 tide.

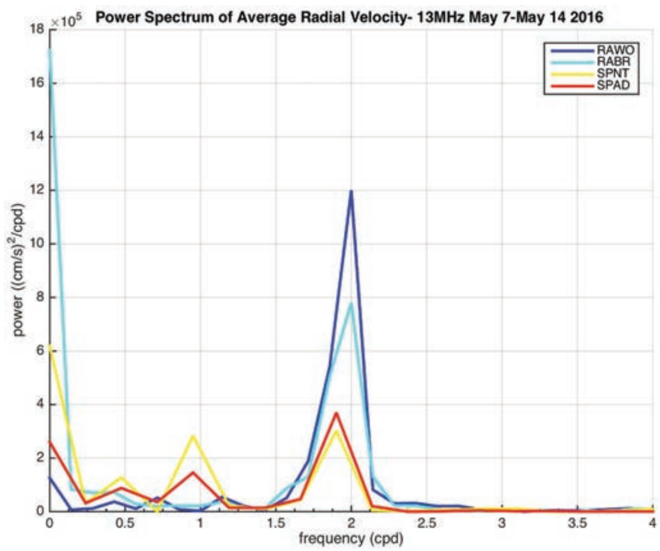

Figure 6: Power spectra for the 13MHz sites. Comparing power $((cm/s)^2$/cycles per day) and frequency (cycles per day)

III. Discussion and Conclusion

These results suggest that running a multistatic system for the entire HF network is possible and in doing so it appears to increase the coverage of the network. The proposed pairing schema proved challenging to implement so a paired down version was adopted. In general the elliptical velocity files showed an increase in the coverage when compared to their corresponding radial files suggesting that GDOSA was correct in estimating an increase accuracy and resiliency.

Total area coverage maps are being generated for the current multistatic system. These maps will be compared to the GDOSA total coverage maps to test if GDOSA was accurate in its estimates. It will also allow for a more accurate analysis of resiliency impact of the elliptical files.

IV. Acknowledgements

This work was funded by NOAA Award Number NA11NOS0120038 “Towards a Comprehensive Mid-Atlantic Regional Association Coastal Ocean Observing System (MARACOOS)”. Sponsor: National Ocean Service (NOS), National Oceanic and Atmospheric Administration (NOAA) NOAA-NOS-IOOS-2011-2002515 / CFDA: 11.012, Integrated Ocean Observing System Topic Area 1: Continued Development of Regional Coastal Ocean Observing Systems.

I. References

[1] Sullivan, D., and L. Uccellini. "Hurricane/post-Tropical Cyclone Sandy, October 22–29, 2012." *NOAA Service Assessment, NOAA* 1 (2013).

[2] Baskin, Chloe, et al. "High Frequency radar measurement resiliency with bistatics." *OCEANS 2015-MTS/IEEE Washington*. IEEE, 2015.

[3] Glaser, J. I. "Fifty years of bistatic and multistatic radar." *Communications, Radar and Signal Processing, IEE Proceedings F* 133.7 (1986): 596-603.

[4] Roarty, Hugh, et al. "Operation and application of a regional high-frequency radar network in the Mid-Atlantic Bight." *Marine Technology Society Journal*44.6 (2010): 133-145.

Fast Gap Filling of the coastal ocean surface current in the seas around Taiwan

Erick Fredj
Department of Computer Sciences, Lev Academic Center
21 Havaad Haleumi Street PO Box 16031, 91160
Jerusalem, Israel.
erick.fredj@gmail.com

Hugh Roarty
Department of Marine and Coastal Sciences Rutgers,
The State University of New Jersey. 71 Dudley Road,
New Brunswick, NJ 08901, U.S.A.
hroarty@marine.rutgers.edu

Josh Kohut
Department of Marine and Coastal Sciences Rutgers,
The State University of New Jersey. 71 Dudley Road,
New Brunswick, NJ 08901, U.S.A.
kohut@marine.rutgers.edu

Jian-Wu Lai
Taiwan Ocean Research Institute, National Applied
Research Laboratories. No.196, Henan 2nd Rd., Qianjin
Dist., Kaohsiung City 80143, Taiwan
laijw@narlabs.org.tw

***Abstract*— A fast, recently developed, Least Square regression method based on Discrete Cosine Transform (DCT-PLS) algorithm has been adapted to the mapping of hourly High Frequency Radar (HFR) data in the seas surrounding Taiwan. HFR is a shore based remote sensing system, and can be subject to unexpected observation failure. This algorithm produces both solution and error estimates of oceanographic data. The method explicitly uses both space and time information to predict missing values. In contrast to previous methods, our approach uses all HFR measurements to provide estimation error statistics while permitting long-range correlations, while allowing arbitrary HFR measurement locations.**

The approach is demonstrated by reconstructing the Hourly HFR data with a spatial resolution of 9km in the Taiwanese seas.

We validated the method during the summer 2015 against typical gap scenarios. A major advantage of the approach is the ability to perform fast and robust computation while requiring a small amount of memory storage, showing the feasibility of a real-time application for filling HFR missing data.

Keywords*— *Penalized least square regression; OMA; OI; EOF; gap filling; HF-Radar

I. Introduction

The coastal ocean is a complex system that forms the boundary between the land and the deep ocean. Deeper understanding of surface currents can be extremely valuable when one seeks to characterize and quantify the transport of plankton and anthropogenic material in the coastal ocean. The Taiwan Ocean Research Institute (TORI) of the National Applied Research Laboratories (NARLabs) since 2009 provides consistent and accurate hourly surface current information in the seas around Taiwan. This is based on a significant effort to ensure hardware and software resiliency, quality control, and quality assurance. Spatial coverage with good data percentage more than 50% according to the past three years records has been observed to vary on daily seasonal scales because ionospheric interference at the lower HF radio spectrum and variable state conditions (Liu et.al. 2010).

A fast, recently developed, Least Square regression method based on Discrete Cosine Transform (DCT-PLS) algorithm has been adapted to the mapping of hourly High Frequency Radar data observation in the seas surrounding Taiwan.

In this study, we attempt to solve a very difficult analytical problem: filling gaps with spatial scales of up to 100 km over a domain that spans roughly 450 km along the coast and 150 km offshore, while maintaining a spatial resolution of nine kilometers. It is obvious that no gap filling method can reliably reconstruct variability at a scale as small as nine kilometers over gaps as large as 100 km in all scenarios. If there is no small-scale variability in the gap, available data will likely provide enough constraints for credible reconstruction. If the gap includes a small-scale structure, the reconstruction will likely be very poor.

The DCT-PLS algorithm produces both solution and error estimates of oceanographic data across these gaps. The method explicitly uses both space and time information to predict missing values. In contrast to previous methods, our approach uses all HF Radar measurements to provide estimation error statistics while permitting long-range correlations, while allowing arbitrary HF Radar measurement locations.

This method tackles a particularly difficult problem, and finding a comparable existing method may be extremely difficult. The Open boundary Modal Analysis (OMA) basis set then will consist of at least 2000 Dirichlet modes and 2000 Neumann modes, or a total 4000 of modes (Kaplan and Lekein, 2007). OMA mappings of HF Radar generally use no more than a few hundred modes. In the nine kilometer resolution, the 450 km x 450 km domain requires roughly 60 modes in the along shore direction and at least 60 modes in the offshore direction. Fourier methods like Normal Mode Analysis (NMA) or OMA are not appropriate because they will certainly produce large, non-physical velocity magnitudes in the gap regions when a nine-kilometer resolution is required, as it is in this case. In addition, it is likely not numerically feasible to compute the several thousand modes, so the OMA toolbox PDE solver will fail to compute all of these modes, because the numerical solutions become extremely sensitive at higher mode numbers. Another alternative, Empirical Orthogonal Functions (EOF) might be considered (Yaremchuk et.al. 2011), but EOFs are sensitive to gappy data and are not suitable for interpolation or extrapolation.

Optimal Interpolation (OI) developed by Kim et.al. (2008), or other covariance-based techniques include no boundary constraints, and can easily generate non-physical normal flow at solid boundaries.

In this article we will describe the fast Filling algorithm giving a special attention of the Taiwan Ocean Radar Observing System Network (section 2). In Section 3, we will describe the Gap Filling Method. Finally in Section 4 we present some typical gap-filling scenario of the Taiwanese network.

II. The Network

The Taiwan Ocean Radar Observing System (TOROS) of TORI consists of 17 SeaSonde type radars around the Taiwan Island (Figure 1), 12 of which are long range, 4 of which are medium range, and 1 of which is standard range. Table 1 provides the typical characteristics of the different types of systems. Each site consists of two categories of hardware: the radar equipment purchased directly from CODAR Ocean Sensors and the ancillary site specific hardware required for communications, power, backup power, temperature control, weather proofing, security, and antenna foundations. High Frequency Radar (HFR) systems (Kohut 2012) are one technology deployed along the coast to remotely measure the complex surface current dynamics over these highly variable seas.

TABLE I. CHARACTERISTIC OF TOROS LONG-, MEDIUM-, AND STANDARD RANGE HF RADAR SYSTEMS.

System Type	Radio Frequency (MHz)	Range (km)	Resolution (km)
Long Range	4.58	150	3.75
Medium Range	13.4	70	1.5
Standard Range	24.3	40	1.5

All of the sites are managed by Taiwan Ocean Research Institute (TORI), National Applied Research Laboratories (NARLabs) since 2009 and the primary function of the radars was to map surface currents. The TORI headquarters in Kaohsiung processed all data, combined to surface current map, checked for quality control, and saved to the archive.

According to the 2014 TOROS annual report (Lai et al., 2015), the correlation coefficient of surface current between HFR observed and 11 drifter-derived current velocities are 0.70 and 0.84 in u and v directions, respectively. And the mean differences are 0.019 m/s and -0.033 m/s in u and v directions.

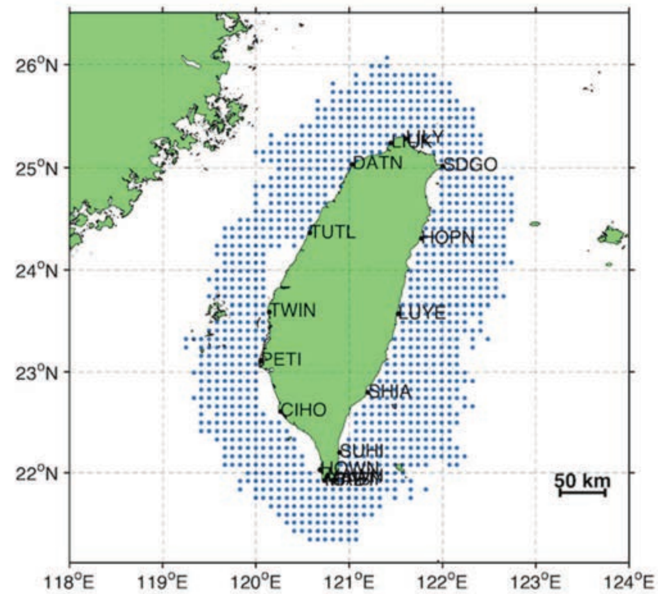

Fig. 1. Location of long-range HF radar locations (black circle) within the TORI domain with four-letter site code next to station location overlay with the 70% mean coverage from May 01, 2015 to July 31, 2015 in seas around Taiwan.

III. The Gap Filling Method

Fredj 2016 introduces for the first time a DCT-PLS method applied to HFR data processing. We now give a short introduction of the DCT-PLS algorithm. For more details on the mathematics of the method, the reader is referred to Fredj et. al. (2016).

$$F\left(\hat{X}\right) = RSS + sP = \left\| W^{1/2} \circ \left(\hat{X} - X\right)\right\|^2 + s\left\|\nabla^2 \hat{X}\right\|^2 \quad (1)$$

Let X stands for a spatial-temporal dataset with gaps, and W a binary array of the same size indicating whether or not the values are missing. The technique consists in minimizing a criterion that balances the fidelity to the data, measured by the residual sum of squares (RSS), and a penalty term (P) that reflects to the roughness of the smooth data $\hat{X}$ measured. The DCT-PLS seeks for $\hat{X}$ that minimizes the error function F. $\|\cdot\|$ is the Euclidian norm, ∇^2 and ° stand for the Laplace operator and the Schur (element wise) product respectively. The term s is a positive scalar that controls the degree of smoothing. As s increases, the smoothness of $\hat{X}$ also increases. For small values of s, the value of $\hat{X}$ will be dominated by noise.

To investigate the best fit of the model coefficients, we apply the Generalized Cross Validation (GCV) score method (Craven and Wahba 1978) to find a good compromise between goodness and smoothness of $\hat{X}$. In the case of equispaced data, Strang (1999) simplified considerably the complexity of the GCV calculation by rewriting the GCV score in terms of the type-2 DCT and its inverse (IDCT), which forms

$$\hat{X} = IDCT\left(\Gamma \circ DCT\left(W \circ \left(X - \hat{X}\right) + \hat{X}\right)\right) \tag{2}$$

Where Γ are the components of the diagonal three-dimensional tensor defined by Yueh (2005)

$$\Gamma_{i_1,i_2,i_3} = \left[1 + s\left(\sum_{j=1}^{3}\left(2 - 2\cos\left(i_j - 1\right)\pi / n_j\right)\right)^2\right]^{-1} \tag{3}$$

Where i_j denotes the i elements along the direction j, and n_j denotes the size of X along the direction j. The DCT-PLS technique relies only on the choice of the smoothing parameter s. In the case of gap filling the parameter s has an infinitesimal value to reduce the effect of smoothing. A high s value leads to the loss of high frequency variability in the HFR surface current fields. To avoid any subjectivity in the choice of the smoothing parameter, this parameter is determined by minimizing the GCV score. Minimization of the GCV score helps to optimize the trade-off between bias and variance. The bias measures how well the smoothed velocity field approximates the true velocity field, and the variance measures how well the smoothing velocity field can estimate the original experimental velocity field.

IV. Regional Results

The gap-filling algorithm was tested for two main scenarios observed in the hourly HFR current data in the seas around Taiwan. Based on the last three months (Figure 1) dataset the hourly in the seas around Taiwan coverage is characterized both spatial and temporal to provide at least 70% spatial coverage and 70% temporal coverage.

In this study we defined two scenarios, which reproduce the most common two failure situations (Figure 2).

A. Scenario 1

The first scenario tested mimic a major hardware failure in July 9, 2015 14:00:00 at least one site from the network. Observed gaps under this scenario can be best described as a gap that extends along the coast from the shore to the offshore edge of the coverage explicitly splitting the TORI HFR network into two.

The size of the band with no data depends of the number of sites that are not reporting data. For the purpose of this analysis we are simulating the loss in contributing radials from a single site in HOPN region in the eastern part of Taiwan Island.

B. Scenario 2

The second scenario tested imitates more common situations in which each site is contributing radials vectors, but there is a reduction in the number of radial data from one or more sites. The most common cause is an increase on external noise that lowers the signal to noise ratio and therefore limits the range of detectable signal used to determine radial velocity. The size and location of the gaps depend on the location and magnitude of the reduction of coverage from each individual site. For long-range SeaSonde HF radar the ionosphere effects increase the range at which a given site receives an external noise. June 11, 2015 16:00:00 cause serious effect on the system.

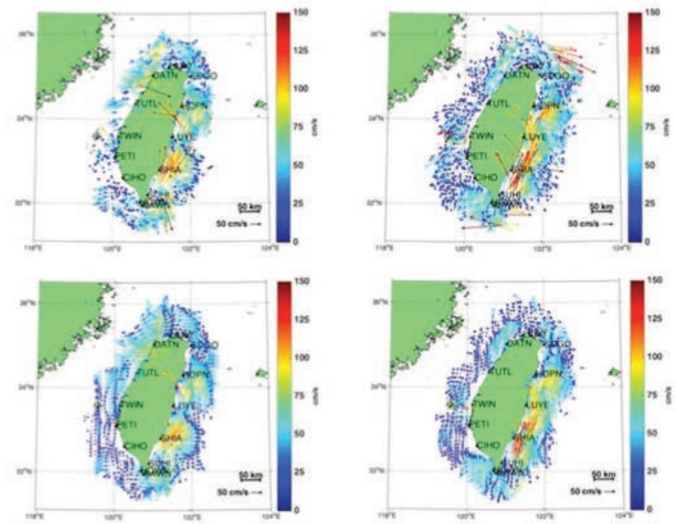

Fig. 2. Surface current maps showing the scenario 1 in July 9, 2015 14:00:00 on the right column, and the scenario 2 in June 11, 2015 16:00:00 on the left column. The observed velocity field by TORI HFR is on the top and the smoothed velocity field map with 70% mean coverage is on the bottom.

Based on TORI on 7 years analysis from 2009 HFR coastal radar network, scenario 1 occurs less than 6 % of the time and the scenario 2 occurs almost 60 % of the time.

For the both scenarios 1 and 2 we estimated the validity DCT-PLS velocity fields by comparing the removed vectors and the predicted vectors. The correlation shows a strong agreement from both meridional and zonal velocity components.

V. Conclusions

In this study we introduce an efficient automated DCT-PLS method for filling the data gaps in the HFR ocean Spatial-Temporal dataset applied to TOROS domain in the seas around Taiwan.

The DCT-PLS approach was demonstrated by reconstructing the Hourly HF Radar observation with a spatial resolution of nine-kilometer in the Taiwanese seas. We validated the method during the summer 2015 against typical gap scenarios. A major advantage of the approach is the ability to perform fast and robust computation while requiring a small amount of memory storage, showing the feasibility of a real-time application for filling HF Radar missing data. The user, however, should be aware of some limitations of the automatic gap filling procedure. Under the less common scenario in which more significant outages can remove entire sites from a coastal network, the effectiveness of the method depends on the characteristics of the surrounding flow. Individual HFR network operators will need to assess the scales of variability in their operating area to determine the optimal way to apply this method in either a real-time or post-processed application.

Acknowledgment

This study was supported by a grant from the Israel Science Foundation and the Taiwan Ministry of Science and Technology. Taiwan Ocean Research Institute (TORI), National Applied Research Laboratories (NARLabs), sponsored the HFR dataset.

References

[1] Craven P., Wahba G. 1978. Smoothing noisy data with spline functions. Estimating the correct degree of smoothing by the method of generalized cross-validation. Numer Math 31:377–403.

[2] Fredj E., Roarty H., Kohut J., Smith M. and Gleen S. " Gap Filling of the Coastal ocean surface current from HFR data: Application to the Mid Atlantic Bight Network", JTECH, accepted for publication, February 16 (2016).

[3] Kaplan, D.M., Lekein, F. 2007. Spatial interpolation and filtering of surface current data based on open-boundary modal analysis. J. Geophys. Res. 112, C12007.

[4] Kohut, J., Roarty, H., Randall-Goodwin, E., Glenn, S., & Lichtenwalner, C. 2012. Evaluation of two algorithms for a network of coastal HF radars in the Mid-Atlantic Bight. Ocean Dynam. 62:953-68.

[5] Kim, S.Y., Terrill, E., Cornuelle, B., 2008. Mapping surface currents from HF radar radial velocity measurements using optimal interpolation. J. Geophys. Res. 113, C10023.

[6] Lai, J.W., Lin, K.I., Yu, C.M., Hsu, T.C., Yang, Y.C., Huang, Y.H., Wu, C.C., Chen, S.H., Chen, S.H., Lee, C.W. 2015. TOROS 2014 Annual Report. TORI Tech Note, p. 443 (in Chinese)

[7] Strang, G. 1999. The discrete cosine transform. SIAM Review 41, 135–147.

[8] Yaremchuk, M. and Sentchev,A. 2011. A combined EOF/variational approach for mapping radar-derived sea surface currents. Continental Shelf Research. 31, 758–768.

[9] Yueh, W.C. 2005. Eigenvalues of several trigonal matrices. Applied Mathematics E-notes 5, 66-74.

Stratified Coastal Ocean Processes in Hurricanes and Typhoons Enhance Ahead-of-Eye Cooling and Reduce Storm Intensity

Scott Glenn, Travis Miles, Greg Seroka, Robert Forney, Hugh Roarty, Oscar Schofield and Josh Kohut
Rutgers University
New Brunswick, NJ 08901, USA
glenn@marine.rutgers.edu

Yi Xu
State Key Laboratory of Estuarine and Coastal Research
East China Normal University
Shanghai 200062, China

Fei Yu
Institute of Oceanology
Chinese Academy of Sciences
Qingdao 266071, China

***Abstract*— Integrated ocean observations from Hurricane Irene (2011) reveal widespread and significant ahead-of-eye cooling (at least 5°C and up to 11°C) as it crossed the seasonally stratified continental shelf of the Mid-Atlantic Bight of North America. Buoys and gliders deployed in the storm allow the detailed evolution of the surface temperature to be examined at select points, revealing 76%-94% of the total cooling occurs before eye passage. A range of ocean models were used to diagnose the processes responsible for the observed cooling. In Irene, 1D vertical mixing models generate only 17% of the total cooling ahead of eye, while deepwater 3-D models forced by Irene's nearly symmetrical offshore windfield produce an approximately 50-50 split in the cooling between the front and back side. A 3-D coastal ocean model (ROMS) generates a wind-forced two-layer circulation in the stratified MidAtlantic not present in the 1-D and 3-D deepwater models. The resultant shearinduced mixing more accurately reproduces both the magnitude and timing of the surface cooling with respect to eye passage. Atmospheric simulations establish that this cooling was the missing contribution required to reproduce Irene's accelerated reduction in intensity over the Mid Atlantic Bight. Historical buoys from 1985 to present show that ahead-of-eye cooling occurred beneath all 11 tropical cyclones that traversed along the Mid Atlantic Bight continental shelf during stratified summer conditions. The buoys also reveal that an average of about 75% of the cooling in these 11 hurricanes occurs ahead of eye, indicating a robust process in the Mid Atlantic. Similar to the Mid Atlantic Bight, the Yellow Sea have had 26 typhoons cross its shallow highly stratified waters in summer before making landfall in China or Korea. Typhoon Muifa (2011), whose intensity was also overpredicted, generated significant SST cooling (up to7C) in the Yellow Sea, and a Yellow Sea buoy array similarly revealed 85% of the cooling was ahead of eye. These findings establish that including realistic 3D coastal ocean processes in forecasts of landfalling storm intensity and impacts will be increasingly critical to mid-latitude population centers as sea levels rise and tropical cyclone maximum intensities migrate poleward.**

***Index Terms*—Hurricane Forecasting, U.S. IOOS, Underwater Gliders, HF Radar, Ocean Modeling, Atmospheric Modeling.**

I. INTRODUCTION

Tropical storms are some of the most destructive and deadly weather phenomena on Earth, and have killed more people than any other natural catastrophe (Keim et al. 2006). For example, in the United States during the 20th-century, ten times as many deaths and >three times as much damage occurred from these extreme weather events as compared with earthquakes (Gray, 2003). The impacts are magnified given the human population density found along the coastlines that are prone to hurricanes. Despite the potential devastation, advances in technology, communication, and forecasting have resulted in significant declines in hurricane-related mortalities

978-1-4673-9724-7/16/$31.00 ©2016 IEEE

between 1900 and present day (Walker et al. 2006). Most recently these declines reflect the developments in global atmospheric models and an ensemble forecasting approach that have successfully reduced hurricane track forecast errors by factors of 2-3 over the last two decades, allowing communities sufficient time to proactively prepare for the storms and evacuate prior to their arrival. Despite the progress in predicting hurricane tracks, the predictive skill for hurricane intensity forecasts has remained "flat" over the last twenty years (Pasch & Blake, 2012).

The Mid-Atlantic Regional Association Coastal Ocean Observing System (MARACOOS), one of eleven Regional Associations comprising the regional component of the U.S. Integrated Ocean Observing System (IOOS), operates a Regional-Scale Coastal Ocean Observatory that includes coastal weather mesonets, satellite data ground stations, a 1000 km long High Frequency (HF) Radar network (Roarty et al., 2010), and a distributed fleet of autonomous underwater gliders (Schofield et al., 2010). Observatory data is assimilated into global and regional-scale ocean models, and an ensemble of regional atmospheric models beginning to use the ocean surface conditions as a boundary condition. The Regional-Scale Coastal Ocean Observatory was fully operating during both hurricanes. In this paper, we discuss selected highlights of real-time ocean data acquired by the MARACOOS regional-scale network during Irene. This network identifed coastal baracolinic circulation induced by the strong winds ahead of Irene's eye as the key process causing rapid ahead of eye cooling on fhte ocean. The cold ocean reversed the sign of the heat flux as the eye passed over, rapidly deintensifying the storm. The newly identified process in Irene was found to occur in every hurricane crossing the Mid Atlantic bight in summer in the last 30 years, and in a Yellow Sea typhoon.

II. Hurricane Irene & Typhoon Muifa

We illustrate the current state of the science by comparing two tropical cyclones, Hurricane Irene (Fig. 1) and Super-Typhoon Muifa (Fig. 2). Both occurred during the summer of 2011.

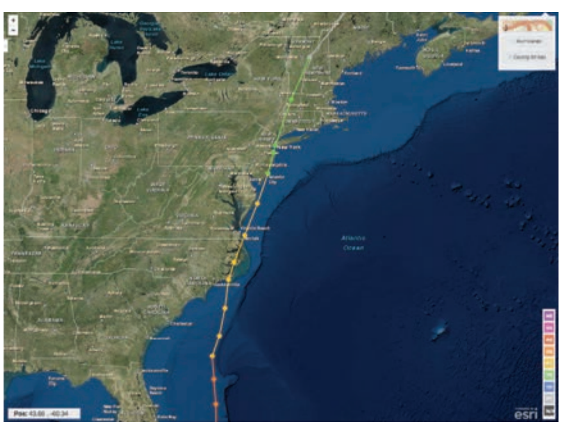

Fig. 1. National Weather Service track and intensity for Hurricane Irene, 26-29 August 2011.

Despite the tendency of many east coast hurricanes to recurve out to sea, Hurricane Irene's track straight up the east coast of the United States was well forecast days in advance. The intensity forecast did not fair as well. Dire warnings of hurricane winds and intense storm surge were issued by the President of the United States, Governor of New Jersey and the Mayor of New York City. Over 2 million people were ordered to evacuate. But as Irene crossed the Mid Atlantic coastal ocean, its intensity plummeted to Tropical Storm. There was little storm surge experienced at the coast. The devastation caused by the tropical storm was instead well inland and caused intense rainfall and flooding of rivers.

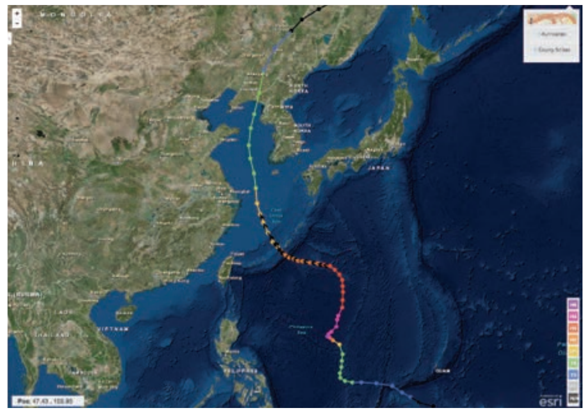

Fig. 2. National Weather Service track and intensity for Typhoon Muifa, 26 July – 9 August, 2011.

Typhoon Muifa had a similar history with of dire warnings as it approached the Yellow Sea. With landfall expected in China, hundreds of thousands of residents were ordered to evacuate the coast. But again, as Typhoon Muifa crossed the Yellow Sea on its way to landfall, its intensity plummeted. The dire warnings were unrealized, and bloggers thanked the weather service for a long weekend.

What do these two tropical cyclones from the summer of 2011 have in common?

III. Coastal Baroclinic Circulation & Mixing in Irene

The day before final landfall in New Jersey, Irene was located over the warm water of the South Atlantic Bight and was still an intense Category 1 hurricane (Fig. 3). The scale of the storm vissible in the cloud pattern is the same scale has the Mid Atlantic's HF Radar network. The storm remained intense until the eye left the South Atlantic Bight and entered the Mid Atlantic Bight just north of Cape Hatteras.

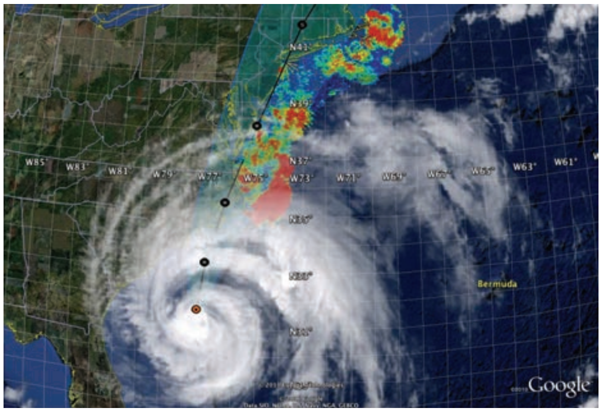

Fig. 3. Hurricane Irene approaches the Mid Atlantic Regional Association Coastal Ocean Observing System (MARACOOS) on August 27, 2011

The eye of Hurricane Irene made landfall in southern New Jersey near Atlantic City about 0935 UTC on August 28, 2011. Irene was moving rapidly northward, fully crossing the state of New Jersey in about 6 hours. The rapidly evolving surface current response as Irene propagated along the New Jersey coast was observed (Figure 4) using the Mid-Atlantic's High Frequency (HF) Radar network (Roarty et al., 2010). At 0600 GMT, Irene's eye is still over water, with its location observed in the CODAR currents offshore southern New Jersey. Strong onshore currents over the entire width of the shelf are observed north of the eye. At 1200 GMT, the eye is over land in central New Jersey.

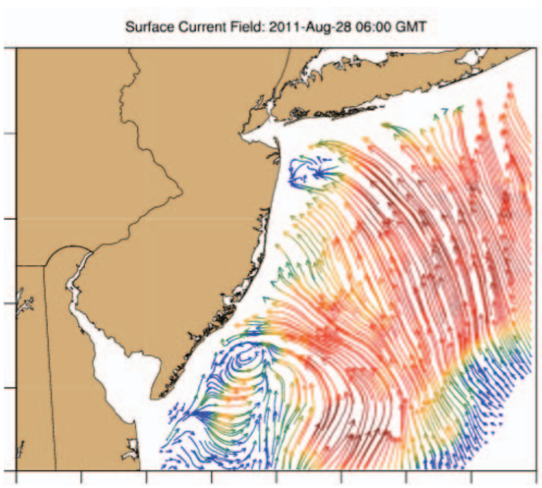

Fig. 4. Onshore surface currents observed by the HF Radar network ahead of the Irene's eye.

The satellite-derived sea surface temperature (SST) difference before and after Irene is shown in Figure 5. Cooling on the shelf was intense, up to 11C maximum. But satellite infrared SST sensors cannot see the ocean through cloud cover, so all we cn say is that the intense cooling occurred sometime between the start of the cloud cover shown in Figure 3 and the end of the cloud covered time period.

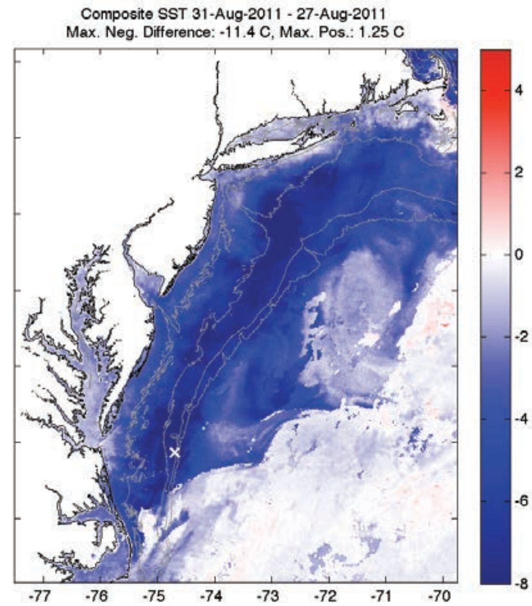

Fig. 5. SST cooling during Hurricane Irene. Maximum cooling is 11C.

An autonomous underwater glider was deployed about 2 weeks before Irene along the New Jersey coast (Figure 6). It was on a routine water quality monitoring mission (blue line) when the first warnings of Irene's appear. Glider RU16 was directed to fly out to the 40 m isobath to ride out the storm in the relative safety of the deeper water. During the 24 hour period of the storm, Glider RU16 barely moved from its assigned location (green portion of line)

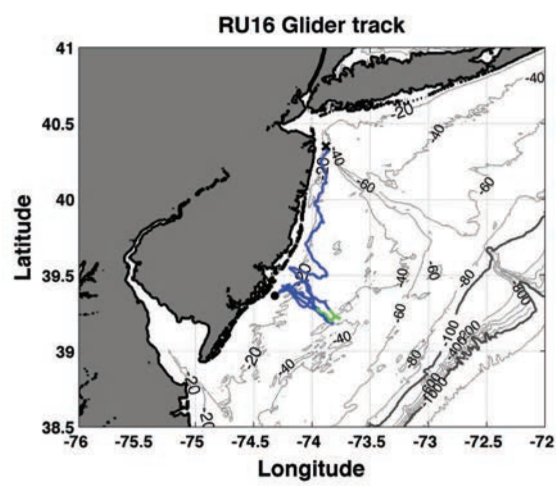

Fig. 6. Glider RU16 track from EPA water quality monitoring mission along coastal New Jersey. Green segment shows the portion of the glider track during Hurricane Irene.

Data from the glider was first used to determine when intense cooling from Hurricane Irene occurred (Figure 7). Wind data (7a) from the closest coastal station indicates Irene passed over the glider at about 10:00 GMT on 28 August. Temperature data from the glider (7b) indicates that most of the cooling occurred before the eye passage.

Data from the glider and CODAR network where them combined to determine why the intense cooling occurred so rapidly. As noted above, the glider hardly changed its position during the storm (Figure 6), despite the over 50 cm/sec currents observed by the CODAR (Figure 4). Since the glider depth averaged current (green line in 7c & 7d) was nearly zero the entire storm, and the surface layer current from CODAR (red line) before the storm is quite large, there must be a compensating bottom current in the lower layer (blue line) that keeps the glider in approximately the same location.

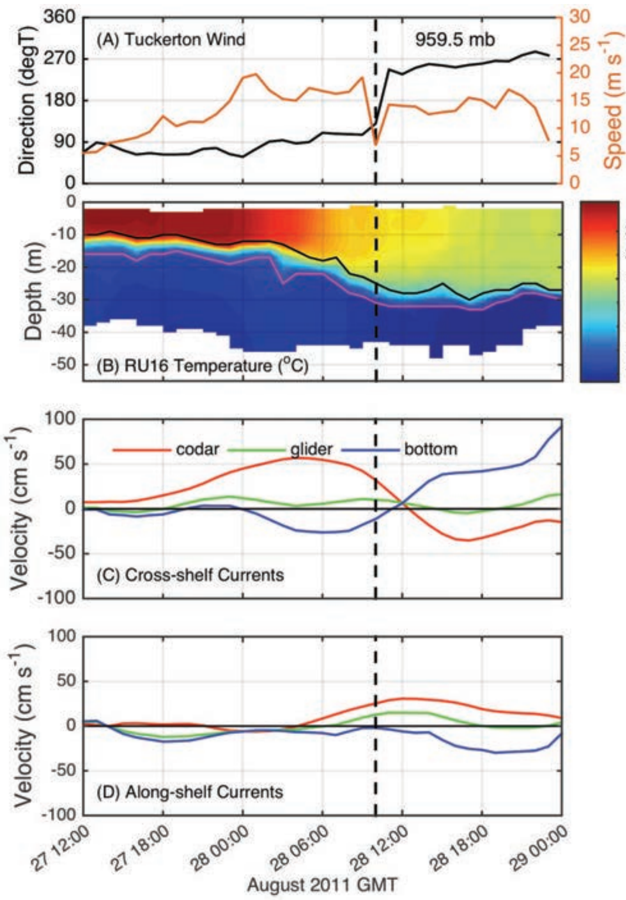

Fig. 7. Data from Hurricane Irene. (a) Wind speed and direction for the Tuckerton weather station near glider RU16. (b) Glider RU16 temperature section. (c) Cross-shore currents (positive onshore). (d) Alongshore currents (positive northwest).

This two layer ahead-of-eye flow is the baroclinic circulation observed by the network. It is the rapid increase in shear across the thermocline that then causes the mixing that results in the cooling of the surface layer ahead of the eye (Glenn et al., 2016).

But is this ahead of eye coolling unique to the glider location? To check, three coastal buoys along Irene's track were examined (Figure 8). Plotted here are the air temperatures (red) and ocean temperatures (blue). The time of eye passage and the value minimum sea level pressure are indicated by the vertical dashed black line. In all three buoys, most of the cooling occurs ahead of eye passage.

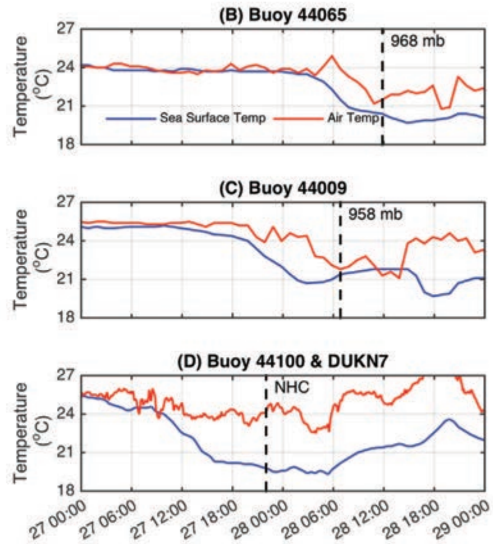

Fig. 8. Air (red) and ocean (blue) temperature records from 3 NDBC buoys deployed along Irene's track. The vertical black dashed line indicates the time of eye passage.

To further quantify the impact of the baroclinic processes on ahead of eye cooling, the water depth, the value of the ahead of eye cooling, the total cooling during the forced stage of the storm, and the percent ahead of eye are tabulated in Table 1. The percentage of cooling occurring ahead of eye ranges from 76% to 94%. In deepwater away from the coast, where coastal baroclinic processes are absent, cooling occurring during the direct storm forced period is typically split 50-50 between ahead of eye and after the eye. The coastal baroclinic processes discovered in Irene bias the cooling to occur before eye passage.

Storm Name	Buoy	Water Depth (m)	Ahead-of-Eye Cooling (°C)	Total Cooling (°C)	% Ahead-of-Eye
Irene (2011)	44065	25	4.7	5.5	85%
Irene (2011)	RU16 Glider	37-46	5.1	6.7	76%
Irene (2011)	44009	31	4.5	5.5	80%
Irene (2011)	44100	26	6.8	7.2	94%

Table 1. Percent ahead of eye cooling in Hurricane Irene observed by 3 surface buoys and 1 underwater glider.

IV. Ahead of Eye Cooling Observed in Other Mid Atlantic Hurricanes.

Following this discovery, the next question to examine is does this same process occur in other hurricanes. Can we observe it in the historical record. First the most recent 30 years of hurricane tracks crossing the Middle Atlantic Bight in summer were examined. A total of 11 hurricanes were found to fit this criteria (Figure 9). water of the South Atlantic Bight and was still an intense Category 1 hurricane (Fig. 3). The scale of the storm vissible in the cloud pattern is the same scale has the Mid Atlantic's HF Radar network. The storm remained intense until the eye left the South Atlantic Bight and entered the Mid Atlantic Bight just north of Cape Hatteras.

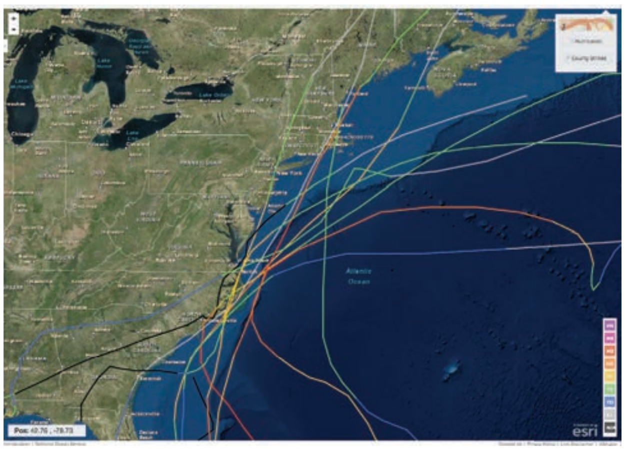

Fig. 9. Historical record of hurricane tracks crossing the Mid Atlantic Bight during the summer stratified season.

The coincident 30 year NDBC buoy record was then used to determine the amount of cooling ahead of eye, the total cooling occurring during the direct forcing phase, and the percentage ahead of eye. The percentage of ahead of eye cooling ranges from 50% to 100%. The average is 75%, indicating that this a common occurrence for hurricanes satisfying this criteria.

Storm Name	Buoy	Water Depth (m)	Ahead-of-Eye Cooling (°C)	Total Cooling (°C)	% Ahead-of-Eye
Arthur (2014)	44014	48	1.4	2.4	58%
Irene (2011)	44100	26	6.8	7.2	94%
Barry (2007)	ALSN6	29	5.1	5.1	100%
Hermine (2004)	44009	31	0.9	1.1	82%
Allison (2001)	CHLV2	14	2.3	2.6	88%
Bonnie (1998)	CHLV2	14	4.2	4.2	100%
Danny (1997)	44009	31	2.1	3.6	58%
Arthur (1996)	44009	31	2.3	3.5	66%
Emily (1993)	44014	48	2.3	2.8	82%
Bob (1991)	44025	41	2.1	4.6	46%
Charley (1986)	44009	31	2.7	5.4	50%
Average		**31**	**2.9**	**3.9**	**75%**
STD		**11**	**1.7**	**1.7**	**20%**

Table 2. Percent ahead of eye cooling in 11 hurricanes that crossed the Mid-Atlantic Bight shelf during summer.

V. Ahead of Eye Cooling Observed in Typhoons.

But does this same process occur in other regions. The Yellow Sea is known th have strong summer stratification like the Mid Atlantic Bight, and is an area significantly impacted by typhoons. The 30 year history of typhoon tracks over the Yellow Sea in summer is shown in Figure 10. A total of 26 typhoons were found. All of these summer Yellow Sea typhoons had a significant ipact on the Korean penisula.

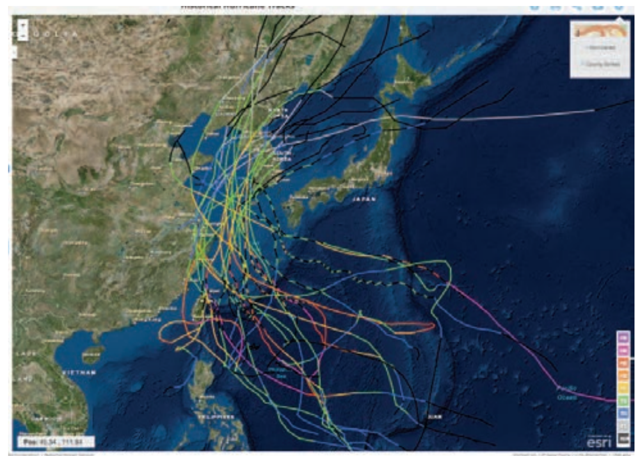

Fig. 10. Historical record of typhoon tracks crossing the Yellow during the summer stratified season.

A Chinese buoy deployed in the Yellow Sea captured data from one of these storms, Super Typhoon Muifa. Wind, pressure and temperature data from this buoy indicate that 85% of the cooling observed in Typhoon Muifa occurred ahead of eye (Table 3).

Storm Name	Buoy	Water Depth (m)	Ahead-of-Eye Cooling (°C)	Total Cooling (°C)	% Ahead-of-Eye
Muifa (2011)	37.0445N 122.6558E	31	4.1	4.8	85%

Table 3. Percent ahead of eye cooling in Typhon Muifa that crossed the Yellow Sea during summer.

VI. Conclusions

The back-to-back landfalls of hurricanes Irene and Sandy along the coast of New Jersey have hightened awareness of hurricanes and their potential impacts in the Mid-Atlantic. Irene's alongshelf track was accurately forecast but the intensity was over-predicted. Ocean observations by U.S. IOOS provide guidance as to why. Operational SST products did not pick up the 8-10C cooling caused by Irene even several days after the weather had cleared. An autonomous underwater glider that flew through the storm indicated that the cooling occurred rapidly as the leading edge of the hurricane approached and well ahead of the eye. Even if the operational

SST products were reconfigured to pick up the cooling after the storm, they could not be applied in time to impact Irene. A more useful SST mapping product that accurately captures the timing and spatial extent of the cooling can only be supplied by an ocean forecast model. The ocean observations indicate what processes the ocean model must capture. Specifically, the initial thermocline must be better represented as the starting point. Second, the model must be 3-D, with a coast and a bottom. An infinitely deep 1-D model, one potential option for coupled atmosphere-ocean modes, will not capture the processes observed here. These include the initial onshore transport in the surface layer towards the coast, and the delayed response of the bottom layer to produce an offshore transport that limits the net shoreward transport. When there are two layers, the water transported onshore has an escape route through the bottom layer that appears to limit the storm surge. It also appears that the bottom layer also should be sufficiently thin for the offshore transport to produce a large shear across the interface. It is when this large shear is present that the mixing and cooling occurs.

The coastal baroclinic process responsible for enhanced ahead of eye cooling described above was not limited to Irene. A historical record of 30 years of buoy data indicates that for the 11 hurricanes crossing the Mid Atlantic shelf during the stratified summer, an average of 75% of the coolling is observed to occur ahead of eye. In the Yellow Sea, similar buoy data indicates 85% of the cooling was ahead of eye in Typhoon Muifa. All of these results indicate there is an ahead of eye enhancement of the cooling in shallow water that is not observed in the deep ocean where the split is nearly 50-50 between before and after the eye.

The U.S. IOOS observations of hurricanes Irene as implemented by MARACOOS for the Mid-Atlantic provided unprecedented real-time views of the evolving coastal ocean as the hurricane made landfall in New Jersey. Combined with the lomg-term historical records, the significance of this new process could be established. These results provide further evidence that one step towards improving hurricane intensity forecasting is to provide atmospheric modelers a better forecast of the rapidly changing coastal ocean beneath hurricanes.

ACKNOWLEDGMENT

Base support was provided by the National Oceanic and Atmospheric Administration (NOAA) led Integrated Ocean Observing System (IOOS) through the Mid-Atlantic Regional Association Coastal Ocean Observing System (MARACOOS, NA11NOS0120038), the Environmental Protection Agency (EP-11-C-000085), the New Jersey Department of Environmental Protection (WM13-019-2013) and Board of Public Utilities (2010RU-COOL) and the NOAA Cooperative Institute for the North Atlantic Region (CINAR, NA13OAR4830233), Disaster Recovery Act. The authors thank Teledyne Webb Research and Rutgers University for student support, and the NOAA National Centers for Environmental Prediction for student engagement.

REFERENCES

[1] S. Glenn, O. Schofield and J. Kohut, "Hurricane Irene 2011: Mid-Atlantic IOOS response to the hurricane", http://maracoos.org/sites/macoora/files/downloads/Hurricane_Irene_blog_2011.pdf, pp. 65, 2011.

[2] W. Gray, 2003. Twentieth century challenges and milestones. In: Hurricanes! Coping with Disaster, R. Simpson, ed., American Geophysical Union, Washington, DC. 10.1029/055SP02.

[3] B. Keim, R. Muller and G. Stone, Spatiotemporal patterns and return periods of tropical storm and hurricane strikes from Texas to Maine, Journal of Climate, 20, 3498-3509, 2007.

[4] H. Roarty, S. Glenn, J. Kohut, D. Gong, E. Handel, E. Rivera, T. Garner, L. Atkinson, W. Brown, C. Jakubiak, M. Muglia, S. Haines, H. Seim, "Operation and Application of a Regional High-Frequency Radar Network in the Mid-Atlantic Bight" Marine Technology Society Journal, 44 (6), 2010.

[5] Pasch, R. and E. Blake, 2012. 2012 Review of the NCEP Production Suite: Report from NHC, National Centers for Environmental Predictions, Maryland, December 4, 2012,

[6] O. Schofield, J. Kohut, S. Glenn, J. Morell, J. Capella, J. Corredor, J. Orcutt, M. Arrott, I. Krueger, M. Meisinger, C. Peach, F. Vernon, A. Chave, Y. Chao, S. Chien, D. Thompson, W. Brown, M. Oliver, W. Boicourt, "A regional Slocum glider network in the Mid-Atlantic coastal waters leverages broad community engagement." Marine Technology Society 44(6): 64-74, 2010.

[7] N. Walker, A. Haag, S. Balasubramanian, R. Leben, I. van Heerden, P. Kemp and H. Mashriqui, 2006. Hurricane prediction: A century of advances, Oceanography, 19(2), 24-36.

[8] Glenn, S. M. et al. Stratified coastal ocean interactions with tropical cyclones. Nat. Commun. 7:10887 doi: 10.1038/ncomms10887 (2016).

Automated Quality Control of High Frequency Radar Data II

Hugh Roarty, Laura Palamara, Josh Kohut, Scott Glenn
Center for Ocean Observing Leadership
Rutgers University
New Brunswick, NJ USA
hroarty@marine.rutgers.edu

***Abstract*—A paper was presented at OCEANS'12 by the authors on a similar topic. The original paper was more of a formulation of ideas for automated quality control of HF radar data with only a listing of potential tests. This paper lays out the framework for the quality assurance methods and quality control tests for the entire data processing chain. The paper also synthesizes a number of papers that have been presented recently on this topic of HF radar data quality control**

Keywords—radar, remote sensing, quality control, MARACOOS

I. Introduction

The Mid Atlantic High Frequency radar (HFR) network consists of three components. The first is a 5 MHz long range network that covers from Cape Hatteras to Cape Cod with a 150 km range offshore. The second are five 25 MHz networks that provide high resolution sampling of the major estuaries in the region : Chesapeake Bay, Delaware Bay, New York Harbor, Western Long Island Sound and Block Island Sound. The third component of the HF radar network is a 13 MHz network that provides mesoscale coverage along the coast of New Jersey. See [1] for a detailed description of the network.

All the radars within the Mid Atlantic are of the SeaSonde variety manufactured by CODAR Ocean Sensors, So the methods developed in this paper are specific to the data processing chain of this particular instrument. Another type of HF radar in use is the WERA manufactured by Helzel Messtechnik GmbH. The reader is referred to [2] for a discussion of the quality control methods utilized by this instrument.

In addition to the 46 radars that make up the Mid Atlantic network, there are approximately 400 High Frequency (HF) radars deployed around the globe making real time measurements of the surface currents in the coastal ocean. The HF radar network within the Mid Atlantic Regional Association Coastal Ocean Observing System (MARACOOS) has been delivering surface current measurements to the United States Coast Guard since May 2009. This model was expanded nationally and the Integrated Ocean Observing System (IOOS) National HF Radar Network became operational with the Coast Guard in March 2011. It is essential for effective search and rescue that the surface current measurements from the HF radar are of the highest quality.

II. Methods

The first step we took was to map the components of the HF radar data processing chain onto the data levels presented in the NASA Earth Science Reference Handbook (Table 1)[3]. There are a total of 5 layers with Level 0 representing the unprocessed instrument data at full resolution and Level 4 signifying derived products. We present quality assurance and quality control techniques for each data level.

Level 0 to 2 takes place out at the individual radar station. For these steps we follow the procedures laid out by CODAR Ocean Sensors [4]. Level 2 represents the radial vector file generation stage. The radial files are transferred back to the data assembly center once an hour via secure shell. A collection of instantaneous and time series tests are applied to the radial files. In order to perform the time series tests, five hourly radial files are loaded and concatenated. The quality control tests are applied to each time series of a particular range and bearing grid cell.

Table 1: Data levels as defined in the NASA Earth Science Reference Handbook and the corresponding data product in the HF radar processing chain.

Data Level	Associated HF Radar Data Product
0	Time series files that represent received signal power
1	Radar spectra file
2	Radial vector file
3	Total vector file
4	Derived products from total vector files e.g. daily averages or drifter trajectories

978-1-5090-1537-5/16/$31.00 ©2016 IEEE

The flags used to identify the quality of the data are taken from the United States Integrated Ocean Observing System (US IOOS) Quality Assurance of Real Time Oceanographic Data (QARTOD) [5, 6]. The flags are then written as new columns to the SeaSonde radial file, the thresholds used in the quality control tests are written into the metadata of the file and the file extension is replaced with a ".qcv".

The tests we are currently using are:

- Global range (required)
- Local range
- Trend test
- Stuck sensor
- Gradient test

The radial measurement is also assigned an overall flag for quality. If the radial measurement passes all the tests then it assigned a 1 indicating that it has passed the required quality control tests. If the radial measurement fails any of the nonrequired tests it is assigned a 3 indicating that it is questionable. If the radial measurement fails any of the required tests then it is assigned a flag of 4. If the quality control tests cannot be performed due to missing data then the data point is assigned a 2 as being not evaluated.

III. RESULTS

The next step was to define what the thresholds should be used for each of the tests. A four month data set of HF radar surface currents and the closest surface bin from an acoustic doppler current profiler (ADCP) [7] were utilized to develop the thresholds. Figure 1 and Figure 2 show the statistics of the temporal derivative of the surface current measurements. Based on these figures we chose a threshold of 0.005 cm/s^2 or a change of 18 cm/s over an hour as being excessively large and should be flagged.

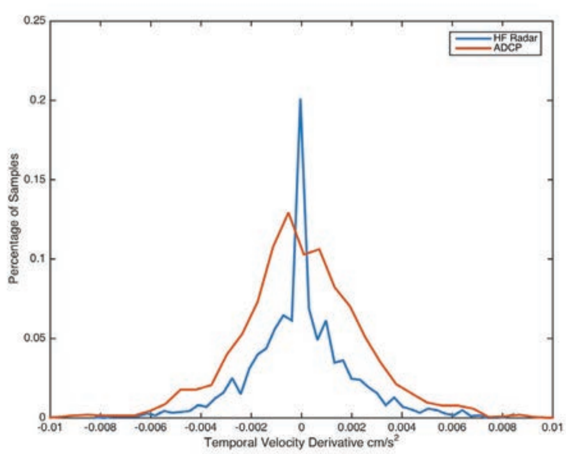

Figure 1: Percentage histogram of radial velocity temporal derivative from the HF radar (blue) and ADCP (red).

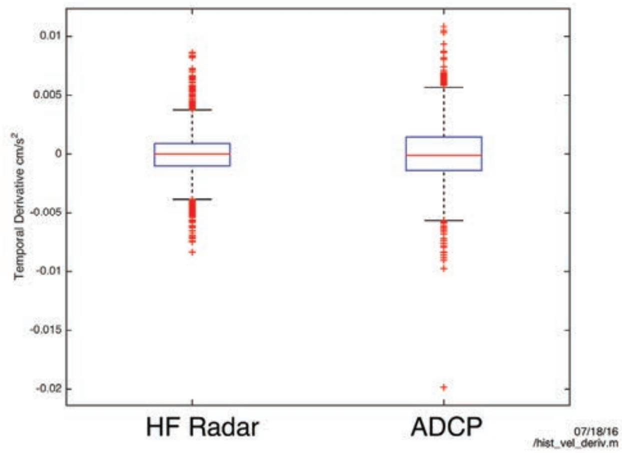

Figure 2: Box plot of the radial velocity temporal derivative from the HF radar (left) and ADCP (right). The central mark is the median, the edges of the box are the 25th and 75th percentiles, the whiskers extend to the most extreme data points the algorithm considers to be not outliers, and the outliers are plotted individually.

The full list of quality control thresholds are listed in Table 2. The low value of 40 cm/s for the local range test was chosen to make sure the function was properly flagging data.

Table 2: Quality control thresholds applied to the HF radar data.

Test Name	*Threshold*
Global range	300 cm/s
Local range	40 cm/s
Stuck Sensor	0.01 cm/s over 3 hours
Gradient Test	0.005 cm/s^2

The thresholds shown in Table 2 were used to flag the HF radar measurements. Results of the quality control flagging are shown in Figure 3. This shows a scatter plot of ADCP currents along the x-axis with HF radar currents along the y-axis. The data points that have been flagged by the range, stuck sensor and gradient test are shown as green. This scatter plot corresponds to Test 8 in Table 3.

Eight combinations of quality control tests were utilized to see if they made any improvement in the comparison between the HF radar and ADCP measurements. Test 1 indicated no data would be flagged and removed while Test 8 removed all data not passing the three tests. Both the correlation and rms error remain unchanged as data was removed. By enacting all three quality control flags up to 9% of the record would be removed, something to consider by the user of the data and flags.

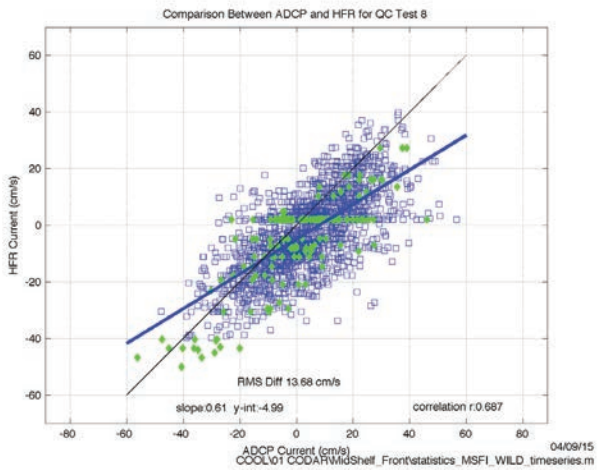

Figure 3: Scatter plot of radial current from the ADCP along the x-axis and radial velocity from the HF radar along the y-axis. The one to one line is shown as the thin black line; the linear least squares fit is the thick blue line (y=0.61x-4.99)

Table 3: Correlation (r), root mean square error (rms error cm/s), number of samples (N) and percentage decrease of the original data record based upon 8 combinations of quality control tests.

Test	Category	r	rms error	N	% Decrease	# Decrease
1	All Data	0.7	13.57	1846	0%	0
2	Speed	0.69	13.58	1832	1%	14
3	Stuck	0.7	13.68	1706	8%	140
4	Gradient	0.7	13.56	1843	0%	3
5	Speed & Stuck	0.69	13.69	1692	8%	154
6	Speed & Gradient	0.69	13.57	1829	1%	17
7	Stuck & Gradient	0.7	13.67	1703	8%	143
8	Speed & Stuck & Gradient	0.69	13.68	1689	9%	157

IV. CONCLUSIONS

We have enacted quality assurance and quality control tests for the real time distribtion of HF radar surface current measurements. These procedures are applied at each level of the data processing chain. In a comparison with an insitu current meter, utilizing the flags did not dicernbaly improve the quality of the data but this is only one sample so we will look to apply this technique to other data sets. This procedure also acts as a feedback mechanism to the operators to evaluate their performance in operating and maintaining the radars. The techniques discussed here can serve as data quality checks for the vast number of systems operating today. They will ensure that the data being produced is of the highest quality, which will in turn ensure that the products being generated with this data are sound and reliable.

ACKNOWLEDGMENT

This work was funded by NOAA Award Number NA11NOS0120038 “Towards a Comprehensive Mid-Atlantic Regional Association Coastal Ocean Observing System (MARACOOS)”. Sponsor: National Ocean Service (NOS), National Oceanic and Atmospheric Administration (NOAA) NOAA-NOS-IOOS-2011-2002515 / CFDA: 11.012, Integrated Ocean Observing System Topic Area 1: Continued Development of Regional Coastal Ocean Observing Systems.

REFERENCES

[1] H. J. Roarty, S. M. Glenn, J. T. Kohut, D. Gong, E. Handel, E. Rivera Lemus, T. Garner, L. Atkinson, C. Jakubiak, W. Brown, M. Muglia, S. Haines, and H. Seim, "Operation and Application of a Regional High Frequency Radar Network in the Mid Atlantic Bight," *Marine Technology Society Journal,* vol. 44, pp. 133-145, 2010.

[2] R. Gomez, T. Helzel, L. Petersen, M. Kniephoff, C. R. Merz, Y. Liu, and R. H. Weisberg, "Real-time quality control of current velocity data on individual grid cells in WERA HF radar," in *OCEANS 2014 - TAIPEI*, 2014, pp. 1-7.

[3] C. L. Parkinson, A. Ward, and M. D. King, "A Guide to NASA's Earth Science Program and Earth Observing Satellite Missions," *Earth Science Reference Handbook,* p. 291, 2006.

[4] D. Barrick, "QA/QC & Related Practices at CODAR," *CODAR Ocean Sensors,* p. 14, 2012.

[5] U. S. I. O. O. System, "Manual for the Use of Real-Time Oceanographic Data Quality Control Flags," *Quality Assurance of Real Time Oceanographic Data,* p. 19, 2013.

[6] U. S. I. O. O. System, "Manual for Real-Time Quality Control of High Frequency Radar Surface Currents Data: A Guide to Quality Control and Quality Assurance of High Frequency Radar Surface Currents Data Observations," *Quality Assurance of Real Time Oceanographic Data,* p. 54, 2016.

[7] J. Kohut, H. Roarty, E. Randall-Goodwin, S. Glenn, and C. Lichtenwalner, "Evaluation of two algorithms for a network of coastal HF radars in the Mid-Atlantic Bight," *Ocean Dynamics,* vol. 62, pp. 953-968, 2012.

Evaluation of Environmental Data for Search and Rescue

Hugh Roarty, Scott Glenn
Center for Ocean Observing Leadership
Rutgers University
New Brunswick, NJ USA
hroarty@marine.rutgers.edu

Arthur Allen
Office of Search and Rescue
United States Coast Guard
New London, CT USA
Arthur.A.Allen@uscg.mil

***Abstract*— Ocean Environmental data is a key component utilized by the United States Coast Guard (USCG) when developing and executing a search and rescue mission. The Search and Rescue Optimal Planning System (SAROPS) became operational with the USCG in 2007 and is the main tool for developing search and rescue mission plans. This tool utilizes environmental data (wind, ocean currents, etc.) to estimate the drift of an object in the ocean and also calculate a probability of detection for the object based upon the various search sensors. The environmental data used by the Coast Guard is a combination of model output, in situ and remote sensing measurements. Recent work by the Coast Guard Office of Search and Rescue has shown that the various environmental data sources available in SAROPS have shown skill but none on a consistent basis. In the Mid Atlantic Bight we compared the predicted drift of several surface drifters that were advected with High Frequency radar measurements and regional and global ocean model surface currents. The results shown here indicate that an ensemble of surface current estimates is useful when trying to predict the path of an object drifting on the surface of the ocean.**

Keywords—radar, remote sensing, algorithm, wave, measurement, MARACOOS

I. Introduction

The Mid Atlantic High Frequency radar (HFR) network consists of three components. The first is a 5 MHz long range network that covers from Cape Hatteras to Cape Cod with a 150 km range offshore. The second are five 25 MHz networks that provide high resolution sampling of the major estuaries in the region : Chesapeake Bay, Delaware Bay, New York Harbor, Western Long Island Sound and Block Island Sound. The third component of the HF radar network is a 13 MHz network that provides mesoscale coverage along the coast of New Jersey. See [1] for a detailed description of the network.

The main purpose for the Mid Atlantic radar network is measurement of ocean surface currents. These measurements have been used to characterize the climatology of the region [2, 3] and study flow events with shorter time scales[4, 5]. The measurements from the 5 MHz network have been utilized by the US Coast Guard since 2009 for operational search and rescue. The measurements are sent to the Coast Guard Environmental Data Server (EDS). Once the data resides on the EDS, it can be retrieved by any of the thirteen Rescue Coordination Centers via the Search and Rescue Optimal Planning System (SAROPS)[6].

II. Methods

A. Coast Guard Database

The Coast Guard maintains an up to date skill evaluation of all the environmental data available within SAROPS. The separation distance between the observed and modeled trajectories of a surface drifter are used to generate the skill metric.

B. High Frequency Radar

The measurements from the 5 MHz radar network were utilized to generate the modelled drifter trajectories. Each radar station in the Mid Atlantic is a SeaSonde HF radar manufactured by CODAR Ocean Sensors. The radar network was damaged by Hurricane Sandy [7] in 2012 but has been restored to full operations.

C. Drifter Skill Score

In previous studies the separation distance between actual and virtual drifter trajectories has been used to evaluate the skill of HF radar measurements [8, 9]. However, only analyzing the distance between the drifters at their respective endpoints ignores the paths that the drifters took. A new skill score (*ss*) has been proposed to evaluate trajectory model performance [10].

A trajectory index is defined as

$$s \quad \sum_{i=1}^{N} di / \sum_{i=1}^{N} loi \qquad (1)$$

where *di* is the separation distance between the modeled and observed endpoints at time step *i*, *loi* is the length of the observed trajectory and *N* is the total number of time steps. If the modeled trajectory were in perfect agreement with the observed drifter then s would equal zero. But conventional skill scores indicate higher values mean better model

978-1-4673-9724-7/16/$31.00 ©2016 IEEE

performance, so a skill score (*ss*) for trajectory models based on *s* is given here

$$ss = \begin{cases} 1 - s, & (s \le 1) \\ 0, & (s > 1) \end{cases} \qquad (2)$$

It was this skill score that was used in the analysis.

III. Results

The Coast Guard database was accessed and drifter information was retrieved for 26 drifters in the Mid Atlantic region between July 2014 and June 2015. The drifters were then sorted to see which ones passed through the coverage area of the HF radar network. This left 5 drifters for comparison with HFR and ocean models. There are approximately 45 different surface current products available within the Coast Guard environmental data server. The data products shown in Table 1 exhibited the average highest skill score. They are the MARACOOS HF radar product that uses optimal interpolation [8], the National HF radar product that uses unweighted least squares [11], New York Harbor Observing and Prediction System (NYHOPS) operated the Stevens Institute of Technology, HYCOM Global operated by the National Centers for Environmental Prediction (NCEP) and the Navy and the Experimental System for Predicting Shelf and Slope Optics (ESPreSSO) operated by the Rutgers Ocean Modelling Group. Each model showed varying levels of skill in predicting the trajectory of a surface drifter. It was disappointing to see that the measured surface currents did not show an appreciable difference over the ensemble of models.

Table 1: **Drifter skill score after Liu et al. (2011) for the various data sources available to SAROPS. The green box indicates which data source had the highest skill for the particular drifter case.**

Drifter	MARACOOS HFR	National HFR	NYHOPS	HYCOM Global	HYCOM Global Navy	ESPRESSO
38689	0.29	-	0.37	0.29	0.29	0.34
43356	0.18	0.08	-	0.15	0.48	-
43361	0.31	0.21	0.25	0.21	0.18	0.09
43466	0.12	0.34	0.37	0.16	0.22	0.23
43484	0.10	0.23	0.29	0.14	0.31	0.29

The authors obtained a copy of the skill score code and repeated the analysis. An example of the reanalysis is shown in Figure 1 and Figure 2. For this particular drifter the authors calculated an average skill score of 0.61, double what was originally found in the Coast Guard database.

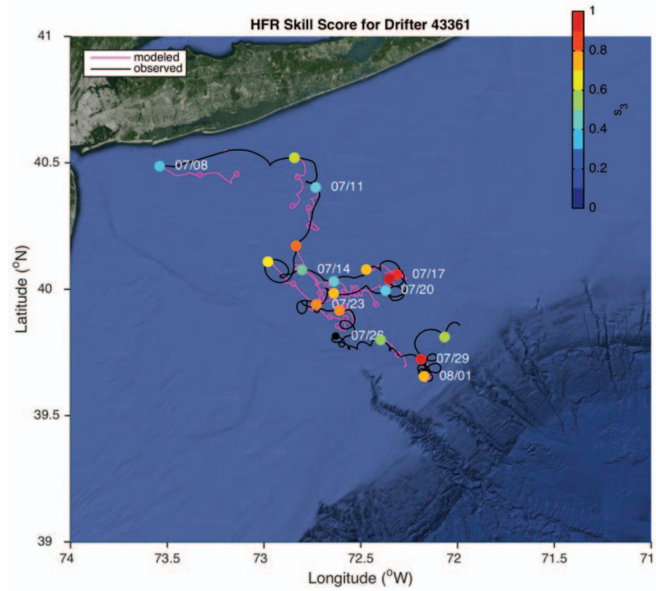

Figure 1: Map of the Mid Atlantic Bight showing the observed trajectory of drifter 43361 (black) along with the two day simulation using HF radar (pink). The skill score for the HF radar data source is shown as the colored dot referenced to the Colorbar in the upper right.

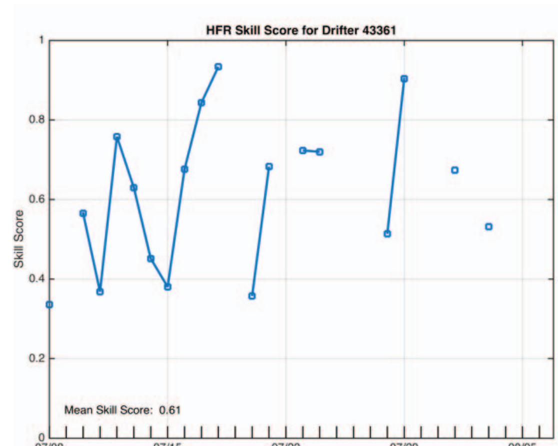

Figure 2: HF radar skill score as a function of time for drifter 43361 deployment July 8 to August 7, 2014.

Table 2 shows the average skill score as calculated by the authors for the five drifters used in the reanalysis. For drifter 43356, the coverage of the HF radar in the vicinity of the drifter was lacking due to the downtime of the radar station in Nauset, MA so no skill score was calculated. In all other cases the skill score calculated here was 2-4 times greater than what was calculated in the Coast Guard database. This will be repeated for the ensemble of ocean models and presented at the conference.

Table 2: Average drifter skill score for the five drifter cases analyzed by the authors.

Drifter	MARACOOS HFR
38689	0.49
43356	-
43361	0.61
43466	0.43
43484	0.40

IV. CONCLUSIONS

The effectiveness of HF radar in predicting the trajectory of virtual surface drifters was evaluated against the trajectory of in site surface drifters. Upon reanalysis HF radar proved to be rather good in predicting the trajectory of ocean surface drifters.

ACKNOWLEDGMENT

This work was funded by NOAA Award Number NA11NOS0120038 "Towards a Comprehensive Mid-Atlantic Regional Association Coastal Ocean Observing System (MARACOOS)". Sponsor: National Ocean Service (NOS), National Oceanic and Atmospheric Administration (NOAA) NOAA-NOS-IOOS-2011-2002515 / CFDA: 11.012, Integrated Ocean Observing System Topic Area 1: Continued Development of Regional Coastal Ocean Observing Systems. Thanks to Yonggang Liu and Robert Weisberg for providing the MATLAB skill score code.

REFERENCES

[1] H. J. Roarty, S. M. Glenn, J. T. Kohut, D. Gong, E. Handel, E. Rivera Lemus, T. Garner, L. Atkinson, C. Jakubiak, W. Brown, M. Muglia, S. Haines, and H. Seim, "Operation and Application of a Regional High Frequency Radar Network in the Mid Atlantic Bight," *Marine Technology Society Journal,* vol. 44, pp. 133-145, 2010.

[2] D. Gong, J. T. Kohut, and S. M. Glenn, "Seasonal climatology of wind-driven circulation on the New Jersey Shelf," *J. Geophys. Res.,* vol. 115, p. 25, 2010.

[3] B. Dzwonkowski, J. T. Kohut, and X.-H. Yan, "Seasonal differences in wind-driven across-shelf forcing and response relationships in the shelf surface layer of the central Mid-Atlantic Bight," *J. Geophys. Res.,* vol. 114, p. C08018, 2009.

[4] B. Dzwonkowski, B. L. Lipphardt Jr, J. T. Kohut, X.-H. Yan, and R. W. Garvine, "Synoptic measurements of episodic offshore flow events in the central mid-Atlantic Bight," *Continental Shelf Research,* vol. 30, pp. 1373-1386, 2010.

[5] E. Hunter, R. Chant, L. Bowers, S. Glenn, and J. Kohut, "Spatial and temporal variability of diurnal wind forcing in the coastal ocean," *Geophys. Res. Lett.,* vol. 34, p. L03607, 2007.

[6] T. M. Kratzke, L. D. Stone, and J. R. Frost, "Search and Rescue Optimal Planning System," in *Information Fusion (FUSION), 2010 13th Conference on*, 2010, pp. 1-8.

[7] D. Malakoff, "Scientists Assess Damage From Sandy's Deadly Punch," *Science,* vol. 338, pp. 728-729, 2012.

[8] J. Kohut, H. Roarty, E. Randall-Goodwin, S. Glenn, and C. Lichtenwalner, "Evaluation of two algorithms for a network of coastal HF radars in the Mid-Atlantic Bight," *Ocean Dynamics,* vol. 62, pp. 953-968, 2012.

[9] D. S. Ullman, J. O'Donnell, J. Kohut, T. Fake, and A. Allen, "Trajectory prediction using HF radar surface currents: Monte Carlo simulations of prediction uncertainties," *J. Geophys. Res.,* vol. 111, p. C12005, 2006.

[10] Y. Liu and R. H. Weisberg, "Evaluation of trajectory modeling in different dynamic regions using normalized cumulative Lagrangian separation," *Journal of Geophysical Research: Oceans,* vol. 116, pp. n/a-n/a, 2011.

[11] J. Harlan, E. Terrill, and B. Burnett, "National high frequency radar network: Update," in *OCEANS 2009, MTS/IEEE Biloxi - Marine Technology for Our Future: Global and Local Challenges*, 2009, pp. 1-7.

Improving CODAR SeaSonde Wave Measurements

Jaden Dicopoulos
Department of Marine and Coastal Sciences, Rutgers University
New Brunswick, NJ, United States of America
jad438@scarletmail.rutgers.edu

Dr. Hugh Roarty
Department of Marine and Coastal Sciences, Rutgers University
New Brunswick, NJ, United States of America
hroarty@marine.rutgers.edu

Maeve Daugharty
CODAR Ocean Sensors
Mountain View, CA, United States of America
maeve@codar.com

Dr. Scott Glenn
Department of Marine and Coastal Sciences, Rutgers University
New Brunswick NJ, United States of America
glenn@marine.rutgers.ed

***Abstract*—High Frequency (HF) Radar functions not only as a way to measure currents, but significant wave height, wave period and wave direction as well. Being a secondary product from CODAR Ocean Sensors' SeaSonde, wave current and direction being the primary, there is much room for wave height measurements improvement. The opportunity to validate existing and future wave models is also a factor because much of an oceanographer's decision making comes from interpreting these models. Spatial validation of the wave model from additional wave measurement tools will help strengthen new and existing tools. CODAR has also changed and improved how their software calculates wave measurements and those improvements significantly and helped wave period. For the research into what causes certain gaps or anomalies in the data, several wave-inducing factors were examined. These examined factors include wind direction and speed. Buoy wave measurements were also analyzed on whether or not two peak readings in spectral density graphs from Buoy 44065 had an effect on wave measurements. The most promising of the research lies on the noise environment and noise floor of HF radar sites. We have validated CODAR's wave height measurement techniques by comparing them to wave factors and we have narrowed down the possible causes of wave height discrepancies between buoy and CODAR data.**

Keywords—High Frequency Radar, CODAR, wave height, waves, wave model

I. INTRODUCTION

There is an opportunity to use already established HF Radar networks for their secondary product, wave measurements such as wave height. The coverage of SeaSonde HF Radar includes several coasts around the world, but the focus for this study will be on the New Jersey coastline, where there is consistent HF Radar coverage. HF Radars sites in relation to buoy locations are displayed in Figure 1. This map does not show all HF Radar locations but the ones that were used for our analysis, BRMR, BRNT, and SPRK as they had the highest percent data returns. Site uptime also played a factor as the sites that were picked needed to be comparable to buoy data.

Figure 1: A map of the 13MHz HF Radar sites SPRK, BRNT and BRMR used in this analysis and the location of relevant buoys 44025 and 44091.

HF Radar is not only an established network but also is consistently updated with new hardware and software. During this research the SeaSonde software that calculates wave data was drastically improved, moving from Release 7 to Release 8. In order for these improvements to be made accurately and regularly, the research behind them must coincide with what we know about wave development. Figure 2 shows how drastic of an improvement can be made to data when the proper measurements and advancements are applied, Wave period can be a vital asset in solving further wave related problems. If we can have these same improvements that would help push forward the other wave measurements the accuracy of the data would beneficial. This paper outlines the basic understanding of how waves form and checks that the radar is collecting the data with that in mind.

978-1-5386-1654-3/18/$31.00 ©2018 IEEE

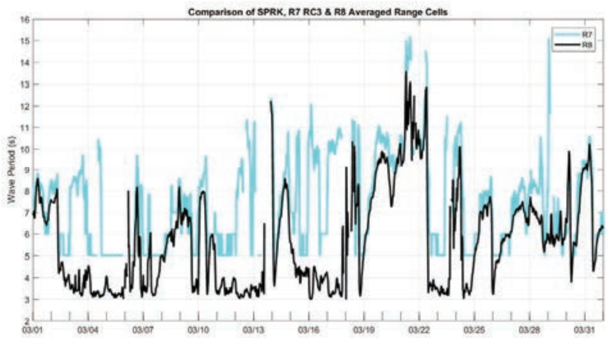

Figure 2: Wave period comparison between Release 7 (aqua) and Release 8 (black) products from March 1-31, 2017.

In an era of increasing storm intensity an opportunity to make accurate wave measurements is crucial. Being able to research wave height and wave height anomalies help build evidence for the changing ocean. Buoys can be far spaced and accurate in one location, HF Radar has a larger coverage radius and reach out radially to 30 km on 13MHz sites and 60 km on 5MHz. The reach, coverage, and accuracy of HF radar when properly tuned and applied can far surpass other data acquisition units for wave measurements.

II. METHODS

The research and analysis of the wave measurements was conducted using Matlab and SeaSonde software to create several figures and time series analyses across several sites. Then, the comparisons to the different forms of wave data to different wave inducing factors were made to solidify knowns about wave creation. All data was pulled directly from the HF Radar sites and buoys and then compiled and binned internally. The first step was finding the most accurate and consistent HF Radar site for wave data. Figure 3 displays percent data return of the three main 13MHz HF Radar sites with respect to each individual range cell.

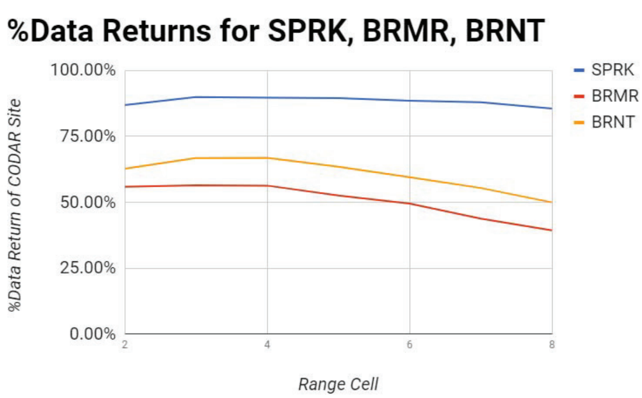

Figure 3: Graph relating percent data return of the HF Radar sites BRNT, BRMR, and SPRK in relation to their range cells. Data covers two months from January 1 to March 1, 2017.

After comparing a selection of New Jersey HF Radar sites, it was found that SPRK, the call sign for Seaside Park's HF Radar site, had the highest percent data return and wave height correlation when compared to the closest buoy. SPRK also has the longest and consistent uptime compared to any other New Jersey sites. When it comes to the buoy comparisons, there are three buoys in the vicinity, but buoy 44091 is the closest to the last range cell of SPRK and the most reliable for comparisons. 44091 only records wave measurements so when wind data is needed buoy 44065 is used for its wind measurements. Buoys are the best fit for comparisons due to their consistent and accurate data. The only discrepancy is their single point locations, far from other forms of measurements. Another statistic we ran was the correlation between wave height measurements on both HF Radar and buoy 44091, Figure 4.

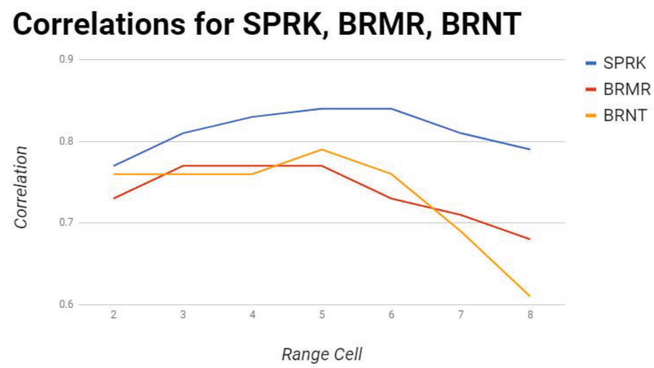

Figure 4: Graph representing correlation between SPRK, BRMR, BRNT wave heights when compared to buoy 44091. Data covers two months from January 1 to March 1, 2017.

Seaside Park remains dominant in these statistics and returns the best correlation across all range cells. For both Figure 3 and 4 we see dips at range cells 2 and 8. These are the closest and furthest range cells tested.

Wind direction and speed were used to find inconsistencies in data and to confirm that as waves build from consistent wind across a fetch and their wave heights increased across the range cells. This increase in wave height across range cells can be seen in Figure 5.

978-1-5386-1654-3/18/$31.00 ©2018 IEEE

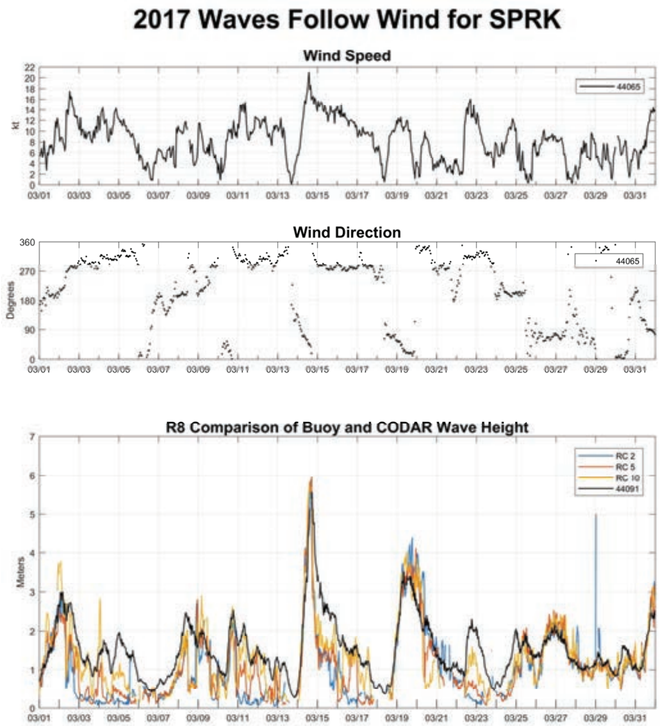

Figure 5: A figure comparing wind speed, wind direction, and wave height from three selected CODAR range cells. Buoys 44065 and 44091 used for wind and wave data respectively from March 1-31, 2017.

Where we see wind the early days of January blowing away from the shore, wave height increases across the range cells. And any time where wind is in the 270 to 360-degree direction, waves build in height from range cell 2 to 10. It can also be seen on the strong wind events going the opposite direction on the 19th where waves got smaller the farther from the coast. These northeast winds are the most devastating to the east coast. Buoy 44091 also sits on the outer range of range cell 10, so it also shows the consistency the waves increase based on wind events.

Following consistencies in wind, wave relationships, wind direction readings were binned on whether they were offshore or onshore. This was to see if the wave height measurements were consistent with longshore waves or if readings were inconsistent based on what direction the wind blew. It was consistently seen that when wind blew across the fetch that the range cells covered that waves would build in size corresponding to the direction of the wind. Also, from separating wave height based on the direction of the wind it became evident that a pattern was found on approaching and receding waves seen in Figure 6.

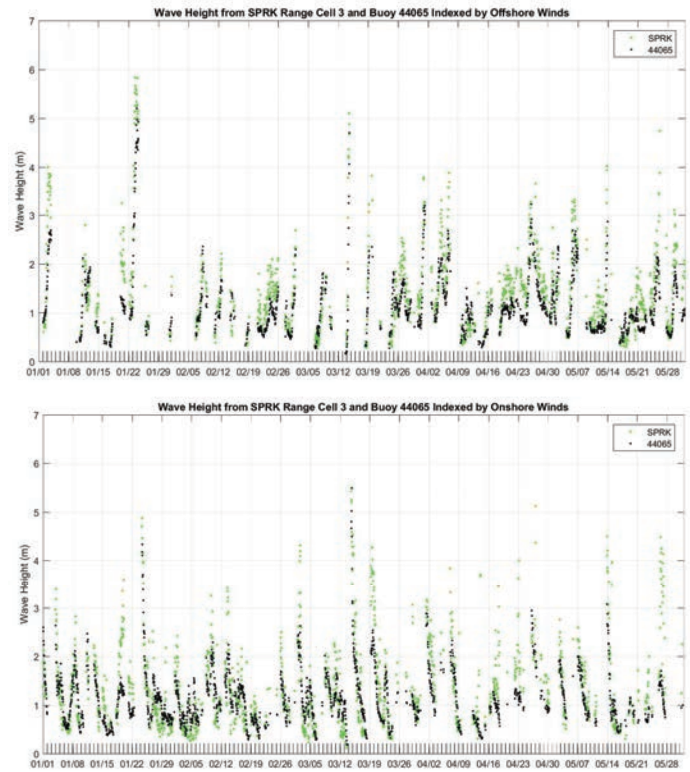

Figure 6: Wave height from CODAR site SPRK binned by times of offshore winds then onshore winds respectively. Buoy 44065 used for the wind indexing and wave height comparison from January 1 to June 1, 2017.

It was from here that the waves follow wind setting was toggled on to test a boost in percent data return and correlation between the wave height of the buoy and the radar. What was found was that the waves follow wind setting lowered percent data return overall but increased it drastically in certain wind circumstances. The development of a dynamic waves follow wind measure was put into place so that it would turn on to obtain the higher correlated data then turned off when the wind event passed and the waves follow wind setting would not be detrimental.

III. Conclusion

With wave height measurements substantiated by the basics of wave height generation we can create a basis of understanding of how accurately HF radar measures waves. With all wave measures in check we can move on to study other factors that cause the differences we see in HF Radar and make improvements and adjustments as they become known. Dynamic waves follow wind is an example of an area of improvement discovered from the basis of wave development and the wind-wave relationship. If these improvements continue to be made we can take advantage of the opportunity of the already established radar networks and improve our wave models.

978-1-5386-1654-3/18/$31.00 ©2018 IEEE

ACKNOWLEDGMENT

Thank you to everyone at the Department of Marine Sciences at Rutgers for accepting me into their community and research and special thanks to the CODAR Ocean Sensors team for making this paper possible.

978-1-5386-1654-3/18/$31.00 ©2018 IEEE

Evaluation of Environmental Data for Search and Rescue II

Hugh Roarty
Center for Ocean Observing Leadership
Rutgers University)
New Brunswick, NJ 08901 USA
hroarty@marine.rutgers.edu

Arthur Allen
Office of Search and Rescue
United States Coast Guard
New London, CT 06320 USA
Arthur.A.Allen@uscg.mil

Scott Glenn
Center for Ocean Observing Leadership
Rutgers University)
New Brunswick, NJ 08901 USA
glenn@marine.rutgers.edu

Josh Kohut
Center for Ocean Observing Leadership
Rutgers University)
New Brunswick, NJ 08901 USA
kohut@marine.rutgers.edu

Laura Nazzaro
Center for Ocean Observing Leadership
Rutgers University)
New Brunswick, NJ 08901 USA
nazzaro@marine.rutgers.edu

Erick Fredj
Department of Computer Sciences
Jerusalem College of Technology
Jerusalem, Israel
erick.fredj@gmail.com

***Abstract*—The Mid Atlantic Ocean Observing System (MARACOOS) conducted a validation experiment of its High Frequency radar network from May 10 to July 12, 2016. The goal of the experiment was to evaluate its two surface current products, test quality control software and algorithms and evaluate new bistatic data streams. The experiment was conducted in collaboration with the United States Coast Guard Office of Search and Rescue and RPS an environmental consulting company. The Coast Guard provided 9 drifters that were deployed in the coverage area of the radar network. Six were deployed south of Martha's Vineyard and 3 were deployed off New Jersey, which focused on the validation of the 13 MHz network. The position data from the drifters was used to generate surface drift velocity estimates. These velocity estimates were compared against the radial velocity measurements of the radars. The actual path of the drifters over 48 hours was compared against virtual paths generated using the radar currents and other surface current estimates. The Lagrangian skill score was computed for several different surface current products. The regional surface current product from MARACOOS proved to be the best at predicting the path of the drifters.**

Keywords—remote sensing, radar, MARACOOS, geoscience, oceans, currents

I. Introduction

The United States Coast Guard utilizes the Search and Rescue Optimal Planning System (SAROPS) [1] to conduct all of their maritime searches. SAROPS requires an estimate of surface winds and surface currents in order to generate a drift trajectory for search planners. . Table 1 lists the top ten surface current data sources that were requested by the Coast Guard between November 1, 2016 and May 1, 2017. RPS, an international consulting company, provided the data in Table 1. RPS manages the Environmental Data Server (EDS) for the US Coast Guard. SAROPS requests environmental data (winds and currents) from the EDS. Models are preferred over measurements because of the forecast capability of the models. Regional models are preferred over global models for their increased spatial and temporal resolution. But as Table 1 shows the most requested model by the Coast Guard for surface current information is Global HYCOM. One goal of this paper is determine which data source is best at predicting drift in the coastal ocean.

This experiment used two components of the Mid Atlantic High Frequency Radar (HFR) Network, the long-range 5 MHz network and the mid range 13 MHz network. The 5 MHz network makes hourly measurements of surface currents within 150 km of the coast. The 5 MHz network utilizes a 3-hour averaging interval in the calculation of the hourly currents. The 13 MHz network also makes hourly measurements of the surface currents off New Jersey but only utilizes a 1-hour averaging interval in the calculation. The 13 MHz network has a range of 60 km from the coast. See [2] for a detailed description of the network.

Table 1: Top 10 surface current data products as ordered by the US Coast Guard for Search and Rescue from November 1, 2016 to May 1, 2017.

Rank	Product	Orders	Percent	Orders/ Week
1	Global HYCOM (Navy)	11,836	38%	455
2	NAVGEM (Navy)	4,244	14%	163
3	North Atantic HYCOM (NCEP)	3,826	12%	147
4	Espresso ROMS	3,425	11%	132
5	Global HYCOM (NCEP)	3,213	10%	124
6	HF Radar Data & Predictions	1,541	5%	59
7	Chesapeake Bay (NOS) Currents	1,379	4%	53
8	Mariano - Ship Drift	976	3%	38
9	NY HOPS (Stevens Institute)	514	2%	20
10	FVCOM Mass Bay (UMass)	427	1%	16
	Total	**31,381**	**100%**	**1,207**

The goal of the experiment was to compare the trajectory of in situ surface drifters to the trajectory of virtual drifters that were advected with a variety of surface current products. The

978-1-5386-1654-3/18/$31.00 ©2018 IEEE

previous paper on this topic [3] utilized drifters of opportunity that were in the coverage area of the HFR Network. Thanks to the US Coast Guard Office of Search and Rescue providing the drifters we were able to choose the deployment locations of the drifters with this experiment and paper.

II. Methods

The United States Coast Guard provided the surface drifters [4] utilized in the experiment. Three clusters of drifters were released, one along the 30 m isobath in the northern area of the 5 MHz network, one along the 70 m isobath in the northern area of the 5 MHz network and one along the 30 m isobath in the central region of the 5 and 13 MHz network. The average surface drift is towards the southwest, so the hope was that the drifters deployed in the northern region of the network would drift through the majority of the network coverage. The drifters remained in the northern and central region for the experiment so the full network wasn't tested but the drifters endured for an average of 36 days so it provided a robust data set. The details of the drifters are given in Table 2 and the trajectories of the drifters are shown in Figure 1.

The drifters reported position data every 30 minutes. The drifter data was interpolated to once an hour to match the temporal sampling of the radar data and models. The location of the drifter once a day at 00:00 GMT was used as a starting point for the release of a virtual drifter that was advected using several surface current data sources. The virtual drifter was moved for 48 hours and then stopped. This process was repeated every day for as long as position information from the in situ drifter was available.

Here is a description of the surface current data sources. The radial surface currents from the 5 MHz network were combined on a 6 km grid [5] using the optimal interpolation algorithm [6, 7] to produce hourly total surface currents. The radial surface currents from the 13 MHz network were combined on a 2 km grid using the optimal interpolation algorithm with different configuration parameters to produce hourly total surface currents. Another product that was tested was a quality controlled 2 km surface current product. The radial data from the 13 MHz network was passed through a series of quality control algorithms, combined on the 2 km grid and then the total surface currents were gap filled and smoothed using penalized least squares regression [8]. Lastly, the surface currents from the Global Real Time Ocean Forecast System (Global RTOFS) Region 1 were used to advect a virtual drifter. Region 1 covers from the equator to 70 degrees north latitude and from 50 to 100 degrees west longitude. The spatial resolution of this data set is 1/12 degree and temporal resolution was 3 hours.

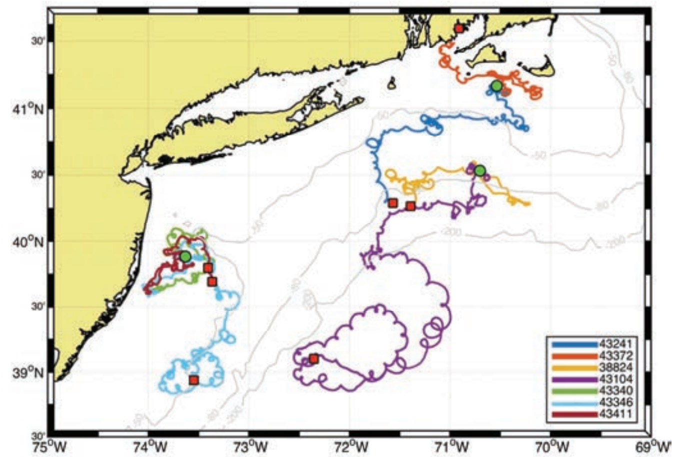

Figure 1: Trajectory of 7 drifters from May 10, 2016 to July 6, 2016. The release point of the drifters is marked as the green circle; the last known position for the drifters is marked as the red square.

Table 2: List of drifters deployed during the experiment with release date, end date and location.

#	Buoy Number	Release Date	End Date	Group	Description
1	43241	5/10/16	6/9/16	1	Northern 30 m isobath
2	43372	5/10/16	5/30/16	1	Northern 30 m isobath
3	38824	5/10/16	6/9/16	2	Northern 70 m isobath
4	43104	5/10/16	7/5/16	2	Northern 70 m isobath
5	43340	5/10/16	6/9/16	3	Central 30 m isobath
6	43346	5/10/16	7/6/16	3	Central 30 m isobath
7	43411	5/10/16	6/9/16	3	Central 30 m isobath

III. Results

The Lagrangian skill score [9] was computed for each of the four surface current data sources once a day over the course of two days. An example of this skill score calculation for drifter 43346 that was tracked using data from the 13 MHz network shown in Figure 2. The skill score of this data source varied from 0.5 to as high as 0.9. A skill score of 1 implies a perfect fit between model and observation. If the separation distance between model and observation becomes larger than the length of the observed trajectory then the skill becomes negative and is capped at 0. The skill score was not calculated on May 25 because a gap developed in the coverage of the 13 MHz radar network and we were unable to calculate a trajectory for this time period. This gap was not counted against the data source in calculating the average skill score. This will be addressed in a future publication.

The average skill scores for the different drifters and different data sources are given in Table 3. Each of the HFR data sources displayed a high degree of skill and outperformed the global model by a significant margin. The authors expected 13 MHz network to outperform the 5 MHz network with respect to skill score because of the increased spatial resolution and shorter temporal averaging. But 5 MHz network had equal skill compared to the 13 MHz network in predicting the path of a surface drifter over 48 hours.

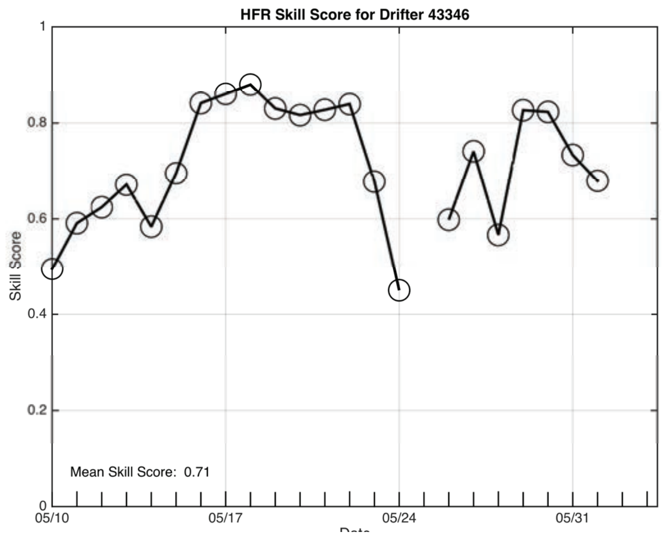

Figure 2: 13 MHz/ 2 km surface current product skill score as a function of time for drifter 43346 from May 10 to June 1, 2016.

Table 3: Individual and average drifter skill score after [9] for the various surface current data sources.

#	Buoy Number	5 MHz	13 MHz	13 MHz QC	RTOFS-1
1	43241	0.65			0.05
2	43372	0.44			0.20
3	38824	0.62			0.07
4	43104	0.45			0.04
	Average	**0.54**			**0.09**
5	43340	0.65	0.61	0.59	0.12
6	43346	0.65	0.69	0.68	0.12
7	43411	0.69	0.67	0.66	0.09
	Average	**0.66**	**0.66**	**0.64**	**0.11**

IV. CONCLUSION

Surface currents from several HF radar derived products along with currents from a numerical model were evaluated in their skill of estimating the trajectory of a surface drifter over 48 hours. The various HF radar products outperformed the numerical model when judged against the Lagrangian skill score. Therefore, the authors recommend that the regional models like ESPRESSO that assimilate HFR surface currents be utilized in Coast Guard search planning.

ACKNOWLEDGMENT

This work was funded by NOAA Award Number NA16NOS0120020 “Mid-Atlantic Regional Association Coastal Ocean Observing System (MARACOOS): Preparing for a Changing Mid Atlantic”. Sponsor: National Ocean Service (NOS), National Oceanic and Atmospheric Administration (NOAA) NOAA-NOS-IOOS-2016-2004378 / CFDA: 11.012, Integrated Ocean Observing System Topic Area 1: Continued Development of Regional Coastal Ocean Observing Systems.

REFERENCES

[1] T. M. Kratzke, L. D. Stone, and J. R. Frost, "Search and Rescue Optimal Planning System," in *Information Fusion (FUSION), 2010 13th Conference on*, 2010, pp. 1-8.

[2] H. J. Roarty, S. M. Glenn, J. T. Kohut, D. Gong, E. Handel, E. Rivera Lemus, T. Garner, L. Atkinson, C. Jakubiak, W. Brown, M. Muglia, S. Haines, and H. Seim, "Operation and Application of a Regional High Frequency Radar Network in the Mid Atlantic Bight," *Marine Technology Society Journal,* vol. 44, pp. 133-145, 2010.

[3] H. Roarty, S. Glenn, and A. Allen, "Evaluation of environmental data for search and rescue," in *OCEANS 2016 - Shanghai*, 2016, pp. 1-3.

[4] A. Allen, "Performance of GPS/Argos self-locating datum marker buoys (SLDMBs)," in *OCEANS '96. MTS/IEEE. 'Prospects for the 21st Century'. Conference Proceedings*, 1996, pp. 857-861 vol.2.

[5] E. Terrill, M. Otero, L. Hazard, D. Conlee, J. Harlan, J. Kohut, P. Reuter, T. Cook, T. Harris, and K. Lindquist, "Data Management and Real-time Distribution in the HF-Radar National Network," in *OCEANS 2006*, 2006, pp. 1-6.

[6] S. Y. Kim, E. J. Terrill, and B. D. Cornuelle, "Mapping surface currents from HF radar radial velocity measurements using optimal interpolation," *J. Geophys. Res.,* vol. 113, p. C10023, 2008.

[7] J. Kohut, H. Roarty, E. Randall-Goodwin, S. Glenn, and C. Lichtenwalner, "Evaluation of two algorithms for a network of coastal HF radars in the Mid-Atlantic Bight," *Ocean Dynamics,* vol. 62, pp. 953-968, 2012.

[8] E. Fredj, H. Roarty, J. Kohut, M. Smith, and S. Glenn, "Gap Filling of the Coastal Ocean Surface Currents from HFR Data: Application to the Mid-Atlantic Bight HFR Network," *Journal of Atmospheric and Oceanic Technology,* vol. 33, pp. 1097-1111, 2016.

[9] Y. Liu and R. H. Weisberg, "Evaluation of trajectory modeling in different dynamic regions using normalized cumulative Lagrangian separation," *Journal of Geophysical Research: Oceans,* vol. 116, pp. n/a-n/a, 2011.

978-1-5386-1654-3/18/$31.00 ©2018 IEEE

Mitigation of Offshore Wind Turbines on High-Frequency Coastal Oceanographic Radar

D. Trockel, I. Rodriguez-Alegre, D. Barrick, C. Whelan
CODAR Oceans Sensors
Mountain View, USA
dale@codar.com

J. F. Vesesky
Electrical Engineering Dept.
University of California Santa Cruz
Santa Cruz, USA

H. Roarty
Department of Marine and Coastal Sciences
Rutgers University
New Brunswick, USA

***Abstract*— Observations in Europe [1] indicate that the spinning blades of offshore wind turbines cause interference in HF radars. With the first five U.S. offshore wind turbines in the monitoring area of the Mid-Atlantic Regional Association Coastal Ocean Observing System (MARACOOS) SeaSonde network already installed, the proximity of radars and turbines prompted a study to better understand the potential effects on the U.S. National HF Radar Network. The construction of several more offshore wind turbines is planned to begin in the coming years, begging the question: what can be done to minimize the impact on the U.S. National HF Radar Network? Using the relation between the rotation rate of the turbine and the structure of the interference found in range-Doppler space of a SeaSonde cross spectra we developed and tested several mitigation techniques. Tests were performed using simulated wind turbine interference added to SeaSonde Doppler spectra.**

Keywords—HF radar; interference; wind energy

I. Introduction

Coastal HF surface-wave radars (HFSWRs) have evolved over the past 50 years to aid in beyond-the-horizon ocean surveillance detecting and measuring surface currents, waves, tsunamis and vessels. There are now about 600 HFSWR units operating worldwide, most of them in national networks. With CODAR SeaSonde® radars accounting for over 85% of the HFSWRs. The premier example is the U.S. IOOS network of over 140 units, with another 15 in Canada [3].

The data from the HFSWR are used for operational purposes such as Coast Guard Search and Rescue, Hazardous Materials Spills Response and Marine Navigation, among others. The environmental data products are obtained from echoes from the rough sea waves, and the Doppler shifts produced by their motions. Two other echoes are seen in the echo Doppler spectra: vessel echoes and returns from offshore wind turbines in the radar field of view. The spinning large blades are excellent reflectors because their lengths are greater than the radar wavelength. The problem is, these turbine echoes constitute interference that can mask the other desired surface returns.

Observations in the U.K., on Liverpool Bay, indicate that the spinning blades of offshore wind turbines cause interference in HFSWR [1]. The first offshore wind farm in the USA, the Block Island Wind Farm, consisting of five wind turbines was installed off Block Island, RI in 2016. Additional wind farms, with many more wind turbines, are currently in planning. It is therefore crucial that we understand the possible impact of these wind farms on the national HF radar network, and that we develop techniques to mitigate the impact of turbine interference on all the radar data products.

In September 2016 we began an investigation funded by the Bureau of Ocean Energy Management (BOEM) to study the impact of wind turbine interference on HFSWR. We collected data for a two-year period from six HF radar sites near the five turbines installed off the Southern coast of Block Island, RI. We also used NEC (Numerical Electromagnetic Code®) [2] combined with CODAR's FMCW current processing algorithms, to characterize the wind turbine interference and obtain a functional relationship between the rotation rate of a turbine and the range-Doppler cells that may contain interference.

In this paper we focus on identifying and testing four mitigation filters. In particular we look at filters applied to SeaSonde "cross spectra" files, which contain the auto and cross spectra from the three CODAR antennas (monopole and two orthogonal loop antennas). We start with an overview of our simulation methods, following which, we define each of the mitigation filters. The strengths and weakness of each are identified through the application of various combinations of the filters to simulated data.

978-1-5386-4814-8/18/$31.00 ©2018 IEEE

II. Wind turbine Interference

A. Interference Charateristics

The turbine echoes show up as spikes in the Doppler spectral, which may also contain desired oceanographic information. The mechanism that produces them is not conveniently described by Doppler shift of a translating target (like a ship). Rather, it is better described as modulation. As the blades rotate, the echo time series varies, but repeats precisely every third of a revolution (120°) due to the three-bladed symmetry. A Fourier transform (to get a Doppler spectrum) of this periodic time series gives output points at discrete frequency bins, the first being the fundamental (the reciprocal of the period). Successive bins are the harmonics. These are essentially the "spikes" seen as interference in the radar spectral echoes.

By tracing the harmonic modes of the RCS of a wind turbine through a 120° of rotation through demodulation-processing, we find that given the revolutions per minute (RPM), frequency f_c, bandwidth B, sweep rate repetition T, and the distance R_t of the turbine from the receiver, the eight range-Doppler bins containing wind turbine interference are given by:

$$R_m = R_t + \frac{c}{2B}\left\lfloor \frac{\frac{3(RPM)}{60}+\frac{1}{2T}}{\frac{1}{T}} \right\rfloor \tag{1}$$

$$f_d = \left[\left(\frac{3m(RPM)}{60}+\frac{1}{2T}\right) \bmod \frac{1}{T}\right] - \frac{1}{2T} \tag{2}$$

where the harmonic number m is an integer ranging from -4 to 4. Equations (1) and (2) make it possible to identify the impacted range-Doppler bins given a rotation rate.

Through observation and comparison with the simulated cross spectra we identified three ways that interference from offshore turbines, like the five found in the Block Island Wind Farm, impacts oceanographic surface current map products:

1. biasing the measurement of the actual background noise level (affecting the Bragg sea echo peak identification algorithms)
2. changing the boundaries of the sea echo peaks by mischaracterizing turbine echoes as part of the sea echo
3. changing the bearing assignment of the radial current vectors by causing turbine echoes to be convolved within the Bragg sea echo peaks

The first two impacts listed above affect the current measurements by shifting the boundaries that define the first order region. To illustrate how wind turbine interference separated from the sea echo in the Doppler spectra can change

Fig. 1. An illustration of the ways wind turbine interference change the bins assigned to Bragg region.

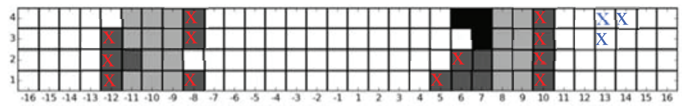

the boundary determination of the Bragg region, consider the simplified depiction in Fig. 1. To be consistent with SeaSonde cross spectra, the horizontal axis in Fig. 1 represents the Doppler bin and the vertical axis the range bin. The range-Doppler bins containing wind turbine interference are demarcated with an X. The light gray and black bins show the bins that correctly belong to the Bragg region, while the dark gray bins are range-Doppler bins that have been added to the Bragg region as a result of the wind turbine interference. The black bins are bins that have been removed from the Bragg region due to the impact of the wind turbine interference. When the wind turbine interference is near the correct Bragg boundaries, as with the bins marked with a red X, the first order lines (FOL) are shifted to include the wind turbine interference, resulting in the addition of the dark gray bins to the Bragg regions. In contrast, if the interference is found near the edges of the spectra, bins marked with a blue x, then the noise floor is over estimated and bins can be removed, as shown in range cells 3 and 4 of Fig. 1.

The other possibility is that some of the wind turbine interference peaks fall in the Bragg region. When the wind turbine interference is in the Bragg regions there is less impact, but the wind turbine interference is more difficult to detect. When the wind turbine interference is in the Bragg region it is difficult to distinguish it from the sea echo. However, since it does not affect the location of the FOL fewer current vectors are changed. The wind turbine interference peaks in the Bragg region span at most three range- Doppler bins, limiting the impact to at most three radial vectors. The wind turbine interference changes the radial vector calculations either by changing velocity at a given bearing or by shifting the bearing determination, meaning the desired bearing will be misplaced to an erroneous bearing position, resulting in consequent errors in radial velocities.

III. Mitigation Methods

A. Filters

Each of the four filters tested in this paper are intended to reduce one or more of the three impacts identified above. The four filters we developed include:

Edge Filter (EF): The EF mitigates the impact of wind turbine interference near the edges of the Doppler spectra. The EF is applied directly to the cross spectra via a median filter used on the edges of the Doppler spectrum of the range cell containing the wind turbine.

Bearing Removal Filter (BR): The BR filter removes all radial current measurements within a given range and bearing of the turbines.

Table 1. Mitigation methods and the filters they use.

Method	EF	BR	R1	R2
BR		X		
EFBR	X	X		
EFR1	X		X	
EFR1BR	X	X	X	
EFR2	X			X
EFR2BR	X	X		X

Rotation rate estimation techniques, R1 and R2: The R1 and R2 filters both estimate the rotation rates of the turbines and then use (1) and (2) to form a set of range-Doppler bins to be excluded from the current measurements.

The first step for both R1 and R2 is to estimate the possible rotation rates. A set of possible rotation rates is formed from all the rotation rates that have at least three of the eight range-Doppler bins predicted with (1) and (2) with a signal to noise ratio (SNR) of at least 10 dB. Once the set of possible RPMs has been determined, the steps in the R1 filter deviate from those taken with the R2 filter.

The next step for the R1 filter is to form a set s containing the union of the range-Doppler bins predicted by (1) and (2) for each of the possible rotation rates. Before the currents are extracted from the cross spectra files, each of the range-Doppler bins outside of the Bragg region are set to the value of the noise floor. The range-Doppler bins in s found in the Bragg regions are flagged so they are not processed for current measurements.

Alternatively, the R2 filter first finds the most probable rotational states of all the turbines and uses those specific rotation rates to calculate the set s of bins flagged for removal as mentioned above.

While each of the filters discussed in the previous section can be used individually as a mitigation technique, they are insufficient by themselves. For example, while the BR filter may reduce wind turbine interference in the Bragg region it does not effectively remove the wind turbine interference near the edge of the Doppler spectrum. In turn, if the wind turbine interference near the edge of the Doppler spectrum is not removed, the FOL can shift leading to inaccurate current measurements. However, the shifting of the FOL may be avoided if the BR and EF filter are used together.

Table 2. Parameters used for NEC modeling

Parameter	Value
Mast Height	100 m
Hub Length	10 m
Blade Length	40 m
Number of Blade Segments	20
Number of Mast Segments	50
Number of Hub Segments	2
Frequency	4.538
Sweep Bandwidth	25 KHz

To find effective combinations of the filters, we designed and tested six different mitigation methods. The mitigation methods are listed in Table 1 along with the filters they include. The methods are named using the concatenation of the two-letter abbreviations of all the filters they use. The mitigation methods include: BR, EFBR, EFR1, EFR1BR, EFR2, and EFR2BR.

IV. Simulations

Simulations provide the ability to fine tune each parameter independently while also allowing us to remove other sources of interference. The interference found in HF-radar resulting from a wind turbine is a consequence of the amplitude modulation of the signal reflected from the turbine [4]. As the turbine blades rotate, the RCS of the turbine changes, causing a proportional change in the voltage signal at the receiver. The changing RCS causes an amplitude and phase modulation of the complex voltage signal at the receiver.

Following [4] we use NEC to simulate the expected wind turbine interference in SeaSonde "cross spectra" from a single wind turbine, for various rotation rates and nacelle angles.

The parameters used for the NEC simulations are displayed in Table 2. After the wind turbine interference had been simulated, it was scaled to be of similar magnitude to the wind turbine interference observed at the Block Island BLCK 4.538 MHz radar. The scaled simulated wind turbine interference was added to cross spectra collected before the turbines were

Fig. 2. Range -Doppler bins added to the radial current measurements after filtering

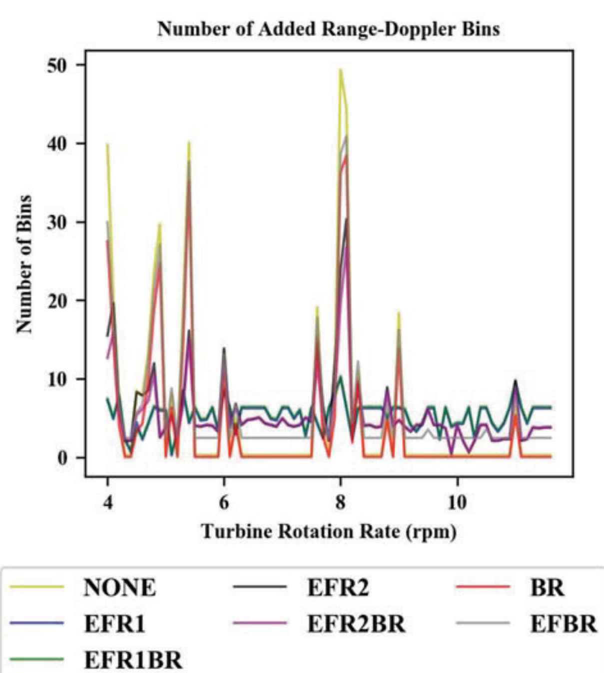

Fig. 3. Range-Doppler bins removed from the radial current measurements after filtering

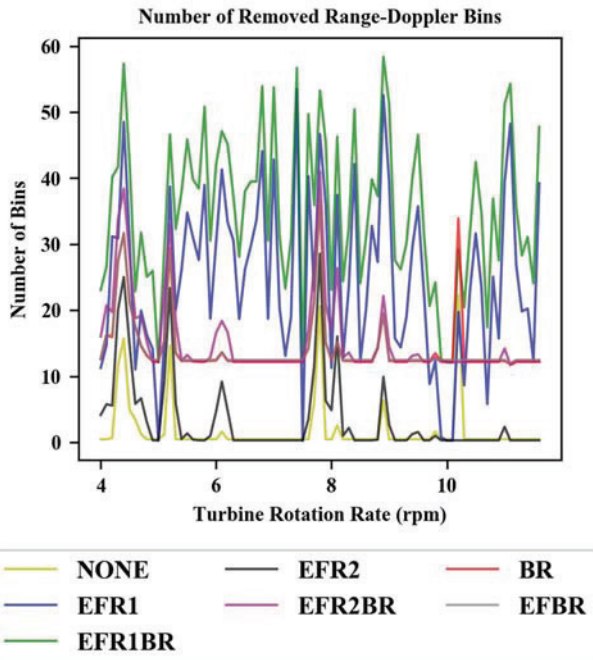

spinning, resulting in cross spectra files containing simulated wind turbine interference.

Using the method outlined above we generated a set of 1463 cross spectra with simulated wind turbine interference, each corresponding to a specific RPM and nacelle angle pair. In the set of 1463 simulated cross spectra, the rotation rates range from 4 to 11.6 rpm at 0.1 increments, while the nacelle angle ranges from 0° to 90° at 1° increments.

V. PERFORMANCE

The set of 1463 simulated cross spectra were filtered with each of the six mitigation methods listed in Table 1. The radial current measurements were extracted from the filtered cross spectra and compared to the radial currents obtained from the original cross spectra before the addition of simulated wind turbine interference. The radial vectors added and lost are plotted in Fig. 2 and Fig. 3 respectively. To show the impact of the filtering, we have included the result of no filtering, labeled NONE, in Fig. 2 and Fig. 3. A summary of the average performance of the methods across all rotation rates and nacelle angles is found in Table 2.

Fig. 2 and Fig. 3 show that EFR1 and EFR1BR are the best at eliminating erroneous radial current measurements added by the wind turbine interference, at rotation rates that add a large number of range-Doppler bins to the Bragg region. However, EFR1 and EFR1BR also tend to over-filter the data, removing more of the actual current measurements than any other method. In contrast, EFR2 removes the least amount of correct current measurements, but it is not as effective at filtering out radial currents added by the wind turbine interference.

Furthermore, both BR and EFBR perform poorly at both removing the added measurements and removing the valid current measurements. However, BR and EFBR performed the best at reducing the number of current vectors with a changed bearing assignment.

In addition to the number of erroneous current vectors added and the number of correct currents removed, it is also important to consider the magnitude of the current measurement error. In the simulations, the error was found to be as large as 92.164 cm/s. In the last column of Table 3 we show the average maximal error in the current measurement after each of the mitigation techniques had been applied. Table 3 indicates that methods using the BR filter tend to perform the best at reducing the maximal error. However, as we show below this is not likely true for non-simulated data, as the error in the bearing determination can be much larger.

One of the added benefits of using the R2 filter is that in addition to reducing the impact of the wind turbine interference,

Table 1. Simulation filtering test results

Filter Method	Average Number of Bins Added	Average Number of Bins Lost	Average Number of Bearings Changed	Average Maximum Current Error
None	5.23	1.40	0.83	15.9 cm/s
BR	4.03	14.00	0.25	7.5 cm/s
EFBR	6.06	13.70	0.25	7.5 cm/s
EFR1	5.04	24.58	1.79	14.7 cm/s
EFR1BR	5.01	35.01	1.59	12.9 cm/s
EFR2	5.70	3.04	0.77	11.6 cm/s
EFR2BR	5.18	15.27	0.39	6.9 cm/s

Fig. 4. Antenna 3 self spectra: unfiltered (top), EFR1 (middle), EFR2 (bottom). The turbine interference peaks are marked with red arrows.

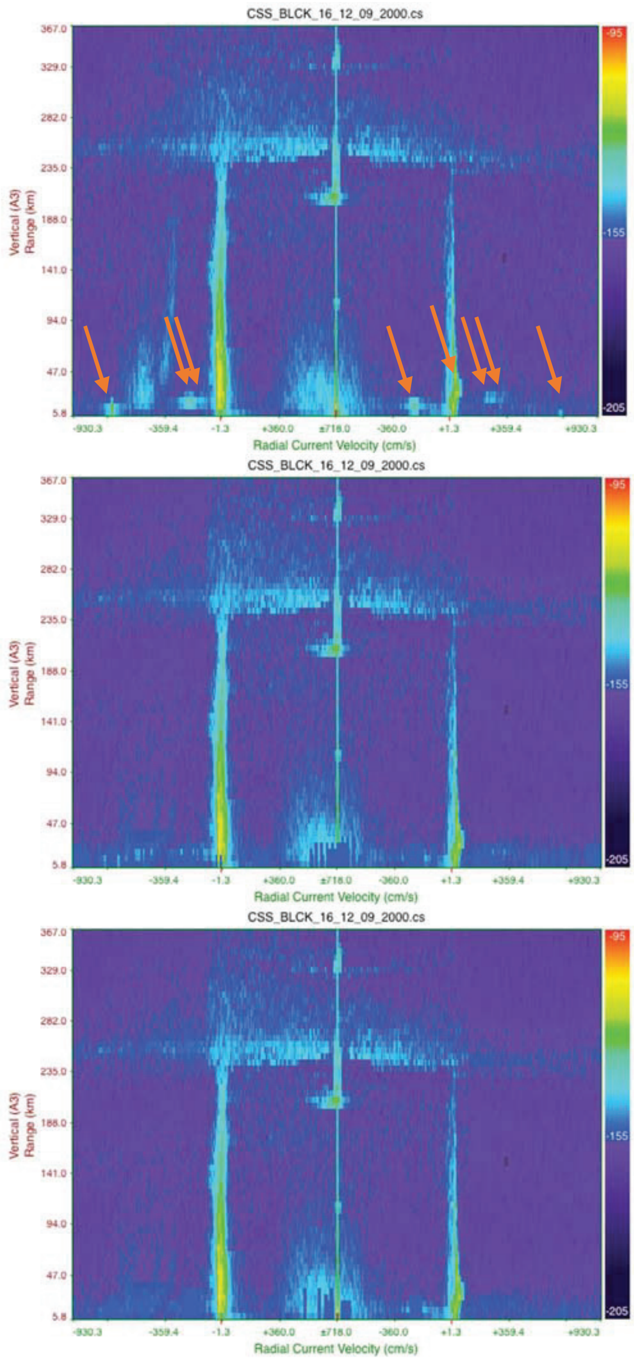

the filter also gives an estimation of the rotational state of each of the turbines. When filtering the simulated data with the R2 filter, we find that the R2 filter correctly predicts the rotation rate within 0.3 RPM of the turbines 44% of the time. The disadvantage of the R2 filter is its high computational cost, which makes it unsuitable for real time filtering as the number of turbines increases.

VI. Example

To further investigate the effectiveness of each of the mitigation techniques, we filtered a set of 32 cross spectra obtained from the 4.538 MHz Block Island SeaSonde "BLCK" radar during times when the wind turbines were in operation. Without any "ground-truth measurement" for the currents, we are unable to determine the quality of the filtered radial currents quantitatively. However, the comparisons do provide some qualitative differences.

We display one of the 32 filtered cross spectra taken from BLCK on 12/09/2016 at 20:00 UTC in the top plot of Fig. 4. At the time the cross spectra were collected, two of the five turbines were rotating with rotation rates between 11.1 rpm and 11.5 rpm. The variability in the rotation rates accounts for the spreading of the wind turbine interference peaks visible outside of the Bragg regions. Equations (1) and (2) show that for the RPMs near 11.1, there is wind turbine interference peaks in or near the edges of the Bragg regions providing an ideal mitigation test case. We show the resulting radial currents in the top plot of Fig. 5. The large velocity vectors in the first range bin are the result of the wind turbine interference peaks found along the boundaries of the Bragg regions. The plots second from the top, second from the bottom, and at the bottom of Fig. 5 show the resulting current measurements when using EFR2, EFR1, and EFR1BR respectively. While we do not show the result of using the other mitigation techniques, we can infer their effectiveness from the other plots in Fig. 5.

The BR filter was set to remove any current measurement assigned to a bearing within five degrees of any of the five turbines, resulting in the loss of current measurements in a sector from 125° to 170° as shown in the bottom plot of Fig. 5. This highlights two of the shortcomings of the BR filter.

First, the method over-filters, removing indiscriminately all measurements for a given bearing. The over-filtering problem becomes worse as the number of turbines increases, making the method unsuitable for large wind farms.

Second, the BR filter may not even remove the erroneous current vectors introduced by the wind turbine interference. The direction finding algorithm is not reliable when more than two signals from different directions are found in the same range-Doppler bins.

Comparing the bottom plot in Fig. 5 we can see how the BR and EFBR mitigation methods would have no positive impact on the resulting current measurements but rather cause the loss of good data.

Fig. 5 Radial Current Maps From BLCK: Unfiltered (Top), EFR1 (Second From the Top), EFR1BR (Second From the Bottom), and EFR2 (Bottom).

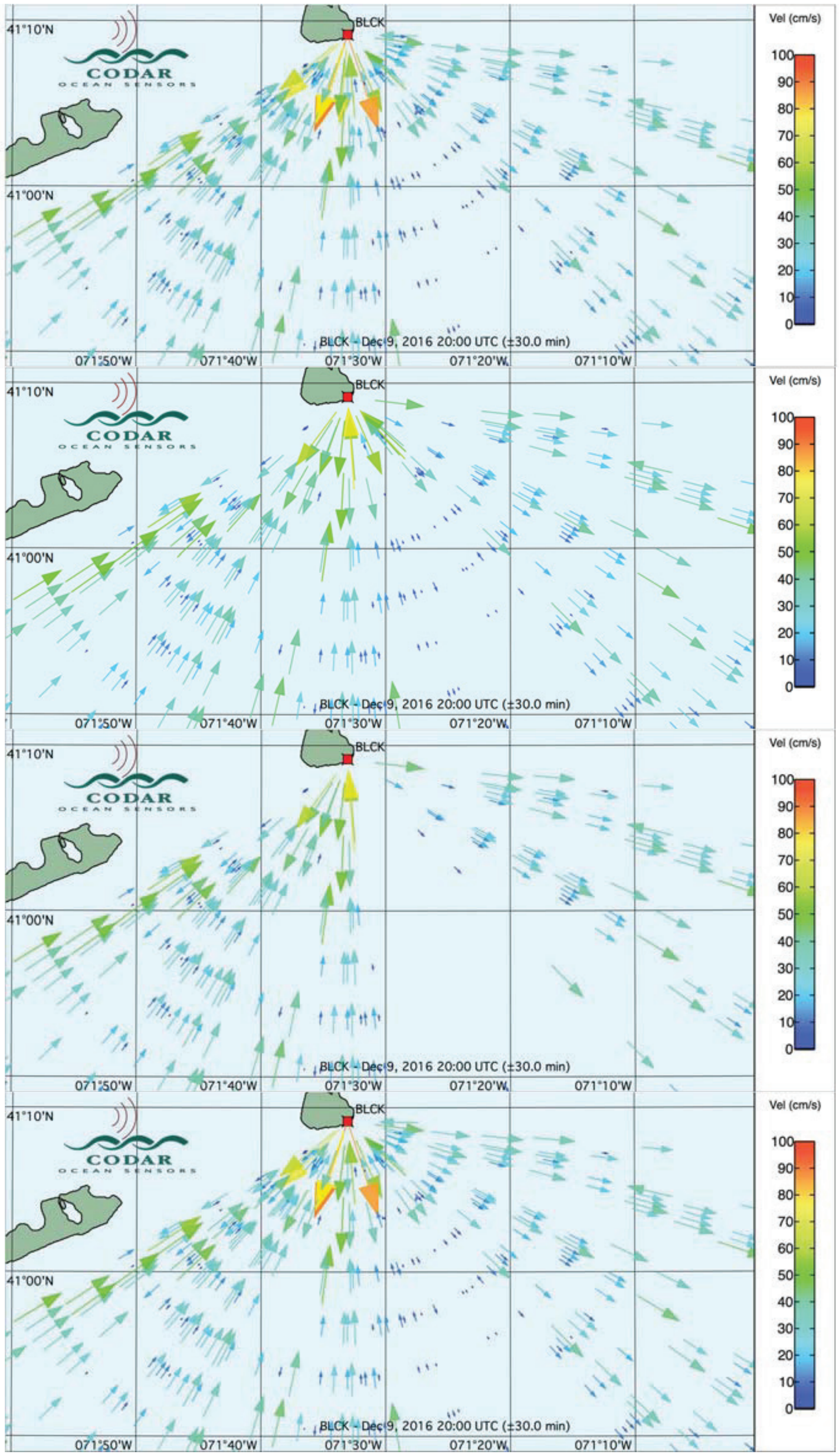

The bottom plots in Fig 4 show the result of filtering the cross spectra using EFR1 and EFR2 respectively. Note that all peaks filtered by EFR2 were also filtered using EFR1. However, since EFR1 removes peaks from all possible rotation rates the EFR1 method does a better job at removing peaks that have been spread due to a varying rotation rate, as is the case in this example. To illustrate this, observe the resulting current measurements shown in the middle plots in Fig. 5. In this case, even though the proper rotation rate was predicted using the R2 filter, not all the erroneous current vectors added by the wind turbine interference were removed. This is a result of only removing the best-fit rotation rates for each of the turbines, which misses interference spread out in Doppler. In contrast, the R2 filter removes peaks corresponding to each of the possible rotation rates. The downside is that if there is a large amount of interference, from any source, the method may over-filter the velocity currents

It is difficult to predict how the EFR1 method would scale with the number of turbines in the wind farm. The computational cost of EFR1 is only O(1) which is favorable, but the method may tend to over-filter the current measurements as the number of turbines and other sources of interference increase. The EFR2 method has the benefit of not over-filtering the data but consumes too many computational resources to even be feasible for a wind farm with only five wind turbines.

We find that overall, regarding both computational resources and accuracy, the EFR1 method is the most efficient. While it does over-filter the data in some cases, it does so discriminately as opposed to the BR filter. In our simulated comparisons, the EFR2 method performed better than any other method at not over-filtering the data while still reducing the number of current measurements added from the wind turbine interference.

VII. Conclusion

Bearing notching was shown to be insufficient for mitigating wind turbine interference, in some cases doing more harm than good. The inconsistency of the bearing assignment, especially when there were more than two signal sources in a single range-Doppler bin makes filtering by bearing alone ineffective. Additionally, it is necessary to filter wind turbine interference near the edges of the spectral Bragg peaks for consistent determination of the FOL.

We found that methods that incorporate the structure of the wind turbine interference in SeaSonde cross spectra result in effective mitigation techniques. The lack of a priori knowledge of the rotation rates of the turbines makes these methods challenging. However, once the rotation rates are known, the methods effectively reduce the impact of turbine interference.

As the number of offshore wind farms increases, real-time mitigation software will become increasingly necessary to preserve the integrity of the national network of coastal HF radar. In the work present here, we developed several radial current-flagging methods to inform radar operators which radial vectors could be affected by turbine interference. The mitigation methods presented above have laid the groundwork for the development of a real-time solution.

As larger wind farms are installed in the observation fields of coastal HF radars we will have the opportunity to test the scalability of the mitigation algorithms. However, the simulation methods we have developed will allow us to preemptively test the impact of a larger scale offshore wind farm and the effectiveness of the mitigation methods. Ultimately, this gives us the foundation to develop the real-time mitigation software needed to preserve the integrity of the coastal HF radar network data.

Acknowledgment

Acknowledgement of Funding: Study funding was provided by the U.S. Department of the Interior, Bureau of Ocean Energy Management, Environmental Studies Program, Washington, D.C, under Contract Number M16PC00017.

References

[1] L. Wyatt, A. Robinson, M. Howarth, Wind farm impacts on HF radar current and wave measurements in Liverpool Bay. IEEE OCEANS , pp. 1-3, 2011.

[2] G. Burke, A. Poggio, J. Logan, J. Rockway, (1979). Numerical electromagnetic code (NEC). IEEE International Symposium on Electromagnetic Compatibility, pp. 1-3, 1979

[3] J. Harlan, E. Terrill, L. Hazard, C. Keen, D. Barrick, C. Whelan, S. Howden, J. Kohut, The Integrated Ocean Observing System High-Frequency Radar Network: Status and Local, Regional, and National Applications, Marine Technology Society Journal, Vol. 44, 122-132

[4] C. Teague, D. Barrick, Estimation of Wind Turbine Radar Signature at 13.5 MHz., IEEE OCEANS, pp. 1-4, 2012

Evaluation of Wave Data from HF Radar by the National Weather Service

Hugh Roarty
RUCOOL
Rutgers University
New Brunswick, NJ USA
hroarty@marine.rutgers.edu

Jared Klein
WFO Binghamton
National Weather Service
Binghamton, NY USA
jared.klein@noaa.gov

Siena Dante
NOAA CREST
The City College of New York
New York, NY USA
sdante000@citymail.cuny.edu

Al Cope
WFO Philadelphia/Mt. Holly
National Weather Service
Mt. Holly, NJ USA
alan.cope@noaa.gov

Sara Johnson
WFO Philadelphia
National Weather Service
Mt. Holly, NJ USA
sarah.johnson@noaa.gov

Maeve Daugharty
CODAR Ocean Sensors
Mountain View, CA USA
maeve@codar.com

Abstract— **The National Weather Service issues a marine zone forecast and surf zone forecast daily. NWS currently uses wave information collected from nearby buoys as part of the forecast process. However, the buoy data is limited in spatial coverage and are sited offshore. The Integrated Ocean Observing System (IOOS) selected a limited number of marine Weather Forecasting Offices to evaluate the utility of HF radar-derived significant wave height and direction in their marine forecasts. Wave data was provided to the National Weather Service in Mt. Holly, NJ via a web interface which allowed forecasters to view and download recent wave measurements. The wave height from the HF radar stations were compared to nearby buoys. Several wave products (individual range cell wave estimates and a composite wave product) from the HF radar were provided to the WFO for evaluation. There was good agreement between the buoys and the HF radar, especially for periods of buildings seas. However, there were instances (April 2018) where the wave height measurements from the HF radar decreased more rapidly than the wave measurements from the nearby buoys. There were also other instances of the HF radar wave heights being higher than those from the buoys. This high bias began to appear late last spring 2018 and seems to be still present in the fall. In both these cases, it is unclear at the moment if the difference we are seeing between the HF radar and the buoy is due to environmental variability or fundamental difference in how the sensors are estimating wave conditions for the area of interest. In our initial communication with the National Weather Service, the measurements from the HF radar have proved valuable to their forecast operations. We have concluded that the HF radar can provide information to bridge the gap between the buoy measurements. We will continue to explore the two measurements and look for reasons that explain the differences.**

Keywords—remote sensing, radar, MARACOOS, oceans, waves, HF radar, weather service

I. Introduction

The Integrated Ocean Observing System (IOOS) in partnership with the National Weather Service (NWS) Office of Science and Technology Integration selected a limited number of volunteers at marine Weather Forecast Offices (WFOs) to evaluate the utility of High Frequency (HF) radar derived significant wave height (SWH) and direction in daily marine forecasts. This is a new data product that will be created and delivered by IOOS academic partners in near-real-time. Pilot projects in several coastal areas are envisioned that should last at least 6 months. At the end of the pilot projects, the NWS Analyze, Forecast and Support (AFS) Office should be able to decide whether this new data product has utility for marine forecasting.

IOOS partners provided a near-real-time display of wave data for access by WFOs in the area of the HF radars. The partners were available for clarification, discussion and analysis with the WFO(s) in their area. Forecasters at each participating WFO evaluated the HFR-derived products. The frequency with which the products are used will be determined by the WFO. Opinions from WFOs were sought about the displays so that the displays were improved during the span of the pilot project. Each pilot project should last approximately 6 months although an evaluation that lasts longer would be preferred so that a greater variety of sea states can be monitored. The exact length will be determined by the WFO as well as the start and end dates. It is expected that WFOs will have other sources of wave data available to them to help in the evaluation.

The marine WFOs selected, corresponding IOOS regional association and partner are listed in Table 1. The results

978-1-5386-5485-9/19/$31.00 ©2019 IEEE

discussed in this paper will be focused on the Mid Atlantic and the Philadelphia WFO.

Table 1:Partners in the project

WFO	IOOS Regional Association	IOOS Partner
Philadelphia/Mt Holly (PHI)	MARACOOS	Rutgers University
Eureka, CA (EKA)	CENCOOS	University of California Davis
San Juan, PR (SJU)	CARICOOS	University of Puerto Rico Mayaguez.

II. BACKGROUND

A. Previous HFR Wave Research

Rutgers has been researching ways to improve the wave measurement from the SeaSonde HF radar for quite some time. Initial investigations sought to determine if the shallow water of the continental shelf would bias the wave measurements [1] but our findings found no such bias [2]. We then sought to quantify the difference we should expect to see when comparing buoy measurements with HFR since there was sizable separation between the measurements. We should expect a correlation above 0.8 for any of the 13 MHz radars in New Jersey with wave heights from NDBC buoys 44009, 44025 or 44065. The correlations of the radars with the wave buoys were on the order of 0.4 [3]. One possible explanation for the difference we were seeing in the wave measurements was due to wind direction. When the wind is blowing from the east, the fetch is similar for the radars and the buoys and the measurements agreed. When the winds are from the west the fetch is small for the radar wave measurements compared to the buoy measurements and there can be as much as a 1 m difference between wave estimates. Under certain scenarios, we could observe the growth of wave heights in each of the radars range cells when winds were from the west [4]. Another possible explanation for the difference seen in the radar and buoy measurements is the modality of the wave spectrum. The radar processing assumes a single mode wind sea, specifically a Pierson-Moskowitz wave spectrum. If the wave spectrum is bimodal with a wind and swell sea, then that can lead to an incorrect measurement of the wave parameters by the radar. CODAR is currently exploring the use of a bimodal spectrum in its wave processing software. Changing the radio wave parameters to focus more of the transmitted energy in the nearby range cells improved wave measurements. We also explored changing the averaging scheme to test its impact on data coverage but concluded that the existing settings of a 75 minute average was best [5].

B. NWS Marine Forecasts

The Philadelphia WFO produces a five-day marine zone forecast 20 nautical miles from the coast (Figure 1) with information for wave height, period and direction as well as wind speed and direction. Those elements are forecast year-round. The WFO also produces a surf zone forecast and rip current risk index from mid-May to the end of September. Other offices further south forecast this element year-round. The marine forecasting process starts with analyzing model output from the Nearshore Wave Prediction System (NWPS) [6] and NOAA WaveWatch III [7] (the latter model has an extratropical and tropical version). There is also probabilistic guidance from these models that the forecasters utilize. Part of the forecast process is to compare modeled wave heights, period, swell (the three parameters that are included in the marine forecast at PHI) to observations at select offshore buoys to estimate how well the models had initialized. Forecasters can then populate the gridded forecast database with one of the models or even take a blend of several models and/or our previous NWS forecasts. Forecasters also look at text products that contain output from these models at select buoys (e.g., 44009, 44025, 44091). This is an important step because the primary wave group (based on energy of a particular wave height, period, swell) that is depicted in the gridded output for a particular model is not always the correct one. Looking at these text products will help decipher which wave group would be the predominant one and this can always be drawn manually in the forecast grids. The forecast is updated every three hours focusing on the first few hours of the forecast and can be updated at any time if the forecasters determine the forecast does not reflect current conditions.

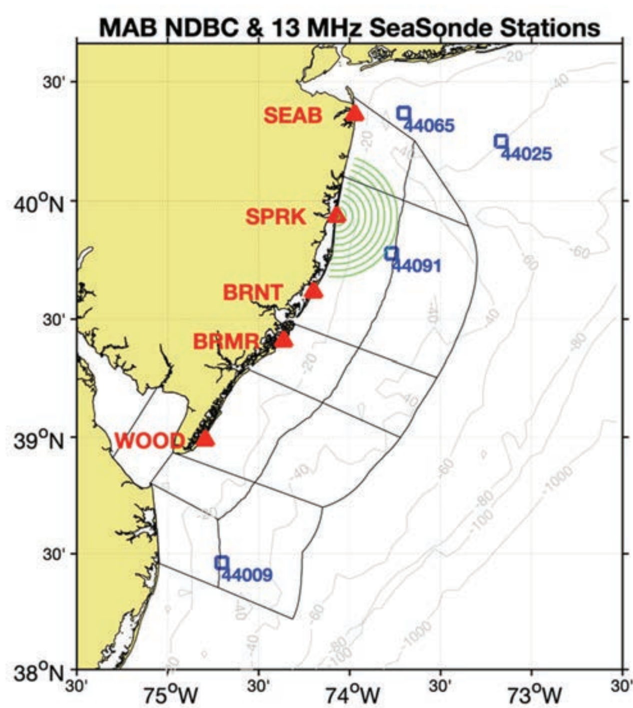

Figure 1: Map showing the study area. The location of the HF radar stations (red triangles) and NDBC wave buoys (blue squares) are noted. The marine forecasting zones for WFO Mt. Holly are indicated by the thin black line and the 3 km range cells from the Seaside Park radar station are shown in green.

III. RESULTS

The program in the Mid Atlantic began in December 2017. Philadelphia WFO submitted monthly progress reports on the utility of the wave data in their forecasts. The radar wave measurements were also used in a hindcasting mode to analyze past storms.

A Nor'easter passed through the Mid Atlantic on March 14, 2017 producing a swath of heavy snowfall across a large portion of the Northeast. Predictions of the storm in the New York metropolitan area were criticized due to the overestimation of the forecasted snowfall amount. A surface low developed off the coast of Georgia and the pressure began to rapidly drop as it moved parallel to the Eastern Seaboard. The storm reached its peak just inland over Long Island on the evening of March 14. The track of the storm could be seen in the wave heights off the coast (Figure 2). The wave heights peaked at the southern sensor locations first and then moved north. Buoy 44009 was offline during this storm so there was 365 km between station 44014 off Virginia to the next buoy measurement at 44091. The HFR stations helped fill in this gap by providing wave height measurements as the storm moved towards the northeast. The winds gradually rotated from the northeast to the northwest as the storm moved northwards. The peak in wave heights could been seen travelling from south to north in the buoy and radar data (Figure 2) where the peak wave height at the Wildwood HFR station (WOOD) occurred at 12:00 UTC while the peak wave height at the Sea Bright HFR station (SEAB) occurred at 18:00 UTC, some six hours later with 170 km between the two stations. Each of the HFR wave measurements were taken in range cell 10 (30 km from shore).

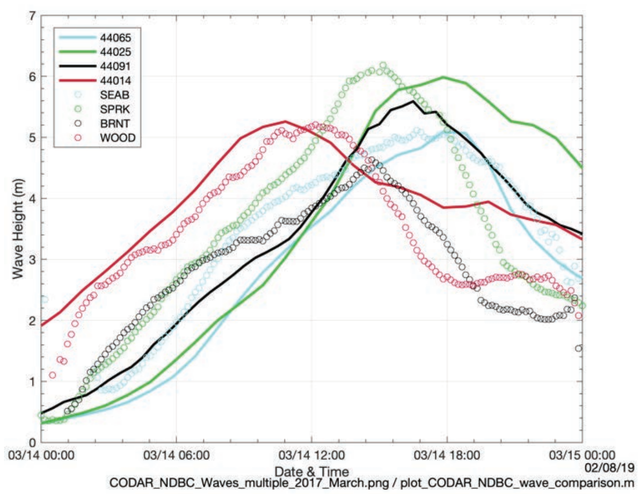

Figure 2: Time series plot of wave height for March 14, 2017 UTC. The solid lines are wave heights from NDBC buoys and the open circles are from range cell 10 of the HFR stations. The legend explains where each wave measurenent was made and Figure 1 provides the location of the measurements.

Another storm passed through the region a few weeks later on March 22, 2017 where the wind shifted from a weak southwest wind to a strong northwest wind (Figure 3). For this case, the HFR station at Seaside Park was able to measure the growth in wave height with increasing fetch. The radar measures wave parameters in each of its range cells. The range cells for the 13 MHz radar at Seaside Park were set to 3 km. The radar typically measures ocean currents in range cells 2-30 while wave processing is performed on range cells 2-10.

Figure 3 shows that the waves only reached 1.5 m significant wave height within range cell 2 (6 km from shore) for this particular storm while the wave heights in range cell 8 (24 km from shore) peaked over 2 m in close agreement with NDBC buoy 44025 which is 70 km offshore.

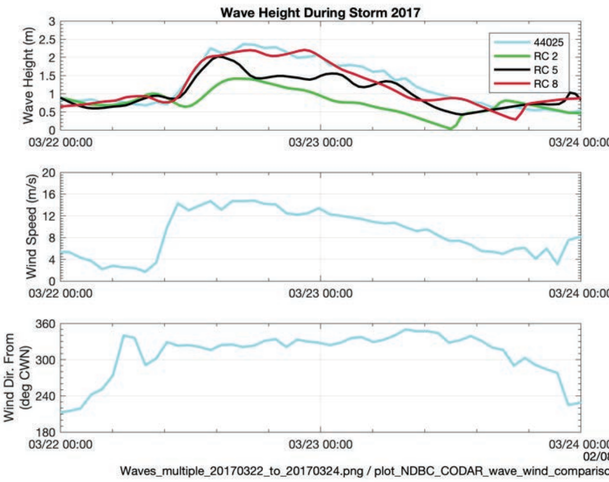

Figure 3: Time series plot of wave height from NDBC buoy 44025 (cyan) and HFR station at Seaside Park, NJ for range cells 2 (green), 5 (black) and 8 (red) (top panel). The middle panel shows wind speed (m/s) and bottom panel shows wind direction from (degrees clockwise from north) for buoy 44025.

Lastly, the weather service noticed some wave measurements by the HF radar that deserved further analysis. A low-pressure system moved east from the Ohio River Valley on April 15, 2018. Winds were out of the east from April 12 to April 15. The wave measurements from the Seaside Park HFR agreed with the nearby NDBC buoys. Then the wind shifted to blowing out of the west on April 17 and there was a sharp drop in waves measured by the HFR while the wave buoys displayed a more gradual decrease in wave heights over two days (Figure 4). The weather service noticed this pattern in two other instances on March 13th and March 21st . In all three cases the steep drop in HFR waves coincided with the shift in wind direction from the northeast (onshore) to the northwest (offshore). It should be expected that the waves would diminish after the wind shifts from east to the west. However, the rate of this drop deserves further investigation. Previous research has found that wave attenuation by an opposing wind was higher than predicted by theory [8]. So, the wave attenuation observed by the radar may be realistic.

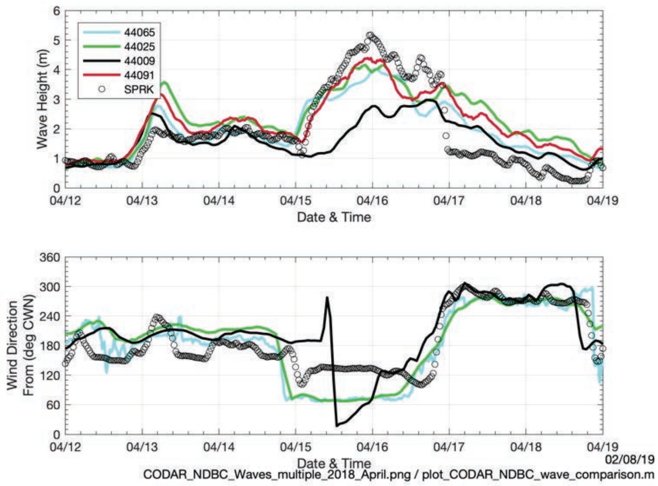

Figure 4: Time series plot of significant wave height (top) and wind direction (bottom) from April 12 to April 19, 2018. The legend explains the data sources.

IV. Conclusion

The National Weather Service Weather Forecast Office in Mt. Holly, NJ has been evaluating the wave measurements from several HF radar stations along the New Jersey coast since December 2017. Initial feedback indicates that the measurements from the HFR can be valuable in validating their Coastal Waters Forecast and for providing additional wave measurements along the coast of New Jersey for their surf zone forecast and rip current risk index. The lack of marine observations and the predominately offshore siting of the wave buoys (i.e., not in the surf zone) hinders the forecasters ability to analyze how well marine forecasts and numerical weather prediction (NWP) guidance have been verified or initialized in the surf zone and coastal waters. Furthermore, the conversion between offshore wave heights and surf heights remains challenging but hopefully the nearshore wave measurements by the HF radar can help interpret this wave transformation.

Acknowledgment

Thank you to Dr. Jack Harlan and Mr. Dennis Atkinson for developing the wave evaluation program. This work was funded by NOAA Award Number NA16NOS0120020 “Mid-Atlantic Regional Association Coastal Ocean Observing System (MARACOOS): Preparing for a Changing Mid Atlantic”. Sponsor: National Ocean Service (NOS), National Oceanic and Atmospheric Administration (NOAA) NOAA-NOS-IOOS-2016-2004378 / CFDA: 11.012, Integrated Ocean Observing System Topic Area 1: Continued Development of Regional Coastal Ocean Observing Systems.

References

[1] B. Lipa, B. Nyden, D. Barrick, and J. Kohut, "HF Radar Sea-echo from Shallow Water," *Sensors,* vol. 8, no. 8, pp. 4611-4635, 2008.

[2] C. W. Evans, H. J. Roarty, J. T. Kohut, and S. M. Glenn, "Examination of the SeaSonde wave processing settings and the effects of shallow water on wave measurements," in *2012 Oceans*, 2012, pp. 1-6: IEEE.

[3] H. Roarty, C. Evans, S. Glenn, and Z. Hao, "Evaluation of algorithms for wave height measurements with high frequency radar," in *Current, Waves and Turbulence Measurement (CWTM), 2015 IEEE/OES Eleventh*, 2015, pp. 1-4.

[4] B. Lipa *et al.*, "Developments in compact HF-radar ocean wave measurement," *Advances in sensors: Reviews,* vol. 5, pp. 469-495, 2018.

[5] R. Forney, H. Roarty, and S. Glenn, "Measuring waves with a compact HF radar," in *OCEANS 2015-MTS/IEEE Washington*, 2015, pp. 1-5: IEEE.

[6] A. van der Westhuysen *et al.*, "4.5 DEVELOPMENT AND VALIDATION OF THE NEARSHORE WAVE PREDICTION SYSTEM1," 2013.

[7] H. L. Tolman, "User manual and system documentation of WAVEWATCH III TM version 3.14," *Technical note, MMAB Contribution,* vol. 276, p. 220, 2009.

[8] W. L. Peirson, A. W. Garcia, and S. E. Pells, "Water wave attenuation due to opposing wind," *Journal of Fluid Mechanics,* vol. 487, pp. 345-365, 2003.

Evaluation of the CODAR Tsunami Detection Algorithm and Software

Hugh Roarty
Ctr. for Ocean Observing Leadership
Rutgers University
New Brunswick, NJ USA
hroarty@marine.rutgers.edu

George Garcia
Department of Computer Science
Passaic County Community College
Paterson, NJ USA
peralta.george973@gmail.com

Terry Nichols
National Tsunami Warning Center
NOAA
Palmer, AK USA
terry.nichols@noaa.gov

***Abstract*— Coastal hazards pose a threat to human life and property around the globe. Tsunami waves and storm surge are some examples of coastal hazards we must try to mitigate over the coming decades. High Frequency radars have emerged as possible technology capable of mitigating the destruction from these hazards by providing early detection of these disturbances out at sea. Rutgers University has worked with CODAR Ocean Sensors by collecting and analyzing data from four HF radar stations for potential tsunami signals from October 2016 to June 2019. CODAR has developed a pattern recognition process to detect the presence of tsunami waves. The output of the process is quantified as an alongshore and cross shore q-factor. If there is a spike in the q-factor measurement then arrival of a tsunami could be imminent. The statistics of the q-factor measurements at the four stations were calculated and compared against the radio noise spectrum and other environmental data like nearby water level and atmospheric pressure. Recently, on May 30, 2019 a weather system moved through the region that generated a small meteotsunami (amplitude 15-30 cm) that was detected by a DART buoy, water level gauges and one of the HF radar stations. The data from all three system covered a large spatial area which allowed us to study the propagation of the wave through the region. The different detection schemes with each technology also allowed us to study the characteristics of the tsunami signal.**

Keywords—MARACOOS, coastal hazards, tsunami, remote sensing, HF radar

I. INTRODUCTION

Tsunamis are a coastal hazard that inflict death and destruction along the world's coastlines. The cost of tsunamis will increase over time as population growth and migration is trending towards coastal areas. The ability to detect a tsunami wave and forecast its severity and arrival time is critical for the protection of life and property.

A special kind of tsunami that is generated by meteorological events is referred to as a meteotsunami. The oscillations from a meteotsunami are similar to ordinary tsunami waves but have typically been observed only in bays and inlets. Recent instances of more energetic events have been observed along the coastal United States [1, 2] and have spurred increased interest.

One of the recent events was a meteotsunami that struck the coast of New Jersey on June 13, 2013. It was generated by a weather system, referred to as a derecho, that had passed through the area. The system displayed a spike in atmospheric pressure that gave rise to an ocean wave that propagated outwards [3]. The wave reflected off the continental shelf break and travelled back towards land and impacted the coast six hours later. The data from the SeaSonde HF radars operated along the NJ coast were post processed and the tsunami wave was visible in the radar data, some 43 minutes before it made landfall.

The CODAR SeaSonde radar (http://www.codar.com) is unique in that it detects the oncoming tsunami wave through its orbital velocity, rather than the amplitude of the wave as most other sensors observe. SeaSonde HF radars have observed tsunami waves in the near-field region (2-50 km from the coast) on multiple occasions [4]. Water depth is a critical determinant for the visibility of the tsunami waves. As the tsunami waves propagate into shallow water, their height increases but their orbital velocities increase much faster than their amplitude [5]. The shallow continental shelf of the Mid Atlantic Bight makes it an excellent study area to test the CODAR radar and software's ability to detect tsunami waves.

CODAR Ocean Sensors has developed a methodology for the detection of tsunami waves. The method entails calculating radial velocity maps from short-term radar cross spectra. The radial velocities are partitioned by 2 km strips (Figure 1) that are constructed parallel to the bathymetry contours and then resolved into components perpendicular and parallel to the depth contour. All the resolved velocities within a particular strip are then averaged to create a time series of cross shore and along shore velocity for each band. A pattern recognition algorithm is then applied to the time series to detect the oncoming tsunami waves. The algorithm looks for correlation in the adjacent bands in nearby times. The output of the algorithm is called a q-factor. A positive q-factor in the crossshore indicates a wave moving toward the coast and the radar, and a positive q-factor in the alongshore indicates a tsunami wave moving +90 degrees from crossshore, or in this case towards the northeast. More background on this process has been published previously [6].

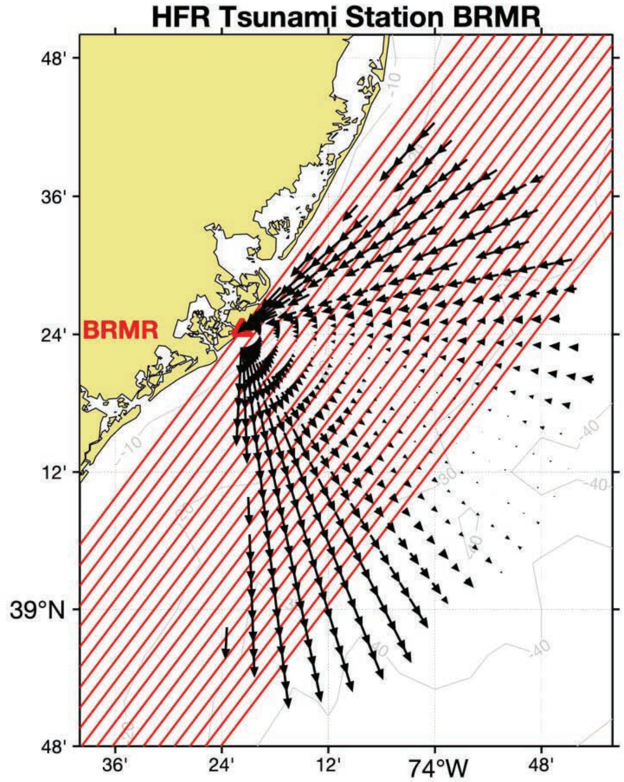

Figure 1: Radial map from the Brigantine 13 MHz radar BRMR (black arrows) overlaid with 2 km averaging strips for the tsunami processing.

In this paper we discuss the q-factor output from four HF radar stations in New Jersey. The statistics and behavior of the q-factor data are analyzed and discussed. Attention is paid to the data from January to June 2019. Lastly, a meteotsunami was detected on May 30, 2019 and the performance of the four stations during that event is discussed. One main goal of the present study is to determine an appropriate threshold for a q-factor warning that will warrant further investigation and minimize the number of false alarms.

II. Methods

CODAR tsunami software was operated and q-factor data was collected at four HFR stations along the New Jersey coast. Three of the stations operated in the 13 MHz band, Bradley Beach (BRAD), Brant Beach, BRNT and Brigantine (BRMR) and one station in the 5 MHz band Loveladies (LOVE)(Figure 2). Each station is denoted by a four-letter site code and are a part of the Mid Atlantic HF Radar Network [7]. The q-factor data is derived from Doppler spectra that is collected every 128 seconds for the 13 MHz systems and 256 seconds for the 5 MHz system. This recording time is reduced compared to spectra that is utilized in the ocean current processing that is collected every 256 seconds for the 13 MHz and 1024 seconds for the 5 MHz system. Data was collected from June 2016 to June 2019.

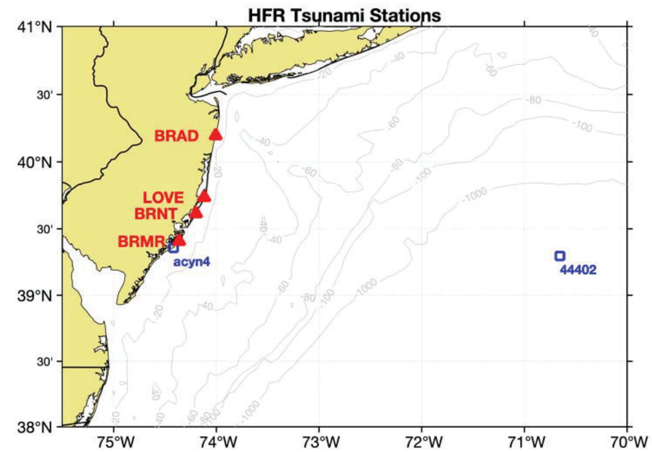

Figure 2: Study area showing the location of the four HF radar stations (red triangles), NOAA water level gauge in Atlantic City, NJ acyn4 (blue square) and NOAA DART sensor 44402 (blue square).

The configuration settings for the tsunami software processing are given in Table 1. The strip width for the 13 MHz stations was 2 km while it was 6 km for the 5 MHz station. The strip orientation denotes the true bearing of a line perpendicular to the coast. The depth contours are parallel to the coastline along this section of coast. The tsunami processing has its own gap detection and allowance where the standard setup requires 26 minutes of continuous cross spectra data in order to output data.

Table 1: Tsunami software configuration settings for the four HF radars.

Station	Detection Method	Strip Orientation (degrees True)	Strip Width (km)	Number of Strips	Background Span (minutes)
BRAD	4	130	2	20	26
LOVE	4	130	6	10	52
BRNT	4	125	2	20	26
BRMR	4	130	2	20	26

Water level and atmospheric pressure data was collected at NOAA station 8534720 (acyn4) in Atlantic City, NJ. The update rate on the atmospheric pressure data was every 6 minutes while it was every minute for the water level data.

III. Results

Data collection began in August 2016. For this paper we focus on data collected between January 1 and June 16, 2019. The cross shore (Figure 3) and along shore (Figure 4) q-factor data from each of the four stations hover around zero with excursions from there. The statistics of the onshore and alongshore q-factor are given in Table 2. The q-factor for all stations ranges from -3,000 to 6,000 while a majority (90%) of time the q-factor is between -500 and 500. The median and mode q-factor for all stations is zero. The mean for all stations is slightly above zero. The maximum and minimum q-factor from the software appears to be 6,300 and -2,520 respectively. Histograms of onshore q-factor were created from the data (Figure 5). The y-axis in the figure is logarithmic in order to display the five orders of magnitude in the data frequency plot. All sites display a positive skewness. The BRNT station displayed the largest number of spikes above 2,000 (60 in the onshore and 64 in the alongshore).

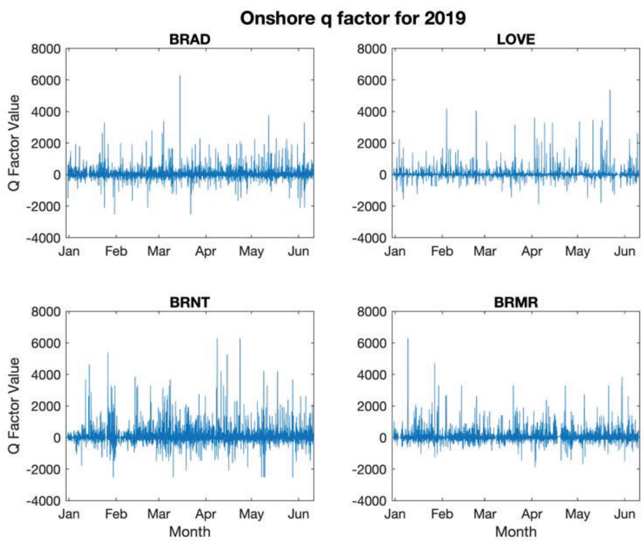

Figure 3: Onshore q-factor values from January to June 2019 for the four HFR stations in the study.

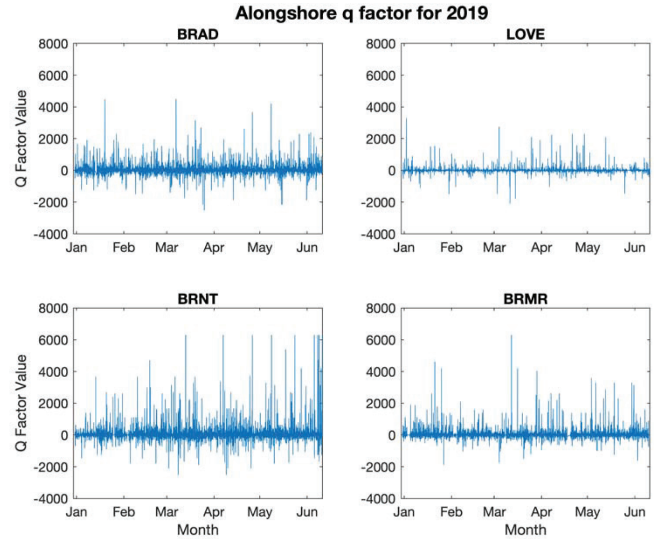

Figure 4: Alongshore q-factor values from January to June 2019 for the four HFR stations in the study.

If a spike in the q-factor indicates an oncoming tsunami wave then we wanted to investigate the high q-factor spikes. Table 3 shows the station, time and value for q-factor spikes above 4,000. We then examined the spectra nearest the time of the q-factor spike to see how the spectra was behaving and if it had an influence on the q-factor. For example, Figure 6 shows the spectra from each of the three channels of the SeaSonde from the BRMR station on January 26, 2019 at 23:00:49 UTC. There was a considerable amount of interference plaguing the spectra at this time as evidenced by the green and yellow vertical striping on the left side of the figure near -4 m/s Doppler velocity. Each of the spectra were graded on a low, medium or high noise level. The spectra for this time period was graded as a high noise level. The last column in Table 3 shows the qualitative assessment of the noise level at the time of the q-factor spike. The spectra noise level was medium to high on 70% of the q-factor spikes above 4,000.

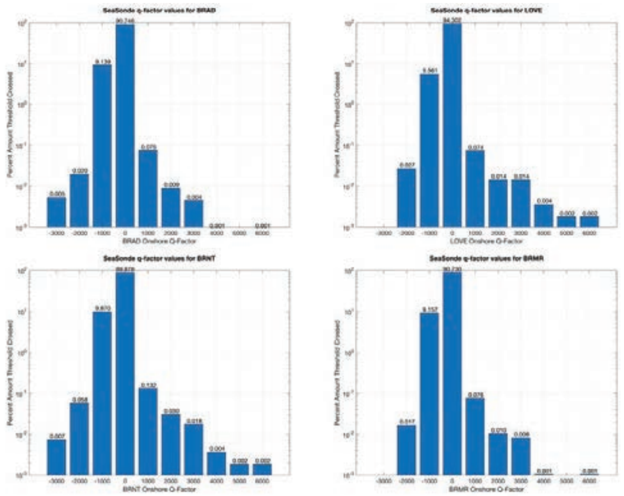

Figure 5: Histogram of the onshore q-factor from the four HFR stations in the study. The percentage occurrence for each bin is shown at the top of each bar.

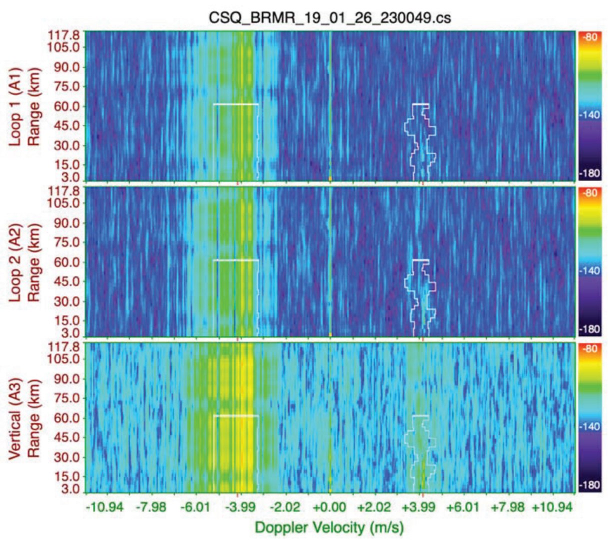

Figure 6: Spectra file from the BRMR station for January 26, 2019. Each panel represents the spectra from the three channels in the receive antenna. Note the large amount of interference on the left side of the Doppler.

Table 2: Summary statistics of the q-factor reading for each of the four HFR stations used in the study from January 1-June 16, 2019.

Onshore	BRAD	BRNT	LOVE	BRMR
mean:	3	5	3	3
median:	0	0	0	0
mode:	0	0	0	0
std:	78	116	91	83
n:	111,983	108,472	55,743	96,328
max:	6,300	6,300	6,300	6,300
min:	-2,520	-2,520	-1,890	-1,890
Alongshore	**BRAD**	**BRNT**	**LOVE**	**BRMR**
mean:	2	5	1	3
median:	0	0	0	0
mode:	0	0	0	0
std:	75	122	52	75
n:	111,983	108,472	55,743	96,328
max:	4,500	6,300	3,300	6,300
min:	-2,520	-2,520	-2,100	-1,890

Table 3: Instances when the onshore q-factor broke 4,000 and the accompanying qualitative assessment of the noise level in the spectra at the time.

Station	Date	q-factor	Noise Level
BRAD	3/14/19 23:00	6,000	low
BRAD	6/11/19 1:00	4,000	low
BRMR	1/9/19 10:00	6,000	medium
BRMR	1/26/19 23:00	4,000	high
BRNT	1/14/19 7:00	4,000	low
BRNT	1/26/19 12:00	5,000	medium
BRNT	4/8/19 8:00	6,000	low
BRNT	4/10/19 22:00	4,000	medium
BRNT	4/14/19 23:00	5,000	medium
BRNT	4/23/19 9:00	5,000	medium
BRNT	5/9/19 0:00	4,000	medium
BRNT	5/18/19 2:00	4,000	medium
LOVE	2/3/19 19:00	4,000	low
LOVE	2/23/19 6:00	4,000	medium
LOVE	5/22/19 7:00	5,000	medium
LOVE	6/13/19 3:00	6,000	medium

A. Meteotsunami 2019

A storm system moved through the study area on May 29, 2019. A spike in atmospheric pressure was observed at NOAA gauge acyn4 in Atlantic City, NJ (Figure 7). This spike was most likely the result of a short-lived localized high-pressure zone associated with the downdraft of the squall line that moved through. This weather pattern was similar to the one that generated a meteotsunami in 2013 [8, 9]. This down burst of air generated a ripple on the surface of the ocean that propagated outwards. Anomalous water levels were detected in Atlantic City, NJ (Figure 8) Lewes, DE and Montauk, NY. DART buoy 44402 also detected the wave at May 30, 2019 00:45 GMT with only an amplitude of 1.8 cm. Station BRMR was the only radar site that showed spikes in the q-factor reading after the passage of the storm (Figure 9). The q-factor spike for this event broke 3,000 in the onshore and alongshore direction. The timing of the first q-factor spike occurred at 00:40 GMT while the water level spike occurred at 02:40 GMT. So, the first signal of this small meteotsunami was detected by the HF radar two hours before the water level gauge on shore.

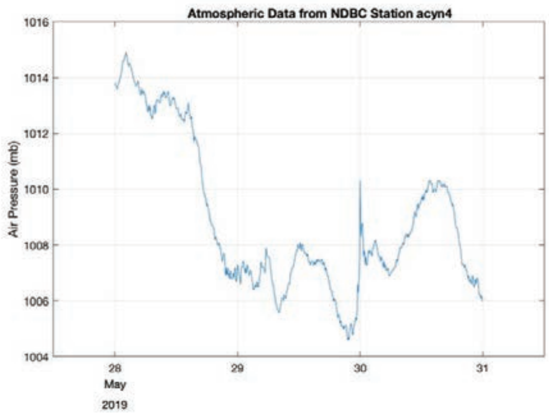

Figure 7: Atmospheric pressure from May 28-31, 3019 from station acyn4. The record shows a spike in the pressure record at the beginning of May 30.

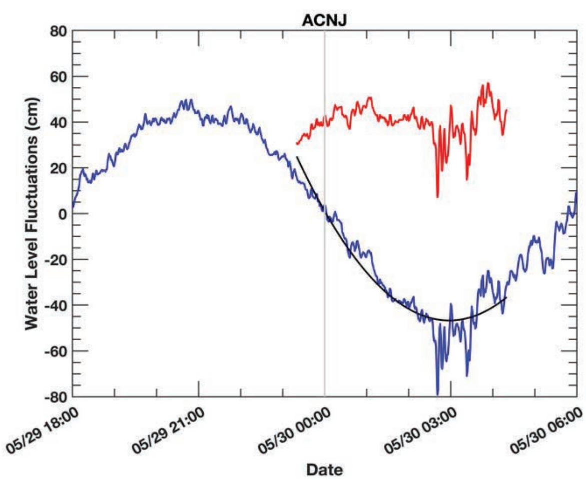

Figure 8: Water level data from gauge in Atlantic City, NJ (acyn4) from May 29-30, 2019 (blue line). The residual (red line) from the polynomial fit (black line) of the water level data is also shown. The residual is offset +40 cm/s from the x axis.

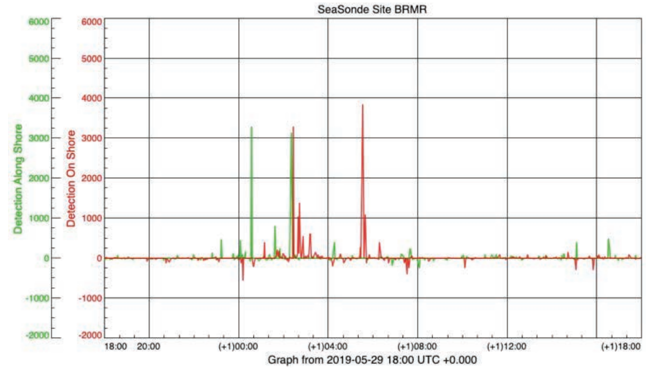

Figure 9: Onshore (red) and alongshore (green) q-factor from the BRMR station from May 29-30, 2019. Note the q-factor spikes at the beginning of May 30.

IV. Discussion

Based on the findings in Table 2, the presence of HF noise is a likely contributor to generating false alarms in the tsunami detection. For the SeaSonde HF radar external noise is much greater than internal thermal noise, so it is worthwhile examining the causes of external noise and developing ways to minimize its effects on the radar measurements. External noise originates from natural sources like lightning and man-made signals like switching-mode power supplies, power transmission lines and radio transmissions in the HF band. The noise from lightning can be generated locally or travel long distances through the ionosphere. There is also a daily cycle of the noise level as measured by the SeaSonde. Figure 10 shows the noise floor measurement of the radar as a function of the hour of the day. The 13 MHz stations (BRAD, BRNT and BRMR) all display lower noise levels between 0 and 12 hours and higher noise levels between 12 and 23 hours. The 5 MHz station (LOVE) is just the opposite with higher noise levels at night and lower during the day. The local time for the stations is five hours behind UTC, so 0-12 UTC is roughly night and 12-23 UTC is daylight. The noise floor is highest at the BRNT station and that location has 3 times q-factor above 2,000, so there appears to be a linkage between the noise level at a station and the q-factor output.

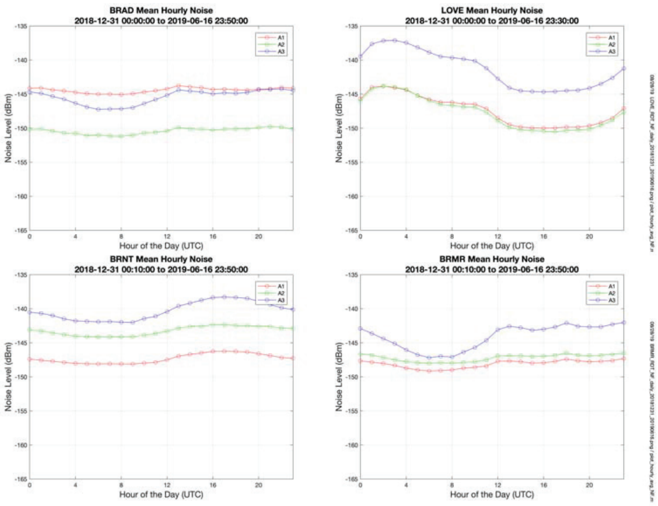

Figure 10: Average noise floor measurements (y axis) for channel 1 (red), channel 2 (green) and channel 3 (blue) vs time of day (x axis) for the four HFR stations in the study from December 31, 2018 to June 16, 2019.

We would like to determine an appropriate threshold for the q-factor to generate a tsunami warning. The threshold is currently set at 1,000 but that was done with no prior testing of the software for the Mid-Atlantic region. In the Results section the statistics of the q-factor were presented and the stations generated a q-factor that exceeded 1,000 an average of five times a week. The stations generated a q-factor that exceeded 2,000 an average of one time per week. This seems like a better threshold as it would not generate an excessive amount of false alarms and this would have generated a correct detection for the May 30 event.

V. Conclusions

Tsunami detection software from CODAR Ocean Sensors has been operating at four High Frequency radar stations since June 2016. The data recorded from January to June 2019 was analyzed for this paper. The output of the software is a q-factor that is updated with each time step which is approximately every two minutes. When there is a spike in the q-factor reading, that signals the potential for an oncoming tsunami wave. The statistics of the q-factor were calculated at each of the four stations. The median and mode q-factor at each station was zero for the five-month analysis and the range is between +6,300 and -2,520. On average, the stations generate a q-factor above 2,000 once a week. This seems like a good threshold to generate a warning as it will not tax the operator too much to further investigate if a tsunami is approaching.

Acknowledgment

Funding for this research was provided through a grant from CODAR Ocean Sensors and the NOAA Tsunami Research Advisory Council (TRAC).

References

[1] I. Vilibić *et al.*, "Atmospheric processes responsible for generation of the 2008 Boothbay meteotsunami," in *Meteorological Tsunamis: The US East Coast and Other Coastal Regions*: Springer, 2013, pp. 25-53.

[2] E. J. Anderson, A. J. Bechle, C. H. Wu, D. J. Schwab, G. E. Mann, and K. A. Lombardy, "Reconstruction of a meteotsunami in Lake Erie on 27 May 2012: Roles of atmospheric conditions on hydrodynamic response in enclosed basins," *Journal of Geophysical Research: Oceans,* vol. 120, no. 12, pp. 8020-8038, 2015.

[3] C. A. Wertman, R. M. Yablonsky, Y. Shen, J. Merrill, C. R. Kincaid, and R. A. Pockalny, "Mesoscale convective system surface pressure anomalies responsible for meteotsunamis along the US East Coast on June 13th, 2013," *Scientific reports,* vol. 4, p. 7143, 2014.

[4] B. Lipa, D. Barrick, and J. Isaacson, "Coastal Tsunami Warning with Deployed HF Radar Systems," *Tsunami,* p. 73, 2016.

[5] B. J. Lipa, D. E. Barrick, J. Bourg, and B. B. Nyden, "HF radar detection of tsunamis," *Journal of Oceanography,* vol. 62, no. 5, pp. 705-716, 2006.

[6] B. Lipa, J. Isaacson, B. Nyden, and D. Barrick, "Tsunami arrival detection with high frequency (HF) radar," *Remote Sensing,* vol. 4, no. 5, pp. 1448-1461, 2012.

[7] H. J. Roarty *et al.*, "Operation and Application of a Regional High Frequency Radar Network in the Mid Atlantic Bight," *Marine Technology Society Journal,* vol. 44, no. 6, pp. 133-145, 2010.

[8] B. Lipa, H. Parikh, D. Barrick, H. Roarty, and S. Glenn, "High-frequency radar observations of the June 2013 US East Coast meteotsunami," (in English), *Natural Hazards,* pp. 1-14, 2013/12/17 2013.

[9] G. Dusek *et al.*, "A meteotsunami climatology along the US East Coast," *Bulletin of the American Meteorological Society,* no. 2019, 2019.

The Impact of Reprocessing Efforts on the Mid-Atlantic's Surface Current Product

Teresa G. Updyke
Center for Coastal Physical Oceanography
Old Dominion University
Norfolk, VA, USA
garner@ccpo.odu.edu

Hugh J. Roarty, Michael Smith, and Laura Nazzaro
Rutgers University
New Brunswick, NJ, USA
hroarty@marine.rutgers.edu

***Abstract*— The Mid-Atlantic Regional Association Coastal Ocean Observing System (MARACOOS) has undertaken a reprocessing effort for their 6-kilometer gridded surface current product which utilizes data from the network of long-range High Frequency (HF) radar systems. Radar data from January 2017 to December 2017 have been re-examined and reprocessed. It is worthwhile to consider how errors in the real-time processing may be corrected by reprocessing and what improvements may be realized in the total vector map product by such an effort.**

Keywords—high frequency radar; surface currents; Mid-Atlantic; quality control

I. INTRODUCTION

A network of 17 long-range High Frequency (HF) radar stations contribute radial data to a MARACOOS 6-kilometer gridded surface current data product (Fig. 1). The 5 MHz network covers the 1,000 km of Mid Atlantic Bight Shelf from Cape Hatteras to Cape Cod. The near real-time version of the data product is computed from radial data that is subject to several quality assurance (QA) and quality control (QC) procedures [1,2].

These procedures include quality assurance methods that are conducted on the radar hardware and site visits at least once every six months. Operators periodically check the settings that extract first order sea echoes (or Bragg echoes) from the rest of the radar Doppler spectra. This extracted data is processed to radial data. The goal is to include all first order echo, but to exclude any noise or interference as much as possible. Antenna calibrations are performed typically once a year or when site diagnostics indicate that the calibration file needs to be updated. These calibrations are important for accuracy in "direction finding", the process which places radial vectors into bearing bins within a range ring on the radial grid.

Quality control of radial data involves routine remote inspection of the radial data and system diagnostics. For QC purposes, radial vectors are plotted with the blue/red colormap where blue indicates vectors that are travelling towards the radar and red vectors indicating currents that are travelling away from the radar, consistent with redshift and blueshift from electromagnetic Doppler phenomenon. We utilize the 25-hour mean radial map and a weekly plot of average radial velocity and radial vector count as quick diagnostics for station health. These diagnostics are similar to those of previous researchers. If a station or data type (ideal or measured) is not in agreement with surrounding stations, the operator begins an inspection of the system to look for problems. We have also found that a consistent average radial bearing [2] is an indication of a properly operating station and if this measurement has a step change or becomes erratic then that is an indication of a failure somewhere within the system.

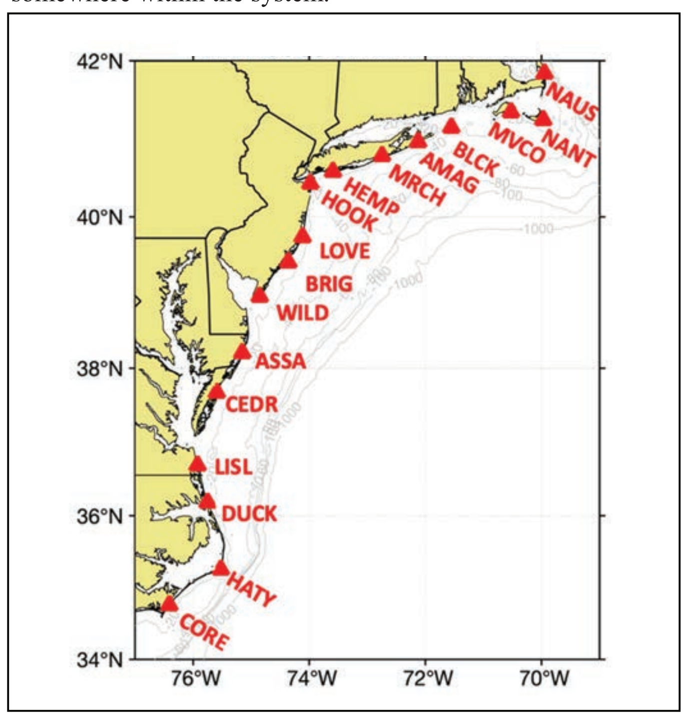

Fig. 1. Locations of the 5 MHz High Frequency radar stations that contribute to the MARACOOS surface current product.

Despite the routine use of QA and QC procedures, the real-time product carries the potential for errors that might be corrected in post-processing. For example, events may occur

This work was funded by NOAA Award Number NA16NOS0120020 "Mid-Atlantic Regional Association Coastal Ocean Observing System (MARACOOS): Preparing for a Changing Mid Atlantic". Sponsor: National Ocean Service (NOS), National Oceanic and Atmospheric Administration (NOAA) NOAA-NOS-IOOS-2016-2004378 / CFDA: 11.012, Integrated Ocean Observing System Topic Area 1: Continued Development of Regional Coastal Ocean Observing Systems.

978-0-578-57618-3 ©2019 MTS

that invalidate a calibration pattern or damage a radar and there is typically some delay between the time of the event and when the data is pulled from the real-time processing. This delay is often a reason to reprocess a portion of the radial maps from spectra or to choose a different pattern than the one that was used in real-time total processing.

II. Methods

A. Data Review & Radial Reprocessing

The first step in the reprocessing effort was to check for data gaps in the real-time product and collect the missing hourly radial files into the appropriate directories at the data assembly center (DAC) if those files could be found. If the radial files were not found, it was sometimes possible to generate the files from Doppler spectra. A more common problem was that a site communication problem and/or delay in file transfer excluded a radial file from real-time processing, but the file later became available. The real-time software is able to handle up to a 7 day delay in data transfer latency.

The next step involved a review of the logs, diagnostics, radial distributions and averages from each station to check for any events that might signal a change in radial quality. Radial maps surrounding those events were reviewed to check for velocities that did not appear to be realistic or were inconsistent with nearby data or data from neighboring stations. In some cases, data from a station needed to be excluded from total vector processing for a period of time. In other cases, applying configuration changes and reprocessing from spectra significantly improved the radial maps. Radial maps processed using a measured pattern were preferred over maps processed using the assumption of an ideal pattern if a suitable pattern measurement was available [3].

Diagnostics we found particularly useful included sea echo amplitudes and phases, signal to noise, noise floor, and average radial bearing. For example, a step change in the sea echo amplitude of the receive antenna often signals a change in the antenna pattern. In this case, spectra might be reprocessed to radials using a pattern that was measured after the step change. A step change in average radial bearing with no coinciding change in antenna bearing can also signal an error in the configuration that might be corrected in reprocessing. Data from stations reporting low signal to noise and/or high background noise diagnostics for long periods of time were often indicative of equipment failures and were excluded from processing.

Weekly average and distribution plots were reviewed by the QC team (a group including operators, technicians and scientists). Plots for ideal pattern and measured pattern radial maps were reviewed side-by-side. Angular gaps in the weekly radial distribution plots or anomalously placed radials in the average maps were indications that a pattern type might not suitable or that maps might need to be reprocessed from spectra.

B. Radial Quality Control

A major component of the reprocessing effort focused on the implementation of QARTOD quality control (QC) tests [4,5]. Version 1.0 of the QARTOD Manual for Real-Time Quality Control of High Frequency Radar Surface Current Data describes several QC tests that may be performed at different levels of radar data processing including tests for the spectra, radial component and total vector processing stages. The present study has focused on the tests for radial data. The North Carolina station radials had an additional radial metric QC test applied [6]. The QARTOD radial tests that have been applied are listed in Table 1 along with threshold values that were chosen to implement the tests. The QC06 and QC09 test flags apply to the entire file and are reported in the header metadata. In this case, a failure flag means that none of the radials in file are included in total vector computations. The QC07, QC08 and QC10 apply to individual radial vectors within the file and are reported in extra columns for each row of radial data contained in the file.

The syntax test requires that the following metadata be present in the file: file type LLUV, site code, timestamp, site coordinates, antenna pattern type and time zone. Other requirements include 1) the file name timestamp must match the timestamp reported within the file, 2) radial data tables (Lon, Lat, U, V, ...) must not be empty 3) radial data table columns stated must match the number of columns reported for each row 4) site location must be within range: $-180 \leq \text{Longitude} \leq 180$ $-90 \leq \text{Latitude} \leq 90$ and 5) time zone must be Greenwich Mean Time.

TABLE I. QARTOD RADIAL QC TESTS APPLIED

Test Code	Radial QC Test List		
	Test Name	***Suspect Flag***	***Fail Flag***
QC06	Syntax	N/A	see text
QC07	Max Threshold	N/A	velocity > RSPDMAX *RSPDMAX = 300 cm/s*
QC08	Valid Location	N/A	*VFLG = 128*
QC09	Radial Count	RCMIN[a] >= count <= RCLOW[a]	count < RCMIN[a]
QC10	Spatial Median	N/A	velocity > CURLIM *RCLIM=2.1 cells, ANGLIM = 10 degrees, CURLIM[b] = 30 or 50 cm/s*

a. RCMIN and RCLOW are site dependent thresholds.

b. Stations LISL, DUCK, HATY, CORE use 50 cm/s. All others use 30 cm/s.

The radial count test will flag a radial file if it contains less than a minimum number of radial vectors (RCMIN). The RCMIN threshold is site specific and dependent on the number of radial grid cells that are available given 40 range cells, five degrees of bearing resolution and omitting any cells that are invalid (e.g. over or behind land). RCMIN is defined as 10% of the available radial grid cells "rounded" to the nearest 25. RCLOW is defined as 30% of the available radial grid cells "rounded" to the nearest 25.

Each of the QARTOD tests were converted into Python code and are assembled in a GitHub repository (https://github.com/rucool/codar_processing). The assembled radial data is then run through the QC code and new radial files with QC metadata and QC flags are generated.

C. *Total Vector Generation*

Measured pattern radials were chosen as the preferred radial type for most radar stations for the 2017 reprocessing. DUCK, HATY, and CORE contributed ideal pattern radials. Ideal pattern radials were also used for BRIG (July-Sept) and NANT (Aug-Sep) stations.

Radial vectors that received failure flags for one or more of the QC tests were excluded from total vector processing. After radial reprocessing and radial filtering based on QARTOD test flags, an updated "best" set of radials were used to recompute total vectors maps. Two sets of totals were computed: one set using an unweighted least squares (UWLS) method and the other set using an optimal interpolation (OI) method [7,8]. In this paper, we focus on the UWLS product. At least three radial vectors and a minimum of two contributing radar stations were required to compute a total vector. The search radius for total vector processing was set to 10 kilometers. Vectors with GDOP total error values greater than 1.25 were removed from the vector maps. Computations were performed using the HFR-Progs MATLAB toolbox. An online summary of the reprocessing effort is available at this url: https://marine.rutgers.edu/~michaesm/reprocessed/index.html

D. *Evaluation*

An analysis of the QARTOD radial QC flag data has indicated which tests flag the most radials and where failure flags occur most often within radar coverage areas.

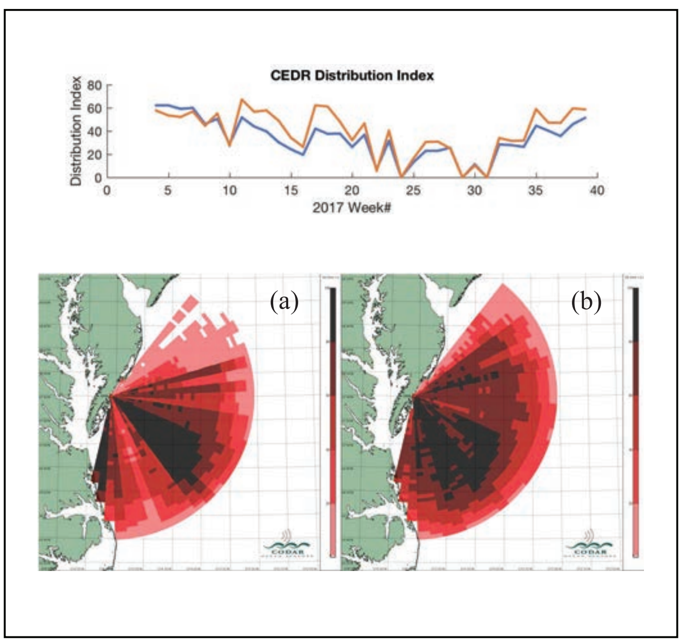

Fig. 2. Top panel: Weekly radial distribution index for real-time (blue) and reprocessed (orange) radials at the CEDR radar station. Bottom panels: Weekly radial distributions at CEDR station using (a) real-time and (b) reprocessed radial maps for April 24 – Apr 30 2017.

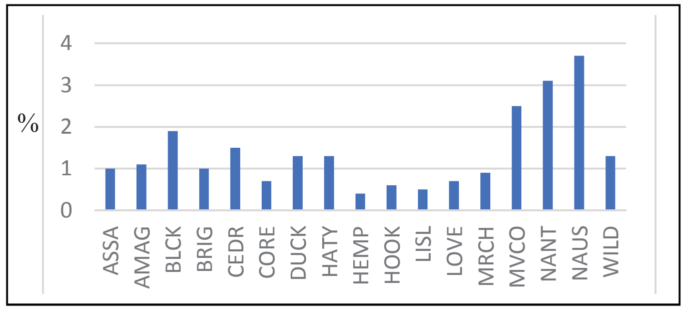

Fig. 3. On average, the percent of radials in a file that fail the spatial median QC test. Only failures for radials at valid locations were considered for this chart.

Finally, the real-time and reprocessed total vector map products were compared to assess the overall impact of the effort. Complex correlations [9] and root mean square differences were calculated between the real-time velocity time series and the reprocessed velocity time series. The impact of reprocessing on monthly averages was also investigated.

III. Results

A. *Real-time Radials vs Reprocessed Radials*

In 2017, radials were reprocessed from spectra for several radial sites to apply updated patterns and this improved data coverage. For example, CEDR station radials from January 26, 2017 through September 25, 2017 were reprocessed with a pattern that was measured on September 25, 2017. Fig. 2 compares a weekly radial distribution index for the real-time measured pattern maps and the reprocessed measured pattern maps. The weekly index is the number of radial grid cells containing data at least 80% of the time divided by the total number of radial grid cells expressed as a percentage. The total number of grid cells was the count of all cells that contained at least one radial vector during the week. No cells over land were included. The weekly distributions of reprocessed radials often showed improved radial coverage according to this metric. Week 17 of 2017 (Apr 24 to Apr 30) is one example of a dramatic improvement. The bottom panels of Fig. 2 compare the distributions for that week. The reprocessed radials also produced average velocity maps containing less outliers.

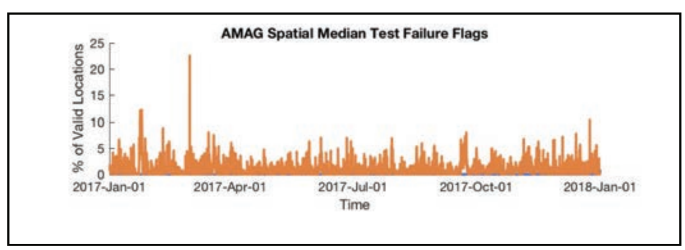

Fig. 4. Percent of radials in each hourly file that were flagged by the spatial median QC test at the AMAG station.

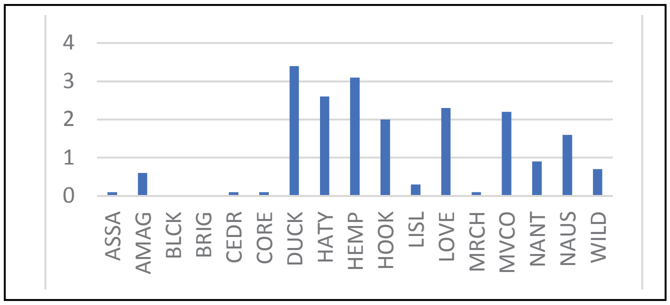

Fig. 5. Percent of available radial files that failed the radial count QC test.

The North Carolina stations (DUCK, HATY and CORE) had been producing radial maps in near-real-time on site using radial metric QC [5] since August 2017 but those versions, called the QCD versions, of the radial maps were not used for total generation in the real-time totals data product until late in 2017. In the reprocessing effort, QCD versions were used for the entire year.

Filling in data gaps due to missing or delayed files resulted in the inclusion of 7,270 more files in the reprocessed data set for 2017.

B. *Radial Quality Control Flag Statistics*

The real-time product did not make use of radial QC flags. It did however, exclude radials in invalid locations which were identified by codes produced by the manufacturer software.

The syntax test failed for a small set of files at six sites coinciding (surprisingly) with the 2017 switch from Eastern Daylight Time to Eastern Standard Time. Timestamps in the file headers of four hourly files were offset by one hour from the times given in the filenames. Data at all stations were collected in UTC time.

The maximum velocity QC test was put into practice for this reprocessing effort. However, in 2017, radar stations had a limit set on the maximum velocity that was allowed to pass from the spectra to radial stage of processing and this maximum was less than the maximum of 300 cm/s chosen for the QC test. Therefore, this test failed no radials. In future processing, the velocity limits will no longer be set at the radar station or they will be set at a much higher level in this earlier processing stage so that the QC max threshold test flags will become effective and will provide flag statistics that may be analyzed.

On average, the spatial median test failed between 0 and 4% of the radials (at valid overwater locations) in hourly files (Fig. 3). NAUS had the highest average of 3.7%. At most stations, the hourly time series show that the percent of radials with fail flags usually varies within the 0-7% range and includes some spikes up to 12% or 25%. Fig. 4 is an example for a single station. Sudden shifts in amounts of failures often coincide with changes to site configuration settings.

For the spatial median test, maps were created to highlight the most frequently flagged locations at each station. Highlighted bearing spokes near coast or edges of coverage are common in these maps. Most radials in the reprocessed data set were measured pattern radials and the measured radial type is more likely to show a pattern that lines up along a bearing or set of bearings since errors may concentrate along bearing lines. The arcs as well as partial spokes in mid to far ranges are signs of the test removing ionospheric interference. Close ranges at all bearings were more frequently flagged at NANT and MVCO. Maps for stations near the Gulf Stream showed that the test was often flagging the Gulf Stream gradient. In order to minimize this erroneous flagging, the current difference threshold at those sites (DUCK, HATY, CORE and LISL) was increased from 30 cm/s to 50 cm/s. The problem was not completely eliminated but flag counts decreased as a result.

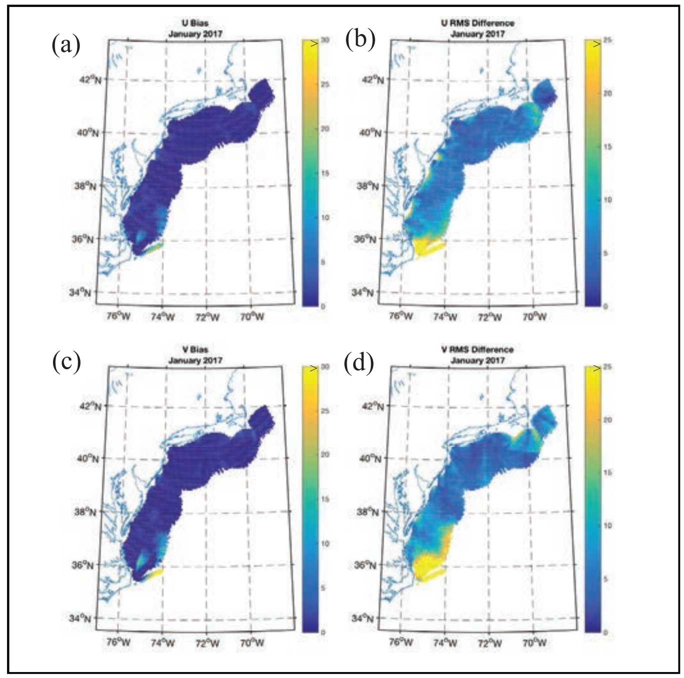

Fig. 6. Biases between the real-time and reprocessed surface currents for the U and V components of velocity are shown in (a) and (c) respectively. Unbiased root mean square differences between the real-time and reprocessed surface currents for the U and V components are shown in (b) and (d) respectively.

Fig. 5 shows radial count file failures given as a percent of files that failed out of a total number of available radial files for 2017. 1794 radial files were excluded based on the radial count test.

C. *Real-time versus Reprocessed Total Vector Products*

A comparison of surface current maps for the month of January shows that the bias, or difference between means, for U and V components is below 10 cm/s for most of the coverage area (Fig. 6). The unbiased root mean square differences are typically less than 15 cm/s. In the south, in locations where radial data was added, where radial metric QC was applied, and where currents are stronger due to the presence of the Gulf Stream, there are greater biases as well as greater unbiased root mean square differences. Fig. 7 shows the monthly average vectors at grid locations with 60% data availability after removing data with GDOP > 1.25 for a southern section of the Mid-Atlantic. Data coverage is greater in the reprocessed product and reveals the Gulf Stream currents. Also, a number of suspect vectors near the coast with strong average currents directed offshore have been eliminated in the reprocessed product.

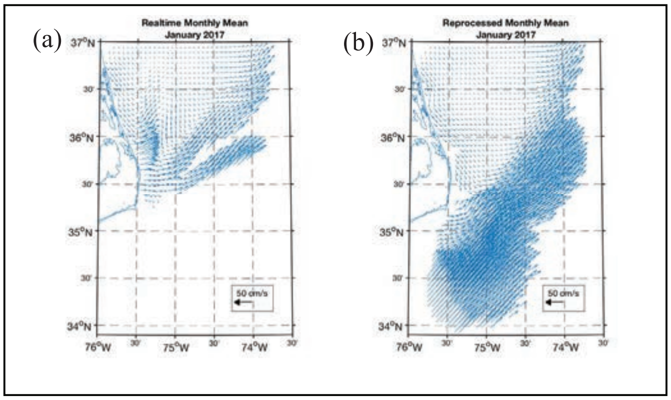

Fig. 7. January 2017 average current vectors for the (a) real-time and (b) reprocessed surface current products.

IV. Discussion

Observing system networks should weigh the potential benefits that may result from reprocessing HF radar data with the time commitment. The initial radial review relied heavily on the expertise of the QC team to make judgment calls and reprocess radials from spectra when deemed appropriate. This is a time-consuming step, but the impact on the radials and totals can be quite significant. The application of radial QC flags is comparatively more objective and efficient. Once QC test thresholds are assigned, this process is completely automated. However, QC flags may not catch some errors that would be easily noticed by an operator looking at a radial map.

Many types of problems can be addressed by reprocessing from spectra. Cable swaps are a good example of a mistake that is easy to correct in reprocessing and one that is extremely important to correct because it can affect a large area in a significant way. Cable swaps can even generate maps with radials going the opposite direction of the true ocean current.

First order determination and direction finding are crucial steps in the creating the radial map and yet they are also parts of the process that can be dramatically altered for reprocessing. For example, if new algorithms are developed that improve removal of ionospheric interference from spectra, software running those algorithms could be utilized for reprocessing. This has the potential to make substantial improvements to data collected years ago and provide better quality data sets for researchers.

Differences between real-time and reprocessed data will be greatest in hourly plots and daily average plots. Weekly or monthly averages of total vector data and averages over large spatial areas will not differ as much. A researcher who would like to use surface current data to inform a study involving shorter time scales and/or a smaller geographic area may see significant benefit to using a reprocessed data product.

V. Conclusions

This paper has presented initial findings on the impact of reprocessing HFR data and has shown that significant differences occur between real-time and reprocessed products. However, much more may be done to show the impact on data quality. Future analysis will compare the real-time and reprocessed products to other data sources.

Acknowledgment

We thank the University of North Carolina and the Coastal Studies Institute for the use of HF radar data from the North Carolina radar stations. Sara Haines applied radial metric QC to radial data from UNC stations and kindly provided us with those reprocessed radial files for this effort. Thanks to the radar operators who helped maintain the long-range radar systems in 2017: Ethan Handel, Rich Arena, Mike Muglia, Patterson Taylor, Nicolas DeSimone and Anthony Whipple. Josh Kohut provided guidance on how to approach this reprocessing effort and helped determine our initial steps in the effort. Josh Kohut and Travis Miles also helped review and annotate hourly maps of reprocessed totals.

References

[1] H. Roarty, M. Smith, J. Kerfoot, J. Kohut, and S. Glenn, "Automated quality control of High Frequency radar data," in *Oceans, 2012*, 2012, pp. 1-7.

[2] H. Roarty, L. Palamara, J. Kohut, and S. Glenn, "Automated quality control of high frequency radar data II," in *OCEANS 2016 MTS/IEEE Monterey*, 2016, pp. 1-3.

[3] J. Kohut and S. Glenn. "Improving HF radar surface current measurements with measured antenna beam patterns." Journal of Atmospheric and Oceanic Technology., vol. 20(9), pp. 1303-1316. 2003.

[4] Manual for Real-Time Quality Control of High Frequency Radar Surface Current Data: a Guide to Quality Control and Quality Assurance for High Frequency Radar Surface Current Observations. Version 1.0. Integrated Ocean Observing System (U.S.), U.S. Department of Commerce, National Oceanic and Atmospheric Administration, National Ocean Service, Integrated Ocean Observing System, Silver Spring, MD, 2016.

[5] Manual for the Use of Real-Time Oceanographic Data Quality Control Flags. Version 1.1. Integrated Ocean Observing System (U.S.), U.S. Department of Commerce, National Oceanic and Atmospheric Administration, National Ocean Service, Integrated Ocean Observing System, Silver Spring, MD, 2017.

[6] Haines, S., H. Seim and M. Muglia. "Implementing Quality Control of High-Frequency Radar Estimates and Application to Gulf Stream Surface Currents," Journal of Atmospheric and Oceanic Technology, vol. 34(6), pp. 1207-1224. 2017,

[7] Kim, S. Y., E. J. Terrill, and B. D. Cornuelle, "Mapping surface currents from HF radar radial velocity measurements using optimal interpolation," J. Geophys. Res., vol. 113(C10), 2008.

[8] Kohut, J., Roarty H.J, Randall-Goodwin, E., Glenn, S. and C. S. Lichtenwalner, "Evaluation of two algorithms for a network of coastal HF radars in the Mid-Atlantic Bight," Ocean Dynamics, vol. 62, pp. 953–968. 2012.

[9] Kundu, P. "An analysis of inertial oscillations observed near Oregon coast," Journal of Physical Oceanography, vol. 6(6), pp 879-893, 1976.

Evaluation of Bistatic High Frequency Radar Data

Laura Nazzaro
Center for Ocean Observing and Leadership
Department of Marine and Coastal Sciences
Rutgers University
New Brunswick, NJ
nazzaro@marine.rutgers.edu

Hugh Roarty
Center for Ocean Observing and Leadership
Department of Marine and Coastal Sciences
Rutgers University
New Brunswick, NJ
hroarty@marine.rutgers.edu

***Abstract*—High Frequency radar data is typically collected using a monostatic configuration, in which a single HFR antenna acts as both a transmitter and a receiver. We analyze data collected with a bistatic configuration, where the transmitter and receiver are on separate HFR antennas. We compare bistatic data to monostatic data and regional drifter data, and compare errors and coverage of totals generated with monostatic and bistatic data to totals generated with only monostatic data. Error values in bistatic data were slightly higher than in monostatic data, but data correlated well with other surface current data sources in the region. Further, totals error decreased with inclusion of bistatic data, which has potential to increase data coverage during periods of large data gaps. Inclusion of bistatic data can provide large benefits to surface current data available in the Mid-Atlantic Bight, particularly given that it uses pre-existing antennas so there is very little cost associated with collecting the additional data.**

Keywords—bistatic; high frequency radar; Mid-Atlantic Bight; ellipticals; surface currents

I. Introduction

Typical High Frequency radar (HFR) surface current data are measured by a signal transmitted and received by a collocated antenna, referred to as a monostatic configuration. This results in a field of radial current components directed towards and away from the antenna (Fig. 1a). Radial fields from multiple antennas can be combined to create a regional map of total current vectors [1]. Another type of surface current measurement is performed by transmitting a radio signal from one location and receiving it at a geographically separate radar, referred to as a bistatic geometry [2, 3]. This creates an elliptical field of surface current components with focal points at the locations of the two antennas (Fig. 1b); while radial vectors are measured with headings (direction of velocity component measured) that effectively point directly towards the radar antenna, the headings of measured elliptical velocity components are pointed in between those two focal points. Because the elliptical fields can be generated using antennas that are simultaneously measuring radial fields, they can provide additional information that can be used to improve data coverage and reduce uncertainty in regional totals products, without any additional equipment.

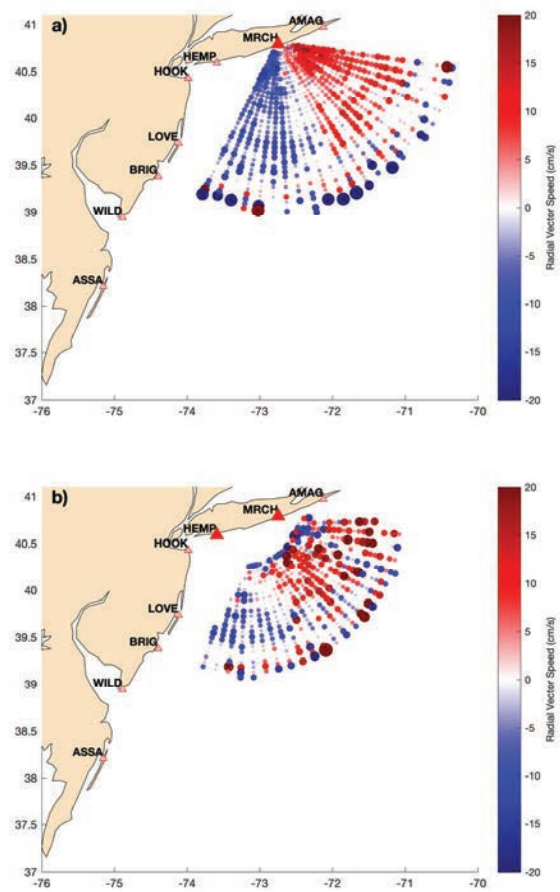

Fig. 1. Twenty-four hour average map of vector currents from radial station with monostatic data from MRCH (a) and bistatic data generated by transmitter HEMP and receiver MRCH (b) from January 15-16, 2021. The colormap and size of the dot are scaled to the mean current velocity (blue away from the radar, red towards) over the 24 hours. Pink triangles denote HFR antennas for the long-range MAB network, with transmit and receive sites for each map indicated by larger red markers.

Surface currents along the U.S. Mid-Atlantic Bight (MAB) shelf have been well sampled by HF radar for over a decade [4,5]. The long-range network is comprised of 17 antennas extending from Cape Hatteras, NC to Cape Cod, MA. Radial and elliptical fields from these sites can be combined to generate a field of totals vectors, u and v velocity components that extend from shallow water (starting in water depths greater than 15 m) out to the shelf break (180 km from the coast). Thus far, however, while some elliptical fields have been generated, only radial fields have been used for totals generation. We evaluated five sets of bistatic data in the New York Bight from the long-range MAB HFR Network. This additional data can increase regional vector component data by about 20% (Fig. 2). Three of the elliptical fields covered the northern NY Bight, based on one HFR receiver (Moriches/MRCH) coupled with three different HFR transmitters (Sandy Hook/HOOK, Hempstead/HEMP, and Amagansett/AMAG), and two additional elliptical fields covered the southern NY Bight based on one receiver (Brigantine/BRIG) coupled with two different transmitters (Loveladies/LOVE and Wildwood/WILD). Each HFR station also operated as a collocated transmitter and receiver generating radial fields. Elliptical data fields were compared to neighboring radial data fields as well as to drifter data available in the region, and the effect of including elliptical data fields in the regional totals product was also evaluated.

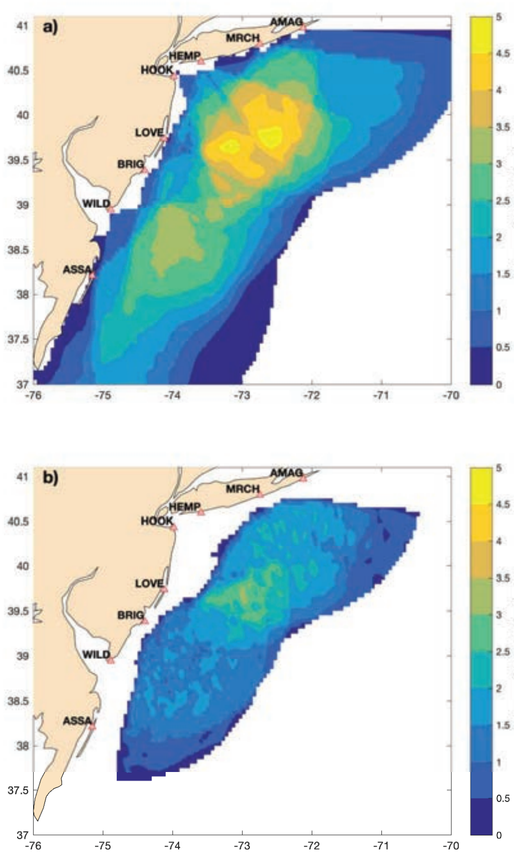

Fig. 2. Average number of radial data points per single map from monostatic data available to use as input to and used in standard totals products (a), and average number of additional data points available if the five bistatic datasets used in this analysis are also used as input (b). Calculated using data from January 2021.

II. Analysis

A. Ellipticals Compared to Radials

The elliptical vector data was compared to the radial data from the seven contributing HFR stations (MRCH, HOOK, AMAG, HEMP, BRIG, LOVE, and WILD) during three week-long periods with good coverage (April 18-25, 2018 in the southern NY Bight, August 18-25 in the northern NY Bight, and January 13-20, 2021 for both sets) by mapping a set of radials and a set of ellipticals to the same spatial grid and comparing component velocities in areas of the grid where velocity heading was within a 15° difference. Only radial data with measured antenna patterns were utilized in the analysis. Correlation strength (r) and root mean square difference (RMSD) was calculated for the component vectors. Correlation largely exceeded 0.6 (many exceeding 0.8), and while RMSD varied widely it remained below 15 cm/s for many of the paired comparisons (Table 1, Fig. 3). While this RMSD is somewhat high, on about the same scale as average radial vector speed, we believe that is not necessarily indicative of poor data quality considering the high variability in both sets of data, plus the offset in the headings for comparable vectors which introduces additional variability. Elliptical fields with particularly low correlation, specifically transmitter HEMP paired with receiver MRCH (especially in August 2018) and transmitter HOOK paired with receiver MRCH, had the majority of the poor correlations at the outer edge of the field suggesting possible ionospheric interference or issues with settings at the site(s).

Table 1. Comparisons between data from radial fields generated by a collocated transmitter and receiver and elliptical fields generated by separate transmit and receive sites. Radial components were only compared where vector heading differed by less than 15 degrees and there were at least 12 hours of data available for comparison during the given time period. N refers to the number of grid points meeting that criteria, and ranges listed for correlation coefficient (r) and RMSD include the 25th-75th percentiles.

January 13-20, 2021 Northern NY Bight				
Collocated Radial Site	**Elliptical Transmitter-Receiver Site**	**N**	**Correlation Coefficient**	**RMSD (cm/s)**
AMAG	AMAG-MRCH	155	0.45-0.72	11.8-16.1
MRCH	AMAG-MRCH	169	0.42-0.67	13.0-19.8
HEMP	HEMP-MRCH	53	0.38-0.65	13.3-17.4
MRCH	HEMP-MRCH	108	0.42-0.71	13.2-18.4
HEMP	HOOK-MRCH	120	0.08-0.52	15.8-23.4
MRCH	HOOK-MRCH	37	0.74-0.86	10.6-14.2
January 13-20, 2021 Northern NY Bight				
Radial	**Elliptical**	**N**	**r**	**RMSD**
BRIG	LOVE-BRIG	195	0.43-0.75	10.5-15.6
LOVE	LOVE-BRIG	167	0.45-0.71	11.7-16.3
BRIG	WILD-BRIG	131	0.37-0.70	13.5-19.3
WILD	WILD-BRIG	97	0.38-0.65	13.1-21.1
August 18-25, 2021 Northern NY Bight				
Radial	**Elliptical**	**N**	**r**	**RMSD**
AMAG	AMAG-MRCH	169	0.42-0.67	13.0-19.8
MRCH	AMAG-MRCH	206	0.56-0.77	10.9-15.4
HEMP	HEMP-MRCH	63	0.38-0.75	11.2-19.3
MRCH	HEMP-MRCH	113	0.18-0.58	14.7-26.6
April 18-25, 2018 Southern NY Bight				
Radial	**Elliptical**	**N**	**r**	**RMSD**
BRIG	LOVE-BRIG	198	0.49-0.75	9.6-15.0
LOVE	LOVE-BRIG	148	0.48-0.71	9.9-13.7

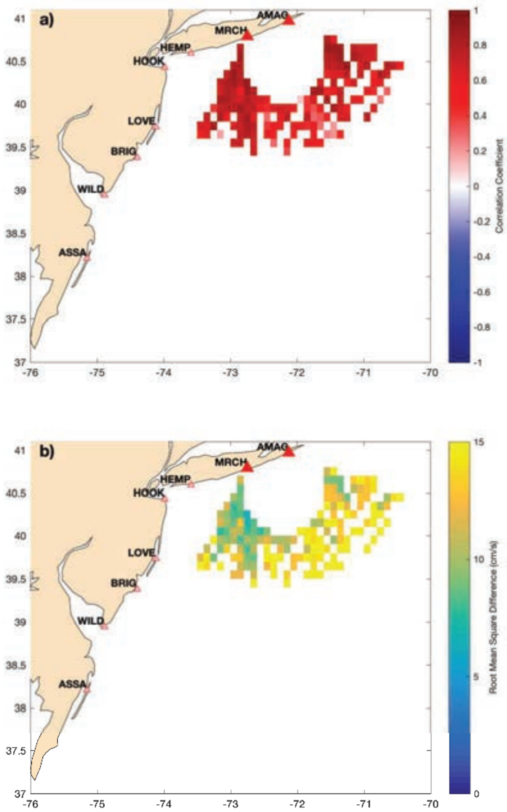

Fig. 3. Correlation coefficient r (a) and root mean square difference RSMD (b) of data from radial field generated by monostatic data collection from MRCH compared to bistatic data generated by transmitter AMAG and receiver MRCH, where vector heading was similar. Transmit and receive sites used to generate data for this comparison are marked by large red triangles.

B. Ellipticals and Radials Compared to Drifters

Drifter data from the US Coast Guard (USCG) and NOAA Northeast Fisheries Science Center was available during both 2018 case studies and used for comparison with elliptical and radial data. For these drifters overlapping with areas of good elliptical coverage, drifter velocities were matched to neighboring elliptical and radial data, the component matching elliptical or radial heading calculated, and correlation strength and RMSD determined along the drifter path. Data from two drifters (one USCG and one NOAA) were within the southern NY Bight coverage for the April 2018 time period, and data from one USCG drifter was available in the northern NY Bight coverage for the August 2018 time period. Dates for the April 2018 USCG southern NY Bight drifter were modified slightly in order to preserve more data within HFR coverage. Correlation between drifters and elliptical data was fair (about 0.65), but lower than the correlation between drifters and radial data from a collocated transmitter and receiver (many >0.75); RMSD varied widely for both types of data, but was generally a few cm/s higher for elliptical data compared to radial data (Table 2, Fig. 4). While this suggests that bistatic data may not be quite as reliable as monostatic data, correlation strength is still encouraging and the additional data can add value to the total vector products.

Project funded by Mid Atlantic Regional Association Coastal Ocean Observing System (MARACOOS).

Table 2. Radial and elliptical velocity data as it compares to nearby drifter data rotated to match HFR vector heading. HFR site listed is either the individual site for collocated radial data or the transmitter-receiver site pair for elliptical data. N indicates the number of drifter velocities available for comparison to each site or site pair.

USCG Drifter 65141730, Northern NY Bight, August 18-25, 2018			
HFR Site	**N**	**r**	**RMSD (cm/s)**
MRCH	150	0.85	8.8
AMAG	121	0.72	12.2
HEMP	150	0.78	14.8
HOOK	147	0.88	10.4
AMAG-MRCH	131	0.68	13.4
HEMP-MRCH	149	0.65	16.3
USCG Drifter 65903190, Southern NY Bight, April 14-21, 2018			
HFR Site	**N**	**R**	**RMSD**
BRIG	46	0.53	15.0
WILD	128	0.62	14.9
NOAA Drifter 184390731, Southern NY Bight, April 18-25, 2018			
HFR Site	**N**	**R**	**RMSD**
LOVE	106	0.84	7.5
BRIG	118	0.59	10.6
LOVE-BRIG	118	0.59	10.6

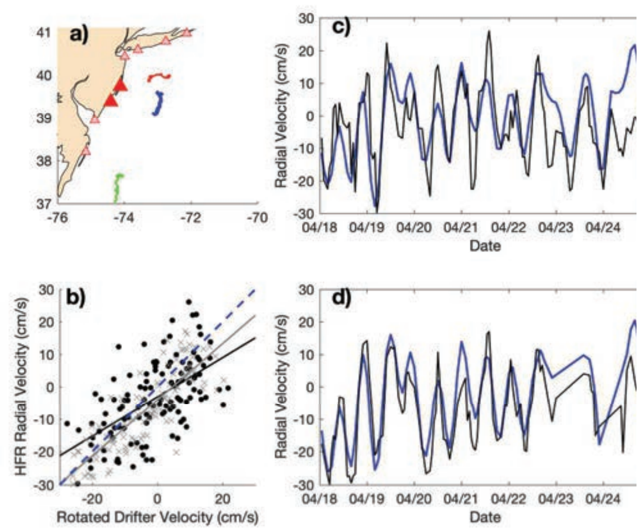

Fig. 4. Drifter tracks for the three available comparisons (a). Red trajectory is US Coast Guard drifter from August 2018, green US Coast Guard drifter from April 2018, and thicker blue line NOAA drifter from April 2018, used in b-d. Red markers indicate transmit and receive sites used in b-d (BRIG and LOVE). Scatterplot (b) shows drifter data compared to radial data from LOVE (gray x) and compared to elliptical data from transmitter LOVE with receiver BRIG (black dots), with best-fit lines in the same color and 1:1 in dashed blue. Line plots show the time-series of the rotated drifter data (blue) and the nearest HFR radial velocity (black) from transmitter LOVE and receiver BRIG (c) and collocated transmitter and receiver LOVE (d).

C. Totals With Elliptical Data

Because it had good coverage for all five sets of elliptical data, we used the full month of January 2021 to evaluate the effect of including ellipticals in addition to radials during optimal interpolation (OI) totals calculations [6]. For the most part, incorporating ellipticals into totals did not change the totals or the coverage by any significant amount, but did decrease the estimated normalized error within the calculated totals – at times by more than 20% (exceeding a decrease of 0.1 at errors <0.6, Fig. 5a). We also calculated the change in data coverage during January 2021 for monostatic and bistatic data compared to monostatic-only data based on a maximum accepted normalized error of 0.6 for MAB OI totals products (i.e., how many hours a grid point met the error < 0.6 requirement for totals using both types of data, but failed to meet that requirement for totals using only monostatic data). Widespread improvements in data coverage were rarely observed, mainly during brief time periods with large data gaps (e.g. during site outages) in the totals calculated using only monostatic data (Fig. 5b). In order to estimate the effect of including bistatic data in totals during a time period with persistent large data gaps, we did an additional case study for the same month simulating a scenario where the receiver at a site (LOVE) was not working by generating totals that excluded radial data from this site, thus creating a gap in the data field along the shelf. In this scenario, there was even greater improvement in error when bistatic data was included in the totals (Fig. 5c), and elliptical data filled in data gaps for many hourly maps throughout the month, especially off southern NJ at the edge of the shelf (Fig. 5d).

III. Conclusions

Compared to radial data sources available in the region, elliptical data fields may have a slightly increased error. However, correlation is typically strong, verifying it as a valuable data source in the region, particularly for features that are naturally high in variability. Further, totals are by far the HFR product most frequently utilized by end-users, and the majority of error introduced is averaged out with other data, both bistatic and monostatic, during totals generation. Overall, bistatic data can be extremely valuable to regional HFR products, particularly given their ability to fill in large data gaps (e.g. due to site outages) and the fact that there is only a slight cost associated with collecting and using bistatic data.

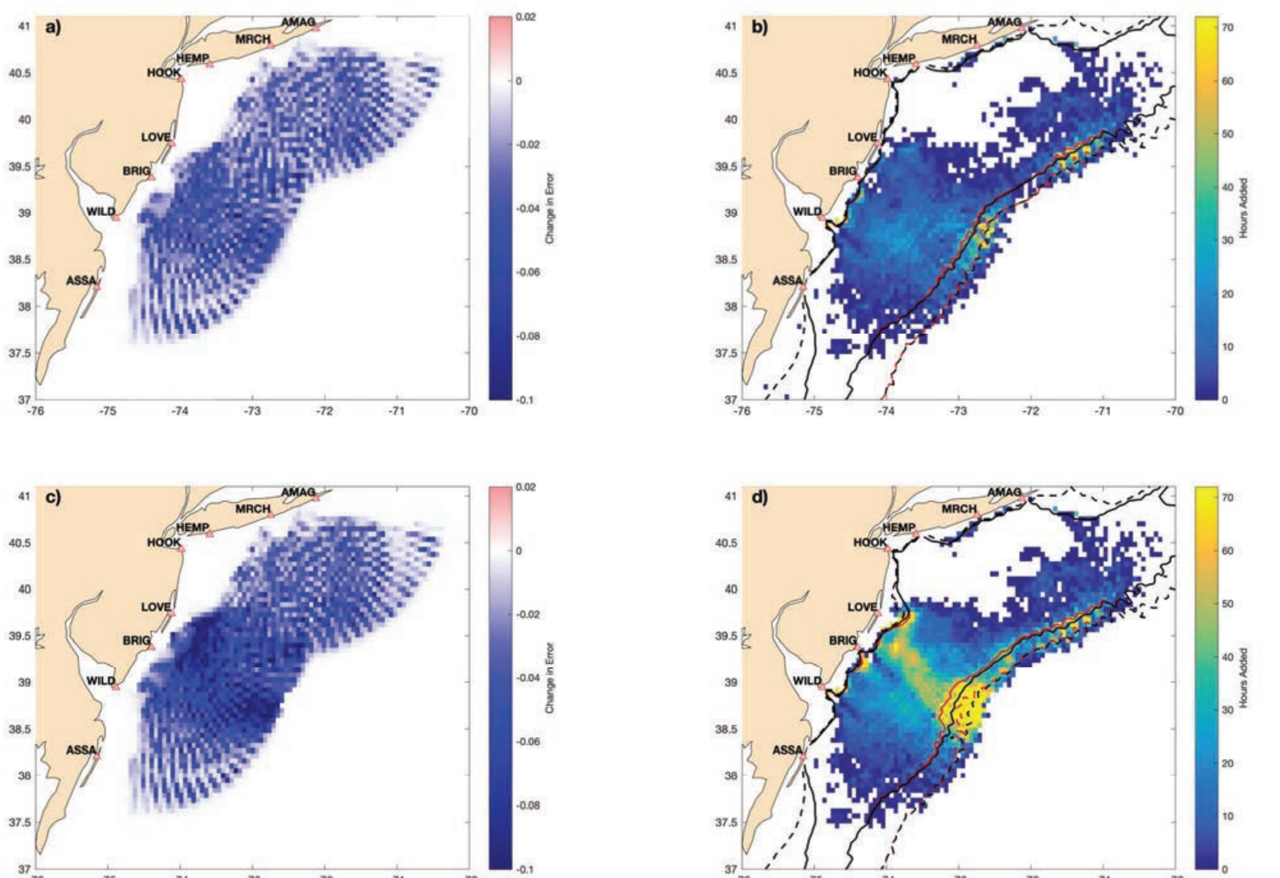

Fig. 5. Average change in totals error with inclusion of bistatic data (blue=improvement) for January 2021 (a), and number of hours added to coverage over the month based on a maximum normalized error of 0.6 (b), with 80% (solid lines) and 50% (dashed lines) coverage contours for monostatic-data-only totals coverage (red) and monostatic+bistatic totals coverage (black). The same change in error (c) and additional coverage (d) images are shown for totals generated without radial site LOVE, simulating a data gap due to an issue with the receiver at LOVE.

REFERENCES

[1] H. Roarty, S. Glenn, J. Kohut, D. Gong, E. Handel, et al., “Operation and application of a regional high-frequency radar network in the Mid-Atlantic Bight,” Marine Technology Society Journal, vol. 44, pp. 133-145, November 2010.

[2] B. Lipa, C. Whelan, B. Rector, and B. Nyden, “HF radar bistatic measurement of surface current velocities: Drifter comparisons and radar consistency checks,” Remote Sens., vol. 1, pp. 1190-1211, December 2009.

[3] H. Roarty, J. Kerfoot, J. Kohut, S. Glenn, C. Whelan, and M. Hubbard, “Improving the measurements of high frequency radar: Reduced averaging times and bistatics,” 2013 MTS/IEEE Oceans – Bergen, pp. 1-6, 2013.

[4] H. Roarty, J.T. Kohut, L.J. Palamara, W.S. Brown, H. Seim, et al., “Observations of the surface circulation over the Mid Atlantic Bight continental shelf,” American Geophysical Union, Ocean Sciences Meeting, 2016

[5] H. Roarty, S. Glenn, J. Brodie, L. Nazzaro, M. Smith, et al., “Annual and seasonal surface circulation over the Mid-Atlantic Bight continental shelf derived from a decade of high frequency radar observations,” JGR Oceans, vol. 125, November 2020.

[6] J. Kohut, H. Roarty, E. Randall-Goodwin, S. Glenn, and C.S. Lichtenwalner, “Evaluation of two algorithms for a network of coastal HF radars in the Mid-Atlantic Bight,” Ocean Dynamics, vol. 62, pp. 953-968, April 2012.

Mid Atlantic Drifter Program: Development of Software Toolbox to Manage Drifter Data

Hugh Roarty
Dept. of Marine and Coastal Sciences
Rutgers University
New Brunswick, NJ USA
hroarty@marine.rutgers.edu

Laura Nazzaro
Dept. of Marine and Coastal Sciences
Rutgers University
New Brunswick, NJ USA
nazzaro@marine.rutgers.edu

***Abstract*— A MATLAB toolbox has been developed to calculate drifter velocities at regular timesteps matching High Frequency radar (HFR) data output. This allows the user to compare drifter velocities to nearby radial and total velocities, calculate statistics (correlation coefficient and root mean square error (RMSE) and create figures of the comparisons. The drifter data is quality controlled and output as netCDF files. Drifter velocities are rotated to obtain the velocity component matching the heading angle of the nearest radar radial measurement, and plotted as time-series line plots of radial vector components with matching rotated drifter velocity component. Multiple HFR datasets can be compared at once for the same drifter dataset, allowing for easy comparison of quality controlled vs. non-quality-controlled data, for example. The toolbox is curated at https://github.com/lnazzaro/hfr-drifters/wiki The toolbox was utilized to process and organize drifter data from NOAA and the United States Coast Guard. This regional drifter dataset was compared to the NOAA Global Drifter Data set.**

Keywords—remote sensing, geoscience, radar, ocean currents, drifters, MARACOOS

I. Introduction

A regional climatology of ocean surface currents is valuable for a variety of reasons. Knowledge of the surface circulation is relevant for search and rescue operations, improved ship routing, and for assessing the fate and transport of marine debris, oil spills and microplastics. Long-term surface current measurements also describe the physical conditions in which organisms of the Mid-Atlantic Bight (MAB) live and reproduce. Global drifter data sets provide circulation information on basin scale but seldom cover the continental shelves where regional associations like the Mid-Atlantic Regional Association Coastal Ocean Observing System (MARACOOS) are responsible for monitoring. The temporal and spatial averaging for global drifter datasets are large compared to HFR. Therefore, we aim to organize the drifter deployments within the Mid-Atlantic and provide it as a resource to the community.

The Mid Atlantic of the United States is a densely populated region with 79 million people (24% of the US population) and includes some of the largest shipping centers for maritime commerce. The Port of Virginia, New York and Philadelphia and others in the MARACOOS domain account for 13% of trade by volume. MARACOOS [1] supports the safety, health and economy from Cape Hatteras to Cape Cod by providing data and products that address five stakeholder-defined theme areas:

1. Improving maritime commerce and safety – Mid Atlantic surface currents and predictions have been an operational data source to Coast Guard search and rescue since May 2009.

2. Reducing coastal hazards – surface currents can be utilized in rip current models and be used as a validation data source for storm surge models.

3. Improved water quality – surface current measurements and forecasts can be utilized to predict where floatables will go after a large rain storm or the fate of harmful algal blooms, and for oil spill response.

4. Sustainably managed fisheries and natural resources – seasonal surface current maps can describe the environment for fish habitat and larval transport.

5. Improved planning and development of energy from Mid Atlantic offshore waters – a decade of surface current measurements are available for historical analysis and wind model validation.

Surface current measurements contribute to each of these five theme areas. MARACOOS is part of the Integrated Ocean Observing System (IOOS) [2] network, a public-private partnership that includes 17 federal agencies as well as the external or non-governmental entities from the 11 regional associations across the United States. IOOS is supported through the Integrated Coastal and Ocean Observation System Act of 2009 and was recently reauthorized in 2020. IOOS is the United States contribution to the Global Ocean Observing System (GOOS) [3].

II. Methods

A software toolbox written in the MATLAB programming language has been developed to organize surface drifter data. The toolbox is named hfr-drifters and is maintained on the GitHub repository at https://github.com/lnazzaro/hfr-drifters/wiki. The toolbox uses drifter data in netCDF format that is structured following the Climate and Forecast (CF) convention [4] for a trajectory feature type. The template was borrowed from National Centers for Environmental Information (NCEI) trajectory template version 2.0. The toolbox requires the HFR-Progs toolbox and the associated file directory structures.

The toolbox has three main functions:

1. Processing raw drifter data and saving it using a netCDF template

2. Matching drifter data to HFR radial and total vector data
3. Comparing and analyzing the drifter data to HFR radial and total vector data

The toolbox calculates drifter surface velocities at regular timestamps which allows for the comparison with High Frequency radar surface velocity measurements. The user chooses which drifter file and the appropriate HFR stations to compare against. Typically, you would choose a drifter for comparison that spent some amount of time within the coverage area of the HFR station or total vector product. If you are comparing the drifter against the radial current vectors from a particular HFR station then the toolbox creates a MATLAB structured array containing the drifter velocity rotated into reference frame that aligns in heading with the nearest radial measurement of the HFR station. If you are comparing the drifter against a total vector product then the toolbox saves the northward (u) and eastward (v) velocity of the HFR total surface current product closest to the drifter in space and time. The toolbox allows a single drifter dataset to be used for comparison with multiple HFR datasets at once.

The drifter data is mapped to hourly timesteps on the hour and removes any successive drifter locations that display velocities over 300 cm/s or under the minimum precision defined by MATLAB. If quality control flags following the QARTOD [5] standard are present in the radial or drifter files, then flags having a value of 3 for questionable or 4 for failed are removed.

Lastly the toolbox provides statistics and visualization of the drifter and HFR comparison. For radial vector comparisons, the statistics include the sample size, the correlation coefficient (r), and the root mean square error (RMSE) of the comparison. The visualizations include a map showing the drifter track and the location of the HFR stations, a line plot comparing nearest radial velocity at each timestep to rotated drifter velocities and scatter plot of the same data with a best fit and 1:1 line included (Figure 1). For total vector comparisons, the statistics include sample size, RMSE of the u and v velocities, and complex correlation strength and directional offset. The visualizations include (1) a map showing the drifter track over a specific time period, (2) a current rose for drifter data and matching total vector data, and (3) map of drifter track overlaid with drifter velocity and each set of total velocities plotted as colored arrows at each drifter location (Figure 2).

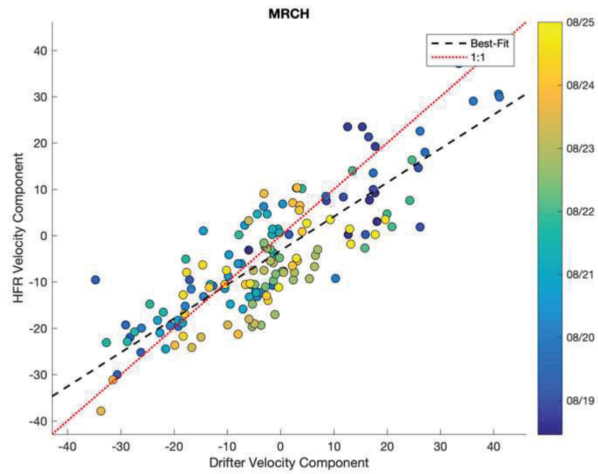

Figure 1: Scatter plot of drifter radial velocity (x axis) plotted against HF radar radial velocity (y axis). The time period of the comparison (August 19-25, 2018) is displayed as the color of the data points in the colorbar. The best fit line (black) and 1:1 (red) line are also shown.

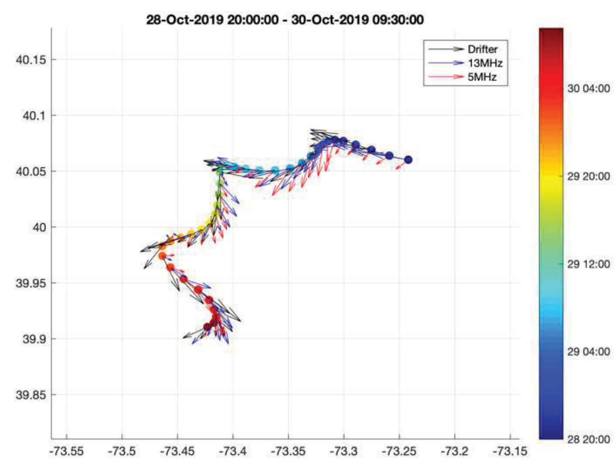

Figure 2: Map of drifter track overlaid with drifter velocity (black) and each set of total velocities 5 MHz (red) and 13 MHz (blue) plotted as colored arrows at each drifter location. The colorbar indicates the timestamp of the drifter location from October 28-30, 2019.

III. Results

Drifter data were assembled from several sources over the Mid-Atlantic region from 2014 to 2019. Drifter data from the United States Coast Guard (USCG) was assembled and is shown in Figure 3. The USCG utilizes the Self Locating Data Marker Buoy (SLDMB) [6] in most search and rescue cases to provide a validation data set to evaluate the particular ocean model they are utilizing in the case. Drifter data [7] from the Northeast Fisheries Science Center were also collected and are shown in Figure 4.

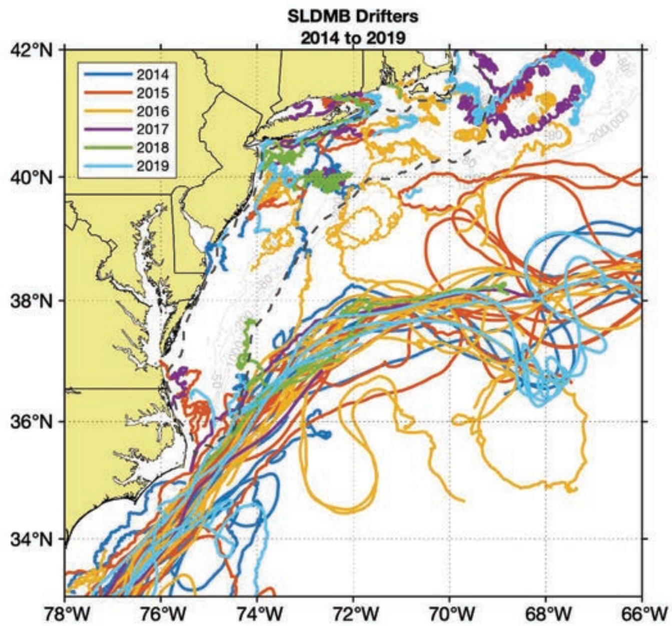

Figure 3: US Coast Guard drifter tracks for the Mid Atlantic region. The drifters are colored by deployment year (2014-2019), with the 50% data coverage contour for the MARACOOS HF radar network as a dashed black line.

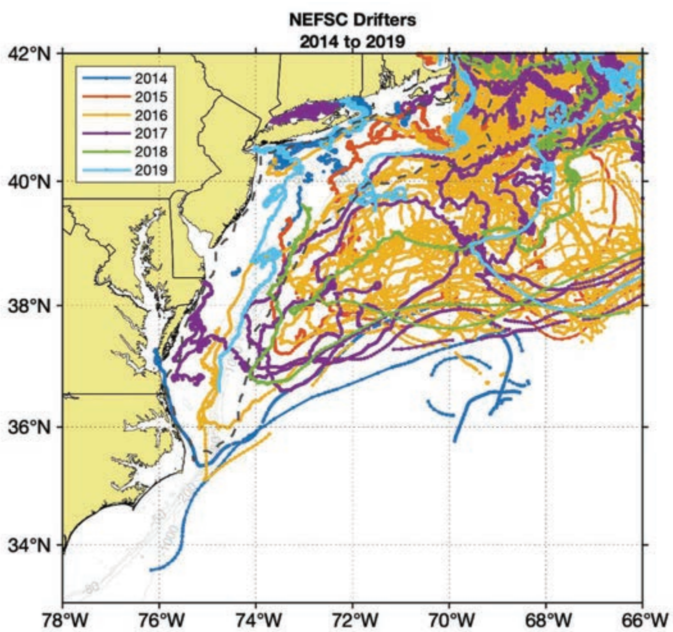

Figure 4: NOAA Northeast Fisheries Science Center drifter tracks for the Mid-Atlantic region. The drifters are colored by deployment year (2014-2019), with the 50% data coverage contour for the MARACOOS HF radar network as a dashed black line.

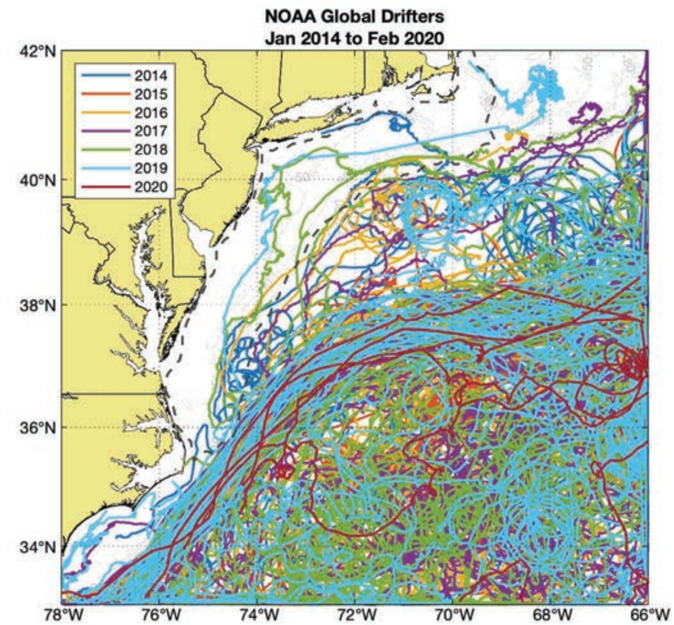

Figure 5: NOAA Global Drifter Program drifter tracks for the Mid-Atlantic region. The drifters are colored by deployment year (2014-2019), with the 50% data coverage contour for the MARACOOS HF radar network as a dashed black line.

For comparison, drifter data were downloaded from the Global Drifter Program [8] for the same time period (Figure 5). The Global Drifter Program provided 160 drifters for the Mid-Atlantic region. A total of 111 drifter data sets were collected from the USCG and 143 from NOAA for a total of 254. So, the regional drifter data sets can more than double the data supply for the Mid Atlantic area. (Figure 6). The regional drifter data also provide increased data density near the coast to help fill in the gap that the Global Drifter Program has in this area.

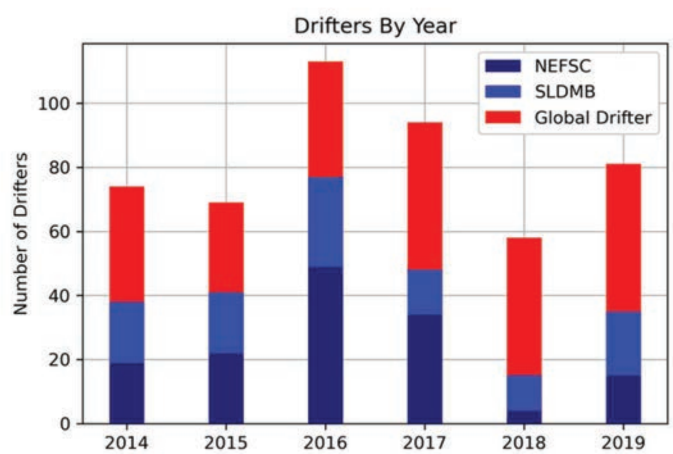

Figure 6: Relative abundance of drifter tracks in the Mid Atlantic from 2014-2019.

IV. Discussion

Having regional drifter data can serve as a validation data set for the Mid Atlantic regional HF radar network. It also has the potential to help bridge the gap between regional measurements and global scale measurements. The near surface current climatology for the Mid-Atlantic region as derived from the Global Drifter Program is shown in Figure 7. This climatology covers 1979 to 2020 and is version number 3.06. The Gulf Stream is the dominant ocean feature displaying currents toward the northeast on the order of 1 m/s. The currents are weak on the shelf on the order of 10 cm/s. There are also some gaps in the climatology on the shelf and near Georges Bank. Having an organized regional drifter dataset could help fill in some of these gaps.

Recently a decade of HFR surface current measurements were collected for the Mid Atlantic Bight [9]. The measurements show a mean surface flow that is offshore and equatorward with speeds between 2-12 cm/s (Figure 8). The current speeds increase with water depth, are most variable near the coast, and uniform along the shelf break. If the global drifter climatology is plotted on the same speed and geographic bounds as the HFR data, the currents are much faster than those measured by the HFR (Figure 9). The global drifter current direction on the shelf overall agrees with the HFR measurement showing a drift towards the southwest, but the variability of the global data set can be erratic with some vectors that should be revisited. This should not be surprising as the data density off the shelf is three times higher than near the coast inside the 200 m isobath.

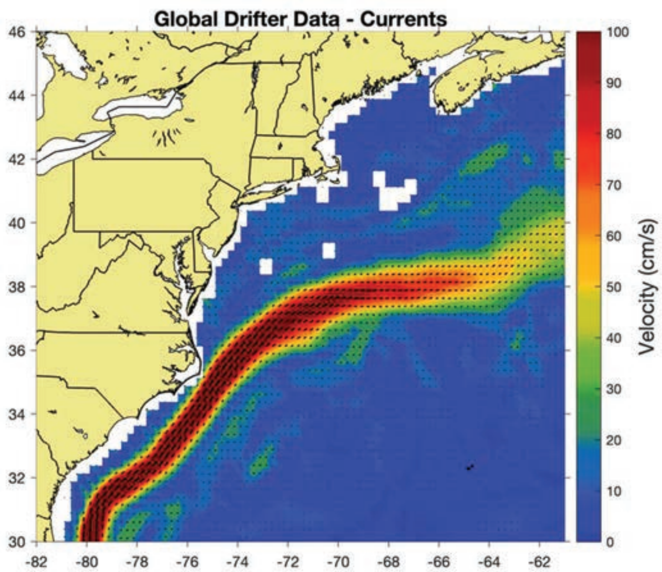

Figure 7: Climatology of near-surface currents (cm/s) for northwest Atlantic. Data taken from the NOAA Global Drifter Program.

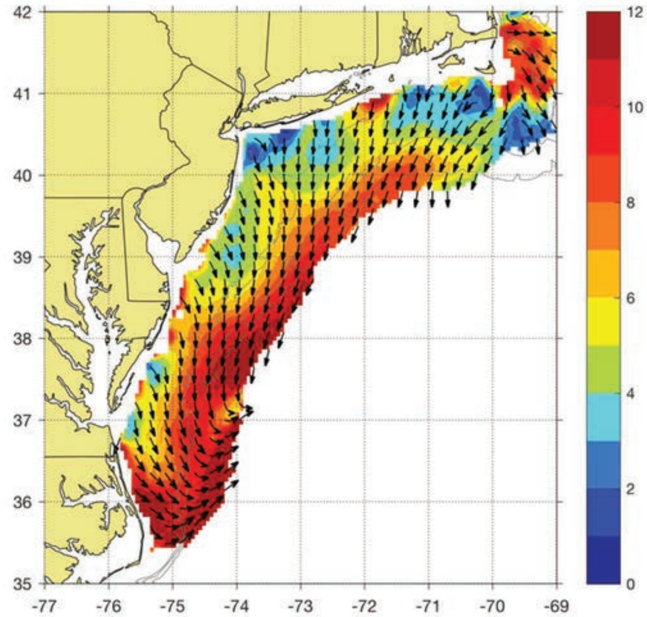

Figure 8: Climatology of near-surface currents (cm/s) for the Mid Atlantic. Data taken from the MARACOOS HF Radar network.

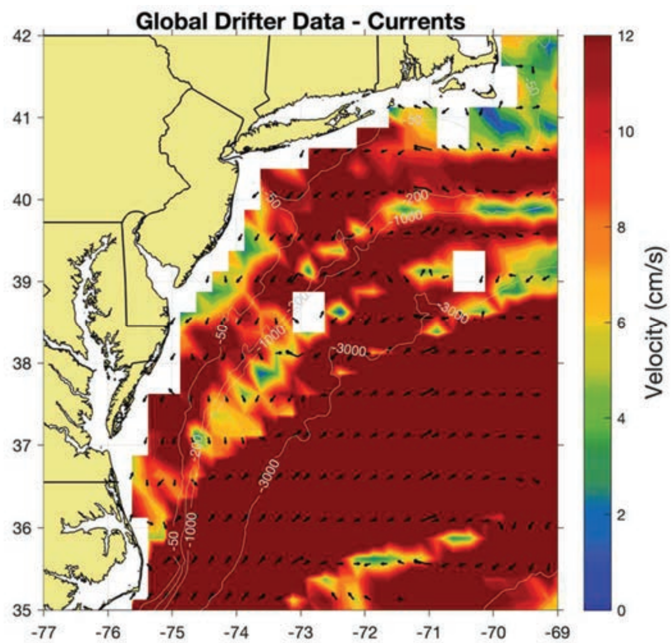

Figure 9: Climatology of near-surface currents (cm/s) for the Mid Atlantic. The data is the same as Figure 7, only the geographic bounds of the plot are zoomed in and bounds of the colorbar are reduced to 0-12 cm/s.

V. Conclusions

We have developed a MATLAB toolbox to help organize surface drifter data in the Mid-Atlantic region. This allows for comparison of the surface current measurements from drifters and HF radar. This will allow for a deeper understanding of the surface flows of the MAB. Regional drifter data sets can dramatically improve coverage density for regions like the Mid Atlantic. We would welcome accepting other drifter data sets into this growing database.

ACKNOWLEDGMENT

This work was funded by NOAA Award Number NA16NOS0120020 “Mid-Atlantic Regional Association Coastal Ocean Observing System (MARACOOS): Preparing for a Changing Mid Atlantic”. Sponsor: National Ocean Service (NOS), National Oceanic and Atmospheric Administration (NOAA) NOAA-NOS-IOOS-2016-2004378 / CFDA: 11.012, Integrated Ocean Observing System Topic Area 1: Continued Development of Regional Coastal Ocean Observing Systems.

REFERENCES

[1] G. F. Kuska, C. A. Thoroughgood, S. Glenn, M. Crowley, and P. Moore, "Raising the bar in the Mid-Atlantic: Moving MARACOOS observations to next generation forecasting and product development," in *2012 Oceans*, 2012: IEEE, pp. 1-6.

[2] J. Snowden *et al.*, "The U.S. Integrated Ocean Observing System: Governance Milestones and Lessons From Two Decades of Growth," (in English), *Frontiers in Marine Science,* Review vol. 6, no. 242, 2019-May-14 2019, doi: 10.3389/fmars.2019.00242.

[3] T. Moltmann *et al.*, "A Global Ocean Observing System (GOOS), Delivered Through Enhanced Collaboration Across Regions, Communities, and New Technologies," (in English), *Frontiers in Marine Science,* Review vol. 6, no. 291, 2019-June-28 2019, doi: 10.3389/fmars.2019.00291.

[4] B. Eaton *et al.*, "NetCDF Climate and Forecast (CF) metadata conventions," ed: Version, 2003.

[5] M. Bushnell, "Quality Control of Real-Time Water Level Data: The US IOOS® QARTOD Project," *Marine Technology Society Journal,* vol. 52, no. 2, pp. 13-17, 2018.

[6] A. Allen, "Performance of GPS/Argos self-locating datum marker buoys (SLDMBs)," in *OCEANS '96. MTS/IEEE. 'Prospects for the 21st Century'. Conference Proceedings*, 23-26 Sep 1996 1996, vol. 2, pp. 857-861 vol.2.

[7] J. P. Manning, D. J. McGillicuddy Jr, N. R. Pettigrew, J. H. Churchill, and L. S. Incze, "Drifter observations of the Gulf of Maine Coastal Current," *Continental shelf research,* vol. 29, no. 7, pp. 835-845, 2009, doi: http://dx.doi.org/10.1016/j.csr.2008.12.008.

[8] L. C. Laurindo, A. J. Mariano, and R. Lumpkin, "An improved near-surface velocity climatology for the global ocean from drifter observations," *Deep Sea Research Part I: Oceanographic Research Papers,* vol. 124, pp. 73-92, 2017.

[9] H. Roarty *et al.*, "Annual and seasonal surface circulation over the Mid - Atlantic Bight Continental Shelf derived from a decade of High Frequency Radar observations," *Journal of Geophysical Research: Oceans,* vol. 125, no. 11, p. e2020JC016368, 2020.

A Unified Approach to HF Radar Radial Quality Control for Understanding Gulf Ocean Systems

Smith, Michael
Rutgers University
New Brunswick, NJ, USA
michaesm@marine.rutgers.edu

Glenn, Scott
Rutgers University
New Brunswick, NJ, USA
glenn@marine.rutgers.edu

Merz, Clifford
University of South Florida
St. Petersburg, FL, USA
cmerz@usf.edu

Liu, Yonggang
University of South Florida
St. Petersburg, FL, USA
yliu@usf.edu

Weisberg, Robert
University of South Florida
St. Petersburg, FL, USA
weisberg@usf.edu

Shay, Lynn
University of Miami
Miami, FL, USA
nshay@rsmas.miami.edu

Howden, Stephan
U. of Southern Mississippi
Stennis Space Center, MS, USA
stephan.howden@usm.edu

Knap, Anthony
Texas A&M University
College Station, TX, USA
tknap@geos.tamu.edu

***Abstract*—There are seven planned CODAR SeaSonde High Frequency radar (HFR) sites to observe surface currents in the Straits of Florida, northern Gulf of Mexico, and Straits of Yucatan as part of the Understanding Gulf Ocean Systems (UGOS) project. UGOS is a project funded by the National Academies of Sciences, Engineering, and Medicine (NASEM) to study Loop Current dynamics in the Gulf of Mexico. A unified approach to delayed-mode quality control of radial data is developed and implemented. The first two steps involving reviewing radial distributions and diagnostics and identify any time periods that may require special attention. The third step is to plot all Doppler spectra and ensure that the first-order Bragg are identified by the first order line settings and any interference is filtered out or noted as suspect. The fourth step is to recalculate the radial currents from the Doppler spectra with the best available measured antenna patterns and first order line settings to produce the best radial current vectors based on the preceding steps. The fifth step is to apply the full suite of Quality Assurance/Quality Control of Real-Time Oceanographic Data (QARTOD) radial tests to the reprocessed radials. Finally, the post-processed radial currents are compared to the original radial files produced at the remote site.**

Keywords—delayed mode; codar; seasoned; quality control; surface currents; high frequency radar;

I. INTRODUCTION

University of South Florida, University of Miami, Rutgers University, Texas A&M University, and University of Southern Mississippi have partnered to install seven high frequency radar (HFR) surface current mapping systems around the Gulf of Mexico to advance the understanding of the Loop Current Dynamics for the purpose of improving predictive skills of the Loop Current and associated eddies. The first of these HFR systems was deployed by the University of South Florida in Marathon, Florida (MARA) in December 2019 to observe the surface currents in the Straits of Florida across to Cuba. Six more HFR sites, two each in the Florida Keys, Gulf of Mexico, and Straits of Yucatan are scheduled for installation in 2021. Rutgers is leading the development and implementation of a unified delayed-mode quality control (QC) routine that utilizes the tests defined in the Quality Assurance/Quality Control of Real-Time Oceanographic Data (QARTOD) manual for Real-Time Quality Control of High Frequency Radar Surface Current Data [1]. This routine is to be performed on all seven of the Coastal Ocean Dynamics Applications Radar (CODAR) SeaSonde HFR systems for the Understanding Gulf Ocean Systems (UGOS) Loop Current Project.

After each new HFR site is deployed, data will be submitted to Rutgers on a biannual basis, where it is put through a thorough quality control process examining every intermediate step in the production of a radial file. A brief description of the quality control process is provided as a part of the work in Liu et al. [2]. Here in this paper, we elaborate the process in more details and provide some results as an example. The quality control process has five steps: The first step involves reviewing daily and weekly radial distributions. The second step involves reviewing radial diagnostics to identify any time periods that may require special attention. The third step is to plot all the spectra. Once the spectra are plotted, each timestep is checked to ensure that the first order portion of doppler spectra are properly defined as identified by the first order line settings. The first order line settings inform the radial processing software what portion of the Doppler spectra it should process target echoes into radial currents. This step is also used to identify any sources of outside interference that may affect data quality. The fourth step is to recalculate the radial currents from the Doppler spectra with the best available measured antenna patterns and first order line settings to produce the best radial current vectors based on steps one and two. The fifth step is to apply the full suite of ‘required’ and ‘recommended’ QARTOD radial tests to the reprocessed radials, flagging each vector for each of the tests that are not passed. Finally, the post-processed radial currents are plotted and compared to the original radial files produced at the remote site [2].

II. RADIAL DATA REVIEW

The first step in the delayed-mode reprocessing is a review of the radial data for the latest available six-month time period. The data curator creates daily and weekly-averaged radial distribution plots of the real-time measured pattern radial files. These plots are useful to identify when a site has physically changed or a measured antenna pattern is no longer performing well. When an averaged radial velocity map shows angular gaps or misplaced radial velocities over an extended period of time, this often indicates an incomplete or obsolete antenna pattern measurements (APM) [3]. The initial review of radial distributions allows the data evaluator to track the performance of the HFR site throughout the entire time period and make any necessary changes to the APM during reprocessing.

978-0-692-93559-0 ©2021 MTS

APMs are crucial in improving the direction-finding capabilities of the system. APM are the receivers measured response to a known signal as a function of direction and are used to provide the direction-finding algorithm information on what angle in relation to the receiver to place radial velocities at a given range [4]. APM can be measured manually by the HFR site operator using a transponder or by utilizing automatic APM generating software that matches ship echoes in the backscatter doppler spectra with known ship positions derived from automatic identification system signals.

Figure 1 shows an example of variations in the extent of the measured offshore radial velocities obtained with differing APMs. Initial Marathon HFR site measurements were made by USF in December of 2019 using a transponder walking along shore after initial installation which was followed in February 2020 by an APM made by boat 1 km offshore. The region covered by the red triangle illustrates the additional coverage obtained by the boat APM that was previously obscured by physical shoreline obstructions during the initial alongshore APM.

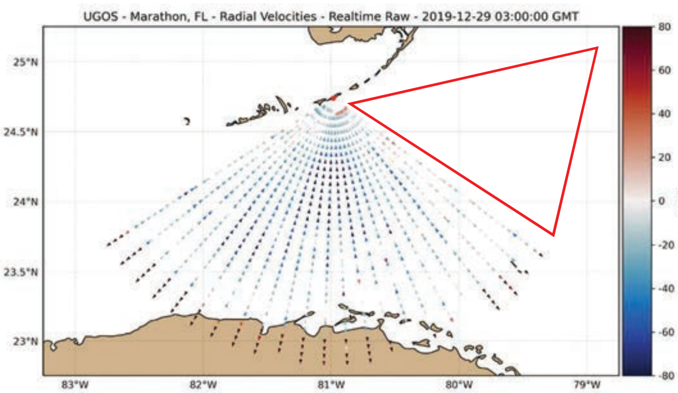

Fig. 1. Weekly radial distribution plot showing variations in offshore coverage at the USF Marathon HFR site. The red triangle to the East-Southeast of Marathon, FL reveals additional offshore coverage obtained from a follow-on APM that was previously obscured by physical shoreline obstructions in the initial alongshore APM .

III. Diagnostics Review

The next step in the delayed-mode reprocessing effort is a thorough review of the site's radial diagnostics. Radial diagnostic files contain information on measured sea amplitude and phase, measured signals, number of radial vectors, noise floor, and average radial bearing. Diagnostics can help identify significant changing in antenna setup or transmitter problems that have occurred. Change in sea echo phases and amplitudes or in average radial bearing with no coinciding change in antenna bearing can signal an error in the configuration that will need to be corrected in reprocessing. Data from stations reporting low signal to noise and/or high background noise diagnostics for long periods of time are often indicative of equipment failures and were excluded from processing. The diagnostics are used to identify possible events that may require a new antenna pattern measurement or equipment checks [3].

IV. Doppler Spectra Review

The observed Doppler spectrum of sea surface wave echoes contain current and wave information which must be processed by the SeaSonde software into usable data. SeaSonde backscatter cross spectra have a characteristic appearance: dominant first-order peaks surrounded by a second order continuum [5]. The first-order Bragg spectral peaks contain sea surface current information whereas the second-order peaks contain wave information [6]. Fig. 2 shows an example of a clean Doppler spectra displaying a clear first-order Bragg peak along with a second-order peak from the USF Marathon site. The quality of radial data is dependent on the quality of the Doppler spectra produced from the backscatter of radio waves off the ocean surface [2, 7].

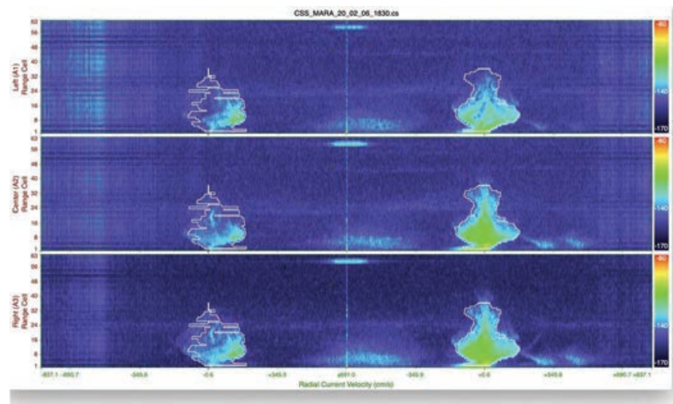

Fig. 2. Observed Doppler Spectrum from each of the three receiver antennas at the USF HFR Marathon, FL site. The first-order Bragg peaks (currents) are centered on approximately +/-0.6cm/s. Second-order peaks (waves) are centered on +300cm/s. The white lines surrounding the first-order Bragg are the first order lines that help the software define the Bragg peak.

The determination of the frequencies that define the first-order Bragg region in the doppler spectra is a critical step in HFR analysis. These are known as the 'first-order region boundaries' or 'first-order lines (FOL).' It is important that the software be able to differentiate these echo regions properly because this region is processed by the SeaSonde software into radial currents [5]. The complete Doppler spectra of the dataset is reviewed to ensure that the FOL are adjusted appropriately in order to define the first-order Bragg scattering peak during different environmental conditions.

Occasionally, HFR receivers will receive unwanted background noise which has the potential to be processed by the radial processing software if the noise intrudes on the boundaries set by the first order line settings. This noise may be either in the form of a man-made radio interference (RF) or naturally occurring ionospheric echoes [2, 7]. RF interference presents in the Doppler spectra as strong vertical banding while ionospheric interference appears as a band of range cells with strong returns across a broad range of Doppler frequencies. In order to ensure the processing software processes the first order Bragg region correctly, this introduced noise must be filtered and removed. The HFR site has built-in spectra averaging software that combines the spectra and removes most interference. Any remaining interference that persists after the spectra is filtered and noted in a database. This database is used to populate quality controlled radial files with operator flags (QCOP) that tell users that the data may be suspect at the exact time, range, and bearing at which the interference appears in.

V. REPROCESS RADIALS

Once all radials, diagnostics, and spectra are reviewed, the data evaluator will recalculate the radial currents from the Doppler spectra with the best available measured antenna patterns and first order line settings to produce the best radial current vectors based on the preceding steps.

VI. QARTOD ALGORITHMS

UGOS Data Quality Control procedures for radial files were designed with the goal of meeting IOOS QARTOD standards. Table I shows the six required and recommended radial quality control algorithms from version 1.0 of the QARTOD HFR manual [1]. These algorithms were ported in the Python programming language and implemented into an open-source GitHub repository called HFRadarPy [8]. This toolbox reads standard CODAR Tabular Format (CTF) files into standardized radial object. This radial object contains all original header/footer metadata, radial data, and diagnostic data. The underlying radial data is loaded into a tabular Pandas dataframe where the data can be analyzed using built-in Pandas tools. This toolbox will work with any surface current measuring HFR system that outputs files in the CTF format including the CODAR's SeaSonde, Helzel Messtechnik's Wellen Radar (WERA), and University of Hawaii's Least Expensive Radar (LERA).

Each algorithm, other than the Syntax test (QC06), has site specific inputs that must be defined by each HFR site's operator. A successful QC effort is highly dependent upon selection of the proper thresholds, which should not be determined arbitrarily but can be based on historical knowledge or statistics derived from recently acquired data [1].

The flags for each radial current are appended to the radial data table as a new column that corresponds to each QC test. The resulting radial object can be exported into either the standard CTF tabular format, a tabular NetCDF file, or a multidimensional NetCDF file [9].

TABLE I. QARTOD RADIAL QC TESTS

Code	**Name**	**Flag**
QC06	Syntax	See *Syntax Test* in text
QC07	Max Threshold	Fail: RSPD > RSPDMAX
QC08	Valid Location	Fail: If VFLG == +128 or if source point intersects over land mask
QC09	Radial Count	Suspect: RCLOW< = count <= RCMIN Fail: count < RCMIN
QC10	Spatial Median	Fail: VELO > CURLIM
QC11	Temporal Gradient	Suspect: GWARN < ΔTEMP < GFAIL Fail: ΔTEMP > GFAIL

A. Syntax Test

The syntax test is a collection of tests that verify that radial files are properly formatted and radial data fields exist within. The radial file is tested for proper parsing and content, file format, site code, time stamp, time zone, site coordinates, antenna pattern type, and internally consistent row/column specifications [1].

According to the QARTOD manual, the test is operator defined, however, the test as written in HFRadarPy is written to the same standards as the HFR National Network [1]. The test requires that the following metadata be present in the file: file type, site code, timestamp, site coordinates, antenna pattern type and time zone. Other requirements include 1) the file name timestamp must match the timestamp reported within the file, 2) radial data tables (Longitude, Latitude, U, V) must not be empty, 2) radial data table columns stated must match the number of columns reported for each row 4) site location must be within the following ranges: -180 ≤ Longitude ≤ 180 and -90 ≤ Latitude ≤ 90, and 5) time zone must be Greenwich Mean Time. If any of the tests fail, the radial file is not created to community standards and the entire file is flagged as rejected [3].

B. Max Threshold Test

RF and ionospheric interference can cause strong radar echoes in the doppler spectra, often near the first order Bragg peaks where currents are processed from. These echoes show as high velocities in the radial current maps [6]. A maximum velocity threshold test was written to ensure that a radial current speed is not unrealistically high. The maximum radial speed threshold (RSPDMAX) represents the maximum reasonable surface radial velocity for the given domain. If a radial speed (RSPD) exceeds the RSPDMAX as defined by the HFR operator, then this speed realization will be flagged [1].

C. Valid Location Test

HFR surface current data are measured from a stationary land-based remote sensor and are placed on a fixed grid created based on range and bearing from the receiver location. Occasionally, the real-time radial processing software may place velocity data over land or behind an island or some other unmeasurable area. On the HFR site, operators can visually create a reference area filter (AngSeg) file that will tell the real-time radial processing software to add flags where the operator deems that surface currents are unmeasurable. These flags are output as +128 in the VLFG column that is saved in the real-time radial files [1].

The valid location test performs two operations. First, it checks the VFLG column in the radial file for any +128 flags that the real-time processing output and converts this information into the standard QARTOD flags as part of the valid location test column. If the AngSeg is not setup or adjusted correctly, the real-time processing software will miss any unmeasurable areas over land. During the second part of the test, a high-resolution coastline shape file is loaded and joined using GeoPandas on latitude and longitude with a specific radial file. The joined matrix shows where radial points intersect with land (+1) or water (-1). With the results of this test, we can be sure whether a point near is a valid ocean point or an unmeasurable land point. All points that do not lay over water or points that lie in other unmeasurable areas are flagged.

D. Radial Count

Low radial counts indicate poor radial map coverage. The radial count test rejects radial files that contains less than a minimum number of radial vectors (RCMIN) and flag as suspect any that contain more than RCMIN but less than or equal to the warning threshold (RCLOW). The RCMIN threshold is site specific and dependent on the number of radial grid cells. The radial count test does not apply to beam-forming systems [1].

E. Spatial Median

A spatial median filter is used to reduce outlier velocities in each radial file. For each separate radial source vector, the median of all velocities within a specified radius whose vector bearing is within a specified angle from the source vector's bearing is computed (VELO). If the difference between the source vector and the median velocity is greater than the specified speed threshold (CURLIM), the vector is flagged. If the difference is less than the threshold, the vector value is changed to the median velocity. The spatial median test does not apply to beam-forming systems [1].

F. Temporal Gradient

The temporal gradient test checks for satisfactory temporal rate of change of radial components between successive files. The test determines whether changes between successive radial velocity (ΔTEMP) measurements at a specific radial source point are within an acceptable range defined by the HFR operator. If the temporal change between successive radial velocities exceeds the gradient failure threshold (GFAIL), the source point is flagged as fail. If the change is less than the failure threshold, but more than the warning threshold (GWARN), the source point is flagged as suspect [1].

G. Interpreting QC Flags

TABLE II. QARTOD FLAG STANDARDS

Code	Meaning	Definition
1	Pass	Data have passed critical quality control tests
2	Not Evaluated	Data have not been QC-tested
3	Suspect	Data are considered to be suspect based off of site warning thresholds
4	Fail	Data are considered to have failed QC based off of site failure thresholds
9	Missing	Data are missing

The flag meanings used in the quality controlled radial files are displayed in Table II. Data are not removed based on the results of the QC tests. Once each algorithm completes testing, the results are appended to a new column that corresponds to the QC test that was executed. This column contains the QARTOD flag information that the end user can utilize to filter out points that the QC test deemed suspect or failed. After every QC test has completed, the flags are combined into a primary flag that is set to the worst case of all QC flags within the data record for each radial source vector. This provides a convenient way for users to filter the results of all executed tests rather than filtering each one separately [10].

VII. REPROCESSED DATA ANALYSIS

Once the QC flags have been added to the radials, we compare the flagged radials to the original radials. Fig. 3 shows useful comparison consisting of two different plot that allows us to quickly see how well the QARTOD algorithms are flagging problematic radial points as we scroll through time. We compare the pass/fail plots in Fig. 3b to the original radials in Fig. 3a to make sure that any bad or suspect data that we can see in the original file has been removed or flagged. The process is repeated for every UGOS HFR site as each new six-month dataset is retrieved by the operator. All quality controlled radial data is made available to UGOS modelers via an ERDDAP server and sent to various data archival centers including the National Centers for Environmental Information (NCEI), Gulf of Mexico Research Initiative Information and Data Cooperative (GRIIDC), and GulfHub for permanent data storage. A schematic of the entire UGOS real-time and delayed mode radial quality control process can be seen in Fig 4.

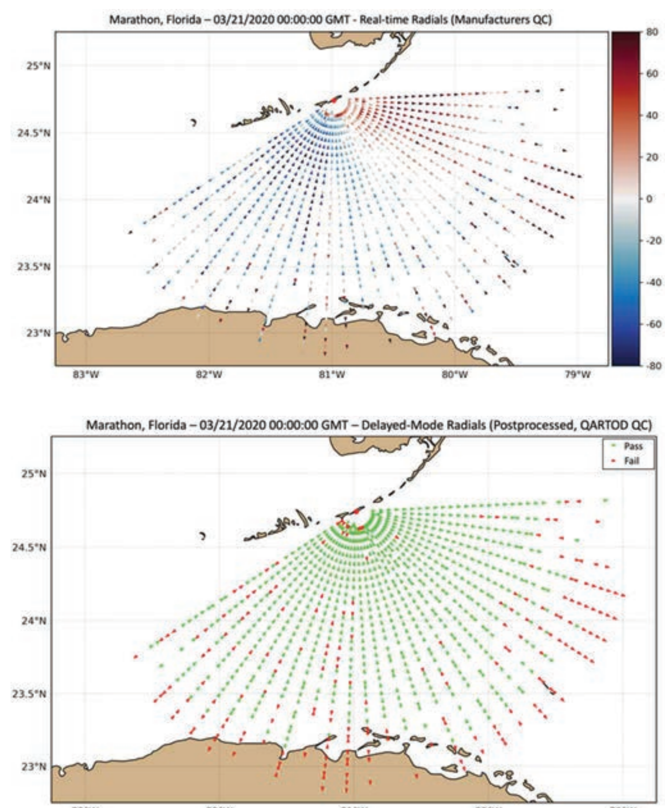

Fig. 3. USF MARA radial maps. a) Real-time, no qc - Interference is present in unrealistically high radial velocities at the outer range cells. Radials present over land and behind islands b.) Delayed-mode, qc – Primary Flag plot. The

outer range cells are flagged for inteference that was not filtered out. Radials over land and behind islands are flagged.

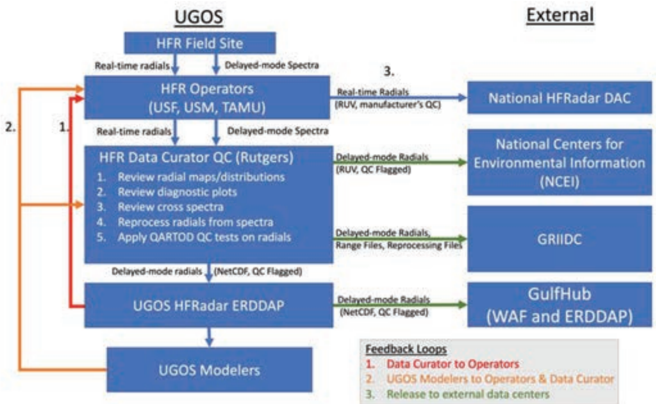

Fig. 4. UGOS Data Flow

VIII. DISCUSSION

As HFRs increasingly become an important component of coastal ocean observing systems [11], implementation of the unified quality control procedure is critical prior to applications of radial data, e.g., in generating total currents or for assimilation into numerical ocean models [12]. Even though the HFR quality control procedure was developed for the UGOS project, the software is open-source developed and can be can be used by many other groups in the HFR community. It has been successfully demonstrated on CODAR SeaSonde radial data. It can be similarly applied to other HFR (WERA and LERA) data CTF files.

ACKNOWLEDGMENT

This work was supported by the Gulf Research Program of the National Academies of Sciences, Engineering, and Medicine under the Grant Agreement number: 2000009917. The content is solely the responsibility of the authors and does not necessarily represent the official views of the Gulf Research Program or the National Academies of Sciences, Engineering, and Medicine. We thank Teresa Updyke (Old Dominion University), Kyle Wilcox (Axiom Data Science), and Laura Nazzaro (Rutgers University) for their contributions to the continued development of the HFRadarPy Python toolbox and Hugh Roarty (Rutgers University) and Ethan Handel (Rutgers University) for ongoing discussion of HF radar quality control.

REFERENCES

[1] Integrated Ocean Observing System. "Manual for Real-Time Quality Control of High Frequency Radar Surface Current Data," 2016 https://ioos.noaa.gov/ioos-in-action/manual-real-time-quality-control-high-frequency-radar-surface-current-data/).

[2] Y. Liu, C. Merz, R. Weisberg, L. Shay, S. Glenn, and M. Smith, "Chapter 5: An Initial Evaluation of High-Frequency Radar Radial Currents in the Straits of Florida in Comparison with Altimetry and Model Products," Ocean Remote Sensing Technologies: High Frequency, Marine and GNSS-Based Radar, The Institution of Engineering and Technology, 2021, in press.

[3] T. G. Updyke, H. J. Roarty, M. Smith, and L. Nazzaro, "The Impact of Reprocessing Efforts on the Mid-Atlantic's Surface Current Product," OCEANS 2019 MTS/IEEE SEATTLE, 2019, pp. 1-5, doi: 10.23919/OCEANS40490.2019.8962804.

[4] T. G. Updyke, "Antenna Pattern Measurement Guide," 2020, Online, Available: http://www.ccpo.odu.edu/currentmapping/documents/guides/Antenna_Pattern_Measurement_Guide_2020.pdf.

[5] B. Lipa, "Defining First-Order Region Boundaries," 2002, Online, Available: http://support.codar.com/Technicians_Information_Page_for_SeaSondes/Docs/Informative/FirstOrder_Settings.pdf.

[6] Integrated Ocean Observing System, "CODAR QA/QC & Related Practices", 2012, Online. https://cdn.ioos.noaa.gov/media/2017/12/cos_qaqc_document.pdf.

[7] Merz, C., Y. Liu, and R. Weisberg, "Chapter 4: Sea surface current mapping with HF radar – A Primer," Ocean Remote Sensing Technologies: High Frequency, Marine and GNSS-Based Radar, The Institution of Engineering and Technology, 2021, in press.

[8] M. Smith, "HFRadarPy", 2021, Online, GitHub repository, https://github.com/rucool/HFRadarPy/.

[9] M. Otero. "Encoding NetCDF Radial Data in the HF-Radar Network," 2013, Coastal Observing Research and Development Center, Scripps Institution of Oceanography. https://cordc.ucsd.edu/projects/mapping/documents/HFRNet_Radial_NetCDF.pdf.

[10] Integrated Ocean Observing System, "Manual for Real-Time Oceanographic Data Quality Control Flags," 2020, Online, https://cdn.ioos.noaa.gov/media/2020/07/QARTOD-Data-Flags-Manual_version1.2final.pdf.

[11] Y. Liu, H. Kerkering, and R.H., Weisberg (Editors), *Coastal Ocean Observing Systems*, 2015, 461 PP., Elsevier (Academic Press), London, UK.

[12] A. Barth, A. Alvera-Azcárate, and R.H. Weisberg, "Assimilation of High-Frequency Radar Currents in a Nested Model of the West Florida Shelf", *Journal of Geophysical Research*, 2008, 113, C08033, doi:10.1029/2007JC004585.

Implementation of Quality Flags in the Processing of High Frequency Radar Surface Current Data

Teresa G. Updyke
Old Dominion University
Norfolk, VA, USA
garner@ccpo.odu.edu

Hugh J. Roarty
Rutgers University
New Brunswick, NJ, USA
hroarty@marine.rutgers.edu

Michael Smith
Rutgers University
New Brunswick, NJ, USA
michaesm@marine.rutgers.edu

Laura Nazzaro
Rutgers University
New Brunswick, NJ, USA
nazzaro@marine.rutgers.edu

***Abstract*—The Mid-Atlantic Regional Association Coastal Ocean Observing System (MARACOOS) produces hourly regional surface current maps for an area of coastal ocean stretching from the Outer Banks to Cape Cod. An updated and more formal implementation of quality control (QC) in the real-time processing has been tested over the past year using QC tests described in the QARTOD Manual for Real-Time Quality Control of High Frequency Radar Surface Current Data [1]. Quality checks are performed at spectra, radial and total vector levels of processing. At the radial and total vector levels, primary and secondary flags are written to the data files. The primary flag is intended to provide data users with an overall assessment of data quality that can be used to quickly filter out bad data. The secondary flags are the results of individual QC tests and provide information that the radar operator(s) could use to address specific quality issues in order to improve the real-time data feed.**

An analysis of the flag information recorded in the radial and total vector files for the time period of March 1, 2021 to May 31, 2021 is presented in this paper. Percentages of over-water radial vectors that fail the QC tests are typically under 10%. The valid location test fails more radials than other tests followed by the spatial median test, the radial count test and the syntax test. A comparison of test failures is made between thirteen different radar stations. Details are provided on how QC test thresholds are assigned. Finally, the impact of the quality control on the surface current maps is described.

Keywords*—*high frequency radar, surface currents, Mid-Atlantic, quality control

I. INTRODUCTION

This paper describes a new implementation of real-time quality control within the Mid-Atlantic Regional Association Coastal Ocean Observing System (MARACOOS) high frequency (HF) radar processing and compares the output of two different versions of MARACOOS real-time data processing, which produced 6-km gridded regional surface current maps each hour over the focus time period from March 1, 2021 to May 31, 2021. Version 1 processing, which will be referred to as V1, uses data management procedures and programming scripts that were originally put in place in 2012. Although changes have been made since that time, the basic processing flow and computer code are effectively the same as they were in 2012. Version 2 (V2) processing contains the new implementation of QARTOD. It builds on previous work in automated quality control by the HF radar group at Rutgers University [2][3]. Important goals in the development of this version were to document QC through the use of quality flags and create a process that was extensible so new QC tests could be easily added in the future. V2 uses the HFRadarPy community toolbox code (available at https://github.com/rucool/HFRadarPy) to run the QARTOD QC tests and features newly developed file formats that include flag metadata in radial and total vector data files. There are other significant differences in the V1 and V2 processing, but the data comparisons presented here will focus on the differences that result from the new quality control procedures.

The MARACOOS 6-km gridded surface current maps are calculated using radial data from seventeen long range CODAR HF radar systems (Fig. 1). Fourteen are owned and operated by MARACOOS. The three stations located on North Carolina's

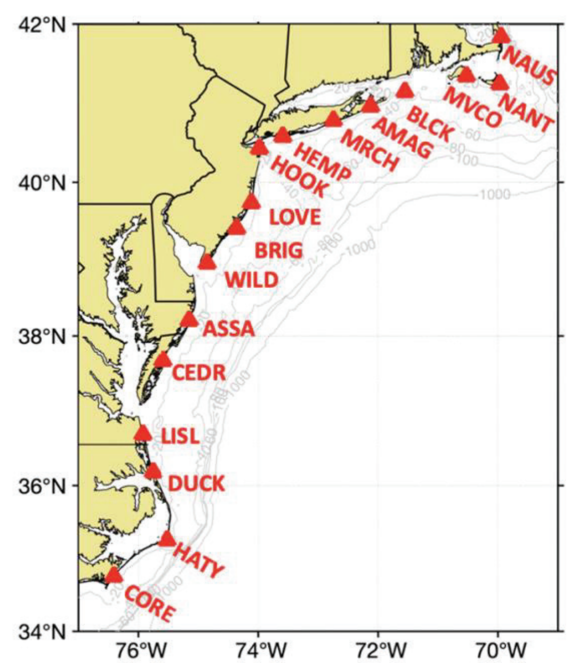

Fig. 1. 5 MHz radar stations contributing to MARACOOS surface current maps. DUCK, HATY and CORE stations are operated by SECOORA.

Outer Banks (DUCK, HATY and CORE) are operated by the Southeast Coastal Ocean Observing Regional Association (SECOORA). During the analysis time period, four stations were not operational (NAUS, NANT, MVCO and CEDR).

II. Methods

Radar operators in the region follow several quality assurance and quality control procedures. Operators routinely monitor hardware and radial diagnostic plots to look for potential problems. Operators also review radial maps and radial map distributions to check for suspect radials and poor distributions. The Doppler spectra first order line settings are periodically evaluated to maximize the amount of Bragg sea echo data that is processed to radials and minimize the inclusion of various types of interference as much as possible. Antennas are calibrated with measured antenna patterns and appropriate patterns are applied in data processing [4].

In addition to the quality measures described above, real-time processing incorporates automated quality control. Quality checks are performed at spectra, radial and total vector levels. In the MARACOOS new V2 processing, primary and secondary flags are written into the data files. Both levels of flags follow the IOC 54:V3 Primary Level flagging standard (UNESCO 2013) which has been adopted by QARTOD [5] (Table 1).

TABLE I. PRIMARY AND SECONDARY FLAG CODES

Flag Value	*Flag Meaning*
1	Good
2	Not Evaluated
3	Questionable/Suspect
4	Bad

A. *Spectra Level Quality Control*

Although QARTOD signal (spectra) level QC tests are used in real-time processing, the flags are not saved at this level of processing. All stations use signal-to-noise ratio thresholds for each antenna as well as other tests that are embedded in the manufacturer's software. At the DUCK, HATY and CORE stations, additional radial metric QC tests are performed on site with qccodar Python toolbox scripts [6]. In the HFR QARTOD manual, these tests are included as Test 2 (Cross Spectra Covariance Matrix Eigenvalues), Test 3 (Single and Dual Angle Solution - Direction of Arrival (DOA) Metrics (magnitude)) and Test 4 (Single and Dual Angle Solution - Direction of Arrival (DOA) Function Widths (3 dB)).

B. *Radial Level Quality Control*

The QC tests performed on the radial data in both V1 and V2 processing are the syntax, maximum speed, and valid location tests. V2 adds the radial count and spatial median tests (Table II).

TABLE II. QARTOD RADIAL QC TESTS APPLIED

Test Code	**Radial QC Test List**		
	Test Name	***Suspect Flag***	***Fail Flag***
QC06	Syntax	N/A	See text
QC07	Max Threshold	velocity > RSPDHIGH <= RSPDMAX	velocity > RSPDMAX *RSPDMAX = 300 cm/s*
QC08	Valid Location	N/A	VFLG = 128, identified by regional mask file
QC09	Radial Count	RCMIN[a] >= count <= RCLOW[a]	count < RCMIN[a]
QC10	Spatial Median	N/A	velocity > CURLIM *RCLIM=2.1 cells, ANGLIM = 10 degrees, CURLIM[b] = 30 or 50 cm/s*

a. Threshold values are determined for each station.

b. DUCK, LISL, HATY and CORE use 50 cm/s. All others use 30 cm/s.

The syntax test requires that the following metadata be present in the file: file type LLUV, site code, timestamp, site coordinates, antenna pattern type and time zone. Other requirements include 1) the file name timestamp must match the timestamp reported within the file, 2) radial data tables (Lon, Lat, U, V, ...) must not be empty 3) radial data table columns stated must match the number of columns reported for each row 4) site location must be within range: $-180 \leq \text{Longitude} \leq 180$ $-90 \leq \text{Latitude} \leq 90$ and 5) time zone must be Greenwich Mean Time.

The maximum threshold test ensures that a radial current speed is not unrealistically high. The maximum threshold is set to 300 cm/s for all stations. This is consistent with the National HF Radar Network's threshold. The high threshold, above which the vector is considered suspect, is station-dependent and based on a knowledge of current speeds for that area and a review of several months of previously recorded data.

Any vector that is placed over land or any other area that is out of view of the radar (e.g. water behind a point of land) is flagged by the valid location test. Radar operators use CODAR SeaSonde software to create a mask file for the station that will set a flag (+128) in the "VectorFlag" column of the CODAR LLUV radial file. The regional processing looks for that flag to set the QARTOD fail flags for the invalid location test. It also uses a separate land mask, independent of the station-specific mask, to fail any over-land radials.

The radial count test will flag all radials in a file that contains few radials. Often a very low number of radials indicates a problem with the radar system or a high level of interference. Any file with less radials than the minimum count threshold value is assigned fail flags and any file with greater than or equal to the minimum count but less than or equal to the low count threshold is assigned suspect flags. The minimum threshold value for a station is based on a percentage of the number of possible radials given a 6-km range cell interval, 5-degree directional bins and a maximum of 40 range cells. The

Sponsor: National Oceanic and Atmospheric Administration (NOAA)
NOAA-NOS-IOOS-2016-2004378 / CFDA: 11.012

minimum threshold is 10% of the possible number of radials "rounded" to the nearest 25. The low threshold is three times the minimum threshold.

The spatial median test is based on a CODAR SeaSonde spatial filter and is designed to fail a radial if it is significantly different from its neighbors. Fig. 2 shows an example of how the spatial median test can be used to remove bad radial data. In the QARTOD implementation, a radial velocity is flagged if it differs by more than 30 cm/s from the median value of neighboring velocities (located within a radius of 12 km and bearing of 10 degrees of that radial). At stations in the vicinity of the Gulf Stream, the speed difference threshold had to be increased from 30 cm/s to 50 cm/s in order to avoid flagging the edge of the Gulf Stream.

In V2 processing, secondary flags for these radial tests are written to a radial QC file. The new radial QC file retains the same name as the original radial file and keeps all of the information from the original file. QC test metadata is added to the file header and the flag code results for each test are appended to the CODAR main data table in separate data columns. Presenting the flag information in this way requires more space than using a binary or hex code to locate multiple flags in a single column, but the file is simpler to read and codes are easier to interpret. When an entire file fails based on a test such as syntax or radial count, fail flags are set for every vector in the file. The primary flag for a radial is set to a fail code if any of the secondary flags has a fail code and radials that fail are excluded from the total vector calculation.

C. *Total Vector Level Quality Control*

Total vectors are calculated using an optimal interpolation method described in [7] using code from the MATLAB community toolbox HFR-Progs. A copy of this toolbox is available at https://github.com/rowg/hfrprogs. Total vectors are subject to data density, maximum speed, valid location, U-component uncertainty and V-component uncertainty tests (Table III). These tests were in place for both V1 and V2 processing. The valid location test wasn't formally implemented with flags in V1, but a land mask file was used. V2 keeps all locations in the grid and sets fail flags for those grid points that are invalid.

TABLE III. TOTAL VECTOR QC TESTS APPLIED

Test Code	Total Vector QC Test List		
	Test Name	***Suspect Flag***	***Fail Flag***
QC14	Data Density	N/A	N/A (see text)
QC16	Max Threshold	velocity > RTPDHIGH[b] <= TSPDMAX	velocity > TSPDMAX *TSPDMAX = 300 cm/s*
QC18	Valid Location	N/A	Identified by regional mask file
QC19	U-component Uncertainty	N/A	Uerr > 0.6
QC20	V-component Uncertainty	N/A	Verr > 0.6

[c] Threshold values are determined for each station.

A data density requirement is enforced, but this test does not use flags. A minimum of three radial velocities must be sourced from at least two radar stations in order to compute a total velocity vector.

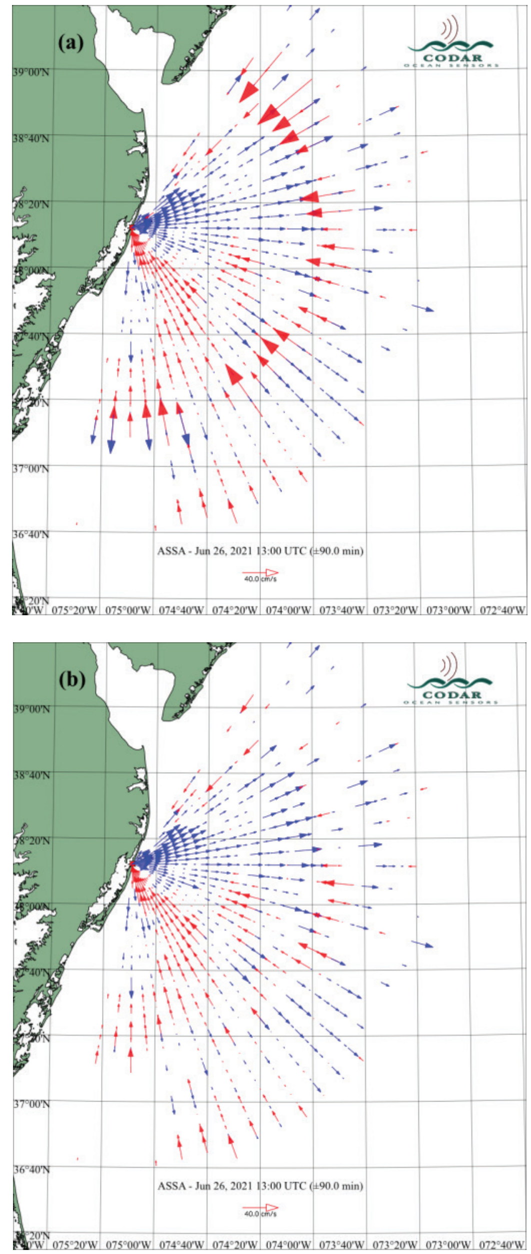

Fig. 2. a) Original ASSA radial map. b) ASSA map after radials that failed the spatial median test were removed.

The U-component and V-component uncertainties are normalized uncertainties that are calculated as part of the optimal interpolation algorithm [8]. A value of 0 is good and a value of 1 is poor. In the Mid-Atlantic, a previous study by Kohut et al. showed that a threshold value of 0.6 improved data quality while preserving good data coverage in the maps [7].

Total vector flags are recorded with total velocities in Matlab MAT files. They are saved in the HFR-Progs community toolbox TUV structure as additional fields. When the Matlab file is converted to NetCDF, the flags are represented as additional variables and those variables include attributes that describe the flags. Following Climate and Forecast (CF) metadata conventions, the "ancillary variable" attributes of the velocity variables provide a reference to the flag variables.

III. Results

A large percentage (91.1%) of the hourly files from thirteen stations were available for total vector processing. There were 2531 hourly radial files missing. An additional 314 radial files were taken out of processing due to the QC test failures (142 due to syntax errors and 172 that failed the radial count test). Only 1.2% of available radial files were removed from processing by implementing the QARTOD tests.

A. *Radial Quality Control Flag Statistics*

Overall, the test that fails the most radials is the invalid location test followed by the spatial median test, the radial count test and the syntax test. As an example, Fig. 3 shows time series of percent failures for each test at a single station.

Fig. 4a shows invalid location test failures at each station as the average percentage of radials in the hourly files that failed the tests. The failure averages at most stations fell between 10% and 25%. BLCK had the largest average at 33.5%. At the North Carolina stations, the radial metric QC already removed data in bad locations, therefore, no failures were identified at the regional processing level.

The radial count test failed radials in 172 hourly radial files. The percentage of files that failed for the three-month time period varied between stations, but the percentage was under 1% for all stations except ASSA and DUCK (Fig. 4b). ASSA had 68 files fail (3.1% of files) and DUCK had 44 failures (2.1% of files).

Some syntax failures were present in the DUCK, HATY and CORE files. The cause is a mismatch in the timestamp in the header of the file and the time indicated by the radial file name. The radials from 142 files were removed from total vector processing due to syntax errors. Failures occurred for 2.9% of

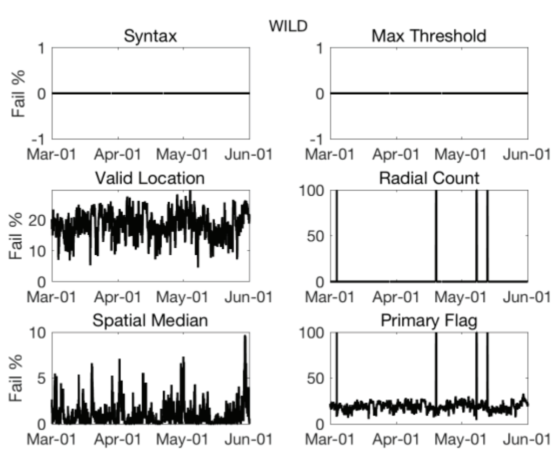

Fig. 3. QC test results for the WILD radar station. Percentage of radials in the hourly files that received fail flags for the radial QC tests.

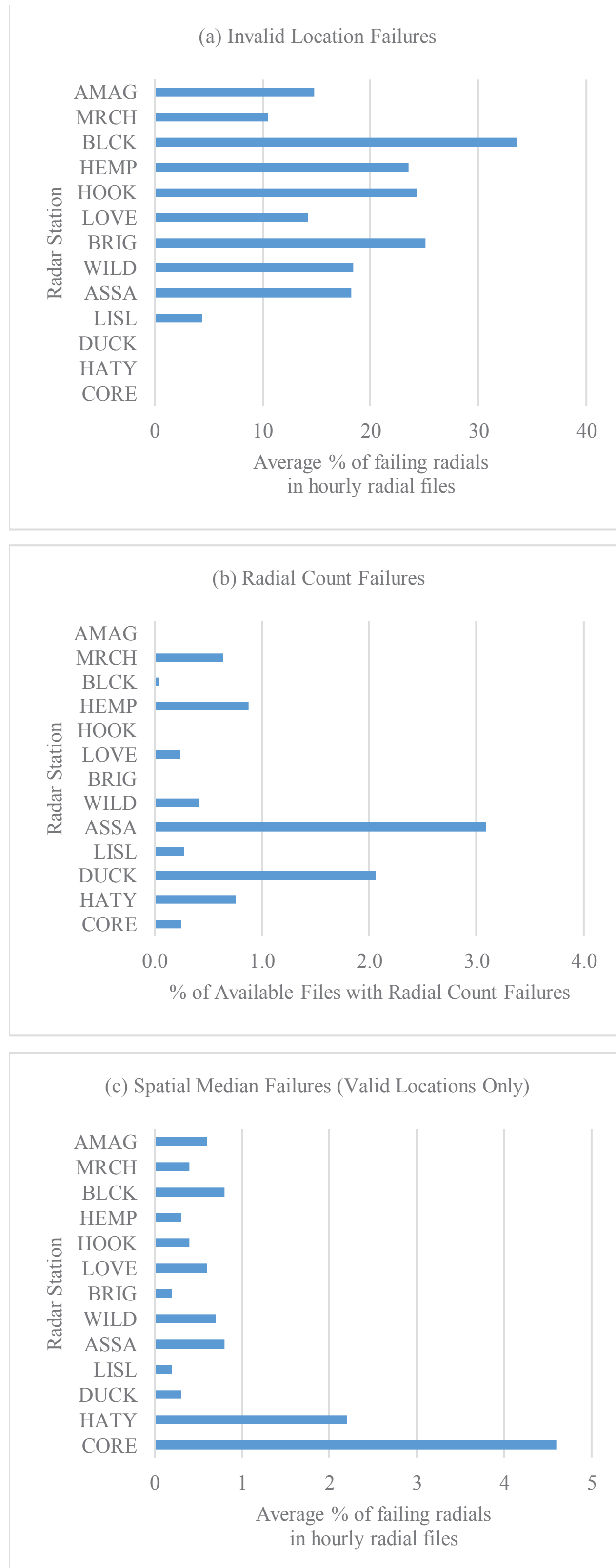

Fig. 4. Radial QC test failure statistics for the (a) invalid location test, (b) radial count test and (c) spatial median test.

available hourly files at DUCK, 1.9% of CORE files, and 1.7% of HATY files. The mismatch happens only when radial metric QC [6] is implemented on site and the number of merged radials is lower than the normal merged radial count of five.

The maximum threshold flags were put into practice in V2 processing; however, at this time, the radar stations have a limit on the maximum velocity that is allowed to pass from the spectra to radial stage of processing and this maximum is less than the maximum of 300 cm/s chosen for the QC test. Therefore, this test failed no radials. In future processing, the velocity limits may be set at a higher level in this earlier processing stage so that the QC max threshold test flags will become effective and provide flag statistics that may be analyzed.

On average, the spatial median test failed less than 5% of the radials placed in valid over-water locations in the hourly files (Fig. 4c). At all but two stations, the average failure rate for the spatial median test was less than 1%. CORE and HATY had the highest average failure rates of 4.6% and 2.2% respectively.

For the spatial median test, maps were created to highlight locations that most frequently failed for each radar station. Several stations show more frequent failures at points in the first few range cells. Highlighted bearing spokes near coast or edges of coverage are also common in these maps. WILD, HOOK, LOVE and MRCH stations have fail flags concentrated in one to three bearing spokes. The measured pattern radial type is more likely to show a pattern that lines up along a bearing or set of bearings since errors may concentrate along bearing lines. Highlighted arcs as well as partial spokes in mid to far ranges are signs of the test removing ionospheric interference. This pattern of failures is shown at ASSA, LISL, DUCK, AMAG and BLCK. Maps for stations HATY and CORE showed that the test was still often flagging the Gulf Stream gradient. In order to minimize this erroneous flagging, the current difference threshold for those two sites may need to be increased.

B. *Surface Current Map Comparisons*

The additional quality control in V2 resulted in a very slight decrease in surface current map data coverage at some grid points. The V1 and V2 maps have 11,430 grid point in common. The difference in percent data availability at these grid locations (V1-V2) ranged from 0 to 0.102% and the average decrease in percent availability was 0.005%.

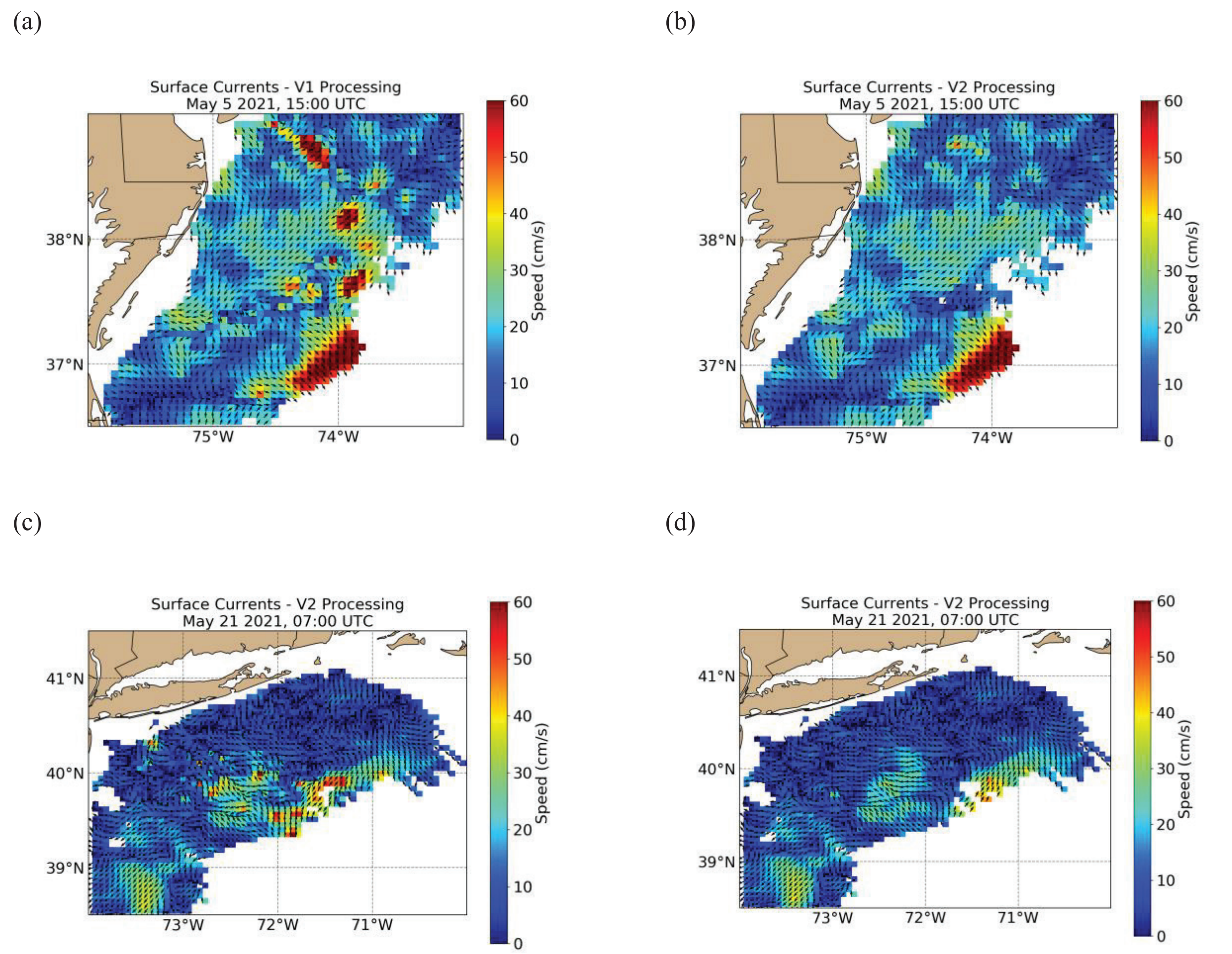

Fig. 5. Surface current map comparisons (a) V1 May 05 2021 15:00 UTC, (b) V2 May 05 2021 15:00 UTC, (c) V1 May 21 2021 07:00 UTC and (d) V2 May 21 2021 07:00 UTC

The greatest differences in surface current velocities between V1 and V2 total vector maps are expected to occur from the implementation of the spatial median test. This test removes spatial outliers from the data and in particular, it helps remove ionospheric interference that is interpreted as Bragg echo and erroneously processed into radials. Those radials often appear in the radial maps as high velocities concentrated in certain range rings. In the total maps, they can show up as patches or arcs of high current velocity in areas of otherwise low current speed. Thirty hours of V1 maps containing data contaminated by ionospheric interference, were compared with corresponding V2 maps and all show some removal of this bad data in V2. The high velocity patches were completely removed or much improved in half of those maps (Fig. 5). Seven maps had little improvement and an investigation into those cases would be worthwhile in order to see what changes might be made to automatically assign fail flags to more of this bad data.

IV. Conclusions

A new implementation of QARTOD quality control in the MARACOOS HF radar processing has proven beneficial for flagging bad data in the real-time Mid-Atlantic surface current maps. The primary flag provides a simple way for data users to filter out bad data. The inclusion of secondary flags is useful to radar operators and data providers. By knowing when, where and how often specific types of failures occur, steps may be taken to mitigate these problems. More quality control work remains to be done and more tests can easily be added into the testing framework that has been built into the new version of processing.

Acknowledgment

The authors would like to acknowledge their fellow HF radar team members who operate and maintain the long-range radar systems in the Mid-Atlantic: Ethan Handel, Rich Arena, Mike Muglia, Patterson Taylor, Nicolas DeSimone and Anthony Whipple. We also thank the University of North Carolina and the Coastal Studies Institute for the use of HF radar data from the North Carolina radar stations.

References

[1] Manual for Real-Time Quality Control of High Frequency Radar Surface Current Data: a Guide to Quality Control and Quality Assurance for High Frequency Radar Surface Current Observations. Version 1.0. Integrated Ocean Observing System (U.S.), U.S. Department of Commerce, National Oceanic and Atmospheric Administration, National Ocean Service, Integrated Ocean Observing System, Silver Spring, MD, 2016.

[2] H. Roarty, M. Smith, J. Kerfoot, J. Kohut, and S. Glenn, "Automated quality control of high frequency radar data," in *Oceans, 2012*, 2012, pp. 1-7.

[3] H. Roarty, L. Palamara, J. Kohut, and S. Glenn, "Automated quality control of high frequency radar data II," in *OCEANS 2016 MTS/IEEE Monterey*, 2016, pp. 1-3.

[4] J. Kohut and S. Glenn. "Improving HF radar surface current measurements with measured antenna beam patterns." Journal of Atmospheric and Oceanic Technology., vol. 20(9), pp. 1303-1316. 2003.

[5] Manual for the Use of Real-Time Oceanographic Data Quality Control Flags. Version 1.2. Integrated Ocean Observing System (U.S.), U.S. Department of Commerce, National Oceanic and Atmospheric Administration, National Ocean Service, Integrated Ocean Observing System, Silver Spring, MD, 2020.

[6] Haines, S., H. Seim and M. Muglia. "Implementing Quality Control of High-Frequency Radar Estimates and Application to Gulf Stream Surface Currents," Journal of Atmospheric and Oceanic Technology, vol. 34(6), pp. 1207-1224. 2017,

[7] Kohut, J., Roarty H.J, Randall-Goodwin, E., Glenn, S. and C. S. Lichtenwalner, "Evaluation of two algorithms for a network of coastal HF radars in the Mid-Atlantic Bight," Ocean Dynamics, vol. 62, pp. 953–968. 2012.

[8] Kim, S. Y., E. J. Terrill, and B. D. Cornuelle, "Mapping surface currents from HF radar radial velocity measurements using optimal interpolation," J. Geophys. Res., vol. 113(C10), 2008.

Evaluation of the NOAA Operational Forecast System in Delaware Bay

Hugh Roarty
Dept. of Marine and Coastal Sciences
Rutgers University
New Brunswick, NJ USA
hroarty@marine.rutgers.edu

***Abstract*— Ocean models play a large role in helping to understand the ocean's influence on climate and weather. Ocean models can also provide information on to mariners to help them in the piloting of their vessels. The Delaware Bay Operational Forecast System (DBOFS) provides nowcasts and forecasts of water levels, currents, water temperature and salinity. A High Frequency radar station was installed in Lewes Delaware in 2021 that dramatically increased the coverage inside Delaware Bay. Two months of surface current data from the HF radar network were utilized to validate the surface current measurements from the NOAA Operational Forecast System model for Delaware Bay. The HF radar surface current measurements showed that the model displayed good skill in estimating the phase of the currents but underestimated the speed by 50%. Also, the HF radar measurements highlighted eddies and complex flow regimes that were not represented in the model. Hopefully, continued measurements by the HF radar network can help improve the skill of the model.**

Keywords—remote sensing, geoscience, radar, ocean currents, numerical model, MARACOOS

I. Introduction

The US Integrated Ocean Observing System (IOOS) federal and nonfederal network of ocean observations, analyses and communications that delivers information on the past present and future state of the coastal ocean. IOOS meets the nation's need for ocean information by integrating across seven societal benefit areas [1, 2] which include improving the safety and efficiency of maritime commerce and better predictions of climate and weather effects on coastal communities.

As part of this effort, one tool that NOAA provides to the maritime community is the Physical Oceanographic Real Time System (PORTS). PORTS provides observations and predictions of water level and currents amongst other physical measurements critical for safe navigation. A component of Delaware Bay PORTS is the Delaware Bay Operational Forecast System (DBOFS) which provides nowcasts of surface winds, water levels, currents, temperature and salinity and forecasts these estimates 48 hours into the future.

One of the coastal communities that rely on IOOS observations and forecasts is the shipping associated with the Port of Philadelphia. The port of Philadelphia has the largest oil refinery capacity on the U.S. East Coast and is the 5th largest U.S. port complex. Port traffic in the winter amounts to 1,000 vessels per month or 30 vessels per day and this traffic doubles in the summer months. Each one of these vessels could potentially be utilizing forecasts of winds, waves and currents from IOOS.

Another stakeholder in the Delaware Bay region is the United States Coast Guard. In 2018 the United States Coast Guard conducted the Ports and Waterways Safety Assessment of the Delaware River with the goal of making the waterway as safe, efficient, and commercially viable as possible. The tool that the Coast Guard used in that assessment is the Waterway Risk Model which lists six categories of risk. The categories are existing conditions for 1) vessels 2) traffic 3) navigation 4) waterway and the corresponding consequences 5) immediate and 6) subsequent of a marine incident. The navigational risk conditions include winds and water movement, two of the variables that are estimated by DBOFS. And the maritime community has listed DBOFS as one of the tools that they use to mitigate the risk associated with the water movement. So having accurate and timely surface currents will help reduce the navigational risk inside the Delaware Bay.

An HF radar network has been operated near the entrance to Delaware Bay for the past decade [3]. Three 25 MHz radars are operated at Cape Henlopen, DE (HLPN), Cape Shore Lab (CAPE) and Cape May Point (CMPT). A 13 MHz radar is also operated in North Wildwood, NJ (WOOD). Recently a 25 MHz radar was installed in Lewes, DE (LEWE) in June 2021 to help increase the coverage inside Delaware Bay. Figure 1 shows the radial coverage for the five stations in the vicinity of the Bay.

For this study surface currents from the HF radar network were compared to estimates from the DBOFS model to assess model accuracy.

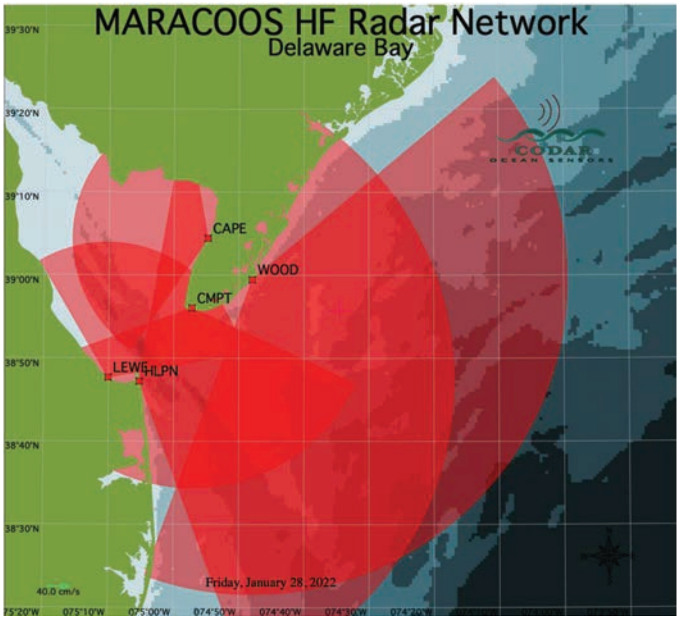

Figure 1: Map of the study area showing the locations of the HF radar stations (red square) around Delaware Bay. The four-letter site code is next to each station marker. The theoretical radial coverage from each station is shown as red semi-circle. Areas of deeper red indicate overlap from several stations.

II. METHODS

Two weeks of data from July 18, 2021 to August 1, 2021 from the DBOFS model and HF radar network were compared. Maps of surface currents were generated for both products each hour. Figure 2 shows the map of surface currents from the DBOFS model for July 21, 2021 18:00 GMT while Figure 3 shows the surface current measurements. The model captures the ebb tidal current and the faster currents on the western side of the Delaware Bay Channel but there are several features in the HF radar map not captured by the model. A cyclonic eddy has developed just south of Cape May NJ and the flow has reversed towards the northwest along the coast of Delaware. Both features are not represented in the model.

The data from the DBOFS model was interpolated onto the grid used for the surface current maps. A point inside the shipping channel near the entrance to Delaware Bay was chosen to perform a statistical comparison between the two current estimates. The coordinate for the point was 75°01' W and 38°51' N. Any data points within 3 km of that point were averaged to increase the confidence in the statistics which equated to 7 grid points for both data sets. The u and v surface current data were rotated into along and cross channel directions. The bearing of the along channel direction was 145° degrees (true north) from the point in the channel (Figure 4).

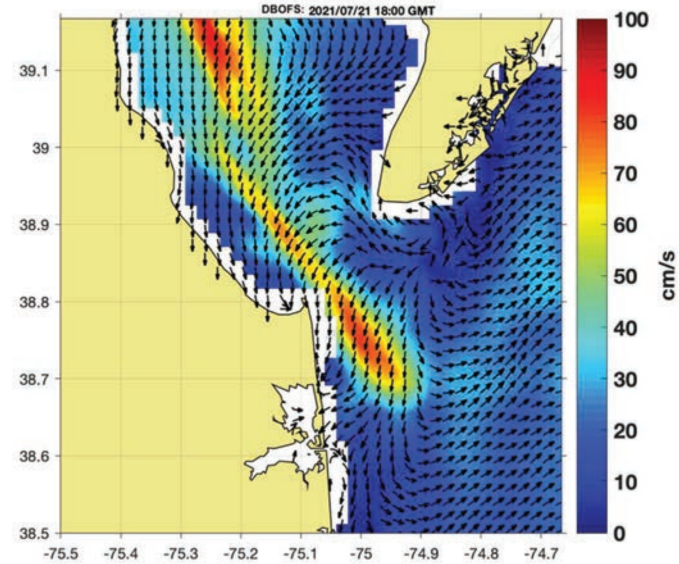

Figure 2: Map of surface currents from the Delaware Bay Operational Forecast System for July 21, 2021 18:00 UTC. The colorbar on the right indicates speed (0-100 cm/s) and the black arrows on the map indicate current direction.

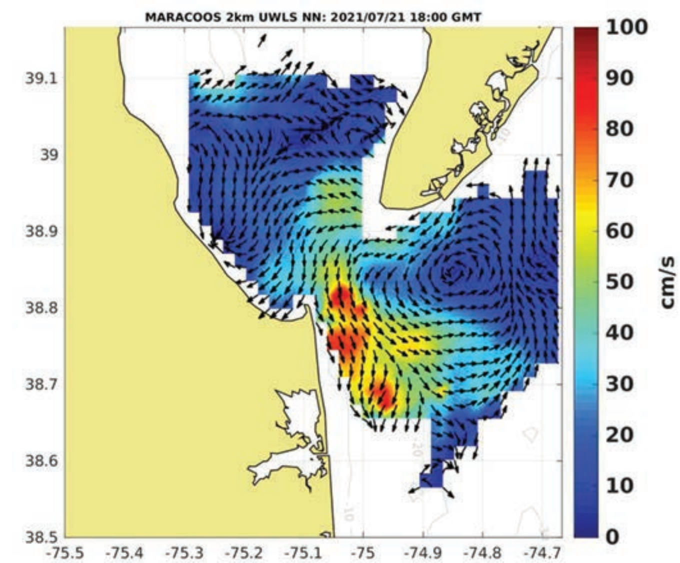

Figure 3: Map of surface currents from the Delaware Bay HF Radar Network for July 21, 2021 18:00 UTC. The colorbar on the right indicates speed (0-100 cm/s) and the black arrows on the map indicate current direction.

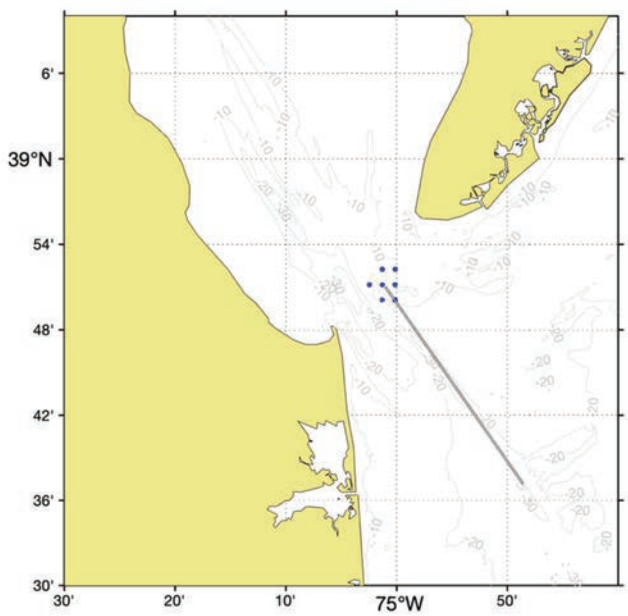

Figure 4: Map showing the points that were used int he comparison (blue dots) and the orientation of the along channel axis (black line).

III. Results

The two-week comparison of along and cross channel currents for the DBOFS model are shown in Figure 5 and Figure 6 shows the same for the HF radar surface currents. The model estimates the along channel current range to be 229 cm/s while the HF radar measured the range to be 305 cm/s. In the cross-channel direction, the model estimated the current range to be 118 cm/s while the HF radar only measured a current range of only 62 cm/s. Both the model and HF radar measured a period of 12.44 hours in the along channel direction which matches the period of the semidiurnal lunar tide (M2). However, there is a 33-degree phase shift between HF radar and DBOFS estimate in the along channel direction. This equates to a one-hour difference and the model is ahead of the HF radar surface currents by this one hour.

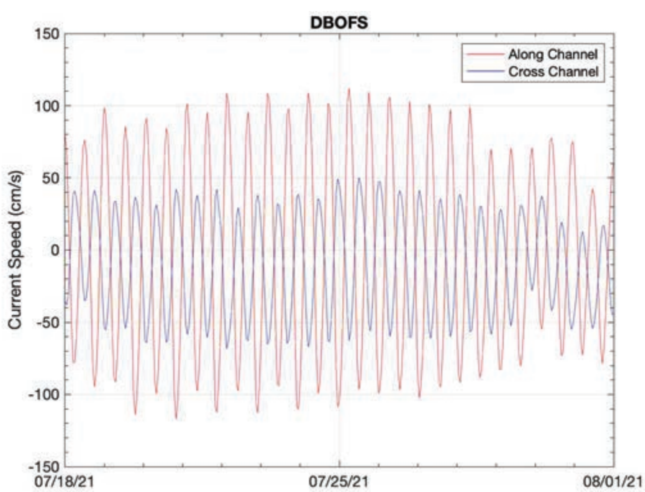

Figure 5: Time series of along (red) and cross (blue) channel currents at the mouth of Delaware Bay from July 18, 2021 to August 1, 2021 from the Delaware Bay Operational Forecast System.

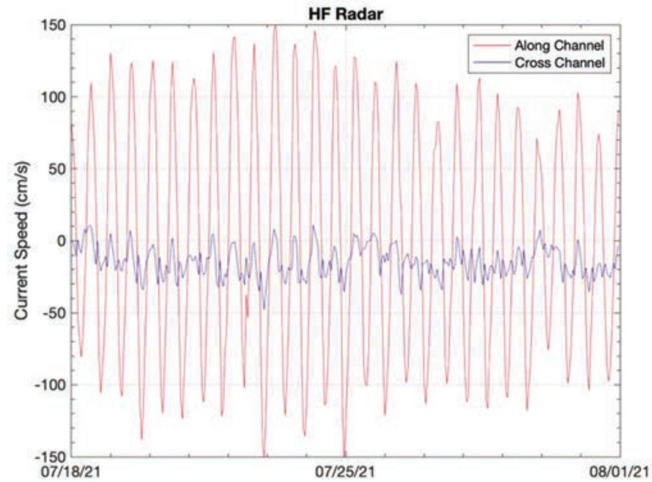

Figure 6: Time series of along (red) and cross (blue) channel currents at the mouth of Delaware Bay from July 18, 2021 to August 1, 2021 from the 2 km HF radar surface current product.

The same data were plotted to compare the along and cross channel estimates between he two products (Figure 7). The HF radar currents were plotted along the x axis while the DBOFS currents were plotted along the y axis. The top panel shows the along channel currents while the bottom panel displays the cross-channel currents.

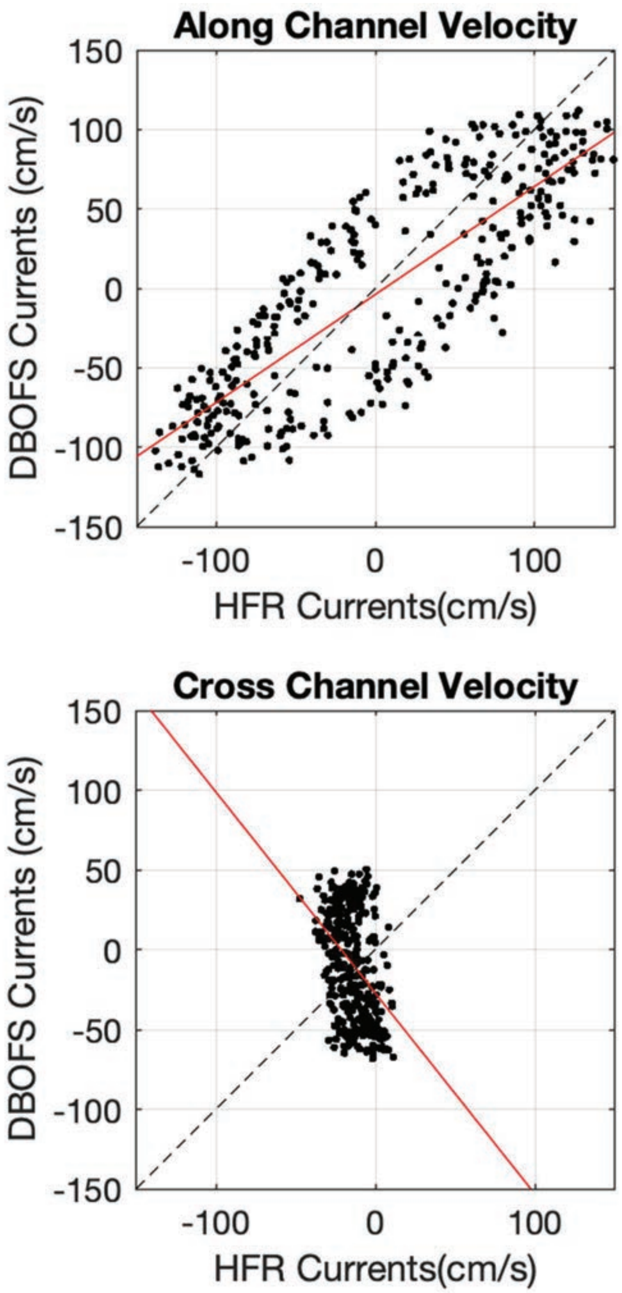

Figure 7: Scatter plot of HF radar currents (x-axis) vs. DBOFS currents (y-axis) for the along channel (top) and cross channel (bottom) direction. The 1:1 line is shown as the black dashed line and the red line is the least squares regression line.

IV. Discussion

The DBOFS model shows good skill in the along channel and only underestimates the current range by 25%. However, in the cross-channel direction the model is overestimating the current range by 90% and the correlation between the model and data is negative.

These results suggest that adjustments can be made to improve the Operational Forecast System for Delaware Bay. One improvement could be the assimilation of the surface current data into the model. One of the first operational HF radar networks was deployed in Delaware Bay in 1984 [4]. The authors of that publication noted the features in the surface currents repeat with semidiurnal regularity in calm conditions, but the CODAR measurements showed that stiff winds caused significant departures from the norm. It is now 38 years later from this assesment and there are features in the surface currents around Delaware Bay that the DBOFS model has yet to capture. The lack of mesoscale eddies and velocity contours that are closely tied to bathymetry are some of the essential features that could be improved in the model.

The accepted error criteria for skill assessment of the NOAA model is 26 cm/s for current speed and 22.5° for current direction [5, 6]. Further analysis will be required to determine if the model is within the accepted error criteria for skill assessment.

V. Conclusions

The Delaware Bay Operational Forecast System has been evaluated using two weeks of HF radar surface current data. The model was shown to be underestimating the maximum along channel velocity while overestimating the current in the cross-channel direction.

Acknowledgment

This work was funded by NOAA Award Number NA16NOS0120020 “Mid-Atlantic Regional Association Coastal Ocean Observing System (MARACOOS): Powering Understanding and Prediction of the Mid-Atlantic Ocean, Coast, and Estuaries”. Sponsor: National Ocean Service (NOS), National Oceanic and Atmospheric Administration (NOAA) NOAA-NOS-IOOS-2021-2006475, Integrated Ocean Observing System Topic Area 1: Implementation and Development of Regional Coastal Ocean Observing Systems.

References

[1] A. Lehmann, J. Masò, S. Nativi, and G. Giuliani, "Towards integrated essential variables for sustainability," vol. 13, ed: Taylor & Francis, 2020, pp. 158-165.

[2] (2018). *US IOOS Enterprise Strategic Plan 2018-2022*.

[3] P. Muscarella, N. Barton, B. Lipphardt Jr, D. Veron, K. Wong, and A. Kirwan Jr, "Surface currents and winds at the Delaware Bay mouth," *Continental Shelf Research,* vol. 31, no. 12, pp. 1282-1293, 2011.

[4] D. E. Barrick and B. J. Lipa, "Mapping surface currents," *Sea Technol,* vol. 26, pp. 43-48, 1985.

[5] K. W. Hess *et al.*, "NOS standards for evaluating operational nowcast and forecast hydrodynamic model systems," 2003.

[6] A. Zhang, K. W. Hess, E. Wei, and E. Myers, "Implementation of model skill assessment software for water level and current in tidal regions," 2006.

Surface Current Coverage of the Mid Atlantic United States

Hugh Roarty and Chris Shivock
Dept. of Marine and Coastal Sciences
Rutgers University
New Brunswick, NJ USA
hroarty@marine.rutgers.edu

Abstract— **Remote sensing technologies provide data across a large geographic area without the cost associated with in situ observations. Sensor placement is critical in maximizing the effectiveness of an organization's remote sensing strategy. While technical specifications of oceanographic sensors are easy to compare, the coverage and performance of a remote sensing network when applied to a specific location can be more challenging. The complex coastal and estuarine environment of the Mid Atlantic United States is constantly changing and remote sensing is an effective tool for measuring these changing waters. Accurately assessing the coverage that a remote sensing network delivers will provide justification for future investments and sensor placement. This paper provides a method for calculating the marine surface area of the Mid Atlantic and how it relates to the coverage of the High Frequency radar network. This method can be applied globally to evaluate observing network design and implementation.**

Keywords—remote sensing, geoscience, radar, ocean currents, GIS, MARACOOS

I. Introduction

The Integrated Ocean Observing System is a national-regional partnership that collects and communicates ocean information to meet the safety, economic and stewardship needs of the United States. The eleven regional associations of IOOS guide development and stakeholder input to regional observing activities. The Mid Atlantic of the United States from Cape Cod to Cape Hatteras encompasses the region for the Mid-Atlantic Coastal Ocean Observing System (MARACOOS).

IOOS recently adjusted the boundaries of the eleven regional associations. IOOS provided a GIS shapefile of the MARACOOS boundary that was coarse. We were unsure if this rough boundary would lead to problems in the future if it was used for area calculations. Therefore, a more refined boundary was created and subregions of the MARACOOS region were created. The surface area of each of the subregions and the overall boundary were compared between the IOOS shapefile and the refined boundary.

The paper also examines the radial coverage for several radar stations in the network. The SeaSonde HF radar is capable of measuring ocean currents over a full 360 degrees of angular coverage if not blocked by land. The presence of land will attenuate the signal. Antenna pattern measurements are typically performed utilizing the AIS package from CODAR Ocean Sensors. The question arises as to what angular coverage can be achieved from this method for measuring the antenna pattern. The angular coverage of each antenna pattern is gauged against the possible angular coverage from the coastline adjacent to a particular radar station.

II. Methods

U.S. IOOS has grown to include 17 Federal partners and 11 Regional Associations (RAs) that implement regional observing systems covering all U.S. coasts and Great Lakes with activities spanning from head of tide to the U.S. exclusive economic zone (EEZ) [1]. MARACOOS has colloquially been described as "1,000 km of coastline from Cape Hatteras to Cape Cod".

Recently IOOS has adjusted the boundary of MARACOOS. The waters east of Cape Cod and the inland waters of North Carolina were removed from the area of responsibility (Figure 1). The water surface area of the boundary file provided by IOOS was 417,750 km^2. The coverage of the new updated boundary file reduced the area to 378,121 km^2.

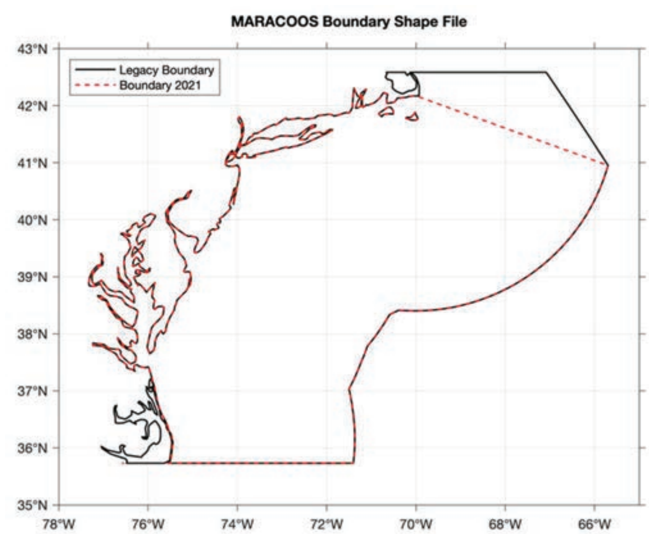

Figure 1: Map of Mid Atlantic United States. Area of responsibility for MARACOOS from 2007-2021 (black) and 2021-present (red).

The coastline in both boundary files is coarse and Block Island, RI is missing from the shape file. In order to create a more refined boundary file the National Hydrography Dataset from the United States Geological Survey's National Map was used to generate a more detailed boundary of the MARACOOS region. Hydrography data was processed in ArcGIS Pro and features of interest were selected using custom polygons. Subset polygons were created based on maritime criteria. Inland or estuarine waters were included from the head of tide to the Convention on the International Regulations for Preventing Collisions at Sea, 1972 (COLREGS) line of demarcation (Figure 2). Offshore waters were delineated from the COLREGS line seaward to the Exclusive Economic Zone boundary (200 nautical miles from the coast). The selected features were clipped from the original hydrography data and individual features were merged to create unified water bodies. Finally, water feature boundaries were dissolved to create one complete detailed feature within the general confines of the IOOS designated MARACOOS observation area.

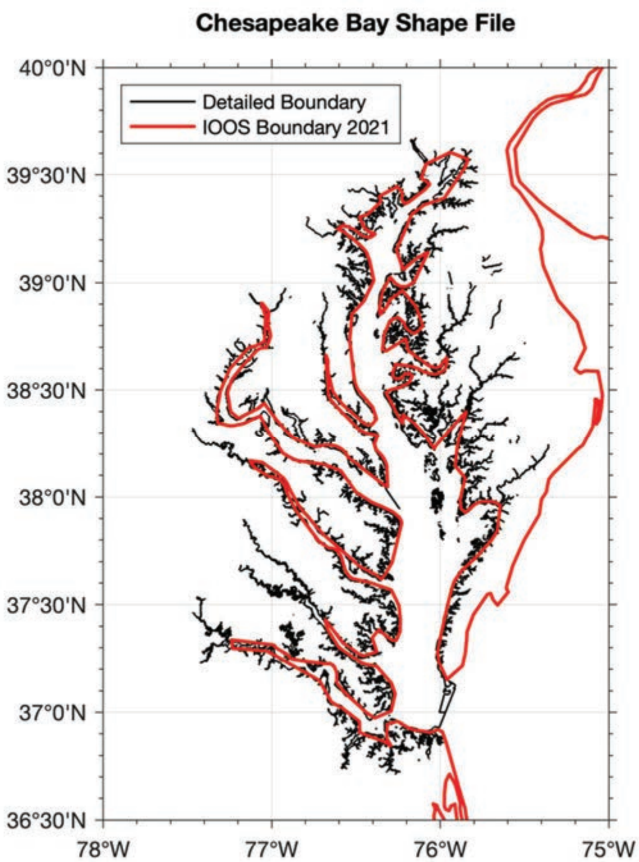

Figure 2: Map of Chesapeake Bay showing the MARACOOS boundary from IOOS (red) and the more detailed boundary file that was created for this research project (black).

III. RESULTS

Detailed shapefiles for eleven coastal subregions of the Mid Atlantic and an overall boundary for the MARACOOS region were created and the surface area of each polygon was calculated. The subregions for the MARACOOS area are listed from north to south in Table 1 and plotted in Figure 3.

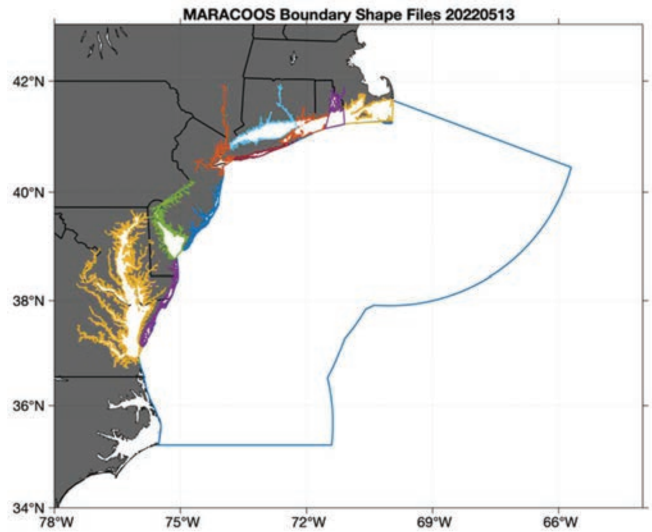

Figure 3: Detailed shapefiles for eleven coastal subregions of the Mid Atlantic and an overall boundary for the MARACOOS region

Table 1: Subregions within the MARACOOS area of responsibility. The columns are the surface area from the IOOS shape file, surface area of detailed shape file generated by Rutgers, percent difference between two products and the overall percentage of the detailed shapefiles.

#	Subregion	IOOS Area (km^2)	Rutgers Area (km^2)	Pct. Diff.	Rutgers Overall Pct.
1	Nantucket Sound	3,854	3,515	-9.6%	0.9%
2	Narragansett Bay	1,373	1,365	-0.6%	0.4%
3	Block Island Sound	2,124	2,036	-4.3%	0.5%
4	Long Island Sound	2,872	3,050	5.8%	0.8%
5	Great South Bay	0	420	100%	0.1%
6	New York Harbor	746	851	12.3%	0.2%
7	New Jersey Coast	0	577	100%	0.2%
8	Delaware Bay	2,054	2,225	7.7%	0.6%
9	DelMarVa Coast	0	997	100%	0.3%
10	Chesapeake Bay	11,040	11,816	6.6%	3.1%
11	Atlantic Ocean	354,058	352,050	-0.6%	92.9%
	Total	378,121	378,902	0.2%	100.0%

MARACOOS has sponsored the operation of HF radar since its inception. The networks that were first sponsored included a 5 MHz network that covered the shelf region and

25 MHz networks for Chesapeake Bay, Delaware Bay, New York Harbor, Western Long Island Sound and Block Island Sound. Recently MARACOOS has added sponsorship of a 13 MHz network for the coast of New Jersey and 16 MHz network for the Martha's Vineyard Shelf.

The metric for radar performance has been to cover 80% of the expected HFR coverage for 80% of the time [2]. For the 5 MHz shelf network, the expected coverage is 140,000 km^2. With the existing technology of HFR, that only covers 40% of the MARACOOS region. That coverage could be expanded through the use of dual transmitters at each station or the deployment of at sea bistatic transmitters [3, 4]. Table 2 provides the expected HFR coverage for the subregions and the surface current coverage for the subregions.

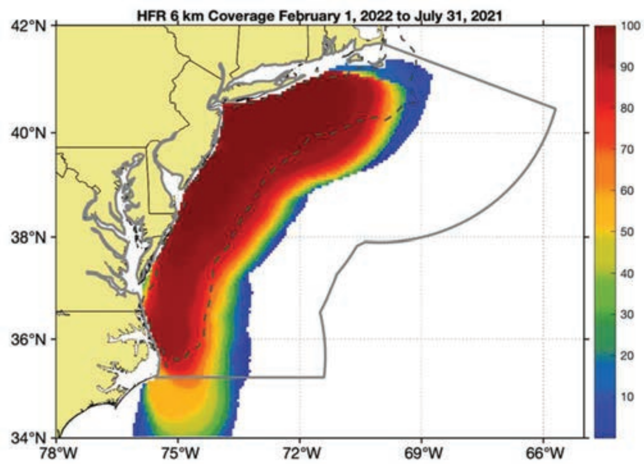

Figure 4: Percent coverage of the 5 MHz HFR Network from February 1 to July 31, 2022. The dashed gray line is the historical 50% coverage boundary for the network [5]. The solid gray line is the 2021 MARACOOS boundary and the outer edge coincides with the Exclusive Economic Zone (EEZ) boundary.

Table 2: Subregions within MARACOOS that currently have HF radar coverage and the percent coverage of that subregion by HFR.

Subregion	Area (km^2)	HFR Coverage (km^2)	Pct. Coverage (%)
Atlantic Ocean	352,050	140,000	40
Block Island Sound	2,036	968	48
Long Island Sound	3,050	267	9
New York Harbor	851	220	26
Delaware Bay	2,225	820	37
Chesapeake Bay	11,816	810	7

Another topic that deals with HF radar performance and spatial coverage is the coverage of individual radar stations. Figure 5 shows the radial coverage for a single HF radar station over 25 hours. When the station is performing optimally, then coverage should average between 90-100% for all the radar cells over water. The SeaSonde HF radar typically bins the data in 5° angular bins and this particular station is achieving 155° of coverage over the water.

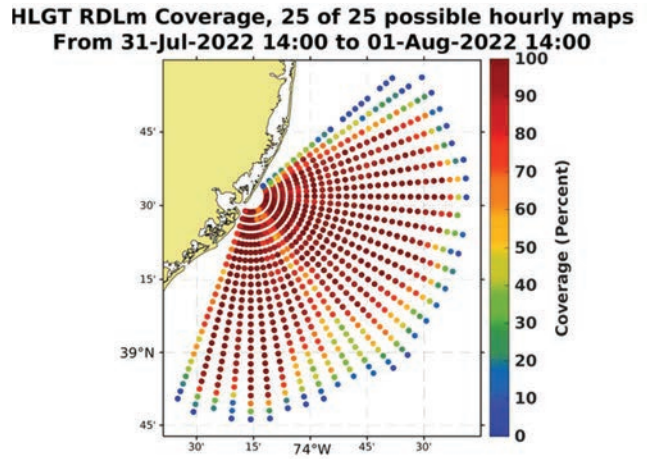

Figure 5: Spatial coverage for the 13 MHz radar located in Holgate, NJ (site code HLGT) over 25 hours. The colormap represents coverage, 100% red to 0% blue.

The bearing coverage for the Rutgers owned or operated HF radar stations within the MARACOOS area are shown in Figure 6. The red indicates the bearing coverage of the measured antenna pattern [6] for the station while the blue indicates the bearing coverage of the coastline over water. For example, the station from Figure 5 HLGT has a coastline from 30° to 205° true north and has an antenna pattern that covers from 50° to 200° true north. This particular station covers 86% of the angular sector over water. On average the stations listed in Figure 6 cover 83% of the over water angular swath between the coastlines.

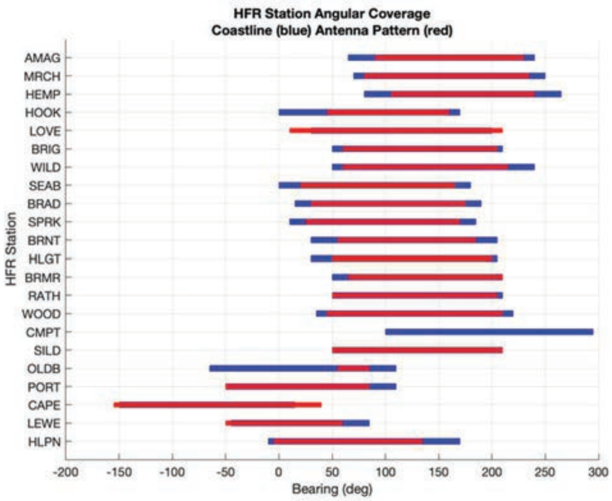

Figure 6: Angular coverage for the Rutgers owned or managed HF radar stations. The blue bar indicates the angular swath of the coastline and the red bar indicates the angular swath of the measured antenna pattern for the particular station. The four-letter site code for the particular station is shown along the y axis.

IV. Discussion

Overall, the added detail of the shoreline accounted for only a 0.2% increase in the surface area of MARACOOS designated waters (378,902 km^2) as compared to the original IOOS provided boundary (377,317 km^2). Area differences in the subregions were much more significant with as much as a 100% increase for Great South Bay, New Jersey Coast and DelMarVa coast, 14% increase for the New York Harbor area and a 9% reduction in the area around Nantucket Sound. Having accurate surface area measurements of subregion water bodies will allow for proper delegation of resources for improved ocean observing.

The Atlantic Ocean dominates the surface waters of the MARACOOS region accounting for 352,050 km^2 or 93% of the area. The existing HF radar coverage is only able to cover 40% and is not able to measure out to the edge of the EEZ (Figure 4). Many of the requirements NOAA has for surface current measurements encompass the coastal US or EEZ US so additional resources will be needed to cover the entire MARACOOS region. These requirements were accessed via the Technology, Planning and Integration for Observation (TPIO) program's database.

The HF radar coverage for the subregions vary from as high as 48% to as low as 7%. Additional resources will be needed to increase the surface current coverage of the subregions. There is a caveat to this strategy as HF radar will not be the optimal sensor for surface current measurements in the inland estuaries. Propagation of HF ground waves is greatly reduced by the poor conducting properties of fresh water [7].

This factors into the build out plan for a National Surface Current Monitoring Network [8]. The plan calls for a total of 52 HF radars for the Mid Atlantic. There are currently 39 HF radar stations within the MARACOOS region. The findings of this paper could help decide how radars are distributed within the Mid Atlantic.

V. Conclusions

The surface areas of each subregion were used to calculate how well the HF radar network covers the surface waters of the Mid Atlantic. Other researchers, students and organizations can use these shapefiles to accurately define study areas, brief personnel on areas of operation, or evaluate asset distribution. Future work will include could include a decision matrix that helps answer the question of where to allocate resources. We will look to compare the percentage of marine activity that takes place in these subregions to the corresponding surface area percentages to further guide asset distribution and allocation decisions.

Acknowledgment

This work was funded by NOAA Award Number NA16NOS0120020 "Mid-Atlantic Regional Association Coastal Ocean Observing System (MARACOOS): Powering Understanding and Prediction of the Mid-Atlantic Ocean, Coast, and Estuaries". Sponsor: National Ocean Service (NOS), National Oceanic and Atmospheric Administration (NOAA) NOAA-NOS-IOOS-2021-2006475, Integrated Ocean Observing System Topic Area 1: Implementation and Development of Regional Coastal Ocean Observing Systems.

Special thanks to David Helms and Martin Yapur for providing the NOAA requirements for surface currents, winds and waves.

References

[1] J. Snowden *et al.*, "The U.S. Integrated Ocean Observing System: Governance Milestones and Lessons From Two Decades of Growth," (in English), *Frontiers in Marine Science,* Review vol. 6, no. 242, 2019-May-14 2019, doi: 10.3389/fmars.2019.00242.

[2] H. Roarty, M. Smith, J. Kerfoot, J. Kohut, and S. Glenn, "Automated quality control of High Frequency radar data," in *Oceans, 2012*, 14-19 Oct. 2012 2012, pp. 1-7, doi: 10.1109/oceans.2012.6404809.

[3] J. Harlan, P. M. Kosro, and P. Barletto, "Next generation use of high power and bandwidth in the NE Pacific—A component of the NSF Ocean Observing Initiative," in *OCEANS 2009*, 2009: IEEE, pp. 1-8.

[4] H. J. Roarty, M. Smith, E. Handel, S. M. Glenn, and D. E. Barrick, "Expanding the coverage of HF radar through the use of wave powered buoys," in *Oceans, 2012*, 14-19 Oct. 2012 2012, pp. 1-4, doi: 10.1109/oceans.2012.6404810.

[5] H. Roarty *et al.*, "Annual and seasonal surface circulation over the Mid‐Atlantic Bight Continental Shelf derived from a decade of High Frequency Radar observations," *Journal of*

Geophysical Research: Oceans, vol. 125, no. 11, p. e2020JC016368, 2020.

[6] J. T. Kohut and S. M. Glenn, "Improving HF Radar Surface Current Measurements with Measured Antenna Beam Patterns," *Journal of Atmospheric and Oceanic Technology,* vol. 20, no. 9, pp. 1303-1316, September 01, 2003 2003. [Online]. Available: http://dx.doi.org/10.1175%2F1520-0426%282003%29020%3C1303%3AIHRSCM%3E2.0.CO%3B2

[7] H. F. R. S. S. Team, "High Frequency Radar Freshwater Performance Evaluation," NOAA Integrated Ocean Observing System, 2012.

[8] J. Harlan, "A Plan to Meet the Nation's Needs for Surface Current Mapping," *NOAA IOOS,* p. 64, September, 2009 2015.

Surface current velocity observations of the Yucatan Channel using High-Frequency Radar

Steven F. DiMarco
Geochemical and Environmental Research Group
Texas A&M University
College Station, TX, USA
sdimarco@tamu.edu

Scott Glenn
Center for Ocean Observing Leadership
Rutgers University
New Brunswick, NJ, USA
glenn@marine.rutgers.edu

Michael Smith
Center for Ocean Observing Leadership
Rutgers University
New Brunswick, NJ, USA
michaesm@marine.rutgers.edu

Rafael Ramos
Woods Hole Group, LLC.
Houston, TX, USA
rramos@woodsholegroup.com

Anthony H. Knap
Geochemical and Environmental Research Group
Texas A&M University
College Station, TX, USA
tknap@tamu.edu

Rosalinda Monreal Jiménez
Facultad de Ciencias
Universidad Nacional Autónoma de México
Mexico City, MX
rmonrealj@ciencias.unam.mx

David Salas de Léon
Instituto de Ciencias del Mar y Limnologia
Universidad Nacional Autónoma de México
Mexico City, MX
dsalas@unam.mx

Victor Kevin Contreras Tereza
Facultad de Ciencias
Universidad Nacional Autónoma de México
Mexico City, MX
vcontreras@ciencias.unam.mx

***Abstract*— We report on surface current velocity observations from two 5 MHz coastal radars deployed in Quintana Roo, Mexico (Puerto Morelos and Isla Contoy) on the west side of the Yucatan Channel. The instrument systems are funded by the National Academy of Sciences Understanding the Gulf Ocean System (UGOS) program (Knap et al. 2023). Deployed in June 2022, the radar system provides hourly estimates with 6-km spatial resolution of the surface current velocity field between the west coast of Cuba and the east coast of the Yucatan Peninsula. The data are used to assess the current velocity structure found in multiple operational numerical ocean models operated by federal agencies (RTOFS, GOFS, CMEMS and AMSEAS), university researchers (CNAPS), and industry (TOPS). The radar observations are also part of a larger field campaign of the southeastern Gulf of Mexico that targets adaptive sampling strategies for the Yucatan in-flow region to improve prediction skill of numerical models of the Loop Current System (DiMarco et al. 2023). Maximum speed of the along-channel flow can reach 2 m/s. Model/data comparison metrics were established along a cross-Strait line through the highest quality data in the HF Radar field. Metrics include the maximum downstream velocity and its distance from the Yucatan coast, along with the total downstream surface transport. The variability of the Yucatan Current in space and time reveals how the speed core position changes with Loop Current orientation and state. For example, when the Loop Current is in a retracted state (i.e., the current enters the Gulf of Mexico and turns eastward and flows along the northern Cuban coast and exits the Gulf through the Florida Straits), the Yucatan Current speed core is close to the channel midpoint. As the Loop Current extends into the Gulf of Mexico, the speed core tends to move to the western edge of the Channel. In February of 2023, the HF Radar network observed a rapid transition from a high transport offshore mode to a lower transport nearshore mode. This corresponds to a time when the Loop Current itself was transitioning from a fully retracted state flowing eastward along the coast of Cuba to the Florida Straits with little interaction with the Gulf to a deeply extended state where it flowed northward along the Yucatan Escarpment and interacted with a previously formed Loop Current Eddy. When the Loop Current is in the nearshore mode, a double peak in the downstream speed is often observed, with the local minimum between the two peak currents located downstream of the island of Cozumel. Tidal current variability is also evident in the observational record as diurnal current variability dominates the tidal bands. Variations in the easterly wind speed on scales of 1-2 weeks are correlated with variations in the downstream transport. On the western side of the Yucatan Channel, frequent current reversals of southward flow from the western Cuban coast to the Caribbean Sea are observed; this current reversal has been documented previously in cross-channel transects, however, the magnitude, persistence and variance of the reversals and the spatial extent can now be quantified for the first time. The HF-radar observations are compared against sparse historical observations from the 19th and 20th century.**

Keywords*— *Yucatan Strait, Gulf Loop Current, high frequency radar, model-data comparison, real-time observations

I. INTRODUCTION

Two High-Frequency Radar (HFR) systems were deployed in Quintana Roo, Mexico, (northeastern Yucatan peninsula) to investigate the spatial and temporal variability of the Yucatan Current at the entrance to the Gulf of Mexico. The operating frequency of the long-range radars is near 5 Mhz. Figure 1 shows the locations of the radar systems. Station UASA is located near Puerto Morelos along the eastern coast between Cozumel and Cancun; Station ISCY is located on Isla Contoy, an island 30 km north of Cancun. The system was deployed in June 2022 and has provided nearly-continuous hourly surface current observations in a five-kilometer grid that extends approximately 100 km into the Yucatan Channel between Mexico and Cuba.

979-8-218-14218-6 ©2023 MTS

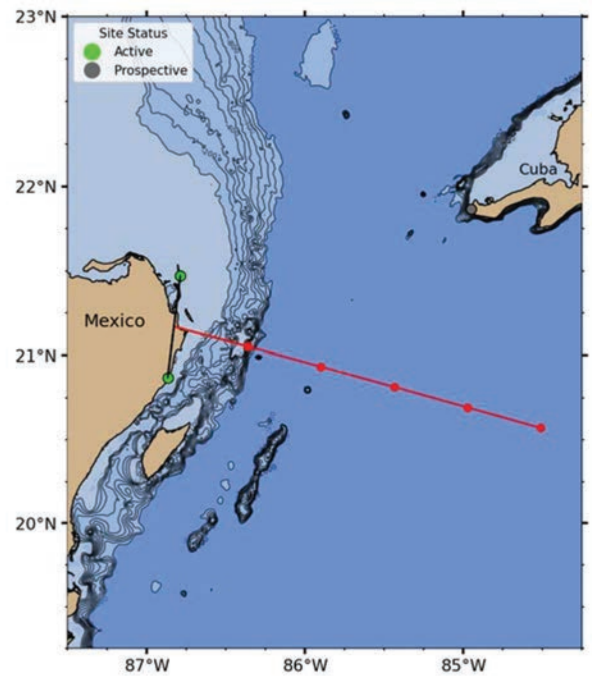

Fig. 1. Map of Yucatan Channel showing location of high-frequency radar stations (green circles) at the inflow region of the Gulf of Mexico. Red line indicates "best" transect location referred to in the text. Red dots are placed every 50 km along the red transect line. Note the shallow bathymetry located near 21°N, 86.5°W known as Banco Arrowsmith.

The Yucatan Current (YC) is part of the western boundary current (WBC) system in the northern Atlantic Ocean. The precursor of the YC is the north Brazil Current, which enters the eastern Caribbean Sea. After flowing westward across the Caribbean Sea, the current turns northward, west of the Cayman Islands and south of Cuba, as it encounters the obstruction of the North American continent near Honduras. The region between Mexico and Cuba, which forms the Yucatan Channel, serves as a choke-point for the current as it focuses the flow northward. After passing through the channel and entering the Gulf of Mexico, the YC becomes associated with the Loop Current (LC) System of the Gulf. In the Gulf, the dynamics become complex as the current evolves into several phases involving interaction with topography, coasts, bathymetry, and eddies. The evolution of the LC state determines the fate of the water masses and whether the LC detaches an anticyclonic eddy from the main current or whether the current leaves the Gulf of Mexico through the Florida Straits (between the northern Cuban coast and southern Florida). The Florida Current then turns northward along the US east coast and joins with other currents of the western Atlantic to form the Gulf Stream.

Because of the relatively unique position of the Yucatan Current in the WBC system (i.e., a strong jet constrained to a relatively narrow geographical location), observations of the YC at spatial and temporal resolutions that resolve processes controlling the variability and dynamical characteristics of the flow into the Gulf of Mexico can lead to improved numerical models of meridional heat and volume transport.

The HFR system is an element of the Understanding Gulf Ocean System (UGOS) Program funded by the National Academy of Sciences Gulf Research Program (Knap et al. 2023). Other UGOS observational elements include buoyancy gliders, drogued drifters, APEX-EM floats, and Argo floats (DiMarco et al. 2023). Operation of the HFR is organized through an international partnership of US and Mexican academic and commercial organizations.

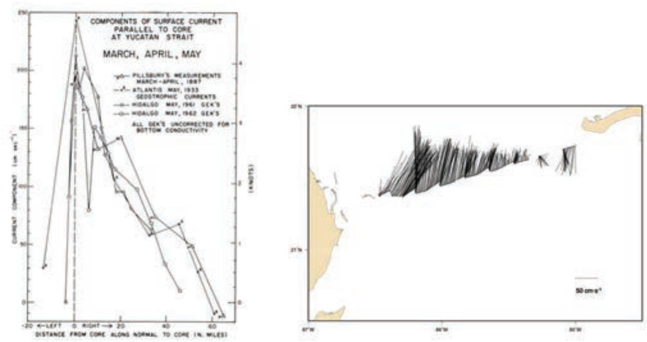

Fig. 2. Left: Along-channel velocity component across the Yucatan Channel from Pillsbury (1887), Atlantis (1933), and Cochrane (1961, 1962) using direct measurements, geostrophic estimates, and GEK observations, respectively. Right: Vessel-mounted acoustic doppler current profiler (VMADCP) observations at 15 m depth during November 1999. Left panel: Taken from Cochrane (1963). Right panel: modified from Nowlin et al. 2001.

Historical observations (Figure 2: Left) show the western intensified along-channel current velocity component of the Yucatan Current inflow. The zonal structure of the inflow is shown to have multiple peaks as the current enters into the Gulf of Mexico. The eastern Yucatan Current is shown to be a minimum and with indication of flow from the Gulf of Mexico back into the Caribbean Sea. The YC structure of western intensification and eastern minima, with reversal from the Gulf of Mexico into the Caribbean Sea, has also been shown in moored subsurface current meter observations (Bunge, 2001; Bunge et al. 2002; Sheinbaum et al. 2002) and numerical model output (Dukhovskoy et al. 2023). The vessel-mounted ADCP transect (Figure 2: Right) shows the velocity speed and direction of the YS at 15 m below the surface (Nowlin et al. 2001). The VMADCP observations were made in November 1999.

II. Data Processing and Analytical Methods

A. Data Collection

Raw radar data collected by the two stations were hosted on local servers for initial processing. Initial processing includes the assembly of individual radial data for each station. Radial data are subjected to standard data quality protocols, consistent with NOAA-IOOS QARTOD standards for HFR data. Radial data were then merged to form estimates of the surface ocean current flow field. Additional processing using simultaneously collected ship-based AIS information to refine the current velocity estimates and improve the error covariance (Liu et al. 2022; Smith et al. 2021; Smith et al., 2022; Updyke et al. 2019; Updyke et al. 2021). The resulting dataset consisted of hourly fields of current velocity vectors (east-west and north-south components) on a regular 6-km grid. The spatial coverage of the HFR observation varied in size and was dependent on several factors that include: obstructions, atmospheric conditions, ocean surface salinity, and sea state. Temporal gaps in the data were caused by several factors that include: power outages at one or both stations, computer resiliency (i.e., system crash), mechanical issues, software incompatibility, and more.

After processing into vector components, time-series at individual grid locations were analyzed for range, persistence, and first-order differences. Outliers were identified and removed. After this step, the surface current observations were ready for analysis and interpretation.

B. *Current Vector fields*

The gridded surface current velocity data were converted into surface current fields using the Objective Analysis (OA) mapping technique of Gauss-Markov optimal interpolation (Denman and Freeland, 1985; Wilkin et al., 2002; Thomson and Emery, 2015). The OA results in a regular grid of surface current velocity and include uncertainty estimates that vary in space and time. Stream lines of current velocity are estimated from the horizontal gradient of the velocity field and superimposed on the gridded field to indicate current velocity direction.

A collection of visualization products are constructed from the surface current fields (https://rucool.marine.rutgers.edu/ugos-hfr/). These products are produced, updated, and disseminated in near-real time as the radar radial current vector data become available from each site. The near-real time products include maps of the surface currents, and of the covariance error uncertainty based on standard approaches used in the U.S. National HF Radar network. The red line representing the cross-Strait transect used in our analyses was chosen to go through the area of lowest uncertainty based on the fields displayed in our operational plots.

Analysis and inspection of the gridded daily surface current fields and time series of velocity components at individual geographical locations shows a continuous spectrum of variability in the YC. The spectral range of variability resolvable by the HFR system is defined by sampling interval 1 hour and the length of the longest continuous time series about 2 months. Therefore the range is 0.01 to 8 cpd. At relatively high-frequencies, spectral peaks at about 1 cpd indicate tidal and inertial contributions to the variability. Lower frequency variance is aligned with weather-band and other variability as detailed in the results section. Because of the tidal and inertial variability present in the records, filtered and unfiltered versions of the fields were generated to highlight the different processes known to exist.

C. *Along channel transport*

To define the along-channel transport, an objective measure of the "best line" across the HFR radar footprint was determined using the OA error covariance metric (Wilkin et al. 2002) based on the integrated error covariance field estimate from the OA maps referenced above during the period 28 JAN 2023 to 12 JUL 2023. The plot shows that the error covariance is best (i.e., the least error) in the region between the radar station and is degraded (i.e., the largest error) away from the center and at the periphery of the HFR footprint. The region of least error extends from the Mexican coast to the east-southeast into the Caribbean Sea. The superimposed red line (Figure 1) indicates the longest continuous line from the coast through the radar footprint. This subjective line indicates the "best" line through the radar data and will be used in this manuscript to estimate the along-channel and cross-channel velocity components of the YC in the Yucatan Channel. Space-series of the along-channel velocity (positive: into the Gulf of Mexico; negative: out of the Gulf of Mexico) will serve as a proxy for surface transport of the YC.

Hovmöller diagrams of the along-channel velocity are constructed along the cross-Strait transect (red line in Figure 1) to illustrate the temporal and spatial evolution of the YC transport into the Gulf of Mexico. Similarly, surface currents were sampled from the publicly available operational ocean forecast models. The primary model used for comparison's is NOAA's global Real-Time Ocean Forecast System (RTOFS). Other global models include the U.S. Navy's publicly available Global Ocean Forecast System (GOFS) 3.1, and the European Copernicus Marine Environment Monitoring Service (CMEMS). We also include three higher resolutions models, the Navy's intra American Seas model (AmSeas), the North Carolina State University (NCSU) Coupled Northwestern Atlantic Prediction System (CNAPS) and the Woods Hole Group (WHG) Tendral Ocean Prediction System (TOPS).

Identify applicable funding agency here. If none, delete this text box.

III. Results

A. *YC Structure from HFR Observations*

Cross-channel Current Structure. The HFR surface currents fields show that current vectors are typically flowing from the Caribbean Sea into the Gulf of Mexico with maximum speeds in the western Yucatan Channel. The observations indicate that the Yucatan Current has two modes of variability that associated with the position of the velocity maximum within the Yucatan Channel. The two modes are: nearshore mode, speed maximum between 25-75 km from the coast and offshore mode, speed maximum 100-150 km from the coast. Figure 3 illustrates the two modes. Figure 3 (top panel) shows the surface current velocity field on 6 Feb 2023 (1800z) during the offshore mode configuration. The maximum velocity is located mid-Channel near 85.9°W (about 120 km from the Mexican coast). The maximum velocity exceeds 1.8 m/s. In the nearshore mode (Figure 3, bottom panel, 22 FEB 2023, 1200z), the speed core (maximum speed: ~1.0 m/s) is about 40-80 km from the Mexican coast.

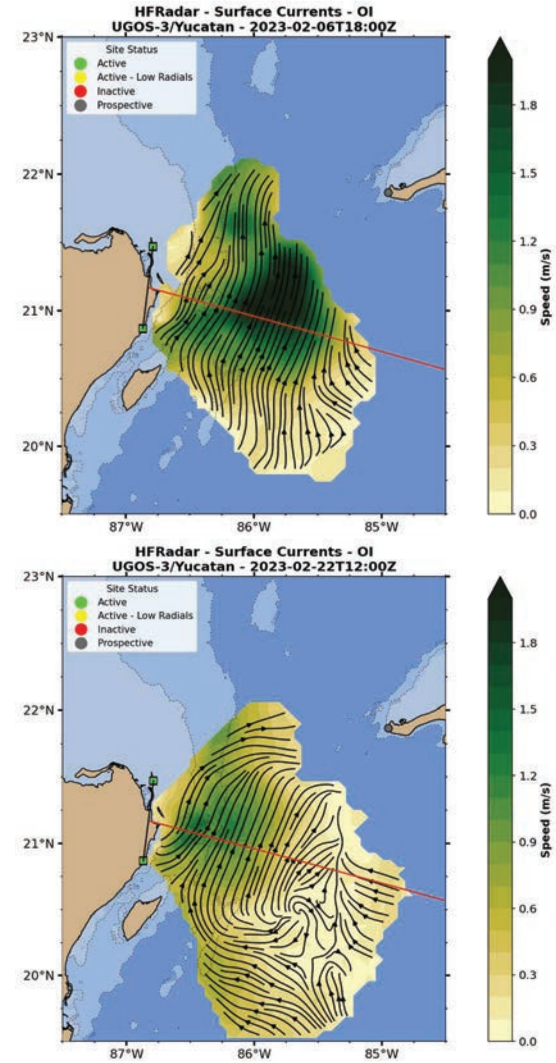

Fig. 3. (Top): HF Radar surface currents showing the Loop Current entering the Gulf during the higher transport offshore mode. (Bottom): HF Radar surface currents showing the Loop Current entering the Gulf during the lower transport nearshore mode.

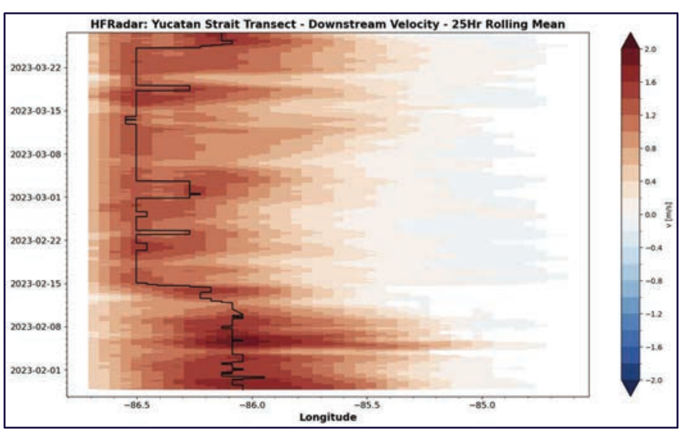

Fig. 4. (Left): Hovmöller plot (y-axis: date increasing up; x-axis: longitude °W) of along-channel velocity component (color bar) in the Yucatan Channel as observed by the HFR in Quintana Roo, Mexico. Velocity estimates are taken along the red line in the radar field shown in Figure 1. Red hues indicate that the velocity components is into the Gulf of Mexico from the Caribbean Sea; blue hues indicate flow into the Caribbean Sea from the Gulf of Mexico. Heavy black line indicates the position of the maximum speed.

The temporal and spatial evolution of the YC structure is shown in Figure 4. Early in the record (bottom of Figure 2; 28 JAN 2023 - 10 FEB 2023), the YC is in the offshore mode with the speed maximum centered around 86°W. The YC abruptly transitions to the nearshore mode (around 13 FEB 2023) with the speed maximum centered around 86.5°W. The maximum speed when the YC is in the nearshore mode tend to be less than the maximum speed of the offshore mode. The speed core (i.e., location of maximum speed) position is variable as short (1-2 day) shifts move the core to the east. Additionally, the speed core breaks into two or more peaks (e.g., 01 MAR 2023 and 15 MAR 2023).

Effect of Topography on Horizontal YC Structure. The bathymetry of the western Yucatan Channel has a shallow feature northeast of Cozumel known as Banco Arrowsmith. This bank rises to within less than 50 m of the ocean surface and is nearly 20 km long by 10 km wide. Banco Arrowsmith is coincident with the location where the YC is observed to bifurcate into two velocity cores. The location of the bathymetric feature is roughly 50 km from the baseline between the two HFR sites (see Figure 1).

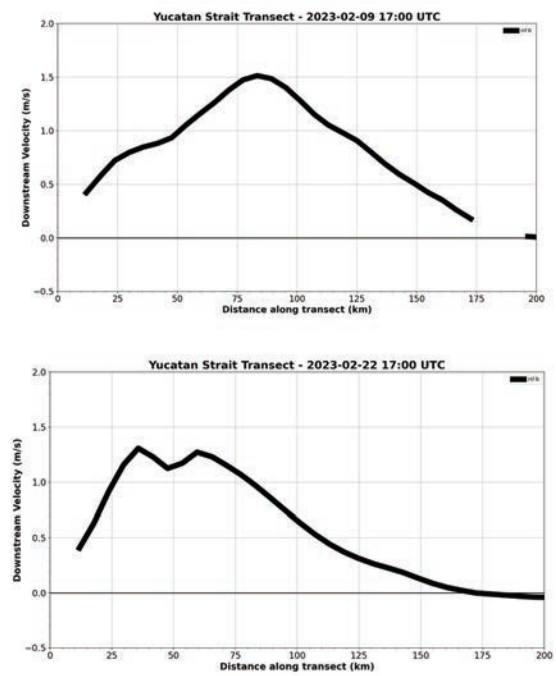

Fig. 5. Effect of topography. Top: Downstream velocity from Figure 4 Hovmöller on February 9 at 17:00 UTC when the LC maximum velocity core is in the offshore location. Bottom: Downstream velocity from Figure 4 Hovmöller on February 22 at 17:00 UTC when the LC maximum velocity core is in the nearshore location.

When the YC is in the offshore mode, the velocity core is west of the bathymetry feature (Figure 5: Top). On 22 FEB 2023, when the YC is in the nearshore mode, the velocity core has moved west towards the Mexican coast (Figure 5: Bottom). When the velocity peak is nearshore (Figure 5: Bottom), a speed minimum is seen 50 km from the Mexican coast with an inshore maxima at 35 km and offshore maxima at 65 km. Sometimes the offshore peak is a bit higher, and the black line in the Hovmöller (Figure 4) jumps back and forth between the offshore peak and the onshore peak.

When the peak velocity is further offshore, e.g., ~80 km, the highly horizontal shear on the western face of the velocity core is in the downstream island and topographic shadow zone. The shadow zone near 50 km appears as a break in the steep horizontal sheer in the downstream currents.

B. Comparison with Numerical Model Output

Maximum YC Velocity. The time series of Figure 6 (Top) shows the temporal variability of the maximum along-channel velocity (m/s) from 28 Jan 2023 thru 25 MAR 2023. The range of the HFR maximum is 1.0 to 1.8 m/s.

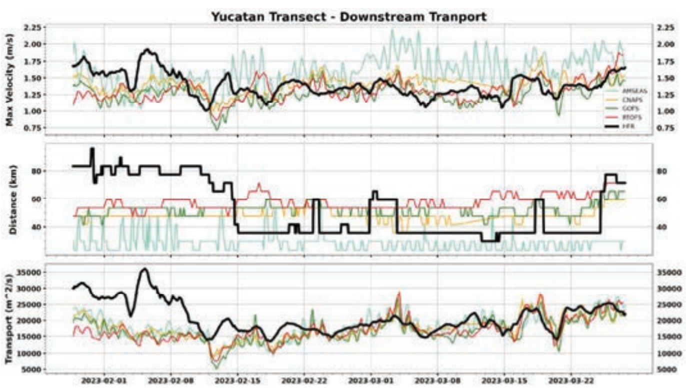

Fig. 6. Time series of a) maximum velocity (m/s), b) distance of speed core from Mexican coast (km), and c) integrated transport (m^2/s) along the cross-channel (red) line of Figure 1. Black line: HFR observations, cyan, magenta, green, red lines indicate numerical output from the AMSEAS, CMEMS, GOFS, and RTOFS models, respectively. Numerical output is taken at model grid points nearest to the cross-channel line of the HFR observations.

Velocity core maximum from four models (CMEM, GOFS, AMSEAS, RTOFS) is superimposed on the observations time series. In general, the range of the velocity core from the models is consistent with those found in the HFR observations. However, the core speeds found in AMSEAS does show a double peak in the YC along channel velocity and tends to consistently exceed those of the observations with the greatest core velocity (between 2.0 and 2.25 m/s); this model output also shows considerable high-frequency (on the order of diurnal and inertial periods, i.e., ~24 hours) variability as compared with other models and the observations.

The models (CMEMS, GOFS, RTOFS) have a tendency to align with each other during the observation period and with reduced variability at high-frequency than that seen in the AMSEAS output. The HFR observations have been smoothed from high-frequency variability to filter out the variability associated with the diurnal tides. The HFR observations differ considerably from all four models during the offshore mode period of early February 2023. During the offshore mode the observations are about 0.5 m/s greater than the values found in the numerical models. After 15 FEB 2023, the HFR observations and the model output are consistent and within 0.25 to 0.5 m/s.

The time series of the velocity core distance from the Mexican coast (Figure 6: Middle panel) shows less consistency between the observations and the models. All four models show a nearshore mode throughout the observation period. None of the numerical models show an offshore mode in the late January to early February time frame. After 15 FEB 2023, when the HFR observations show a nearshore mode of the YC, all of the models show the YC velocity core to be within 60 km of the coast. The AMSEAS model has the closest nearshore mode with the speed core typically within 20 km of the coast but with multiple speed peaks (as observed in the HFR).

The integrated transport of the YC across the Yucatan Channel is shown in Figure 6: bottom Panel). The integrated transport is similar to the velocity core distance result. When the YC is in the offshore mode, the integrated transport of the numerical models are consistently less than the transport observed in the HFR (by a factor of 2, and observations about 15k m^2/s greater than numerical output). After 15 FEB 2023, when the YC is in the nearshore mode, all four numerical models are consistent with the observations and show 15k - 20k m^2/s transport.

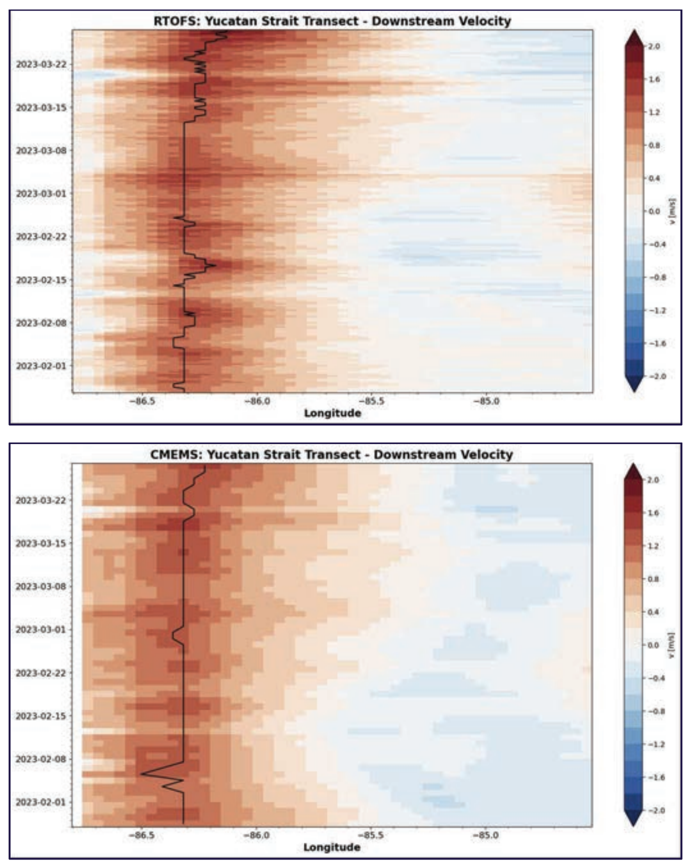

Fig. 7. Hovmöller plot (y-axis: date increasing up; x-axis: longitude °W) of along-channel velocity component (color bar) in the Yucatan Channel from numerical model output (Left) RTOFS and (Right) CMEMS. Velocity estimates are taken along the red line in the radar field shown in Figure 1. Red hues indicate that the velocity component is into the Gulf of Mexico from the

Caribbean Sea; blue hues indicate flow into the Caribbean Sea from the Gulf of Mexico. Heavy black line indicates the position of the maximum speed.

YC Horizontal Structure. The spatial and temporal evolution of the velocity core estimated from the RTOFS and CMEMS numerical models are shown in Figure 7. As can be seen, the YC velocity core, as estimated in the model, remains in the nearshore mode throughout the observation time period. The numerical model output also does not show any vestige of the bathymetric shadowing present in the observations. This is likely due to the coarseness of global numerical model spatial resolution and the inability to resolve the local bathymetric features. The eastern region of the Yucatan Channel also has a wider area of southward flow (into the Caribbean Sea) than that expressed in the HFR observations. The mechanisms, which control the southward flow in the models, are currently under investigation.

IV. Discussion

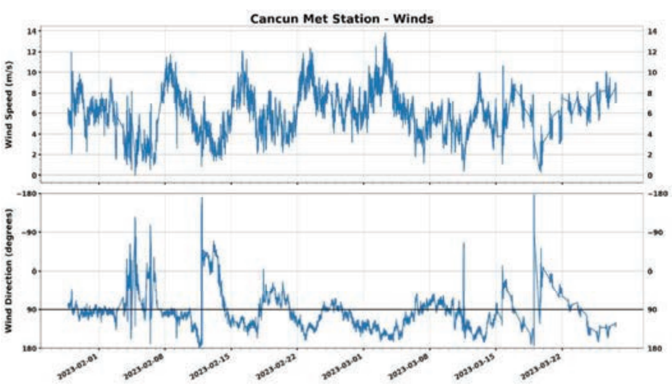

Fig. 8. (Top) wind speed (m/s) and (Bottom) wind direction (°T) from the Weatherflow weather station at Cancun Mexico.

The Cancun Weatherflow Station is located at the water's edge near the midpoint between the UASA and ICSY HFR sites. The site reports wind speeds and directions every 5 minutes. The data from late January through the end of March are plotted in Figure 8. Direction in meteorological convention (winds from) is measured in degrees positive clockwise from true north. The wind is predominantly from the east (90 degrees) to southeast. Increases in the easterly wind speed are visually correlated with increases in downstream surface transport (Figure 6, Bottom). Early in the record when the LC was in the offshore mode, short duration events with winds from the north are visually correlated with reductions in the downstream surface transport. Changes in Loop Current surface transport are often observed during passing hurricanes. Here we see the impact of less extreme weather changes on surface transport.

Historical context. The HFR observations of the Yucatan Channel are generally consistent with previous understanding of the characteristics of the inflow region of the Gulf of Mexico. Specifically, the YC is a western intensified current that has periodic reversals in the eastern channel near the Cuban coast. Before 1999, estimates of the Yucatan Channel transport and YC vertical and horizontal structure were rare, i.e., Pillsbury's 1887 observations (Pillsbury, 1890) are the first published quantification of the flow (Figure 2). Pillsbury's and others (Cochrane 1963) observations have also indicated that the Gulf of Mexico inflow can have multiple peaks across the YC and eastern reversal into the Caribbean.

The frequency, persistence, and magnitude of the eastern current reversal has not been quantified. Owing to the importance of the YC as a key component of the climate system by contributing to the control of meridional transport of heat and volume through the channel, advancing understanding of the processes that drive latitudinal exchange can impact, hopefully improve, the ability of numerical climate models to forecast future ocean variability.

The addition of the HFR station on the western coast of Cuba, at Cabo de San Antonio (Figure 1: gray circle) will increase the spatial coverage of the HFR network of the channel and will improve the accuracy of the surface velocity estimates across the channel. We recommend and are presently pursuing the implementation of a HFR station at Cabo de San Antonio, Cuba.

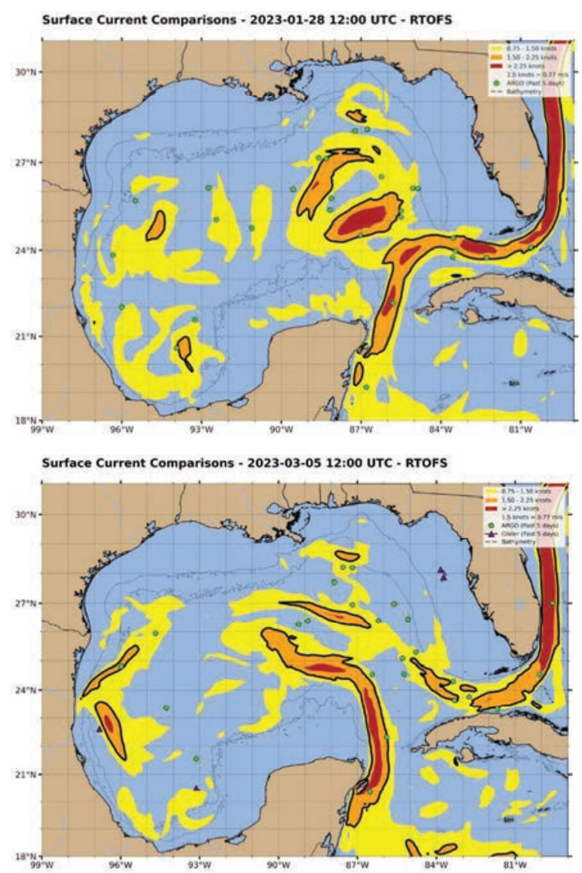

Fig. 9. Gulf of Mexico basin showing representative numerical circulation model output from RTOFS on January 28 and March 5, 2023. Shading

represents current speed classifications, e.g., yellow: 0.75-1.5 kt (25-75 cm/s), orange: 1.5 – 2.5 kt (75-125 cm/s), and red: in excess of 2.5 kt (> 125 cm/s). The yellow, orange, and red colors represent warning zones associated with the location of the industry standard 1.5 knot line. The solid black line represents the model forecast location of the 1.5 knot line. Dashed blue lines represent bathymetric depths of 100 m and 1000 m.

The YC mode is associated with the configuration of the Loop Current in the Gulf of Mexico. Figure 9 shows two LC configurations (left) retracted and (right) extended). When the LC is retracted (left), the YC is in the offshore mode and is further from the Mexican coast. When the Loop Current is extended (right), the YC is in the nearshore mode and is closer to the Mexican coast. The two dates chosen for Figure 9 encompass the February transition time period for the LC from fully retracted to fully extended states, with Jan 28 being the first date that the Loop Current interaction with the Loop Current Eddy begins, and March 5 is the first day when the Loop Current is fully extended into the Gulf with none of the surface flow taking the shorter route directly out of the Gulf.

V. Conclusions

In summary, we have reported on surface current velocity observations from two 5 MHz HF Radars deployed in Quintana Roo, Mexico (Puerto Morelos and Isla Contoy) on the west side of the Yucatan Channel. The instrument systems are funded by the National Academy of Sciences Understanding the Gulf Ocean System (UGOS) program (Knap et al. 2023). Deployed in June 2022, these systems have provided hourly estimates with 6-km spatial resolution of the surface current velocity field between the west coast of Cuba and the east coast of the Yucatan Peninsula. The data are used to assess the current velocity structure found in multiple operational numerical ocean models operated by federal agencies (RTOFS, GOFS, CMEMS and AMSEAS), university researchers (CNAPS), and industry (TOPS). The radar observations are also part of a larger field campaign of the southeastern Gulf of Mexico that targets adaptive sampling strategies for the Yucatan in-flow region to improve prediction skill of numerical models of the Loop Current System (DiMarco et al. 2023).

Maximum observed surface speeds of the along-channel flow can exceed 2 m/s. Metrics presented include the maximum downstream velocity and its distance from the Yucatan coast, along with the total downstream surface transport. The HF-radar observations are compared with sparse historical observations from the 19th and 20th century.

The variability of the Yucatan Current in space and time reveals variability of the speed core position that is associated with changes in Loop Current orientation and state, i.e., extended or retracted. For example, when the Loop Current is in a retracted state (i.e., the current enters the Gulf of Mexico and turns eastward and flows along the northern Cuban coast and exits the Gulf through the Florida Straits), the Yucatan Current speed core is close to the channel midpoint. As the Loop Current extends into the Gulf of Mexico, the speed core tends to move to the western edge of the Channel. In February of 2023, the HFR network detected a rapid transition from a high transport offshore mode to a lower transport nearshore mode. This corresponds to a time when the Loop Current itself was transitioning from a fully retracted state flowing eastward along the coast of Cuba to the Florida Straits with little interaction with the Gulf to a deeply extended state where it flowed northward along the Yucatan Escarpment and interacted with a previously formed Loop Current Eddy.

When the Loop Current is in the nearshore mode, a double peak in the downstream speed is often observed, with the local minimum between the two peak currents located downstream of the island of Cozumel and Banco Arrowsmith. Tidal current variability is also evident in the observational record as diurnal current variability dominates the tidal bands. Variations in the easterly wind speed on scales of 1-2 weeks are correlated with variations in the downstream transport. On the eastern side of the Yucatan Channel, frequent current reversals of southward flow from the western Cuban coast to the Caribbean Sea are observed; this current reversal has been documented previously in cross-channel transects, however, the magnitude, persistence and variations of the reversals and their spatial extent can now be quantified for the first time.

Acknowledgment

This work was funded by the Gulf Research Program of the National Academy of Sciences (Grant Award Number SCON-10000542). Numerical model output shown in this manuscript is provided by: Naval Research Laboratory (AMSEAS), Naval Oceanographic Office (GOFS 3.1), NOAA (RTOFS), and Copernicus (CMEMS). Weather data (wind speed and direction) is courtesy of WeatherFlow, Inc. The institutional members of the GulfCORES consortium are Texas A&M University, Rutgers University, University of Southern Mississippi, University of Miami, University of South Florida, Universidad Nacional Autonoma de Mexico (UNAM, Mexico), Woods Hole Group, and Ensenada Center for Scientific Research and Higher Education (CICESE, Ensenada, Mexico). NASEM-GRP-UGOS has funded two additional consortia under the UGOS umbrella: GOFFISH (Lead PI: Eric Chassignet, Florida State University) and GODEEP (Lead PI: Amy Bower, Woods Hole Oceanographic Institution). Additional partners in this research include Naval Research Laboratory, NOAA IOOS, GCOOS, Ocean Sierra LLC.

References

[1] Bunge, L., (2001) “La relación de los flujos profundos en el Canal de Yucat'n con la extensión de la Corriente del Lazo y la anomal ía de volumen en el Golfo de México” M. Sc., thesis, CICESE, 2001

[2] Bunge, L, Ochoa, J, Badan, A, Candela, J, Sheinbaum, J. 2002. Deep flows in the Yucatan channel and their relation to changes in the Loop Current extension. Journal of Geophysical Research 107:3233. DOI: 10.1029/2001JC001256.

[3] Cochrane, J.D., 1963. Oceanography and Meteorology of the Gulf of Mexico, Annual Report, Project NR 093-036.ONR Report. Texas A&M University, 11p.

[4] Denman, K. L. & H. J. Freeland, 1985. Correlation scales, objective mapping and a statistical test of geostrophy over the continental shelf. J. Mar. Res. 43: 517–539.

[5] DiMarco, S.F., Glenn, S., Jaimes de la Cruz, B., Knap, A.H., Liu, Y., Magnell, B., Mahmud, S., Miles, T., Pallas-Sanz, E., Ramos, R.J., Shay, L.N., Smith, M., Tenreiro, T., and Weisberg, R.M. (2023). Applications Of Adaptive Sampling Strategies Of Autonomous Vehicles, Drifters, Floats, And HF-Radar, To Improve Loop Current System Dynamics Forecasts In The Deepwater Gulf Of Mexico. Offshore Technology Conference, Houston Texas. American Society of Civil Engineers,

Brazilian Petroleum, Gas, and Biofuels Institute, Society of Naval Architects and Marine Engineers. OTC-32459-MS.

[6] Dukhovskoy, D.S., Chassignet, E.P., Bozec, A. and Morey, S.L. (2023) Assessment of predictability of the Loop Current in the Gulf of Mexico from observing system experiments and observing system simulation Experiments. Frontiers of Marine Science, Sec. Physical Oceanography, 10. DOI10.3389/fmars.2023.1153824.

[7] Emery, W. J., and R. E. Thomson, *Data Analysis Methods in Physical Oceanography*. Elsevier, 2014. 638 pp. Third Edition.

[8] Knap, A.H., DiMarco, S.F., Glenn, S., Ramos, R., Magnell, B. and Salas, D. (2023). Understanding the Gulf Ocean System Program: Informing Stakeholders and Improving prediction of the Loop Current System using advanced observational and numerical tools. Offshore Technology Conference, Houston Texas. American Society of Civil Engineers, Brazilian Petroleum, Gas, and Biofuels Institute, Society of Naval Architects and Marine Engineers. OTC-32392-MS.

[9] Liu, Y., Merz,C., Weisberg, R., Shay, L., Smith, M. and Glenn, S. (2021). An initial evaluation of High-Frequency Radar radial currents in the Straits of Florida in comparison with altimetry and model products, *Ocean Remote Sensing Technologies: HF, Marine and GNSS-Based Radar*, IET, edited by Huang, W. and Gill, E., 29 pp.

[10] Nowlin, Jr., WD, Jochens, AE, DiMarco, SF, Reid, RO, and Howard, MK. 2001. Deepwater Physical Oceanography Reanalysis and Synthesis of Historical Data: Synthesis Report. OCS Study MMS 2001-064, U.S. Dept. of the Interior, Mineral Management Service, Gulf of Mexico OCS Region, New Orleans, LA. 528 pp.

[11] Pillsbury, J.E. (1890). The Gulf Stream, Methods of the Investigation and Results of the Research. Appendix 10- Report for 1890

[12] Sheinbaum, J., Candela, J,, Badan, A. and Ochoa, J. (2002) Flow Structure and transport in the Yucatan Channel. Geophysical Research Letters, 29:3 10-1-10-4. https://doi.org/10.1029/2001GL013990

[13] Smith, M.J, Updyke, T. and Haines, S. (2022) Open-source software to support high frequency radar data analysis and quality control, *OCEANS 2022, Hampton Roads*, Hampton Roads, VA, USA, pp. 1-4, doi: 10.1109/OCEANS47191.2022.9977323.

[14] Smith, M., Glenn, S., Merz, C., Liu, Y., Weisberg, R., Shay, L., Howden, S. and Knap, T. (2021). A Unified Approach to HF Radar Radial Quality Control for Understanding Gulf Ocean Systems, *OCEANS 2021: San Diego – Porto*, 2021, pp. 1-5, doi: 10.23919/OCEANS44145.2021.9705910.

[15] Updyke, T., Roarty, H., Smith, M. and Nazzaro, L. (2021). Implementation of Quality Flags in the Processing of High Frequency Radar Surface Current Data, *OCEANS 2021: San Diego – Porto*, pp. 1-6, doi: 10.23919/OCEANS44145.2021.9706013.

[16] Updyke, T.G., Roarty, H.J., Smith, M. and Nazzaro, l. (2019). The Impact of Reprocessing Efforts on the Mid-Atlantic's Surface Current Product, OCEANS 2019 MTS/IEEE SEATTLE, Seattle, WA, USA, pp. 1-5, doi: 10.23919/OCEANS40490.2019.8962804.

[17] Wilkin, J.L., Bowen, M.M., Emery, W.J., 2002. Mapping mesoscale currents by optimal interpolation of satellite radiometer and altimeter data. Ocean Dynamics 52: 95–103 DOI 10.1007/s10236-001-0011-2.

Nearshore Wave Climatology of the New Jersey Shelf

Hugh Roarty
Dept. of Marine and Coastal Sciences
Rutgers University
New Brunswick, NJ USA
hroarty@marine.rutgers.edu

***Abstract*— Knowledge of ocean surface conditions including waves and winds are a valuable asset to the mariner as well as the oceanographer. While global climatology provides an overview for the general wave environment, regional studies provide more detail that may be useful to the stakeholder. The coast of New Jersey is important economically to the state for the coastal tourism and revenue. Having a nearshore wave climatology is important to protect the natural resource of the Jersey Shore. A decade of wave measurements were collected at several locations along the coast of New Jersey utilizing High Frequency (HF) radar measurements. HF radar is a remote sensing technology that covers the coastal ocean up to 200 km from shore. These measurements were compared to nearby wave buoys as provided by the National Data Buoy Center. The statistics of the nearshore waves were comparable with the offshore buoy measurements on a yearly or monthly time scale. However, during individual storm events there could be large differences between the two measurements due to wind direction and fetch limitations. The availability of this nearshore wave measurement has applications for validation of operational weather models. The nearshore measurements will also fill gaps between offshore measurements (buoys and satellite altimeters) and temporary nearshore observations during severe events. The data could also be utilized as a model assimilation data source as well.**

Keywords—remote sensing, geoscience, radar, waves, New Jersey, MARACOOS

I. Introduction

Measuring ocean waves is essential for improving safety of life at sea, providing accurate measurements for coastal engineering and developing renewable energy estimations. The use of accelerometers on buoys are a popular method for measuring wave parameters. The National Data Buoy Center maintains five such platforms in the New York Bight region (Figure 1). The buoy wave measurements in the region date back as far as 1984 (Table 1).

High Frequency radar (HFR) measurements of ocean surface currents in the Mid Atlantic began in 1998 (REF) and has remained a sustained measurement in the region (REF). The main measurement of an HFR station is a radial map of surface currents typically once an hour. The sensors have also shown the ability to measure wave height, period and direction with some caveats. In the Mid Atlantic region HFRs that operate in the 5 MHz band are not able to provide consistent wave measurements in low sea states. It's not until a storm passes through to generate waves above 2 m that the SeaSonde will return a measurement. However, the 13 and 25 MHz SeaSonde have provided reliable wave measurements over the past 15 years (Table 1: Year and length of time that wave measurements have been collected in the NY Bight region.Table 1). The wave measurement from the SeaSonde is derived from the second order Bragg scatter that is captured in the Doppler spectra of the radar (Figure 2).

A 13 MHz HF radar network consisting of eight stations has been operated on the New Jersey shelf for the past decade (REF). For this study we focused on using the wave data from four of those stations. The stations are located in Sea Bright (SEAB), Seaside Park (SPRK), Holgate (HLGT) and Brigantine (BRMR).

In this paper we seek to develop a nearshore wave climatology for the New Jersey shelf using wave data from several HF radar stations. We compare the wave measurements from the HFR stations with nearby wave buoys for consistency.

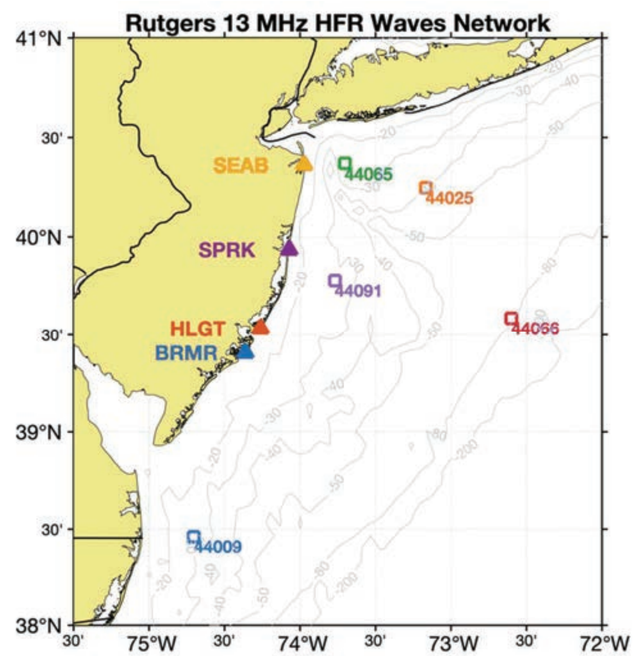

Figure 1: Map of the study area showing the locations of the HF radar stations (triangles) and NDBC wave buoys (squares). The HF radar four-letter site code is next to each station marker and the names of the NDBC buoys are detailed. Bathymetry contours are displayed as thin gray lines.

979-8-218-14218-6 ©2023 MTS

Table 1: Year and length of time that wave measurements have been collected in the NY Bight region.

Platform	Year Measurements Started	Number of Years
44009	1984	40
44025	1991	33
44065	2008	16
44066	2009	15
44091	2014	10
SEAB	2009	15
SPRK	2011	13
HLGT	2011	13
BRMR	2022	2

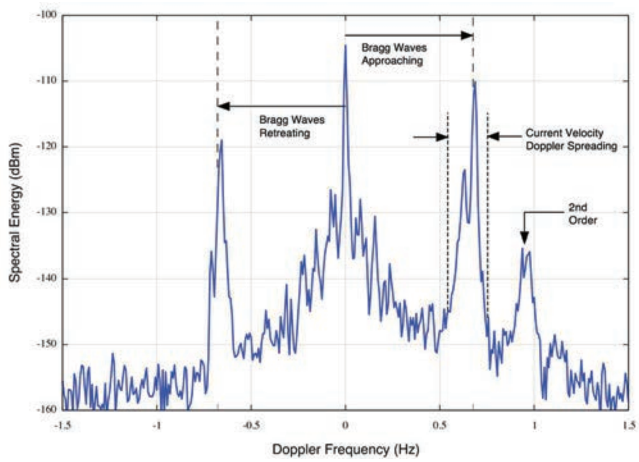

Figure 2: Doppler spectrum from a SeaSonde HF radar. The Doppler frequency (Hz) is shown along the x axis while the y axis shows spectral energy (dBm). The Bragg peaks which provide current information are located at ±0.6 Hz while the second order Bragg peak located near +1.0 Hz provides wave information.

II. Methods

Data from the wave buoys were downloaded from the NDBC website via the yearly standard meteorological data ASCII text files. The yearly files were concatenated into a single MATLAB binary MAT-file and plotted (Figure 3). Buoy 44009 displayed consistent coverage from 2017 to 2022 with only a brief outage in 2017 and 2021.

Wave data from the HFR stations are recorded in monthly ASCII text files. These files were transferred back to Rutgers once an hour in real time via rsync. The text files were converted to climate and forecast (CF) compliant netCDF files and posted to the Rutgers ERDDAP server. This process was started in 2017 so only the data from 2017 to present is available online. We aim to move the HFR wave data from 2009 to 2017 onto the ERDDAP server. The HFR wave data at SPRK also showed good coverage (Figure 4) over the time period with only an outage between 2018 and 2019 when the antenna at the station needed to be removed for a beach replenishment project.

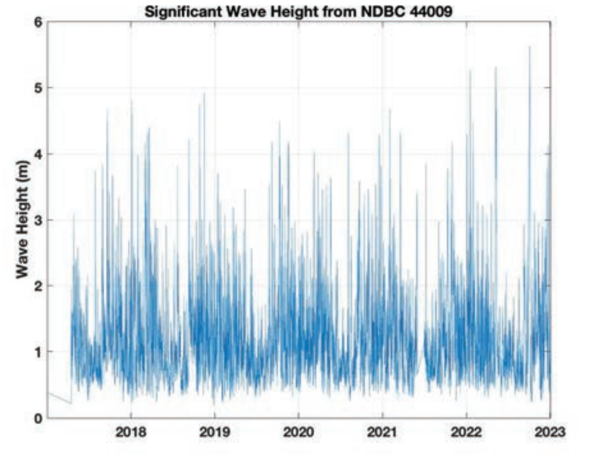

Figure 3: Time series plot of significant wave height at NDBC buoy 44009 from 2017 to 2023.

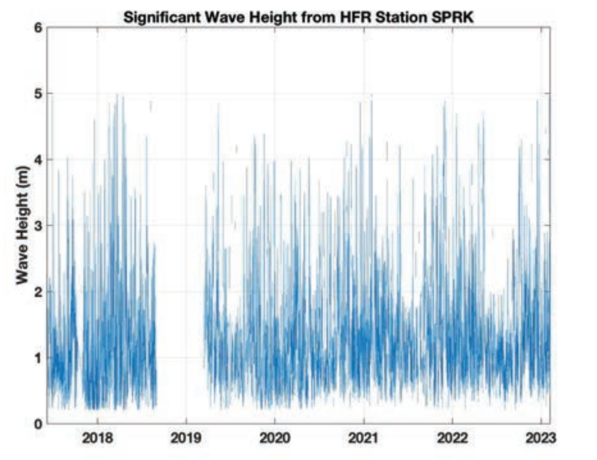

Figure 4: Time series plot of significant wave height at HF radar station SPRK from 2017 to 2023.

III. Results

Using data from 2017 to 2022, monthly statistics of significant wave height were generated for buoy 44009 (Figure 5) and HFR station SPRK (Figure 6). The figures show mean significant wave height for each month (blue line) along with one standard deviation error bars on each data point. The figures also show maximum wave height from each month (red line). The wave measurements for the radar have a 5 m threshold applied to them to eliminate abnormally large waves for the area.

The radar is limited in the range of wave heights it can measure. During high wave conditions the radar spectrum can saturate where the first order echo merges with the second order and the wave extraction using existing methods is not possible [1]. For a 13 MHz SeaSonde the saturation wave height is 7.4 m.

In addition to the monthly statistics, we compared buoy and radar measurements on a quarterly basis to evaluate radar measurement effectiveness. Figure 7 shows a time series plot

Significant wave height time series plot from January 1 to March 6, 2023 from wave rider buoy 44091 (black) and Holgate (HLGT) HFR (green) and Figure 8 shows the same data as a scatter plot.

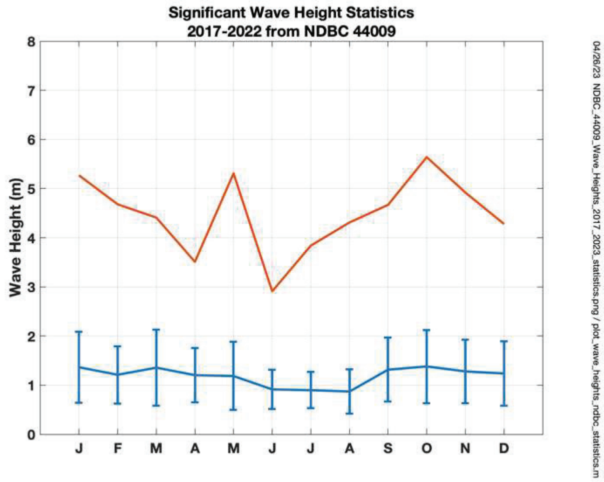

Figure 5: Monthly statistics of mean (blue line), standard deviation (error bars) and maximum (red line) wave height from NDBC buoy 44009.

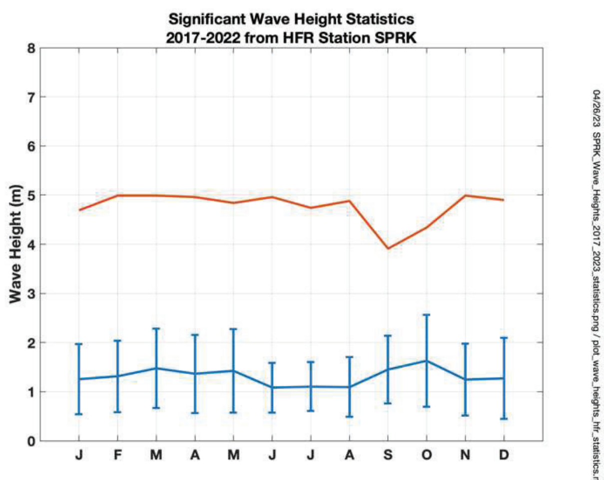

Figure 6: Monthly statistics of mean (blue line), one standard deviation (error bars) and maximum (red line) wave height from HF radar station at Seaside Park, NJ (SPRK).

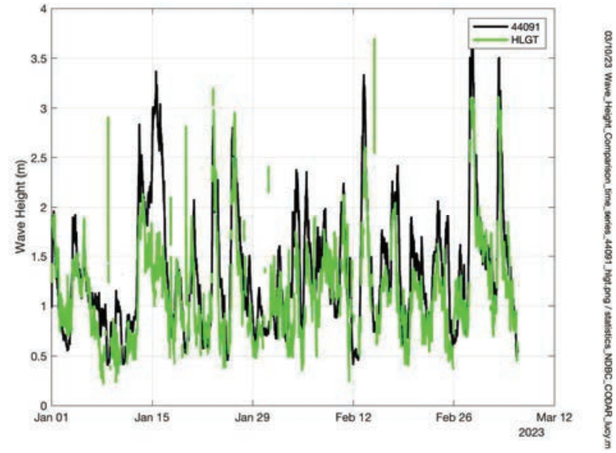

Figure 7: Significant wave height time series plot from Jan. 1 to Mar. 6, 2023 from wave rider buoy 44091 (black) and HLGT HF radar (green).

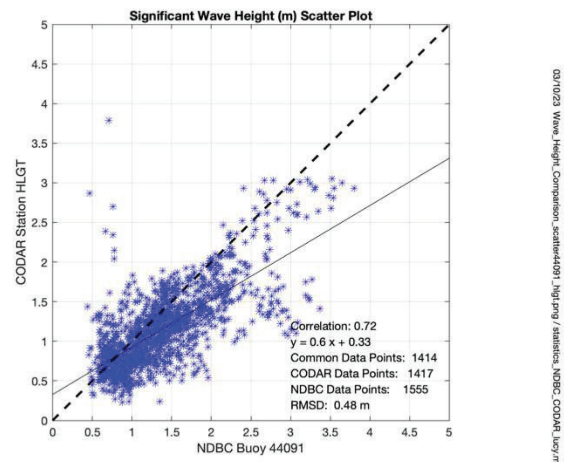

Figure 8:. Significant wave height scatter plot from January 1 to March 6, 2023 from wave rider buoy 44091 (x axis) and HLGT HF radar (y axis).

IV. Discussion

The buoy and HFR displayed similar monthly statistics for mean, maximum and variability of wave height for the New Jersey shelf. The mean wave height varied between 1.0 and 1.6 m for SPRK and 0.9 and 1.4 m for buoy 44009. Both measurements showed lower wave heights in the summer months of June to August and higher wave heights in the spring, fall and winter when Nor'easters pass through to produce some of the largest wave heights. The variability within each month is similar with the average standard deviation being 1.5 m for both the buoy and HFR.

The largest difference between the measurements is the maximum wave height estimate. The HFR station shows a consistent 5 m maximum wave height while the buoy shows a maximum wave height of 5 m in January and October with only a 3 m maximum wave height in June. The buoy data also shows a spike in maximum wave height for May. This is reflected in the climatic summary plots for Station 44009 found on the NDBC website which also show a spike in maximum wave height in the month of May.

Looking at the wave data on a quarterly basis reveals some differences between the buoy and HFR wave measurements. The data sets are strongly correlated with a correlation coefficient of 0.72 and a root mean square difference (RMSD) of 0.48 m between the two data sets. However, the HFR wave measurements are biased low when compared to the buoy measurements. Also, the HFR displays a few outliers estimating large wave heights when the buoy is measuring less than 1 m. This is likely due to low signal returns to the radar due to a calm sea and the radar interpreting noise as valid signal. But the outliers only represent 0.5% (7 out of 1,1417 data points) so it should have minimal impact on the evaluation.

V. Conclusions

Wave measurements from several HF radar stations were evaluated against nearby NDBC wave buoys. The HFR wave measurements showed similar statistics on a monthly basis for mean, maximum and variability. But on shorter time scales the radar measurements showed lower wave heights compared to the buoys. It is unclear if the radar has a bias or the difference is due to spatial variability in the wave field.

Acknowledgment

This work was funded by NOAA Award Number NA16NOS0120020 “Mid-Atlantic Regional Association Coastal Ocean Observing System (MARACOOS): Powering Understanding and Prediction of the Mid-Atlantic Ocean, Coast, and Estuaries”. Sponsor: National Ocean Service (NOS), National Oceanic and Atmospheric Administration (NOAA) NOAA-NOS-IOOS-2021-2006475, Integrated Ocean Observing System Topic Area 1: Implementation and Development of Regional Coastal Ocean Observing Systems.

References

[1] B. Lipa and B. Nyden, "Directional wave information from the SeaSonde," *Oceanic Engineering, IEEE Journal of,* vol. 30, no. 1, pp. 221-231, 2005, doi: 10.1109/joe.2004.839929.

Best Practices for SeaSonde Antenna Pattern Measurements

Timothy Stolarz
Center for Ocean Observing Leadership
Rutgers University
New Brunswick, NJ USA
tstolarz@marine.rutgers.edu

Hugh Roarty
Center for Ocean Observing Leadership
Rutgers University
New Brunswick, NJ USA
hroarty@marine.rutgers.edu

Scott Glenn
Center for Ocean Observing Leadership
Rutgers University
New Brunswick, NJ USA
glenn@marine.rutgers.edu

Michael Smith
Center for Ocean Observing Leadership
Rutgers University
New Brunswick, NJ USA
michaesm@marine.rutgers.edu

Ethan Handel
Center for Ocean Observing Leadership
Rutgers University
New Brunswick, NJ USA
handel@marine.rutgers.edu

***Abstract*— The SeaSonde is one type of High Frequency Radar (HF Radar) which is a coastal ocean current monitoring sensor developed and manufactured by CODAR Ocean Sensors Ltd. HF Radar is a highly efficient, low impact method for generating near real-time surface current velocities. Antenna Pattern Measurements (APMs) are a form of calibration performed on the SeaSonde antenna to attune it to local distortions which impact the bearing determination of the received radio signals. Several methods exist to perform APMs. Those methods include moving a transponder around the antenna by someone carrying it on land or placing the transponder on a boat. Drone patterns are conducted by placing a compact signal source aboard an uncrewed aerial vehicle and performing a similar semicircle around the antennas like the walking or boat pattern. The last method involves using signals from the Automatic Identification System (AIS) to determine the bearing of vessels relative to the radar antenna and using that information to derive the antenna beam pattern. This is accomplished by a radar operator analyzing the output from the AIS method or more recently CODAR has developed artificial intelligence to output an antenna pattern. Each type of APM method comes with its strengths and weaknesses for data quality as well as ease of performance. CODAR recommends the boat pattern whenever possible, but for many HF Radar operators, the APM is a subjective matter and many utilize their preferred methods accessible to them.**

Keywords—High Frequency Radar, oceans, vessel detection, drone, calibration, currents, bearings, SeaSonde

I. Introduction

The SeaSonde, a commercial High Frequency radar manufactured by CODAR Ocean Sensors, is low power and low impact oceanographic sensor which allows for continuous measurements of surface currents in near-real time. These sensors are located along coastlines, both beaches and cliff-faces, enabling the generation of surface current velocity maps. SeaSondes operate in the High Frequency (HF) band between 3 MHz and 30 MHz, (wavelengths ~100 m – 10 m), with models that focus operations near three frequencies which are 5 MHz, 13 MHz, and 25 MHz. These frequencies allow data to be collected in range resolutions of 6 km, 2 km, and 1 km respectively. The HF Radar determines velocity by measuring the Doppler shift of the first order Bragg peak from surface wind waves [1]. The shift detected from surface waves moving toward or away from the radar allows velocity to be measured. The velocity measurement is attributed to a depth proportional to $\lambda/8\pi$, where λ is the radar wavelength [2].

SeaSonde HF Radars utilize antenna beam patterns to determine the bearing of a radio signal scattered off the ocean surface [3]. The beam patterns can assume an ideal shape or be measured to account for any distortion of the pattern caused by coupling in the near field of the antenna. Operators of the SeaSonde must conduct a process known as an antenna pattern measurement (APM) as a form of calibration for the radar to produce a measured pattern. The APM measures the natural distortions of the surrounding environment which will disrupt the propagation of the radio signal back to the antenna creating errors in bearing assignment of sea echo during data processing [4]. Sources of distortions include metal objects, buildings, ionospheric disturbances, electromagnetic interference, and space weather events [5]. Many of these distortion factors can be limited when choosing a site to set up the SeaSonde [6], but do not account for future changes in conditions usually made by local municipalities. Over time, due to changes in the environment or conditions of the hardware of the HF Radar, the phases can distort leading to errors in total surface current generation [5]. APMs are important for calibrating the antenna to these distortions to improve data quality (Figure 1). Data from the HF Radar is used for purposes such as algal bloom and oil spill tracking, and the data is utilized by the United States Coast Guard for search and rescue operations [7]. Hence if surface current data is used for critical lifesaving purposes, we must ensure the highest data quality by performing APMs on a consistent and as needed basis.

979-8-218-14218-6 ©2023 MTS

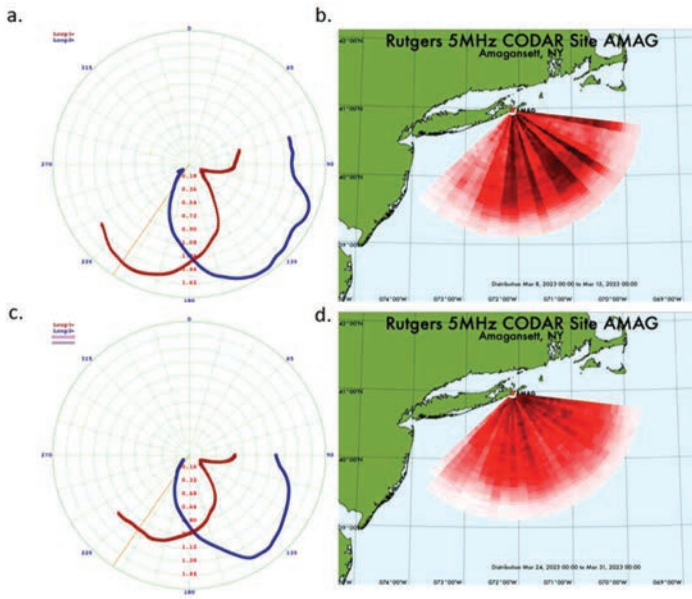

Fig. 1. Measured antenna patterns at Rutgers' HF Radar site AMAG in Amagansett, NY created on July 25, 2022 (a) and the new pattern created on March 24th 2023 (c). The density of the radial vectors for 7 days from March 8-15, 2023 (b) using the APM from July 25, 2022 and the 7-day distribution of radial data from March 24-31, 2023 (d) using the APM from panel c. Overall, coverage increased in the two regions we saw lower coverage (100 ° – 120 °,200 ° - 225 °) and the smoothness of the pattern was greater with the pattern in panel c.

This document will provide an overview of the procedures for performing the different types of APMs available at this time. These methods include the boat pattern, walking pattern, Automatic Identification System (AIS) pattern, auto AIS pattern, and drone pattern. This document will provide brief synopses of more detailed documents that instruct operators in the various methods for measuring antenna patterns.

II. METHODS

Antenna pattern measurements can be conducted using five separate methods: boat, walking, AIS, auto AIS, and drone. Each method for conducting an APM possesses its own benefits and drawbacks which will influence the method the operators prefer in the long-term operation of their HF Radar network.

The first APMs that will be examined are the boat and walking APMs. These two APM methods will be considered together since they follow the same procedure. To begin, the operator must possess a transponder which is a battery-operated device which receives, amplifies and adds a unique signature to the radio signal transmitted by the SeaSonde [8]. This device must be tuned to the frequency of the station. Once it is tuned to the correct frequency using the SeaSondeTransponder application, the operator must adjust the radio signal characteristics of the SeaSonde and enable the collection of time series files, which are a collection consecutive time sweeps consisting of received signal power over time, to enable collection of the proper data needed for the APM. Once the transponder signal is confirmed to be received by the antenna, the pattern is ready to measured.

Both methods require making at least 2 equidistant semi-circle arcs with the transponder around the receive antenna, but one method involves walking over land and one requires making the arcs over water on a boat. For a successful pattern, the arcs must encompass all the bearings where data is expected over water, and the arcs must be completed very slowly (1 minute of time for each 10 degrees of bearing coverage). Moving through the arcs too quickly does not allow for the generation of enough data points for an accurate measurement of the pattern [9]. It is also recommended by CODAR for boat patterns, if possible, to gather extra data at bearings which the boat cannot reach using a walking pattern and coupling the APM data. This creates a pattern with greater bearing coverage than if just done by boat. Once the measurement is complete, a single loop file is generated by overlaying the time series data with a GPS TRAK file. This loop file is then processed into the measured pattern for installation. The radar is then re-configured back to its original operating settings and the pattern is processed. The best reference for a boat or walking pattern is found in the Antenna Pattern Measurement Guide provided by Old Dominion University [9].

Boat pattern measurements are the preferred method in conversations with CODAR. Walking APMs have a steeper sightline from the top of the receive antenna to the transponder compared to the sightline of the transponder in boat APMs. This steeper sightline will create a pattern measurement which will not completely represent the distortion experienced by sea echo. CODAR also states that walking patterns have an increased chance for the transponder signal to multi-path due to its closer proximity to distorting objects which can also cause the distortion to not be measured properly. With boat APMs, there are caveats to this method in the form of cost, time and coverage. Depending on the region it can be costly to charter a vessel and the availability and the cost of chartering a vessel can be dissuasive to frequent boat pattern measurements. While walking patterns are simpler, less time-consuming, and less costly, they do not permit the signal to propagate over water, which is the intended function of the SeaSonde's signal. Many sites such as those on the West Coast of the United States have the antenna positioned on a cliff's edge overlooking the ocean which makes a walking pattern impossible.

AIS APMs are generated by comparing the radar bearing estimate of the echo generated by passing marine vessels with the vessel bearing calculated from AIS information. The AIS antenna is separate from the SeaSonde and has its own independent processing for listening to AIS signals and signal processing. The SeaSonde is able to track the speed, bearing and location of vessels from backscattered signals off of the vessels. This data can land in the Bragg region and is removed during the averaging and processing from CSQ files to the final cross spectra product (CSS) [10]. Using the SeaSonde's projected location of the vessel and the location of the vessel broadcasted from the vessel to the AIS listening antenna, a pattern measurement can be generated. While the collection of AIS data is recommended for at least one week after the discovery of the need for new pattern, generating the pattern measurement can be done remotely in a very short time frame.

AIS kits are provided separately from the SeaSonde which are necessary for conducting AIS APMS. The quality of the pattern generated is controlled by the availability of AIS data from local ship traffic. Regions that have low ship traffic would have reduced effectiveness for AIS pattern generation.

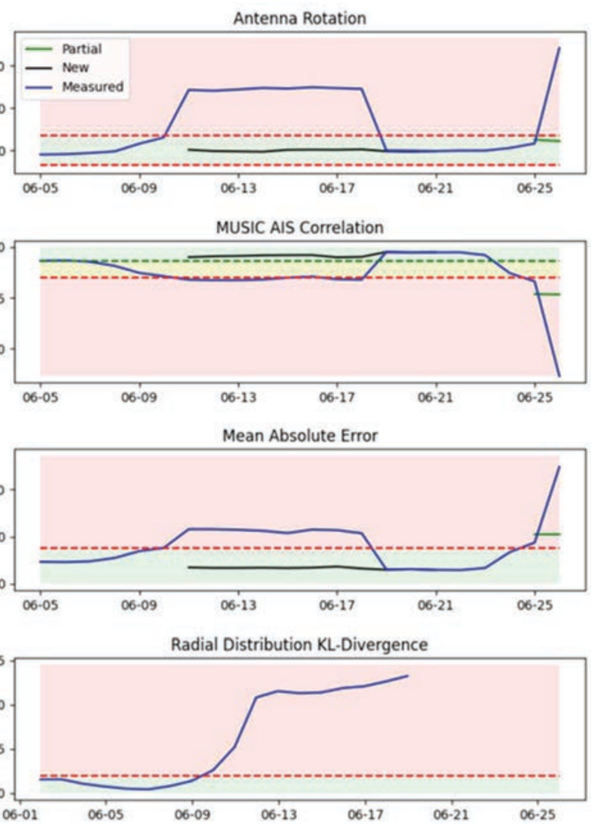

Fig. 2. The statistical data report generated by CODAR Ocean Sensors on June 26th 2023 as part of their (at time of writing) novel Auto AIS APM software. This report was generated for the HF Radar site in Sandy Hook, NJ owned by Rutgers University. The plots show the current measured pattern in blue, the new suggested pattern in black, and a partially built pattern in green. Plot (a) shows the deviation of antenna rotation bearing assignment, (b) the strength of correlation between SeaSonde's bearing assignment algorithm MUSIC and the AIS bearing assignment, (c) the mean absolute error, (d) the KL-Divergence of the radial distribution of the current pattern at the current time vs when the pattern was initially installed. Data that is within the green bounds is acceptable to the Auto APMs software conditions and the red bounds indicate the pattern has fallen out of

Recent iterations in CODAR software have allowed for patterns to be generated automatically by the AIS software rather than from the operator. These APMs are called Auto AIS APMs. The new software generates daily reports which visualize the results of four criteria the software tests the existing antenna pattern against to assess its quality and also recommends a smoothing value to be used when implementing the suggested pattern. These criteria are 1) mean absolute error, 2) KL-divergence, 3) correlation between MUSIC and AIS bearing assignment, and 4) the mean rotation error in direction finding bearing. Along with testing the current pattern, the software generates a new pattern which is assessed using the same criteria. This statistical data is represented visually in the report (Figure 2). This new iteration in AIS software still requires the operator to examine and install the generated pattern, but it is an innovative step toward consistently evaluating the quality of an installed measured pattern.

Drone APMs are the last type of APM and are typically conducted using a quadcopter drone. The APM is performed by flying the drone in a semi-circle around the receive antenna over water. The effectiveness of the drone APM is demonstrated in [11] where they found results using the drone APM are similar to those generated with a boat APM. The drones follow pre-programmed path determined by the operator around the receive antenna. The benefits to the drone APM are that sea state is no longer an issue for data collection, cost is lower in the longer term, and there is no worry of vessel availability. Like the boat APM, the drone APM also allows the signal to propagate over water. Drawbacks to drone APMs include requiring an FAA drone piloting license, requiring permission to fly the drone over parks or public/protected areas, technical skill in programming and operating the drone, and vulnerability to harsh weather conditions. The best reference for a drone pattern can be found by the University of California, Santa Barbara [12]. This manual is the most up-to-date guide for the drone APM using the DJI Phantom model drone.

III. Conclusion

This document sought to provide an overview of the current methods for conducting a SeaSonde antenna pattern measurement and provide resources for helping operators conduct them themselves. APMs are a vital procedure that must be performed to increase the quality of the data produced by the HF Radar and detect changes in near field region due to natural or anthropogenic sources. CODAR, the manufacturer of the SeaSonde recommends boat patterns paired with walking patterns as the 'gold standard' for pattern measurements. In some cases, this becomes impractical due to cost, vessel scheduling, and weather issues. Drone patterns [11] can replicate the boat pattern well and can be performed at a much lesser cost, but run into issues of weather susceptibility as well. Newer releases in SeaSonde software allow for AIS and Auto AIS APMs. The procedures can be done remotely and quickly at the operator's leisure. The quality of the AIS APM relies on the quantity of the AIS data retrieved from passing vessels.

Acknowledgments

This work was funded by NOAA Award Number NA16NOS0120020 "Mid-Atlantic Regional Association

Coastal Ocean Observing System (MARACOOS): Powering Understanding and Prediction of the Mid-Atlantic Ocean, Coast, and Estuaries”. Sponsor: National Ocean Service (NOS), National Oceanic and Atmospheric Administration (NOAA) NOAA-NOS-IOOS-2021-2006475, Integrated Ocean Observing System Topic Area 1: Implementation and Development of Regional Coastal Ocean Observing Systems.

This document was written the guidance of documents provided by Teresa Updyke of Old Dominion University and the University of California Santa Barbara, and the manufacturer CODAR Ocean Sensors.

References

[1] H. Zhou and B. Wen, "Wave Height Extraction From the First-Order Bragg Peaks in High-Frequency Radars," *IEEE Geoscience and Remote Sensing Letters,* vol. 12, no. 11, pp. 2296-2300, 2015, doi: 10.1109/LGRS.2015.2472976.

[2] J. Paduan and H. Graber, "Introduction to High-Frequency Radar: Reality and Myth," *Oceanography,* vol. 10, pp. 36-39, 01/01 1997, doi: 10.5670/oceanog.1997.18.

[3] D. E. Barrick and B. J. Lipa, "Using antenna patterns to improve the quality of SeaSonde HF radar surface current maps," in *Proceedings of the IEEE Sixth Working Conference on Current Measurement (Cat. No.99CH36331)*, 13-13 March 1999 1999, pp. 5-8, doi: 10.1109/CCM.1999.755204.

[4] C. W. Evans, H. J. Roarty, E. M. Handel, and S. M. Glenn, "Evaluation of three antenna pattern measurements for a 25 MHz seasonde," in *2015 IEEE/OES Eleveth Current, Waves and Turbulence Measurement (CWTM)*, 2-6 March 2015 2015, pp. 1-5, doi: 10.1109/CWTM.2015.7098147.

[5] J. T. Kohut and S. M. Glenn, "Improving HF Radar Surface Current Measurements with Measured Antenna Beam Patterns," (in English), *Journal of Atmospheric and Oceanic Technology,* vol. 20, no. 9, pp. 1303-1316, 01 Sep. 2003 2003, doi: https://doi.org/10.1175/1520-0426(2003)020<1303:IHRSCM>2.0.CO;2.

[6] C. Mantovani *et al.*, "Best Practices on High Frequency Radar Deployment and Operation for Ocean Current Measurement," (in English), Review vol. 7, 2020-April-09 2020, doi: 10.3389/fmars.2020.00210.

[7] H. Roarty *et al.*, "Operation and Application of a Regional High-Frequency Radar Network in the Mid-Atlantic Bight," *Marine Technology Society Journal,* vol. 44, pp. 133-145, 11/01 2010, doi: 10.4031/MTSJ.44.6.5.

[8] D. M. Fernandez, J. Vesecky, and C. Teague, "Calibration of HF radar systems with ships of opportunity," in *IGARSS 2003. 2003 IEEE International Geoscience and Remote Sensing Symposium. Proceedings (IEEE Cat. No.03CH37477)*, 21-25 July 2003 2003, vol. 7, pp. 4271-4273 vol.7, doi: 10.1109/IGARSS.2003.1295486.

[9] T. Updyke, "Antenna Pattern Measurement Guide," 2020.

[10] B. M. Emery, L. Washburn, C. Whelan, D. Barrick, and J. Harlan, "Measuring Antenna Patterns for Ocean Surface Current HF Radars with Ships of Opportunity," (in English), *Journal of Atmospheric and Oceanic Technology,* vol. 31, no. 7, pp. 1564-1582, 01 Jul. 2014 2014, doi: https://doi.org/10.1175/JTECH-D-13-00181.1.

[11] L. Washburn, E. Romero, C. Johnson, B. Emery, and C. Gotschalk, "Measurement of Antenna Patterns for Oceanographic Radars Using Aerial Drones," (in English), *Journal of Atmospheric and Oceanic Technology,* vol. 34, no. 5, pp. 971-981, 01 May. 2017 2017, doi: https://doi.org/10.1175/JTECH-D-16-0180.1.

[12] E. Romero, "AAPM Guide (DJI) Using Drones for Antenna Pattern Calibrations," 05/01/2018 2018.

Strategies for Operating HF Radars in Field of View of Offshore Wind Turbines

1st Joshua Trockel
CODAR Ocean Sensors Ltd
Mountain View, CA
josh@codar.com

2nd Brian Emery
UC Santa Barbara
Santa Barbara, CA
brian.emery@ucsb.edu

3rd Anthony Kirincich
Woods Hole Oceanographic Institution
Falmouth, MA
akirincich@whoi.edu

4th Mike Muglia
East Carolina University
Greenville, NC
mugliam@ecu.edu

5th Hugh Roarty
Rutgers University
New Jersey, USA
hroarty@marine.rutgers.edu

6th Patterson Taylor
East Carolina University
Greenville, NC
patterson.taylor.iii@gmail.com

7th Dale Trockel
CODAR Ocean Sensors Ltd
Mountain View, CA
dale@codar.com

8th Teresa Updyke
Old Dominion University
Norfolk, VA
garner@ccpo.odu.edu

9th Chad Whelan
CODAR Ocean Sensors Ltd
Mountain View, CA
chad@codar.com

***Abstract*— Oceanographic High Frequency (HF) radars are used to monitor coastal ocean conditions, such as waves and surface current velocities, up to 250 km from shore in near real-time. Applications using HF radar outputs include search and rescue, oil spill response, harmful algal bloom monitoring, tsunami detection, among others. Offshore wind turbines in the field of view of HF radars act as strong reflectors and can cause interference, leading to loss and/or bias in the oceanographic measurements. With the current U.S. administration's goal of deploying 30 gigawatts (GW) of offshore wind by 2030, offshore wind farms in the United States are expected to drastically increase in the coming years from the seven turbines currently operating in U.S. waters.**

This paper summarizes current understanding of wind turbine interference (WTI) on HF radar data as well as current best practice recommendations for mitigating the effects of WTI on HF radar networks. Present mitigation methods fall into three categories including, altering how radars are configured or run, using software to flag data containing WTI, and altering the design of the radar network to increase redundancy.

I. Introduction

Coastal oceanographic high frequency radars (HFRs) are observational tools used to monitor ocean conditions. They collect beyond-the-horizon observations with high spatial and temporal resolution. HFRs are primarily used to monitor surface current measurements. These observations are used by government agencies, industry professionals, and scientists for applications such as search and rescue, ocean current modeling, and oil spill response [1]. Other HFR observations include wave measurements [2], wind measurements [2, 3], and tsunami detection.

HFR networks have operated around the world for the past 30 years [4]. These HFR observations have been identified by the Integrated Ocean Observing System (IOOS) as being an effective tool to measure some of the 30 essential ocean observations [5].

Recent years have seen an increased focus on renewable energy sources globally, including generating electricity from atmospheric winds over the ocean from fixed or floating offshore wind turbines. By harnessing the strong and consistent winds at sea, offshore wind farms have the capacity to produce substantial electricity. The expansive offshore environment also offers ample space for the installation of larger turbines, resulting in increased power output. There has been an increase in the plans of projected offshore turbine farms, as well as the projected size of these turbines. The U.S. Department of the Interior (DOI) has set a goal to deploy 30 GW of offshore wind capacity by 2030 [6].

When offshore wind turbines are in the coverage area of HFR networks, they act as reflectors which cause signals that can mix with oceanographic current information [7]. These mixed signals cause loss and/or corruption of ocean observations. This paper reviews recent findings on both WTI and mitigation methods.

II. Wind Turbine Interference

WTI in HFRs was first observed in Cornwall, UK by Wyatt et al. [7]. These observations led the community to investigate the effects of WTI on HFR networks. Teague and Barrick, [8], first identified the harmonic components of periodic amplitude modulated WTI signal as the cause of the interference. Trockel et. al [9] derived the analytical solution for the location of the interference based on a wind turbine's rotation rate.

The characteristics of WTI in HFR data are primarily determined by the wind turbine rotation rate, yaw angle, and the variation in rotation rate over the radar's Doppler integration period. WTI is identifiable in HF Doppler spectra by the resulting harmonic peaks. The rotation rate of wind turbines is determined by the turbine manufacturer's power-curve and offshore wind conditions. As rotation rate increases, the location of the positive WTI harmonic peaks increase in Doppler frequency and the negative WTI harmonic peaks decrease in Doppler frequency, pushing them away from the center. If the rotation rate places the harmonic peak at a frequency that exceeds the Nyquist frequency of the radar, the peak is aliased in Doppler and pushed out in range for positive harmonics or pulled back in range for negative harmonics.

Fig. 1 shows the effect of rotation rate on the Doppler Frequency location of the WTI. The black lines represent the location in Doppler of the first three positive and first four negative harmonic peaks as a rotation rate increases. The blue line shows the fourth positive harmonic. Four green dots are used to show the location in Doppler of the first four positive harmonic peaks at a rotation rate of 4.5 and 11.3rpm. The fourth harmonic peak aliases in Doppler at higher rotation rates, as can be seen by the blue line and the higher green dots.

The yaw of the turbine blades is determined by the prevailing wind direction near the turbine. The yaw of the turbine (also known as the nacelle angle) determines the amplitude of the different harmonic peaks of the WTI. Fig. 2 shows the radar cross section of the first four positive and negative harmonics at different nacelle angles relative to the radar. The nacelle angle of 0° has turbine blades orthogonal to the radar radial lines. Conversely a nacelle angle of 90° has the turbine blades parallel to the radar radial lines. The nacelle angle affects the relative amplitude of the harmonic peaks observed in HFR data. Thus, the nacelle angle determines the number of observable harmonic peaks in HFR data.

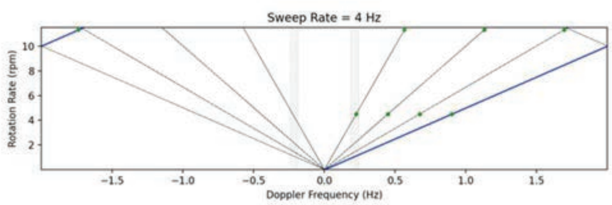

Fig. 1. The locations in Doppler of the first four positive and negative harmonic peaks of WTI are shown at different turbine rotation rates. The blue line shows the aliasing that can occur when the frequency of the interference is greater than the Nyquist frequency of the radar. The signal of the fourth positive harmonic loops from positive Doppler to negative at rotation rates greater than 10. This aliasing also pushes the peak up in range. Green dots show the location of the four positive harmonic peaks at rotation rates of 4.5 and 11.3. At 11.3, the fourth harmonic peak aliases around to the negative frequencies. This occurs with the negative harmonic peaks as well.

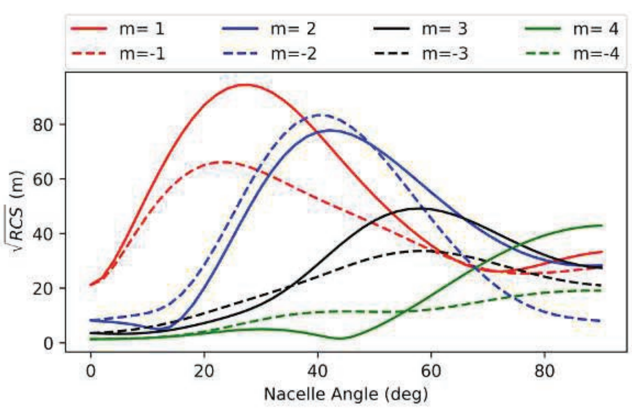

Fig. 2. The radar cross section of the first four positive and negative harmonic peaks (m=-4… m=4) as a function of Nacelle angle.

Outside of the optimal rotation rate of the turbines, variable wind conditions lead to variable turbine rotation rates. The changes in the rotation rate over the course of a HFR Doppler integration period (for example 17 minutes at 5 MHz) cause the WTI peaks to spread out in Doppler. This leads to wider WTI peaks which mixes with a greater portion of the HFR data. The way the rotation rate varies over the course of an integration period determines the shape of these wider peaks. Fig. 3 shows simulated WTI added to the same range bin of the same cross spectra file with the same starting rotation rate but three different rotation rate variance characteristics over the integration period of the spectra. The WTI with no variance produces sharp, thin peaks. The other two simulations both have a variance in rotation rate of 2 rpm over the integration, but the first varies linearly while the second varies non-linearly. Although both result in wider peaks, the shape, relative width, and amplitude of the peaks differ. The sensitivity of WTI to subtle changes in rotation rate has prevented efforts to-date of removing WTI from ocean current signal in HFR Doppler spectra [10]. Using the analytical understanding of the effect of turbine characteristics on the HFR WTI, CODAR Ocean Sensors has developed simulation software that can add WTI to radar data [10]. Fig. 4 shows an example of WTI placed into a Doppler Cross spectra in the fifteenth range bin. The figure shows two simulated turbines, one with a starting rotation rate of 11.3 rpm with a yaw angle of 44 and increasing to a rotation rate of 11.5 over the integration period. The second turbine has a starting rotation rate of 4.2 with a yaw angle of 44 and increasing to a rotation rate of 4.3 over the integration period.

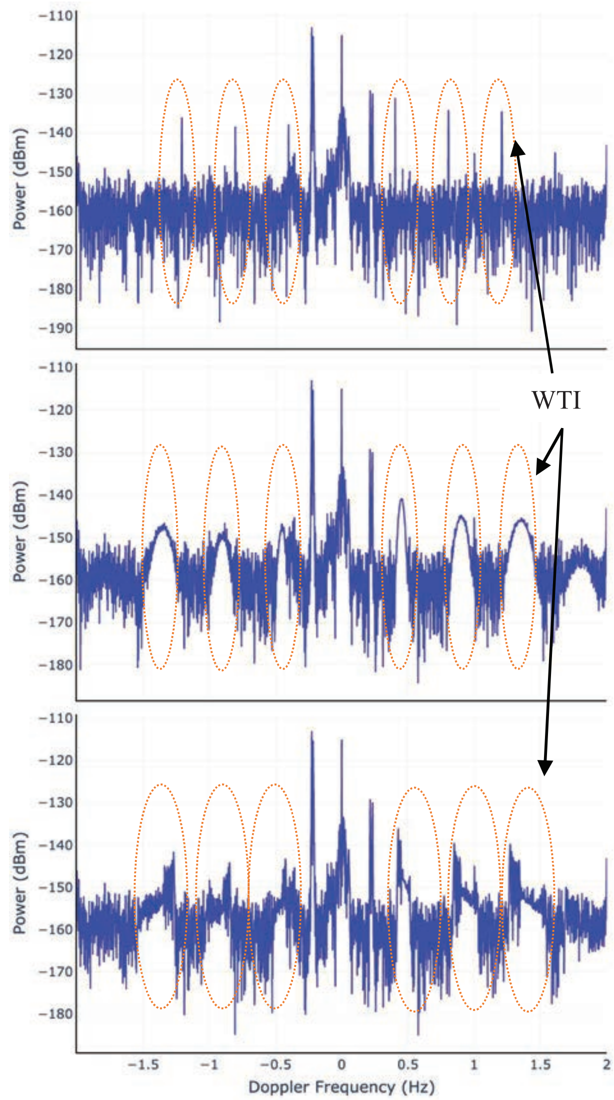

Fig. 3. Range slice of the fifteenth range bin of a cross spectra with simulated WTI added. The first three positive and negative harmonic peaks are circled in yellow dotted lines. All three plots show the addition of one simulated turbine with a starting rotation rate of 8 rpm. The top plot does not change rotation rates during the integration period. The middle plot increases from 8 to 10 rpm linearly over the integration period. The bottom plot increases from 8 to 10 rpm non-linearly.

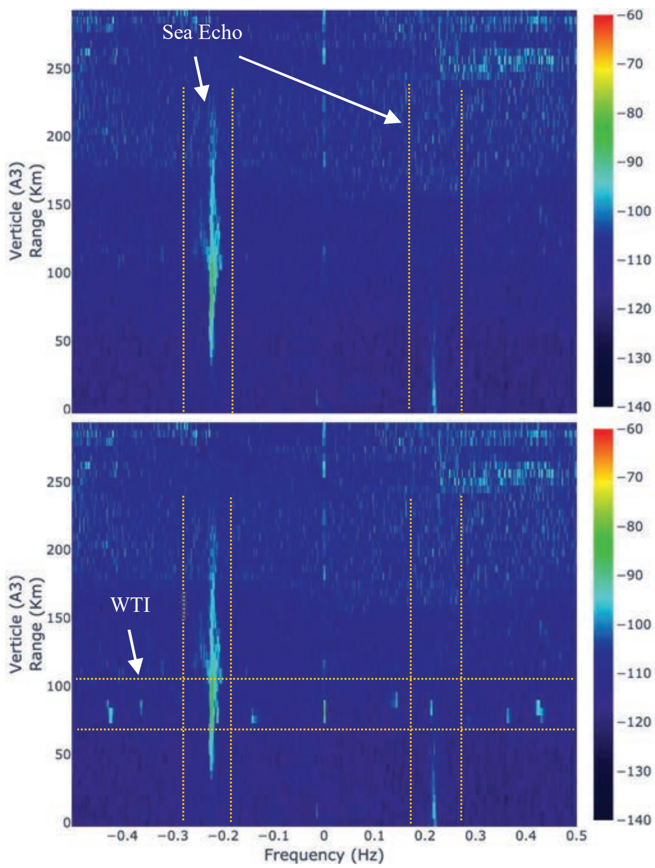

Fig. 4. WTI is simulated into a cross spectra at the fifteenth range bin. The original cross spectra is shown in the top figure, the bottom shows the WTI addition. The sea echo and WTI are labeled and highlighted in dotted lines. Two turbines are simulated here have rotation rates of 11.3 – 11.5 and 4.2 – 4.3 rpm and yaw angles of 44°.

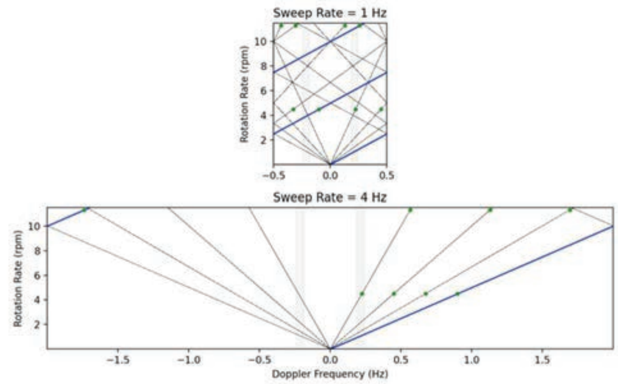

Fig. 5. Aliasing of harmonic peaks at 1 Hz vs 4 Hz as rotation rate increases. At 4 Hz, only the fourth positive and negative harmonic peaks are aliased and that only once. At 1 Hz, all harmonic peaks are aliased and the fourth is aliased twice (the blue line in both plots). Green dots show the location of the first four positive harmonic peaks at rotation rates of 4.5 and 11.3. At 1Hz, the fourth harmonic peak is aliased back into the Sea Echo at 11.3 rpm.

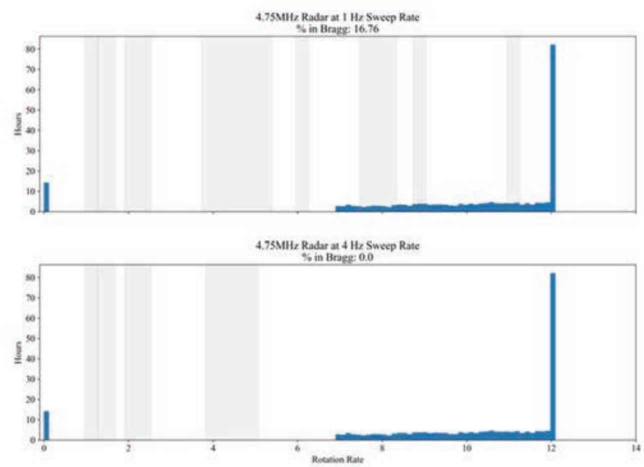

Fig. 6. Rotation rates generated using a simulated power curve [11] are shown using local wind conditions observed at Block Island, RI over the course a month. The simulated power curve has a cut in rotation rate of 6.9 rpm at wind speeds of 3m/s and an optimal rotation rate of 12.1 reached at wind speeds of 11.4 m/s. The rotation rates are then used to calculate the percentage of time (number of hours in the bar graph) at least one turbine would be found within the Sea Echo region if the site were operating at 1 Hz and 4 Hz. Rotation rates placed in the Sea Echo are shown as grey bars.

III. Mitigation Methods

A. Parameter Optimization

The location of WTI in range and Doppler is affected by the rotation rate of the turbine and the Nyquist frequency of the HFR. At lower radar sweep rates, aliasing of WTI occurs at lower rotation rates. As peaks are aliased multiple times, more range bins are affected by WTI and the percentage of turbine rotation rates placing WTI within the Sea Echo region of the Doppler cross spectra is increased. By increasing the sweep rate of the radar, the harmonic WTI peaks that experience aliasing over the normal operating rotation rate range of wind turbines decrease drastically. Fig. 5 and Fig. 7 show this decrease. The gray bars in Fig. 5 show the sea echo region. By increasing the sweep rate, there are fewer rotation rates where the rotation rate is placed into the sea echo, and there are fewer affected range bins.

The percentage of time the rotation rates place interference into the sea echo can be approximated using historical wind data and simulated turbine power curves. Fig. 6 shows the percentage of time rotation rates place at least one of five turbines' WTI into the sea echo at BLCK where five offshore turbines are operating in the first range bin. By increasing the sweep rate, the percentage of time at least one turbine peak is placed within the Sea Echo goes down from 17% to 0%.

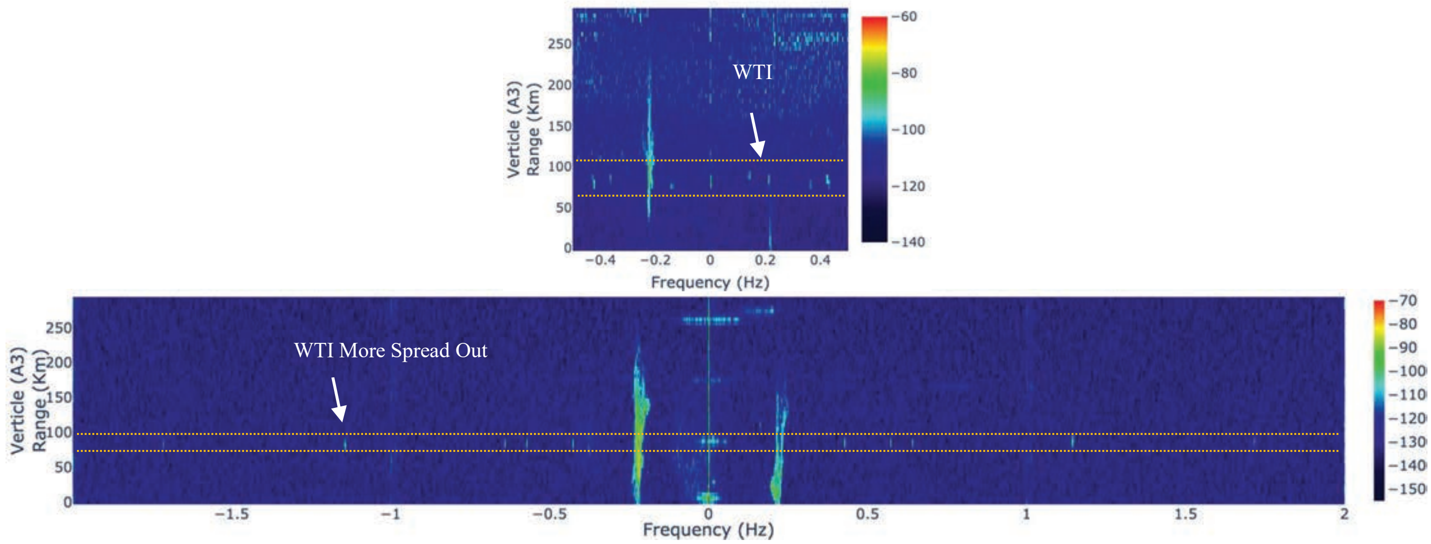

Fig. 7. A visualization of the effect of increasing the sweep rate. WTI from two turbines are simulated into a cross spectra from a site operating at 1 Hz (top) and another operating at 4 Hz (bottom). The rotation rate, yaw angle, and variance in rotation rate are all the same in both top and bottom plots, but the WTI is no longer in the Sea Echo and only spans one range bin in the cross spectra from 4 Hz.

B. Flagging

Recent efforts [9, 10, 12, 13] have developed two different methods of estimating the rotation rate of the turbines within the field of view of the radars. Using these rotation rates, the locations in range and Doppler of WTI peaks can be determined and flagged.

1) Estimating Rotation Rates

Trockel et al. [9, 12] describes a method that uses the symmetrical nature of WTI at higher sweep rates to measure the gaps between peaks and thus determine the rotation rates of the turbines. This approach is limited to HFR operating at 4 Hz because the symmetrical nature of the WTI is only present without aliasing.

More recent efforts developed deep learning algorithms which estimate the rotation rate of wind turbines within the field of view of the radar from cross spectra [10]. This approach showed a high degree of accuracy, estimating rotation rates of up to two turbines with a mean error of 0.14 rpm. This accuracy was consistent at both sweep rates of 4 Hz and 1 Hz. Machine learning (ML) models were also combined with a modified version of the BOEM [9, 12] analytical method to further correct the ML model estimates.

2) Flagging Peaks

Once the rotation rate is predicted, the observed harmonic peaks associated with that rotation rate are measured to determine the estimated average width of the peaks. This width is then used to flag all the harmonic peaks associated with the rotation rate. This step is essential for times when the interference is placed in the Sea Echo. In those cases, the only peaks that matter for processing and flagging are the ones that are unobservable because they are mixed with the sea echo. By using information from the other observable peaks, the width and location of the peak within the Sea Echo can be determined. Fig. 8 shows an example of the flags produced by this method. The red boxes show the location of the flags identified by the software. The tool was able to accurately identify and flag the affected range-Doppler bins, including those in the Sea Echo region.

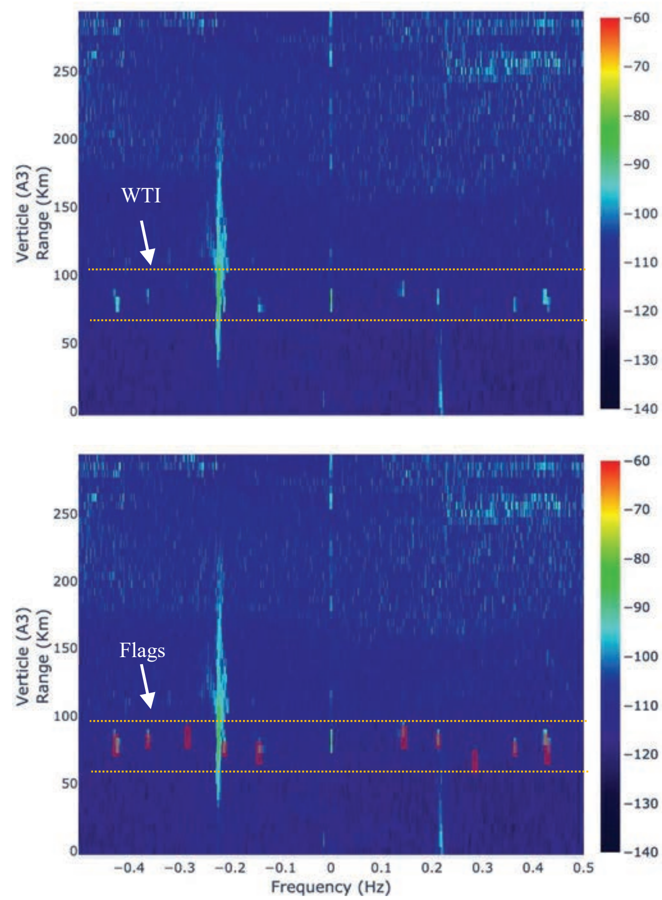

Fig. 8. Example of flagging performed using deep learning algorithms and analytical correction. WTI peaks are seen on the top as light blue dashes. The Red boxes on the bottom over those dashes represent the flags identified by the software.

C. Increasing Radar Redundancy

Networks of HF radars produce total vector ocean surface currents when multiple radars have overlapping coverage. Overlapping coverage can be obtained in two forms: monostatic radial component measurements, and bistatic component measurements. Monostatic measurements are when a HFR transmits and receives its own signals.

Monostatic measurements can be increased by adding additional radars to a radar network. Bistatic measurements are obtained when signals are transmitted from one site and received at another. Bistatic measurements can also be included in the combining step used to produce totals. Bistatic measurements can be added to a radar network by operating the radars on the same frequency and using multiplexing technology [14-18].

Radar observation redundancy works because WTI places interference at the same Doppler location at each of the sites observing the turbines. However, since each site only measures the radial component of the sea surface in the direction of the HFR, that patch of ocean associated with the Doppler location will be different at each site. The range bin of the WTI at each site can also be different depending on the relative distances of the HFRs to the wind turbines. This means that ocean data lost or corrupted by WTI at one site will not be the same ocean data lost or corrupted by WTI at a different site. Increasing the number of sites looking at the turbines and/or including bistatic detections, adds redundancy in the surface current component measurements which can be protective against interference.

Trockel et al. [10] aimed to quantify the effect of added redundancy on mitigating impacts of WTI. To test this, the NOWRDC effort flagged a 3 by 3 range-Doppler box to be removed from processing at each of the sites corresponding to the location of the turbines relative to each radar. One month of data was then processed using these flagged range-Doppler bins at each of the sites individually. The data were then combined to produce totals in three different ways: 1) using monostatic data from two sites, 2) using monostatic data from three sites, and 3) using monostatic data from three sites and bistatic data from one site. Fig. 9 shows the coverage area of the sites used in the study. Totals were produced in the same three ways mentioned above, with and without the flagged range-Doppler bins. Using data from two monostatic sites led to the loss of 1,168 total vectors and a root mean squared difference RMSD in changed vectors of 10.94 cm/s with the introduction of flagged range-Doppler bins. The vectors lost were reduced to 106 and RMSD to 5.58 cm/s with the addition of a third monostatic site, then 94 and 5.38 cm/s with the addition of a third monostatic site and one bistatic site (Fig. 10).

Trockel et al [10] repeated the same study design outlined above but with simulated WTI added at each of the three sites instead of flagging a three-by-three range-Doppler bin window. The trend seen in the previous analysis was consistent. The number of vectors lost, and RMSD of changed vectors due to the introduction of WTI was 1002 and 10.85cm/s respectively, for two monostatic sites, 105 and 5.48cm/s for three monostatic sites, and 98 and 5.33cm/s for three monostatic site and one bistatic site (Fig. 11).

Trockel et al [10] found that increasing the amount of redundancy significantly reduced both missing data and the error introduced by both WTI mixed vectors as well as reducing both error measures when range-Doppler bins were removed from processing within the Sea Echo.

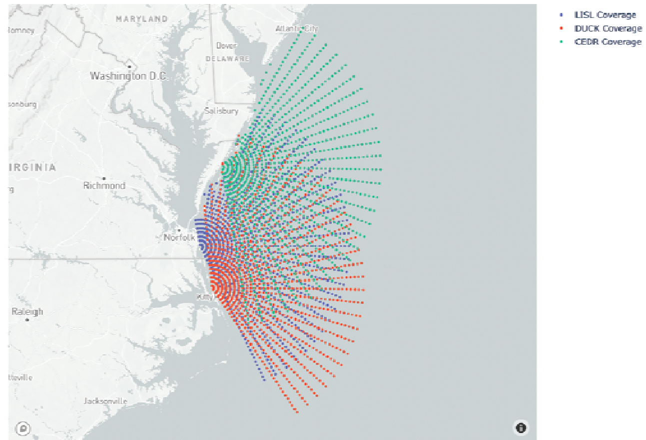

Fig. 9. Coverage map of sites used for NOWRDC study. The color of the dot represents the particular radar station Cedar Island, VA (green), Little Island, VA (blue) and Duck, NC (red).

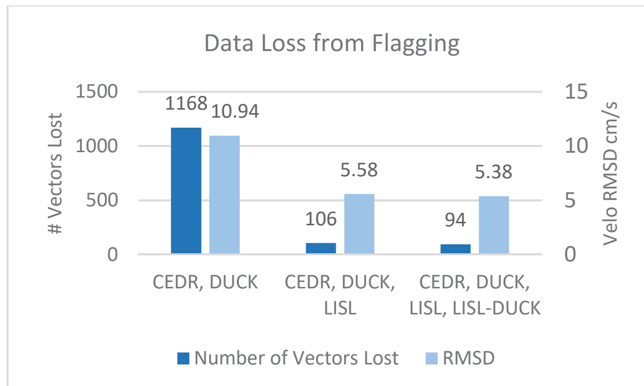

Fig. 10. The number of total vectors lost and the root mean square difference (RMSD) of changed vectors caused by flagging a 3x3 range-Doppler bin window in the positive and negative Sea Echo peaks as more sites were used to produce totals.

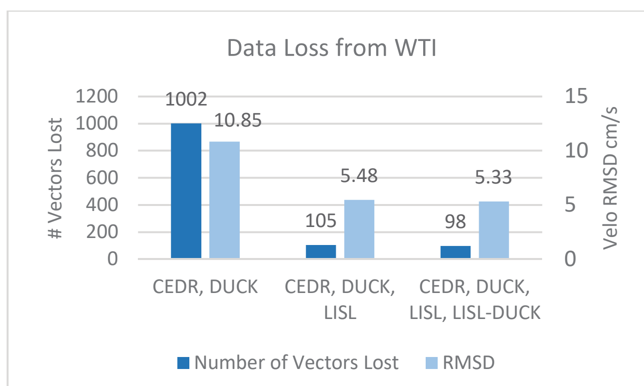

Fig. 11. The number of total vectors lost, and the root mean square difference (RMSD) of changed vectors caused by flagging simulated WTI as more sites were used to produce totals.

IV. Discussion

A. *Limitations*

Each presented method for mitigating WTI has associated limitations. Increasing the sweep rate of the radar and increasing the radar redundancy are both limited by the HFR permitted operating frequency band as outlined by the International Telecommunication Union (ITU) [19] and implemented in the United States by the Federal

Communication Commission [20]. In particular, when increasing the sweep rate from 1 Hz to 4 Hz, the limited bandwidth of the ITU band makes it difficult to operate multiple radars on the same band near each other. Increasing the sweep rate increases the number of spurious images that appear in the range Doppler spectra from blanking, complicating timing adjustments, and making it more difficult to keep adjacent radars from interfering with each other. This interference can be mitigated by properly timing the offset of the radars but provides an additional unresolved challenge to operating a network of many radars.

Flagging has limitations as well. Even when flags are placed perfectly, the flagged sea echo data is lost. Flagging is also limited by the ability of software to identify interference peaks. As wind farms increase in number, flagging alone may not be as effective in mitigating the effects of WTI.

B. Recommendations

It is unlikely that any single method of mitigation is sufficient to solve the problem of WTI, but when used in conjunction, WTI can be effectively mitigated in HFR. For sites operating in isolation, increasing the sweep rate is an effective way to ensure WTI stays out of the sea echo. Data lost by flagging can be recovered using the increased redundancy offered by HFR networks with increasing levels of overlapping coverage obtained through deployment of additional sites and/or bistatic operation. Our findings suggest that increasing redundancy in HF radar networks will become essential for the observation of surface currents in the vicinity of the large number of planned offshore wind turbines.

C. Next Steps

The effects of larger wind farms on HFR networks is currently being investigated through an NOAA Ocean Technology Transfer funded effort which will end in 2024. This effort will collect in-situ measurements of ocean currents via drifters as the 64 turbines from the Vineyard Wind's turbine farm are deployed off the coast of Massachusetts. These measurements will be used to validate the efficacy of the mitigation methods described here on large-scale wind farms in the field of view of multiple HF radars operating at different frequencies. Cameras will also be placed on buoys to collect rotation rates of the off-shore wind farm and this dataset will be used for validation of future mitigation and flagging schemes. Efforts to simulate the effects of much larger numbers of turbines (O(~100)) are also needed and in progress.

ACKNOWLEDGMENTS

This work was funded by NOAA Award Number NA16NOS0120020 "Mid-Atlantic Regional Association Coastal Ocean Observing System (MARACOOS): Powering Understanding and Prediction of the Mid-Atlantic Ocean, Coast, and Estuaries". Sponsor: National Ocean Service (NOS), National Oceanic and Atmospheric Administration (NOAA) NOAA-NOS-IOOS-2021-2006475, Integrated Ocean Observing System Topic Area 1: Implementation and Development of Regional Coastal Ocean Observing Systems.

Funding for this study was provided in part by the U.S. Department of the Interior, Bureau of Ocean Energy Management, Environmental Studies Program, Washington, D.C, under Contract Numbers M16PC00017 and 140M0120C0002.

Funding for this study was provided in part by the National Offshore Wind Research & Development Consortium under Task Work Order No. 111 to Agreement No. 140398

REFERENCES

[1] Abascal, A.J., et al., *Operational oil spill trajectory modelling using HF radar currents: A northwest European continental shelf case study.* Mar Pollut Bull, 2017. **119**(1): p. 336-350.

[2] Lipa, B., et al., *Brahan Project High Frequency Radar Ocean Measurements: Currents, Winds, Waves and Their Interactions.* Remote Sensing, 2014. **6**(12): p. 12094-12117.

[3] Kirincich, A., *Remote sensing of the surface wind field over the coastal ocean via direct calibration of HF radar backscatter power.* Journal of Atmospheric and Oceanic Technology, 2016. **33**(7): p. 1377-1392.

[4] Roarty, H., et al., *The Global High Frequency Radar Network.* Frontiers in Marine Science, 2019. **6**.

[5] *IOOS 30 essential: U.S. Integrated Ocean Observing System, 2010: A Blueprint for Full Capability. Tech. rep.* 2010, IOOS Office: Maryland, MD, USA.

[6] FACT SHEET: President Biden's Budget Lowers Energy Costs, Combats the Climate Crisis, and Advances Environmental Justice. The White House Office of Management and Briefing, 2023.

[7] Wyatt, L., A. Robinson, and M. Howarth. Wind farm impacts on HF radar current and wave measurements in Liverpool Bay. in OCEANS 2011 IEEE-Spain. 2011. IEEE.

[8] Teague, C.C. and D.E. Barrick. *Estimation of wind turbine radar signature at 13.5 MHz*. in *2012 Oceans*. 2012. IEEE.

[9] Trockel, D., et al., *Impact Assessment and Mitigation of Offshore Wind Turbines on High Frequency Coastal Oceanographic Radar.* Sterling, VA: US Department of the Interior, Bureau of Ocean Energy Management. OCS Study BOEM, 2018. **53**: p. 49.

[10] Trockel, J., et al., Oceanographic HF Radar Data Preservation in Wind Turbine Interference Mitigation. 2023.

[11] Jonkman, J., et al., *Definition of a 5-MW Reference Wind Turbine for Offshore System Development* 2009.

[12] Trockel, D., J. Trockel, and C. Whelan, Coastal High Frequency Radar Wind Turbine Interference Mitigation. Sterling, VA: US Department of the Interior, Bureau of Ocean Energy Management. 37 p. Report No.: OCS Study BOEM 2021-081. Contract, 2021(140M0120C0002).

[13] Trockel, D., et al. *Mitigation of Offshore Wind Turbines on High-Frequency Coastal Oceanographic Radar*. in *OCEANS 2018 MTS/IEEE Charleston*. 2018. IEEE.

[14] Baskin, C., et al., Effectiveness of a bistatic system on high frequency radar resiliency. 2016. p. 1-5.

[15] Baskin, C., et al., High Frequency radar measurement resiliency with bistatics. 2015. p. 1-7.

[16] Lipa, B., et al., HF Radar Bistatic Measurement of Surface Current Velocities: Drifter Comparisons and Radar Consistency Checks. Remote Sensing, 2009. **1**(4): p. 1190-1211.

[17] Nazzaro, L. and H. Roarty, Evaluation of Bistatic High Frequency Radar Data. 2021. p. 1-5.

[18] Roarty, H., et al., Improving the measurements of high frequency radar: Reduced averaging times and bistatics. 2013. p. 1-6.

[19] World Radiocommunication Conference. in World Radiocommunication Conference. 2012. Geneva: International Telecommunication Union.

[20] *Radio Spectrum Allocation*. 2022; Available from: https://www.fcc.gov/engineering-technology/policy-and-rules-division/general/radio-spectrum-allocation.

Event: Offshore Technology Conference

Manuscript Number: **OTC-35072-MS**

Title:

Results of the Mini-Adaptive Sampling Test Run (MASTR) Experiment: Autonomous Vehicles, Drifters, Floats, ROCIS, and HF-Radar, to Improve Loop Current System Dynamics and Forecasts in the Deepwater Gulf of México

SF DiMarco[1], S Glenn[2], M Smith[2], B Jaimes de la Cruz[3], R Ramos[4], E Pallas-Sanz[5], M Tenreiro[5], S Mahmud[1], U Nwankwo[1,9], TN Miles[2], R Monreal Jiménez[7], D Salas de León[6], AH Knap[1], LK Shay[3], B Magnell[4], J Storie[4], G Stuart[8], J Marble[8], VK Contreras Tereza[10]

[1]Geochemical and Environmental Research Group, Texas A&M University, College Station, TX USA

[2]Center for Ocean Observing Leadership, Rutgers University, New Brunswick, NJ USA

[3]Rosenstiel School, University of Miami, Miami, Florida USA

[4]Woods Hole Group LLC, Houston, Texas USA

[5]Physical Oceanography, CICESE, Ensenada, B.C., México

[6]Facultad de Ciencias, Universidad Nacional Autónoma de México, México City, México

[7]Instituto de Ciencias del Mar y Limnología, Universidad Nacional Autónoma de México, México City, México

[8]Fugro, Houston, Texas USA

[9]Gulf of México Coastal Ocean Observing System, Texas A&M University, College Station, Texas USA

[10]Mexican Institute for Water Technology, Paseo Cuauhnáhuac 8532 Progreso, México

Abstract

We report the preliminary results of the international MASTR (Mini-Adaptive Sampling Test-Run) Experiment of the UGOS (Understanding the Gulf Ocean Systems) Program, which simultaneously deployed multiple autonomous measurement platforms (i.e., ocean buoyancy gliders, subsurface floats, surface drifters) and high-frequency coastal radar in the Deepwater south-eastern Gulf of México. The state-of-the-art ocean observing technologies provide near-real-time surface and subsurface co-located temperature, salinity and velocity observations and were assessed for improvements to the predictive capability of multiple federal and industry operational ocean circulation models. Six ocean buoyancy gliders were deployed in the western Yucatan Strait near Mahahual, México - four of the gliders were deployed in January 2024, two gliders were deployed from July thru November 2023. The summer and fall 2023 glider data was assimilated into the NOAA RTOFS numerical model and significantly improved the model performance to accurately represent the vertical hydrographic structure of the inflowing water from the Caribbean Sea to the Gulf of México via the Yucatan Strait. The high-frequency radar system deployed near Cancun, México was operational throughout the experiment. Radar observations of surface velocity during fall 2023 observed the passage of extreme weather events, including Hurricane Idalia (26 August – 2 September). Additionally, the hi-frequency radar observed the spatial and temporal position of the Yucatan Current speed core as the Loop Current System in the Gulf of México evolved from a retracted state to an extended state, to a detached state, with numerous reattachment sequences. The research underscores the complexity of the four-dimensional structure of the Loop Current system and the spatial and temporal evolution of the circulation in response to topographic, tidal, geostrophic, ageostrophic, and wind forcing.

Additional observations from airborne and subsurface observational platforms reveal sub-mesoscale variability and the correlation between surface and subsurface current patterns.

Introduction

The Loop Current transports nearly 27 million cubic meters per second of water into the Gulf of México through the Yucatan Strait between México and Cuba (Candela et al., 2019). Despite decades of effort in the public and private sector, accurate and timely prediction of arrival time, location, and intensity of the current and its associated eddies into the Northern Gulf of México has remained elusive (Forristall et al., 1991, DiMarco et al., 2001, Nowlin et al., 2001). Ocean buoyancy gliders and subsurface float technology that are equipped with direct velocity observations provide the capability to estimate total kinematic variability in addition to the traditional hydrography methodologies that provide geostrophic velocities only (Knap et al., 2023).

Adaptive sampling strategies indicate the ability for observational assets to be guided or directed to regions of poor model skill and where the availability of additional observations can reduce model uncertainty. Improvements to prediction accuracy and precision of deep-water features are assessed. Recommendations for transition to operations include co-located temperature, salinity, and velocity profiles. The high-frequency radar (HFR) observations in the Yucatan Strait provide the first near-real-time observations of the surface currents and their variability into the basin. In total, a dozen autonomous platforms were deployed in 2023. The impact of assimilating subsurface observations in the Yucatan Strait shows improvements to all numerical ocean models considered by improving the vertical hydrographic structure of the inflowing water masses. Additionally, the inflowing Yucatan Current is shown to be spatially complex and temporally dynamic (Bunge et al., 2002) by abruptly (time scales of days) transitioning from coastal (< 50 km) to offshore (> 70 km) states and correlated with changes to the Loop Current structure in the Gulf's interior. The results have the potential to impact offshore industry safety by providing improved information of the offshore environment (stakeholder industries include energy transition, renewables, and fisheries) and improved extreme weather intensification prediction through better estimates of upper ocean heat content.

Understanding the Gulf Ocean System (UGOS)

The National Academies of Sciences Engineering and Medicine (NASEM) has funded a five-year (2022-2027) international private-public-partnership (NASEM Report 2018) of academic and industry organizations, and federal agencies led by Texas A&M University, Florida State University and the Woods Hole Oceanographic Institution and partnered with several federal government agencies (including NOAA, NRL, BOEM, BSEE). UGOS is explicitly engaging a wide range of Stakeholders including agencies, Energy Sector Industries, Fisheries managers, as well the general public.

Objectives

Previously, we reported on the adaptive sampling element of UGOS (Understanding the Gulf Ocean Systems) to simultaneously deploy multiple autonomous measurement platforms (i.e., ocean buoyancy gliders, subsurface floats, drogued drifters) and high-frequency coastal radar to provide near-real-time surface and subsurface observations of the deep-water southeastern Gulf of México (DiMarco et al. 2023a, Knap et al. 2023). The state-of-the-art ocean observing technologies, are available for inclusion in cutting-edge machine learning, artificial intelligence, and modern data science methodologies to improve the predictive capability of ocean models. In this paper, our focus is on the results from the initial deployment of observing platforms in the southeast Gulf of México and western Caribbean Sea.

International Partnership

The unique placement of the study region within three independent exclusive economic zones necessitated the research be carried out in partnership between scientists of each participating country.

MASTR Operations

Study Region and observational platforms

The region of study for the MASTR experiment is the inflow region of the Gulf of México that includes the Yucatan Strait and the western Caribbean Sea (Figure 1). The study region overlaps three sovereign exclusive economic zones: US, México, and Cuba. The green color bar shows the magnitude of near surface currents from the NOAA RTOFS operational global ocean circulation model.

Fig. 1—Map of southeast Gulf of México showing possible buoyancy glider, APEX-EM float, and surface drifter deployment locations for Adapted Sampling experiments: MASTR. Green color bar represents surface (0m) current speed (m/s) from NOAA RTOFS numerical ocean circulation model from 15 January 2024, 0000 UTC. Four buoyancy gliders were deployed (green circle) in January 2024 near Mahahual, México. The intended trajectories include the western Caribbean and Cayman Sea and entrance to Yucatan Strait (red and green arrows), Yucatan Strait cross-section and possible trajectories into Gulf of México (magenta arrows) showing potential branches leading to Florida Straits, West Florida

Shelf, and Gulf of México interior. Highlighted light orange in the Yucatan Strait shows the nominal footprint of the Yucatan HFR system. Drifter and float deployment locations (dark red boxes) are guided by adaptive sampling strategies and will complement glider mission objectives. RTOFS model output courtesy of NOAA.

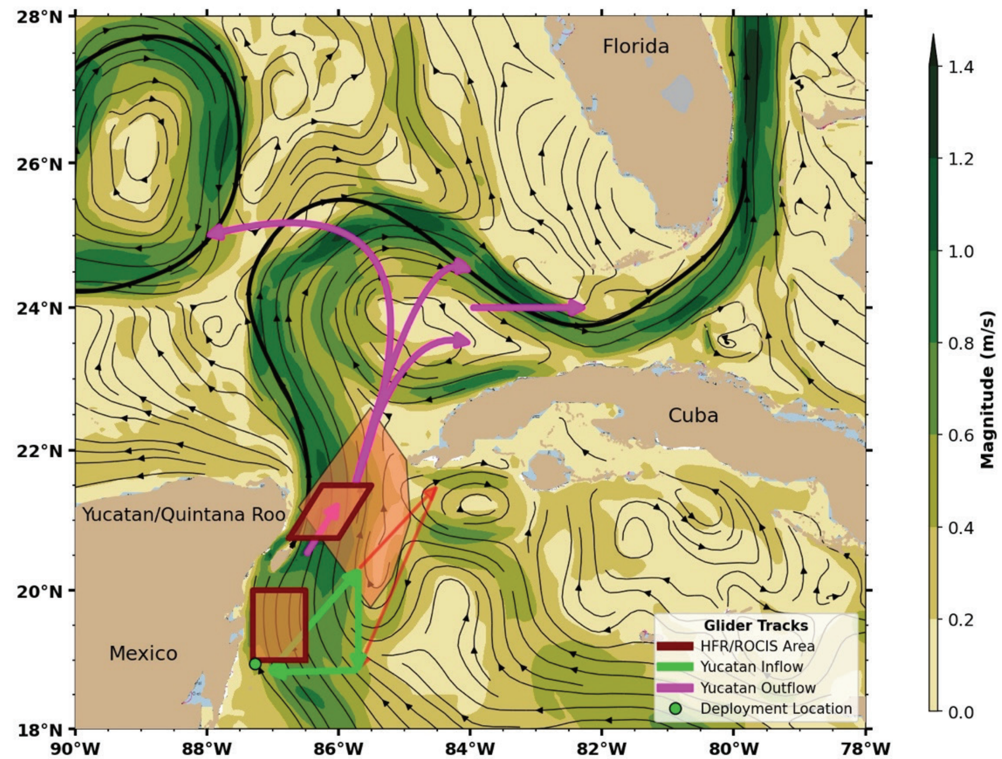

High-frequency radar (HFR). Since June 2022, a HFR system (CODAR Oceansonde, operating frequency is 5-Mhz) deployed at two locations on the eastern México coast (Quintana Roo, Puerto Morelos and Isla Contoy) have provided hourly estimates of near-surface current velocity (six-kilometer grid) across 70% of the Yucatan Strait and effectively capturing the magnitude and variability of the velocity core of the Yucatan Current (precursor to the Loop Current and eventually the Gulf Stream) as it enters into the Gulf of México (DiMarco et al. 2023b). The location of the footprint of the HFR stations in the Yucatan Strait is shown in orange in Figure 1. During the roughly 20 months of operations, the Yucatan HFR has provided about 80% data return. The primary reason for data dropout during this time was due to power outages at the remote station at Isla Contoy. Power outages were often due to tropical weather or excessive cloudiness that interfered with solar panel abilities to recharge the battery supply. There is no electricity at this remote site.

Raw radar data collected by the two stations were hosted on local servers for initial processing. Initial processing includes the assembly of individual radial data for each station. Radial data are subjected to standard data quality protocols through full implementation of the NOAA-IOOS QARTOD standards for HFR data (Smith et al., 2021). Radial data were then merged to form estimates of the surface ocean current flow field. Additional processing using simultaneously collected ship-based AIS information to refine the current velocity estimates and improve the error covariance (Liu et al. 2021; Smith et al. 2021; Smith et al., 2022; Updyke et al. 2019; Updyke et al. 2021). The resulting dataset consisted of hourly fields of current velocity vectors (east-west and north-south components) on a regular 6-km grid.

Buoyancy gliders. Ocean buoyancy gliders (Testor et al., 2019) provide vertical profiles of collocated temperature, salinity, and current velocity to 1000m depth up to several times per day (depending on depth of profile and environmental factors that can impact vehicle flight characteristics). The glider models used in MASTR are Slocum gliders (Model G2 and G3, Teledyne Webb Research) and Seaglider (Kongsberg). A total of six ocean buoyancy gliders were deployed for the MASTR experiment. Two deployments occurred in late summer and fall of 2023. These deployments targeted the hydrographic structure of the western Caribbean Sea as waters entered the Yucatan Strait and the southeastern Gulf of México. The planned deployment duration for the MASTR gliders is 30 days, however, the gliders carried enough Lithium-battery power for up to 90 days for extended sampling or long transits to recovery sites. The extended configuration of the Loop Current led to focusing the glider deployments initially in the western Caribbean Sea.

Surface drifters provide Lagrangian estimates of near surface current velocity (using differential positioning of the drifter) (DiMarco et al. 2005, Storie et al. 2023). Industry deployed surface drifters (e.g.,the Woods Hole Group - Far Horizon Drifters (FHD) and EddyWatch service) have established the standard for metrics associated with Gulf of México Loop Current and LC eddies dynamics, position, magnitude, and intensity. Six FHD drifters were deployed in the Yucatan Strait during MASTR. One drifter was deployed with each glider deployment operation (two drifters), with the remaining drifters deployed from the southern HFR station at Puerto Morelos.

APEX-EM float. One APEX float (Shay et al. 2019) was deployed for MASTR. Each float provides vertical profiles of collocated temperature, salinity, and current velocity to a maximum depth of 2000m and can be programmed to cycle from surface to depth up to two times per day. Argo float mission duration can exceed one year.

Argo floats. At the time of the MASTR experiment, about 45 Argo floats occupied the Gulf of México (Furey et al., 2018), with most of the floats occupying the eastern Gulf beneath the Loop Current and Eddy Berek (Figure 2). During the summer and fall of 2023, three severe tropical weather systems passed thru the Gulf of México (Harold, Arlene, and Idalia). Of these, Hurricane Idalia passed through the Yucatan Strait in late August (Glenn et al., 2024).

ROCIS airborne observations. A series of five overflights is planned in the MASTR region using the Remote Ocean Current Imaging System (ROCIS) (Anderson et al., 2015). ROCIS has the capability to provide maps of current vectors at 250 m resolution along the flight path and in near real-time and with current speed accuracy of 5 cm/s. The target regions for the overflight are the Yucatan Current and Loop Current frontal boundaries of the Yucatan Slope and Gulf of México interior, the Yucatan HFR footprint, and the western Caribbean Sea as the Yucatan Currents enters the channel. Direct comparisons of the ROCIS current vector observations with the HFR and velocities derived from the drogued drifters will provide quantitative assessment and validation of the ROCIS observations.

Timeline for MASTR

The timeline for the MASTR experiment consists of four Phases. **Phase 1: Diplomacy** was principally active from September 2022 to December 2023. During Phase 1, the MASTR team communicated with the US State Department, and the Mexican and Cuban Consulates to secure all necessary permissions, manage expectation, and define the scope of the research (including data access, geographical limitations, start/stop dates, durations, environmental parameters measured, sampling metrics (e.g., sampling interval and frequency). Elements of Phase 1 extend into Phase 3: Operations (described below) because of notification requirements to inform domestic and foreign authorities when MASTR platforms pass in and out of non-US EEZs.

Phase 2: Mobilization. During Phase 2, instrumentation platforms were prepared for deployment. Activities included scientific sensor calibration, instrument refurbishment, ballasting diagnostics, system diagnostics and power supply servicing and maintenance. Observation platforms were shipped to the final deployment destination of Puerto Morelos, México using domestic and international service providers. Phase 2 involved personnel from each institution and occurred in Fall/Winter 2023. Some logistical considerations during Phase 2 were necessarily delayed until diplomatic permissions were granted under Phase 1 activities. Data-flow pathways were tested and, in some cases established, to ensure end-to-end continuity of collected data to accessible data servers and federal (Data Assembly Centers) and international (Global Telecommunications Service) access points.

Phase 3: Operations. The field campaign was operational during Phase 3 of MASTR. Operations included the deployment and recovery operations of each platform. Most deployment and recovery operations proceeded with the use of small local commercial fishing vessels and dive boats. In this way, local expertise and indigenous knowledge were used to ensure safe and efficient action. While deployed, guidable instrument platforms, i.e., gliders, floats, and airborne instruments (ROCIS), were piloted by the responsible team members. All near real-time data transmissions were monitored and assessed for quality. Active piloting was coordinating using web tools and services designed for voice and data communications and sharing.

Phase 4. Analysis. Following the operations phase, the team will be engaged in the processing, analysis, synthesis, and archival of data, data products, and numerical output. The timeline for analysis is to be coincident with the *in-situ* field program and provide guidance for the Grand Adaptive Sampling Experiment (GrASE) now scheduled for deployment in 2025. The best practices and lessons learned during MASTR will be directly applied to the planning and operations for GrASE.

Fig. 2— Location of Argo float profiles during the 2023 hurricane season. The SST map is from 21 August 2023—five days prior to the formation of Hurricane Idalia. Color in the storm tracks signifies wind intensity from the Saffir-Simpson Hurricane Wind Scale as per the legend. Hurricane Idalia: 27-29 August; Tropical Storm Harold: 20 August; Tropical Storm Arlene: 1-3 June 2023.

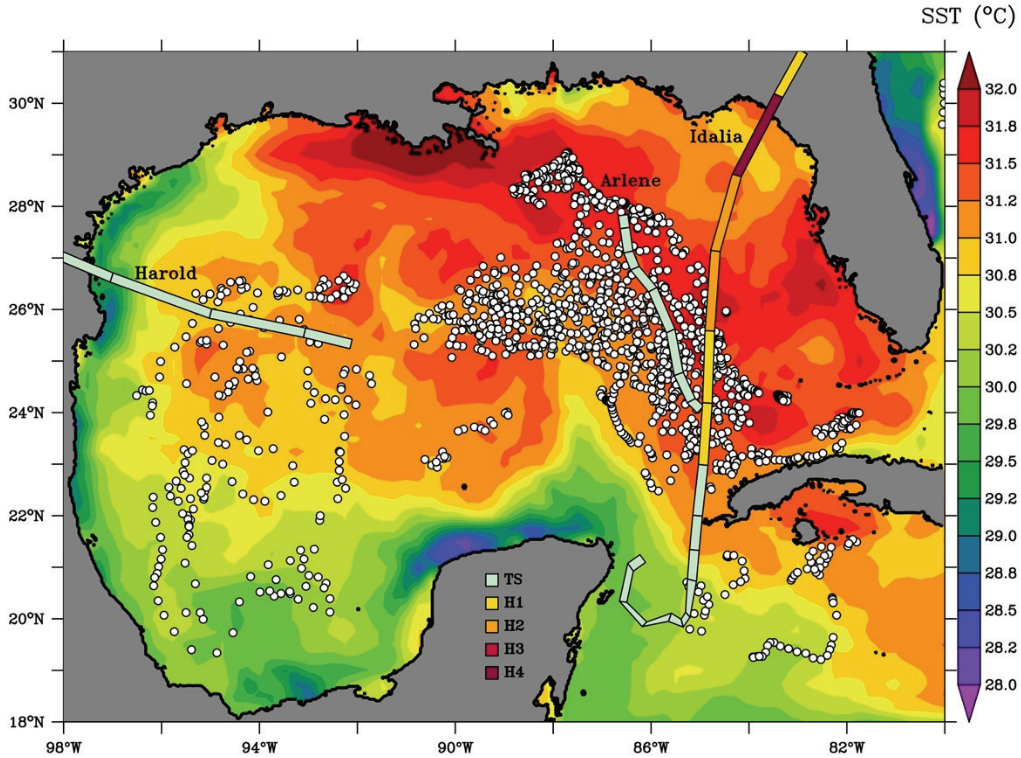

Oceanographic Conditions in January 2024

At the beginning of the intensive field campaign (mid-January 2024), the Yucatan Current speed core occupied the western half of the Yucatan Straight. The Loop Current was in an extended configuration into the Gulf of México (northward extension to about 26°N). A Loop Current Eddy (LCE), nicknamed Eddy Berek, had separated from the Loop Current stem and migrated westward with the center of rotation near 26°N, 89°W. Northwest of Cuba, the surface circulation between the Loop Current and the island forms a closed circulation cell. Eddy Berek had undergone several transitions from separation in mid-2023, to reattachment, and separation in the latter period of 2023 and early 2024.

Numerical Circulation Models: Operations

The MASTR experiment will incorporate the use of several agency and industry numerical models to guide the observing assets during deployment. Priority is given to position and direct mobile platforms to regions of high variability. However, caution is also advised due to the potential for current speeds to far exceed the forward speed of the gliders, which makes arbitrary navigation difficult. Additionally, the presence of submarine obstacles in the form of shallow banks and reefs further complicates piloting operations. The numerical output is also available to provide context to the observations and to assist with interpretation. Four operational models are available for direct comparison of MASTR observations. NOAA's Global Real-time Operational Forecast System (RTOFS), the US Navy Global Ocean Forecast System (GOFS 3.1), and the European Copernicus Marine Environment Monitoring Service (CMEMS). We also have access to three higher resolutions models, the Navy's intra American Seas model (AmSeas), the North Carolina State University (NCSU) Coupled Northwestern Atlantic Prediction System (CNAPS), and the Woods Hole Group (WHG) Tendral Ocean Prediction System (TOPS) model.

Observed vertical profiles collected by the gliders and floats of temperature, salinity, and density are made available and displayed on the multiple websites and include the glider data portals maintained by GCOOS (gandalf.gcoos.org) and NOAA's National Glider DAC. The observed profiles are plotted against vertical profiles of similar variables extracted from CMEMS, RTOFS, and GOFS as maintained by the US IOOS Hurricane Glider consortium.

Results

Yucatan Evolution from High-Frequency Radar

The data map of Figure 3 shows a horizontal view of the Yucatan Strait region of the southeastern Gulf of México. The graphic is routinely produced every hour using processed observations from the two radar sites located in Quintana Roo México (Stations ISCY and UASA shown as green squares). The observations were collected 11 November 2023 1500 UTC and processed QA/QC'd data extend across the Strait, almost reaching the Cuban mainland. At this time, the Yucatan Current surface speed core was in the western part of the Strait, northward flowing with maximum speeds exceeding 1.4 m/s. On the eastern side of the Strait, surface current speeds are markedly diminished at less than 0.4 m/s and with direction of flow more variable with possible southward flow at the Cuban west coast near Cabo de San Antonio.

Fig. 3— Map of southeast Gulf of México highlighting the entry to the basin between México (left) and Cuba (right). Color bar represents current speed (m/s) observations from two high-frequency radar stations at Puerto Morelos (green square, south) and Isla Contoy (green square, north), Quintana Roo, México. Yucatan Radar observations taken on 11 November 2023 1500 UTC. Dashed lines represent depth contours of 100, 500, and 1000 m. Gray circle at Cabo de San Antonio, Cuba, shows site of prospective HFR location on eastern Yucatan Strait. White dashed line represents uncertainty level of optimal interpolation (roughly equivalent to 95% significance level, Wilkin et al., 2002). Yellow triangles represent locations of simultaneously deployed bottom mounted CPIES (current meter – profiling inverted echo sounders) in the Yucatan Strait Interior.

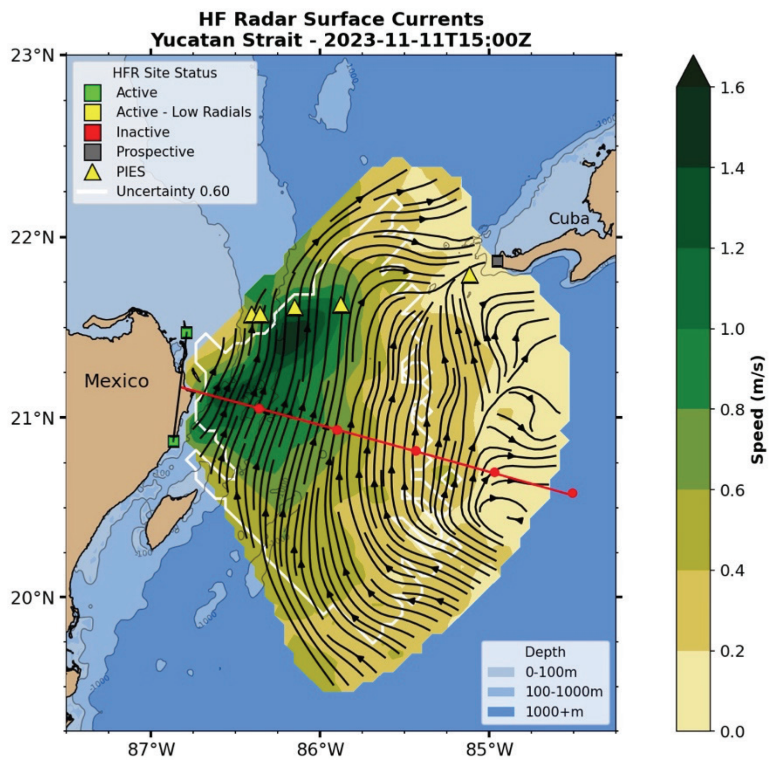

Decision Support Tools: Glider Piloting Operation

Buoyancy gliders require active piloting by trained technical personnel to navigate the vehicle from point to point. Navigation is further complicated by the inability to communicate directly with the glider and course correct once the glider submerges. During the MASTR experiment, gliders were commanded to descend from the surface to 1000 m depth (when depth conditions allow). The forward speed of a typical buoyancy glider is about 0.20 m/s (about 15 km per day). As shown in Figure 3, surface current speeds of the Yucatan Strait can far exceed the forward speed of the glider. To efficiently achieve the desired waypoints, glider pilots must carefully consider the integrated (surface to 1000 m) current speed to maneuver the glider across the region. A decision support tool was developed to graphically display the depth averaged currents using available numerical model output (nowcast and forecast) to provide glider pilots near real-time environmental information.

Figure 4 shows an example of the depth averaged currents from the NOAA RTOFS model (output from 02 February 2024 0000 UTC). The relatively high current speed of the Yucatan Current, Loop Current (26°N, 87°W), and Florida Current (24°N, 81°W) are seen in green shading. Note that integrated current speeds are considerably smaller than the current speed observed near surface from the HFR observations (typically less than 0.3 m/s subsurface as compared to greater than 1 m/s at the surface). The reduced relative speed of the glider (current advection plus forward speed) to the fixed earth, allows for greater confidence that the glider will not deviate far from planned trajectories. However, pilots also need to limit time that the glider is at the surface and transmitting data so to not be swept downstream by high surface currents.

Fig. 4—Map of southeast Gulf of México highlighting the entry to the basin between México (left) and Cuba (right). Color bar represents current speed (m/s) output from the NOAA RTOFS numerical model from 03 February 2024 0000 UTC. The current speed is the depth averaged speed from the surface to 1000 m. Contour lines represent isolines of current speed; arrowheads indicate direction of flow. Triangles represent the most recent glider locations with the white tails representing the track over the last three days.

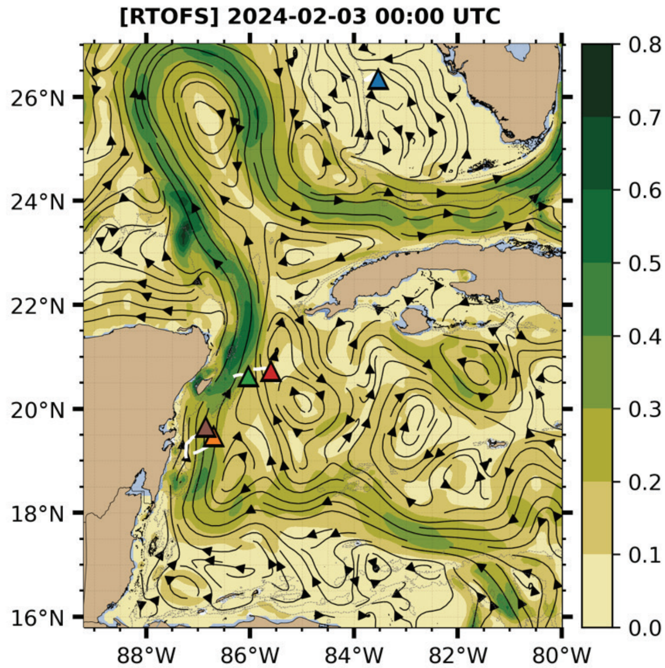

Decision Support Tools: Offshore Energy Platform Operation

Figure 5 shows an example of a decision support tool used to guide operations and safety decisions for offshore energy applications. The black line on each panel represents 75 cm/s (1.5 kt) contour of current speed estimated from the analysis of available *in situ*, remote sensing, and satellite observations. The contour defines the frontal boundary of the Loop Current and its associated eddies. Offshore operations on fixed and mobile platforms in deep water (depths greater than 1000 m) will stop when currents exceed the 75 cm/s threshold. Therefore, nowcasts and forecasts of the contour location will guide when and where operations will occur. The sequence below from October 2023 to January 2024 shows a separated LCE (top left panel: October) remain stationary while the LC stem meanders from east to west and north to south. By 25 December, the meander moves the LC close to the LCE to form a reattachment. By 8 January 2024, the LCE separates from LC and slowly moves westward. Eventually, separated eddies will continue to move west until they dissipate by interacting with bathymetry (the western boundary of the Gulf of México) and other eddies.

Fig 5 —Sequence of temporal and spatial evolution of Loop Current and detached Loop Current Eddy from October 2023 to January 2024. Black line is the analyzed 1.5 kt (~75 cm/s) speed contour.

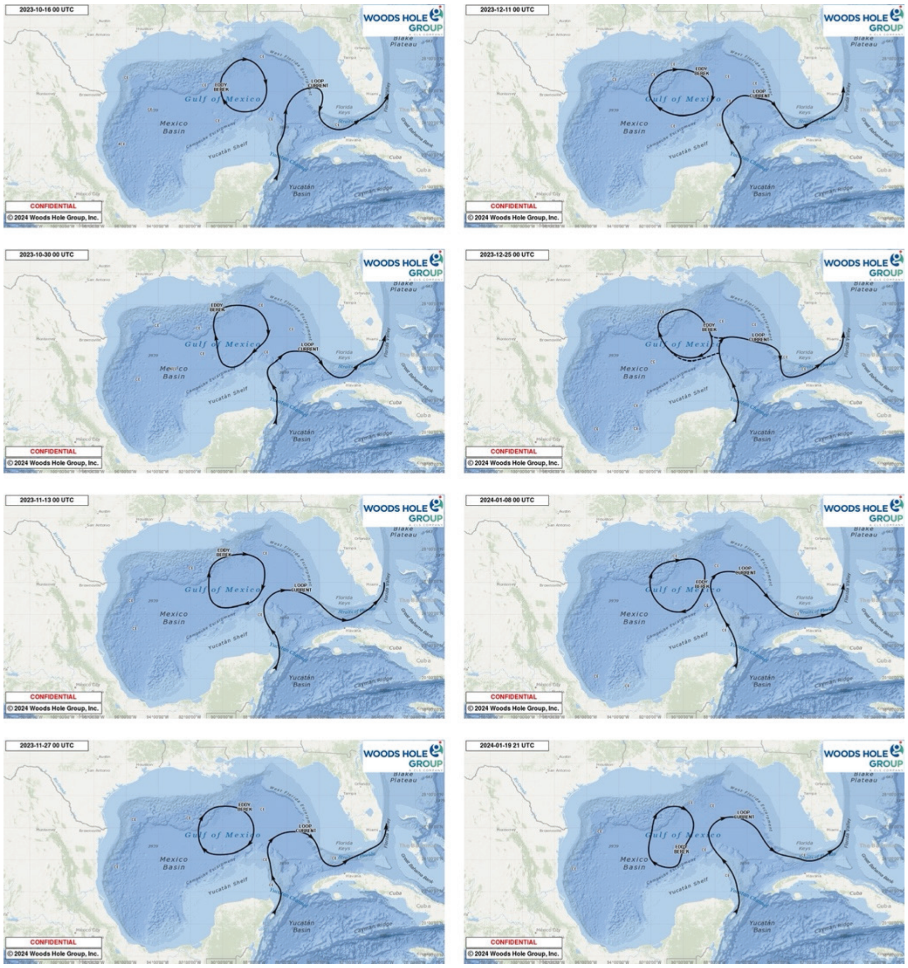

Gulf of México Inflow Hydrography

The sequence of graphics shown in Figure 6 indicate the locations of multiple observational assets in the MASTR region at the beginning of the experiment (late January 2024). The map (top left) shows locations of 4 gliders (two Slocum and two Seaglider), 50-m drogued drifter, and one Argo float on 01 February 2024. The vertical plot (lower left) shows a time history of salinity in the upper 1000 m. The subsurface maximum salinity associated with the movement of Subtropical Underwater (STUW) formed in the Atlantic Ocean is prevalent between 100 and 200 m depth. The impact of the glider observations on the ability of numerical models to accurately represent the salinity structure of the Caribbean basin as the water enters the Yucatan Strait and flows to the Gulf of México is shown in the right panel of Figure 6. The close alignment of property profiles for CMEMS to the gliders observations reveals that both SUT from the NOAA RTOFS and GOFS models are fresher and cooler than the observations. The implications downstream (into the Gulf of México and beyond, i.e., into the Gulf Stream) of this difference on ocean dynamics and climate are currently being assessed.

Fig. 6— a) Map of western Caribbean Sea and east coast of Yucatan Peninsula showing the location of two Seagliders (yellow), two Teledyne Slocum gliders (red), one Far Horizon Drifter (FHD) (purple), and one Argo float (blue) on 01 February 2024. b). Hövmuller graph of salinity (date versus depth) recorded by Seaglider (SG562) 18 Jan 2024 to 01 Feb 2024. c) Average of ten vertical profiles of Temperature, Salinity, and Density from glider SG652 (blue) (31 January 2024) and nearest neighbor profiles from NOAA RTOFS (red), GOFS (green), and CMEMS (purple) numerical models. Graphics from GANDALF.GCOOS.org, CICESE, and the IOOS Hurricane Glider consortium.

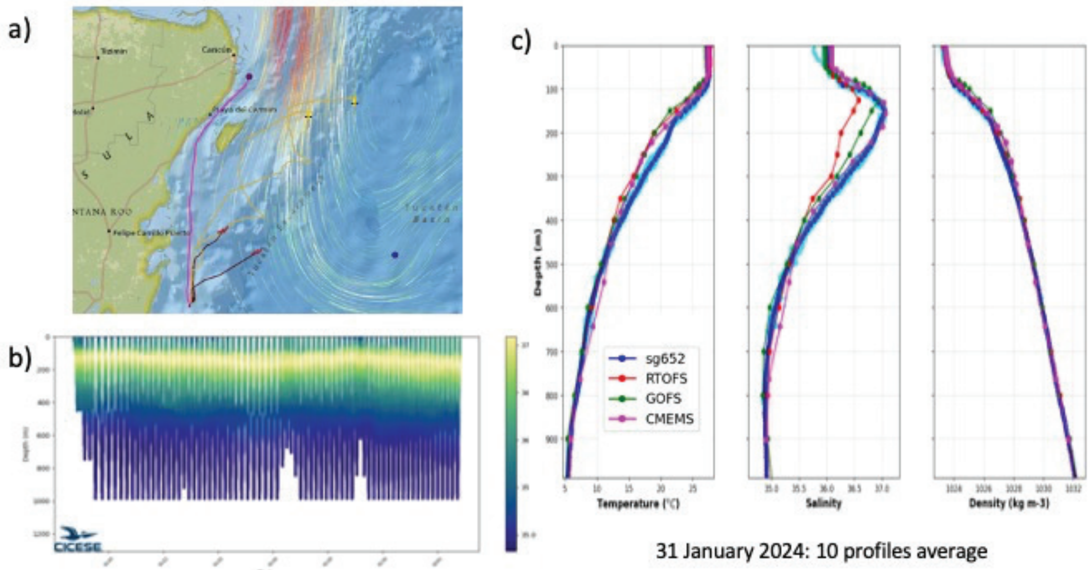

Expectations

Transition to Operations

The knowledge, data products, and decision support tools described here and developed during this experiment are expected to be transitioned into routine and widely available operational services. Ultimately, the findings of MASTR, and the follow-up experiment GrASE, and other activities of the UGOS program will inform future prediction system development and will guide additional transition to operations. Clear communication pathways among implementation teams and coordinated integration of observations, forecasting systems and products are needed to ensure that the stakeholder requirements and expectations are met. As the example described in this paper demonstrate, products and services can be developed that meet the specific needs of a large range of stakeholders and users, which include industry, government agencies, scientific community, as well as the general public.

MASTR Evolution to GrASE

The lessons learned and best practices developed during MASTR are expected to guide the planning of the GrASE experiment, which is tentatively scheduled for early summer 2025. It is anticipated that the number and variety of observational platforms will increase during GrASE. New observing platforms, e.g., the SWOT satellite of high-resolution altimetry, are expected to become fully operational for GrASE. It is also expected that the spatial resolution of some numerical models will improve to ~1 km. Also, under development are statistical models that can optimize the trajectories of adaptive observational platforms and address the issue of reachability for slowly moving platforms in a swiftly moving environment, e.g., estimating the probability that a glider can reach a destination in a specific time given the speed of the glider and speed of the current.

In the coming months, the GrASE team will outline the tasks necessary to plan and execute the experiment. The planning will follow the four-phase protocol developed during MASTR. Most importantly, the diplomatic phase will require early identification of all instrument platforms and sensor types that will be deployed so that research applications in foreign waters can be submitted to appropriate consulate offices and embassies. This step we have found is the controlling factor for the timing and execution of the research plan.

Acknowledgements

The activities described in this manuscript are funded through a contract from the National Academies of Science, Engineering, and Medicine – Gulf Research Program – Understanding Gulf Ocean Systems (NASEM-GRP-UGOS) to the GulfCORES research consortium. The institutional members of the GulfCORES consortium are Texas A&M University, Rutgers University, University of Southern Mississippi, University of Miami, University of South Florida, Universidad Nacional Autonoma de México (UNAM, México), Woods Hole Group LLC, and Ensenada Center for Scientific Research and Higher Education (CICESE, Ensenada, México). NASEM-GRP-UGOS has funded two additional consortia under the UGOS umbrella: GOFFISH (Lead PI: Eric Chassignet, Florida State University) and GODEEP (Lead PI: Amy Bower, Woods Hole Oceanographic Institution). Additional partners in this research include Naval Research Laboratory, NOAA IOOS, GCOOS, Ocean Sierra LLC. The authors are extremely thankful to the group of technicians who fiercely worked in Quintana Roo México to mobilize and deploy the gliders, drifters and float: Brian Buckingham, Kaycee Coleman, Jessica Leonard, Becca Horwitz, David Aragon, Nicole Waite (Rutgers), Donovan Bright, Emily Caulder, Andrew Dancer (TAMU), Bob Currier (GCOOS). The authors also thank the US State Department – Marine Science, the Cuban Consulate, the Mexican Consulate General who worked cooperatively to approve the international research application. We also thank Doug Wilson (UVI, CoastalOceanObs) for assistance in preparing the research application and navigating diplomatic channels.

Anderson, SP, S. Zuckerman and G. Stuart, "Real-time airborne optical remote sensing of ocean currents," 2015 IEEE/OES Eleveth Current, Waves and Turbulence Measurement (CWTM), St. Petersburg, FL, USA, 2015, pp. 1-5, doi: 10.1109/CWTM.2015.7098113.

Bunge, L, Ochoa, J, Badan, A, Candela, J, Sheinbaum, J. 2002. Deep flows in the Yucatan channel and their relation to changes in the Loop Current extension. Journal of Geophysical Research 107:3233. DOI: 10.1029/2001JC001256.

Candela, J, J Ochoa, J Sheinbaum, M López, P Pérez, M Tenreiro, E Pallàs-Sanz, G Athie and L Arriaza-Oliveros, 2019:The Flow Through the Gulf of Mexico. *J. Phys. Oceanogr*. https://doi:10.1175/JPO-D-18-0189.1

DiMarco, SF, RO Reid, and WD Nowlin, Jr., 2001. "Vertical Current Structures in the Deep Gulf Using EOF Analysis" April 30–May 3, 2001. Offshore Technology Conference Manuscript 12994. DOI: https://doi.org/10.4043/12994-MS

DiMarco, SF, RO Reid, WD Nowlin, Jr., 2005. A Statistical Description of the Near-surface Velocity Field from Drifters in the Gulf of Mexico. Geophysical Monograph Series, **Volume 161**, *Circulation of the Gulf of Mexico: Observations and Models*. Eds. W. Sturges and A. Lugo-Fernandez. American Geophysical Union, pp. 101 – 110.

DiMarco, SF, S. Glenn, M. Smith, R. Ramos, AH Knap, R. Monreal, D Salas de Léon, VK Contreras-Tereza, 2023b. Surface current velocity observations of the Yucatan Channel using High-Frequency Radar, 25-28 September 2023. IEEE *OCEANS 2023 - MTS/IEEE U.S. Gulf Coast*, Biloxi, MS, USA, pp. 1-8, doi: 10.23919/OCEANS52994.2023.10337389.

DiMarco, SF**,** S Glenn, B Jaimes de la Cruz, AH Knap, Y Liu, B Magnell, S Mahmud, T Miles, E Pallas-Sanz, RJ Ramos, LK Shay, M Smith, M Renreiro, RH Weisberg, 2023a. Applications Of Adaptive Sampling Strategies Of Autonomous Vehicles, Drifters, Floats, And HF-Radar, To Improve Loop Current System Dynamics Forecasts In The Deepwater Gulf Of Mexico. Offshore Technology Conference, Houston Texas. American Society of Civil Engineers, Brazilian Petroleum, Gas, and Biofuels Institute, Society of Naval Architects and Marine Engineers. OTC-32459-MS. DOI 10.4043/32459-MS

Forristall, GZ, KJ Schaudt, C Cooper, 1992. Evolution and kinematics of a Loop Current Eddy in the Gulf of Mexico in1985. *J. Geophys. Res.* **97**(C2), 2173–2184. DOI: https://doi.org/10.1029/91JC02905

Furey, H, A Bower, P Perez-Brunius, P Hamilton, R Leben, 2018. Deep eddies in the Gulf of Mexico observed with floats. *Journal of Physical Oceanography* **48** (11), 2703–2719

Knap, AH, SF DiMarco, SM Glenn, R Ramos, B Magnell, D Salas, 2023. Understanding the Gulf Ocean System Program: Informing Stakeholders and Improving prediction of the Loop Current System using advanced observational and numerical tools. Offshore Technology Conference, Houston Texas. American Society of Civil Engineers, Brazilian Petroleum, Gas, and Biofuels Institute, Society of Naval Architects and Marine Engineers. OTC-32392-MS. DOI 10.4043/32392-MS

Liu, Y., Merz, C., Weisberg, R., Shay, L., Smith, M. and Glenn, S. (2021). An initial evaluation of High-Frequency Radar radial currents in the Straits of Florida in comparison with altimetry and model products, *Ocean Remote Sensing Technologies: HF, Marine and GNSS-Based Radar*, IET, edited by Huang, W. and Gill, E., 29 pp.

National Academies of Sciences, Engineering, and Medicine. 2018. Understanding and Predicting the Gulf of Mexico Loop Current: Critical Gaps and Recommendations. Washington, DC: The National Academies Press. https://doi.org/10.17226/24823.

Nowlin, Jr., WD, Jochens, AE, DiMarco, SF, Reid, RO, and Howard, MK. 2001. Deepwater Physical Oceanography Reanalysis and Synthesis of Historical Data: Synthesis Report. OCS Study MMS 2001-064, U.S. Dept. of the Interior, Mineral Management Service, Gulf of Mexico OCS Region, New Orleans, LA. 528 pp.

Shay, LK, J Brewster, B Jaimes, C Gordon, K Fennel, P Furze, H Fargher, and R He, 2019. Physical and biochemical variability from APEX-EM floats. Current, Waves, Turbulence Measurement Workshop, IEEE Oceanic Engineering Society Proceedings, 10–13 March 2019, San Diego, CA. doi:10.1109/CWTM43797.2019.8955168

Smith, M., Glenn, S., Merz, C., Liu, Y., Weisberg, R., Shay, L., Howden, S. and Knap, T. (2021). A Unified Approach to HF Radar Radial Quality Control for Understanding Gulf Ocean Systems, *OCEANS 2021: San Diego – Porto*, 2021, pp. 1-5, doi: 10.23919/OCEANS44145.2021.9705910.

Smith, M., S. Glenn, C. Merz, Y. Liu, R. Weisburg, L. Shay, S. Howden, A. Knap, A Unified Approach to HF Radar Radial Quality Control for Understanding Gulf Ocean Systems, Oceans 2021: San Diego, https://ieeexplore.ieee.org/document/9705910

Storie, J, RJ Ramos, M Leber, H Nowack, L Ivanov, B Magnell, 2023. Evaluation Of Loop Current/loop Current Eddy Fronts To Guide Offshore Oil & Gas Operations. Offshore Technology Conference, Houston Texas. American Society of Civil Engineers, Brazilian Petroleum, Gas, and Biofuels Institute, Society of Naval Architects and Marine Engineers.OTC-32643-MS.

Testor, P, B de Young, D Rudnick, S Glenn, D Hayes, CM Lee, C Pattiaratchi, K Hill, E Heslop, V Turpin, P Alenius,C Barrera, J Barth, N Beaird, G Bécu, A Bosse, F Bourrin, A Brearley, Y Chao, S Chen, J Chiggiato, L Coppola, RCrout, J Cummings, B Curry, R Curry, R Davis, K Desai, S DiMarco, C Edwards, S Fielding, I Fer, E Frajka-Williams,H Gildor, G Goni, D Gutierrez, P Haugan, D Hebert, J Heiderich, S Hanson, K Heywood, P Hogan, L Houpert, S Huh,ME Inall, M Ishii, S-I Ito, S Itoh, S Jan, J Kaiser, J Karstensen, B Kirkpatrick, J Klymak, J Kohut, G Krahmann, MKrug, S McClatchie, F Marin, E Mauri, A Mehra, MP Meredith, T Meunier, T Miles, J Morell, L Mortier, S Nicholson,J O'Callaghan, D O'Conchubhair, P Oke, EP Sanz, M Palmer, J Park, L Perivoliotis, P-M Poulain, R Perry, B Queste, LRainville, E Rehm, M Roughan, N Rome, T Ross, S Ruiz, G Saba, A Schaeffer, M Schönau, K Schroeder, Y Shimizu,B Sloyan, D Smeed, D Snowden, Y Song, S Swart, M Tenreiro, A Thompson, J Tintore, R Todd, C Toro, H Venables,T Wagawa, S Waterman, R Watlington and D Wilson, 2019. OceanGliders: A Component of the Integrated GOOS.*Front. Mar. Sci.* **6**:422. doi: 10.3389/fmars.2019.00422

Updyke, T., Roarty, H., Smith, M. and Nazzaro, L. (2021). Implementation of Quality Flags in the Processing of High Frequency Radar Surface Current Data, *OCEANS 2021: San Diego – Porto*, pp. 1-6, doi: 10.23919/OCEANS44145.2021.9706013.

Updyke, T.G., Roarty, H.J., Smith, M. and Nazzaro, l. (2019). The Impact of Reprocessing Efforts on the Mid-Atlantic's Surface Current Product, OCEANS 2019 MTS/IEEE SEATTLE, Seattle, WA, USA, pp. 1-5, doi: 10.23919/OCEANS40490.2019.8962804.

Wilkin, J.L., Bowen, M.M., Emery, W.J., 2002. Mapping mesoscale currents by optimal interpolation of satellite radiometer and altimeter data. Ocean Dynamics 52: 95–103 DOI 10.1007/s10236-001-0011-2.

WMO Technical Conference on Meteorological and Environmental Instruments and Methods of Observation (TECO-2024)

23-26 September 2024, Vienna (Austria)

THE YUCATAN HF RADAR NETWORK AS A PATHFINDER FOR CARIBBEAN-WIDE OPERATIONS

Glenn, Scott[1]; Smith, Michael[1]; Miles, Travis[1];
Knap, Anthony[2]; Dancer, Andrew[2]; Nwankwo, Uchenna[2]; DiMarco, Steven[2];
Monreal Jimenez, Rosalinda[3]; Salas de Leon, David Alberto[4];
Parikh, Hardik[5]; Whelan, Chad[5]

[1] Rutgers University, Center for Ocean Observing Leadership, New Brunswick, NJ, USA

[2] Texas A&M University, Geochemical & Environmental Research Group (GERG), College Station, TX, USA

[3] Mexican Institute of Water Technology, Morelos, Mexico

[4] Universidad National Autonoma de Mexico (UNAM), Laboratorio de Oceanografia Fisica, Mexico City, Mexico

[5] CODAR Ocean Sensors, Mountain View, CA, USA

Corresponding author: Glenn, glenn@marine.rutgers.edu

Abstract:

The Yucatan High Frequency Radar (HFR) network is envisioned as a trilateral collaboration between the US, Mexico and Cuba to provide sustained surface current observations of the Yucatan Current component of the global ocean conveyor belt circulation. Immediate applications are improved forecasting of the Loop Current extension and eddy formation cycles in the Gulf of Mexico, and improved coupled atmosphere-ocean forecasting of hurricanes.

The initial two HF Radar installations, funded by the U.S. National Academies, included self-contained power and communication modules for operations on uninhabited islands, as well as software systems to calculate and monitor receiver antenna patterns using AIS ship location data. Calibrated and sustained data collection began in 2023. Numerous software upgrades were developed, tested, implemented and shared.

Hourly radial and total vector current fields are displayed on a web-based viewer for easy browsing and are distributed through an ERDDAP server. Software to implement all the QARTOD manual quality control flags has been implemented and applied. Beyond maps of surface currents, one popular new derived product includes plots of the along-channel and cross-channel currents along a cross-channel line through the center of the current field. The total vector maps generated by the HF Radar are currently compared to models for validation, and eventually will be assimilated into hindcasts and forecasts.

These methodologies provide a framework for a sustained Caribbean-wide HFR radar network that includes both the inflow through the Antilles Island chain passages and the outflow through the Yucatan Strait. Full implementation will require continued capacity building initially enabled by existing education programs and international investments.

1. Introduction

Installation and the initial 5-years of operation of a Yucatan High Frequency Radar (HFR) network is sponsored by the U.S. National Academies of Sciences, Engineering and Medicine (NASEM) Gulf Research Program (GRP) Understanding Gulf Ocean Systems (UGOS) activity. The network is envisioned to grow into a trilateral collaboration between the U.S., Mexico and Cuba to provide sustained surface current observations of the Yucatan Current segment of the global ocean conveyor belt circulation. The purpose of the network is to contribute to improved understanding of the Loop Current and what controls its evolution by monitoring the surface inflow from the Caribbean basin into the Gulf of Mexico. Immediate applications are improved forecasting of the Loop Current extension and eddy formation cycles in the Gulf of Mexico, and improved coupled atmosphere-ocean forecasting of hurricanes (Knap et al., 2023). Surface current data generated by the network are openly shared in near-real-time for the mutual benefit of the people in all three countries.

The Loop Current enters the Gulf of Mexico through the Yucatan Strait, flows northward into the Gulf before looping back to the south along the West Florida Shelf, and then exits the Gulf through the Florida Strait. The Loop Current can grow into an extended state where it penetrates deep into the Gulf. At irregular intervals between 3-18 months, an extended Loop Current will break off into a large Loop Current Eddy that propagates slowly westward, leaving the Loop Current itself in a retracted state flowing from Yucatan along the north coast of Cuba to the Florida Strait. Figure 1 illustrates the Loop Current in an extended state prior to eddy formation as depicted in the surface currents of NOAA's operational global Real Time Ocean Forecast System (RTOFS).

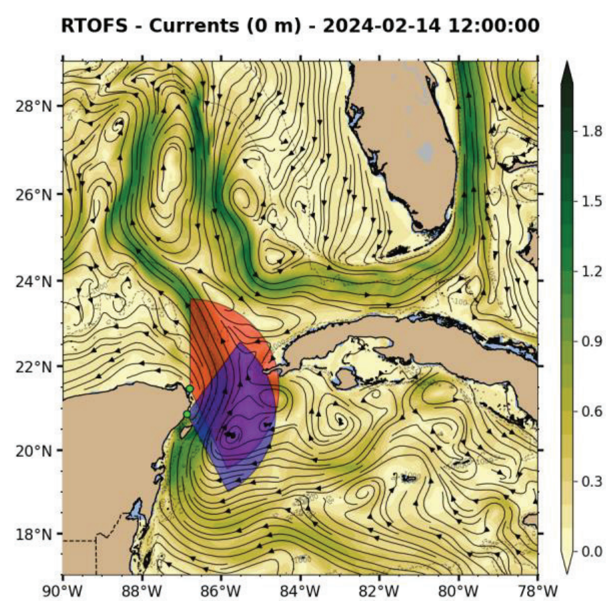

Figure 1: Map of ocean surface currents from the NOAA RTOFS global model showing the Loop Current in an extended state flowing deep into the Gulf during the MASTR field experiment described in Section 3. The potential coverage areas of the first two Yucatan HF Radars are indicated, where the red coverage from the northern site combines with the blue coverage from the southern site to produce a purple color in the overlap region.

To better understand the influence of the Yucatan Current inflow to the Gulf of Mexico on the downstream evolution of the Loop Current and its eddy shedding events, a multi-national HF Radar network was envisioned as a Caribbean contribution to the Global HF Radar Network (Roarty, 2019). The first two HF Radars were deployed in Mexico along the Yucatan coast in 2022 as COVID travel restrictions relaxed (two green dots in Figure 1). The northern site is located in a natural sanctuary on the uninhabited Isla Contoy, and the southern site is located within the built environment of the UNAM marine operations facilities. Each HF Radar is used to generate a field of surface current velocity components in the radial direction towards or away from the radar. In regions where the coverage overlaps, the radial current components from the individual radars can be combined into a total vector field. The pie-slice shaped radial current coverage area potentially available for each HF Radar location is shown for the northern site in red and the southern site in blue so that the overlap region between the two turns purple.

2. Methods

CODAR Ocean Sensors (COS) SeaSonde direction finding HF Radars were chosen for this application. The compact SeaSonde single transmit and single receive antennas offered distinct advantages in these challenging tropical environments (Figure 2). The northern Isla Contoy site is only accessible by small boat, has no electrical power or communications, wind turbines for power generation are not allowed to protect the sanctuary's birds, and deployment space was limited to the immediate area around the small boat landing. This site, call sign ISCY, required the use of all the SeaSonde low power options, the installation of solar power panels with a limited amount of fuel for a backup generator, and satellite communications. One advantage is that the antenna installations areas were relatively free of man-made clutter that could disrupt the antenna patterns. In contrast, the southern UNAM site, call sign UASA, was surrounded by dense tropical vegetation that extended to the water's edge except within the facility itself. Antennas would have to be mounted on facility rooftops, where ample power and highspeed internet communications is available, but where both stationary and moving metal objects could distort the receiver antenna patterns in unknown amounts. This would require measurement of the antenna pattern for any distortion caused by stationary objects, but also regular monitoring and adjustment of the receiver antenna pattern as large metal objects within the facility could be moved. Such monitoring would be required of any HF Radar receiver antenna used within the built environment.

Figure 2: CODAR Ocean Sensors Seaonde transmit and receive antennas installed at the northern ISCY site (left two photos) and the southern UASA site (right two photos).

Calibrated and sustained data collection began in 2023. Numerous software upgrades were developed, tested, implemented and shared via SeaSonde software updates or on GitHub. These include: (a) Automatic Identification System (AIS) derived ship locations for calculating antenna patterns, (b) increased flexibility for identifying bimodal Bragg scattering peaks in regions with strong boundary currents, (c) improved separation of vertical ionospheric radio interference from the horizontal Bragg scattering, (d) adjustment of the MUSIC direction finding algorithms to favor more single angle solutions for the radial current bearings expected in a strong boundary current region than the usual dual angle solutions expected in coastal eddy fields, and (e) full implementation of the QARTOD quality control flags for both radial and total currents.

Here we highlight the new SeaSonde software used to derive receiver antenna patterns from ship locations collected by an AIS antenna co-located at each SeaSonde HF Radar site (Figure 3). Antenna patterns are often calculated using transponders on small boats or drones that move in a circular arc around the HF Radar to compare the known location of the transponder with the location observed in the strong spectral peak the transponder generates in the HF Radar returns. Use of these standard methods are logistically difficult or not allowed in the remote regions we are working. However, both sites have large vessels transiting through the Yucatan Strait directly in front of the HF Radars. The large ships can be detected as hard target peaks in the received signal spectra that are distinct from the Bragg peaks used to calculate surface currents. By pairing the hard target range and bearing detections with the AIS ship location data, small adjustments to the receiver antenna patterns can be made to minimize the difference between the HF Radar detection position and the AIS reported position. Optimizing the fit over a large number of AIS detections distributed across the full range of ocean viewing directions produces smooth antenna patterns that can then be used to determine the bearing for each radial current observation derived from the Bragg peaks.

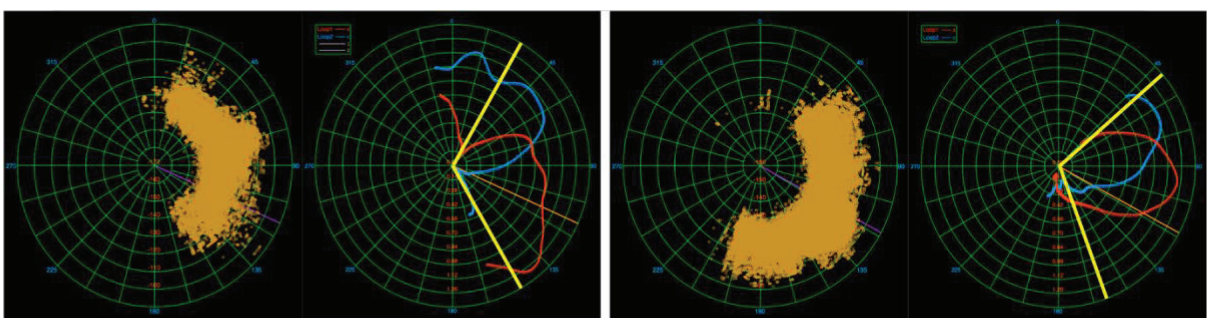

Figure 3: Range and bearing plots of AIS ship positions paired with SeaSonde HF Radar ship detections (orange) and the resulting best fit receiver antenna patterns (Loop 1 in red, Loop 2 in blue) for the northern ISCY site (left) and the southern site (right). The obtuse angle between the two yellow lines are the range of bearings where sea-echo is detected by each receiver.

The northern ICSY site is relatively pristine with few electrical conducting materials surrounding the antennas that can distort the antenna pattern. Here we used a month of AIS data with 46,856 paired detections from February 1 to March 1, 2023 to calculate the antenna pattern. The pattern was checked multiple times up to one year later and there was virtually no change. RMS bearing differences to known ships were within 3 degrees. Little change in the antenna pattern is expected and confirmed in this pristine environment. The antenna pattern could be calculated over a wide range of bearings from -10 degrees to 160 degrees as some ships could go around the northern small island. Still radial current velocities from ISCY were only developed in the area seaward of the antenna with bearings between 30 degrees and 150 degrees (yellow lines in Figure 3) based on the locally measured bearings along the beach.

In contrast, the southern UASA site in the built environment of a marine lab can be expected to be distorted and possibly change over time. Here we recalculated antenna patterns at regular intervals. In this paper we focus on the time period of our first field experiment described below, January 15 through May 15, 2024, when 277,357 AIS ship locations could be paired with HF Radar detections. Sensitivity to the first month versus the last month showed little time variability in the antenna patterns, so we use AIS data from the full duration of the field experiment. Here radial currents solutions with bearings between 50 and 160 degrees were developed based on the along beach bearings.

3. Results and discussion

After the initial year of operations in 2023 (DiMarco et al., 2023a), the Yucatan HF Radar network was used to support the Mini-Adaptive Sampling Test Run (MASTR) from January through May of 2024, in preparation for the Grand Adaptive Sampling Experiment (GrASE) in 2025 (DiMarco et al., 2023; DiMarco et al., 2024). Fields of radial current components towards or away from each HF Radar are calculated from the quality controlled spectra and AIS generated antenna patterns every hour (Figure 4). The radial current fields are quality controlled using all the Quality Assurance/control of Real Time Ocean Data (QARTOD) tests in the most recent manual (Bushnell & Worthington, 2022). Each vector is flagged as passing or not passing every test to provide users with the most flexibility in which vectors to use and a sense of which tests are causing any failures. Most commonly the user will choose to accept only those radial currents that passed all the QARTOD tests. The quality controlled radial data is often used for assimilation in models as the area of coverage extends beyond the overlap region.

Total surface current vectors are then calculated in the overlap region by both the UnWeighted Least Squares (UWLS) or the Optimal Interpolation (OI) method commonly used in throughout U.S. National HF Radar network. QARTOD tests are similarly applied to the total current vectors (Roarty et al., 2024). Figure 4 includes a plot of the total vectors using the OI method that includes calculation of the uncertainty field that includes the effect of geometry (combining radial currents at right angles to each other have least geometric dilution of precision). Relative values of the uncertainty used in the Mid Atlantic are 0.65 for their extensive multi-radar network while values of 0.95 are used in more sparse networks. Here we identify the location of the 0.65 and 0.9 relative uncertainty contours for reference. Which level of uncertainty to accept can be chosen by the user based on their application.

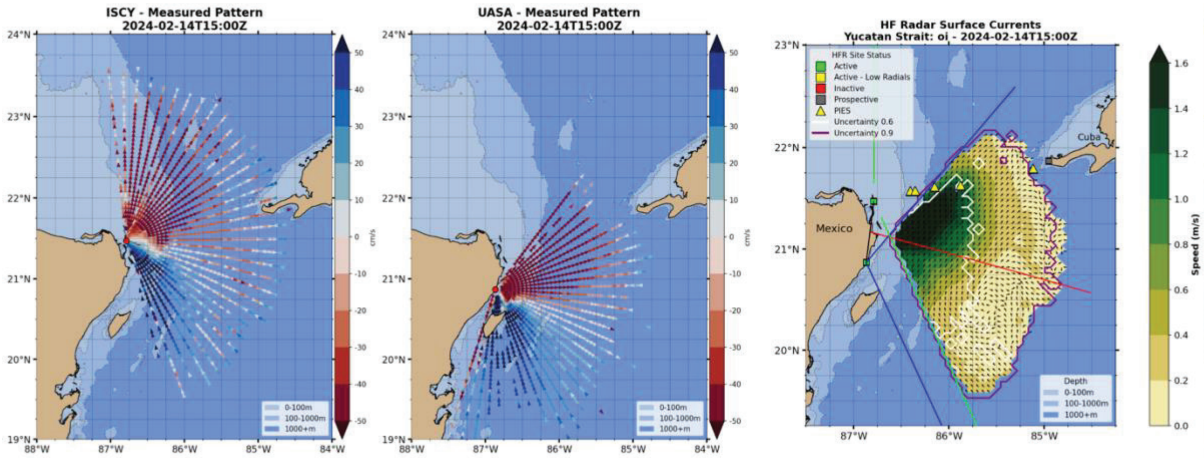

Figure 4: Radial current components towards (blue) or away (red) from the northern ISCY site (left) and the southern UASA site (center). The radial currents from each site are combined into total vector currents (green plot on the right) for analysis. The red line through the center of the total vector field is the line with the lowest uncertainty calculated after combining the radial currents into total vector currents by the OI method.

Hourly radial and total vector current fields are web-displayed for easy browsing and are distributed through an ERDDAP server. One popular new derived product includes plots of the downstream and cross-stream velocity transects along the cross-channel line through the center of the HF Radar current field shown as the red line in Figure 4. Similar products are also regularly produced for the operational ocean models (e.g. RTOFS in Figure 1) for comparison. Hovmöller diagrams of these velocity components reveal the impact of small-scale topography and the occasional storm or hurricane reversing the predominantly westward cross-shore currents. Alongshore current observations indicate that the current maximum alternates between onshore and offshore of the Cozumel and Banko Arrowsmith shadow zone, but the maximum current in the operational models remains offshore. Operational data flows for HF Radar assimilation in future higher resolution regional operational models have been designed.

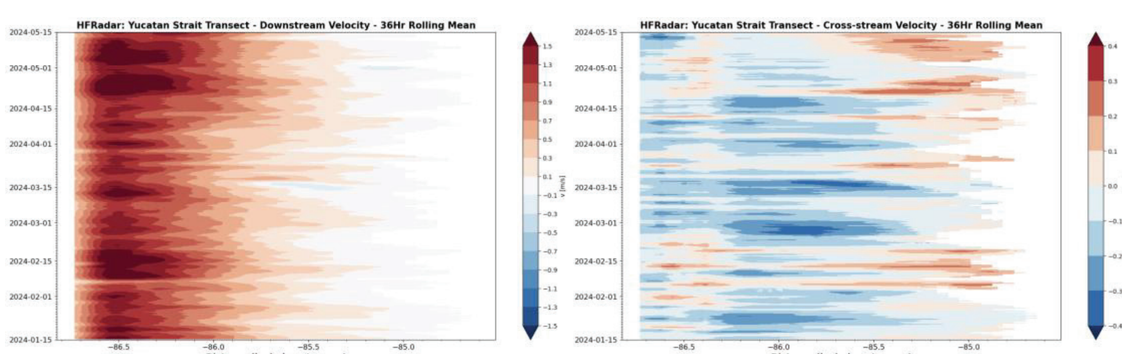

Figure 5: Hovmöller diagrams of the downstream velocity with positive to the north (left) and the cross-stream velocity with positive to the east (right) along the cross-strait line with the lowest uncertainty identified in Figure 4.

4. Conclusions

The first two SeaSondes in the Yucatan HF Radar Network were initially installed in late 2022, underwent their first year of exploratory operations in 2023, and supported the MASTR field program in 2024 with real time data. It will be part of the GrASE field program in 2025. The data is currently used for model/data comparisons, is expected to be assimilated in hindcast models in the near future, and eventually transitioned to real time assimilation in forecast models. It is envisioned that in 2026, the operation will be transitioned to government entities such as the U.S. Integrated Ocean Observing System (IOOS). It is anticipated that additional SeaSonde HF Radars will be deployed along the Yucatan coast and at INSMET facilities in Cabo de San Antonio, the most western tip of Cuba.

These methodologies provide a framework for a sustained Caribbean-wide HF Radar network that contributes to the Global Ocean Observing System (GOOS) Global HF Radar Network (Roarty, 2019). Plans for the Tropical Americas and Caribbean Ocean Observing and Forecast System (TAC-OOFS) include HF Radar monitoring of both the inflow through the Antilles Island passages and the outflow through the Yucatan Strait. Full implementation will require continued capacity building that could be enabled by existing education programs and international investment.

5. References

Bushnell, M., & Worthington, H., 2022. Manual for real-time quality control of high frequency radar surface current data: a guide to quality control and quality assurance for high frequency radar surface current observations.

DiMarco, SF, S Glenn, M Smith, B Jaimes de la Cruz, R Ramos, E Pallas-Sanz, M Tenreiro, S Mahmud, U Nwankwo, TN Miles, R Monreal Jiménez, D Salas de León, AH Knap, LK Shay, B Magnell, J Storie, G Stuart, J Marble, VK Contreras Tereza, 2024. Results of the Mini-Adaptive Sampling Test Run (MASTR) Experiment: Autonomous Vehicles, Drifters, Floats, ROCIS, and HF-Radar, to Improve Loop Current System Dynamics andForecasts in the Deepwater Gulf of México (2024). Offshore Technology Conference, Houston Texas. 6-9 May 2024. American Society of Civil Engineers, Brazilian Petroleum, Gas, and Biofuels Institute, Society of Naval Architects and Marine Engineers. OTC-35072-MS. DOI 10.4043/35072-MS.

DiMarco, SF, S Glenn, M Smith, R Ramos, AH Knap, R Monreal, D Salas de Léon, VK Contreras-Tereza, 2023a. Surface current velocity observations of the Yucatan Channel using High-Frequency Radar, 25-28 September 2023. IEEE *OCEANS 2023 - MTS/IEEE U.S. Gulf Coast*, Biloxi, MS, USA, pp. 1-8, doi: 10.23919/OCEANS52994.2023.10337389.

DiMarco, SF, S Glenn, B Jaimes de la Cruz, AH Knap, Y Liu, B Magnell, S Mahmud, T Miles, E Pallas-Sanz, RJ Ramos, LK Shay, M Smith, M Renreiro, RH Weisberg, 2023b. Applications Of Adaptive Sampling Strategies Of Autonomous Vehicles, Drifters, Floats, And HF-Radar, To Improve Loop Current System Dynamics Forecasts In The Deepwater Gulf Of Mexico. Offshore Technology Conference, Houston Texas. American Society of Civil Engineers, Brazilian Petroleum, Gas, and Biofuels Institute, Society of Naval Architects and Marine Engineers. OTC-32459-MS. DOI 10.4043/32459-MS

Roarty, H., Updyke, T., Nazzaro, L., Smith, M., Glenn, S., & Schofield, O., 2024. Real-time quality assurance and quality control for a high frequency radar network. *Frontiers in Marine Science*, *11*, 1352226.

Roarty, H., Cook, T., Hazard, L., George, D., Harlan, J., Cosoli, S., ... & Grilli, S., 2019. The global high frequency radar network. *Frontiers in marine science*, *6*, 164.

Knap, AH, SF DiMarco, SM Glenn, R Ramos, B Magnell, D Salas, 2023. Understanding the Gulf Ocean System Program: Informing Stakeholders and Improving prediction of the Loop Current System using advanced observational and numerical tools. Offshore Technology Conference, Houston Texas. American Society of Civil Engineers, Brazilian Petroleum, Gas, and Biofuels Institute, Society of Naval Architects and Marine Engineers. OTC-32392-MS. DOI 10.4043/32392-MS.

Determining the Seasonality of Oceanic eDNA Source Waters

Brendan Henley
Center for Ocean Observing Leadership
Rutgers University
New Brunswick, NJ USA
bvh16@scarletmail.rutgers.edu

Hugh Roarty
Center for Ocean Observing Leadership
Rutgers University
New Brunswick, NJ USA
hroarty@marine.rutgers.edu

Timothy Stolarz
Center for Ocean Observing Leadership
Rutgers University
New Brunswick, NJ USA
tstolarz@marine.rutgers.edu

Josh Kohut
Center for Ocean Observing Leadership
Rutgers University
New Brunswick, NJ USA
kohut@marine.rutgers.edu

Jason Adolf
Urban Coast Institute
Monmouth University
West Long Branch, NJ USA
jadolf@monmouth.edu

2024 IEEE/OES Thirteenth Current, Waves and Turbulence Measurement (CWTM) | 979-8-3503-9391-0/24/$31.00 ©2024 IEEE | DOI: 10.1109/CWTM61020.2024.10526335

***Abstract*— With offshore wind development planned for US coastal waters, there are potential impacts construction and operations may have on traditional surveys used to assess the marine species within the turbine farm areas. Environmental DNA (eDNA) offers a uniquely efficient method of monitoring marine communities since species do not have to be actively caught with a traditional trawl survey. It is important to quantify the past trajectory of the sampled water to properly interpret the representative space of the processed eDNA. To better understand the range and movement of the ocean water containing the eDNA samples backwards drift models were utilized to identify the origin of the sample and the dependence of sample range on location and season. Using a 10-year HF Radar surface current data set from 2007 to 2016, the reverse drift of particles were simulated off the coast of southern New Jersey. This was accomplished using the OpenDrift model that was seeded with 100 virtual particles and advected backwards in time for five days, encompassing the likely detection threshold of eDNA in the water. This analysis tested particle movement distances by varying location from the shore, as well release date within each season of the year. These findings suggest that eDNA has the potential to travel farther in the fall compared to the other seasons. A more practical result of the analysis is that around the 24-hour mark, particles originated within 10 km of sampling location regardless of season or location. This is an important time scale to observe because an estimate of the half-life of eDNA is around 24 hours. Variability in travel distance was only seen in time periods beyond 24 hours.**

Keywords—High Frequency Radar, ocean currents, ocean modeling, eDNA, particle tracking

I. Introduction

Acquiring samples of marine species and communities can be costly, with fishing and trawl-based surveys being expensive and capable of harming the animals that are caught and released [1]. Additionally, the development of offshore wind farms will make it difficult to perform trawl-based surveys within the wind farm areas. These two factors necessitate new ways to make species assessments and characterize marine communities. A developing method for species assessment is the collection of water samples and analyzing it for environmental DNA (eDNA). eDNA originates from any genetic material that fish or other marine species shed into the water, such as mucus, tissue, and bodily fluids in both cellular and extracellular form [2]. This sampling method can be accomplished without the need to catch or trawl, but there is still not enough known on how eDNA moves within the ocean. Understanding the movement of eDNA in the marine waters will provide information necessary to use eDNA as a reliable sampling method.

Acknowledging that the ocean environment the eDNA samples are taken from is not static, it is therefore important to understand the movement of the sampled water to quantify where that water was over the lifetime of the DNA. Only with this information can one properly associate the region of the ocean from which the fish presence derived from the eDNA can be assigned. This research gathers more information on the distance and path that particles travel in the ocean, how their movement in the ocean depends on the seasons of the year, as well how the magnitude and direction of currents change with distance from the coast.

II. Methods

A. Surface Currents

This project utilized the MARACOOS 06 km resolution HF (High Frequency) radar data set of hourly surface currents in the Mid-Atlantic Bight [3] which spans 10 years (2007-2016). The HF radar data was used in conjunction with the Python software package OpenDrift [4] from the Norwegian Meteorological Office. This package generates virtual Lagrangian drifters that will move with the direction and magnitude of the surface current vectors. Drifter release locations were chosen based on the planned offshore wind lease areas off New Jersey. The model was seeded with virtual drifters and the HF radar data surface current vector fields (Figure 1). To gauge the range of eDNA source waters, a negative timestep of one hour was used to advect the virtual drifters every hour in reverse for a total of five days. By tracking the particle location and calculating the distance from release, we can observe differences in location or season of these drifters. Maps and animations which show the vector field of currents and the path of the particles from start to finish were generated.

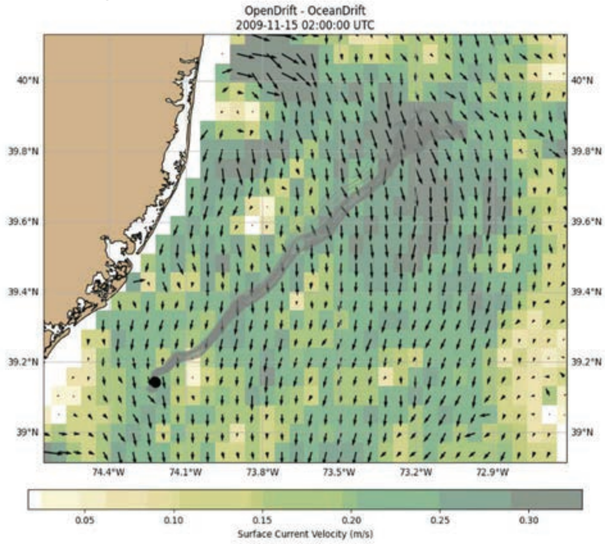

Figure 1: Surface current map from HF radar for November 15, 2009 (colormap and vectors). The path of virtual surface particles are shown as the black circle and gray lines.

B. Drift Model

The OpenDrift model was used to test surface particle trajectory 1) dependence on season 2) dependence on starting location 3) variability in time (between years and within months) and 4) variability in space (maps of drifter end locations). The starting location was chosen based on two existing eDNA sampling sites in the study area, one close to shore and one farther offshore. The offshore site was located at 38.99105° N, 73.9725° W and the inshore site was at 39.21736° N, 74.4406° W (Figure 2). Each release contained 100 virtual drifters surrounding the release location, and the resulting distance data was the mean path of these 100 drifters. We selected an arbitrary starting date, the 15th of the month, centered in each season (February for winter; May for spring; July for summer; November for fall). The drift model was run for each of the 10 years and the position data was averaged the distances from the starting point over all years, separated based on season. To measure the inter-annual variability, each average particle displacement for each year was plotted as a separate line. To measure intra-month variability, we varied the starting date by five days and then compared these results to the yearly plots. When studying drifters in terms of eDNA, it is important to remember that eDNA has a half-life within the water, so over time it will diminish. For this analysis, we focused on the movement of the virtual drifters at around one half-life. A current estimate of eDNA half-life in the coastal ocean is close to 24 hours [5], so drifter locations at this time period were of importance. We used this half-life estimation to observe the spatial variability of the eDNA locations at the 24-hour mark by season, since the percentage of eDNA in a location five days in the past is many times smaller than at 24 hours.

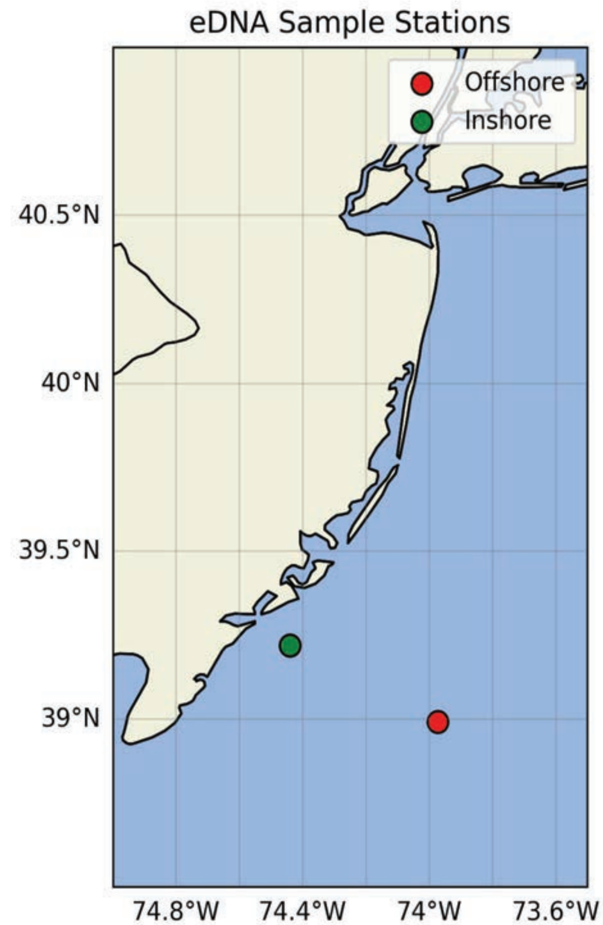

Figure 2: Study area map showing release site locations, offshore (red) and inshore (green).

III. Results

The results of the surface drift models were first analyzed by observing the averages over all 10 years, separated by season and location. Figure 3 compares the seasonality of the particle movement over 120 hours with separate graphs based on the starting location (inshore vs. offshore). The fall displayed the farthest travel distance of any season, being able to reach over 50 km at the end of the 120 hours. In the offshore case, winter and spring had similar travel distances in the middle ranges while the movement in the summer was the least. The inshore release site had little difference between spring, winter, and summer. However, we wanted to look specifically at the 24-hour mark because it is a good estimate for the half-life of marine eDNA. This focus represents the idea that a significant portion of the eDNA collected at a particular spot will have originated in the previous 24 hours. Therefore, this data will be more reliable on shorter time scales. So, when observing the transport at 24 hours, we see that the distances traveled are similar in every season. In the offshore plot at the 24-hour mark, there is a small variability from about 7-15 km, and in the inshore plot the range is smaller, from around 9-13 km. It is only after 24 hours that the seasonal averages start to diverge from each other. These results suggest that travel distances are similar within the first day, but beyond 24 hours the main variability is a result of the seasons.

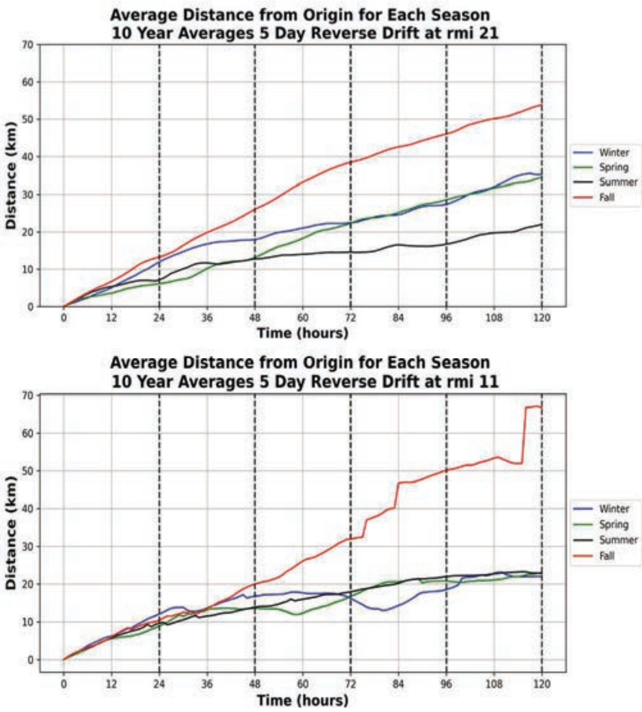

Figure 3: Average particle distance from release point for offshore release site (top) and onshore release site (bottom).

By plotting the drifter distance for each year (Figure 4), the inter-annual variability of the drifter distance can be examined. For winter both in both the offshore and inshore locations, the drifter distances span between 10-20 km from the origin at 24 hours, and 15-40 km over the entire time scale. For the inshore site, virtual drifters that were impacted by offshore currents were sent towards the coast, and when they contacted the coast, the model stopped advecting the particles and the path of the drifters stopped before the full five days elapsed. However, looking at the graphs qualitatively, the drifters follow similar paths regardless of location. For spring, drifters traveled around 10 km from the origin at 24 hours and is like winter, with one standout event in 2008 that showed much farther transport than usual. Summer has no standout years like this, with a greater concentration of lines around 20 km at the end of the five days, smaller than previous seasons. In the final set of plots, we see that fall had the farthest transport because there were multiple years which exhibited an explosive increase in distance traveled as a result of high velocity currents. Fall has the greatest spread of particle distance at the 24-hour mark, spanning from 0-30 km. The maximum distance traveled was 140 km from 2009, with other years like 2010 reaching 130 km and 2011 reaching 70 km (Figure 4g).

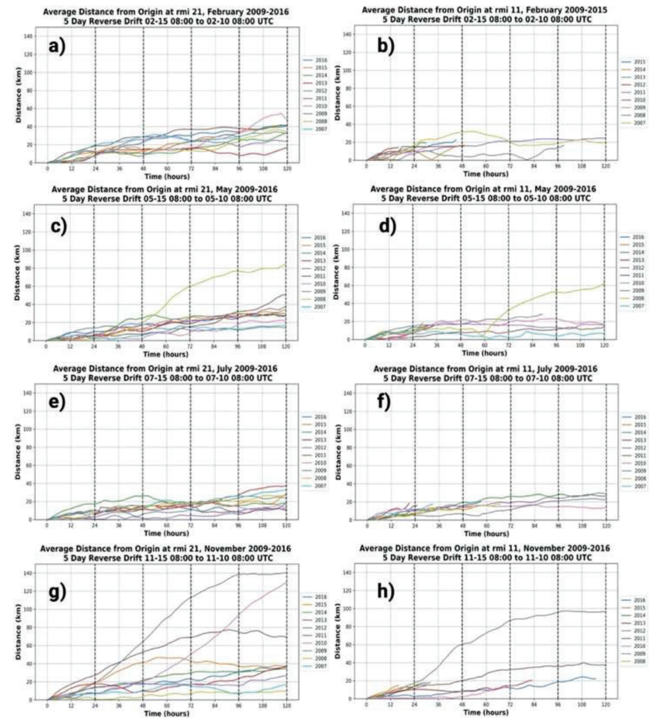

Figure 4: Distance (0-140km) from release point versus time (0-120 hours), where each line is data from a different year. a) offshore winter b) inshore winter c) offshore spring d) inshore spring e) offshore summer f) inshore summer g) offshore fall; h) inshore fall.

Figure 5 displays the spatial variability of the drifters at the end of the 24-hour mark. First looking at the offshore site, the red and blue points (fall and winter, respectively) have the farthest distance from the origin (yellow dot). The points for summer and spring closely surround the origin. Of note, the points exist on either side of the origin, meaning currents travel in both directions rather than a single uniform current movement. The shape of the spread of points suggests that the currents governing the drifter movement are in the alongshore direction, parallel to the coast which matches climatology [3]. The farthest points are northeast and southwest of the origin, with none of the far points appearing to the east or west. Next looking at the inshore plot (Figure 5 bottom), the overall spread of the points is not in the alongshore direction like the offshore point, but rather a higher concentration of points towards the coast relative to the origin, which means that the predominant currents come from the coast pushing offshore. There are still points on the other sides of the origin, meaning currents also originate from both up and down the coast, as well as offshore moving towards the coast, but the majority of the points are closer to the shore. In terms of seasonality, fall is the only season that displays great travel distances from the origin, with the other three seasons being relatively similar. These visuals agree with the mean plot from Figure 3, keeping in mind that the scatter plot is only after 24 hours of drift.

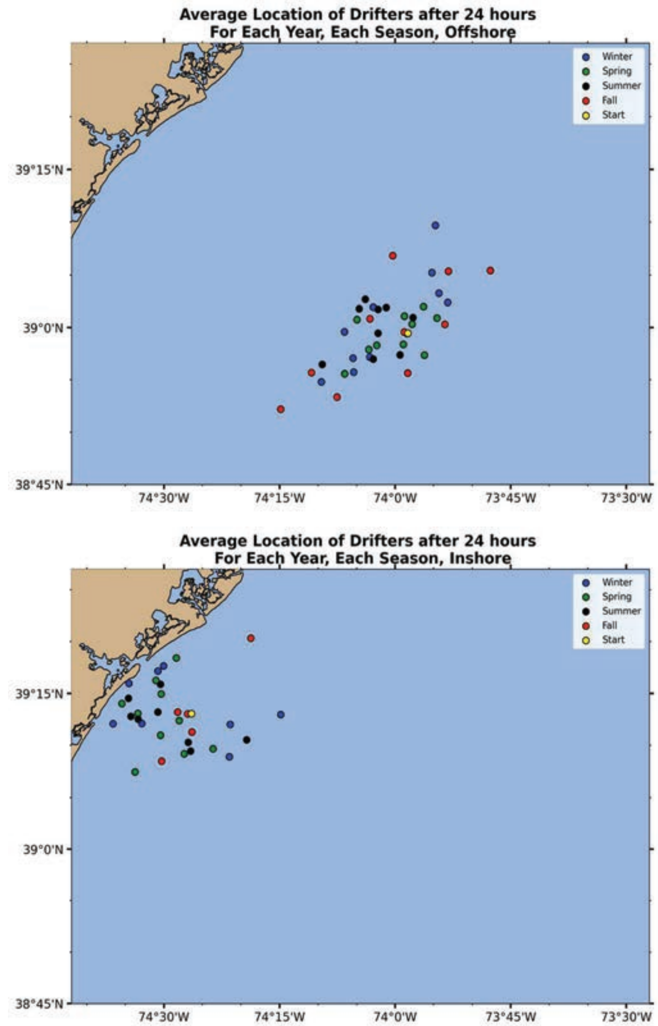

Figure 5: Average location of drifters after 24 hours elapsed, for each year (2007-2016) and season (winter-blue, spring-green, summer-black and fall-red) for the offshore (top) and inshore release location (bottom).

Lastly, we investigated the specifics of these differences in transport through intra-month variability. Figure 6 highlights different scenarios when comparing variability within a month to variability across multiple years. The results showed that there are starting dates in which the variability within months is greater than, smaller than, and about the same as variability across years. For example, in November 2016 (Figure 6d) there was little difference between the drifter releases at different times throughout the month. But that same month in other years exhibited significant variability (Figure 6c). In February of that same year (Figure 6e-f), there was a completely different response in which the winter season showed similar results across the 10-year time period, but within the single month there were larger differences. For July (Figure 6a-b), there was little difference within a month or between years. These results highlight the sensitivity of results to specific high current events on the dates of starting the reverse drift.

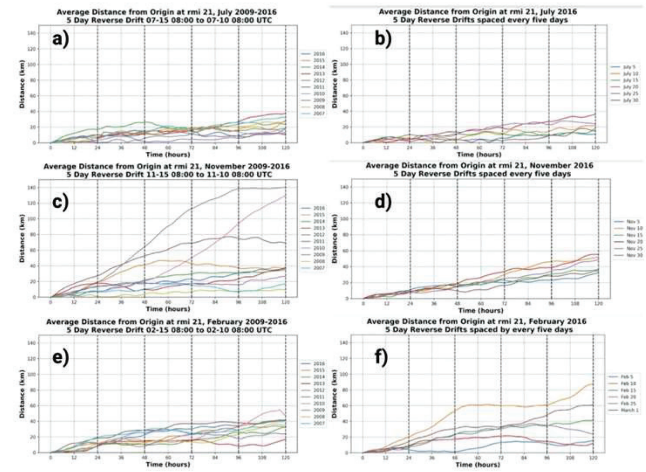

Figure 6: Comparison of distance from origin based on release time between different years (2007 -2016) or different days within a month (5th, 10th, 15th, 20th, 25th, 30th) a) all years summer; b) all days summer 2016 c) all years fall d) all days fall 2016 e) all years winter f) all days winter 2016.

IV. Discussion

Based on eDNA half-life (24 hours) [5], the virtual drifters traveled about 10 km away from the starting point. The 10 km excursion over 24 hours was consistent regardless of season and location (Figure 3). The eDNA samples likely come from within 10 km of the sample location. Beyond 24 hours, there was a larger difference between release location and season with seasonal variability larger than location. The degradation of eDNA occurring over time in the marine environment suggests that detections of 'displaced fish' in eDNA data is more likely to be found at trace levels than as a major component of the eDNA fish community. Viewing animations of the drifters revealed that this difference in particle trajectories was due to fast currents in the fall, while in summer, with more relaxed winds, the particles are advected by the tides and remained close to the release point. Looking closer at the direction of arrival of a particular drifter release, there was a difference between locations. Inshore, currents mainly come from the coast, and all seasons except for fall have a close spread to the origin. Offshore, currents mainly travel in the alongshore direction, where points from the fall and winter are far from the origin whereas spring and summer form a tighter spread around the origin.

In all observations, large ocean current events played an important role in determining the excursion distance and direction of the drifters. These events are mainly storms, which create high velocity currents that can push the drifters far from the starting point. In November 2009, the coast of New Jersey experienced the residual nor'easter from Hurricane Ida, named Nor'Ida [6]. During this event the drifters travel 140 km over the five-day release, much further than any other season and year without a storm. For years that had storm events drifters traveled farther within the first 24 hours if high currents were present. And, as seen in November 2010 (Figure 4gh), the high velocity currents can appear at any time and instantly push drifters far distances in a short period of time. These events caused the different cases from Figure 6, because if there was a storm coincident on the date picked, the drifter trajectory would be drastically different. In general, the fall season exhibited more storm events than other seasons, which resulted in fall having the farthest drifter movement. This means that eDNA sampling must consider the timing of sampling relative to these events, acknowledging that certain seasons with greater storm frequency will be most impacted. A potential strategy could be to sample in calmer conditions between storm events when possible. Regardless, it is important to understand how these storm events impact ocean transport.

V. Conclusions

eDNA metabarcoding is a novel and cost-effective way to measure biodiversity within the ocean. However, it is important to remember that while fish are generally nektonic, fish eDNA behaves more like plankton in the ocean, including passive transport by prevailing physical currents. Understanding the origin of eDNA samples through drifter modeling tools like OpenDrift, can allow the use of existing physical oceanographic measurement platforms to aid in biological and ecological marine research. By examining drifters advected by HFR surface current data over ten years, it is evident that fall was the season in which eDNA samples traveled the farthest after a five-day trial period, with summer being the shortest distance traveled. The offshore drifters generally traveled farther than the inshore drifters and displayed more spread in the alongshore direction after 24 hours, likely due to the strong alongshore flows off the coast of New Jersey. Inshore drifter movements were generally found to be tidally dominated and had more spread in the cross shelf after 24 hours. Intra-monthly variability was equally important for the distance traveled from the origin. February 2016 (Figure 6f) showed the greatest intra-month variability ranging about 40 km. November showed the greatest inter-year variability ranging 130 km due to storm events (Figure 4gh). This finding of strong fall variability coincides with our understanding the stormy season in the Mid Atlantic [3]. Lastly, we conclude that after 24 hours, the proposed half-life for marine eDNA, the eDNA samples originated within 10 km of the sampling site. This trend was found to be generally true across all seasons and years.

For future work it will be important to consider the velocities further down in the water column. This research was limited to HF radar surface current data, so to improve it we may need to consider vertical drifter movement and bottom currents. Considering eDNA sampling of water from trawls, it may be of more use to analyze modeling for bottom currents. However, recent comparisons between trawl surveys and surface samples showed little difference in eDNA composition [1], so for the scope of this project it was assumed they were the same. Additionally, as these measurements were taken by modeling backwards in time, the 'origin' of the virtual drifters is a distance away from the sampling location. If the goal of eDNA sampling is to understand species composition in a certain region, then perhaps sampling needs to include points at some distance away from the desired region of focus, considering the expected ocean transport. In this case, a forward run of the model may be useful to identify where to sample for species from the target region. Nonetheless, it will be valuable to keep in mind all these factors when sampling, so that reasonable estimates can be made. Understanding this dependence on seasonality, location, and storm events will be valuable to improve the quality of eDNA sampling.

Acknowledgments

This work was funded by NOAA Award Number NA16NOS0120020 "Mid-Atlantic Regional Association Coastal Ocean Observing System (MARACOOS): Powering Understanding and Prediction of the Mid-Atlantic Ocean, Coast, and Estuaries". Sponsor: National Ocean Service (NOS), National Oceanic and Atmospheric Administration (NOAA) NOAA-NOS-IOOS-2021-2006475, Integrated Ocean Observing System Topic Area 1: Implementation and Development of Regional Coastal Ocean Observing Systems.

The eDNA sampling was supported by a grant from the New Jersey Department of Environmental Protection (NJDEP) Research and Monitoring Initiative (RMI).

References

[1] M. Y. Stoeckle, J. Adolf, Z. Charlop-Powers, K. J. Dunton, G. Hinks, and S. M. VanMorter, "Trawl and eDNA assessment of marine fish diversity, seasonality, and relative abundance in coastal New Jersey, USA," *ICES Journal of Marine Science,* vol. 78, no. 1, pp. 293-304, 2021.

[2] M. A. Barnes and C. R. Turner, "The ecology of environmental DNA and implications for conservation genetics," *Conservation genetics,* vol. 17, no. 1, pp. 1-17, 2016.

[3] H. Roarty *et al.*, "Annual and seasonal surface circulation over the Mid - Atlantic Bight Continental Shelf derived from a decade of High Frequency Radar observations," *Journal of Geophysical Research: Oceans,* vol. 125, no. 11, p. e2020JC016368, 2020.

[4] K.-F. Dagestad, J. Röhrs, Ø. Breivik, and B. Ådlandsvik, "OpenDrift v1. 0: a generic framework for trajectory modelling," *Geoscientific Model Development,* vol. 11, no. 4, pp. 1405-1420, 2018.

[5] R. A. Collins, O. S. Wangensteen, E. J. O'Gorman, S. Mariani, D. W. Sims, and M. J. Genner, "Persistence of environmental DNA in marine systems," *Communications Biology,* vol. 1, no. 1, p. 185, 2018.

[6] M. Olabarrieta, J. C. Warner, B. Armstrong, J. B. Zambon, and R. He, "Ocean–atmosphere dynamics during Hurricane Ida and Nor'Ida: an application of the coupled ocean–atmosphere–wave–sediment transport (COAWST) modeling system," *Ocean Modelling,* vol. 43, pp. 112-137, 2012.

The History of Oceanographic High Frequency Radar at Rutgers University

Hugh Roarty
Dept. of Marine and Coastal Sciences
Rutgers University
New Brunswick, NJ USA
hroarty@marine.rutgers.edu

Josh Kohut
Dept. of Marine and Coastal Sciences
Rutgers University
New Brunswick, NJ USA
kohut@marine.rutgers.edu

Tim Stolarz
Dept. of Marine and Coastal Sciences
Rutgers University
New Brunswick, NJ USA
tstolarz@marine.rutgers.edu

Michael Smith
Dept. of Marine and Coastal Sciences
Rutgers University
New Brunswick, NJ USA
michaesm@marine.rutgers.edu

Jacquelyn Veatch
Dept. of Marine and Coastal Sciences
Rutgers University
New Brunswick, NJ USA
jveatch@marine.rutgers.edu

Ethan Handel
Dept. of Marine and Coastal Sciences
Rutgers University
New Brunswick, NJ USA
handel@marine.rutgers.edu

Scott Glenn
Dept. of Marine and Coastal Sciences
Rutgers University
New Brunswick, NJ USA
glenn@marine.rutgers.edu

2024 IEEE Radar Conference (RadarConf24) | 979-8-3503-2920-9/24/$31.00 ©2024 IEEE | DOI: 10.1109/RADARCONF2458775.2024.10548298

***Abstract*—Oceanographic High Frequency radars (HFR) have been mapping currents in the U.S. Mid-Atlantic Bight since 1998 when two stations were installed in New Jersey at Brant Beach and Brigantine as part of the Rutgers University Long Term Ecosystem Observatory (LEO-15). Twenty-five years later, that seminal duo has grown into the 41-site Mid Atlantic HFR network providing continuous current maps along more than 1,000 km of coastline from Cape Cod to Cape Hatteras. The expansive gridded current velocities serve a variety of stakeholders including federal agencies like the U.S. Coast Guard for search and rescue, NOAA for oil spill response, Homeland Security for vessel detection and ocean scientists developing both short-term forecasting applications as well as longer term, multi-decadal changes in coastal circulation. Long-term archives are now available with calculated decadal mean, annual and seasonally averaged surface currents. This paper provides a history of the network to date and a glimpse towards the future.**

***Keywords*—oceanography, HF radar, remote sensing, direction finding, FMCW**

I. Introduction

The Rutgers High Frequency (HF) radar network was established in 1998 with the installation of 25 MHz CODAR SeaSondes at Brigantine and Brant Beach, NJ (Figure 1). They were installed to support studies focused on the topographic steering of coastal upwelling and its role in driving bottom water hypoxia/anoxia along the New Jersey coast [1].

The Rutgers CODAR HF radar network underwent reconfiguration for the Lagrangian Transport and Transformation Experiment (LaTTE) [2], transforming into a nested, multifrequency system for current mapping across the New Jersey continental shelf. The 25 MHz radars were relocated north to Sandy Hook, NJ and Breezy Point, NY to capture the Hudson River as it exited New York Harbor. The network added 5 MHz systems to cover the entire New Jersey shelf at a 6 km resolution and then added 13 MHz systems at 3 km resolution for the approaches to New York Harbor. The 25 MHz radars created an inner nest at 1.5 km resolution for the harbor entrance and interior. This nested approach increased both spatial and temporal resolution closer to the coast as the variability increases in this direction. Other universities also established HF radar networks to measure ocean surface conditions in their regions. Old Dominion University established a 25 MHz network to cover the entrance to Chesapeake Bay [3] and the University of Connecticut and University of Rhode Island collaborated to measure the currents surrounding Long Island Sound [4]. Rutgers also collaborated with the National Oceanic and Atmospheric Administration (NOAA) to deploy their transportable HF radars for enhanced coverage and rapid response tests in remote locations.

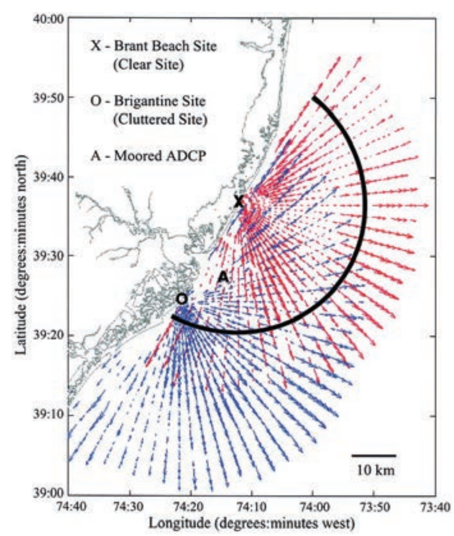

Figure 1: Map of the coastal waters off Atlantic City, NJ showing the location of the HF radar stations and associated radial maps at Brant Beach (X, red) and Brigantine (O, blue). Figure reprinted from [5]

The similar efforts of HF radar remote sensing at several universities led to the establishment of the Mid-Atlantic HF radar Consortium in 2007. Data from participating groups in the Consortium contributed to a regional array along approximately 1,000 km of coastline, from Cape Hatteras, NC to Cape Cod, MA [6]. However, coverage was contingent on the research grant support available to each radar's host institution. The Coast Guard employed surface drifters in field tests to assess improvements in search and rescue planning facilitated by real-time surface currents, while NOAA focused on validating CODAR HF radar parameters for nearshore waves and currents to aid in rip current forecasting. Results from these efforts formed the basis for a plan to transition the current mapping network to sustained operations.

Alongside the development of a regional current mapping capability, ongoing research explored new CODAR hardware, processing algorithms, and products. The use of Global Positioning System (GPS) timing on each radar emerged as a significant improvement allowing radars in close proximity to share frequencies without interference and enabling coordinated multistatic (a radar can process its own echo as well as nearby radars) operations. This improvement, funded by the Office of Naval Research (ONR), led to vessel-tracking experiments, demonstrating the HF radar network's ability to detect and track surface ships. Efforts to extend the range of over-the-horizon vessel detection without increasing radar broadcast power included the deployment of super-directive multistatic receiver antennas and placing bistatic HF radar transmitters on offshore buoys. Both concepts, tested in the Mid-Atlantic HF radar test bed, resulted in enhanced Coast Guard mapping capabilities.

II. Beginning

A coastal ocean observatory was established along the shoreline of New Jersey and continental shelf in 1998. One of the key technologies chosen for the observatory was a High Frequency (HF) radar network. This network comprised two transmit-receive stations in Brant Beach and Brigantine, New Jersey, and a central processing site in Tuckerton, New Jersey. The first experiments conducted with the network tested the bearing determination of HF radar systems and its relation to the receive antenna beam pattern [5]. Analysis of antenna beam pattern measurements conducted on the New Jersey system revealed that these patterns often deviate from the expected shape when antennas are deployed in the field. Test results indicated that environmental factors, rather than system hardware, contribute to distorting the pattern from its theoretical form.

Having ensured that the systems were calibrated and operating properly a year-long dataset was collected from the HF radar [7]. The radar surface current measurements were supplemented with in situ and meteorological observations, to investigate annual and seasonal variations of the coastal ocean. The impact of ocean stratification became apparent through a current response strongly correlated with the wind during the summer stratified season, contrasting with a more variable response less correlated with wind during the mixed season. In mixed water column conditions, the local topography's influence on surface current variability is contingent on the slope of the bathymetry, showing a tendency for variability to align more with steeper topography.

The sustained observatory off the southern coast of New Jersey provided the opportunity for examining both prolonged trends in surface currents as well as transient events like hurricanes. On the evening of September 16, 1999, Tropical Storm Floyd traversed the New Jersey coast directly over the observatory [8]. Despite a noticeable peak in the near-inertial band of the depth-averaged current, the reaction deviated from the usual clockwise ringing response observed in deepwater stratified regions. Instead, the shallow, well-mixed inner shelf exhibited an alongshore current oscillation, balanced by the alongshore pressure gradient and bottom stress. In contrast to a typical nor'easter, where the transport in this location moves alongshore toward the south and onshore, the currents during the hurricane follow an alongshore direction toward the south but with an offshore component.

As the applications for the measurements grew, there was a need for better definitions and assessment of the radar measurement uncertainty [9]. Comparison metrics were computed for various vertical bins of an in situ current profiler, across different current profilers, and between the current profilers and different HF radars. The discrepancies in velocity, both vertically and horizontally, were subsequently described by assessing the observed root-mean-square (rms) differences. Comparisons between HF radars and current profilers yielded differences comparable to the observed environmental disparities at corresponding scales. This suggests that the environment plays a significant role in influencing the observed distinctions between in situ measurements and the remotely sensed currents from the HF radars.

III. Vessel Detection Work

Having established the CODAR SeaSonde as a reliable tool for surface current measurements, the group sought to develop additional applications for the sensor which included a vessel detection capability. Rutgers aimed to develop the dual use capability where the ability to detect vessels within the radar's footprint would not compromise the surface current measurement.

This led to a series of experiments sponsored by the Office of Naval Research (ONR) and the newly created Department of Homeland Security (DHS). The ONR program sought to develop and demonstrate a ship detection capability of multiple radars operating in simpler geometry of monostatic operations where the transmitter and receiver are collocated. The program [10] also sought to develop and demonstrate a more complicated geometry where the radars would be operated bistatically meaning the transmitter and receiver were geographically separated (Figure 2). This was enabled by the patented technology from CODAR that allowed multiple stations to operate on the same frequency utilizing GPS synchronized timing where the time distributed via GPS is accurate to less than 30 nanoseconds

The vessel detection work sponsored by Homeland Security looked to further develop the vessel detection capability and optimize the system to transition from a successful technology demonstration into an operational product. The technology was operated in three test beds at various latitudes to test the system in different environmental and radio conditions. The first testbed was the Mid Atlantic at the entrance to NY Harbor [11], low latitudes off the west coast of Puerto Rico [12] and high latitudes of Alaska [13, 14].

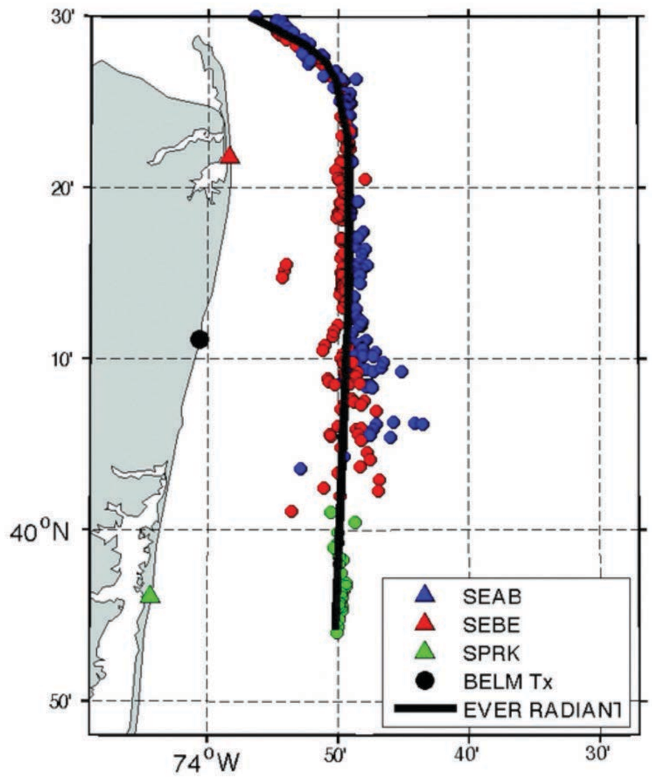

Figure 2: Vessel detections by 13 MHz HF radar stations (dots). Monostatic detections from the Sea Bright (blue) and Seaside Park (green) along with bistatic detections transmitted from Belmar (black circle) and received at Sea Bright (red). The path of the vessel Ever Radiant from AIS is shown as the black line.

IV. Expanding the Network

The network expanded in 2001 with five additional CODAR systems operating in the 5 MHz band. These were deployed along the coast of New Jersey and Nantucket, MA. The systems in New Jersey were operated for 6 years to capture the structure of the mean and seasonal surface circulation along the coast [15]. The mean flow was measured to be 2-12 cm/s towards the south and offshore. The variability of the current was shown to be several times that of the mean. The dominant direction of the wind in each of the seasons played a prominent role in moving the surface current.

The Mid Atlantic Ocean Observing System (MARACOOS) was founded in 2004 as a regional association of partners that collect unique ocean and coastal data that is transformed into information products that support jobs, the economy, safety and well-being for the more than 78 million people living in the Mid-Atlantic region. Again, HF radar was identified as a key sensor for the observing system. In order to cover the entire Mid Atlantic area Rutgers teamed with other HFR operators in the region. The radar network began in 2007 as 13 long-range sites, 2 medium-range sites, and 12 standard-range sites [6]. The group was able to collect surface currents for a decade to provide the most detailed to date picture of the surface current structure (Figure 3) [16]. As with the NJ shelf study, the mean and seasonal patterns of flow were examined. This improved understanding of the coastal circulation over the Mid Atlantic, and what drives its variability, has implications for pollutant transport, plankton transport at the base of the food chain, fish and shellfish reproduction, and multiple ocean based human activities including fishing, marine transportation, and offshore wind energy development.

The state of New Jersey has a goal of 100% clean energy use by 2035 and offshore wind is envisioned as being part of the renewable portfolio. In order to reduce the risk associated with installing these offshore wind turbines, Rutgers undertook a two-year study, sponsored by the NJ Board of Public Utilities, of the ocean winds and currents to provide insight on the best locations for siting the wind turbines. A 13 MHz 4 station HF radar network was installed to measure the surface currents every 2 km out to a range of 60 km from the coast [17]. This grew the 13 MHz network to a total of 7 stations. The study also utilized the Weather Research and Forecast (WRF) model to estimate the variability of the offshore wind resource. The HF radar surface currents showed strong correlation with each of the wind measurements throughout the study period and was a valid source to evaluate the spatial variability of the surface winds in the weather model.

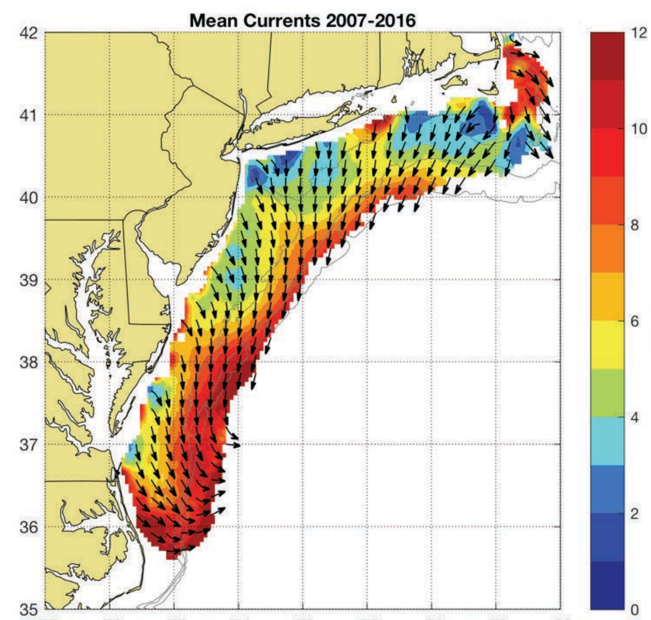

Figure 3: Map of the mean surface currents for the Mid Atlantic United States from 2007-2016.

V. Additional Applications

Surface current maps and vessel detection were the established products from the HF radar network. The group then began to develop additional products to expand the utility of the network. Ocean wave conditions impact navigation, offshore operations, recreation, fisheries, safety of life at sea and hence the economic stability of any country's maritime sector. Making accurate measurements of wave conditions will help validate wave models and will help with forecasts of the wave conditions over the next few days. Several studies by the Rutgers team were conducted comparing HF radar wave measurements with nearby buoys. One of the first studies sought to quantify the spatial variability of wave measurements within the Mid Atlantic Bight to provide context for the radar to buoy comparisons because the evaluations are never collocated [18]. Recent work has focused on the usefulness of the radar wave measurement with the National Weather Service [19].

Coastal hazards like tsunamis and storm surges threaten both lives and property globally. High Frequency radars have emerged as a potential technology to minimize the impact of these hazards by detecting disturbances before they make landfall. On June 13, 2013 a meteotsunami impacted the coast of New Jersey that was detected in post processing utilizing data from the 13 MHz network. The disturbance was measured 23 km offshore or 47 minutes before arrival at the coast [20]. Building upon this successful demonstration Rutgers collaborated with CODAR Ocean Sensors by analyzing data from four HF radar stations between October 2016 and June 2019 to identify potential tsunami signals. CODAR Ocean Sensors devised a pattern recognition algorithm to detect the presence of tsunami waves. Rutgers evaluated the performance of the algorithm throughout a multi-year effort to gauge the impact of radio interference on the detection algorithm. An again on May 30, 2019 a weather system moved through the region that generated a small meteotsunami (amplitude 15-30 cm) that was detected by a DART buoy, water level sensors and one of the HF radar stations [21].

Novel applications of HFR data have used these arrays as ecological sensors, linking dynamic surface currents to spatial ecology in Antarctic ecosystem. In 2015, the first Antarctic HFR array was deployed around Palmer Deep Canyon. The use of remote power modules allowed for the installation outside the range of a power grid [22]. Data collected by this array changed the community's understanding of how the biological hotspot in Palmer Deep Canyon is maintained [23] and linked penguin foraging behavior to ocean currents [24]. Following the success of the first season, the Palmer array was re-deployed in 2020 to map each level of the food web, phytoplankton, Antarctic Krill, and penguin foraging behavior, onto ocean currents. It was hypothesized that currents in Palmer Deep Canyon are transporting and locally concentrating phytoplankton into large patches that are then targeted by mobile grazers and foragers, as if they were visiting a marine "grocery store" where foragers and grazers know they will find a reliable food source. The HFR array around Palmer Deep Canyon allowed this hypothesis to be tested. To quantify advective transport in the HFR observed surface currents, a Lagrangian Coherent Structure (LCS) tool was employed known as a Finite Time Lyapunov Exponent (FTLE) [25]. When applied to a velocity field, attracting LCS will assign a scalar quantity to the strength of attraction that changes in space and time with the inputted velocity field. FTLE calculations begin with virtual particles advected by the HFR observed surface currents. Particle trajectories are then integrated over, and compared to neighboring particle trajectories to look for a ridge where particles are converged to and then diverged along. These ridges have a strong attracting effect on nearby drifting particles. FTLE were computed with the HFR data around Palmer Deep Canyon [26] and compared to phytoplankton and krill abundances measured by small boat surveys conducted in the footprint of the HFR data (Figure 4). It was found that strong FTLEs often collocate with phytoplankton patches and krill swarms, suggesting that krill are using the FTLE-identified attracting ocean features to find reliable sources of phytoplankton. Future work will apply similar techniques to the MARACOOS HFR array on large spatial and temporal scales, investigating ways that local phenology is tied to attracting ocean features. Such a relationship between HFR observed surface currents and spatial ecology will be incorporated into ecosystem models, using HFRs as ecological sensors to predict marine animal distributions.

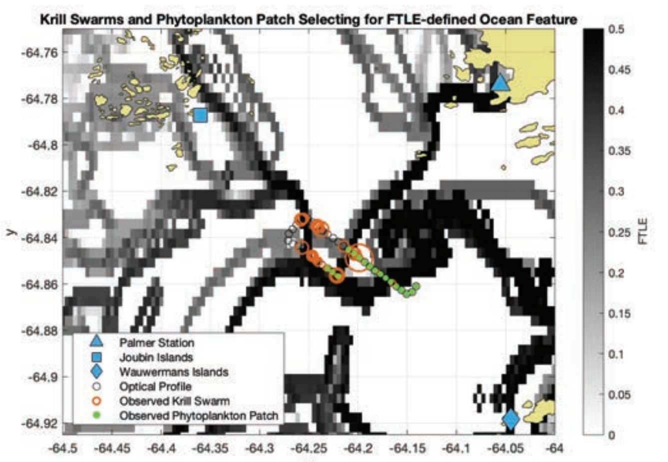

Figure 4: Map of Finite Time Lyapunov Exponent results (black colorbar, hour^{-1}) computed from three HFR stations (blue polygons) at 1km spatial resolution and 1 hour temporal resolution. Phytoplankton abundance was observed with optical instruments aboard a towed ACROBAT survey. Observations of high abundances of phytoplankton are shown in green. Krill swarms observed with active acoustics (EK80) aboard the same towed survey and indicated by orange circles with the diameter scaled to the horizontal length of the krill swarm.

VI. Conclusions

A High Frequency radar network has been operated within the Mid Atlantic Bight of the United States for the past 25 years. This system has captured a detailed picture of the surface flows. Additional applications of the measurements have included vessel detections, wave measurements, wind estimates and meteotsunami detections. The technology was also successfully deployed and operated in the harsh environment of the Antarctic to help explain the food web in the region. We have provided an overview of the development of the network and its many applications. We look forward to the next 25 years of measurements by the network and the insights it will deliver.

ACKNOWLEDGMENTS

We would like to acknowledge the support and collaboration of long-term industry partner CODAR Ocean Sensors who manufactures and maintains the SeaSonde HF radar.

This work was funded by NOAA Award Number NA16NOS0120020 “Mid-Atlantic Regional Association Coastal Ocean Observing System (MARACOOS): Powering Understanding and Prediction of the Mid-Atlantic Ocean, Coast, and Estuaries”. Sponsor: National Ocean Service (NOS), National Oceanic and Atmospheric Administration (NOAA) NOAA-NOS-IOOS-2021-2006475, Integrated Ocean Observing System Topic Area 1: Implementation and Development of Regional Coastal Ocean Observing Systems.

The HF radar deployment in Antarctica was supported by the CONVERGE project (2015) and funded by the National Science Foundation award numbers: ANT-1327248 and DPP-1440435 and the SWARM project (2020) funded by National Science Foundation, award number: 1745009

REFERENCES

[1] S. Glenn and O. Schofield, "Observing the oceans from the COOLroom: Our history, experience, and opinions," *Oceanography,* vol. 16, no. 4, pp. 37-52, 2003.

[2] R. J. Chant *et al.*, "Bulge Formation of a Buoyant River Outflow," *J. Geophys. Res.,* vol. 113, no. C1, p. C01017, 2008. [Online]. Available: http://dx.doi.org/10.1029/2007JC004100

[3] T. G. Updyke and L. P. Atkinson, "A study of surface currents in the coastal ocean outside Chesapeake Bay using HF radar," in *2012 Oceans*, 2012: IEEE, pp. 1-4.

[4] D. S. Ullman, J. O'Donnell, J. Kohut, T. Fake, and A. Allen, "Trajectory prediction using HF radar surface currents: Monte Carlo simulations of prediction uncertainties," *J. Geophys. Res.,* vol. 111, no. C12, p. C12005, 2006. [Online]. Available: http://dx.doi.org/10.1029/2006JC003715

[5] J. T. Kohut and S. M. Glenn, "Improving HF Radar Surface Current Measurements with Measured Antenna Beam Patterns," *Journal of Atmospheric and Oceanic Technology,* vol. 20, no. 9, pp. 1303-1316, September 01, 2003 2003. [Online]. Available: http://dx.doi.org/10.1175%2F1520-0426%282003%29020%3C1303%3AIHRSCM%3E2.0.CO%3B2

[6] H. J. Roarty *et al.*, "Operation and Application of a Regional High Frequency Radar Network in the Mid Atlantic Bight," *Marine Technology Society Journal,* vol. 44, no. 6, pp. 133-145, 2010.

[7] J. T. Kohut, S. M. Glenn, and R. J. Chant, "Seasonal current variability on the New Jersey inner shelf," *J. Geophys. Res.,* vol. 109, no. C7, p. C07S07, 2004. [Online]. Available: http://dx.doi.org/10.1029/2003JC001963

[8] J. T. Kohut, S. M. Glenn, and J. D. Paduan, "Inner shelf response to Tropical Storm Floyd," *J. Geophys. Res.,* vol. 111, no. C9, p. C09S91, 2006, doi: 10.1029/2003jc002173.

[9] J. T. Kohut, H. J. Roarty, and S. M. Glenn, "Characterizing Observed Environmental Variability With HF Doppler Radar Surface Current Mappers and Acoustic Doppler Current Profilers: Environmental Variability in the Coastal Ocean," *Oceanic Engineering, IEEE Journal of,* vol. 31, no. 4, pp. 876-884, 2006. [Online]. Available: 10.1109/JOE.2006.886095

[10] H. J. Roarty, D. E. Barrick, J. T. Kohut, and S. M. Glenn, "Dual-Use Compact HF Radars for the Detection of Mid- and Large-Size Vessels," *Elektrik, Turkish Journal of Electrical Engineering and Computer Sciences,* vol. 18, no. 3, pp. 373-388, 2010.

[11] H. J. Roarty, M. Smith, S. M. Glenn, and D. E. Barrick, "Real-time beyond the horizon vessel detection," *Proc. SPIE 8714, Radar Sensor Technology XVII,* pp. 87140Z-87140Z, 2013, doi: 10.1117/12.2015871.

[12] E. Handel *et al.*, "Increasing the coverage of an island-based HF radar network," in *OCEANS 2015-MTS/IEEE Washington*, 2015: IEEE, pp. 1-5.

[13] H. J. Roarty *et al.*, "Expanding maritime domain awareness capabilities in the arctic: High Frequency radar vessel-tracking," in *Radar Conference (RADAR), 2013 IEEE*, April 29 2013-May 3 2013 2013, pp. 1-5, doi: 10.1109/radar.2013.6586136.

[14] H. Roarty *et al.*, "Multi-use HF radar for arctic maritime domain awareness," in *OCEANS - Bergen, 2013 MTS/IEEE*, 10-14 June 2013 2013, pp. 1-6, doi: 10.1109/OCEANS-Bergen.2013.6608132.

[15] D. Gong, J. T. Kohut, and S. M. Glenn, "Seasonal climatology of wind-driven circulation on the New Jersey Shelf," *J. Geophys. Res.,* vol. 115, no. C4, p. 25, 2010. [Online]. Available: http://dx.doi.org/10.1029/2009JC005520

[16] H. Roarty *et al.*, "Annual and seasonal surface circulation over the Mid‐Atlantic Bight Continental Shelf derived from a decade of High Frequency Radar observations," *Journal of Geophysical Research: Oceans,* vol. 125, no. 11, p. e2020JC016368, 2020.

[17] H. Roarty *et al.*, "Analysis of the wind resource off New Jersey for offshore wind energy development," in *Oceans, 2012*, 14-19 Oct. 2012 2012, pp. 1-4, doi: 10.1109/oceans.2012.6404815.

[18] H. Roarty, C. Evans, S. Glenn, and H. Zhou, "Evaluation of algorithms for wave height measurements with high frequency radar," in *2015 IEEE/OES Eleveth Current, Waves and Turbulence Measurement (CWTM)*, 2015: IEEE, pp. 1-4.
[19] H. Roarty, J. Klein, S. Dante, A. Cope, S. Johnson, and M. Daugharty, "Evaluation of Wave Data from HF Radar by the National Weather Service," in *2019 IEEE/OES Twelfth Current, Waves and Turbulence Measurement (CWTM)*, 10-13 March 2019 2019, pp. 1-4.
[20] B. Lipa, H. Parikh, D. Barrick, H. Roarty, and S. Glenn, "High-frequency radar observations of the June 2013 US East Coast meteotsunami," (in English), *Nat Hazards,* pp. 1-14, 2013/12/17 2013, doi: 10.1007/s11069-013-0992-4.
[21] H. Roarty, G. Garcia, and T. Nichols, "Evaluation of the CODAR Tsunami Detection Algorithm and Software," in *OCEANS 2019 MTS/IEEE SEATTLE*, 27-31 Oct. 2019 2019, pp. 1-6.
[22] H. Statscewich, T. Weingartner, S. Danielsen, B. Grunau, G. Egan, and J. Timm, "A high-latitude modular autonomous power, control, and communication system for application to high-frequency surface current mapping radars," *Marine Technology Society Journal,* vol. 45, no. 3, pp. 59-68, 2011.
[23] J. T. Kohut *et al.*, "Variability in summer surface residence time within a West Antarctic Peninsula biological hotspot," *Philosophical Transactions of the Royal Society A: Mathematical, Physical and Engineering Sciences,* vol. 376, no. 2122, p. 20170165, 2018.
[24] M. J. Oliver *et al.*, "Central place foragers select ocean surface convergent features despite differing foraging strategies," *Scientific reports,* vol. 9, no. 1, p. 157, 2019.
[25] G. Haller, "Lagrangian coherent structures," *Annual review of fluid mechanics,* vol. 47, pp. 137-162, 2015.
[26] J. Veatch, E. Fredj, and J. Kohut, "High Frequency Radars as Ecological Sensors: Using Lagrangian Coherent Structures to Quantify Prey Concentrating Features," in *OCEANS 2022, Hampton Roads*, 2022: IEEE, pp. 1-7.

Determining the Origin and Fate of Marine eDNA

Timothy Stolarz
Center for Ocean Observing Leadership
Rutgers University
New Brunswick, NJ USA
tstolarz@marine.rutgers.edu

Brendan Henley
Center for Ocean Observing Leadership
Rutgers University
New Brunswick, NJ USA
bvh16@scarletmail.rutgers.edu

Hugh Roarty
Center for Ocean Observing Leadership
Rutgers University
New Brunswick, NJ USA
hroarty@marine.rutgers.edu

Josh Kohut
Center for Ocean Observing Leadership
Rutgers University
New Brunswick, NJ USA
kohut@marine.rutgers.edu

Jason Adolf
Urban Coast Institute
Monmouth University
West Long Branch, NJ USA
jadolf@monmouth.edu

***Abstract*— Trawling has been the traditional method for monitoring diversity of benthic communities. Offshore wind is rapidly developing within the Mid Atlantic waters of the United States. Construction of wind turbines will pose challenges to traditional sampling methods because trawling gear in the vicinity of turbine foundations will be limited. Environmental DNA (eDNA) has emerged as a new tool for monitoring marine ecosystems and biodiversity. The use of eDNA is a cost-effective approach to replace traditional sampling. However, there is limited information on the origin, fate and transport of eDNA in the ocean. Therefore, we utilized surface current data from a High Frequency radar network to advect particles backward in time to assess the origin of water that was collected as part of an eDNA sampling campaign. eDNA was sampled west of Cape May, NJ on December 8, 2021. Twenty surface particles were released in the HFR surface current field and allowed to drift backwards in time for five days. Surface and bottom currents from the DOPPIO regional ocean model were also used to transport the passive tracers backwards in time. In this one instance using the HFR surface currents the particles advected to the northwest over the five days originating in the back bays of Cape May NJ. The particles traveled approximately 35 km over the five days. Similarly, the DOPPIO surface currents also indicated a reverse drift to the northwest but after 2 days the currents weakened and particles remained near the sampling location. In contrast the DOPPIO bottom currents displayed a different trajectory indicating source waters originated from the south. These findings underscore the significance of considering various data sources and models when analyzing eDNA transport, as well as the potential for HF radar surface current data to provide valuable insights into the origin and transport of marine genetic material. Such research is crucial as the offshore wind energy industry continues to expand, emphasizing the need for innovative monitoring methods to ensure effective environmental stewardship in the changing coastal landscape.**

Keywords—High Frequency Radar, ROMS, eDNA, models, OpenDrift, transport, currents

I. INTRODUCTION

In the United States, fisheries are a massive contributor to the country's economy and food resources [1]. Fisheries provide a source of protein comparable to sources like beef, poultry and pork [2]. Fisheries also provide job opportunities through the act of fishing itself, and through the countless other employment opportunities to sustain the industry and distribute the products [3]. To help keep the fisheries sustainable, research efforts are pursued either through the fishery industries or through government sponsored research programs to monitor the health of benthic and nektonic communities. Traditionally, methods to measure the health of fishery species was accomplished through trawling surveys and catch reports [4]. Trawling as a metric can be helpful to quantify target species at the cost of also collecting non-target species. However, non-target species experience greater mortality rates dependent on a variety of factors from size, life ecology, closeness to fishing grounds and fishing gear [5] [6].

A novel method for monitoring conservation efforts and fishery biodiversity is by sampling for environmental DNA (eDNA). eDNA is collection of DNA samples ranging from unicellular organisms to larger samples shed off organisms dissolved in the seawater. The spatial and temporal resolution offered by eDNA is greater than traditional physical sampling methods at a fraction of the cost [7]. eDNA collection allows for higher quality biomonitoring analyses to take place which can increase conservation efforts in highly fished ecosystems while also correlating very well to trawl survey catches [6].

Due to eDNA's planktonic nature, transport of eDNA in the ocean is driven primarily by ocean physics and decay of the eDNA samples [7]. When trying to understand the fate and transport of eDNA collected in samples, researchers must not only consider where the samples were found, but where the samples could have originated. Current research indicates that results of eDNA sequencing strongly correlates to vertebrates expected to be found near the sampling site [8-10]. The sequenced data that does not correlate closely with the species near the sampling site can be explained by understanding the potential spatial origins of the samples. This research attempts to understand the transport and fate of eDNA samples when advecting them using near-realtime High Frequency Radar (HFR) and model data from the Regional Ocean Modeling System Doppio.

II. Methods

Two datasets were compared when trying to understand the transport of eDNA in the Atlantic. The first dataset was surface current data produced by the Rutgers High Frequency Radar Network [11, 12]. The HFR Network utilizes the CODAR SeaSonde, which is a stationary, low impact near-realtime surface current measurement instrument. The instrument emits radio waves which reflect off surface gravity waves in the coastal ocean. The backscattered signal is amplified due to Bragg scattering interactions allowing for long range radial velocity measurements of surface currents. More than one SeaSonde is required to create total vector fields for common surface current velocity analysis (Figure 1). Each hourly radial file created by the long range 5 MHz system is a three-hour rolling average of +/- 1.5 hours of the timestamp (i.e. a 12:00 UTC timestamp has data averaged from 10:30 UTC to 13:30 UTC) [13]. The HF radar surface currents data utilized was the 6 km product available on the Rutgers ERDDAP server.

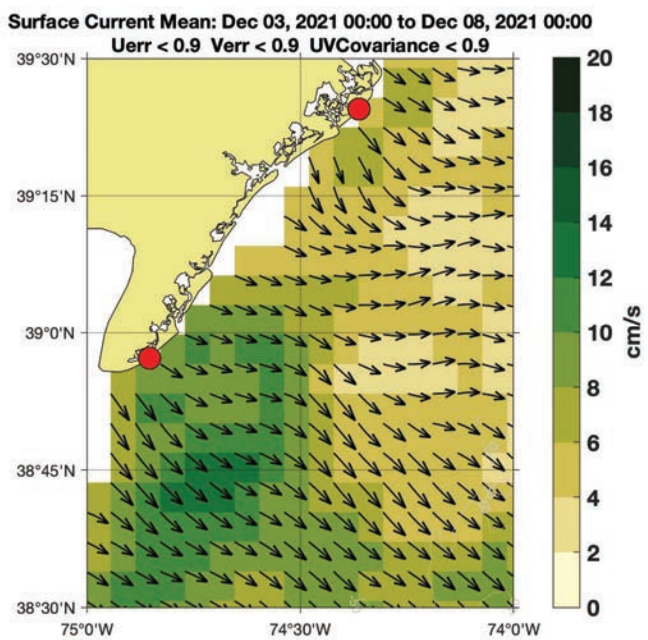

Figure 1: Study area showing the mean surface currents from the HF radar network and location of two of the radar stations (red circles) that contributed to the current maps.

The other dataset used in the analysis were surface and bottom current velocity measurements from Doppio, a Regional Ocean Modeling System (ROMS) for the Mid Atlantic Bight and Gulf of Maine regions [14]. Doppio is specifically focused on generating understanding for biogeochemical interactions, ecosystems analysis, estuarine downscaling and forecasting in the northwestern North Atlantic region. Doppio assimilates measurement data from Slocum gliders, moorings, floats, fishing vessel sensors as well as the HFR surface currents. The integration of HFR surface current data into Doppio's model output creates an interesting space for comparison when trying to utilize both datasets for particle tracking off the coast of New Jersey. The Doppio data was accessed from the Rutgers Ocean Modelling THREDDS server.

In order to validate OpenDrift as an effective tool for tracking drifting marine items, we ran an experiment of opportunity. National Data Buoy Center (NDBC) buoy 44025 located just outside New York Harbor broke free from its mooring during a nor'easter on December 18, 2023. The buoy then proceeded to drift through the study area. A single virtual drifter was released at the time and location where 44025 broke free from its mooring (73°10' W 40°15'N at December 18, 2023 13:00 GMT). The virtual particle was advected forward in time till January 5, 2024, a total of 18 days. The path of the buoy and virtual drifter are given in Figure 2. Buoy 44025 drifted 105 km while the virtual drifter traveled 82 km and they were separated by 22 km after 18 days. This equates to a skill score of 0.8 [15], which is quite good for a drifter validation. Based on this result we were confident that the OpenDrift software and HFR surface currents would be good at describing the flows off the coast of New Jersey.

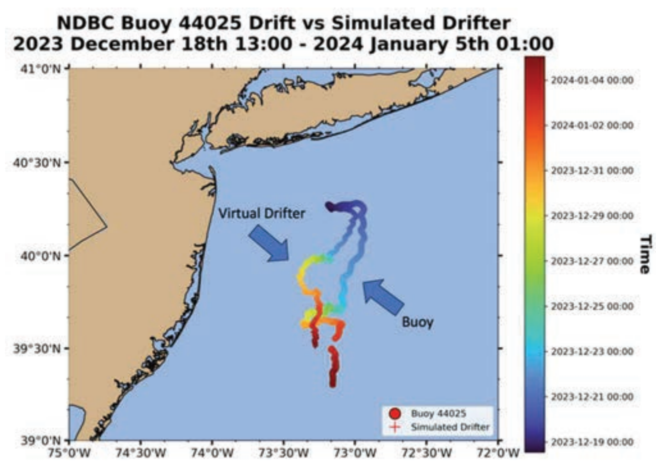

Figure 2: Path of NDBC buoy 44025 (circle) after it broke free from its mooring on December 18, 2023 along with the forward trajectory estimate of the buoy using OpenDrift and HF radar surface currents (plus sign). The identity of the particular drifter on the map is indicated by the label. The time of the drifter position is shown as the colormap.

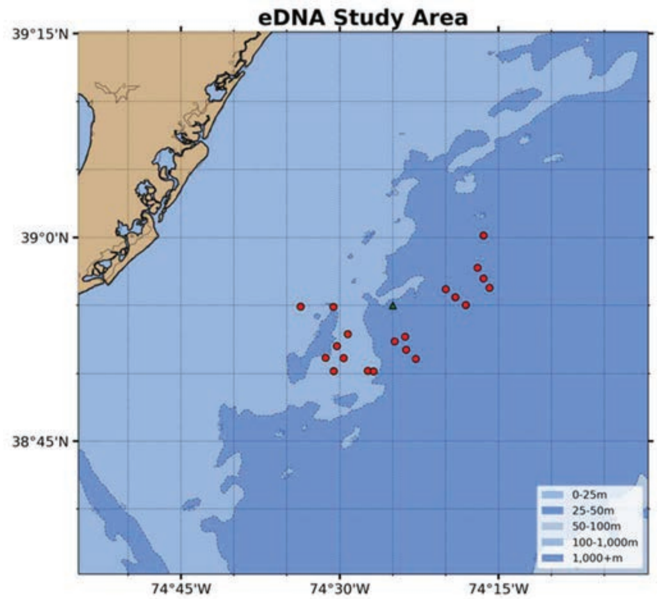

Figure 3: Map of the study areas showing the eDNA sampling locations (red dots) and the release point for the reverse trajectory modelling (green triangle).

For the eDNA drifter experiment, the release point for the particles was chosen to be 74°25’ W and 38°55’ N. This location was representative of the eDNA sampling locations that Monmouth University conducted in December 2018 (Figure 3). To perform the analysis, the software package OpenDrift from the Norwegian Meteorological Office was used to track the eDNA off the coast of New Jersey. The transport of the eDNA was simulated using the OceanDrift model within OpenDrift [16] utilizing the HFR and Doppio datasets to advect the Lagrangian particles.

To ensure the Doppio model run initialized, the location of the release point was modified to be in the center of the nearest grid cell of the model. This adjusted starting position was 1.5 km from the starting position used for the HF radar model run. For each run of OpenDrift’s model OceanDrift, the datasets were placed into readers for the model. The HF radar data fulfilled two climate and forecast (CF) compliant variables within the model (x_sea_water_velocity and y_sea_water_velocity) while the Doppio data fulfilled 11 direct data related variables. These variables include horizontal and vertical velocities, vertical diffusivities, barotropic sea water velocities, surface downward stress, temperature and salinity among others. The Lagrangian particles were advected backwards in time so they describe where the water sampled on December 8, 2021 could have originated. The model was run for 5 days (120 hours) as this represents the amount of time we could realistically expect to detect eDNA at the sampling location. The half-life of eDNA in marine environments has been estimated at approximately one day, allowing travel times determined here to be used to approximate the relative abundance of ‘local’ vs ‘transported’ eDNA at a given sampling location.

Once the model runs were complete, the position data for each drifter at each timestamp were saved and images were produced which shows the track the drifters took colored by time. The saved position data were then used to compare the distance the drifters traveled away from the starting position.

III. Results

The results of the reverse OpenDrift simulation using the HFR currents are shown in Figure 4. The particles advected in reverse towards the west, indicating that the source waters likely originated near the coast. The results of the reverse OpenDrift simulation using the Doppio surface currents are shown in Figure 5a. The particles were moving towards the west similar to the HFR surface currents but then reversed course and headed back east to originate only slightly west of the sampling location. Since the eDNA water samples were taken close to the bottom of the water column, a reverse Doppio run using currents from the bottom most depth layer were utilized in an OpenDrift model run. The path of this simulation is shown in Figure 5b. The particles initially traveled south west then took a sharp turn east and then back west in the last two days of the simulation. The final locations of the drifters in the Doppio trials ended at near the same longitude, just about at 74.5° W, but the bottom water trial ended about 0.1° south of the starting point while the surface water trial ended 0.05° north of the starting position.

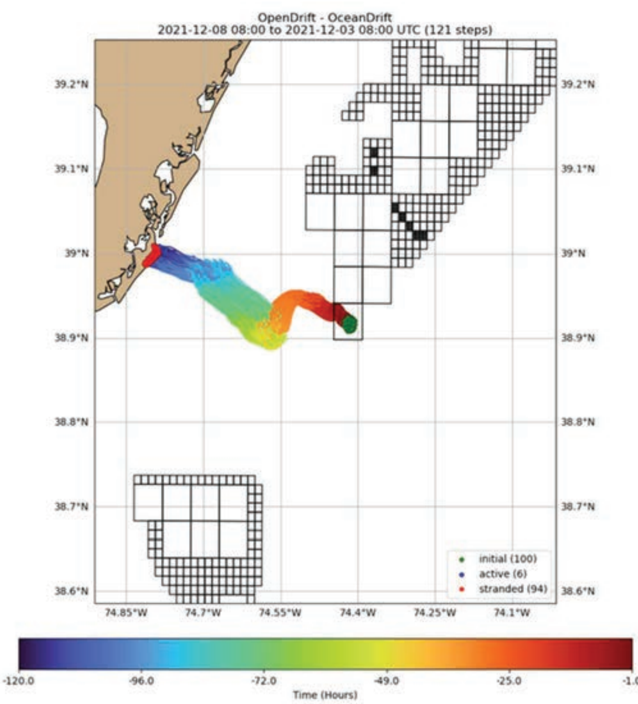

Figure 4: Map showing the reverse trajectory of 20 virtual particles advected by the HFR surface currents. The age of the drifter (hours) is shown as the colormap. The offshore wind lease areas are shown as the black rectangles.

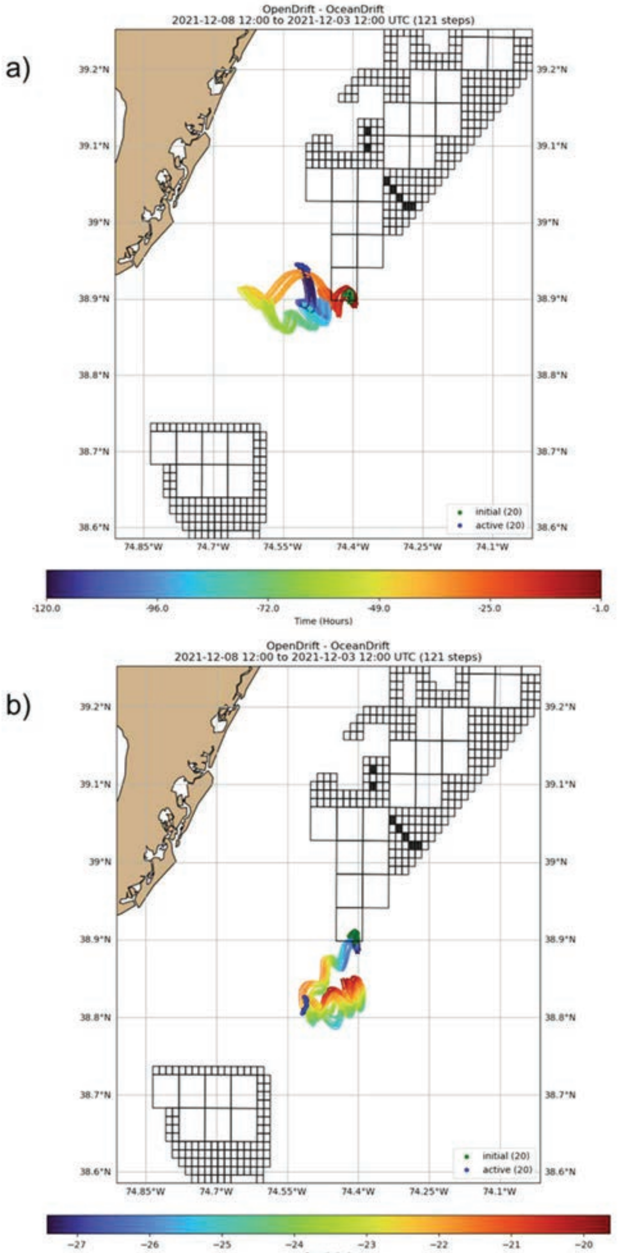

Figure 5: Map showing the reverse trajectory of 20 virtual particles advected by the DOPPIO model a) surface currents and b) bottom currents. The age of the drifter is shown as the colormap. The offshore wind lease areas are shown as the black rectangles.

When examining the distances the drifters travelled relative to the starting position, we can see that the HFR drifters traveled the furthest with a distance of about 35 km (Figure 6). The HFR drifters also have the greatest spread, leading to some drifters hitting land before others both due to distance from one another and the irregular shape of the New Jersey coastline. The next highest distance traveled was the bottom water Doppio drifters which ended at an average of 13 km away from the origin. The surface water Doppio drifters ended at the shortest distance away, 10 km, but had the tightest spread of drifters of all three trials. At 40 hours into the simulation all three data sets converge at 14 km from the origin and then the HFR data drifters make a strong departure from both Doppio runs at about 60 hours into the simulation. Both the Doppio drifter runs tend to be similar in distance traveled from the origin through the entirety of the model runs.

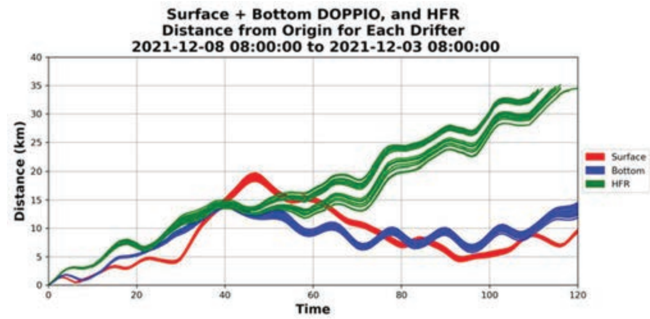

Figure 6: The distance traveled by the virtual particles advected by the HFR surface currents (green), DOPPIO surface currents (red) and DOPPIO 3D currents (blue) relative to the starting location.

IV. Discussion

The Doppio surface drifter simulation agreed well with the HFR surface simulation up to 24 hours from initiation. After that the ocean model diverged from the measurements. The HF radar drifters show the eDNA sampled water originating from the west near the coastline and traveled 30+ km to reach that point. The Doppio surface trajectories initially showed an origin towards the west but then reversed course and ended near the initiation point. Expectedly, the Doppio surface and bottom trajectories correlated well with each other.

The indication that the eDNA samples originated from the west close to the coast was interesting to the team. One species that was detected in the sample from December 8, 2021 was the mummichog. This is a small killifish located along the coast of the United States and Canada. The fish was likely not offshore near the sampling location, but the DNA likely was transported by the currents offshore.

V. Conclusions

The use of environmental DNA (eDNA) coupled with drift modeling offers a promising approach to understanding the transport and fate of genetic material in marine environments. The study compared two datasets, one from the Rutgers High Frequency Radar Network and another from the Doppio model, to simulate the movement of eDNA particles off the coast of New Jersey.

The reverse drift results highlighted differences between the HFR and Doppio datasets, with the HF radar data showing a westward movement while the Doppio data displayed an initial westward movement followed by a reversal towards the east. The Doppio model's surface and bottom current velocity measurements showed a strong correlation, indicating the reliability of the model in tracking water movements.

The study highlighted the importance of the 24-hour half-life mark in understanding the decay of eDNA samples, with the models showing that most of the sample would have decayed by the 4th day. Overall, the findings suggest that eDNA coupled with drift modeling can provide valuable insights into the movement of genetic material in marine environments, aiding in the conservation and management of marine ecosystems.

ACKNOWLEDGMENTS

This work was funded by NOAA Award Number NA16NOS0120020 "Mid-Atlantic Regional Association Coastal Ocean Observing System (MARACOOS): Powering Understanding and Prediction of the Mid-Atlantic Ocean, Coast, and Estuaries". Sponsor: National Ocean Service (NOS), National Oceanic and Atmospheric Administration (NOAA) NOAA-NOS-IOOS-2021-2006475, Integrated Ocean Observing System Topic Area 1: Implementation and Development of Regional Coastal Ocean Observing Systems.

The eDNA sampling was supported by a grant from the New Jersey Department of Environmental Protection (NJDEP) Research and Monitoring Initiative (RMI).

REFERENCES

[1] R. S. de Groot, R. Alkemade, L. Braat, L. Hein, and L. Willemen, "Challenges in integrating the concept of ecosystem services and values in landscape planning, management and decision making," *Ecological Complexity,* vol. 7, no. 3, pp. 260-272, 2010/09/01/ 2010, doi: https://doi.org/10.1016/j.ecocom.2009.10.006.

[2] C. Costello and D. Ovando, "Status, Institutions, and Prospects for Global Capture Fisheries," *Annual Review of Environment and Resources,* vol. 44, no. Volume 44, 2019, pp. 177-200, 2019, doi: https://doi.org/10.1146/annurev-environ-101718-033310.

[3] A. Tursi, P. Maiorano, L. Sion, and G. D'Onghia, "Fishery resources: between ecology and economy," *Rendiconti Lincei,* vol. 26, no. 1, pp. 73-79, 2015/03/01 2015, doi: 10.1007/s12210-014-0372-3.

[4] N. D. Walker, B. García-Carreras, W. J. F. Le Quesne, D. L. Maxwell, and S. Jennings, "A data-limited approach for estimating fishing mortality rates and exploitation status of diverse target and non-target fish species impacted by mixed multispecies fisheries," *ICES Journal of Marine Science,* vol. 76, no. 4, pp. 824-836, 2019, doi: 10.1093/icesjms/fsy205.

[5] M. Pauly D, G.I. , "Theory and Management of Tropical Fisheries," in *ICLARM Conference Proceedings 9*, International Centre for Living Aquatic Resources Management, Manila, Philippines and Division of Fisheries Research, Commonwealth Scientific and Industrial Research Organisation, Cronulla, Australia, 1982, p. 360.

[6] M. Y. Stoeckle, J. Adolf, Z. Charlop-Powers, K. J. Dunton, G. Hinks, and S. M. VanMorter, "Trawl and eDNA assessment of marine fish diversity, seasonality, and relative abundance in coastal New Jersey, USA " *ICES Journal of Marine Science,* vol. 78, no. 1, pp. 293-304, 2020, doi: 10.1093/icesjms/fsaa225.

[7] E. A. Andruszkiewicz *et al.*, "Modeling Environmental DNA Transport in the Coastal Ocean Using Lagrangian Particle Tracking," (in English), *Frontiers in Marine Science,* Original Research vol. 6, 2019-August-07 2019, doi: 10.3389/fmars.2019.00477.

[8] E. A. Andruszkiewicz, H. A. Starks, F. P. Chavez, L. M. Sassoubre, B. A. Block, and A. B. Boehm, "Biomonitoring of marine vertebrates in Monterey Bay using eDNA metabarcoding," *PLoS One,* vol. 12, no. 4, p. e0176343, 2017.

[9] R. P. Kelly, J. A. Port, K. M. Yamahara, and L. B. Crowder, "Using environmental DNA to census marine fishes in a large mesocosm," *PloS one,* vol. 9, no. 1, p. e86175, 2014.

[10] P. F. Thomsen, P. R. Møller, E. E. Sigsgaard, S. W. Knudsen, O. A. Jørgensen, and E. Willerslev, "Environmental DNA from seawater samples correlate with trawl catches of subarctic, deepwater fishes," *PloS one,* vol. 11, no. 11, p. e0165252, 2016.

[11] H. J. Roarty *et al.*, "Operation and Application of a Regional High Frequency Radar Network in the Mid Atlantic Bight," *Marine Technology Society Journal,* vol. 44, no. 6, pp. 133-145, 2010.

[12] H. Roarty *et al.*, "Annual and seasonal surface circulation over the Mid - Atlantic Bight Continental Shelf derived from a decade of High Frequency Radar observations," *Journal of Geophysical Research: Oceans,* vol. 125, no. 11, p. e2020JC016368, 2020.

[13] L. R. Wyatt, J. B. D. Jaffrés, and M. L. Heron, "Spatial Averaging of HF Radar Data for Wave Measurement Applications," (in English), *Journal of Atmospheric and Oceanic Technology,* vol. 30, no. 9, pp. 2216-2224, 01 Sep. 2013 2013, doi: https://doi.org/10.1175/JTECH-D-12-00206.1.

[14] A. G. López, J. L. Wilkin, and J. C. Levin, "Doppio – a ROMS (v3.6)-based circulation model for the Mid-Atlantic Bight and Gulf of Maine: configuration and comparison to integrated coastal observing network observations," *Geosci. Model Dev.,* vol. 13, no. 8, pp. 3709-3729, 2020, doi: 10.5194/gmd-13-3709-2020.

[15] Y. Liu and R. H. Weisberg, "Evaluation of trajectory modeling in different dynamic regions using normalized cumulative Lagrangian separation," *Journal of Geophysical Research: Oceans,* vol. 116, no. C9, pp. n/a-n/a, 2011, doi: 10.1029/2010JC006837.

[16] OpenDrift. "OceanDrift documentation." https://opendrift.github.io/autoapi/opendrift/models/oceandrift/index.html (accessed Apr. 15, 2024, 2023).